LSTM Erlangen

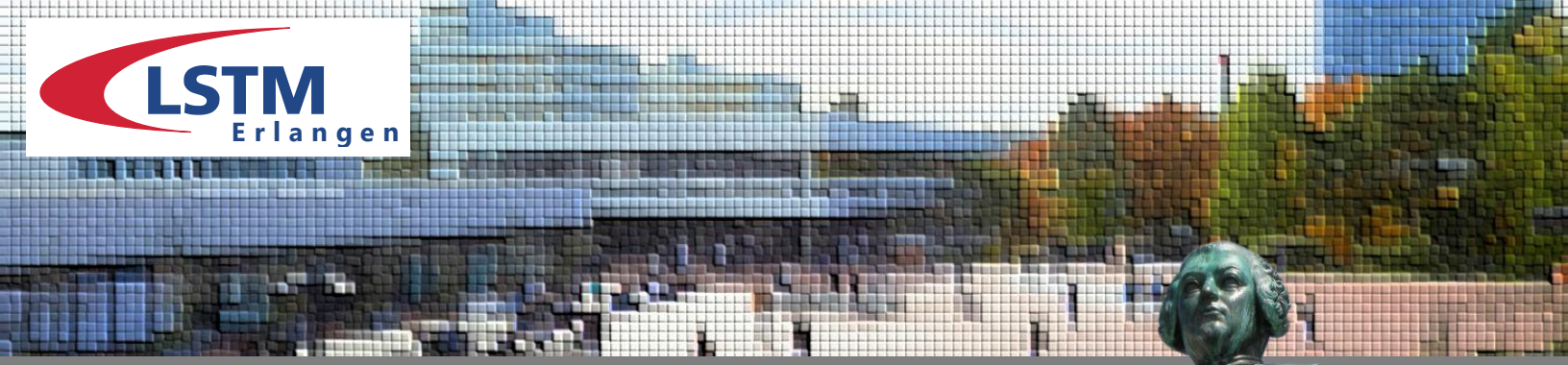

DLES14

Book of Abstracts

Friedrich-Alexander-Universität
Erlangen-Nürnberg

FAU

14th Workshop on Direct and Large-Eddy Simulation

April 10-12, 2024
Erlangen, Germany

https://www.lstm.fau.de/dles/

ERCOFTAC
European Research Community On Flow, Turbulence And Combustion

DLES 14
Ercoftac Workshop
Direct & Large Eddy Simulation

SESSION: Data assimilation and uncertainty quantification I

Wednesday, April 10, 2024

10:00- 11:00

WORKSHOP
Direct and Large-Eddy Simulation 14
April 10-12 2024, Erlangen, Germany

ADJOINT-BASED DATA ASSIMILATION FOR AUGMENTED UNSTEADY SIMULATIONS OF TURBULENT FLOWS

Justin Plogmann[1,2], Oliver Brenner[1] and Patrick Jenny[1]
[1]Institute of Fluid Dynamics, ETH Zurich, Sonneggstrasse 3, CH-8092, Zürich, Switzerland
[2]Automotive Powertrain Technologies Laboratory, Swiss Federal Laboratories for Materials Science and Technology (Empa), Überlandstrasse 129, CH-8600, Dübendorf, Switzerland
justin.plogmann@empa.ch

INTRODUCTION

In recent years, data-driven techniques like data assimilation (DA) and machine learning have been increasingly explored to address inaccuracies from closure models. In addition, DA is often used to extract information from flow measurements. However, often only time-averaged data is available, which poses challenges for DA in the context of unsteady flow problems. Recent works have shown promising results in optimizing Reynolds-averaged Navier–Stokes (RANS) simulations of stationary flows using sparse data through variational data assimilation, enabling the reconstruction of mean flow profiles.

In this study we perform a stationary data assimilation of sparse time-averaged data into an unsteady RANS (URANS) or LES simulation by means of a stationary divergence-free forcing term in the respective momentum equation. Efficiency and speed of our method are enhanced by employing coarse URANS/LES simulations and leveraging the stationary discrete adjoint method for the time-averaged momentum equation.

STATIONARY DATA ASSIMILATION

To describe a turbulent flow with persistent unsteadiness, e.g. wake flows, URANS and LES simulations are widely used in many fields of applications. A forcing is introduced on the right hand side of the momentum equation to account for discrepancies in the modeled Reynolds stresses and is then subjected to a Stokes–Helmholtz decomposition. The unsteady equation reads

$$\frac{\partial \bar{u}_i}{\partial t} + \frac{\partial \bar{u}_i \bar{u}_j}{\partial x_j} = -\frac{\partial p^*}{\partial x_i} + \frac{\partial}{\partial x_j}\left[2\nu_{\text{eff}}\bar{S}_{ij}\right] + \epsilon_{ijk}\frac{\partial \psi_k}{\partial x_j} \,, \quad (1)$$

where the averaged/filtered pressure $\bar{p}$, the isotropic part of the Reynolds stress tensor, and the scalar potential ϕ are absorbed into the modified pressure p^* and the vector potential ψ serves as the stationary parameter for data assimilation. The goal for this work is to leverage the discrete adjoint method for stationary flows from [2] and apply it to unsteady flow problems. Therefore, we introduce temporal averaging $\langle\cdot\rangle$ with the corresponding fluctuation $(\cdot)''$ as

$$\bar{\xi} = \langle\bar{\xi}\rangle + \bar{\xi}'', \quad (2)$$

when applied to a quantity $\bar{\xi}$ that already is Reynolds-averaged or filtered in case of URANS or LES, respectively, yielding the time-averaged momentum equation

$$\begin{aligned} R = &\frac{\partial \langle\bar{u}_i\rangle \langle\bar{u}_j\rangle}{\partial x_j} + \frac{\partial \langle\bar{p}\rangle}{\partial x_i} - \frac{\partial}{\partial x_j}\left(2\left(\nu + \langle\nu_t\rangle\right)\langle\bar{S}_{ij}\rangle\right) \\ &\underbrace{- \frac{\partial}{\partial x_j}\left(2\langle\nu_t''\bar{S}_{ij}''\rangle\right) + \frac{\partial\left\langle\bar{u}_i''\bar{u}_j''\right\rangle}{\partial x_j}}_{\text{additional stress terms}} - \epsilon_{ijk}\frac{\partial\psi_k}{\partial x_j} = 0 \end{aligned} \quad (3)$$

that describes a stationary state. Depending on the choice of the turbulence model, ν_t describes the eddy-viscosity or subgrid scale viscosity for URANS and LES, respectively.

The data assimilation problem requires to minimize the discrepancy between the state variables computed by the model and the existing reference data and thus can be constructed as an optimization problem. In this work the scalar cost function f consists of a regularization function f_ψ and a discrepancy contribution $f_{\bar{u}}$, i. e.,

$$f(\psi, \bar{u}) = f_\psi(\psi) + f_{\bar{u}}(\bar{u}) \,. \quad (4)$$

It is subject to the residual R of the governing equation, that is, one seeks

$$\min_{\psi} \quad f(\psi, \bar{u}) \quad (5a)$$

$$\text{subject to} \quad R(\psi, \bar{u}) = 0 \,, \quad (5b)$$

where ψ is the parameter to be optimized and $\bar{u}$ the forward problem solution.

The optimization involves an inverse problem, which is highly non-linear and usually underdetermined. Hence, a non-linear optimization solver is used, but no assurance is given that there exists a unique solution. Therefore, total variation (TV) regularization is introduced to reduce the ambiguity. For each data assimilation iteration a parameter update is computed with a gradient descent approach. To this end, the stationary discrete adjoint technique is employed to calculate the gradient of the cost function concerning the parameters in question. This strategy demonstrates computational efficiency by yielding a cost of computing the gradient that is akin to solving the stationary forward system. A summary including a derivation is provided in [1]. The latest modifications to the implementation are described in [2] and [3].

In this work, the efficacy of our data assimilation framework is demonstrated by means of the URANS equation as the forward problem.

TEST CASE SETUP

The flow around a two-dimensional square cylinder (e.g. [4]) is considered. All length scales are expressed relative to the cylinder length/height D and the Reynolds number is computed from D, the free-stream velocity u_∞ and kinematic viscosity ν. Boundary conditions for velocity and pressure are taken from [4]. Wall functions for the k-ω SST model are applied at the cylinder wall, 2D BC's are present in spanwise directions and symmetry conditions are used for vertical boundaries. At the inlet, Dirichlet BC's are used and set to a small value reproducing the inflow conditions from [4]. Neumann BC's are set at the outlet. In this work, we analyze the case for

$$\mathrm{Re} = \frac{u_\infty D}{\nu} = 22\,000$$

with DNS velocity reference data from [4]. A time step size of $\frac{\Delta t u_\infty}{D} = 0.2$ is used. The mesh consists of 7496 hexahedral cells. The ratio of the smallest to largest cell is $2.487 \cdot 10^{-3}$.

RESULTS

Here, points near the cylinder and in the cylinder wake are chosen where reference data is taken into account for the assimilation. The velocity profiles near the cylinder as illustrated in Fig. 1 show an improvement toward the reference profiles.

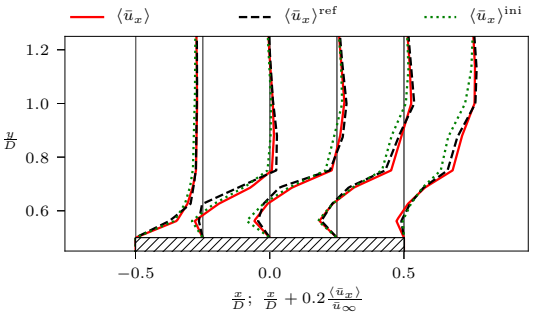

Figure 1: Mean flow velocity profiles near the square cylinder.

Fig. 2 depicts that almost all profiles are very well recovered except for the one closest to the cylinder. One reason is that here the density of reference data points switches quite abruptly.

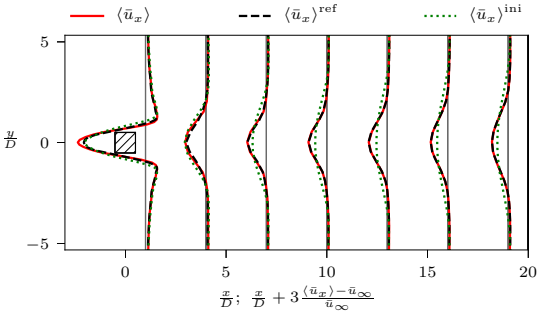

Figure 2: Mean flow velocity profiles in the wake of the square cylinder.

Due to the TV regularization all profiles are very smooth, but it should be noted that it also restricts the optimization. Since the regularization weight has to be chosen quite large to yield smooth fields, the optimization does not result in perfect agreement with the reference data in all regions.

Generally, these results demonstrate the basic capabilities of our approach and also that the time-averaged DNS velocity data can be well matched. In [3] it is presented that the choice of reference data points distribution heavily influences the region where the mean flow velocity is reconstructed, and if the prediction of the flow dynamics, i.e., of the vortex shedding frequency changes.

The baseline solution using the default forward problem solver obtained a Strouhal number differing from the reference [4]. After the assimilation of time-averaged DNS velocity data, the vortex shedding frequency adapted if enough reference data points are distributed in the cylinder near-wall region. A summary of these findings is presented in Tab. 1.

Case	Reference points	St
URANS-BASE	-	0.095
DNS	-	0.132
URANS-OPT-W	90	0.095
URANS-OPT-NW	152	0.122
URANS-OPT-NWW	260	0.120

Table 1: Summary of vortex shedding frequencies expressed by the Strouhal number St for the URANS baseline simulation (URANS-BASE), DNS, optimized URANS simulation with wake reference data points (URANS-OPT-W), optimized URANS simulation with near-wall reference data points (URANS-OPT-NW) and the optimized URANS simulation with near-wall and wake reference data points (URANS-OPT-NWW).

CONCLUSION

Our results demonstrate that data assimilation of sparse time-averaged velocity reference data into an unsteady flow simulation through a stationary parameter not only enables accurate mean flow reconstruction, but also improves the flow dynamics, specifically the vortex shedding frequency. The findings indicate that data points near the cylinder play a crucial role in improving the vortex shedding frequency, while additional data points further downstream are necessary to also reconstruct the time-averaged velocity field in the wake region.

REFERENCES

[1] O. Brenner, P. Piroozmand, P. Jenny, Efficient assimilation of sparse data into RANS-based turbulent flow simulations using a discrete adjoint method, Journal of Computational Physics 471 (2022) 111667. doi:10.1016/j.jcp.2022.111667.

[2] O. Brenner, J. Plogmann, P. Piroozmand, P. Jenny, Robust variational data assimilation of sparse velocity reference data in RANS simulations through a divergence-free forcing term (Oct. 2023). doi:10.48550/ARXIV.2310.11543.

[3] J. Plogmann, O. Brenner, P. Jenny, Variational assimilation of sparse time-averaged data for efficient adjoint-based optimization of unsteady RANS simulations (Oct. 2023). 10.48550/ARXIV.2310.12635.

[4] F. X. Trias, A. Gorobets, A. Oliva, Turbulent flow around a square cylinder at Reynolds number 22,000: A DNS study, Computers & Fluids 123 (22) (2015) 87–98, publisher: Elsevier Ltd. doi:10.1016/j.compfluid.2015.09.013.

WORKSHOP
Direct and Large-Eddy Simulation 14
April 10-12 2024, Erlangen, Germany

DATA ASSIMILATION CLOSURE FOR LES OF RAYLEIGH-BÉNARD CONVECTION

Sagy R. Ephrati[1], **Arnout Franken**[2], **Erwin Luesink** [2], **Bernard J. Geurts**[2,3]
[1]Department of Mathematical Sciences
Chalmers University of Technology and University of Gothenburg, Sweden
sagy@chalmers.se
[2]Mathematics of Multiscale Modeling and Simulation
University of Twente, The Netherlands
{a.d.franken, b.j.geurts, e.luesink}@utwente.nl

INTRODUCTION

Data-driven large-eddy simulation (LES) is an active topic of research. The continued growth of computational resources permits computing flows on increasingly high resolutions. This leads to increased availability of high-fidelity data, which in turn has spurred the development of data-based LES closure models. Machine learning has proven to be a successful approach to empirically estimate closure models from data, for example by learning a variable eddy viscosity [1] or subfilter-scale forces [2]. Despite these encouraging results, no overall-best computational model has been found.

A theoretical best LES model has been presented as 'ideal LES' [3], which minimizes the instantaneous error in the dynamics and yields exact agreement for spatial statistics. The model is defined such that the evolution of the LES solution equals the average filtered evolution of the resolved fields. This average is conditioned to the distribution of fully-resolved solutions with the same large-scale (filtered) fields as the LES solution. Finding this conditional average is challenging in practice, since generally an infinite number of fully resolved solutions correspond to a single filtered solution. Nonetheless, the average may be approximated empirically when sufficient high-fidelity data is available.

Accurately computing this distribution and its mean is the main objective of data assimilation. Data assimilation combines observations (data) with predictions to balance the uncertainties inherent to both these aspects in an optimal way [4]. Commonly, a Bayesian approach is adopted to account for uncertainty and to find a distribution of solutions in a probabilistic setting. The mean of this distribution is the ideal LES model and we therefore consider the applicability of data assimilation algorithms in the context of LES closure models. In particular, this identification aids data-driven LES by prescribing the functional form of the model or by specifying the loss function that the model should minimize.

In this presentation at the workshop, we illustrate how a particular data assimilation algorithm can be used for data-driven LES in statistically steady states. High-fidelity data in the form of flow statistics are gathered in an *offline* phase, which translate to parameters for *online* data-driven forcing. The approach is demonstrated for two-dimensional Rayleigh-Bénard convection.

CLOSURE MODELS VIA THE 3D-VAR ALGORITHM

The approach is based on the premise that the average energy spectrum of a coarse numerical simulation should equal that of the reference solution, up to the smallest resolvable scale on the coarse computational grid. This imposes a constraint on the spectral coefficients of the LES solution [6]. An accurate energy spectrum may be obtained by introducing a control feedback term into the evolution equations of the magnitudes of the spectral coefficients. This is summarized as

$$\mathrm{d}|\mathbf{c}| = L_{\mathrm{coarse}}(\mathbf{c})\mathrm{d}t + \frac{1}{\boldsymbol{\tau}}\left(\boldsymbol{\mu} - |\mathbf{c}|\right)\mathrm{d}t + \boldsymbol{\sigma}\mathrm{d}\mathbf{W}, \qquad (1)$$

where $|\mathbf{c}|$ denotes the vector of magnitudes of the spectral coefficients of the LES solution and L_{coarse} is the operator describing the evolution of these values in a coarse numerical simulation. The last two terms arise as the continuous-time limit of the 3D-Var data assimilation algorithm [5]. Here $\mathrm{d}\mathbf{W}$ denotes Gaussian noise, independent for each coefficient. The symbols $\boldsymbol{\mu}, \boldsymbol{\tau}$ and $\boldsymbol{\sigma}$ contain the mean values, forcing strengths and noise scalings, respectively.

A prediction-correction scheme is used to solve Eq. (1). In short,

$$\tilde{\mathbf{c}}^{n+1} = \mathbf{c}^n + \int_{t^n}^{t^n+\Delta t} L_{\mathrm{coarse}}(\mathbf{c})\mathrm{d}t \quad \text{(time integration)} \qquad (2)$$

$$|\mathbf{c}^{n+1}| = |\tilde{\mathbf{c}}^{n+1}| + \frac{\Delta t}{\boldsymbol{\tau}}\left(\boldsymbol{\mu} - |\tilde{\mathbf{c}}^{\mathbf{n+1}}|\right) + \boldsymbol{\sigma}\Delta\mathbf{W}, \quad \text{(correction)} \qquad (3)$$

where Δt denotes the time step and $\Delta\mathbf{W}$ denotes randomly drawn samples from a standard normal distribution.

The prediction follows from the adopted time-integration method and is not required to be in spectral space. The correction acts only on the magnitude of the spectral coefficients. Note that it is not necessary to know L_{coarse} explicitly, we only require the transformation from the LES solution to its spectral coefficients and vice versa.

We assume that high-fidelity data is available in the form of a time series for each of the magnitudes of the spectral coefficients, yielding means $\boldsymbol{\mu}_{\mathrm{ref}}$ and standard deviations $\boldsymbol{\sigma}_{\mathrm{ref}}$. The prediction-correction scheme can be treated as an autoregressive first-order (AR(1)) process for sufficiently small time steps. Using this assumption, the constraint on the spectral

coefficients of the LES solution require that

$$\boldsymbol{\mu} = \mathbb{E}\left(|\mathbf{c}_{\text{ref}}|\right), \ \boldsymbol{\sigma} = \boldsymbol{\sigma}_{\text{ref}} \sqrt{1 - \left(1 - \frac{\Delta t}{\boldsymbol{\tau}}\right)^2}, \qquad (4)$$

where all arithmetic acts element-wise on the vectors. The forcing strength $\boldsymbol{\tau}$ is a free parameter and is chosen as the correlation time of the measured times series.

APPLICATION TO RAYLEIGH-BÉNARD CONVECTION

The approach is illustrated for two-dimensional Rayleigh-Bénard convection for Pr = 1 and Ra = 10^{10}. DNS is performed on a 4096×2048 computational grid, after which the solution is filtered to make it suitable for the coarse 64×32 grid. The model is applied to each horizontal (wall-parallel) cross-section of the domain. Several model configurations are studied, varying whether the model is applied to the momentum, the temperature, or both. For each case the forcing is applied both at large scales and at all resolvable scales. Full details can be found in Ephrati et al. [7]. Qualitative insight into the results is provided in Figures 2 and 1, in which the DNS, the no model coarse solution and a model coarse solution are compared. In Figures 1 and 2 the wall-parallel temperature spectra in the core of the domain and snapshots of the temperature field are shown, respectively. In Figure 1, it is shown that the energy spectra are accurately reconstructed. In Figure 2, one sees that small-scale features are recovered when using the model. Additionally, large-scale forcing extracted from the high-fidelity simulation leads to accurate Nusselt number predictions across two decades of Rayleigh numbers centered around the targeted reference at $Ra = 10^{10}$, as is shown in Fig. 3. Further work is dedicated to comparing the current approach to eddy-viscosity models, such as the Smagorinsky model and the dynamic subgrid-scale model.

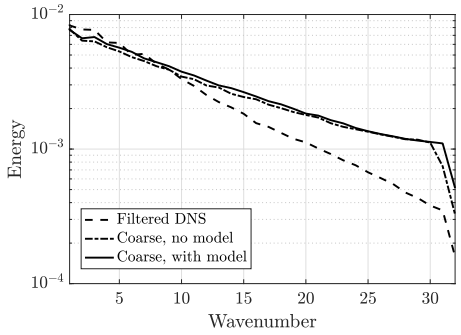

Figure 1: Time-averaged energy spectra for the temperature (right) in the center of the domain.

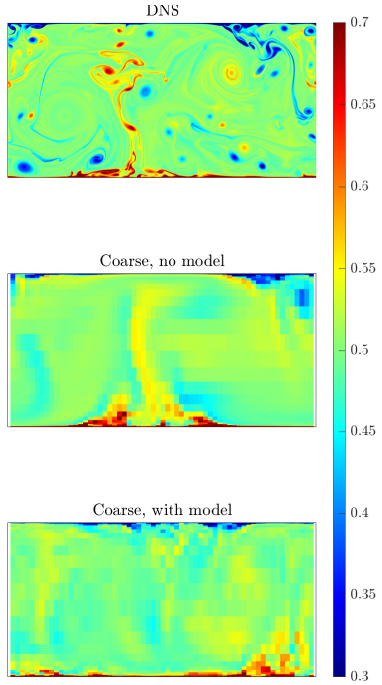

Figure 2: Snapshots of the temperature for the DNS, the no-model coarse simulation, and model coarse simulation.

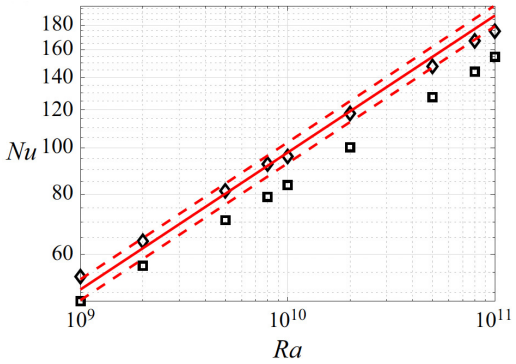

Figure 3: Measured Nusselt number as a function of the Rayleigh number. The solid red lines shows reference Nusselt number predictions from literature with 5% error margins. The no-model and model results are given by the squares and the diamonds, respectively.

REFERENCES

[1]Beck, A., Flad, D. and Munz, C.-D.: Deep neural networks for data-driven LES closure models: *Journal of Computational Physics*, **398**, 108910 (2019).

[2]Xie, C., Wang, J. and Weinan, E.: Modeling subgrid-scale forces by spatial artificial neural networks in large eddy simulation of turbulence: *Physical Review Fluids* **5 (5)**, 054606 (2020).

[3]Langford, J.A. and Moser, R.D.: Optimal LES formulations for isotropic turbulence: *Journal of Fluid Mechanics*, **398**, 321–346 (1999).

[4]Grewal, M.S. and Andrews, A.P.: Kalman filtering: Theory and Practice with MATLAB, (2014).

[5]Blömker, D., Law, K., Stuart, A.M. and Zygalakis, K.C.: Accuracy and stability of the continuous-time 3DVAR filter for the Navier–Stokes equation: *Nonlinearity*, **26 (8)**, 2193 (2013).

[6]Ephrati, S.R., Cifani, P., Viviani, M. and Geurts, B.J.: Data-driven stochastic spectral modeling for coarsening of the two-dimensional Euler equations on the sphere, *Physics of Fluids*, **35 (9)**, 096601 (2023).

[7]Ephrati, S.R., Cifani, P. and Geurts B.J.: Data-driven spectral turbulence modelling for Rayleigh–Bénard convection, *Journal of Fluid Mechanics*, A35 (2023).

WORKSHOP
Direct and Large-Eddy Simulation 14
April 10-12 2024, Erlangen, Germany

AUGMENTED LARGE EDDY SIMULATION FOR THE ANALYSIS OF COMPLEX FLOWS USING ONLINE DATA ASSIMILATION

L. Villanueva[1], Karine Truffin[2] and Marcello Meldi[3]
[1]Institut Pprime, CNRS - ISAE-ENSMA - Université de Poitiers,
11 Bd. Marie et Pierre Curie, Site du Futuroscope, TSA 41123, 86073 Poitiers Cedex 9, France
lucas.villanueva@ensma.fr
[2]Institut Carnot IFPEN Transports Energie, IFP Energies nouvelles,
1-4 avenue de Bois-Préau, 92852 Rueil-Malmaison, France
[3]Univ. Lille, CNRS, ONERA, Arts et Métiers ParisTech, Centrale Lille, UMR 9014- LMFL-
Laboratoire de Mécanique des fluides de Lille - Kampé de Feriet, F-59000 Lille, France

INTRODUCTION

The accurate analysis of progressively more complex flow configurations is becoming an established reality in Computational Fluids Dynamics (CFD). In particular, turbulent closures such as Large Eddy Simulations (LES) are nowadays used for the analysis of industrial configurations, owing to their excellent features in terms of accuracy versus computational cost in time. In addition, scale-resolving simulation has the potential to track in time extreme events such as sudden flow accelerations. The emergence of such conditions, which are usually associated with strong peaks and rapid variations of bulk flow quantities such as the drag and lift coefficient, can lead to main changes in the structural organization of the flow and have a significant impact on the safety of the investigated applications. These extreme events are observed for a large range of high-Reynolds configurations which include external flows such as urban settings [1] as well as internal flows such as combustion cyclic variability [2]. However, uncertainties in initial / boundary conditions and modeling errors significantly affect the instantaneous flow evolution, which can rapidly lose synchronization with reference measurements. This limit has to be overcome to envision online LES applications in the framework of advanced applications such as digital twins [3]. Among the tools available in the literature for model augmentation, sequential Data Assimilation (DA) [4] exhibits strong features for on-the-fly coupling with LES. DA approaches can in fact integrate high-fidelity sparse information from *observations* (usually available at local sensors) to improve the prediction of instantaneous features of the flow as well as to infer the optimized behavior of modeling/boundary conditions.

In the present work, an online DA strategy based on the Ensemble Kalman Filter (EnKF) [4] is used to obtain an augmented prediction based on Large Eddy Simulation (LES) for the analysis of the oscillating compressible flow in a flow rig type geometry (OFR). The test case investigated, which is based on Dellenback flow expansion geometry [5], includes an open valve in its intake to mimic the internal combustion engine configurations. A visualization of the flow field obtained via a refined LES is shown in Figure 1. This kind of flow, which is not permanent owing to the trigonometric behavior of the mass flow rate at the inlet, exhibits difficulties for analyses relying on numerical simulation. In fact, capturing the emergence of instantaneous extreme events is an additional challenge to the accurate prediction of statistical moments of the velocity field.

The algorithm sequentially combines results from an ensemble of LES realizations performed on a coarse grid (LES_c) with sparse instantaneous data from a high-fidelity LES performed over a refined grid (LES_f). The procedure aims to i) infer the trigonometric behavior of the mass flow rate at the inlet, which is supposed to be unknown and ii) provide an augmented state that exhibits higher accuracy than the LES_c model and that synchronizes with the time evolution of the high-fidelity data from the LES_f run.

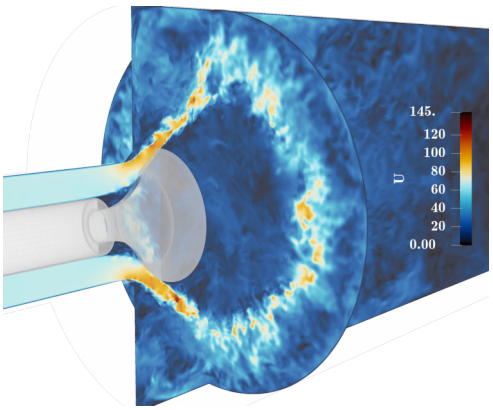

Figure 1: Velocity field around the valve of the OFR. The solution is shown for two orthogonal plans at $y = 0$ and $x = 0.134$.

SETUP FOR DATA ASSIMILATION

Several ingredients are combined with the ENKF formalism:

- **A model**, providing the time-advancement of the physical system studied via an ensemble of realizations. In this study, the forecast of the physical state is performed by the compressible solver *rhoPimpleFoam* available in the solver OpenFOAM, using the LES-WALE turbulent

closure. The simulations are run over a relatively coarse mesh of 8×10^6 mesh elements and $y^+ \approx 4$ close to the port entry walls.

- **Sparse high-fidelity data**, which are used in the DA procedure to update the predicted state of the model and improve its accuracy via parametric optimization. The observation has been sampled from the reference LES_f run. For this simulation, the physical domain is discretized in 1.31×10^8 mesh elements and $y^+ \approx 1$ close to the port entry walls.

The inference capabilities of the DA algorithm are used to optimize the parametric description of the inlet for the ensemble realization relying on the model LES_c. More precisely, the optimization targets the reconstruction of the velocity profile imposed for the simulation LES_f:

$$U_{IN}(t) = U_\infty + asin(\omega t) \tag{1}$$

where the amplitude a and the frequency ω are chosen according to experimental results available to the research group. For the ensemble simulations, these values are supposed to be unknown, and the initial inlet condition prescribed is

$$U^C_{IN}(t) = U_\infty + \sum_{i=1}^{4} a_i sin(\omega_i t + \phi_i) \tag{2}$$

The coefficients a_i, ω_i, and ϕ_i and U_∞ are optimized via the DA procedure. To this purpose, the EnKF utilizes the data sampled from the reference simulation LES_f over subsets of sensors taken from the complete set shown in figure 2. In particular, a sensitivity analysis is performed by choosing different subsets, in order to highlight the global accuracy obtained and the sensitivity of the DA algorithm to the information provided.

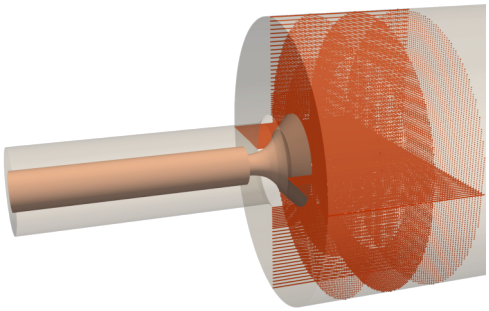

Figure 2: OFR geometry. Red points are sensors where observations is sampled from simulation LES_f.

DA IMPROVEMENTS & RESULTS

The classical formulation of the EnKF would need prohibitive computational resources to investigate this test case, considering the number of degrees of freedom of the flow. Several improvements are performed to improve the speed of the model realizations. First of all, the library CONES (Coupling OpenFOAM with Numerical EnvironmentS), based on CWIPI coupler developed by CERFACS and ONERA, is used to couple online the model LES runs and the DA code. This task dramatically reduces the computational costs, as the resources required to stop/restart ensemble members and write data are eliminated. Also, three different strategies for localization (i.e. reduce the complexity of the DA problem by eliminating part of the correlations between physical variables) are employed. Classical physical and covariance localization algorithms are implemented in order to accelerate the DA problem while keeping a good level of accuracy. In addition, hyper-localization of the Kalman filter is implemented. This strategy decomposes the KF analysis phase in multiple analyses (one per sensor available), providing huge computational gains as well as improved robustness. Table 1 summarizes the computational cost of each procedure, underlying the effectiveness of this last improvement, and its importance in a complex and computationally demanding simulation such as the OFR. At last, parametric inflation is used to increase the variability of the ensemble and allow to target more accurately the optimum provided by the observations.

The first run of the DA algorithm has shown convergence of the optimization of the inlet parametric description. At the same time, it was observed that synchronization of the main structure of the flow close to the valve is successful, thanks to the state update performed by the EnKF. The current analysis, which will be jointly presented at the conference, studies the sensitivity of the DA algorithm to changes in the hyper-parameters (coefficients of localization and inflation, number and position of the sensors).

Type of EnKF	N	N_o	N_e	Completion time (s)
Basic	$350,000 \times 3$	1224	40	166
Physical localization	$154,000 \times 3$	1244	40	94
Physical localization + Filtering of sensors	$154,000 \times 3$	408	40	18
Hyper-localization + Filtering of sensors	$96,500 \times 3$	408	40	2.4

Table 1: Summary of the test performed on an academic test case to evaluate the computational costs required by one analysis phase of the EnKF. N is the number of degrees of freedom used for DA, N_o the number of observations, and N_e the number of members in the ensemble.

REFERENCES

[1]Hemida H., Šarkić Glumac A., Vita G, Vranešević KK, Höffer R.: On the flow over high-rise building for wind energy harvesting: An experimental investigation of wind speed and surface pressure. *Applied Science* , 10-5283, (2020).

[2]Ding, Z., Karine T., Jay, S., Schmidt, M., Foucher, F., Borée, J.: On the Use of LES and 3D Empirical Mode Decomposition for Analyzing Cycle-to-Cycle Variations of In-Cylinder Tumbling Flow. *Flow, Turbulence and Combustion* 111, 1, 235-84 (2023).

[3]Semerano, C., Lezoche, M., Panetto, H., Dassiti, M.: Digital twin paradigm: A systematic literature review, *Computers in Industry*, 130-103469, (2021).

[4]Asch, M., Bocquet, M. and Nodet, M. : Data Assimilation Methods, Algorithms, and Applications, *Society for Industrial and Applied Mathematics*, (2016).

[5]Dellenback, P.A., Metzger, D.E. and Neitzel, G.P.: Measurements in turbulent swirling flow through an abrupt axisymmetric expansion, *AIAA Journal*, 26-6, 669-681 (1988).

[6]Villanueva, L., Valero, M.M., Šarkić Glumac, A. and Meldi, M.: Augmented state estimation of urban settings using on-the-fly sequential Data Assimilation, *Computers and Fluids*, 269-106118 (2024).

[7]Villanueva, L., Truffin, K. and Meldi, M.: Synchronization and optimization of Large Eddy Simulation using an online Ensemble Kalman Filter, *Arxiv 2310.18016*, (2023).

WORKSHOP
Direct and Large-Eddy Simulation 14
April 10-12 2024, Erlangen, Germany

LOOSELY COUPLED UNDER-RESOLVED LES/RANS SIMULATION AUGMENTED BY SPARSE NEAR-WALL MEASUREMENT

A. Pasha Piroozmand[1], B. Oliver Brenner[1], C. Patrick Jenny[1]
[1]Institute of Fluid Dynamics (IFD)
ETH Zürich, Zürich, Switzerland
pasha.piroozmand@ost.ch

INTRODUCTION

Hybrid LES/RANS methods are one of the promising approaches to simulate turbulent flows with high accuracy and low computational costs. On the other hand, data-driven approaches such as data assimilation can further improve the simulations' results by incorporating the available measurement data. In this work, we combine these two powerful methods. We investigate scenarios, where only sparse wall shear stress measurements are available, while accurate wall shear stress and velocity profiles are sought. Applying discrete adjoint-based data assimilation, with only near-wall measurements, accurate wall shear stress profiles are achieved at the expense of unrealistic velocity profiles. We therefore add and employ internal reference data generated by performing a relatively cheap hybrid simulation. We modified the dual-mesh hybrid LES/RANS framework recently proposed by Xiao and Jenny [1] by loosely coupling under-resolved LES in the interior with steady RANS near the walls. The framework was developed in OpenFOAM and tested for flow over periodic hills with Re = 10595. Results show that the devised framework outperforms conventional dual-mesh hybrid LES/RANS and standalone sparse wall-data assimilated RANS models.

METHOD

The method consists of two steps. The first step is to generate the reference data in the internal region for data assimilation by running the loosely coupled dual-mesh hybrid LES/RANS method. The second step is to assimilate the generated data and the near-wall measurement into the RANS model.

The initial version of the dual-mesh hybrid LES/RANS method developed by Xiao and Jenny [1] is outlined below. In this method, two sets of governing equations are solved on different meshes. The generic version of both Reynolds-averaged and the filtered momentum and pressure equations of an incompressible flow with constant density read

$$\frac{\partial U_i^*}{\partial t} + \frac{\partial (U_i^* U_j^*)}{\partial x_j} = -\frac{\partial p^*}{\partial x_i} + \nu \frac{\partial^2 U_i^*}{\partial x_j x_j} - \frac{\partial \tau_{ij}^*}{\partial x_j} + Q_i^* \quad (1)$$

$$\text{and} \quad \frac{\partial^2 p^*}{\partial x_i \partial x_i} = -\frac{\partial^2}{\partial x_i \partial x_j}(U_i^* U_j^* + \tau_{ij}^*) + \frac{\partial Q_i^*}{\partial x_i}, \quad (2)$$

where Q_i^* is the drift force applied to the equations, which ensures consistency between LES and RANS and τ_{ij}^* is the Reynolds or residual shear stress. For a faster and easier-to-implement simulation, we propose the loosely coupled approach. The equations are further simplified by the elimination of all time derivative terms in the RANS equations. We also redefine the drift term Q_i^R, such that the RANS solution gets nudged to the average LES velocity of the previous period, instead of to the exponentially weighted average (EWA) LES velocity. The forcing term Q_i^R remains the same, except that we relax the average LES equation towards the RANS solution.

The source term applied to the corresponding regions are

$$Q_i^R = \begin{cases} (\langle U_i \rangle^{\mathrm{MA}} - \langle U_i \rangle)/\tau_r, & \text{in LES regions,} \\ 0 & \text{in RANS regions,} \end{cases} \quad (3)$$

and

$$Q_i^L = \begin{cases} (\langle U_i \rangle - \langle \bar{U}_i \rangle^{\mathrm{EWA}})/\tau_l, & \text{in RANS regions,} \\ 0 & \text{in LES regions,} \end{cases} \quad (4)$$

where $\langle U_i \rangle^{\mathrm{MA}}$ is the mean time-average LES velocity and τ_r and τ_l are relaxation times for RANS and LES, respectively.

In the next step, the data assimilation is performed through tuning the eddy viscosity of a steady RANS model. The tuned parameter α leads to a correction of the diffusive flux in the steady RANS equation as

$$\frac{\partial (\langle U_i \rangle \langle U_j \rangle)}{\partial x_j} = -\frac{\partial \langle p \rangle}{\partial x_i} + \frac{\partial}{\partial x_j}\left[(\nu + \alpha \langle \nu_t \rangle) \frac{\langle U_i \rangle}{\partial x_j} \right], \quad (5)$$

where $\langle \nu_t \rangle$ is the eddy viscosity computed by the RANS part of the hybrid model. The corrective field α distills the effect of the drift term in the hybrid equations into an optimal eddy viscosity, and it compensates for the shortcomings of the RANS model by incorporating data. To ensure physical results we employed a form of regularization called piecewise linear dimension reduction (PLDR) (see Ref. [3]).

RESULTS

All results are compared with a fully resolved LES simulation (FR-LES) as a reference. The measurement and sampling point locations are shown in Figure 1.

In Figure 2, we see that the loosely coupled approach significantly improves the accuracy of the velocity profiles in comparison with stand-alone under-resolved LES, while the wall shear stresses show no improvement. However, we obtain both accurate velocity profiles and wall shear stresses when the loosely coupled method is combined with the near-wall measurements, as shown in Figure 3. Both stand-alone steady-RANS and under-resolved LES are outperformed. For more detailed discussions, we refer the reader to the Ref. [2].

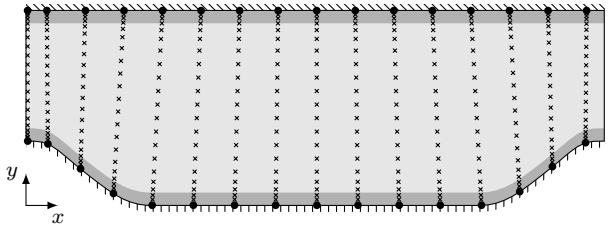

Figure 1: locations of sampling (×) and measurement points at the walls (•).

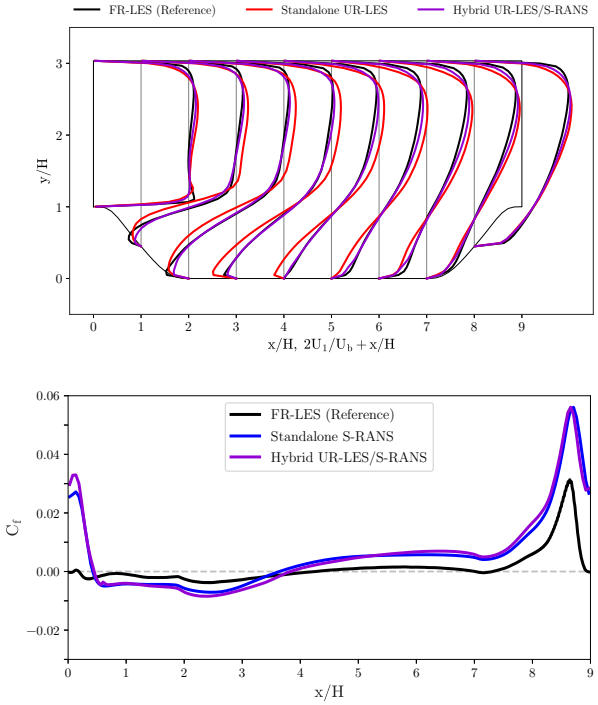

Figure 2: Horizontal mean velocity component U_1 (top plot) and wall shear stress (friction coefficient C_f) profiles at the lower wall (bottom plot) for the loosely coupled LES/RANS method. Note that the friction coefficient of the loosely coupled method is derived from its S-RANS solution.

REFERENCES

[1]Xiao, H., Jenny, P. : A consistent dual-mesh framework for hybrid LES/RANS modeling, *Journal of Computational Physics*, **231**, 1848–1865 (2012).

[2]Piroozmand, P., Brenner, O., Jenny P.: Dimensionality reduction for regularization of sparse data-driven RANS simulations, *Journal of Computational Physics*, **492**, 112404 (2023).

[3]Piroozmand, P., Brenner, O., Jenny P.: Loosely Coupled Under-Resolved LES/RANS Simulation Augmented by Sparse Near-Wall Measurement, available at Research Square, (2023).

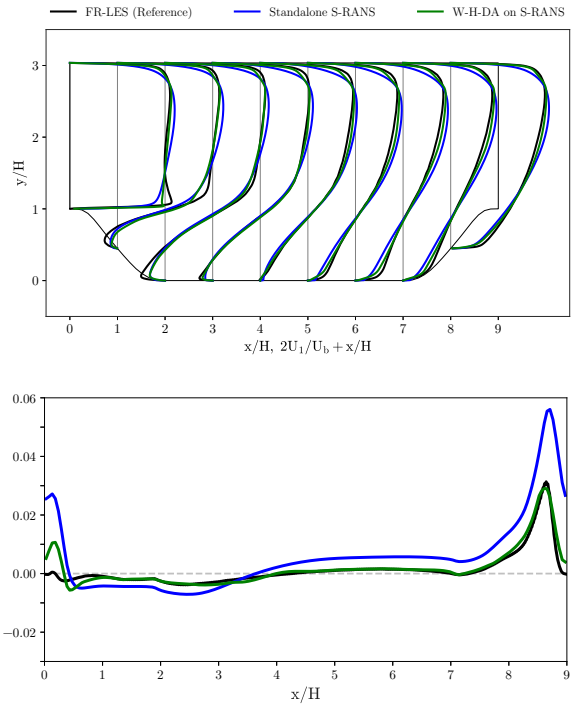

Figure 3: Horizontal mean velocity component U_1 (top plot) and wall shear stress (friction coefficient C_f) profiles at the lower wall (bottom plot) obtained with Steady-RANS (S-RANS) and assimilation of sparse wall shear stress data. W-H-DA stands for wall measurement (W) and hybrid (H) results assimilation (DA).

SESSION: Convection and heat/mass transfer I

Wednesday, April 10, 2024

10:00- 11:00

WORKSHOP
Direct and Large-Eddy Simulation 14
April 10-12 2024, Erlangen, Germany

DLES14: LARGE-EDDY SIMULATION OF SOLID/FLUID HEAT AND MASS TRANSFER APPLIED TO THE THERMAL DEGRADATION OF COMPOSITE MATERIAL

A. Grenouilloux[1], R. Letournel[2], N. Dellinger[3], K. Bioche[1], V. Moureau[1]
[1] CORIA, CNRS UMR6614
Normandie Universite, UNIROUEN, INSA of Rouen,France
[2] Safran Tech
Rue des jeunes Bois, 78117, Châteaufort
[3] ONERA/DMPE
Université de Toulouse, 31055 Toulouse, France
adrien.grenouilloux@coria.fr

INTRODUCTION

The ongoing trend towards improved aircraft efficiency involves the usage of higher-strength materials. In this context, carbon fiber reinforced polymers (CFRP), and more generally composite assemblies, have increasingly been used for the fuselage and nacelle's fairing. They have gradually replaced heavier metallic alloys, thus improving the overall performance. Yet, a critical part of the design phase remains the fire certification of all components. Current international standards, such as the FAR25.856(b):2003 and ISO2685:1998(e), ensure the thermal resistance of these lighter materials when submitted to high-heat loads. Still, certification test campaigns are costly and often require a long time for their set-up. The introduction of numerical tools for the prediction of the degraded material properties could provide supplementary inputs and thus improve the design process. For the past decades, Large-Eddy Simulation (LES) has become a valuable tool for the simulation of unsteady reactive flows [1, 5, 11]. Several Conjugate Heat-Transfer (CHT) approaches have been performed to address the unsteady interactions between a fluid and a solid solver [5, 6]. These efforts have allowed to estimate the impact of the flame on the temperature distribution of solid geometries. However, the number of studies addressing the interaction of a flame leading to a composite plate degradation is limited [4]. In the present paper, a methodology for the coupling between a fluid, a radiation and a solid solver, capable of respectively solving for the reactive, radiative heat losses and the thermal degradation of composite material, is presented. The procedure is first validated under simplified test-bed conditions on a so-called BLADE test [7]. In this context, a high-intensity laser beam replaces the external heat source from a flame.

COUPLING METHODOLOGY

In his work, Biasi et al. [2] presented a methodology for the coupling between a Reynolds Averaged Navier Stokes (RANS) solver and a solid solver for the simulation of a composite material degradation. In addition to temperature and heat-flux exchange, which are standard features of CHT [5, 6], the composite plate out-gassing mass flow rate was added to the coupling. To ensure the thermodynamic equilibrium, Biasi et al. [2] proposed to send to the solid the external fluid pressure. In Dellinger et al. [4] the coupling was improved with additional data sent from the solid. Thus, surface temperature and porosity, as well as mass flow rate and temperature of the decomposition gas were considered for the exchange. In this paper, a coupling methodology for fire certification under realistic conditions is proposed. The procedure relies on the coupling between three solvers. First, a low-Mach number Variable Density Solver (VDS) is used for fluid transport [11] with a multi-species formalism. Second, to take into account radiative effects due to the expected high temperature coming from both the flame and the heated coupon, a radiation solver is used. Note that these two latter solvers are implemented in the massively parallel library YALES2 [8]. Finally, the composite material's degradation is solved using the MoDeTheC code developed by ONERA [3]. In this latter solver, material properties such as anisotropic thermal conductivity are specified based on fiber arrangement. This particular distribution has a significant impact on the heat conduction within the material. The coupling and data interpolation between the different grids is ensured by the CWIPI library [9]. The structure proposed in Dellinger et al. [4] is here considered. Further datas are sent and received between the three solvers to account for radiative effects. Figure 1 summarizes this coupling procedure. Note that in this figure, the direction of the arrows indicates whether the data is sent or received.

VALIDATION TEST-CASE

The BLADE test bed presented by Leplat et al. [7] is considered to validate the coupling procedure. The fluid numerical domain consists of a three-dimensional box and can be seen in Figure 2. In this chamber, the pressure is kept constant at $P_0 = 500$Pa, and the temperature is set at $T_0 = 295$K. This way, convective heat transfer sources are neglected [7]. At its center, a 80mm $\times$ 80mm $\times$ 4mm T700GC/M21 carbon/epoxy solid test coupon is located. A laser of an intensity of 76.2kW/m^2 impinges on the front surface of the test

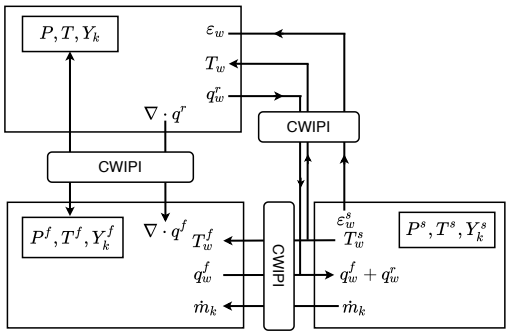

Figure 1: Diagram of the proposed coupling procedure.

coupon for a total duration of 300s and an additional 100s are simulated to account for test coupon cooling. This heat source rapidly increases the temperature of the solid until the composite laminates decompose by pyrolysis and oxidation reactions. At this stage, the plate outgassing can be observed. More precisely, the mass flow rate received by the fluid solver is shown in Figure 3. Note that given the different characteristic time scales between solid and fluid, the coupling is *asynchronous* [2, 6]. Thus, the fluid and solid solvers exchange data at different times to accelerate the temporal convergence.

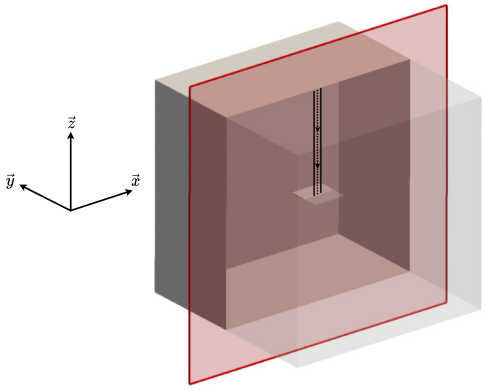

Figure 2: Overview of the numerical domain with incident laser beam.

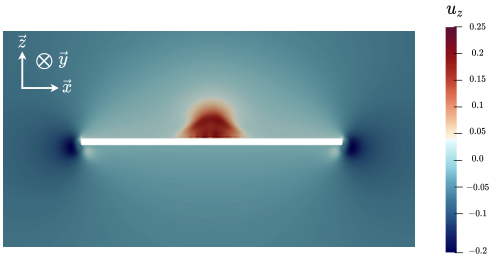

Figure 3: Composite material out-gassing due to laser impingement.

CONCLUSION AND PERSPECTIVES

The proposed methodology is used to perform a coupled simulation of a BLADE test. It relies on the coupling between a Low-Mach variable density solver for the fluid part, a radiation solver for the heat losses and, a solid solver for the composite material degradation. Rear-face temperature distribution will be compared against both experimental and numerical data [2, 7]. Such a case will later be used as a reference benchmark to perform fire certification simulation, with the presence of a burner and a flame as a heat source [4].

ACKNOWLEDGEMENTS

This work is granted access to the HPC resources of CINES/TGCC under the projects 2B06880 and made by GENCI and of CRIANN under the allocation 2012006. This work has been initiated during the Extreme CFD Workshop & Hackathon (`https://ecfd.coria-cfd.fr`).

REFERENCES

[1]Poinsot, T., Veynante, D. : Theoretical and Numerical Combustion,*R.T. Edwards Inc.*, (2005).

[2]Biasi, V. : Thermal Modelling of Decomposing Composite Materials Submitted to Fire,*PhD Thesis*, (2014).

[3]Biasi, V., Leplat, G., Feyel, F. : Numerical modeling and experimental validation of heat and mass transfer within decomposing carbon fibers/epoxy resin composite laminates. *International Journal of Heat and Mass Tranfer*, (2016).

[4]Dellinger, N., Donjat, D., Laroche, E., Reulet, P. : Experimental and numerical modelling of the interaction between a turbulent premixed propane/air flame and a composite flat plate,*Fire Safety Journal* , (2023).

[5]Boulet, L., Bénard, P., Lartigue, G., Moureau, V. : Modeling of Conjugate Heat Transfer in a Kerosene/Air Spray Flame used for Aeronautical Fire Resistance Tests. *Flow Turbulence Combust*, **101**, 579–602 (2018).

[6]Duchaine, F., Mendez, S., Nicoud, N., Corpron, A., Moureau, V., Poinsot, T. : Conjugate heat transfer with Large Eddy Simulation for gas turbine components. *Comptes Rendus Mécanique*, **337**, 550-561 (2009).

[7]Leplat, G., Huchette, C., Biasi, V. : Thermal and damage analysis of laser-induced decomposition within carbon/epoxy composite laminates. *Journal of Fire Sciences*, **34(5)**, 361-384 (2016).

[8]Moureau, V., Domingo, P., Vervisch, L.: Design of a massively parallel CFD code for complex geometries, *Comptes Rendus Mécanique*, (2011).

[9]Coupling with Interpolation Parallel Interface, 2023. `https://w3.onera.fr/cwipi/bibliotheque-couplage-cwipi`. (Accessed 21 November 2023).

[10]Nguye, P.D., Moureau, V., Vervisch, L., Perret, N. : A massively parallel solution strategy for efficient thermal radiation simulation, *Journal of Physics Conference Series*, **369**, (2012).

[11]Analyse et amelioration d'une chambre de combustion centimétrique par simulations aux grandes echelles, *PhD Thesis, INSA de Rouen*, (2015).

WORKSHOP
Direct and Large-Eddy Simulation 14
April 10-12 2024, Erlangen, Germany

ANALYSIS OF BOUNDARY LAYERS BY HIGH-RESOLUTION DNS OF RAYLEIGH-BÉNARD CONVECTION

Roshan J Samuel[1], Mathis Bode[2], Katepalli R Sreenivasan[3], Jörg Schumacher[1,3]

[1]Technische Universität Ilmenau
Ilmenau, Germany

[2]Jülich Supercomputing Center
Jülich, Germany

[3]New York University
New York, USA

INTRODUCTION

Our understanding of thermal convection has progressed greatly over the past many decades. This progress is driven in great part by studies of Rayleigh-Bénard convection (RBC), the paradigmatic system where a fluid is confined between a pair of infinitely extending cold and hot plates placed at the top and bottom respectively [1]. By varying the strength of buoyancy, dictated by the Rayleigh number (Ra), and the dissipation properties of the fluid, set by the Prandtl number (Pr), we can observe a wide variety of flows regimes, ranging from steady laminar to highly turbulent [2, 3, 4].

The convective flow transports both heat and momentum across the two plates at the top and bottom that enclose the fluid layer. This transport is driven by the flow in the boundary layers (BL) and the plumes which rise from them. In the present work, we delve into the flow patterns within the BL which generate the plume ridges typically observed in RBC. Experiments of RBC also indicate the presence of a large-scale circulating flow. However, we show that in the absence of confining side-walls, as in most instances of thermal convection observed in nature, such a large-scale mean flow is absent. Instead, we see intermittent patches of coherent flow interspersed between regions of highly turbulent thermal upwelling.

SIMULATION DETAILS

We perform our direct numerical simulations (DNS) by solving the Navier-Stokes equations in the Boussinesq approximation. We use the GPU accelerated spectral element solver, NekRS [5], for our DNS. This robust and highly scalable solver is based on the acclaimed Nek5000 [6] code.

Ra	N_e	p	N_{BL}	Δt
10^5	$100 \times 100 \times 64$	5	71	1000
10^6	$100 \times 100 \times 64$	7	57	1000
10^7	$100 \times 100 \times 64$	9	42	1000
10^8	$150 \times 150 \times 96$	7	24	1000
10^9	$150 \times 150 \times 96$	9	16	400
10^{10}	$250 \times 250 \times 128$	7	11	200
10^{11}	$500 \times 500 \times 256$	5	11	100

Table 1: Summary of DNS cases with number of spectral elements, N_e, polynomial order, p, number of points inside the thermal boundary layer, N_{BL}, and the averaging time-period, Δt, in free-fall times.

The domain has a wide aspect-ratio $\Gamma = L/H = 4$, where L and H are the length and height respectively. We use no-slip, isothermal walls at the top and bottom, and periodic boundary conditions along the horizontal directions.We fix $Pr = 0.7$, while Ra ranges from 10^5 to 10^{11}. A summary of cases is indicated in Table 1.

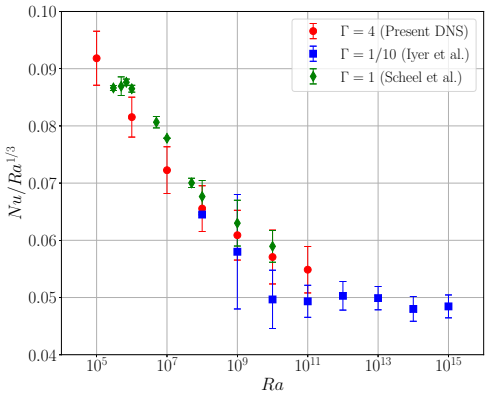

Figure 1: Linear-log plot of $Nu/Ra^{1/3}$ vs $log_{10}(Ra)$ along with the DNS data of simulations in closed cylinders with smaller aspect ratios of $\Gamma = 0.5$ of Scheel et al. [8] and $\Gamma = 0.1$ of Iyer et al. [9]

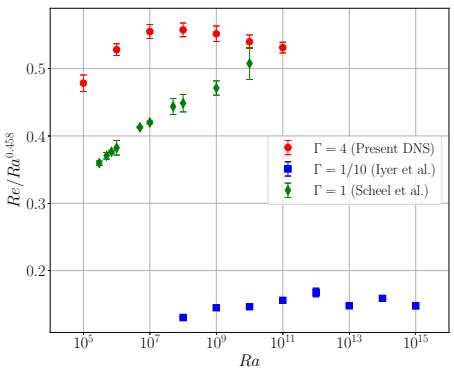

Figure 2: Linear-log plot of $Re/Ra^{0.458}$ vs $log_{10}(Ra)$ along with the DNS data of simulations in closed cylinders with smaller aspect ratios of $\Gamma = 0.5$ of Scheel et al. [8] and $\Gamma = 0.1$ of Iyer et al. [9]

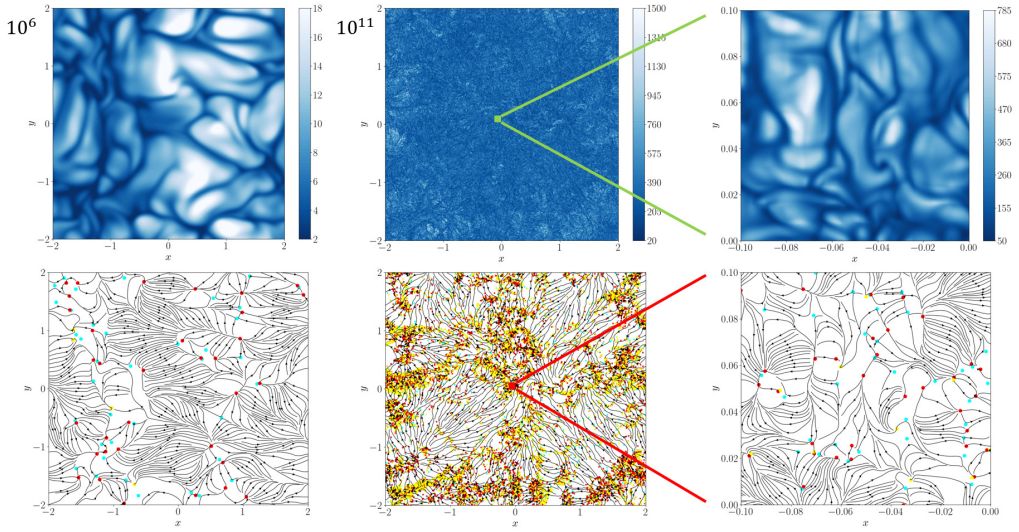

Figure 3: Temperature gradient (top row), and skin-friction field (bottom row) for $Ra = 10^6$ (left column), 10^{11} (middle column), and its zoomed-in section (right column). The critical points of the skin-friction, namely nodes (red), saddles (cyan), and foci (yellow) are also shown. The clustering of critical-points along elongated regions at $Ra = 10^{11}$ (middle column) indicate the presence of turbulent superstructures [11].

OVERVIEW OF RESULTS

The compensated scaling plots of Nusselt number (Nu) and Reynolds number (Re) in Figs. 1 and 2 respectively show that Nu scaling is approaching the classical 1/3 exponent at $Ra \approx 10^{11}$. Moreover, the Re scaling demonstrates the critical role of aspect ratio and confinement in the transport of momentum. The prefactors for $\Gamma = 4$ (from present work), 0.5 (from Scheel et al. [8]), and 0.1 (from Iyer et al. [9]) differ significantly.

To analyse the flow within the boundary layer, we consider the two-dimensional skin friction field $\mathbf{s}$ on the wall, defined from the wall shear stress $\boldsymbol{\tau}_w$ as

$$\mathbf{s} = \boldsymbol{\tau}_w / \rho\nu \quad \Rightarrow \quad \mathbf{s} = \left(\frac{\partial u_x}{\partial z}, \frac{\partial u_y}{\partial z} \right), \tag{1}$$

where ρ and ν are the density and kinematic viscosity respectively. We identify the critical points of $\mathbf{s}$ from the eigenvalues of its Jacobian [7, 10], and thus decompose the flow into nodes, saddles and foci. Consequently we see that the plume ridges are typically defined by groups of node-saddle-node triplets.

At the highest values of Ra, we discover that the critical points tend to cluster in long elongated regions of highly turbulent plume activity. Meanwhile the local patches with mean flow parallel to the plates have very little to no critical points. This clustering of critical points enables us to observe the edges of turbulent superstructures which emerge by averaging the flow field over short intervals of time [11].

Fig. 3 demonstrates the self-similarity of BL at high Ra. The first column shows the temperature gradient (top) and the skin-friction along with its critical points (bottom) over the full extent of the bottom wall for $Ra = 10^6$. The same pair of fields are shown for $Ra = 10^{11}$ in the middle column. Despite the highly turbulent nature of the flow, when we focus on a 0.1×0.1 section of the plate (the green and red boxes) and zoom into it (right column), we recapture the patterns and plume structures seen at lower Ra.

REFERENCES

[1]Kadanoff, L. P., "Turbulent heat flow: Structures and scaling," *Phys. Today*, **54**, 34–39 (2001).

[2]D. Lohse and K.-Q. Xia, "Small-scale properties of turbulent Rayleigh–Bénard convection," *Annu. Rev. Fluid Mech.*, **42**, 335–364 (2010).

[3]F. Chillà and J. Schumacher, "New perspectives in turbulent Rayleigh-Bénard convection," *Eur. Phys. J. E*, **35**, 58 (2012).

[4]M. K. Verma, A. Kumar, and A. Pandey, "Phenomenology of buoyancy-driven turbulence: recent results," *New J. Phys.*, **19**, 025012 (2017).

[5]P. Fischer, S. Kerkemeier, M. Min, Y.-H. Lan, M. Phillips, T. Rathnayake, E. Merzari, A. Tomboulides, A. Karakus, N. Chalmers, and T. Warburton, "Nekrs, a gpu-accelerated spectral element Navier–Stokes solver," *Parallel Computing*, **114**, 102982 (2022).

[6]P. F. Fischer, "An overlapping schwarz method for spectral element solution of the incompressible Navier-Stokes equations," *J. Comput. Phys.*, **133**, 84–101 (1997).

[7]M. S. Chong, J. P. Monty, C. Chin, and I. Marusic, "The topology of skin friction and surface vorticity fields in wall-bounded flows," *Journal of Turbulence*, **13**, N6 (2012).

[8]J. D. Scheel and J. Schumacher, "Predicting transition ranges to fully turbulent viscous boundary layers in low Prandtl number convection flows," *Phys. Rev. Fluids*, **2**, 123501 (2017).

[9]K. P. Iyer, J. D. Scheel, J. Schumacher, and K. R. Sreenivasan, "Classical 1/3 scaling of convection holds up to Ra=10^{15}," *Proc. Natl. Acad. Sci. U.S.A.*, **117**, 7594–7598 (2020).

[10]V. Bandaru, A. Kolchinskaya, K. Padberg-Gehle, and J. Schumacher, "Role of critical points of the skin friction field in formation of plumes in thermal convection," *Phys. Rev. E*, **92**, 043006 (2015).

[11]A. Pandey, J. D. Scheel, and J. Schumacher, "Turbulent superstructures in Rayleigh-Bénard convection," *Nat. Commun.*, **9**, 2118 (2018).

WORKSHOP
Direct and Large-Eddy Simulation 14
April 10-12 2024, Erlangen, Germany

DYNAMIC INTERPLAY OF MASS AND HEAT TRANSFER ALONG WITH REACTIONS IN AN AQUEOUS MDEA DROPLET DURING CO_2 ABSORPTION

S. Jafari[1], S. Zamani[2], L. Brandt[2,3], C. Duwig[1]
[1]Department of Chemical Engineering, Royal Institute of Technology (KTH), Stockholm, Sweden
[2]Department of Energy and Process Engineering, Norwegian University of Science (NTNU), Trondheim, Norway
[3]FLOW, Department of Engineering Mechanics, KTH Royal Institute of Technology, Stockholm, Sweden
sajadja@kth.se

INTRODUCTION TO THE METHODOLOGY

In the pursuit of mitigating carbon emissions, a crucial strategy is the utilization of amine-based solvents in the chemical absorption process, enhancing the overall efficacy of carbon capture technologies[1, 2]. Recent studies emphasize MDEA as an alternative with low heat absorption, high thermal stability, and minimal corrosion susceptibility [1]. However, understanding and modeling the absorption process, as depicted in Fig.1, is challenging because of the intricate aerothermochemical phenomena, encompassing phase transitions, chemical reactions, and multicomponent mixing. The complexity is further increased by the diverse temporal scales and spatial dimensions inherent these phenomena [2]. In response to these challenges, this study introduces a novel numerical approach: the 'Consistent Conservative Form of Two-Scalar Mass Transfer with a diffusive-interface Method,' based on the models in [3, 4], solving equations (1- (5)). This method aims to model CO_2 absorption by integrating the diffuse-interface method[3], Eq.(1), with a novel consistent conservative concept for transport equations. The latter introduces artificial source terms ($\mathbf{S}_{\vec{u}}$, $\mathbf{S}_h$) into momentum and enthalpy equations for improved consistency, as proposed by [4]. Hence, the objective is to integrate two scalar species, Eq. (2), governing mass transfer and species reaction(m, n species in liquid and gas phases), along with one scalar for momentum and enthalpy transports, Equations (4) and (5) .

$$\begin{cases} \frac{\partial \phi}{\partial t} + \nabla \cdot (\vec{u}_\Gamma \phi) = \\ \nabla \cdot \left\{ \Gamma \left[\epsilon(\nabla \phi) - \frac{1}{4} \left(1 - \tanh^2 \left(\frac{\psi}{2\epsilon} \right) \right) (\nabla \psi / |\nabla \psi|) \right] \right\}, \\ \psi = \epsilon \ln \left(\frac{\phi + \epsilon_0}{1 - \phi + \epsilon_0} \right) \rightarrow \epsilon_0 \approx 10^{-16}, \epsilon = \Delta x \end{cases} \tag{1}$$

$$\begin{cases} \frac{\partial c_{1,m}}{\partial t} + \nabla \cdot (\vec{u} c_{1,m}) = \nabla \cdot \left[D_{1,m} \left(\nabla c_{1,m} - \left(1 - \frac{\phi}{\epsilon} \right) \vec{n} c_{1,m} \right) \right] \\ \qquad + S_{J12} + S_R \\ \frac{\partial c_{2,n}}{\partial t} + \nabla \cdot (\vec{u} c_{2,n}) = \nabla \cdot \left[D_{2,n} \left(\nabla c_{2,n} + \frac{\phi}{\epsilon} \vec{n} c_{2,n} \right) \right] - S_{J12} \end{cases} \tag{2}$$

$$\begin{cases} S_{J12}(T, y_m) = A D_{12} \left[K_{eq}(T, y_m) c_2 \phi - c_{1,m}(1 - \phi) \right] \\ \qquad - D_{12} \nabla(\phi) \cdot \nabla(c_{1,m} + K_{eq}(T, y_m) c_2) \\ K_{eq}(T, y_m) = \begin{cases} \frac{RT}{H_{CO_2}(T, y_{mdea})} & \text{Absorption} \\ \frac{c_{1,m}}{\frac{P_{vap}(Y_{1,m}, T)}{RT}} = \frac{c_{1,m} RT}{Y_{1,m} P_{vap}(T)} & \text{Evaporation} \end{cases} \end{cases} \tag{3}$$

$$\begin{cases} \frac{\partial (\rho \vec{u})}{\partial t} + \nabla \cdot (\vec{u}(\rho \vec{u} - \mathbf{S}_{\vec{u}})) = -\nabla \mathbf{P} \\ \qquad + \nabla \cdot \left[\mu \left(\nabla \vec{u} + (\nabla \vec{u}^\top) - \frac{2}{3} (\nabla \cdot \vec{u}) \mathbf{I} \right) \right] \\ \mathbf{S}_{\vec{u}} = \gamma (\rho_l - \rho_g) \left[\epsilon \nabla(\phi) - \phi(1 - \phi) \nabla \cdot \left(\frac{\nabla(\phi)}{|\nabla(\phi)|} \right) \right] \end{cases} \tag{4}$$

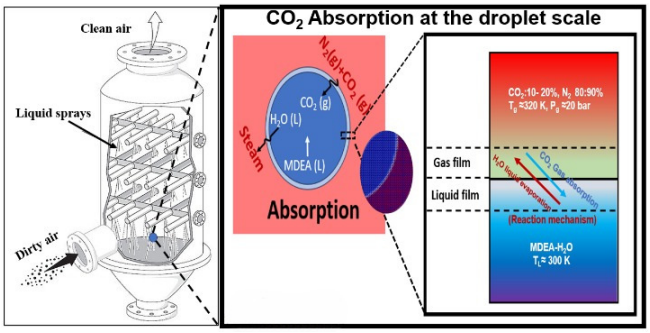

Figure 1: CO_2 Absorption on a single droplet

$$\begin{cases} \frac{\partial \rho h}{\partial t} + \nabla \cdot (\vec{u}(\rho h - \mathbf{S}_h)) = \nabla \cdot (k \nabla T) + H_R(y_m, T) \\ \mathbf{S}_h = \gamma (\rho_l C p_l - \rho_g C p_g) \left[\epsilon \nabla(\phi) - \phi(1 - \phi) \nabla \cdot \left(\frac{\nabla(\phi)}{|\nabla(\phi)|} \right) \right] \end{cases} \tag{5}$$

Two-scalar models (Eq. (2)) are essential in scenarios with significant diffusivity ratios in two-phase flows, here $D_{CO_2(g)}/D_{CO_2(l)} \approx 10^4$, preventing unphysical mass leakage. In contrast, under equilibrium conditions, encompassing both mechanical and thermal equilibrium (refer to Eqs. (4) and (5)) for momentum and enthalpy transport, a single scalar proves sufficient. In the two-scalar transport, a scalar transport term S_{J12} is introduced between phases, dependent on the Henry constant and diffusion coefficients (Eq. (3)) to predict interfacial mass transfer. Additionally, a mechanism of chemical reactions (Eq. (6)) for CO_2 absorption was incorporated to precisely interpret experimental absorption behaviors [6]. The model comprehensively considers all reversible chemical reactions, with the relevant physicochemical properties from existing literature [6].

$$\begin{aligned} CO_2(g) + H_2O + MDEA &\underset{K_1}{\overset{k_1}{\rightleftharpoons}} MDEAH^+ + HCO_3^- \\ CO_2(g) + OH^- &\underset{K_2}{\overset{k_2}{\rightleftharpoons}} HCO_3^- \\ HCO_3^- + OH^- &\overset{K_3}{\rightleftharpoons} CO_3^{2-} + H_2O \\ MDEAH^+ + OH^- &\overset{K_4}{\rightleftharpoons} MDEA + H_2O \end{aligned} \tag{6}$$

Moreover, the presence of mass transfer ($\dot{m}_\Gamma$) leads to a discontinuity in the velocity field, resulting in a non-zero divergent velocity($\nabla \cdot \vec{u}_\Gamma$) caused by interfacial mass flux, see Eq. (7).

$$\begin{cases} \nabla \cdot \vec{u}_\Gamma = \dot{m}_\Gamma \left(\frac{1}{\rho_{g,\Gamma}} - \frac{1}{\rho_{l,\Gamma}} \right) \delta_\Gamma \\ \dot{m}_\Gamma = \sum_{k=1}^{n} \dot{m}^k_{c_{l,g}} = -\sum_{k=1}^{n} D^k_{12} (\nabla c^k_l + \nabla c^k_g) M_{w,k} . n_\Gamma \end{cases} \tag{7}$$

Therefore, it is crucial to establish a mechanism that enables a comprehensive modeling of interfacial velocity calculations. This has been achieved through a divergence-free extension of the liquid velocity field across the entire domain [5]. Once the thermodynamic divergence is computed by Eq. (7), the momentum equation is solved using a standard pressure correction method [5].

$$\begin{cases} \hat{p} = \left(1 + \frac{\Delta t^{n+1}}{\Delta t^n}\right) p^n - \frac{\Delta t^{n+1}}{\Delta t^n} p^{n-1} \\ \vec{u^*} = \vec{u^{**}} - \frac{\Delta t^{n+1}}{\rho_0} \left[\left(1 - \frac{\rho_0}{\rho^{n+1}}\right) \nabla \hat{p} + \nabla p^n \right] \end{cases} \tag{8}$$

Notably, ρ_0 and $\hat{p}$ denote the minimum density across the computational domain and the extrapolated hydrodynamic pressure. Subsequently, the pressure is computed through a time-splitting technique, transforming the variable Poisson equation into one with constant coefficients.

$$\begin{cases} \nabla^2 p^{n+1} = \frac{\rho_0^{n+1}}{\Delta t} (\nabla \vec{u^*} - \nabla \vec{u_\Gamma}) \\ \vec{u^{n+1}} = \vec{u^*} - \frac{\Delta t^{n+1}}{\rho_0} \nabla p^{n+1} \end{cases} \tag{9}$$

This advances the Navier-Stokes equations in time to u^{n+1}, while the interface velocity, crucial for phase-field calculations, is determined through the computation of Stefan flow and extended velocity as follows, more details in Ref. [5].

$$\begin{cases} \nabla^2 p^{n+1}_{\text{stefan}} = -\frac{\rho^{n+1}}{\Delta t} (\nabla \vec{u}_\Gamma) \quad \rightarrow \\ \vec{u}^{n+1}_{\text{stefan}} = -\Delta t^{n+1} \left[\frac{1}{\rho^{n+1}} \nabla p^{n+1}_{\text{stefan}} \right] \\ \vec{u}^{\text{extend}} = \vec{u}^{n+1} - \vec{u}^{n+1}_{\text{stefan}} \\ \vec{u}_\Gamma = \vec{u}^{\text{extend}} + \frac{\dot{m}_\Gamma}{\rho^{n+1}_\Gamma} n_\Gamma \end{cases} \tag{10}$$

RESULTS AND DISCUSSION

The proposed methodology has undergone rigorous scrutiny to predict the absorption of CO_2 on a single MDEA droplet, as depicted in Fig.1. Specifically, a droplet is immersed in a N_2-CO_2 mixture at $T = 320\,\text{K}$, containing a mixture of MDEA-H_2O at $T = 300\,\text{K}$. In Fig. 2, the color velocity vector field reveals the Y-direction interface velocity, demonstrating the absorption of ambient CO_2 by the droplet. The intricate interactions with MDEA initiate the generation of reactions involving various chemical species, as depicted in Fig.3. According to the thermodynamics [6] shown in Fig.4(a), the decline in the diffusion coefficient of dissolved CO_2 in the MDEA+H_2O mixture, correlated with increasing MDEA compositions, is accountable for the decrease in absorbed CO_2 composition, as depicted in Fig.4(b), $C_{l,g}$is the total concentration in both liquid and gas phases. However, as illustrated in Fig.4(c), the HCO_3^- composition, indicative of the reaction, is enhanced with increasing MDEA compositions. This intriguing behavior, observed in CO_2 absorption, can be referred to as *self-regulation*. CO_2 absorption and consumption, influenced by reaction, regulate the process based on the system conditions. Furthermore, higher MDEA compositions lead to reduced water evaporation in the aqueous mixture, as depicted in Fig. 4(d). The results confirm the efficacy of the model.

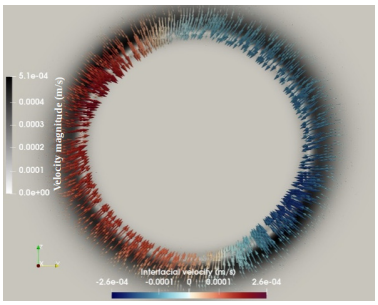

Figure 2: Absorption velocity vector on the droplet interface.

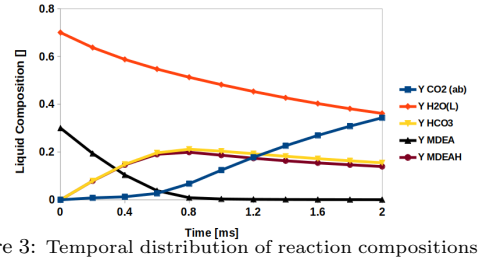

Figure 3: Temporal distribution of reaction compositions under conditions $C_g/C_l = 1000$, $C_l = 50\text{Mole/m}^3$, and $Y_{N_2} = 0.8$.

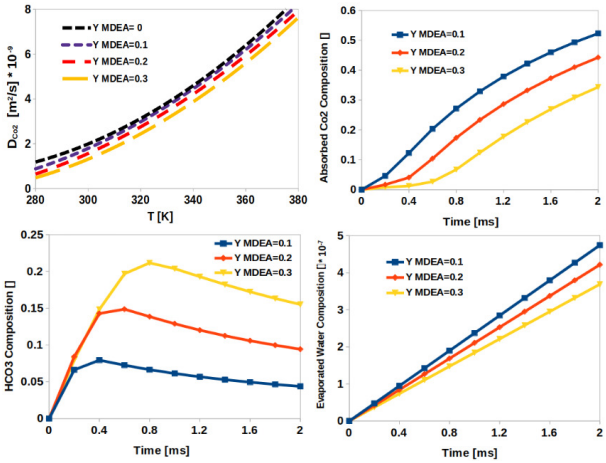

Figure 4: Distribution of the diffusion coefficient of dissolved CO_2 in the MDEA+H_2O mixture (**a**), absorbed CO2 (**b**), $HCO3^-$ (**c**) and evaporated water (**c**) compositions over time under $C_g/C_l = 1000$, $C_l = 50\text{Mole/m}^3$, and $Y_{N2} = 0.8$ for various Y_{MDEA} compositions.

REFERENCES

[1]Ramezani, R., Mazinani, S., Di Felice, R. : Density, Viscosity, pH, Heat of Absorption, and CO_2 Loading Capacity of Methyldiethanolamine and Potassium Lysinate Blend Solutions. *J. Chem. Eng. Data* **66**, 1611, DOI: 10.1021/acs.jced.0c00855.

[2]Stolaroff, J. K., Keith, D. W., Lowry, G. V.: Carbon Dioxide Capture from Atmospheric Air Using Sodium Hydroxide Spray. *Environ. Sci. Technol.* **42** (8), 2728–2735, DOI: 10.1021/es702607w (2008).

[3]Mirjalili, S., Jain, S. S., Mani, A.: A computational model for interfacial heat and mass transfer in two-phase flows using a phase-field method. *Int. J. Heat Mass Transf.*, **197**, 123326.

[4]Mirjalili, S., & Mani, A.: Consistent, energy-conserving momentum transport for simulations of two-phase flows using the phase field equations. *J. Comput. Phys.*, **426**, Article 109918 (2021). DOI: 10.1016/j.jcp.2021.109918.

[5]Scapin, N., Dalla Barba, F., Lupo, G., Rosti, M., Duwig, C., & Brandt, L.: Finite-size evaporating droplets in weakly compressible homogeneous shear turbulence. *J. Fluid Mech.*, **934**, A15 (2022). DOI: 10.1017/jfm.2021.1140.

[6]Kierzkowska-Pawlak, H., & Chacuk, A. (2011). Kinetics of CO_2 desorption from aqueous N-methyldiethanolamine solutions. *Chemical Engineering Journal*, **168**, 367-375. DOI: 10.1016/j.cej.2011.01.001

WORKSHOP
Direct and Large-Eddy Simulation 14
April 10-12 2024, Erlangen, Germany

DNS OF STABLY STRATIFIED TURBULENT FLOWS BEYOND THE OBERBECK-BOUSSINESQ ASSUMPTIONS

S. Kottursheltar[1], P. Costa[1], R. Pecnik[1]
[1]Process & Energy Department
Delft University of Technology, Leeghwaterstraat 39, 2628CB Delft, The Netherlands
s.b.kottursheltar@tudelft.nl

INTRODUCTION

Stratified turbulent flows are encountered in many environmental and industrial flows. Atmospheric boundary layer flows, and mixing of heat and salinity in the oceans are just a few common examples of environmental flows. On the other hand, in industrial settings, we come across these flows in heat exchangers, and in mixing tanks used in oil industries to blend liquids of different densities.

These examples and many others consider stratified wall-bounded turbulence, in which buoyancy acts towards suppressing the turbulence supplied by mechanical shear. In such cases, so-called stably stratified, the fluid layers are averse to mixing and would require energy to overcome a stable potential energy gradient. Here, buoyancy effects alter the structure of the flow, and consequently the dynamics of mass, heat, and momentum transport. Moreover, as density fluctuations become more severe, the so-called Oberbeck-Boussinesq (OB) approximation becomes inaccurate, leading to incorrect predictions.

In the current work, we developed and validated a numerical solver for direct numerical simulations (DNS) of turbulent flows featuring strong property variations. More precisely, we solve the Navier-Stokes (NS) equations in the limit of vanishing Mach number (so-called low-Mach (LM) number limit) with the thermophysical properties (density, viscosity, and thermal conductivity) prescribed as functions of temperature. The solver was then used to study stably-stratified turbulent channel flow under non-Oberbeck-Boussinesq conditions.

The interplay between the turbulence and gravity forces can be characterized in terms of three non-dimensional numbers namely, the shear Reynolds number (Re_τ), shear Richardson number (Ri_τ), and the Prandtl number (Pr), given as:

$$Re_\tau = \frac{u_{\tau 0} h}{\nu_0}, \qquad Ri_\tau = \frac{g \Delta\rho h}{\rho_0 u_{\tau 0}^2}, \qquad Pr = \frac{\nu_0}{\lambda_0}, \qquad (1)$$

where ρ_0, ν_0, λ_0 are reference fluid density, kinematic viscosity, and thermal diffusivity. $u_{\tau 0}$ is the initial shear velocity and is prescribed based on the mean pressure drop. g is the acceleration due to gravity and h is the half channel height. The density difference $\Delta\rho = \rho_b - \rho_t$, is due to the temperature difference between the bottom and top wall.

In the present work, a total of 8 cases corresponding to weakly/moderately stably-stratified turbulent flows are simulated at $Re_{\tau 0} = 180$ and $Pr = 0.76$, as listed in Table 1. We will vary the wall temperature ratios and adjust gravity to maintain similar Richardson numbers between cases, thereby isolating the effects of strong property variations in the flow dynamics. The $T_2/T_1 = 1.01$ case serves as a proxy for the OB approximation and is a benchmark for comparison with the variable property case ($T_2/T_1 = 2$). The dynamics of heat and momentum transport under strong stratification for these conditions is analyzed, also in light of DNS data of the same system under the OB regime.

Case	TR	Ri_τ	$Re_{\tau,cw}$	$Re_{\tau,hw}$	Ri_{bulk}
A0	$T_2/T_1 = 1.01$	0	180	180	0
A1		18	180	180	0.031
A2		36	180	180	0.056
A3		60	180	180	0.081
B0	$T_2/T_1 = 2$	0	194	166	0
B1		18	196	165	0.032
B2		36	195	167	0.057
B3		60	191	170	0.083

Table 1: Summary of cases simulated in the present work.

COMPUTATIONAL SETUP

Stably stratified turbulent flow is simulated in a horizontal straight channel as shown in Fig. 1. The domain size is kept fixed for all the cases. We perform simulations on a channel whose dimensions are $(L_x \times L_y \times L_z) = (4\pi h \times 4\pi h/3 \times 2h)$. The grid for all the cases contains $1024 \times 256 \times 240$ cells. The flow is driven by a constant pressure gradient in the streamwise direction, and gravity acts in the wall-normal direction. Periodic boundary conditions are imposed along the streamwise and spanwise directions. At the walls, no-slip and no-penetration boundary conditions are imposed.

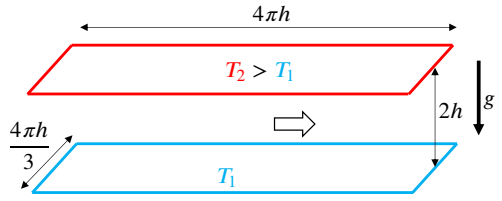

Figure 1: Schematic of the computational domain. The flow is driven by a constant pressure gradient between two isothermal walls.

NUMERICAL METHOD

The LM number approximation [1] of the NS equations is solved to understand the problem of stably-stratified turbulent channel flow in detail. The incompressible NS solver developed by Costa [2] was adapted to solve the LM number approximation. The original code was modified to accommodate large density variations. A third-order WENO scheme was implemented for convection terms in the energy transport equation to avoid discontinuities and have smooth gradients in the temperature field. A pressure-splitting algorithm [3] was implemented to deal with the variable coefficient Poisson equation. The equations are advanced in time using the fully explicit, second-order Adams-Bashforth method.

RESULTS

The buoyancy forces in stably stratified turbulent flows can cause local laminarization of flow, with a major impact on heat and momentum transfer rates. The contours of instantaneous temperature distributions on a $x-z$ cross-section of the channel located at $y = L_y/2$ for a neutrally buoyant case (Case B0) and the stratified case (Case B3) are shown in Fig. 2a and Fig. 2b. The direction of the mean flow is from left to right. The relative magnitudes of inertia and buoyancy forces determine the local behavior of the flow. At $Ri_\tau = 0$, the neutrally buoyant case, we observe that the temperature is well-mixed in the entire domain. In neutrally buoyant flows, the inertial forces are unopposed and the eddies are unconstrained in the entire height of the channel, resulting in larger mixing. With increasing Richardson numbers, the buoyancy forces oppose the inertial forces (for stable stratification). In the near-wall region of stratified flows, turbulence due to mechanical shear always dominates the buoyancy. Hence, the eddies in this region contribute to mixing, and we see that the flow structure resembles that of the neutrally buoyant case. Away from the walls, however, the shear weakens and the buoyancy starts to dominate. In this region, an interface develops, which, in a way, separates the channel into hot (top half) and cold (lower half) regions. The temperature appears to be homogeneously distributed in each of the halves, with a sharp transition at the interface (so-called thermocline). This results in density gradients that facilitate the initiation of so-called internal gravity waves (IGWs).

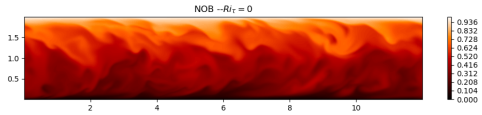

(a) Temperature contour for the case $Ri_\tau = 0$.

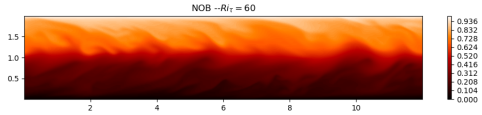

(b) Temperature contour for the case $Ri_\tau = 60$.

Figure 2: Instantaneous temperature contours on a $x-z$ cross-section of the channel located at $y = L_y/2$ for the neutrally buoyant ($Ri_\tau = 0$) and stably stratified ($Ri_\tau = 60$) cases.

It is also evident from Fig. 2b that the position of this thermocline is not at the channel half-height. Instead, it is shifted towards the hot wall. When the temperature difference between the walls is significant, and the thermophysical properties are functions of temperature, we can expect a difference between the shear stress at the top and the bottom walls. The variations in density and dynamic viscosity, result in the deviation of the point of zero stress away from the center of the channel. This is shown in Fig. 3. The shear stress at the cold wall is greater than at the hot wall because of the higher viscosity of the fluid at the cold wall; therefore, the interface is located further away from the cold wall. Aside from the shifting of the thermocline, we do not see any significant differences in the flow characteristics of OB and NOB cases. The comparable Ri_{bulk} values (Table 1) for cases with identical Ri_τ also hint towards the inference that the macroscopic effects do not change markedly.

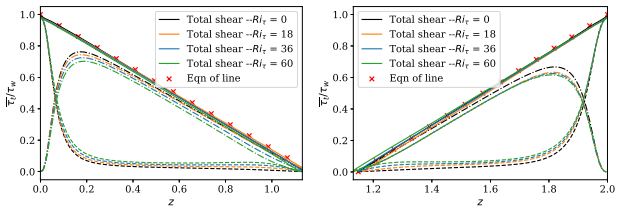

(a) Stress budget in the cold part. (b) Stress budget in the hot part.

Figure 3: Stress budgets for $Ri_\tau = 0,\ 18,\ 36,\ 60$ at $T_2/T_1 = 2$. $--$ is viscous shear stress and $-\cdot-$ is the Reynolds shear stress.

DISCUSSION

From the DNS at $Re_\tau = 180$ and $0 \leq Ri_\tau \leq 60$, with considerable property variations, we observed that the effect of gravity is mainly affecting the central region of the channel, just like for the OB case. The difference between the two cases is the position of the interface between the hot and cold subchannels, wherein the interface for the variable property case is closer to the hot wall. Hence, although the effect seemed identical, the location where the effect was seen was different. It has been reported in the literature that the eddies in the outer region, which are predominantly affected by buoyancy, can be characterized by Obukhov scaling [4]. We could not identify this region in our results due to the lack of scale separation at the simulated Reynolds number, as buoyancy interferes with the logarithmic region of the flow. Hence, we are currently performing DNS at higher Reynolds numbers. The goal is to understand local dominant balances arising from the interaction of buoyancy with eddies of different length scales in these flows.

REFERENCES

[1]McMurtry, P.A., Jou, W.-H., Riley, J., and Metcalfe, R.W. : Direct numerical simulations of a reacting mixing layer with chemical heat release, *AIAA J*, **24**(6), 962–970 (1986).

[2]Costa, P. : A FFT-based finite-difference solver for massively-parallel direct numerical simulations of turbulent flows. *Comput. Math. with Appl.*, **76**(8), 1853–1862 (2018).

[3]Demou, A.D., Frantzis, C., and Grigoriadis, D.G.E. : A low-Mach methodology for efficient direct numerical simulations of variable property thermally driven flows, *Int. J. Heat Mass Transf.*, **132**, 539–549 (2019)

[4]García-Villalba, M., and Del Álamo, J.C. : Turbulence modification by stable stratification in channel flow. *Phys. Fluids*, **23**(4), 045–104 (2011).

SESSION: Combustion and reactive flows I

Wednesday, April 10, 2024

10:00- 11:00

WORKSHOP
Direct and Large-Eddy Simulation 14
April 10-12 2024, Erlangen, Germany

A STOCHASTIC APPROACH TO INVESTIGATE THE EFFECT OF MICRO-MIXING ON THE SPARK EVOLUTION IN MIXTURE FRACTION SPACE

H.S.A.M. Awad[1], S. Gkantonas[1], E. Mastorakos[1]
[1] Department of Engineering
University of Cambridge, UK
hsama2@cam.ac.uk

INTRODUCTION

A thorough understanding of the ignition process at different operating conditions is important for designing reliable combustors. A modelling approach capable of capturing highly transient events such as extinction and ignition is the conditional moment closure (CMC). Most of CMC-based simulations represent the spark as a hot burning distribution in mixture fraction space without considering the initial kernel growth. Here, we investigate the initial spark evolution using an Energy Deposition (ED) model in mixture fraction space. The objective of the present study is (i) to investigate the effect of the scalar dissipation rate (SDR) statistics and the implications of the LES resolution on the spark evolution and (ii) to demonstrate the model performance by conducting an LES-CMC simulation for a bluff-body n-heptane spray swirl burner.

METHODS

The effect of SDR statistics on ignition behaviour is investigated using a zero-dimensional form of the CMC equations. The 0D-CMC equations are given as [1]:

$$\frac{\partial Q_h}{\partial t} = N|\eta \frac{\partial^2 Q_h}{\partial \eta^2}; \quad \frac{\partial Q_\alpha}{\partial t} = N|\eta \frac{\partial^2 Q_\alpha}{\partial \eta^2} + \dot{\omega}_\alpha|\eta \qquad (1)$$

where $Q_\alpha = Y_\alpha|\eta$ and $Q_h = h|\eta$ are the conditional expectation of mass fraction and enthalpy respectively with η being a sample space variable for the mixture fraction ξ. $N|\eta$ is the conditional expectation of SDR and it is modelled with the Amplitude Mapping Closure (AMC) model [1] as $N|\eta = N_0 G(\eta)$, with $G(\eta)$ being an error function and N_0 being $N|\eta$ at $\eta = 0.5$. The spark is represented by adding E_{spk} to the Q_h transport equation and it is assumed to follow a Gaussian distribution in ξ space as follows:

$$E_{\mathrm{spk}} = \frac{1}{\rho t_{\mathrm{sp}}} \frac{E_{\mathrm{d}}}{\sigma_s \sqrt{2\pi}} e^{-\frac{(\eta-\eta_s)^2}{2\sigma_s^2}} \qquad (2)$$

where E_{d} is the energy deposited in J/m^3, t_{sp} is the sparking duration taken as 0.4 ms following [2], η_s is the spark location and σ_s is the spark width in ξ space. The effect of plasma chemical kinetics on O_2 dissociation is represented by adding E_{O} and E_{O2} to Q_α transport equation:

$$E_{\mathrm{O}} = m \frac{Y_{\mathrm{O2}}}{Y^{\mathrm{f}}_{\mathrm{O2}}} \frac{E_{\mathrm{spk}}}{e_{\mathrm{O}}}; \; E_{\mathrm{O2}} = -\frac{W_{\mathrm{O}}}{W_{\mathrm{O2}}} E_{\mathrm{O}} \qquad (3)$$

Where m is the fraction of E_{spk} going into dissociation, $Y^{\mathrm{f}}_{\mathrm{O2}}$ is the O_2 mass fraction in the unburned mixture, and e_{O} is the specific internal energy for O. The influence of SDR statistics on the spark evolution is investigated by allowing N_0 to fluctuate in a stochastic manner. N_0 can be decomposed into resolved and sub-grid scale contributions as $N_0 = N_0^{\mathrm{r}} + N_0^{\mathrm{sgs}}$ where $N_0 \to N_0^{\mathrm{r}}$ and $N_0^{\mathrm{sgs}} \to 0$ if the filter size $\Delta \to 0$. The implication of LES resolution on spark evolution is investigated by considering the time-average ratio of $S_2 \equiv \langle N_0^{\mathrm{r}} \rangle / \langle N_0 \rangle$, which can be estimated according to Obukhov-Corrsin passive scalar spectrum. For well-resolved LES S_2 is about 14.5% suggesting that SGS effects are the main contributor to SDR. The influence of SDR fluctuation on spark evolution is considered by solving a stochastic differential equation (SDE) based on Stratonovich PDF and a log-normal assumption for the statistics of N_0^{r} as follows:

$$dN_0^{\mathrm{r}} = f(N_0^{\mathrm{r}})dt + \sigma_r \varphi(N_0^{\mathrm{r}}) dW_t \qquad (4)$$

where $f(N_0^{\mathrm{r}}) = -(logN_0^{\mathrm{r}} - \log(\langle N_0^{\mathrm{r}} \rangle / exp(0.5\sigma_r^2)) N_0^{\mathrm{r}} / \tau$ and $\varphi(N_0^{\mathrm{r}}) = \langle N_0^{\mathrm{r}} \rangle \sqrt{2/\tau}$. dW_t is a Wiener process, σ_r is the logarithmic distribution parameter for N_0^{r} and τ is the characteristic time scale taken as 0.25 ms. The LES-CMC is based on the experiment conducted by Marchione et al. [3] for n-heptane spray swirl burner. LES-CMC simulations are conducted by coupling OpenFoam 2.3.1 with an in-house CMC code called CLIO [1]. Before initiating the reaction simulations, a cold flow validation has been performed and reasonable agreement with experimental data is observed.

RESULTS

Figure 1 shows the maximum temperature evolution and N_0^{r} during t_{sp} at different filter widths for n-heptane. Changing the filter widths did not result in a significant effect on the spark evolution for the parameters considered here. However, there are some differences in terms of the autoignition delay time especially at higher filter width.

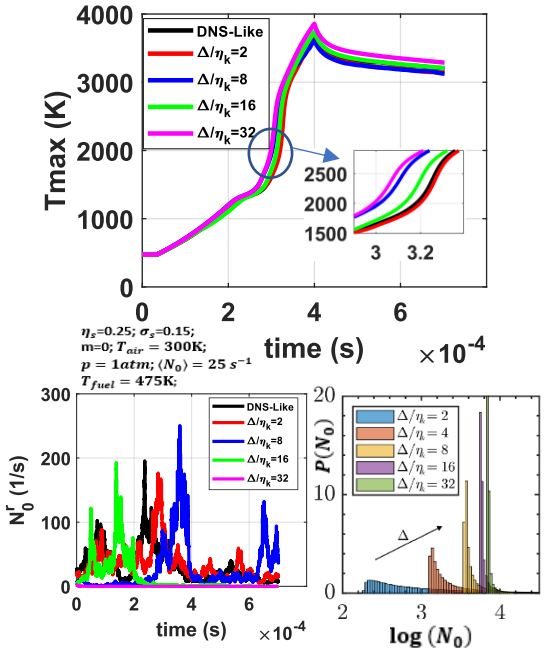

Figure 1 Tmax and N_0^{r} during t_{sp} at $E_{\mathrm{ign}} = E_{\mathrm{d}}/\rho_{\mathrm{u}} c_{\mathrm{p,u}} T_{\mathrm{u}}$=1.7. Bottom right: PDF of N_0 for LES-like Δ.

The spark width in ξ space can be related to the electrode spacing (d_{spk}) according to $N = D\,(\partial\xi/\partial x_{\mathrm{i}})^2 \sim D\,(\sigma_{\mathrm{s}}/d_{\mathrm{spk}})^2$. Figure 2 shows the spark evolution for fixed and variable σ_s, with d_{spk} taken as 1mm following [2]. For all cases, η_s is located in a non-flammable mixture fraction. However, due to the diffusion of heat and reactive scalars into flammable regions, successful ignition is achieved. That behaviour was also observed in laminar counterflow non-premixed flame at non-flammable spark locations in physical space [4]. The fixed σ_s cases correspond to the mean σ_s at a given η_s during t_{sp} (i.e., $\sigma_s = \langle\sigma_s\rangle_{\eta_s}$). Estimating σ_s based on the SDR can affect the outcome of ignition for the parameters considered, suggesting the importance of relating the sparking parameters in ξ space to the SDR for better model predictions. The flame kernel evolution for a successful ignition realization with a spark located at a distance of 5mm from the wall is shown in Figure 3. During early ignition stages, the spark is not significantly affected by the turbulence. However, later in time, the flame kernel undergoes a significant distortion until it gets convected into the central recirculation zone (CRZ). The flame kernel then evolves into the CRZ and a whole flame is established.

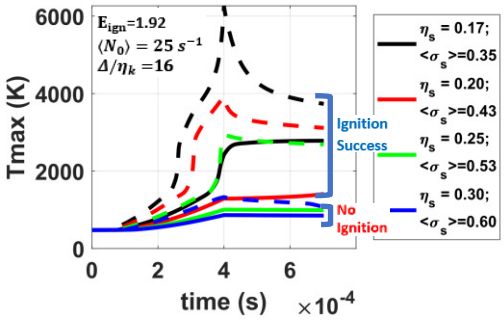

Figure 2 Tmax at fixed (solid) and variable (dash) σ_s.

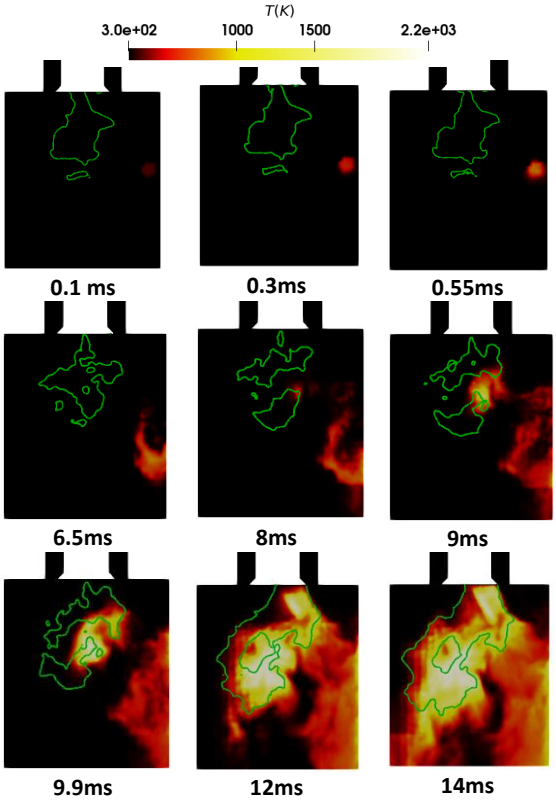

Figure 3. Successful ignition evolution at $E_{\mathrm{ign}} = 1.92$, $\eta_{\mathrm{s}} = 0.2$, $\sigma_s = 0.1$, $m = 0.1$, t_{sp}=0.5ms. Green line: ξ_{st} contour.

REFERENCES

[1] Giusti, A., Mastorakos, E. : Detailed chemistry LES/CMC 85 simulation of a swirling ethanol spray flame approaching 86 blow-off, Proc. Combust. Inst. 36, 2625-2632 (2017).

[2] Ahmed S. F., Mastorakos E. : Spark ignition of lifted 114 turbulent jet flames. Combust. Flame, 146, 215- 114(2006).

[3] Marchione T., Ahmed S. F., Mastorakos E. : Ignition of turbulent swirling n-heptane spray flames using single and multiple sparks,Combust. Flame 156,166-180 (2009).

[4] Richardson, E. S., E. Mastorakos. :Numerical investigation of forced ignition in laminar counterflow non-premixed methane-air flames." Combust. Sci. tech. 179, 21-37(2007).

WORKSHOP
Direct and Large-Eddy Simulation 14
April 10-12 2024, Erlangen, Germany

LES OF BLUFF-BODY STABILISED LEAN HYDROGEN FLAME SUBJECTED TO AN EXTERNAL EXCITATION

L. Caban[1], A. Wawrzak[1], and A. Tyliszczak [1]
[1]Department of Thermal Machinery, Czestochowa University of Technology, Poland
lena.caban@pcz.pl

INTRODUCTION

Active flow control methods have an advantage over passive methods, which rely on optimizing the flow domain for specific flow regimes. It is primarily due to the dynamic ability to adjust their control parameters, such as excitation amplitude and frequency, allowing for real-time adjustments to changing flow conditions, e.g., variations in an inlet velocity or temperature. Passive methods, on the other hand, lack this flexibility. However, the strategic benefit comes from integrating active and passive methodologies. This combined approach takes advantage of the cost-effectiveness of passive methods that operate without the need for additional energy. Simultaneously, it leverages the adaptive capabilities inherent in active technique, thereby increasing overall control efficiency in a wide range of flow regimes.

The study of the flame behavior in a bluff-body burner employing the combined passive and active flow control (sinusoidal velocity excitation) were performed recently by Kypraiou et al. [1]. They revealed a strong impact of the excitation on both a blow-off mechanism and stability limits. For the forced flames, the presence of velocity fluctuations introduces time-varying and spatially-varying equivalence ratio distributions, particularly in cases of imperfect premixing. In fully non-premixed systems, the time-varying mixing rates result in a time-varying heat release rate. Kypraiou et al. [1] examined the forced response of systems characterized by varying levels of premixing to explore the mechanisms influencing flame stability. They found that the non-premixed configuration with an axial fuel injection is characterized by a longer blow-off transient compared to the flame with a radially injected fuel. Furthermore, the blow-off duration in an excited configuration was much longer than the average blow-off duration of unforced non-premixed flames. This suggests that the type of injection and the degree of premixedness, which can be enhanced by the excitation, are crucial for the blow-off dynamics.

In the present work, we focus on a geometry of the injection system and the application of a harmonic forcing, as both these factors are expected to have an important impact on the flame dynamics and stability. Figure 1 shows two analyzed bluff body configurations, a typical cylindrical bluff body, similar to the one used in [1], and a novel star-shaped bluff body. In both the cases the fuel is injected axially. Shedding of small-scale vortices (SV) at the sharp corners changes the flow pattern significantly by destroying the large-scale structures formed in the inner and outer shear layers (IV, OV) [2].

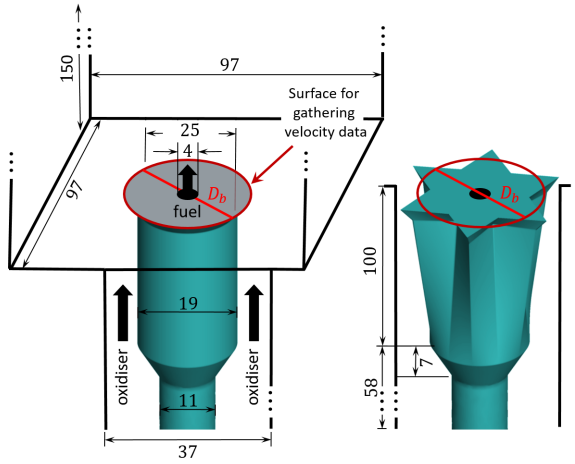

Figure 1: Cylindrical and star-shaped bluff-bodies.

Additionally, the effect of air fluctuations on the behavior of the flames is investigated for various forcing amplitudes and frequencies. The application of external excitation amplifies the formation of strong turbulent structures [3]. They enhance transport of the oxidizer towards the recirculation zone formed in a bluff-body wake. Employing the large-eddy simulation (LES) method, the study offers detailed insights into the complex physics of unsteady flow for a wide range of the control parameters. In order to address the influence of air flow oscillations on the blow-off behavior, we impulsively change the velocity of fuel and/or oxidizer, and thus, create conditions close/far from blow-off.

COMPUTATIONAL CONFIGURATION

Geometrical details of the cylindrical and star-shaped bluff-bodies along with the dimensions of the computational domain are presented in Fig. 1. Both shapes are characterized by the same surface area of the upper bluff body wall ($S_b = \pi D_b^2/4$, $D_b = 25$ mm). The basic cylindrical configuration corresponds to the experimental setup [1] used to determine the blow-off limit of a methane flame. Nevertheless, we introduce two important changes to the original configuration. In the present work, a hydrogen flame is analyzed due to the increasing interest in the use of hydrogen to reduce CO_2 emissions. Fuel is a mixture of hydrogen and nitrogen ($Y_{H_2} = 0.11$, $Y_{N_2} = 0.89$, Y-mass fraction) and is injected into the combustion chamber

through a central fuel pipe of diameter $D_f = 4$ mm. The oxidizer (air) flows around the bluff body and enters the combustion chamber through a flat slot. Additionally, we removed a swirler that was mounted in [1], since the star-shaped bluff-body dumps the swirl completely.

SOLVERS

The computations are performed in a two-stage procedure involving ANSYS software and an in-house high-order code SAILOR. In the first stage, the ANSYS Fluent is used to model the flow around the bluff body using the wall-adapting local eddy-viscosity (WALE) sub-grid model and to generate a time-varying velocity signal at the oxidiser channel exit. This signal is treated as the boundary condition imposed on the inlet plane of the main computational domain (combustion chamber, $L_x \times L_y \times L_z = 97 \times 97 \times 150$ mm) for the second stage of computations where the combustion process is modeled using the SAILOR code. This code is based on high-order compact differences on half-staggered meshes, the time integration is performed using the predictor-corrector approach combined with the projection method for pressure-velocity coupling [4]. The chemical source terms are integrated in time using the VODPK solver, chemical reaction terms are computed with the help of the CHEMKIN interpreter and the hydrogen combustion process is modeled using a detailed chemical mechanism of Mueller et al. [5] involving 9 species and 21 reactions. The chemical source terms representing the net rate of formation and consumption of species are computed using the filtered variables (the laminar chemistry model). There is no experimental data for the hydrogen combustion in the selected configuration. However, to ensure the reliability of the current analyses and to verify the two-stage simulation procedure, the conference presentation will include the results of computations conducted for a benchmark problem (Sydney flame (`https://web.aeromech.usyd.edu.au/thermofluids/bluff.php`)).

RESULTS

Figure 2 presents a structure of the unforced flow downstream cylindrical and star-shaped bluff-bodies visualized by the Q-parameter ($Q = 0.2$ s^{-2}). In the case of the cylindrical shape, one can observe strong toroidal vortices (IV and OV) accompanied by rib vortices (RV). Undoubtedly, for this classical geometry, the mixing process is directed by periodically generated vortices resulting from Kelvin-Helmholtz instability. Contrary, the application of a sharp-corner geometry leads to the formation of small, high-frequency vortices, fostering intense small-scale mixing. As can be observed in Fig. 2, star-shaped bluff-body destroys IV due to the azimuthal instability and the flow contains more small-scale vortices (SV). Figure 3 shows the time averaged axial and radial velocities (U, V_r), mixture fraction (F), and temperature (T) at the distance $0.5D_b$ downstream the bluff-bodies. In the star-shaped configuration, the profiles are shown along two characteristic radii r_1 and r_2. In the region where $r/R_b < 0.8$, both configurations exhibit very similar velocity profiles. Notable differences become apparent only in the oxidizer stream, specifically within the range $1.0 < r/R_b < 1.5$. In the r_2 direction, the axial velocity profile displays a local maximum at $r/R_b = 1.4$. This maximum is preceded by a local minimum in the radial velocity at $r/R_b = 1.15$ indicating flow toward the center of the domain. This behavior is attributed to the flow dynamics around the triangular part of the bluff-body and results in lower temperatures than those observed along r_1 in both configurations. Our findings highlight the significant role of star-shaped bluff-body in flame dynamics, reducing the average temperature by about 200 K. This reduction can potentially mitigate the thermal production of NOx, emphasizing the importance of the bluff-body shape for optimizing the combustion processes. This work stands as part of our ongoing efforts to explore bluff-body influence. The next step is to extend the investigation to flames with external modulations under lean conditions.

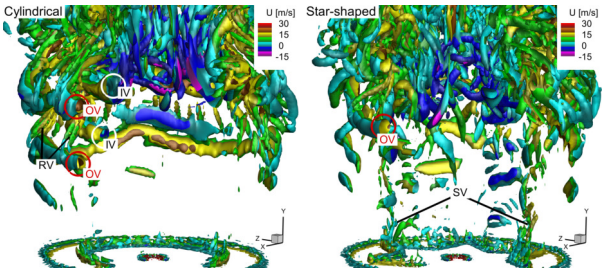

Figure 2: Flow structure (Q-parameter colored by the axial velocity) downstream cylindrical and star-shaped bluff-bodies.

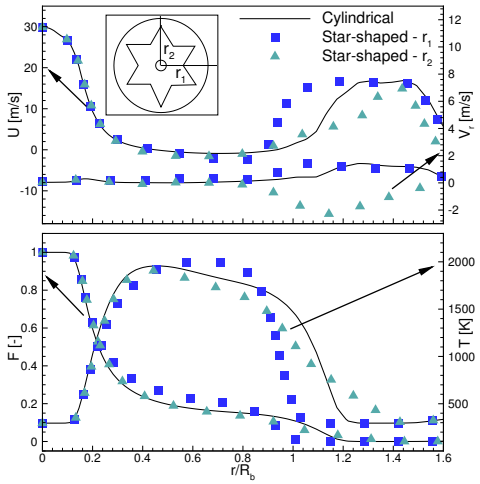

Figure 3: Profiles of time-averaged axial and radial velocity (U,V_r) (upper figure), mixture fraction (F) and temperature (T) (lower figure) along r_1 and r_2 at location $y/D_b = 0.5$.

REFERENCES

[1]Kypraiou, A. M., Giusti, A., Allison, P. M. and Mastorakos, E.: Dynamics of acoustically forced non-premixed flames close to blow-off, *Exp. Therm. Fluid Sci.***95**, 81–87, (2018).

[2]Wawrzak, A., Kantoch, R. and Tyliszczak, A.: LES of a non-premixed hydrogen flame stabilized by bluff-bodies of various shapes, *Tech. Mech.* **43**, 128–137, (2023).

[3]Tyliszczak, A. and Wawrzak, A.: A numerical study of a lifted H2/N2 flame excited by an axial and flapping forcing, *Sci. Rep.* **12**, 2753, (2022).

[4]Tyliszczak, A.: A high-order compact difference algorithm for half-staggered grids for laminar and turbulent incompressible flows, *J. Comput. Phys.*, **276**, 438–467, (2014).

[5]Mueller M. A., Kim T. J., Yetter R. A., and Dryer F. L.: Flow reactor studies and kinetic modeling of the H2/O2 reaction, *Int. J. Chem. Kinet.*, **31**(2), 113–125 (1999).

WORKSHOP
Direct and Large-Eddy Simulation 14
April 10-12 2024, Erlangen, Germany

TURBULENT SPRAY FLAME INFLUENCE ON NANOPARTICLE SYNTHESIS: A DNS INVESTIGATION

A. Abdelsamie[1,2], **D. Thévenin**[1]
[1]Lab. of Fluid Dynamics and Technical Flows,
University of Magdeburg "Otto von Guericke", D-39106 Magdeburg, Germany
[2]Lab of Fluid Mechanics, Mechanical Power Engineering Department,
Faculty of Engineering (Mataria), Helwan University, 11311, Cairo, Egypt
abouelmagd.abdelsamie@ovgu.de

INTRODUCTION

Nanoparticle materials play a crucial role in both industrial and everyday applications, including cancer therapy, drug delivery, carbon black production, catalysts for chemical reactors, and color pigments in paints. Key factors influencing such applications depend on various parameters: thermodynamics and chemical properties, as well as shape and size of these nanoparticles [1]. When relying on combustion, nanoparticles can be generated by introducing specific precursors into the fuel prior to reaction in order to create distinct nanoparticle materials. The characteristics of these produced nanoparticles are contingent upon the combustion properties. Two common types of combustion are typically employed to produce these nanoparticles: either gaseous combustion [2, 3], or liquid spray combustion [1, 4]. The gaseous combustion technique involves a gas-phase process that necessitates precursors either in gaseous form or capable of vaporization, subsequently mixed with combustion gases before reaction within the chamber. However, these volatile precursors are limited to a few elements and are typically derived from costly, corrosive, and/or toxic sources, such as metal chlorides, metal organics, or organometallic compounds. Therefore, the research focus was later extended toward nanoparticle synthesis from spray flames [1, 4, 5, 6], allowing to overcome most of the problems listed above.

In the current work, a configuration similar to the reference SpraySyn burner considered in a collaborative German Research Initiative [4] will be employed to investigate the impact of the turbulent spray flame structure on nanoparticle synthesis.

MATHEMATICAL AND PHYSICAL APPROACHES

In this work, the Navier-Stokes equations are solved while taking into account all relevant physicochemical scales in space and time for the gas phase (i.e., Direct Numerical simulation – DNS – approach). The liquid droplets, being noticeably smaller than the grid resolution, are modeled as point particles. The open-source library Cantera 2.4.0 is used to compute all chemical reactions, thermodynamic terms, and molecular transport processes in the gas phase. The continuous (gas) phase is solved by DNS in a standard manner (Eulerian frame), as described in [7]; whereas the disperse (droplet) phase is tracked in a Lagrangian frame (Discrete Particle Simulation, DPS [1]). Hence, the resulting simulations correspond to the DNS-DPS approach. A two-way coupling between both phases is implemented via the exchange of mass, momentum, and energy. All details regarding the implemented equations describing droplet location, momentum, mass transfer, and heat transfer can be found in previous publications [1]. Concerning the solid phase (nanoparticles), the model developed by Kruis et al. [9] has been employed in this work.

The in-house DNS code DINO [7] was employed in this study to simulate the three aforementioned phases (gaseous, liquid spray, and solid nanoparticles). The simulations discussed here employed a 6th-order central finite-difference method for spatial discretization. For time integration, an explicit 4th-order Runge-Kutta method was used.

NUMERICAL SETUPS

In the standard SpraySyn burner, the solvent is ethanol, which is injected in the form of liquid droplets together with a dispersion gas (pure O_2 for standard conditions) through the central SpraySyn injector. The liquid is evaporated by a pilot flame burning a CH_4/Air mixture under lean conditions (equivalence ratio of 0.25). A pseudo-3D computational domain with dimensions of 4.5 cm (transverse direction) × 9.0 cm (streamwise direction) × 0.064 cm (crosswise direction) is employed, which is discretized over 268 million equidistant grid points, leading to a homogeneous resolution of 22 μm. All simulated cases have a Kolmogorov length scale between 23 and 25 μm, so that the Kolmogorov length scale is properly resolved in these simulations; the same applies to the gas reaction zones. On the other side, for the employed Lagrangian approach for the spray, the ratio of the maximum droplet diameter to grid resolution should not exceed 0.5 [10]. The selected grid resolution in the current work is a suitable compromise for resolving the Kolmogorov scale while ensuring the validity of the Lagrangian approach. The numerical domain is combined with inflow/outflow boundary conditions in streamwise direction, symmetry conditions along the vertical direction, and periodicity in crosswise direction. The computational domain is shown in Fig. 1 together with an instantaneous temperature profile to illustrate the employed computational layout. To reduce computational costs, the inner geometry of the burner is not considered in the present study; the computational domain starts just above the burner

outlet.

RESULTS AND DISCUSSIONS

To investigate the impact of the flame structure on nanoparticle properties, three different cases were tested by changing the dispersion gas composition: Case I (O_2), Case II (CH_4:1.52/O_2:8.), and Case III (Air). Figure 2 shows the temperature contours for these cases and the corresponding distribution of nanoparticle aggregate diameter (histogram). As can be observed from the left side of this figure there are significant differences in the turbulent flames and even qualitative changes in structure due to the different dispersion gas composition. These changes lead in turn to noticeable modifications in the nanoparticle size distribution. Consequently, this would have an impact on practical applications. This will be explained in more detail during the conference.

REFERENCES

[1]Abdelsamie, A., Kruis, F.E., Wiggers, H. and Thévenin, D.: Nanoparticle formation and behavior in turbulent spray flames investigated by DNS, *Flow Turbul. Combust.*, **105**, 497–516 (2020).

[2]Kammler, H.K, Mädler, L. and Pratsinis, S.E.: Flame Synthesis of Nanoparticles, *J. Chem. Eng. Technol.*, **24**(6), 583–596, (2001).

[3]Li, S., Ren, Y., Biswas, P. and Tse, S.D.: Flame aerosol synthesis of nanostructured materials and functional devices: Processing, modeling, and diagnostics, *Prog. Eng. Combust. Sci.*, **55**, 1–59, (2016).

[4]Schneider, F., Suleiman, S., Menser, J, Borukhovich, E., Wlokas, I., Kempf, A., Wiggers, H. and Schulz, C.: SpraySyn-A standardized burner configuration for nanoparticle synthesis in spray flames, *Rev. Sci. Instrum.*, **90**, 085108 (2019).

[5]Stodt, M.F.B., Liu, C., Li, S., Mädler, L., Fritsching, U. and Kiefer, J.: Phase-selective laser–induced breakdown spectroscopy in flame spray pyrolysis for iron oxide nanoparticle synthesis, *Proc. Combust. Inst.*, **38**(1), 1711–1718 (2021).

[6]Gonchikzhapov, M. and Kasper, T.: Decomposition Reactions of Fe(CO)5, Fe(C5H5)2, and TTIP as Precursors for the Spray-Flame Synthesis of Nanoparticles in Partial Spray Evaporation at Low Temperatures, *Ind. Eng. Chem. Res*, **59**(18), 8551–8561 (2020).

[7]Abdelsamie, A., Fru, G., Oster, T., Dietzsch, F., Janiga, G. and Thévenin, D.: Towards direct numerical simulations of low-Mach number turbulent reacting and two-phase flows using immersed boundaries, *Comput. Fluids*, **131**, 123 – 141 (2016).

[8]Abdelsamie, A., Kuns, S., Gonchikzhapov, M., Kasper, T., Karaminejad, S., Endres, T., Wiggers, H. and Thévenin, D.:Comparing Direct Numerical Simulation of the SpraySyn burner with experimental data to investigate the impact of dispersion gas composition on nanoparticle synthesis, *Appl. Energy Combust. Sci.*, under review, 2023.

[9]Kruis, F.E., Kusters, K.A., Pratsinis, S.E. and Scarlett, B.:A Simple model for the evolution of the characteristics of aggregate particles undergoing coagulation and sintering, *Aerosol Sci. Tech.*, **19**(4), 514–526 (1993).

[10]Abdelsamie, A. and Thévenin, D.: Direct numerical simulation of spray evaporation and autoignition in a temporally-evolving jet, *Proc. Combust. Inst.*, **36**(2), 2493–2502 (2017).

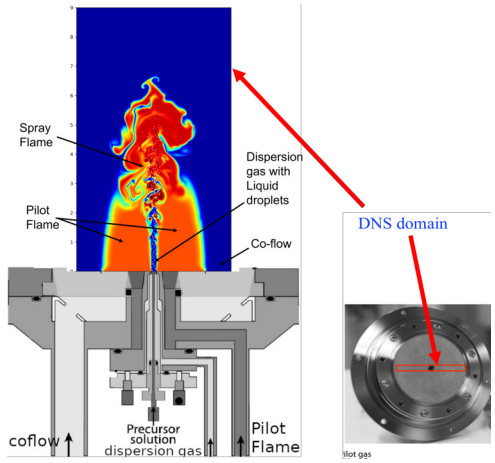

Figure 1: Schematic diagram of the computational domain.

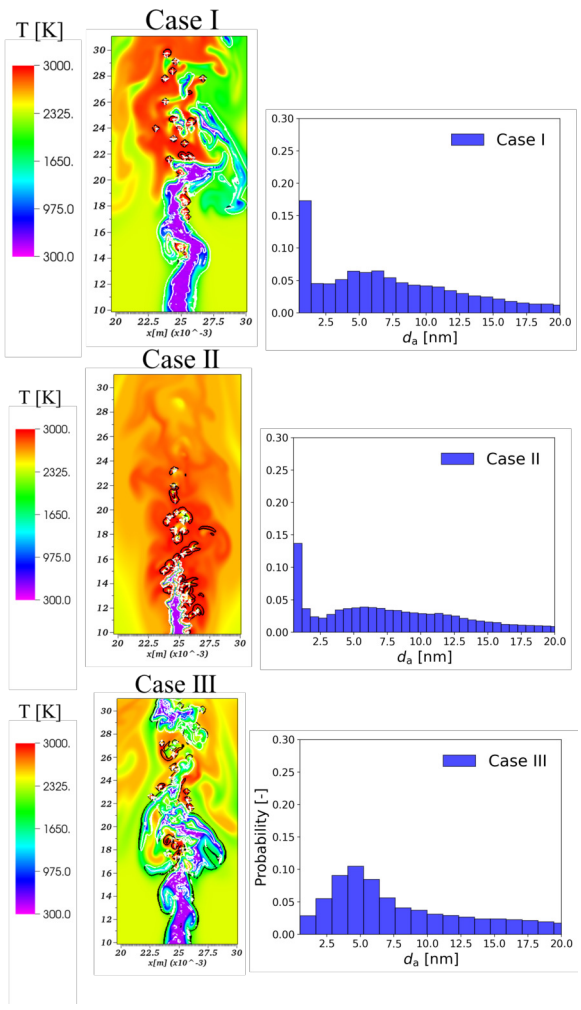

Figure 2: Left: Temperature contour for the three cases under investigation. Right: Histogram of the aggregate diameter of the nanoparticles for the same cases. The data are at quasi-steady state.

WORKSHOP
Direct and Large-Eddy Simulation 14
April 10-12 2024, Erlangen, Germany

EFFECTS OF TURBULENCE ON EARLY FLAME KERNEL DEVELOPMENT OF LEAN HYDROGEN MIXTURE UNDER ENGINE-RELEVANT CONDITIONS

I. Kavroulakis[1], D. Papageorgiou[1], M. Bode[2], Christos E. Frouzakis[3], A. Tomboulides[1]
[1]Department of Mechanical Engineering, Aristotle University of Thessaloniki, Thessaloniki 54124, Greece
[2]Jülich Supercomputing Centre (JSC), Forschungszentrum Jülich (FZJ) GmbH, Germany
[3]Combustion and Acoustics for Power & Propulsion Systems Laboratory, ETH Zürich, Switzerland
ikkavroul@meng.auth.gr

ABSTRACT

A comprehensive series of direct numerical simulations (DNS) is performed to investigate the early flame kernel development (EFKD) in a lean premixed H_2-air mixture in decaying homogeneous isotropic turbulence (HIT) and engine-relevant thermodynamic conditions. Systematic variations of turbulent intensity (u'/S_l) and integral length scale (l_t) within the ranges of 3 to 12 and 15 to 28, respectively, resulting in Ka between 1.9 and 21. Elevated values of u'/S_l lead to increased flame convolution and small-scale wrinkling, while higher l_t values contribute to a smoother flame surface. Higher Ka values correlate with intensified fuel consumption, driven by accelerated flame surface expansion from enhanced wrinkling and increased local consumption speed due to differential diffusion effects.

1. INTRODUCTION

The restricted knowledge of turbulence-flame front interactions and, consequently, cycle-to-cycle variations (CCV) during the early flame kernel developement (EFKD) phase stems from the inherent multiscale and multiphysics nature of turbulent reactive flows that intricately characterize the combustion process within spark-ignition (SI) interna combustion engines (ICEs). Nevertheless, leveraging the capabilities of current Petascale supercomputers and the ongoing shift towards Exascale architectures, recent and anticipated developments in High-Performance Computing (HPC) are poised to open new frontiers in the simulation of combustion systems. As a result, direct numerical simulations (DNS) are turning into an essential tool for combustion simulations, facilitating the incorporation of more realistic conditions, such as higher Reynolds numbers and thermodynamic pressure, and concurrently mitigating the model uncertainties that arise from large-eddy simulations (LES) and Reynolds-Averaged Navier–Stokes (RANS) simulations.

In this vein, a recent series of EFKD DNS for rich iso-octane-air [1] and lean hydrogen-air mixtures [2] under engine-relevant conditions were conducted to explore the effects of differential diffusion on the behavior of flame kernel evolution. Results reveal that lean hydrogen-air flames, due to the formation of strong thermodiffusive effects, lead to more wrinkled flame kernels and therefore faster flame kernel propagation, while iso-otain mixtures tend to recover their laminar behaviour. Moreover, Ozel-Erol et al. [3] explored the impact of water droplet injection on the propagation rate of statistically planar stoichiometric n-heptane-air flames under various turbulent intensities. Their findings indicate that water droplets do not significantly alter the relationships between displacement speed, curvature, and strain rate.

The main objective of this study is to explore the variations induced by turbulence during the EFKD phase in lean hydrogen-air mixtures across various turbulent regimes and assess their influence on the evolution of flame kernels. This is accomplished by utilizing DNS of H_2-air mixture to investigate turbulence-flame interactions under conditions relevant to SI ICEs in decaying HIT.

2. SIMULATION METHODOLOGY

The formation and early propagation of a set of lean premixed lean H_2-air flame kernels were investigated in a decaying HIT field with varying turbulent fluctuations u' and integral length scales l_t, presented in Table 1 which correspond to the thin reaction zone regime, frequently observed in ICEs [4]. The initial HIT flow field is generated in a periodic box of size using the forced HIT turbulence approach of [5]. The initial thermodynamic conditions ($T_u = 800$ K, $p = 40$ atm) are relevant for hydrogen ICE closely resembling those used by Chu et al. [2]. The laminar flame thickness $l_f = (T_b - T_u)/(d/dx)_{max} = 2 \times 10^{-3}$ cm, taken as the reference length scale, is based on the adiabatic flame temperature T_b and the maximum temperature gradient across the planar flame. These quantities along with the laminar flame speed $S_L^0 = 44$ cm/s were computed with PREMIX [6] using the detailed mechanism of [7] resulting in a flame time $t_f = l_f/S_L^0 = 45 \times 10^{-6}$ s. The ignition of the flame kernels is achieved by a heat source term varying smoothly in space and time [8] in the centre of the computational domain, which is active until $t = 0.3t_f$ and forms spherical kernels with an initial radius of $5l_f$. Soret effect is also ecountered for the differential diffusion of the light species H and H_2.

The DNS were carried out using the highly efficient parallel solver Nek5000 [9], where a high-order splitting scheme for low-Mach-number reactive flows [10] is utilized to decouple the hydrodynamic and thermochemistry equation subsytems and the solution, data and geometry are locally expressed in a structured mesh as sums of N^{th} order tensor products of Legendre polynomials, based on the Gauss–Lobatto–Legendre

Case	$\frac{u'}{S_L^0}$	$\frac{l_t}{l_f}$	$\frac{l_t}{\eta}$	Re_t	Ka	Da
U3L15	3	15	47	170	2.6	5
U6L15	6	15	79	341	7.4	2.5
U12L15	12	15	133	682	21	1.3
U3L28	3	28	75	318	1.9	9.3
U6L28	6	28	127	636	5.4	4.7
U12L28	12	28	213	1273	15.3	2.3

Table 1: Summary of DNS turbulent characteristics. η: Kolmogorov length scale, Re_t: turbulent Reynolds number, Ka: Karlovitz number, Da: Damköhler number

(GLL) quadrature points. For the current parametric analysis, a spherical computational domain was adopted instead of a periodic box, allowing the imposition of outflow boundary conditions. Consequently, this methodology maintains a constant thermodynamic pressure within the simulated domain throughout the duration of the simulation and mitigates any impact on the kernel arising from flame to flame interactions, attributed to the periodicity. Thus, zero-Neumann BCs are imposed on all variables on the outer boundaries. Legendre-Lagrangian polynomials of order $N = 9$ were utilized, equivalent to an effective resolution of 10 GLL points per thermal flame thickness.

RESULTS

To assess the influence of turbulence-flame front interactions across diverse turbulent regimes, an analysis was conducted on various global quantities derived from the flame surface density model (FSD). This analysis included parameters such as global consumption speed, wrinkling factor, stretch factor, as well as several local quantities. It is essential to note that this abstract provides only a concise overview, highlighting a limited portion of the comprehensive results obtained.

Figure 1: Iso-surface of H_2 corresponding to it's maximum reaction rate at $t = 1.5t_f$ colored with normalized heat release rate HRR/HRR_0 for the different cases.

Visualizations of the early flame kernels under distinct turbulent conditions are depicted in Figure 1. It is evident that in instances characterized by heightened Ka number, the kernels exhibit an increased propensity for wrinkling, leading to larger flame surface areas, as illustrated from the wrinkling factor in Figure 2. Elevated turbulence intensity (u'/S_L) facilitates surface convolution as the flame traverses an eddy, whereas an increase in turbulent integral length scale (l_t/l_f) appears to exhibit a contrasting effect, diminishing small-scale wrinkling and contributing to a more uniform and smooth flame surface. The distinctive variations in flame area promptly affect the HRR and consequently influence the global flame consumption speed S_c, which is a key quantity of practical and fundamental interest in engine and combustion applications in general. It is important to highlight that, until around $t = 0.5$, the elevated initial consumption speeds can be attributed to the ignition effect, a period beyond the current study's scope.

Subsequent to the dissipation of the ignition effects, S_c rises, closely mirroring the ascending trend of Ξ. A clear trend is apparent, indicating that turbulence enhances the fuel consumption rate, increasing turbulent flame speed S_T up to four times when comparing the cases U3L28 and U12L15, which have the lowest and highest Ka respectively.

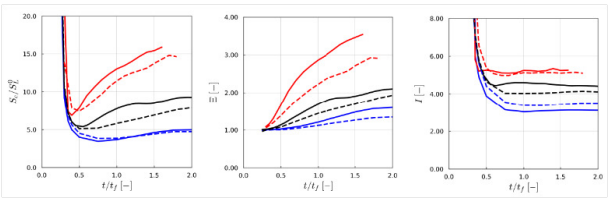

Figure 2: Evolution of the global consumption speed (left), wrinkling factor (middle) and stretch factor (right) in time for the different cases. Red lines: $u'/S_L = 12$, black lines: $u'/S_L = 6$, blue lines: $u'/S_L = 6$. Solid lines: $l_t/l_f = 15$, dashed lines: $l_t/l_f = 28$.

Rather than being solely influenced by the total area, S_c can be significantly impacted by changes in the local flame displacement speed on the flame front, arising from the interplay of differential diffusion and turbulent mixing effects. This influence can be quantified by the global stretch factor I. The significant non-unity stretch factors observed are indicative of the thermodiffusive effects of the lean-hydrogen mixture, which alter the local flame behaviour from that of its unstreched laminar counterpart, and becomes more apparent with increasing Ka, indicating the synergy between turbulence and thermodiffusive effects in agreement with [11], in contrast with flames that exhibit a near unity Le [12]. Hence, the increase of the turbulent flame speed should not only attributed to the increase of flame surface area but also to the increased local reactivity.

REFERENCES

[1]T. Falkenstein, A. Rezchikova, R. Langer, M. Bode, S. Kang, H. Pitsch, The role of differential diffusion during early flame kernel development under engine conditions - part i: Analysis of the heat-release-rate response, Combustion and Flame 221 (2020) 502–515.

[2]H. Chu, L. Berger, T. Grenga, Z. Wu, H. Pitsch, *Effects of differential diffusion on hydrogen flame kernel development under engine conditions*, Proceedings of the Combustion Institute (2022).

[3]Ozel-Erol, G., Hasslberger, J., Chakraborty, N., Klein, M., *Effects of water droplet injection on turbulent premixed flame propagation: a direct numerical simulation investigation.* Flow Turbulence Combust 110, 105–123 (2023).

[4]D. Heim, J. Ghandhi, *A detailed study of in-cylinder flow and turbulence using piv*, SAE International Journal of Engines 4 (1) (2011) 1642–1668.

[5]C. Rosales, C. Meneveau, *Linear Forcing in Numerical Simulations of Isotropic Turbulence: Physical Space Implementations and Convergence Properties*, Phys. Fluids 17 (2005) 095106.

[6]R. Kee, J. Grcar, M. Smooke, J. Miller, E. Meeks, *PREMIX: a fortran program for modeling steady laminar one-dimensional premixed flames*, Sandia Report 143 (1985).

[7]A. A. Konnov, *Yet another kinetic mechanism for hydrogen combustion*, Combustion and Flame 203 (2019) 14–22.

[8]T. Falkenstein, S. Kang, L. Cai, M. Bode, H. Pitsch, *Dns study of the global heat release rate during early flame kernel development under engine conditions*, Combustion and Flame 213 (2020) 455–466.

[9]J.W.L. Paul F. Fischer and S.G. Kerkemeier, *nek5000 Web page (2008).* http://nek5000.mcs.anl.gov.

[10]Tomboulides A., Lee J., and Orszag S., *Numerical simulation of low Mach number reactive flows*, Journal of Scientific Computing 12 (1997), pp. 139–167.

[11]L. Berger, A. Attili, H. Pitsch, Synergistic interactions of thermodiffusive instabilities and turbulence in lean hydrogen flames, Combustion and Flame 244 (2022) 112254.

[12]A. Attili, F. Bisetti, M. E. Mueller, H. Pitsch, Formation, growth, and transport of soot in a three dimensional turbulent non-premixed jet flame, Combustion and Flame 161 (7) (2014) 1849–1865.

SESSION: Data assimilation and uncertainty quantification II

Wednesday, April 10, 2024

11:30- 12:45

WORKSHOP
Direct and Large-Eddy Simulation 14
April 10-12 2024, Erlangen, Germany

MASSIVE ENSEMBLES OF SIMULATIONS TO ASSES PREDICTABILITY OF TURBULENCE DECAY IN PIPE FLOW

Daniel Morón[1], Alberto Vela-Martín[2], Marc Avila[1,3]
[1]Center of Applied Space Technology and Microgravity (ZARM),
University of Bremen, Am Fallturm 2, 28359 Bremen, Germany.
[2]Department of Aerospace Engineering,
Universidad Carlos III de Madrid, Leganés, Spain.
[3]MAPEX Center for Materials and Processes,
University of Bremen, Am Biologischen Garten 2, 28359 Bremen, Germany.
daniel.moron@zarm.uni-bremen.de

INTRODUCTION

Turbulence in pipe flow first appears in the form of localized turbulent patches known as turbulent puffs [2]. See a visualization of a turbulent puff in figure 1. At low Reynolds numbers, puffs tend to decay following a memory-less process, resulting in exponential lifetime distributions. From a dynamical system point of view, decay events correspond to extreme events of transitional pipe flow [1]. Like extreme events in other dynamical systems, such as hurricanes in the weather system, decay events are linked with a certain predictability [5] that, to the best of our knowledge, has not been studied yet. In this project we characterize the predictability of decay events in pipe flow. To that end we perform a massive number of direct numerical simulations, initialized using different instantaneous puffs. By gathering statistics of decay times, we characterize the predictability of decay events. In order to perform such a big number of individual DNS, we use a newly developed `C-CUDA` code, that enables fast DNS.

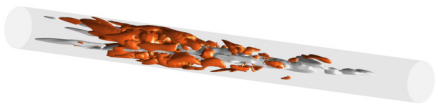

Figure 1: Turbulent puff at $Re = 1850$. In red, isosurfaces of $u_r^2+u_\theta^2 = 0.01U^2$. In grey, low speed streaks with $u_x' = -0.4U$

NUMERICAL METHODS

We consider the flow of a viscous Newtonian fluid with constant properties in a straight smooth rigid pipe of circular cross-section. The flow is assumed to be incompressible and governed by the dimensionless Navier–Stokes equations

$$\frac{\partial \mathbf{u}}{\partial t} + (\mathbf{u}\cdot\nabla)\,\mathbf{u} = -\nabla p + \frac{1}{Re}\nabla^2\mathbf{u} + f_p\,(t)\cdot\mathbf{e}_x \qquad (1)$$

$$\text{and} \quad \nabla\cdot\mathbf{u} = 0. \qquad (2)$$

Here, $\mathbf{u}$ is the fluid velocity, p the pressure, $\mathbf{e}_x$ the unit vector in the axial direction and $f_p\,(t)$ the time-dependent pressure gradient that drives the flow at a constant bulk velocity (U). All variables are rendered dimensionless using the pipe diameter (D), U, and the fluid density (ρ_f). The equations are formulated in cylindrical coordinates (r, θ, x), where the velocity field has three components $\mathbf{u} = (u_r, u_\theta, u_x)$ in the radial, azimuthal and axial directions, respectively.

We integrate the NSE numerically using a newly developed `C-CUDA` version of the pseudo-spectral `nsPipe` code [4]. The equations of motion are discretized using a Fourier-Galerkin ansatz in the azimuthal (θ) and axial (x) directions. In the radial (inhomogeneous) direction, high-order finite differences (FD) are used. The user can select the stencil-length of the FD scheme, being the default one a length of 7. The code assumes periodic boundary conditions in the azimuthal and axial directions. It also considers a non-homogeneously distributed grid spacing in the radial direction, having more points clustered close to the pipe wall than in the pipe center-line. The NSE are integrated forward in time with a predictor-corrector method. The divergence free condition is enforced at each time step after iterating in the corrector step. The boundary conditions at the wall are imposed using an influence matrix method [6].

We perform DNS in a $L_x = 50D$ long pipe domain, at $Re = 1850$. We use a coarse grid that has been optimized so the number of grid points is minimum, but the lifetime distributions of puffs are well captured. We use $N_r = 48$ radial points and $M_\theta = 96$ azimuthal and $M_x = 768$ axial physical points after aliasing. The maximum shear Reynolds number measured is of $Re_\tau \approx 70$ which results in a grid spacing in viscous units of $0.06 \lesssim \Delta r^+ \lesssim 2.2$, $D\Delta\theta^+/2 \gtrsim 4.5$ and $\Delta x^+ \gtrsim 9$. The time step size is set equal to $\Delta t = 0.0025D/U$. As a heuristic threshold we assume that puffs decay when the volume-averaged kinetic energy of the cross-sectional velocity satisfies:

$$\frac{1}{V}\iiint_V \left(u_r^2 + u_\theta^2\right) \mathrm{d}V = \left\langle u_r^2 + u_\theta^2 \right\rangle_{r,\theta,x} \leq 1e-7. \qquad (3)$$

METHOD TO ASSES PREDICTABILITY

We asses the predictability of puff decay performing massive ensembles of simulations. We follow three steps.

Step 1: base trajectories. We run $i = 1, ..., N_b$ base trajectory simulations, each initialized with a different instantaneous snapshot of a puff that decays at a given time T^i_{decay}.

Step 2: sampling the base trajectory. We save the instantaneous state of each base trajectory at several $N_t = 10$ times t^i_j, where $j = 1, 2, ..., N_t$, before the decay event $t^i_j < T^i_{\text{decay}}$. The predictability of each of these instantaneous puff states $N_b \times N_t$ will be assessed.

Step 3: run ensembles of simulations. For each base trajectory i and instantaneous state of the system j, we perform massive ensembles of simulations. Each ensemble has $N_l = 200$ simulations, and all of them are initialized with the corresponding instantaneous field at t^i_j, plus an additive white Gaussian noise in all the d.o.f. of the system with magnitude $\epsilon_0 = 1e-2$.

In total we perform $N_b \times N_t \times N_l$ individual simulations. We use the ensembles of simulations to gather statistics of decay events to characterize predictability.

RESULTS

We compute statistics of puff decay conditioned to be initiated using different instantaneous puffs. See in figure 2 (left) an example of a base trajectory, where points denote the instantaneous puffs we use to compute statistics of decay events. See the lifetimes statistics of each instantaneous puff in figure 2 (right). Note how, the cumulative distribution of lifetimes tends to be clustered close to $\Delta t = 0$, if the puff used to initialize the ensemble is close to the decay event of the base trajectory. On the other hand if the puff is further back in the past, the statistics look more similar to the expected exponential distribution.

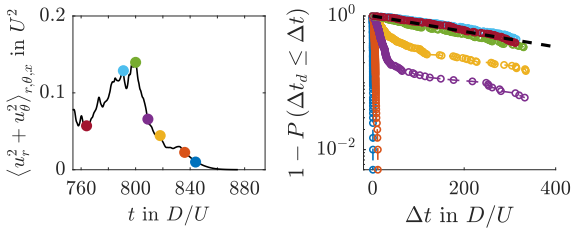

Figure 2: To the left: a zoom in a puff base trajectory i with a decay event at time $t = T^i_{\text{decay}}$. The points denote some instantaneous times t^i_j where massive ensembles of simulations are launched. To the right: survival function of puff decay after a time span Δt, for ensembles of simulations initiated close to different puff states before decay. With a dashed black line, the expected exponential distribution of puff decay without conditioning the statistics, $1 - P_q \approx \exp(-1/\tau)$ [2]. The colors of the lines correspond to the colors of the points in the left plot.

We use these lifetime distributions to characterize the predictability of each puff state. We compute the predictability as the difference between these probability distributions, and the expected exponential one. The Kullback-Leibler divergence (KLD) measures the difference between two probability distributions p and p_q, and is given as:

$$\text{KLD} = \sum_x p(x) \log\left(\frac{p(x)}{p_q(x)}\right). \quad (4)$$

Note that the KLD is minimum when $p \equiv p_q$, then $KLD \to 0$. In our case, p is the normalized probability distribution function $p = \frac{\mathrm{d}P(\Delta t)}{\mathrm{d}\Delta t}$ of the conditional statistics of decay shown in figure 2 (right). The normalized probability distribution p_q corresponds to the expected exponential lifetime distribution, dashed black line in fig 2 (right). The units of the KLD are arbitrary, but the bigger the KLD is, the more different the two distributions are, and therefore, the more predictable a given ensemble is.

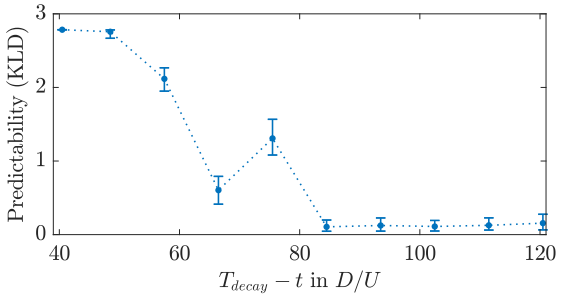

Figure 3: Kullback-Leibler divergence as a metric of predictability with respect to time, for a puff base trajectory i with a decay event at $t = T^i_{\text{decay}}$. The positive horizontal axis represents back in time with respect to a decay event. The error-bars denote the uncertainty of computing the KLD using $N_l = 200$ discrete data points according to a bootstrapping analysis.

See in figure 3 the KLD of one base trajectory. The positive horizontal axis corresponds to back in time with respect to the decay events at T^i_{decay}. Close to the decay event, the instantaneous state of the puff is highly predictable and the KLD is maximum. As one goes back in time, predictability decreases. We report that predictability does not necessarily need to decrease monotonically.

By performing this analysis, for additional base trajectories, we classify puffs according to their predictability and aim to identify what makes some puffs more predictable to decay than others. We believe that, by identifying the features that make a puff more predictable for decay, we can find the causes behind a decay event.

REFERENCES

[1]Nemoto, T., & Alexakis, A. (2021). Do extreme events trigger turbulence decay?–a numerical study of turbulence decay time in pipe flows. Journal of Fluid Mechanics, 912, A38.

[2]Avila, M., Barkley, D., & Hof, B. (2023). Transition to turbulence in pipe flow. Annual Review of Fluid Mechanics, 55, 575-602.

[3]DelSole, T., & Tippett, M. K. (2007). Predictability: Recent insights from information theory. Reviews of Geophysics, 45(4).

[4]López, J. M., Feldmann, D., Rampp, M., Vela-Martín, A., Shi, L., & Avila, M. (2020). nsCouette–A high-performance code for direct numerical simulations of turbulent Taylor–Couette flow. SoftwareX, 11, 100395.

[5]Palmer, T., & Hagedorn, R. (Eds.). (2006). Predictability of weather and climate. Cambridge University Press.

[6]Willis, A. P. (2017). The Openpipeflow Navier–Stokes solver. SoftwareX, 6, 124-127.

WORKSHOP
Direct and Large-Eddy Simulation 14
April 10-12 2024, Erlangen, Germany

EQUATION CONSISTENT DEEP-LEARNING OF SUB-GRID SCALE MODELS FOR LES OF TRANSITIONAL NACA 0012 AIRFOIL FLOWS

T. Hickling[1], J. Sirignano[1], J. MacArt[2]
[1]Mathematical Institute
University of Oxford, UK
[2]Department of Aerospace and Mechanical Engineering
University of Notre Dame, USA
tom.hickling@maths.ox.ac.uk

INTRODUCTION

Developing improved sub-grid scale (SGS) closure models is an important research area within large eddy simulation (LES). Most existing models are limited by their inability to predict back-scatter and their assumption that the SGS stress tensor is aligned with the resolved strain-rate tensor.

With recent advances in machine learning and high-performance computing, there has been a growing interest in using deep neural networks (DNNs) to learn more complex deep learning SGS (DL-SGS) models.

In general, an a priori training approach has been used (e.g. [1, 2]). A priori training trains a closure model as a standard regression problem, where the input to the neural network is the filtered/time-averaged DNS and the output is the DNS' SGS tensor. The training is decoupled from the LES equations; once trained off-line on the DNS data, the closure model is substituted into the LES for an a posteriori simulation. However, in this approach, the training and prediction (LES simulation) are inconsistent. For instance, the model receives DNS data as its input during training while it receives LES data as an input during prediction, and the significant effect of numerical errors on high wavenumbers is unaccounted for. This has been observed to affect accuracy and stability of DL-SGS models, and may play a part in their limited application to only relatively simple flows such as isotropic turbulence, jets, and turbulent channel flows.

Optimizing the DL-SGS in an equation consistent manner using adjoint training methods shows potential for addressing the limitations of a priori DL-SGS model training. It has already been successfully applied to incompressible flows including decaying isotropic turbulence, free jets, and bluff bodies, and has been observed to offer superior performance and improved stability compared to both classical and a priori trained DL-SGS models [3, 4, 5].

In this paper, we develop adjoint methods for optimizing DL-SGS models for compressible flow LES and apply them to the flow around a NACA 0012 airfoil at $\mathrm{Re} = 50,000$ and $\mathrm{Ma} = 0.4$. Both the fluid mechanics and geometry are more complex than previous applications of DL-SGS models: laminar to turbulent transition, separation, and reattachment are all key flow features. The adjoint trained DL-SGS model detailed in this paper provides increased accuracy over both no-model LES and the Smagorinsky eddy viscosity model in out-of-sample computations within the same broad flow regime as the training data, and even out performs no-model LES (and is competitive with the Smagorinksy model) for far out-of-sample simulation of fully separated flow, which contains a large amount of unseen flow physics.

METHODOLOGY

The DNS and LES simulations in this paper are conducted in PyFlowCL, an in-house compressible curvilinear finite difference solver. PyFlowCL is Python native and uses the PyTorch and MPI libraries to enable scalable, distributed simulation and DL-SGS model training with full GPU acceleration.

We model the LES SGS stress and heat flux tensors (τ_{ij}^{SGS} and f_{ij}^{SGS}) with an anisotropic diffusivity approach, such that

$$\tau_{ij}^{SGS} \approx \mu h_{ij}\left(\rho, T, \Delta, \nabla \otimes \boldsymbol{u}; \theta\right) S_{ij}, \tag{1}$$

and

$$f_{j}^{SGS} \approx \mu h_{4j}\left(\rho, T, \Delta, \nabla \otimes \boldsymbol{u}; \theta\right) \frac{\partial T}{\partial x_j}, \tag{2}$$

where ρ, Δ, T and $\boldsymbol{u}$ are density, grid spacing, temperature, and velocity respectively. With these inputs the network is Gallilean invariant. The output layer of the DNN h contains an exponential linear unit (ELU) function, so that net dissipation in the simulation is locally always positive (even neglecting the kinetic energy removed by the implicit filter).

Our adjoint training approach seeks to learn the neural network parameters θ such that the short-time evolution of the LES solution matches the filtered DNS data as closely as possible. To do this, the LES solution is initialized from filtered DNS (fDNS) data and advanced for 1% of a chord flow-through time. The flow field at the end of this period is used to calculate an L_1 loss based on the difference between the LES data and the target fDNS flow field. Then, the auto-differentiation abilities of PyTorch are utilized to advance an adjoint equation backwards in time, accumulating gradients of the loss with respect to θ, which can be used to optimize θ using gradient descent-type algorithms such as RMSprop. We use a minibatch approach, where multiple distributed LES simulations are advanced simultaneously, and their gradients are averaged at the end of each optimization iteration before updating the DNN parameters.

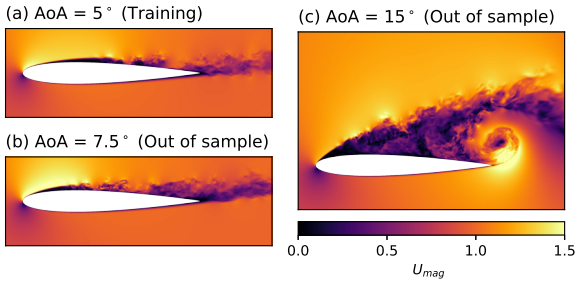

Figure 1: Instantaneous DNS velocity magnitude fields for a NACA 0012 at Re $= 50,000$, and $Ma = 0.4$.

DNS DATASETS

The DL-SGS model is trained on DNS data at $AoA = 5°$. A snapshot of the instantaneous velocity magnitude field predicted by the DNS is shown in Fig. 1a. The PyFlowCL DNS at this condition has been extensively validated, for example showing good agreements with the DNS pressure and friction coefficient distributions in [6]. The DNS shows the expected well-known flow structure of this configuration: there is a leading edge laminar separation bubble, which rolls up into vortices that breakdown, causing turbulent reattachment at around 60% chord. The DNS grid contains 186M points; the LES grid is formed by down-sampling this grid by a factor of $8 \times 4 \times 9$ in the x, y, and z directions, leading to a 2,300-fold reduction in computational cost (288-fold in space, and 8-fold in time).

After training, the model is used in a posteriori LES at $AoA = 5°$, 7.5°, and 15° (shown in Fig. 1a, b, and c respectively. The a-posteriori simulation at $AoA = 5°$ is considered quasi-out-of-sample—this is because, although the model has been trained on DNS data at this angle of attack, this was only over 1% of a chord flow-though time, and not over the 20+ flow-through times required in the LES to expel initial transients and calculate flow-field statistics.

Two fully out-of-sample flow conditions are simulated. The first, at $AoA = 7.5°$ exhibits the same qualitative flow structure as the quasi-out-of-sample case, however it reattaches much earlier at around 30% chord, leading to a more developed turbulent boundary layer over the latter half of the airfoil suction surface. The second, at $AoA = 15°$ is very far out-of-sample. As can be seen in in Fig. 1c, the flow field for this case is fully separated, with the dominant mechanism for unsteadiness in the separation bubble being the roll-up of a large vortex at the trailing edge, which the persists downstream in a vortex street. These flow features are entirely unseen in the training data, meaning that $AoA = 15°$ is expected to be a very challenging case for the DL-SGS model.

RESULTS

The errors (relative to filtered DNS, fDNS) in the lift and drag coefficients (C_L and C_D) predicted by no-model LES, LES with the Smagorinsky SGS model (with $C_s = 0.1$), and LES with the DL-SGS model are shown in Tab. 1. In both the 5° and 7.5° cases, where the DL-SGS has been trained over representative physics, it out performs the no-model LES with errors that are more than 50% smaller in both C_L and C_D. At these conditions, the Smagorinsky model behaves extremely poorly—due to its well-known issues in transitional flows, it incorrectly predicts flow separation.

At $AoA = 15°$, the DL-SGS has similar errors to the Smagorinsky model—this is considered to be extremely encouraging given the far out-of-sample fully separated nature of this flow condition, indicating that the DL-SGS model has learned at least some generalizable properties of turbulence. We highlight that, if we had optimized the value of C_s in the Smagorinsky model at $AoA = 5°$ in a similar way to the DL-SGS, we expect it to be very close to zero, resulting in significantly worse performance of the Smagorinsky model (on a par with no model) at $AoA = 15°$. The no model LES accurately predicts C_L at $AoA = 15°$, but has an error in C_D that is 50% larger than the other two LES simulations, suggesting that the accurate C_L prediction is likely due to a cancellation of errors, not accurately capturing the flow field.

Table 1: fDNS lift and drag coefficients and relative errors of LES simulations.

Angle of attack	5°	7.5°	15°
fDNS C_L	0.605	0.725	0.789
No model C_L error [%]	6.2	12.5	3.5
Smagorinsky C_L error [%]	35.4	16.2	12.9
DL-SGS C_L error [%]	3.0	4.8	13.2
fDNS C_D	0.036	0.050	0.273
No model C_D error [%]	6.8	22.0	29.6
Smagorinsky C_D error [%]	51.9	93.6	14.7
DL-SGS C_D error [%]	2.58	7.24	17.6

CONCLUSION

The results presented here show a significant improvement in the ability of DL-SGS models to predict complex flows and generalize reasonably well to unseen physics. This is attributed to the equation-consistent optimization of the DL-SGS model using an adjoint training method. The full paper will analyze the LES flow fields in detail to yield insights in to what flow-physics the model has learned. It will also assess results of the model at additional out-of-sample conditions (AoA and Re), a model trained with an input space extended to include second derivatives, and a model trained over a longer time-period.

REFERENCES

[1]Beck, A., Flad, D., and Munz, C.-D., "Deep neural networks for data-driven LES closure models," *Journal of Computational Physics,* Vol. 398, 2019, p. 108910.

[2]Meng, Q., Jiang, Z., and Wang, J., "Artificial neural network-based subgrid-scale models for LES of compressible turbulent channel flow," *Theoretical and Applied Mechanics Letters,* Vol. 13, No. 1, 2023, p. 100399.

[3]Sirignano, J., and MacArt, J., "Deep Learning Closure Models for Large-Eddy Simulation of Flows Around Bluff Bodies," *Journal of Fluid Mechanics,* Vol. 966, 2023, p. A26.

[4]MacArt, J., Sirignano, J., and Freund, J., "Embedded training of neural-network subgrid-scale turbulence models," *Physical Review Fluids,* Vol. 6, 2021, p. 050502.

[5]Sirignano, J., MacArt, J., and Freund, J., "DPM: A deep learning PDE augmentation method with application to large-eddy simulation," *Journal of Computational Physics,* Vol. 423, 2020, p. 109811.

[6]Jones, L., Sandberg, R., and Sandham, N., "Direct numerical simulations of forced and unforced separation bubbles on an airfoil at incidence," *Journal of Fluid Mechanics,* Vol. 602, 2008, p. 175–207.

WORKSHOP
Direct and Large-Eddy Simulation 14
April 10-12 2024, Erlangen, Germany

ROBUSTNESS AND UNCERTAINTY OF DIRECT NUMERICAL SIMULATION UNDER THE INFLUENCE OF ROUNDING AND NOISE

Martin Karp[1], Niclas Jansson[1], Saleh Rezaeiravesh[2], Stefano Markidis[1], and Philipp schlatter [2]
[1]KTH Royal Institute of Technology Stockholm, Sweden
[2]The University of Manchester Manchester, United Kingdom
[3]Institute of Fluid Mechanics (LSTM) Friedrich–Alexander–Universität (FAU) Erlangen–Nürnberg, Germany
makarp@kth.se

INTRODUCTION

Numerical precision in large-scale scientific computations has become a frequently discussed topic due to new developments in computer hardware. Low-precision arithmetic offers the potential for significant performance improvements, but the uncertainty added from reducing the numerical precision is a major obstacle for it to reach prevalence in high-fidelity simulations of turbulence [1]. In the present work, the impact of reducing the numerical precision under different rounding schemes is investigated and compared to the presence of white noise in the simulation data to obtain statistical averages of different quantities in the flow. To investigate how this impacts the simulation, an experimental methodology to assess the impact of these sources of uncertainty is proposed, in which each realization u^i at time t_i is perturbed, either by constraining the flow to a coarser discretization of the phase space (corresponding to low precision formats) or by perturbing the flow with white noise.

EXPERIMENTAL METHODOLOGY

We consider the discretized system $u^{i+1} = f(u^i)$ where $u^i = \{u_1^i, \ldots, u_n^i\}$ and $u \in \mathrm{F}^n$ where F^n is a finite precision discretization of the phase space $\mathcal{P}$. In order to assess the sensitivity and robustness of such a discretization we evaluate the impact of the following perturbed system

$$u^{i+1} = g(f(u^i)) \tag{1}$$

where g maps an original state to a slighlty different one. In this work, three different versions of g are considered:

$$g(u) = \quad \mathrm{round}_{\mathrm{RTN,FP}}(u) \tag{2}$$
$$g(u) = \quad \mathrm{round}_{\mathrm{SR,FP}}(u) \tag{3}$$
$$g(u) = \quad (1+\epsilon\delta)u, \quad \delta \sim U^n_{[-1,1]} \tag{4}$$

where $\mathrm{round}_{\mathrm{RTN,FP}}$ corresponds to conventional rounding-to-nearest (RTN) to a numerical representation in floating point precision FP, $\mathrm{round}_{\mathrm{SR,FP}}$ corresponds to stochastic rounding (SR) to precision FP, and the last version adds uniformly distributed white noise to the solution u^i, sampling the new value in the range $f(u^i) \cdot [1-\epsilon, 1+\epsilon]$.

Stochastic rounding for a value x between two values x_1 and x_2 corresponds to rounding up to x_2 with probability $(x - x_1)/(x_2 - x_1)$ and down to x_1 with probability $(x_2 - x)/(x_2 - x_1)$ while round-to-nearest would deterministically round x to x_1 and x_2 whichever is closest to x. The reason for incorporating stochastic rounding is due to recent works indicating that this method avoids so-called stagnation in dynamic systems, where x is repeatedly rounded to the same value, although x changes.

THE LORENZ SYSTEM

To assess the viability of this approach a first study is carried out using the Lorenz system for different parameters. The Lorenz system is commonly written as, for $u = (x, y, z)$:

$$\frac{\mathrm{d}u}{\mathrm{d}t} = (\sigma(y-x), x(\rho - z) - y, xy - \beta z). \tag{5}$$

The system is then discretized with $u^{i+1} = f(u^i)$ with a Runge-Kutta scheme of order four (RK4). Statistics are computed over ensembles of 1000 runs where the initial condition is varied, for each run in the ensemble, the simulation is run for 1500 time units, statistics are collected for 1000 time units, and the first 500 time units of each simulation are discarded. The simulation is carried out first with the commonly used parameters $\rho = 28, \sigma = 10, \beta = \frac{8}{3}$, but also with increasing $\rho = 30, 60$ as well as three different time steps $\Delta t = 0.001, 0.01, 0.1$. The parameters are also varied as we consider six different numerical precisions, namely conventional double-precision (64 bits), single-precision (32 bits), half-precision (16 bits), brain float 16 (bfloat16), as well as the two recently proposed quarter (8 bits) precision formats q43, and q52, with 4 and 5 exponent bits respectively, compared to double-precision's 11 exponent bits. The parameter ϵ for the noisy simulations is then used to match the machine epsilon of each considered floating point precision. Details for each precision can be found in [5] Evaluating the perturbed system $u^{i+1} = g(f(u^i))$ we then collect first and second-order statistics as well as compute the second-order moment of the velocity increments between each time step

$$\langle \Delta u^2 \rangle = \quad \langle (u^{i+1} - u^i)^2 \rangle = \langle (u^{i+1})^2 \rangle + \langle (u^i)^2 \rangle - 2\langle u^{i+1} u^i \rangle \tag{6}$$
$$= \quad 2(\langle u^2 \rangle - \langle u^{i+1} u^i \rangle) \tag{7}$$

as computing the time average over u^i or u^{i+1} is the same due to the system being statistically stationary. Due to this the first order moment is also zero, $\langle \Delta u \rangle = 0$. As we only consider statistical quantities in this study we only consider ergodic, statistically stationary systems.

	$\langle z \rangle$	$\langle \Delta z^2 \rangle^{1/2}$
FP64	23.55, 23.55, 23.55	0.79, 0.79, 0.79
FP32	23.55, 23.55, 23.55	0.79, 0.79, 0.79
FP16	23.50, 23.55, 23.55	0.80, 0.79, 0.79
BF16	24.14, 23.59, 23.58	0.71, 0.79, 0.79
Q43	37.28, 22.77, 24.73	0.00, 1.12, 1.21
Q52	12.49, 25.51, 25.56	0.00, 1.79, 2.21

Table 1: Computed time averages for the Lorenz system for $\rho = 28, \Delta t = 0.01$. The three values in each column correspond to deterministic rounding (RTN), stochastic rounding (SR), and adding noise.

By looking at the results from the Lorenz system in Table 1, we note that stochastic rounding avoids the impact of stagnation that is evident for RTN for lower precisions and performs similarly to the noisy simulations. Second is that the simulation is robust until 16 bits. However, we note in other simulations that the number of bits necessary is also coupled with the length of the time step and also changes when ρ is increased.

CHANNEL FLOW

The same methodology is now applied to direct numerical simulation of turbulent channel flow at $Re_\tau = 182$ and 395, based on the friction velocity u_τ, channel half-height δ and kinematic viscosity ν. The simulation domain is of size $\frac{4}{3}\pi\delta, 2\delta, 4\pi\delta$ for both cases and with periodic boundary conditions in the streamwise and spanwise directions and no-slip boundary conditions at the two walls. Unlike the Lorenz system, we consider only one simulation per rounding procedure, leading to nine simulations per Reynolds number.

In the initial simulations, we employ the pseudo-spectral solver SIMSON [3] with 128 modes in each spatial direction $Re_\tau = 182$ case and $512, 193, 256$ for $Re_\tau = 395$ in the streamwise, wall-normal, and spanwise directions respectively. The rounding at each time step is performed with the library CPFloat [5], all simulations restart from the same initial conditions, and statistics are collected for 500 non-dimensional time units based on the channel centerline velocity U_{cl} and δ. We are applying our methodology to a similar set of simulations by using the recent spectral-element solver Neko [4], to assess whether similar results for these flow cases can be obtained independent of spatial and temporal discretization.

To illustrate our initial results, we assess the impact of different roundings by influencing the state at each time step of the simulation according to(1) with a time step of $\Delta t/(\delta/U_{cl}) = 0.003$. We show the difference between using deterministic and stochastic rounding in Figure 1 . These measurements of the first moment of the streamwise velocity illustrate the same behaviors as we obtained for the Lorenz system in which stochastic rounding converges to the full precision measurements to a larger extent. Using q43, with only 4 exponent bits failed to capture the multiscale behavior of turbulence, and the simulation cannot be obtained for deterministic rounding, while it follows the linear behavior in the near-wall region. For q52 we observe that the statistics are severely impacted when using deterministic rounding, but that when using stochastic, we for this first-order quantity obtain a good match by using higher precision. For noise the first-order moments are preserved well. However, for

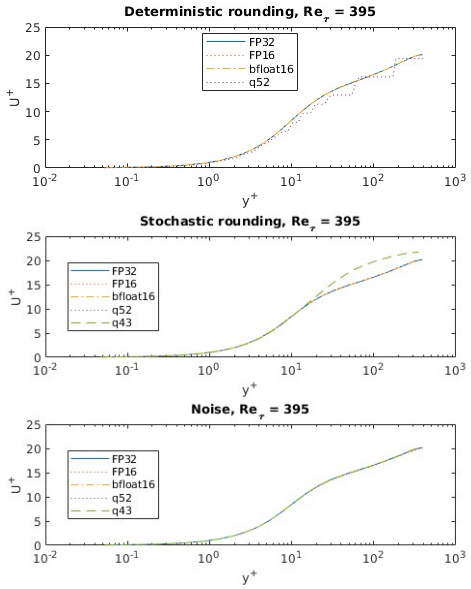

Figure 1: Mean flow profile in plus units for $Re_\tau = 395$ for runs using deterministic and stochastic rounding as well as influencing the flow with noise. For deterministic rounding q43, the simulation became unstable and did not finish.

higher-order moments we observe that the difference for all perturbed systems is significant and the difference between q52 and the other precision is significant. For precisions such as FP16 or bfloat16 though, the results are in good agreement also for higher moments.

We are now in the process of evaluating how the probability density functions of the velocity and velocity increments Δu change as precision and noise influence the simulation. Comparing the sensitivity close to the wall, we see indications that the near-wall region is less impacted as well, similar to previous works looking at the uncertainty of turbulent statistics [2]. Of note in general, is that the flow field and simulation results seem remarkably robust under the influence of rounding and noise for channel flow. An open question is how this translates to more sensitive cases, such as separation, and whether these results can be used to obtain higher performance or for turbulence models and to assess the uncertainty prevalent in simulations of turbulence.

REFERENCES

[1] Witherden, F. D., and A. Jameson.: Impact of Number Representation for High-Order Implicit Large-Eddy Simulations.,*AIAA journal*, 58.1, 184-197, (2020).

[2] Karp, M., Liu, F., Stanly, F., Rezaeiravesh, S., Jansson, N., Schlatter, P., and Markidis, S.: Uncertainty Quantification of Reduced-Precision Time Series in Turbulent Channel Flow, *SC'23 Workshops*, (2023).

[3] Chevalier, M., Schlatter, P., Lundbladh, A., and Henningson, D. S. : SIMSON: A pseudo-spectral solver for incompressible boundary layer flows., (2007)

[4] Jansson, N., Karp, M., Podobas, A., Markidis, S., and Schlatter, P. : Neko: A Modern, Portable, and Scalable Framework for High-Fidelity Computational Fluid Dynamics, `https://arxiv.org/abs/2107.01243`, (2021).

[5] Fasi, M., and Mikaitis, M. : CPFloat: AC library for simulating low-precision arithmetic, *ACM Trans. Math. Softw.* (2023)

WORKSHOP
Direct and Large-Eddy Simulation 14
April 10-12 2024, Erlangen, Germany

LOW COST RECURRENT AND ASYMPTOTICALLY UNBIASED ESTIMATORS OF STATISTICAL UNCERTAINTY ON AVERAGED FIELDS FOR DNS AND LES

M. Boxho[1], M. Rasquin[1], T. Toulorge[1] and K. Hillewaert[1,2]
[1]Cenaero, 29, Rue des Frères Wright, 6041 Gosselies, Belgium
[2]Aerospace and Mechanics dept., Université de Liège, 4000 Liège, Belgium
michel.rasquin@cenaero.be

INTRODUCTION

Due to the rapid increase in available computational resources and the development of high-resolution fluid simulation techniques, Direct Numerical Simulation (DNS) and Large Eddy Simulation (LES) are increasingly used to complement experiments for fundamental flow studies. Moreover, scale-resolving approaches provide access to the statistical moments of the flow variables for the development, calibration, and validation of turbulence models [1]. In this context, a rigorous quantification of the uncertainty on the statistics is essential for numerical studies. Fonseca *et al.* [2] pointed out that the lack of convergence of statistical fields is a source of error in the Reynolds stress tensor and, thus, in the calibration of RANS models. The reporting of uncertainty margins is a common practice in experiments and allows relevant conclusions about the physics under consideration. However, uncertainty is not consistently reported in the DNS literature.

Simulation errors can be classified in three categories. The first category relates to uncertainties linked to numerical approximation errors. The second category correspond to statistical errors. The third category is associated with boundary conditions (i.e., potential reflections and local distortions of the flow). The present work concentrates on the estimation of statistical errors. The evolution of the statistical errors over time can be quantified using sampling error estimators from which the duration of a DNS or LES can be determined by the accepted statistical uncertainty of the quantity of interest. Nonetheless, assessing such an estimate is challenging due to the high and unknown correlation within the time signal. Furthermore, this correlation may vary considerably across the spatial domain.

The basic confidence interval $\epsilon_n = \sigma/\sqrt{n}$ where σ is the standard deviation of a single sample, and n is the number of samples, is constructed on the hypothesis that the data are *identically, independently distributed (i.i.d.)* samples. However, such an assumption does not hold for most real-world problems. The numerical simulation of a continuous-time chaotic system requires a small time step to accurately resolve turbulence structures, resulting in highly correlated successive samples. For this case, several approaches to evaluate the variance of sampling means have been proposed in the literature, e.g. [3, 4] among which many are based on the modelization of the random process and the adjustment of the model parameters via a maximum likelihood formulation. Batch means methods such as the Moving Blocks Bootstrap method (MBB) [5, 6] have been developed to reduce model dependencies. Unfortunately, they require storage of all samples to evaluate the statistic of interest, making them impractical for DNS or LES due to prohibitive memory requirement.

The present work is a first step in the development of a statistical uncertainty quantification methodology for first-order statistics of DNS computations: the development of unbiased estimators to quantify the expected deviation from the infinite-time-averaged statistic without any prior knowledge of the statistical process and with a limited amount of samples. To overcome the memory problem, all statistical quantities are evaluated using cumulative approaches. We developed three estimators for the variance of sample mean and tested them on three representative test problems: a generic autoregressive (AR) process, the solutions of the Kuramoto-Sivashinsky equations, and a DNS of the turbulent flow over a two-dimensional periodic hill, which features a massive separation from a curved wall. In comparison to existing techniques, our estimators are cumulative, work well with short-duration time signals, account for correlation, and result in very little computational overhead.

METHODOLOGY

To get the uncertainty about the sample mean $\overline{x}_n$, one needs to evaluate the variance of the sample mean, defined as,

$$\mathbb{V}\mathrm{ar}\left(\overline{x}_n\right) = \frac{\sigma^2}{n}\left[1 + 2\sum_{k=1}^{n-1}\left(1 - \frac{k}{n}\right)\rho_k\right]. \tag{1}$$

In Eq. 1, the variance σ^2 and the correlation terms ρ_k of the variable x are unknown. Therefore, in this work, three estimators of the ACF (Eqs. 2, 4, and 6) are employed to develop three asymptotically unbiased estimators of the sample mean. The extension to the confidence interval is based on the generalization of the Central Limit Theorem [7]. In the expressions below, the constant m is a truncation of the number of samples n evaluated through an optimization procedure, while the constants a_1, a_2, a_3, and b_3 are functions of n and m.

Estimator 1 This estimator is based on the classical ACF estimator $\hat{\gamma}_k$, defined as,

$$\hat{\gamma}_k = \frac{1}{n-1}\sum_{t=1}^{n-k}(x_t - \overline{x}_n)(x_{t+k} - \overline{x}_n). \tag{2}$$

Based on Eq. 1 and the evaluation of the expectation of Eq. 2, the estimator of the variance of the sample mean is given by

$$\mathbb{V}\mathrm{ar}\left(\overline{x}_n\right) \approx a_1\left(s_n^2 + 2\sum_{k=1}^{m}\hat{\gamma}_k\right), \tag{3}$$

where s_n is the sample variance computed recursively.

Estimator 2 This estimator uses the quadratic variation estimator, initially proposed by Andersen *et al.* [8],

$$\hat{\delta}_k = \frac{1}{n}\sum_{t=1}^{n-k}(x_t - x_{t+k})^2. \tag{4}$$

Following similar manipulation as for Estimator 1, we obtain

$$\mathbb{V}\mathrm{ar}\left(\overline{x}_n\right) \approx \frac{a_2(n-1)s_n^2 - \sum_{k=1}^{m}\hat{\delta}_k}{n(1-a_2)}. \tag{5}$$

Estimator 3 This third estimator is based on the non-centered classical ACF estimator,

$$\hat{\varphi}_k = \frac{1}{n-k}\sum_{t=1}^{n-k} x_t x_{t+k}. \tag{6}$$

The resulting estimator of the variance of the sample mean is

$$\mathbb{V}\mathrm{ar}\left(\overline{x}_n\right) \approx a_3\left[(n-1)s_n^2 + 2\sum_{k=1}^{m}(n-k)\hat{\varphi}_k + b_3\overline{x}_n^2\right]. \tag{7}$$

RESULTS

For the sake of brevity, only the results on a AR(K) process are briefly presented in the present abstract. This AR(K) process is a synthetic model for a stochastic process with known mean, variance and correlation function. It is constructed by computing a new sample value x_i as a finite weighted sum of the K previous sample values plus a white noise:

$$x_i = \sum_{k=1}^{K}\alpha_k x_{i-k} + \epsilon_i\,, \tag{8}$$

where α_k are real coefficients and ϵ_i is a sample of a white Gaussian noise, i.e., $\epsilon_i \sim \mathcal{N}\left(0, \sigma_\epsilon^2\right)$. The resulting system is statistically stationary, with a zero mean, after a "*certain*" initial transient, due to the initialization of the first K value of the process. The coefficients of the auto-covariance function are obtained with the Yule-Walker equations described in the chapter *Autoregressive Processes* of [9].

Figure 1 shows the evolution of the confidence intervals size with increasing realization lengths for our three estimators, taken between 2^7 and 2^{14}, on an ensemble of $B = 100$ distinct time series of an AR(6) process. Because B AR(6) processes are generated, B confidence intervals have been obtained for each n value. Hence, for each n value, the variance over the confidence intervals is evaluated to plot the error bar in Fig. 1. The exact confidence interval size, computed with the analytical expression of μ, σ^2, and ρ_k, is drawn in a red dotted line. The MBB method and the estimator proposed by Beyhaghi *et al* [4] are also compared as additional references. However, both require all samples of the time series, which is impractical for scale-resolving simulations.

Our three estimators behave similarly and are all three asymptotically unbiased. For the highest number of samples of 2^{14}, the relative error with respect to the exact confidence interval is approximately 0.2−0.3%. The MBB method converges more slowly compared to our estimators and slightly underestimates the exact confidence interval size with a relative error of 5.2% at $n = 2^{14}$. The main advantage the Beyhaghi estimator lies in the optimization of the auto-correlation function based on the complete time series, leading to good estimations even for small n. However, the computation of their estimator is expensive. We conclude that the three estimators introduced in the present study converge faster than the MBB method and coincide well with the Beyhaghi estimator at moderate and large n, at a much lower cost though.

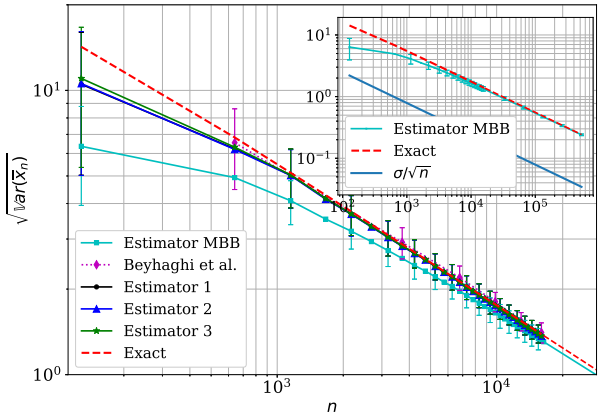

Figure 1: Evaluation of three estimators of the variance of the sample mean on 100 realizations of an AR(6) process.

CONCLUSION AND PERSPECTIVES

Three estimators are presented in this work for the prediction of the variance of the sample mean, i.e., to quantify the uncertainty linked to the approximation of infinite-time-average statistics of statistically stationary ergodic processes. These estimators are asymptotically unbiased and can be computed with a **cumulative approach** and a **small set of correlation coefficients** to reduce the memory storage in scale-resolving flow solvers. The long-term goal of this work is to provide confidence interval maps of all computed statistics for a fair comparison with experimental data and other high-fidelity simulations.

REFERENCES

[1] S. L. Brunton, B. R. Noack, and P. Koumoutsakos, "Machine learning for fluid mechanics," *Annual Review of Fluid Mechanics*, vol. 52, no. 1, pp. 477–508, 2020.

[2] E. Fonseca, V. Rangel, and B. Brener, "Pre-processing dns data to improve statistical convergence and accuracy of mean velocity fields in invariant data-driven turbulence models," *Theor. Comput. Fluid Dyn.*, vol. 36, pp. 435—463, 2022.

[3] S. Alimohammadi and D. He, "Multi-stage algorithm for uncertainty analysis of solar power forecasting," in *2016 IEEE Power and Energy Society General Meeting (PESGM)*, pp. 1–5, 2016.

[4] P. Beyhaghi, S. Alimohammadi, and T. Bewley, "Uncertainty quantification of the time averaging of a statistics computed from numerical simulation of turbulent flow," *arXiv:1802.01056 [physics, stat]*, 2018.

[5] B. Efron, "Bootstrap methods: Another look at the jackknife," *Ann. Statist.*, vol. 7, no. 1, pp. 1–26, 1979.

[6] H. R. Kunsch, "The jackknife and the bootstrap for general stationary observations," *Ann. Statist.*, vol. 17, no. 3, pp. 1217–1241, 1989.

[7] T. A. Oliver, N. Malaya, R. Ulerich, and R. D. Moser, "Estimating uncertainties in statistics computed from direct numerical simulation," *Physics of Fluids*, vol. 26, no. 3, p. 035101, 2014.

[8] T. G. Andersen, T. Bollerslev, F. X. Diebold, and P. Labys, "The distribution of realized exchange rate volatility," *Journal of the American Statistical Association*, vol. 96, no. 453, pp. 42–55, 2001.

[9] G. Box, G. Jenkins, G. Reinsel, and G. Ljung, *Time Series Analysis: Forecasting and Control - Fifth Edition*. Hoboken, New Jersey: Wiley, 2016.

WORKSHOP
Direct and Large-Eddy Simulation 14
April 10-12 2024, Erlangen, Germany

A FRAMEWORK FOR IN-SITU ESTIMATION OF TIME-AVERAGING UNCERTAINTIES IN TURBULENT FLOWS

S. Rezaeiravesh[1], **C. Gscheidle**[2], **A. Peplinski**[3], **J. Garcke**[2,4], **P. Schlatter**[5,3]
[1]Department of Fluids and Environment, The University of Manchester, UK, saleh.rezaeiravesh@manchester.ac.uk
[2]Fraunhofer SCAI, Sankt Augustin, Germany, christian.gscheidle@scai.fraunhofer.de
[3]SimEx/FLOW, Engineering Mechanics, KTH Royal Institute of Technology, Sweden, adam@mech.kth.se
[4]Institute for Numerical Simulation, University of Bonn, Germany, jochen.garcke@scai.fraunhofer.de
[5]Institute of Fluid Mechanics (LSTM), Friedrich–Alexander–Universität (FAU) Erlangen–Nürnberg, Germany
philipp.schlatter@fau.de

INTRODUCTION

Scale-resolving simulations, such as DNS, LES, and hybrid RANS-LES, result in spatio-temporal fields of different quantities of turbulent flows. Among the outcomes of interest from such simulations are the turbulence statistics which are estimated by applying sample mean estimators (SMEs). By nature, such statistics are uncertain up to some level due to the use of finite-size sets of samples in the SMEs. Quantifying such uncertainties has been the subject of a few studies, see e.g. [1, 2, 3]. But all uncertainty quantification (UQ) techniques in the literature have been typically applied in an offline mode, meaning that they require to have access to all samples of the turbulence time series at once. This requires the time samples of quantities to be collected during the simulation and written on disk. The UQ analyses are then performed as a post-processing step. These methods are useful but cannot be used for large amount of data produced in large-scale turbulence simulations which are becoming more affordable due to the progress in high-performance computing technologies. Additionally, we would like to have the possibility of online monitoring of the uncertainties in turbulence statistics in next generation of CFD software [4]. Aligned with these, we have developed a framework for in-situ/online estimation of time-averaging uncertainties in SMEs of turbulent flows statistics [5]. The underlying algorithms which are briefly explained in the following section, are low-storage, flexible (can be used with any CFD software), computationally efficient, and result in accurate estimation of uncertainties on par with the offline methods.

WORKFLOW AND ALGORITHMS

Consider a turbulence time series for variable x, with associated samples denoted by $\mathbf{x} = \{x_i\}_{i=1}^n$, where $x_i = x(t_i)$. The sampling intervals are assumed to be identical. A general characteristic of turbulence time series is that the samples $\mathbf{x} = \{x_i\}_{i=1}^n$ are autocorrelated up to a generally unknown time lag. The SME for a sample time series of x reads as,

$$\hat{\mu} := \hat{\mathbb{E}}[x] = \frac{1}{n}\sum_{i=1}^{n} x_i \,. \tag{1}$$

The uncertainty in $\hat{\mu}$ can be obtained from the following analytical expression [6]:

$$\mathbb{V}[\hat{\mu}] = \sigma^2(\hat{\mu}) = \frac{1}{n}\left[\gamma_0 + 2\sum_{m=1}^{(n-1)}\left(1-\frac{m}{n}\right)\gamma_m\right], \tag{2}$$

where γ_m is the autocovariance of x at lag m. The sample-estimated $\hat{\gamma}_m$ at high lags are, by definition, oscillatory. Therefore, directly using $\hat{\gamma}_m$ in Eq. (2) would result in inaccurate values of $\hat{\sigma}(\hat{\mu})$. Two general remedies have been proposed. First, using a smooth model for the autocovariance function (ACovF) $\gamma(m)$ built based on a limited number of sample-estimated $\hat{\gamma}_m$ with $m \in \mathbf{m}_{\text{train}}$. The second strategy is to avoid using Eq. (2) and rely completely on the batch means, see [2]. The first approach is, however, more intuitive, accurate and less dependent on hyperparameters (such as the batch size in the second approach). The framework introduced in [5] provides streaming algorithms for both strategies, but keeps the main focus on the first strategy. There are a few main elements in the in-situ framework which are shortly reviewed here. An algebraic model is introduced for modelling the autocorrelation functions (ACF), $\rho(m) = \gamma(m)/\gamma(0)$:

$$\rho(m) = a\exp(-b\,m) + (1-a)\exp(-c\,m)\,, \tag{3}$$

where the parameters a, b, and c are estimated using a given a finite set of training $\hat{\gamma}_m$, $m \in \mathbf{m}_{\text{train}}$ where $\mathbf{m}_{\text{train}}$ is flexible (e.g. full or sparse sets associated to fixed or variable sampling intervals). The updating formulations of the sample mean and variance estimators in Ref. [5] rely on the expressions proposed by Welford [7]. For sample-estimated autocovariances, an updating expression has been derived starting from,

$$\Gamma_{i,j}^m = (j-i+1)^{-1}\sum_{k=i}^{j}(x_k - M_{i,j})(x_{k-m} - M_{i,j})\,, \tag{4}$$

where $\Gamma_{i,j}^m$ is the contribution of samples between i and j in $\hat{\gamma}_m$, and $M_{i,j}$ is the corresponding updating sample mean of x. For evaluation of some terms in the expanded form of Eq. (4) which contain x_{j-m}, access to m previous samples is required. To avoid the storage of the whole data samples, the use of an updating buffer array is proposed in [5]. The resulting UQ method is called in-situ modelled ACF (iMACF). Although

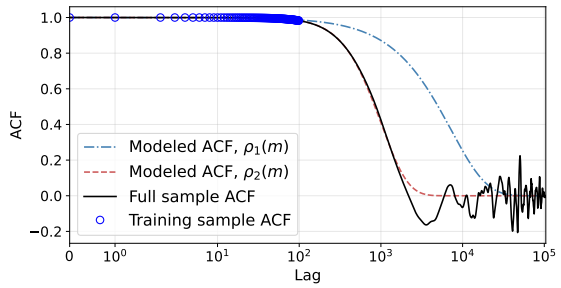

Figure 1: Impact of the function used for modeling the ACF from 10^5 time samples taken from a turbulent channel flow averaged streamwise velocity $\langle u \rangle_{xz}$ at $y^+ = 94$. The training sample-estimated ACF data are taken at the first 100 time lags. The ACF models $\rho_2(m)$ and $\rho_1(m)$ refer to Eq. (3) with all terms and only the first term on the right-hand side, respectively.

the algorithms can be directly implemented in a CFD software, they are wrapped as VTK (Visualisation Toolkit) filters in [5] and executed in a Catalyst [8] pipeline together with native VTK filters, for instance, to extract slices from the original mesh (regions of interest). This makes the whole framework versatile.

RESULTS

The accuracy, robustness and computational efficiency of the described framework have been extensively tested based on the LES of turbulent flows in a channel at $\mathrm{Re}_\tau = 300$ (for a-priori analyses), over a NACA4412 wing section at $\mathrm{Re} = 75000$, and around a rotor built out of four blades with NACA0012 airfoil profiles at $\mathrm{Re} = 10000$. All simulations have been performed by the open-source spectral-element CFD software Nek5000 [9] using conformal meshes except the rotor case for which an adaptive mesh refinement strategy was adopted.

The expression (3) has been demonstrated to be capable of accurately modelling the ACFs, and hence accurately estimating $\hat{\sigma}(\hat{\mu})$. This is shown, for instance, in Figure 1 for the time series of the streamwise velocity of the turbulent channel flow use case at an arbitrary distance from the wall. The model (3) is also robust against how the training samples $\mathbf{m}_{\text{train}}$ are selected. This property is highly beneficial to reduce the memory when streaming algorithms for computing $\hat{\gamma}_m$, $m \in \mathbf{m}_{\text{train}}$ are adopted. Figure 2 represents the contours of the SME of the streamwise velocity along with its associated $\hat{\sigma}^2(\hat{\mu})$ estimated by the iMACF method. The level of uncertainties is higher near the trailing edge of the suction side of the wing. Obtaining such a plot using any offline method would require collecting and storing time samples of the velocity at each of the grid points located within the illustrated region of interest, a task that would have slowed down the simulation and required a considerable disk space and memory. If a batch-based method was used, then the estimated uncertainties could be biased with respect to the selected value for the batch size.

CONCLUSIONS

A versatile, accurate, and computationally efficient framework has been designed and tested for in-situ estimation of time-averaging uncertainties in sample mean estimators appearing in turbulence statistics. The framework can be linked

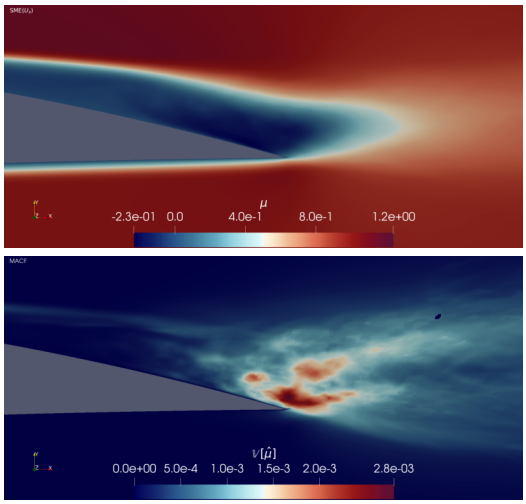

Figure 2: Contours of (top) the SME of streamwise velocity u and (b) associated variance estimated by the iMACF method for the NACA4412 wing use case. The time averaging was performed for overall 5.37 time units equivalent to 200000 time steps. Every 20-th sample was considered in the time averaging.

to any CFD software and handle both conformal and adaptively refined meshes. The weak and strong scaling tests demonstrated a negligible overhead in the computational cost and memory usage by the framework. These results are encouraging to extend the framework to include other in-situ/streaming data analytic techniques in future.

REFERENCES

[1]T. Oliver, N. Malaya, R. Ulerich, and R. Moser, "Estimating uncertainties in statistics computed from direct numerical simulation," *Physics of Fluids*, vol. 26, 02 2014.

[2]S. Russo and P. Luchini, "A fast algorithm for the estimation of statistical error in DNS (or experimental) time averages," *Journal of Computational Physics*, vol. 347, pp. 328 – 340, 2017.

[3]S. Rezaeiravesh, D. Xavier, R. Vinuesa, J. Yao, F. Hussain, and P. Schlatter, "Uncertainty of low- and high-order turbulence statistics in wall turbulence," in *12th International Symposium on Turbulence and Shear Flow Phenomena (TSFP12), Osaka, Japan*, 2022.

[4]J. P. Slotnick, A. Khodadoust, J. J. Alonso, D. L. Darmofal, W. D. Gropp, E. A. Lurie, and D. J. Mavriplis, "CFD vision 2030 study: A path to revolutionary computational aerosciences," 2014.

[5]S. Rezaeiravesh, C. Gscheidle, A. Peplinski, J. Garcke, and P. Schlatter, "In-situ estimation of time-averaging uncertainties in turbulent flow simulations," *arXiv*, no. 2310.08676, 2023.

[6]W. Wei, *Time Series Analysis: Univariate and Multivariate Methods*. Pearson Addison Wesley, 2006.

[7]B. P. Welford, "Note on a method for calculating corrected sums of squares and products," *Technometrics*, vol. 4, no. 3, pp. 419–420, 1962.

[8]A. C. Bauer, B. Geveci, and W. Schroeder, "The ParaView Catalyst User's Guide," 2019.

[9]P. F. Fischer, J. W. Lottes, and S. G. Kerkemeier, "Nek5000 Web page," 2008. http://nek5000.mcs.anl.gov.

SESSION: Numerics and methodology I

Wednesday, April 10, 2024

11:30- 12:45

WORKSHOP
Direct and Large-Eddy Simulation 14
April 10-12 2024, Erlangen, Germany

A COMPARATIVE STUDY BETWEEN VARIATIONAL MULTISCALE AND STREAMLINE-UPWIND PETROV GALERKIN METHOD

Carlo Brunelli[1,2,3], **Bart Janssens**[1], **Georg May**[2], **Mark Runacres**[3]
[1]Mechanical Engineering Department, Royal Military Academy, Belgium
[2]Aeronautics and Aerospace Department, von Karman Institute for Fluid Dynamics, Belgium
[3]Engineering Technology Thermodynamics and Fluid Mechanics Group, VUB, Belgium
mail@carlobrunelli.com

INTRODUCTION

The dynamics of fluid flows is complex and requires advanced numerical techniques for accurate prediction and analysis. Large Eddy Simulation (LES) has gained popularity in recent years, primarily due to advancements in high-performance computing and the proliferation of computer clusters. LES has become the method of choice for simulating flows in scenarios where Direct Numerical Simulation (DNS) is too computationally expensive but Reynolds-Averaged Navier-Stokes (RANS) models provide inaccurate results.

Among the many LES methodologies, the Variational MultiScale (VMS) and the Streamline-Upwind/Petrov-Galerkin (SUPG) method have emerged as powerful tools for addressing the challenges posed by a wide range of flow problems. One can be seen as the evolution of the other. Both have earned recognition for simulating convection-dominated flows capturing a broad spectrum of flow scales, and offer a promising avenue for understanding the intricacies of complex fluid behavior. They have been used successfully to study incompressible flows. Bazilves et al. [1] and Colomés et al. [2] have used the VMS to simulate the turbulent channel up to $Re_\tau = 395$.

We present the results of our research conducted using an in-house code developed in the Julia programming language. Our study focuses on the implementation and utilization of SUPG and VMS to solve fluid dynamics problems using structured quadrangular grids and first-order elements. The two methods are compared while solving in 2D: Taylor-Green vortices, vortex-shedding and lid driven cavity flow. Different aspects are analyzed: how the error decays with the mesh refinement, differences between suing the θ and α (originally introduced in [3]) method for time-marching. Furthermore, an in-depth analysis on the conditioning number of the matrices is carried out, it is investigated how the stabilization terms act on it and how the time step plays a key role in the stability of the resolution.

We also show the capabilities of the Julia programming language [4] for high-performance scientific computing and the advantages of developing an internal code for customized CFD simulations.

The insights and results presented in this paper contribute to the growing body of knowledge regarding advanced CFD techniques and their implementation in Julia, opening doors for improved modeling and simulation capabilities in various engineering and scientific disciplines.

METHODS

The non-linear time dependent formulations of the SUPG and VMS which have been implemented and solved are going to be presented. In both methods, the addition of new terms to the weak form of the governing equations, tailored to the specific instabilities encountered, results in stabilized solutions. The new stabilization terms allow us to use same-order elements for both velocity and pressure. Without the new terms the stability Brezzi-Babuska condition is not statisfied, [5], and the solution is unstable. The new stabilized terms have the fundamental characteristic of being *residual-based*. This means that they approach zero when the original flow-governing equations (mass conservation (1) and momentum conservation (2)) are satisfied.

$$R_c = \nabla \cdot \vec{u} \tag{1}$$

$$\vec{R_m} = \frac{\partial \vec{u}}{\partial t} + (\vec{u} \cdot \nabla)\vec{u} + \nabla p - \nu \Delta \vec{u} - \vec{f} \tag{2}$$

RESULTS

Taylor-Green

The Taylor-Green vortex is a classical two-dimensional test case because an analytical solution is available. The accuracy of the model is tested for different mesh grid sizes, time steps and ODE method.

The report of the relation the velocity error and the size of the mesh is shown in graph 1. Simulations have been performed using the α and θ method for time integration.

Vortex-Shedding

In this example, the classic unsteady flow over a circular cylinder is tested to evaluate the performance of the SUPG and VMS in unsteady problems. This test case allows us to use the method on a non-orthogonal mesh. Figure 2 show an snap-shot of the vortex-shedding behind the cylinder. The shear is extremely regular. To avoid numerical instabilities

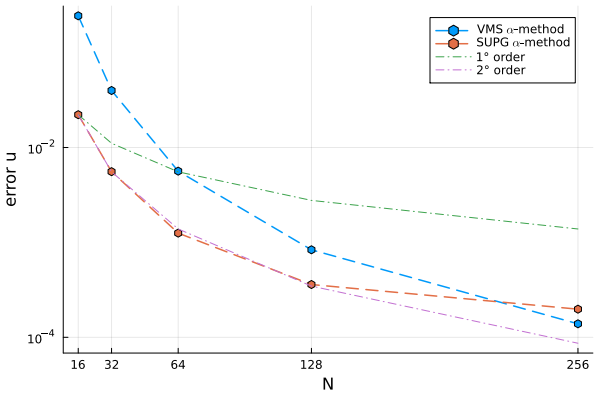

Figure 1: Taylor-Green: velocity mesh error

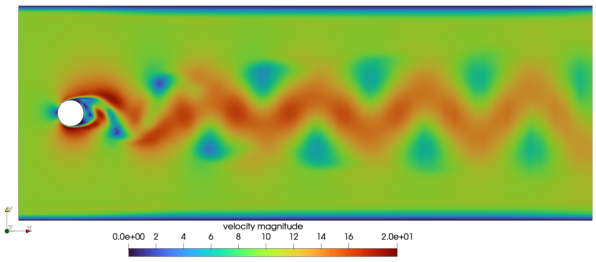

Figure 2: Vortex shedding: instantaneous velocity magnitute, Reynolds 1000

due to the boundary condition at the outlet, a *sponge* fictitious layer has been added. In the last cells the viscosity is increased (according to a parabolic law) to dissipate all the exiting flow. This reduces flow recirculation close to the outlet section, reducing numerical instabilities.

MATRICES AND CONDITION NUMBER

In general, stabilized methods, e. g. SUPG and VMS, are a form of implicit LES that uses a variational approach to separate the flow into scales, and then computes the larger scales explicitly. The unresolved scales are modeled using a residual-based formulation. The idea behind stabilized methods can also be seen from a computational perspective. New terms, which are proportional to the residual of momentum and continuity equations, are added to the variational formulation of the Navier-Stokes equations, in order to reduce the conditioning number of the matrix. In fact, at high Reynolds the matrices are ill-conditioned, and the conditioning number explodes to infinity.

Table 1 shows the matrix conditioning number for the Taylor-Green vortex case using a different stabilized method. It is necessary just to look at the order of magnitude of the condition numbers in the different cases to notice how that non-stabilized formulation is tremendously ill-conditioned. The stabilized method allows one to reduce it by $15 - 20$ orders of magnitude. It is worth noting that the SUPG and VMS methods produce matrices within a very close conditioning number. However, surprisingly, for this case the VMS has a conditioning number which is one order of magnitude higher than the SUPG.

Looking at the sparsity pattern of the matrices is really useful to acknowledge how the variational formulation works

Method	Condition number
Not-stabilized	2.81×10^{22}
SUPG	2.00×10^{6}
VMS	1.90×10^{7}

Table 1: Matrix conditioning number for Taylor-Green Vortex case

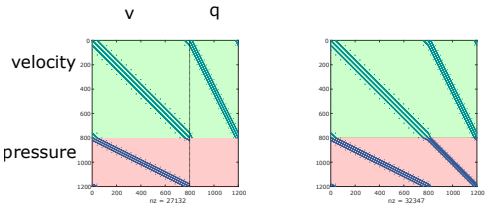

Figure 3: Not-stabilized (left) and VMS stabilized (right) matrices for Taylor-Green vortex

and how the stabilized method modify it.

Figure 3 shows the composition of the final matrix for Taylor-Green case. It is intuitive to identify the rows corresponding to the continuity and momentum due to the lack of pressure terms in the continuity equations. It is the matrix for a coarse grid, 20×20. The total number of degrees of freedom sums up to approximately $20^2 \cdot 3 = 1200$, which is the size of the matrix. The fill-inn is $32347/1200^2 \approx 2.24\%$. Each degree of freedom (dof) in each node is *influenced* by the shape function of the 9 neighboring nodes. It means that each dof is influenced by just 9 shape functions over 400, $9/400 \approx 2.25\%$ which close to the fill-in of the matrix. Stabilized methods increase the fill-in of the matrix.

As mentioned, the continuity equation does not depend on pressure. Therefore, the matrix does not have diagonal elements for approximately 33% of the matrix (25% for a 3D case).

REFERENCES

[1]Bazilevs, Y., Calo, V. M., Cottrell, J. A., Hughes, T. J. R., Reali, A., and Scovazzi, G. (2007). Variational multiscale residual-based turbulence modeling for large eddy simulation of incompressible flows. Computer Methods in Applied Mechanics and Engineering, 197(1–4), 173–201. https://doi.org/10.1016/j.cma.2007.07.016

[2]Colomés, O., Badia, S., Codina, R., énd Principe, J. (n.d.). Assessment of variational multiscale models for the large eddy simulation of turbulent incompressible flows.

[3]Chung, J. and Hulbert, G. M.. A time integration algorithm for structural dynamics with improved numerical dissipation: The generalized-α method. . Journal of Applied Mechanics 1993, vol 60 371-375. 10.1115/1.2900803

[4]Bezanson, Jeff and Edelman, Alan and Karpinski, Stefan and Shah, Viral B (2017). Julia: A fresh approach to numerical computing. SIAM Review. 10.1137/141000671

[5]Arnold, D. N., Brezzi, F., Cockburn, B., Donatella Marini, L.. Unified Analysis Of Discontinuous Galerkin Methods For Elliptic Problems. Numerical Analysis, S. J. . https://doi.org/10.1137/S0036142901384162

[6]Brooks, A. N., and Hughes, T. J. R. (1982). Streamline upwind/Petrov-Galerkin formulations for convection dominated flows with particular emphasis on the incompressible Navier-Stokes equations (Vol. 32).

WORKSHOP
Direct and Large-Eddy Simulation 14
April 10-12 2024, Erlangen, Germany

A ZONAL RANS/LES METHOD FOR WALL-BOUNDED HIGH-SHEAR FLOWS

J. Borgelt[1], **M. Meinke**[1], **W. Schröder**[1,2]
[1]Chair of Fluid Mechanics and Institute of Aerodynamics (AIA), Rheinisch-Westfälische Technische Hochschule (RWTH) Aachen, Germany
[2]JARA Center for Simulation and Data Science, Jülich, Germany
j.borgelt@aia.rwth-aachen.de

INTRODUCTION

Numerical simulations provide valuable insight into the complex unsteady turbulent flow fields at high Reynolds numbers. However, the scale-resolved simulations, e.g. large-eddy simulations (LES) or direct numerical simulation (DNS), of such complex flow problems are challenging even with current computing capabilities. Therefore, they are hardly used in industrial applications. Reynolds-averaged Navier-Stokes (RANS) models offer reduced computational cost due to lower resolution requirements. However, these models are not well suited for unsteady high-shear flows.

An interesting method to efficiently simulate complex unsteady turbulent flows is the zonal RANS/LES concept, sometimes also referred to as segregated RANS/LES, which promises to provide accurate results at reduced computational cost by limiting the turbulence-resolving LES where resolutions beyond the integral length scale are necessary in a region of interest. The main challenge lies in the RANS-LES coupling which has to ensure a smooth transition between non-turbulence-resolved and turbulence-resolved domains. The difference between various RANS-LES forumulations is the hard interface between the predefined computational domains with a discontinuous solution. Hybrid methods use blending functions to switch between the different turbulence modeling.

In general three different zonal interfaces have to be considered. At the inflow of the embedded LES domain turbulent fluctuations have to be created using the time-averaged RANS flow field, whereas the outflow has to be formulated such that no reflections of the fluctuations occur. The third interface is a tangential or wall-parallel RANS/LES interface. This interface has been investigated only in a few of studies. An overview is given in Fröhlich et al. [1] and Arvidson [2]. Quéméré et al. [3] developed a method to calculate velocity fluctuations for the embedded LES domain called enrichment, which was applied to a LES-to-RANS interface inside a turbulent boundary layer. Here the velocity fluctuations described at the ghost cells of the embedded LES domain are calculated by superimposing the velocity obtained by RANS and velocity fluctuations calculated from cells embedded in the LES domain. Terzi et al. [4] and Mary [5] used this method to simulate a curved air intake configuration. They concluded a failure of the tangential coupling described by [3] in cases of non-trivial mean mass fluxes at the tangential interface since inflow fluctuations cannot be obtained.

In the following the zonal method and the numerical setup will be described. Preliminary results are shown and an outlook of future work is given.

ZONAL METHOD

In this work, a semi-coupled zonal RANS/LES method is presented with a novel tangential zonal interface (TZI) formulation. The interface allows an exiting and entering mass flux over the surface determined by the surrounding RANS domain which ensures the correct mass flux in the embedded LES domain. Velocity fluctuations are applied by sampling from cells of the embedded LES domain similar to the enrichment method [3]. However the cells cover an extended area of embedded domain. The sampling distance is set to approx. one correlation length of the velocity fluctuations to mitigate flow dependences. The minimal wall distance of the tangential interface will be part of a parametric investigation. This interface is coupled with wall-normal inflow and outflow boundaries of the embedded LES domain resulting in a further reduction of the overall size of the embedded LES domain. At the inflow the reformulated synthetic turbulence generation (RSTG) method by Roidl et al. [6] is used to generate the turbulent velocity fluctuations from the time-averaged values of the preliminary 2D-RANS solution. The outflow condition is formulated as a characteristic boundary condition (CBC) following Pirozzoli et al. [7]. The amplitude of the incoming wave is modeled using the wall-normal velocity profil and pressure distribution of the preliminary RANS.

The flow variables are exchanged between the RANS regions and the LES region using an underlying Cartesian refer-

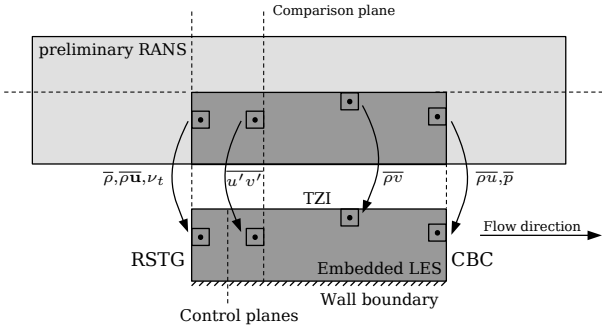

Figure 1: Schematic of cell value exchange.

ence mesh which ensures an efficient exchange without expensive cell value interpolation even for different grid resolutions of the different computational domains. The complete cell value exchange for the three zonal interfaces is shown in figure 1.

NUMERICAL SETUP

The zonal RANS/LES method is used to simulate the separating flow over a curved backward facing step. This flow problem has a non-zero mass flux over the tangential interface. This configuration is considered as a generic problem. Later, the method is to be used to simulate the rim seal flow in an axial tubine, where full LES solutions are extremely expensive.

The geometry and the location of the zonal interfaces are shown in figure 2. The Reynolds number based on the mean velocity and the step height is $Re_h = 28000$ with a Mach number $M = 0.1$. The width in the spanwise direction is set to $4.5h$ with periodic boundary conditions in the spanwise direction. The wall normal distance is set to $\frac{y}{h} = 1.75$. It will be reduced in future work by a parametric study aiming at minimizig the size of the embedded LES domain. This setup, denoted H1, will be compared to a pure LES simulation and a zonal simulation without the tangential interface (woH).

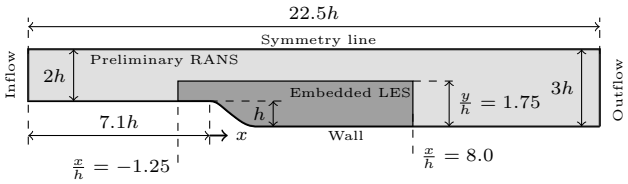

Figure 2: Geometry of total plus embedded domains.

PRELIMINARY RESULTS

Figure 3 shows the wall-normal distributions ostreamwise velocity component u at several streamwise locations. The re-

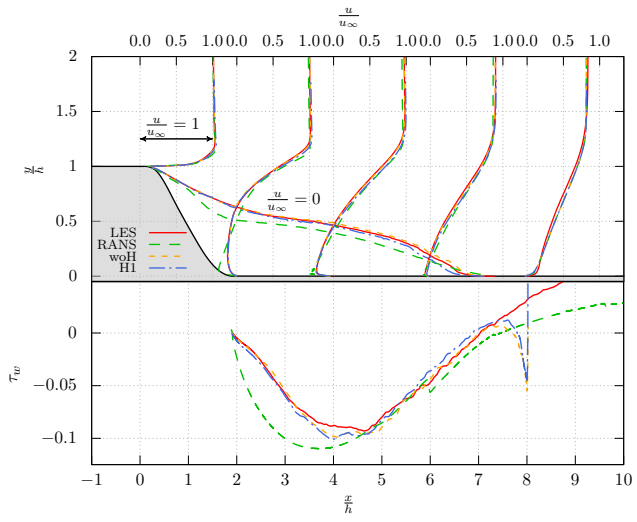

Figure 3: (top) Wall-normal velocity distrubution of the streamwise velocity component u/u_∞, (bottom) non-dimensionalized wall-shear stress τ_W at $y/h = 0.0$.

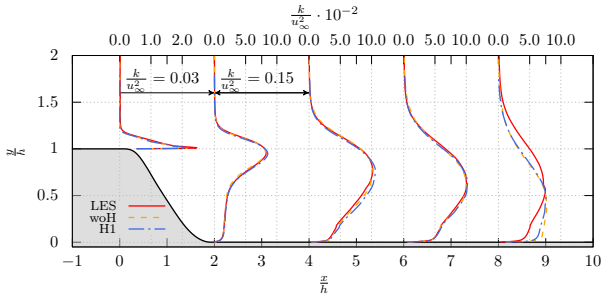

Figure 4: Wall-normal velocity distrubution of the turbulent kinetic energy k.

cirulation region is shown by the contour line $u/u_\infty = 0$. The reattachment position is determined by the vanishing wall-shear stress at the wall $y/h = 0$. The zonal setup H1 shows comparable predictions of the reattachment point compared to the pure LES setup and the zonal setup woH. The CBC ouflow formulation shows only a small upstream effect on the velocity distribution.

The wall-normal distributions of the turbulent kinetic energy k are shown in figure 4. A very good agreement between woH and the pure LES is observed. Furthermore, the setup H1 possesses only a slight difference to woH that shows the quality of the tangential interface formulation. A small discrepancy at the outflow boundary position $x/h = 8.0$ is observed in both setups, i.e., H1 and woH, compared to the pure LES. This is due to the dampening of the streamwise velocity fluctuations by the CBC and the subsequent shift of the remaining velocity fluctuations.

OUTLOOK

The tangential interface will be applied to a stator wake of an axial turbine to efficiently simulate the rim seal flow.

REFERENCES

[1]Fröhlich, J., and Terzi, D.: Hybrid LES/RANS methods for the simulation of turbulent flows, *Progress in Aerospace Science*, **44**, 349–377 (2008).

[2]Arvidson, S.: Methodologies for RANS-LES interfaces in turbulence-resolving simulations, *Dissertation, Chalmers University of Technology, Sweden* (2017).

[3]Quéméré, P. and Sagaut, P.: Zonal multi-domain RANS/LES simulations of turbulent flows, *International Journal for Numerical Methods in Fluids*, **4**, 903–925 (2002).

[4]von Terzi, D., Mary, I., Fröhlich, J.: Segregated LES/RANS Coupling Conditions for the Simulation of Complex Turbulent Flows, *Num. Sim. of Turbulent Flows & Noise Generation*, NNFM **109**, 231–252 (2009).

[5]Mary, I. : RANS/LES Simulation of a Separated Flow in a 3D Curved Duct, *Progress in Hybrid RANS-LES Modelling: Papers Contributed to the 3rd Symposium on Hybrid RANS-LES Methods, Gdansk, Poland, June 2009*, 205–211 (2010).

[6]Roidl, B., Meinke, M., Schröder, W.: A reformulated synthetic turbulence generation method for a zonal RANS–LES method and its application to zero-pressure gradient boundary layers, *International Journal of Heat and Fluid Flow.*, **44**, 28–40 (2013).

[7]Pirozolli, S., Colonius, T.: Generalized characteristic relaxation boundary conditions for unsteady compressible flow simulations, *Journal of Computational Physics*, **248**, 109–126 (2013).

WORKSHOP
Direct and Large-Eddy Simulation 14
April 10-12 2024, Erlangen, Germany

EFFICIENT IMPLICIT TIME-STEPPING FOR HIGH REYNOLDS NUMBER FLOWS AROUND COMPLEX GEOMETRIES

Henrik Wüstenberg[1], Spencer J. Sherwin[1], Joaquim Peiro[1], David Moxey[2]
[1]Deparment of Aeronautics, Imperial College London, United Kingdom
[2]Deparment of Engineering, King's College London, United Kingdom
h.wustenberg@imperial.ac.uk

INTRODUCTION

Solving the unsteady incompressible Navier-Stokes equations for industrial applications requires fast and robust algorithms. Predictions of unsteady flow phenomena are possible via implicit Large-Eddy Simulations (iLES); however, solvers must provide reliable solutions within short design cycles. These constraints are particularly challenging for industrial problems due to complex geometries and high Reynolds numbers flows [1, 2]. Both factors severely restrict the numerical stability of the time-stepping scheme thus the computational efficiency of the algorithm. Therefore, new algorithms are necessary to improve stability and computational efficiency for industrial applications.

We aim to achieve fast and robust simulations using a spectral hp element method and combining it with an implicit time-stepping strategy. The spectral hp element method enables accurate meshes and efficient evaluation of elemental operations for highly curved geometries that are typical for industrial geoemtries [3]. The current workhorse algorithms for incompressible flow use semi-implicit time-stepping which treat diffusion terms implicitly and advection explicitly [4]. Using these schemes on industrial problems, limits the largest time step size Δt through a CFL condition far below what is required for temporal accuracy of the underlying physics and unnecessarily elevates the computational cost. Consequently, numerical stability becomes a limiting factor for the overall time-to-solution.

We investigate an implicit Velocity-Correction scheme based on the work by [5] and [6]. The scheme is unconditionally stable for the advection operator and has previously been shown to give strong improvements in the maximum time step size for two-dimensional problems. While these works have shown strong improvements in stability, they study only low Reynolds number flows. In this work, we employ a slightly modified form of the implicit scheme for three-dimensional simulations of complex geometries. Our aim is to investigate the scheme's robustness at high Reynolds numbers for practical applications.

The next section briefly introduces the implicit Velocity-Correction scheme. The final section shows preliminary results comparing the stability of the implicit and semi-implicit schemes applied to a high Reynolds number flow over a NACA0012 profile.

AN IMPLICIT VELOCITY-CORRECTION SCHEME

The implicit Velocity-Correction schemes belongs to the family of spliting schemes. These schemes efficiently solve the incompressible Navier-Stokes equations by decoupling the full set of equations into a Poisson problem for the pressure p and multiple Advection-Diffusion-Reaction (ADR) problems, one for each velocity coponent u, v, w. The pressure Poisson problem is defined as

$$\nabla p^{n+1} = -\frac{1}{\Delta t}\left(\gamma\tilde{\mathbf{u}}^{n+1} - \sum_{q=0}^{J-1}\alpha_q\mathbf{u}^{n-q}\right) - [\mathbf{u}\cdot\nabla\mathbf{u}]^n \\ -\nu\nabla\times\nabla\times\mathbf{u}^n + \mathbf{f}^{n+1}, \quad (1)$$

where J is the order of the backwards difference formula that appoximates the time derivative. The equation is supplemented with appropriate pressure boundary conditions to enable higher-order time accuracy [4] for the splitting. The boundary conditions are

$$\frac{\partial p}{\partial \mathbf{n}}^{n+1} = \mathbf{n}\cdot\Big[\frac{1}{\Delta t}\sum_{q=0}^{J-1}\alpha_q\mathbf{u}^{n-q} - [\mathbf{u}\cdot\nabla\mathbf{u}]^n \\ -\nu\nabla\times\omega^n + \mathbf{f}^{n+1}\Big]. \quad (2)$$

The velocity equation uses the implicit pressure p^{n+1} to solve for each component with

$$\frac{\gamma}{\Delta t}\mathbf{u}^{n+1} + \tilde{\mathbf{u}}\cdot\nabla\mathbf{u}^{n+1} - \nu\nabla^2\mathbf{u}^{n+1} = \frac{1}{\Delta t}\sum_{q=0}^{J-1}\alpha_q\mathbf{u}^{n-q} \\ -\nabla p^{n+1} + \mathbf{f}^{n+1}. \quad (3)$$

Note that the implicit advection operator is linear because we assume the advection velocity $\tilde{\mathbf{u}}$ is approximated by the extrapolated velocity $\mathbf{u}^{\star n+1} \approx \sum_{q=0}^{J-1}\mathbf{u}^{n-q}$.

The key difference to the semi-implicit scheme is that the velocity problem uses an advection operator. Therefore, the ADR matrices have time-dependent coefficients which makes them less performant when matrices are constructed, however, does not have an impact on performance for matrix-free approaches. Additioanlly, the advection matrix is non-symmetric and requires an adequate iterative solver for the solution of the system. In this work, we employ a restarted Generalised Minimum Residual Method (GMRES) with Jacobi Preconditioner.

PRELIMINARY RESULTS

We aim for industrial applications and therefore require robustness as well as a reasonable time-to-solution for the prediction of turbulent flows. The results compare the stability improvement of an implicit over a semi-implicit time-stepping strategy. We measure the stability of both schemes based on the maximum time-step size that provides a stable solution when time integrating for multiple convective time units (CTU).

The test case for stability and accuracy comparisons is a NACA0012 geometry see Figure 1. It has a chord length $c = 0.2$ and is simulated with a challenging Reynolds number of $Re = 1.44 \times 10^5$. The profile is inclined with respect to the horizontal coordinate axes at an angle of attack of 5°. All simulations are advanced from an initial solution for $10CTU$. CTU is a nondimensional time based on the convection of flow past the chord of the profile and it is defined with $CTU = \frac{U}{c}t$ where t is the physical time and U the farfield velocity $U = 1$. Both, implicit and semi-implicit, schemes are run with increasing time step sizes to identify the stability limit.

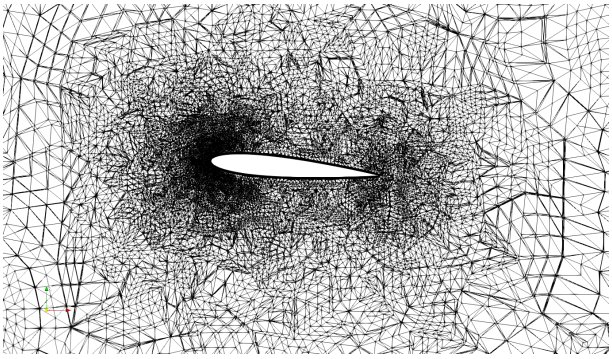

Figure 1: The test case a three dimensional NACA 0012 profile with a 5° angle of attack. The mesh consists of ≈ 40000 tetrahedral and prismatic elements with polynomial order $P = 4$.

Figure 2 shows predictions of the lift coefficient C_L for the NACA0012 profile. The simulations showed that the maximum stable time step size for the semi-implicit scheme is $\Delta t = 8e-5$. In contrast, the implicit scheme increases the stability margin up to $\Delta t = 1e-3$ which gives a 12.5-times larger stability margin.

We compare the accuracy of predictions based on the largest stable Δt for the semi-implicit and implicit scheme as well as intermediate time step sizes. Overall, We observe good agreement between both schemes and at different step size. For the range $CTU = [5-7]$, lift predictions are almost identical. It is interesting that this trend is independent of the time step size and thus the temporal error in the solution. Post $CTU = 7$, the chaotic nature of the turbulent flow at this high Reynolds number leads to instantaneous differences in the predictions. These are likely due to a laminar separation bubble on top of the profile typical for these flow conditions [7]. Nevertheless, the overall trend of the lift coefficient is well predicted even at largely increased time step sizes.

This is confirmed by comparing the time-averaged lift coefficients in Table 1. The averaging is based on the entire 10 CTUs. Both schemes predict the lift coefficient with small error for the largest time step size $\Delta t = 8e-5$ with an error of 0.09%. Further increasing the time step size shows a slightly larger error of about 0.5%, however, this error does not change much for even an order of magnitude increase from $\Delta t = 1e-4$ to $\Delta t = 1e-3$. This further confirms our hypothesis about the temporal error having a minor effect on the overall prediction.

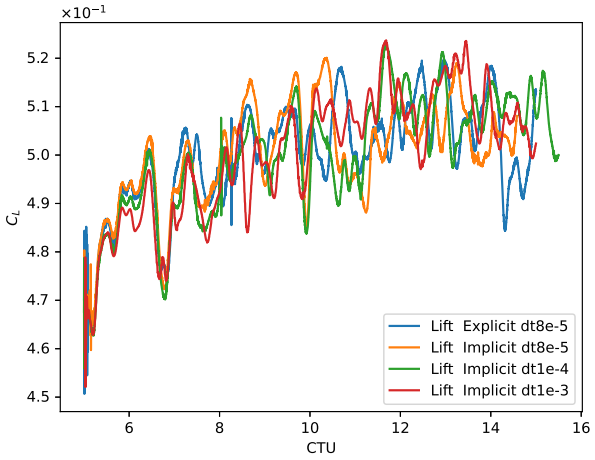

Figure 2: Comparison of Lift predictions between the semi-Implicit and implicit scheme with increasing time step Δt.

Scheme	Δt	Time-avg. C_L	Error
Semi-Implicit	$8e-5$	0.010964	ref
Implicit	$8e-5$	0.010954	0.09 %
Implicit	$1e-4$	0.011022	0.53 %
Implicit	$1e-3$	0.011026	0.57 %

Table 1: Comparison of time-averaged Lift coefficients C_L and their error with increasing time step size Δt.

In summary, the implicit scheme allows more than an order of magnitude increase in the time step size Δt. By comparison, the semi-implicit scheme is stable up to a maximum time step size of $\Delta t = 8e-5$ whereas the implicit scheme gives stable predictions up to $\Delta t = 1e-3$. This improvement in stability provides ample improvement in the robustness and provides leverage for significant reduction in time-to-solution.

REFERENCES

[1]F. F. Buscariolo et al., "Spectral/hp element simulation of flow past a Formula One front wing: Validation against experiments," *Journal of Wind Engineering and Industrial Aerodynamics*, vol. 221, p. 104832, (2022).

[2]J. Slaughter, D. Moxey, and S. Sherwin, "Large Eddy Simulation of an Inverted Multi-element Wing in Ground Effect," *Flow, Turbulence and Combustion*, vol. 110, no. 4, pp. 917–944, (2023).

[3]G. Karniadakis and S. Sherwin, Spectral hp element methods for computational fluid dynamics, 2 ed. *Oxford University Press*, (2013).

[4]G. E. Karniadakis, M. Israeli, and S. A. Orszag, "High-order splitting methods for the incompressible Navier-Stokes equations," *Journal of Computational Physics*, vol. 97, no. 2, pp. 414–443, (1991).

[5]S. Dong and J. Shen, "An unconditionally stable rotational velocity-correction scheme for incompressible flows," *Journal of Computational Physics*, vol. 229, no. 19, pp. 7013–7029, (2010).

[6]J. C. Simo and F. Armero, "Unconditional stability and long-term behavior of transient algorithms for the incompressible Navier-Stokes and Euler equations," *Computer Methods in Applied Mechanics and Engineering*, vol. 111, no. 1, pp. 111–154, (1994).

[7]M. Lahooti, G. Vivarelli, F. Montomoli, and S. Sherwin, Underresolved Direct Numerical Simulation of NACA0012 at Stall. *ECCOMAS Congress 2022, 5-9 June, Oslo, Norway*, (2022).

WORKSHOP
Direct and Large-Eddy Simulation 14
April 10-12 2024, Erlangen, Germany

HOW IMPORTANT IS STRUCTURE-PRESERVING DISCRETIZATION FOR THE PREDICTION OF TAYLOR-GREEN TURBULENCE?

Erwin Luesink[1], Lena Caban[2], Ramy A.M. Rashad[1], Yi Zhang[4], Stefano Stramigioli[1], Artur Tyliszczack[2], Bernard J. Geurts[1,3]
[1]University of Twente, Netherlands
[2]Czestochowa University of Technology, Poland
[3]Eindhoven University of Technology, Netherlands
[4]Guilin University of Electronic Technology, China
{e.luesink, b.j.geurts, r.a.m.rashadhashem, s.stramigioli}@utwente.nl
zhangyi_aero@hotmail.com
{lena.caban, artur.tyliszczak}@pcz.pl

INTRODUCTION

Structure-preserving numerical methods for fluid dynamics have recently been shown to achieve both qualitative and quantitative benefits for the simulation of two-dimensional turbulence [1] . The double cascade mechanism of two-dimensional turbulence as postulated by Kraichnan [2] could be captured accurately at moderate resolutions with a structure-preserving method. The results obtained with these problem-specific lower-order methods compare favorably against very high resolution spectral methods. In fact, the latter that do not properly capture the forward enstrophy cascade, resulting in qualitative descrepancies.

A natural follow-up question is whether structure-preserving methods can achieve similar benefits for three-dimensional turbulence. In the three-dimensional Navier-Stokes equations without forcing on a triply periodic domain, mass is conserved and there are precise expressions that indicate the rate at which energy decays from the initial state [3]. Similar expressions for the rate at which enstrophy and helicity decay are available. The central question we address here is whether the numerical preservation of these foundational characteristics is beneficial for the dynamics captured by the simulations. To provide context for the structure-preserving discretisation we compare the findings to simulations with methods that do not explicitly preserve this structure, but have an established high order of convergence.

The relevance of maintaining the dynamic structure of the underlying problem compared to adopting a discretization method of high order is investigated in the context of the Taylor-Green vortex. To assess the performance of the different methods, simulations of the Taylor-Green vortex for $\mathrm{Re} = 400$ and $\mathrm{Re} = 1600$ are performed and compared with the results of the compact difference scheme in [4] and [5]. The results of both methods are compared with the results presented in the seminal work of [5] to create an independent point of reference.

DUAL FIELD METHOD

The dual field method is a structure-preserving numerical method for the incompressible Navier-Stokes equations based on the preservation of topological characteristics that are present in the continuous problem. Specifically, the dual field method preserves the rate of change of kinetic energy, enstrophy and helicity, while also conserving mass.

We developed a finite element implementation of the dual field method, using the Firedrake framework [6]. This implementation is closely related to compatible finite element methods. Compatible finite element methods and the dual field method are based on the preservation of topological invariants such as the de Rham complex. One of the practical implications of the preservation of the de Rham complex associated with the dual field method is that choosing a suitable finite element space for some of the variables immediately fixes finite element spaces for the other variables by the so-called periodic table of finite elements. The dual field method for the incompressible Navier-Stokes equations written in terms of velocity, vorticity and pressure solves the following problem:

$$\begin{aligned} \frac{\partial}{\partial t} v &= \omega \times v - \nabla p + \frac{1}{\mathrm{Re}} \nabla \times \omega, \\ \omega &= \nabla \times v, \\ 0 &= \nabla \cdot v. \end{aligned} \tag{1}$$

This is a coordinate invariant description of the Navier-Stokes equations. The dual field method solves two coupled linear copies of above equations, with the property that these two linear copies are each other's duals.

TAYLOR-VORTEX SIMULATIONS

The performance of the dual field method for the Taylor-Green vortex at $\mathrm{Re} = 400$ is considered next. In Figure 1 a global impression of the developing flow is presented in terms of the vorticity field. Small-scale features appear from the initial conditions, quickly resulting in a complex flow with turbulent signature. Quantitative findings with the dual field method are presented in Figure 2, using a coarse grid of 16^3 cells and a local basis of third-order polynomials. The predictions relate very closely to findings with the reference compact differencing method at higher resolutions. This is confirmed further in Figure 3 in which we also compare the simulation results with earlier work in [5].

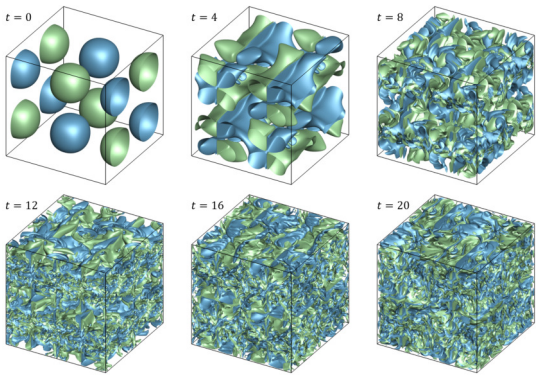

Figure 1: Evolving Taylor-Green vortex simulated with the 6th order compact differencing scheme showing at $Re = 1600$ and a spatial resolution of 256^3.

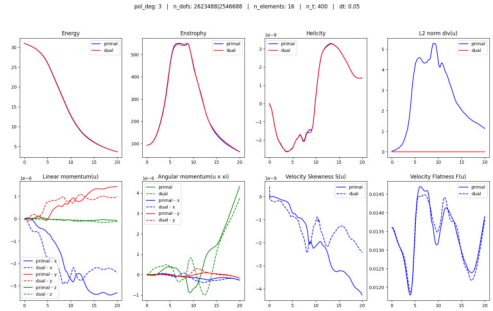

Figure 2: Energy, enstrophy, helicity, L^2-norm of the divergence, linear momentum, angular momentum, velocity skewness and velocity flatness for the Taylor-Green vortex at Re = 400 with the dual field method.

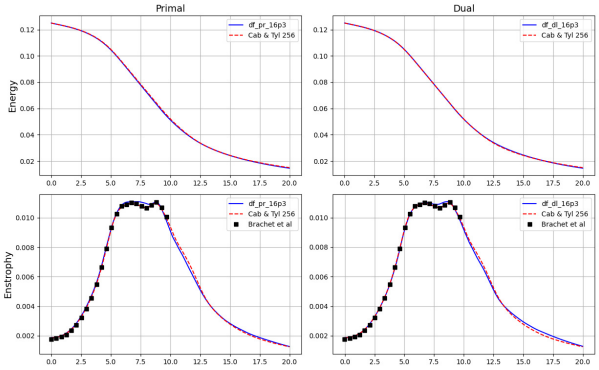

Figure 3: Simulation results for the energy and enstrophy of the Taylor-Green vortex at Re= 400 with the dual field method, the compact differences scheme [7] and verified with [5].

CONCLUSION

We presented first results of incompressible turbulent flow originating from a Taylor-Green vortex. At high Reynolds numbers the flow displays a characteristic evolution from a large-scale dominated initial condition to a field with highly complex small-scale motions. This evolution can be captured well using the 6th order compact differencing method at high spatial resolution and a Reynolds number of 1600.

The simulation of turbulent Taylor-Green flow was also performed based on the dual field method. This method excels by the fact that a number of important properties of the flow are preserved in the numerical model. At a remarkably coarse resolution, this approach showed convincing flow features and also quantitative agreement with sources from literature, as far as the evolution of energy and enstrophy are concerned.

In the full presentation we expect a more complete comparison of the methods and a closer investigation of grid convergence and associated computational challenges and costs.

REFERENCES

[1]P. Cifani, M. Viviani, E. Luesink, K. Modin, and B. J. Geurts, "Casimir preserving spectrum of two-dimensional turbulence," *Physical Review Fluids*, vol. 7, no. 8, p. L082601, 2022.

[2]R. H. Kraichnan, "Inertial ranges in two-dimensional turbulence," *The Physics of Fluids*, vol. 10, no. 7, pp. 1417–1423, 1967.

[3]J. C. Robinson, J. L. Rodrigo, and W. Sadowski, *The three-dimensional Navier–Stokes equations: Classical theory*, vol. 157. Cambridge university press, 2016.

[4]L. Caban and A. Tyliszczak, "High-order compact difference schemes on wide computational stencils with a spectral-like accuracy," *Computers & Mathematics with Applications*, vol. 108, pp. 123–140, 2022.

[5]M. E. Brachet, D. I. Meiron, S. A. Orszag, B. Nickel, R. H. Morf, and U. Frisch, "Small-scale structure of the taylor–green vortex," *Journal of Fluid Mechanics*, vol. 130, pp. 411–452, 1983.

[6]F. Rathgeber, D. A. Ham, L. Mitchell, M. Lange, F. Luporini, A. T. McRae, G.-T. Bercea, G. R. Markall, and P. H. Kelly, "Firedrake: automating the finite element method by composing abstractions," *ACM Transactions on Mathematical Software (TOMS)*, vol. 43, no. 3, pp. 1–27, 2016.

[7]A. Tyliszczak, "A high-order compact difference algorithm for half-staggered grids for laminar and turbulent incompressible flows," *Journal of Computational Physics*, vol. 276, pp. 438–467, 2014.

WORKSHOP
Direct and Large-Eddy Simulation 14
April 10-12 2024, Erlangen, Germany

WAVELET-BASED IMPLICIT LES OF TURBULENT FLOWS

Giuliano De Stefano[1]
[1]Engineering Department
University of Campania, Aversa, Italy
giuliano.destefano@unicampania.it

INTRODUCTION

In large-eddy simulation (LES) of turbulence, the influence of unresolved turbulent eddies is usually approximated through modeling of supplemental subgrid-scale (SGS) terms appearing in the filtered governing equations. As an alternative, the same effect can be implicitly taken into account by exploiting the embedded dissipation of the numerical integration method, without introducing any explicit modeling procedure, which is referred to as implicit large-eddy simulation (ILES) [1].

Traditionally, ILES methods utilize the built-in dissipation introduced by the approximate spatial discretization of the convective terms in the Navier-Stokes equations as a functional model mimicking the physical SGS dissipation. However, the numerical truncation error may not be consistent with turbulent flow physics, with the artificial dissipation provided by the numerical scheme not ensuring the proper amount of local SGS dissipation. To overcome this issue, for instance, specific ILES methods based on truncation error shaping of finite-volume reconstructions have been introduced in [2]. Moreover, if the built-in numerical dissipation is not sufficient, the accumulation of energy at the smallest resolved scales can be reduced by performing an explicit filtering operation. In fact, the use of additional low-pass filters (applied every few time steps during the computation) represents an alternative way to subrogate SGS dissipation, e.g. [3].

WAVELET-BASED IMPLICIT SGS MODELING

The wavelet-based adaptive LES represents a rather novel approach to modeling and simulation of turbulence, which makes use of the adaptive wavelet collocation (AWC) method to resolve the energetic coherent eddies in the turbulent flow field [4]. The method combines the benefits of dynamic grid adaptation and implicit low-pass filtering, where the governing equations are spatially discretized using (relatively) coarse time-dependent meshes, while explicitly modeling the effect of residual SGS coherent eddies, e.g. [5]. Specifically, the simulation approach is based on the wavelet decomposition of the turbulent fields, where the formal separation between resolved (more energetic) and unresolved (less energetic) components is achieved through wavelet threshold filtering.

In this study, following the ILES concept, instead of employing an explicit SGS model, the effect of unresolved coherent flow structures upon the dynamics of the resolved ones is implicitly approximated by exploiting the built-in dissipative properties of the AWC numerical method. Practically, the new proposal consists in using (relatively) low thresholding levels, while not considering any closure term in the wavelet-filtered governing equations. Noteworthily, rather than with classical ILES approaches simply relying on numerical dissipation, the proposed method is more aligned with the modern high-fidelity ILES methods, where the truncation error is suitably designed to resemble physically-motivated SGS modeling, e.g. [6]. In fact, similar to dynamic SGS modeling for explicit LES, here, the numerical viscosity results in being locally and automatically adjusted by refining/coarsening the AWC-based dynamic mesh. That allows to dissipate the right amount of turbulent kinetic energy, which is associated with the local transfer to unresolved coherent eddies. In absence of such a mechanism, where the numerical dissipation is too high, a drastic reduction of the high-frequency components of the resolved turbulence energy spectrum is observed while, where it is too low, the energy incorrectly accumulates at the smallest resolved scales. In both conditions, this fact would ultimately lead to unphysical behavior of the LES solution.

NUMERICAL EXPERIMENTS

The numerical experiments were performed by applying the new wavelet-based adaptive ILES method to the simulation of turbulent supersonic isothermal-wall channel flow, which represents a well-established benchmark for wall-bounded shock-free turbulent compressible flows [7]. The classical flow configuration proposed in the pioneering study by Coleman et al. [8] was considered for the present test, where the computational domain size is given by $4\pi\delta \times 2\delta \times 4\pi\delta/3$, in the streamwsie, wall-normal, and spanwise directions. The bulk flow Reynolds and Mach numbers were prescribed as $\mathrm{Re}_\delta = 3000$ and $\mathrm{Ma} = 1.5$, respectively. The non-adaptive underlying mesh was made of $768 \times 1025 \times 768$ grid points, while only a very small fraction of these points was actually involved by the time-dependent adaptive mesh.

To examine the practical performance of the method, three different calculations were carried out by varying the level ϵ of wavelet thresholding. When making a comparison against reference DNS data, both mean flow features and turbulent fluctuation statistics were correctly reproduced, practically demonstrating both the feasibility and the effectiveness of the newly proposed ILES method. As summarized in Table 1, the number of retained wavelets and, thus, the computational complexity of the method, increased for decreasing threshold. The grid compression, which is measured as the percent of discarded wavelets (or, equivalently, grid points) with re-

Threshold ϵ	Wavelets	Compression	Dissipation
0.01	6.5×10^6	98.9%	11.8
0.02	2.1×10^6	99.6%	12.0
0.03	1.1×10^6	99.8%	12.3

Table 1: Summary of implicit LES calculations with different thresholding level.

spect to the non-adaptive case, remained however very high, as it happens for explicit LES [5]. For decreasing threshold, smaller and smaller turbulent eddies were captured and the DNS solution was practically approached. For instance, this is demonstrated in Figure 1, for the turbulent shear-stress R_{12}, and in Figure 2, for the heat transfer rate H.

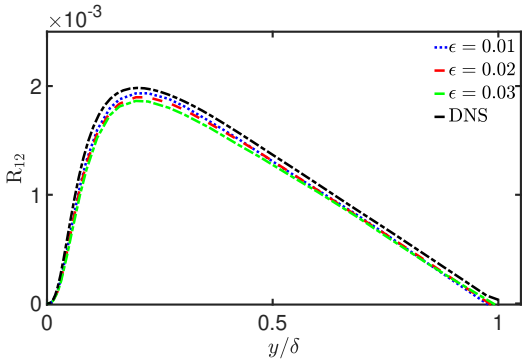

Figure 1: Resolved turbulent shear-stress for different thresholding levels, compared to reference DNS [8].

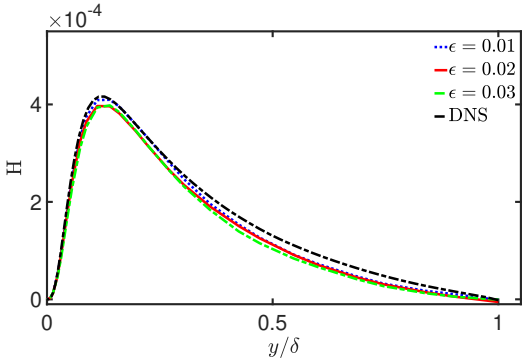

Figure 2: Resolved heat transfer rate for different thresholding levels, compared to reference DNS [7].

The built-in dissipation associated with the use of the AWC method was empirically assessed by using the technique proposed by Schranner et al. [9], which allows for the quantification of the kinetic-energy loss for an arbitrary Navier-Stokes solver, using only information about the resolved flow field (at different discrete-time instants). As reported in Table 1, the resulting numerical dissipation was found to increase with the thresholding level, consistently with the reducing grid resolution [10]. Furthermore, as an example of spectral analysis, Figure 3 shows the (normalized) one-dimensional energy spectra in the streamwise direction, at the wall distance $y/\delta = 0.27$, corresponding to the three different ILES solutions. Apparently, the energy accumulation in the small resolved scales is actually removed before the large scales of interest are contaminated. Again, the importance of low-pass filtering increases with the thresholding level.

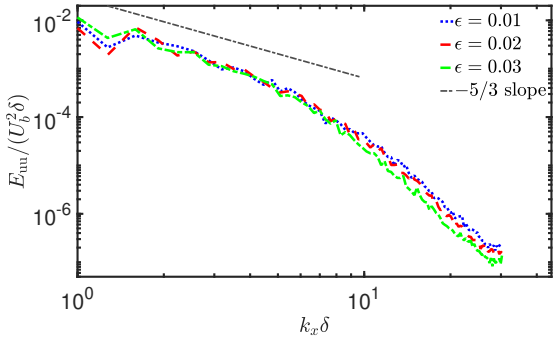

Figure 3: One-dimensional streamwise velocity spectrum for different thresholding levels (U_b stands for the bulk velocity).

CONCLUSION AND PERSPECTIVES

This work introduces the wavelet-based adaptive ILES method, while initially demonstrating its capabilities for wall-bounded compressible turbulence. Depending on the choice of the thresholding level that is used by the AWC solver, the method is able to provide acceptably accurate results, constituting a viable alternative to explicit wavelet-based LES.

Future research will be devoted to better understanding, and effectively exploiting, the intricate coupling between numerical scheme and turbulence modeling that exists for the LES approach based on the wavelet thresholding filter and the AWC method. The matter is complicated by the fact that the prescribed filtering threshold simultaneously controls both the numerical accuracy and the turbulence resolution of the LES solution, where the dynamically adaptive mesh is utilized to determine the relative energy content of the coherent flow structures being resolved.

REFERENCES

[1] Grinstein, F., Margolin, L. and Rider, W. : *Implicit Large Eddy Simulation: Computing Turbulent Fluid Dynamics*, Cambridge University Press, 2007.

[2] Hickel, S., Adams, N.A. and Domaradzki, J.A. : An adaptive local deconvolution method for implicit LES, *J. Comput. Phys.*, **213**, 413–436 (2006).

[3] Sun, G. and Domaradzki, J.A. : Implicit LES using adaptive filtering, *J. Comput. Phys.*, **359**, 380–408 (2018).

[4] De Stefano, G. and Vasilyev, O.V. : Hierarchical adaptive eddy-capturing approach for modeling and simulation of turbulent flows, *Fluids*, **6**, 83 (2021).

[5] De Stefano, G. : Wavelet-based adaptive large-eddy simulation of supersonic channel flow with different thermal boundary conditions, *Phys. Fluids*, **35**, 035138 (2023).

[6] Fu, L., Hu, X. and Adams, N.A. : A targeted ENO scheme as implicit model for turbulent and genuine subgrid scales, *Commun. Comput. Phys.*, **26**, 311–345 (2019).

[7] Morinishi, Y., Tamano, S. and Nakabayashi, K. : Direct numerical simulation of compressible turbulent channel flow between adiabatic and isothermal walls, *J. Fluid Mech.*, **502**, 273–308 (2004).

[8] Coleman, G.N., Kim, J. and Moser, R.D. : A numerical study of turbulent supersonic isothermal-wall channel flow, *J. Fluid Mech.*, **305**, 159–183 (1995).

[9] Schranner, F., Domaradzki, J.A., Hickel, S. and Adams, N. : Assessing the numerical dissipation rate and viscosity in numerical simulations of fluid flows, *Comput. Fluids*, **114**, 84–97 (2015).

[10] De Stefano, G. : Wavelet-based adaptive implicit large-eddy simulation of turbulent channel flow, *Comput. Fluids*, **272**, 106190 (2024).

SESSION: Convection and heat/mass transfer II

Wednesday, April 10, 2024

11:30- 12:45

WORKSHOP
Direct and Large-Eddy Simulation 14
April 10-12 2024, Erlangen, Germany

A ONE-EQUATION VERY-LARGE EDDY SIMULATION APPROACH FOR PREDICTING TRANSVERSE JET MIXING

P. Sander and R. Lechner[1]
[1]Center of Excellence for Cogeneration Technologies,
Ostbayerische Technische Hochschule (OTH) Amberg-Weiden, Germany
p.sander@oth-aw.de

INTRODUCTION

The use of hydrogen is currently investigated also in combined heat and power generation applications. For retrofitting of stationary gas engines port-fuel injection right before the intake valves is preferred to avoid the risk of backfire. Due to the usually low hydrogen system pressures in stationary systems direct-fuel injection into the cylinder is normally not an option. However, port-fuel injection leads to the problem of transverse jet mixing under very low density and velocity ratios of the hydrogen jet to the air crossflow. Transverse jet mixing in general presents significant challenges in accurate prediction and simulation due to the complex interaction of turbulent structures. Traditional Large Eddy Simulation (LES) methods often struggle to balance computational efficiency with the necessary resolution and accuracy. This study introduces a novel approach by integrating one-equation turbulence models, specifically the Spalart-Allmaras and the Wray-Agarwal model, into a Very-Large Eddy Simulation (VLES) framework. This hybrid method aims to efficiently simulate transverse jet mixing under these conditions and evaluates the results in comparison with other computational studies.

METHODOLOGY

The proposed approach leverages the strengths of one-equation turbulence models, memory and computing efficiency, within a VLES framework. VLES, first developed by Speziale [1] as a scale-resolving approach, offers another hybrid methodology for blending between Reynolds-averaged Navier-Stokes (RANS) and LES besides the detached eddy simulation (DES) framework. It also allows for the resolution of larger turbulent scales while modeling the smaller scales. It should offer more robustness against grid-induced separation and a more consistent treatment of turbulence properties across the flow domain. This study adapts two one-equation turbulence models, the classical Spalart-Allmaras model and the more recent approach of Wray and Agarwal, to integrate to the requirements of VLES.

The governing equations for the finite volume method implementation are the compressible Navier-Stokes equations, given by

$$\frac{\partial \rho}{\partial t} + \nabla \cdot (\rho \vec{u}) = 0 \tag{1}$$

$$\frac{\partial (\rho \vec{u})}{\partial t} + \nabla \cdot (\rho \vec{u}\vec{u}) = -\nabla p + \mu \nabla^2 \vec{u} + \nabla \cdot \boldsymbol{\tau} + \rho \vec{g} \tag{2}$$

$$\frac{\partial (\rho E)}{\partial t} + \nabla \cdot (\rho \vec{u} E) + \nabla \cdot (\vec{u} p) = -\nabla \cdot \vec{q} + \nabla \cdot (\boldsymbol{\tau} \cdot \vec{u}) + \rho r + \rho \vec{g} \cdot \vec{u} \tag{3}$$

where ρ is the density, μ the dynamic viscosity, $\vec{u}$ the velocity field, p the pressure, $\boldsymbol{\tau}$ the stress tensor, $\vec{g}$ the gravitational force, E the total energy per unit mass, $\vec{q}$ the heat flux vector and ρr the heat source.

The used Spalart-Allmaras model [2], a one-equation model for turbulence viscosity, is given by

$$\frac{\partial (\rho \tilde{\nu})}{\partial t} + \nabla \cdot (\rho \vec{u} \tilde{\nu}) = c_{b1}(1 - f_{t2}) \rho \tilde{S} \tilde{\nu} - [c_{w1} f_{w1} - \frac{c_{b1}}{\kappa^2} f_{t2}] \rho (\frac{\tilde{\nu}}{d})^2 + \frac{1}{\sigma} \nabla \cdot [\rho(\nu + \tilde{\nu}) \nabla \tilde{\nu}] + \frac{c_{b2}}{\sigma} \rho (\nabla \tilde{\nu})^2 \tag{4}$$

where $\tilde{\nu}$ is the modified kinematic viscosity, ν the molecular kinematic viscosity, $\tilde{S}$ the magnitude of the vorticity, σ, C_{b1}, and C_{w1} are model constants, f_w is a damping function, and d is the distance to the nearest wall.

The Wray-Agarwal model [3] is a wall-distance free model, described by

$$\frac{\partial (\rho R)}{\partial t} + \nabla \cdot (\rho \vec{u} R) = \nabla \cdot [\rho(\sigma_R R + \nu) \nabla R] + \rho C_1 R S + \rho f_1 C_{2k\omega} \frac{R}{S} \nabla R \nabla S - \rho (1 - f_1) \min[C_{2k\epsilon} R^2 (\frac{(\nabla S)^2}{S^2}), C_m (\nabla R)^2] \tag{5}$$

with the turbulent eddy viscosity defined as

$$\mu_t = \rho f_\mu R. \tag{6}$$

In the VLES framework of Han and Krajnović [4], the resolution control function F_r plays a crucial role in blending between the LES and RANS modes and is calculated as

$$F_r = min(1.0, \left[\frac{1.0 - exp(-\beta L_c / L_k)}{1.0 - exp(-\beta L_i / L_k)}\right]^n) \tag{7}$$

where L_c, L_i and L_k are the turbulent cut off length scale, integral length scale and Kolmogorov length scale, defined as

$$L_c = C_x (\Delta_x \Delta_y \Delta_z)^{1/3}, \quad L_i = k^{3/2}/\epsilon \quad \text{and} \quad L_k = \nu^{3/4}/\epsilon^{1/4} \tag{8}$$

with the model parameter C_x, the characteristic cell size $\Delta_x \Delta_y \Delta_z$, the turbulent kinetic energy k and dissipation ϵ.

SIMULATION SETUP AND VALIDATION

The simulation setup involves typical scenarios of transverse jet mixing in a crossflow with circular and rectangular jets, characterized by varying density and velocity ratios. The accuracy is evaluated against benchmark data from numerical studies. The emphasis is on capturing key features such as jet trajectory and the structure of the resulting vortices.

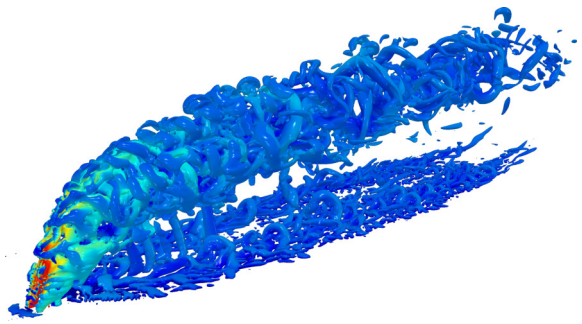

Figure 1: Rectangular tranverse jet mixing, velocity ratio $R = 4$, density ratio $S = 1$, isocontour on $Q = 1 \times 10^{-6}$

RESULTS

Preliminary results demonstrate the ability of the model to accurately predict the jet trajectory and mixing characteristics. Figure 1 shows the development and transport of the turbulent fine structures. The focus of our approach on reducing numerical diffusion with minimal computational effort is particularly evident in the wake of the flow. The model shows a improvement in capturing the anisotropic nature of turbulence in the jet shear layer with a reduced computational cost compared to traditional LES. Figure 2 demonstrates the agreement with the numerical results of the full LES simulation by Zhang and Yang [5]. Both VLES models allow the jet to penetrate deeper into the crossflow while preserving the mean trajectory characteristics. Figure 3 shows a good agreement of the mixture fraction in comparison with the numerical simulations of Prause et al. [6] and experimental results of Andreopoulos et al [7].

CONCLUSION

The integration of one-equation models into a VLES framework presents a promising option for simulating transverse jet mixing with enhanced efficiency and accuracy. This approach provides a practical and computationally feasible alternative to traditional LES, particularly useful for engineering applications where detailed resolution of turbulent structures is essential, but computational resources are limited. Future work will focus on further refining the model parameters, improving the performance and validation on a broad range of jet mixing problems.

REFERENCES

[1]Speziale, C. Turbulence modeling for time-dependent RANS and VLES: a review. *AIAA Journal.* **36**, 173-184 (1998), http://doi.org/10.2514/2.7499

[2]Spalart, P. & Allmaras, S. A one-equation turbulence model for aerodynamic flows. *30th Aerospace Sciences Meeting And Exhibit.* (1992), http://doi.org/10.2514/6.1992-439

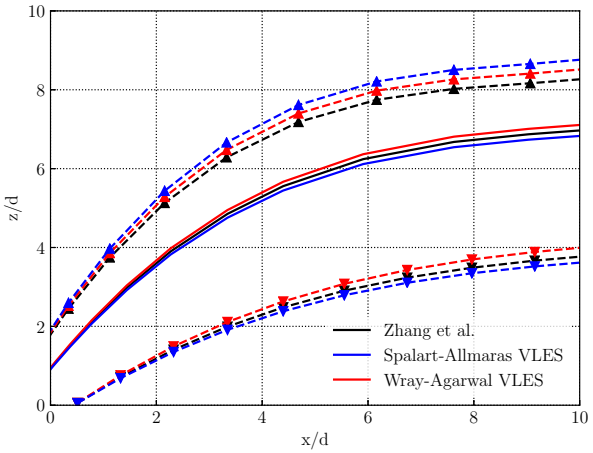

Figure 2: Velocity ratio $R = 4$, density ratio $S = 1$, time-averaged trajectory and lower and upper loci of scalar concentration $C = 0.05$ at jet-center plane, x/z-position by jet diameter d

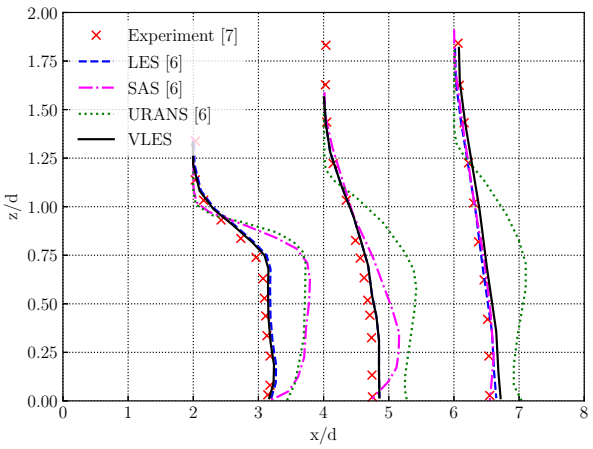

Figure 3: Velocity ratio $R = 0.5$, density ratio $S = 1$, time-averaged mixture fraction at jet-center plane, x/z-position by jet diameter d

[3]Han, X., Rahman, M. & Agarwal, R. Development and application of wall-wistance-free Wray-Agarwal turbulence model (WA2018). *2018 AIAA Aerospace Sciences Meeting.* (2018), http://doi.org/10.2514/6.2018-0593

[4]Han, X. & Krajnović, S. An efficient very large eddy simulation model for simulation of turbulent flow. *International Journal For Numerical Methods In Fluids.* **71**, 1341-1360 (2013), https://doi.org/10.1002/fld.3714

[5]Zhang, L. & Yang, V. Flow dynamics and mixing of a transverse jet in crossflow - part I: steady crossflow. *Journal Of Engineering For Gas Turbines And Power.* **139**, 082601 (2017), https://doi.org/10.1115/1.4035808

[6]Prause, J., Emmi, Y., Noll, B. & Aigner, M. LES/RANS modeling of turbulent mixing in a jet in crossflow at low velocity ratios. *54th AIAA Aerospace Sciences Meeting.* (2016), http://doi.org/10.2514/6.2016-060

[7]Andreopoulos, J. & Rodi, W. Experimental investigation of jets in a crossflow. *Journal Of Fluid Mechanics.* **138** pp. 93-127 (1984), http://doi.org/10.1017/S0022112084000057

WORKSHOP
Direct and Large-Eddy Simulation 14
April 10-12 2024, Erlangen, Germany

DIRECT NUMERICAL SIMULATION OF CONJUGATE HEAT TRANSFER IN THERMAL MIXING SCENARIO IN A T-JUNCTION

A. Mathur[1], T. Nguyen[2], E. Merzari[2], E. Komen[1]
[1]Nuclear Research and Consultancy Group (NRG)
Westerduinweg 3, Petten, The Netherlands
[2]Department of Nuclear Engineering, The Pennsylvania State University
University Park, PA 16802, United States
mathur@nrg.eu

INTRODUCTION

T-junction geometries are widely-used components in the nuclear industry. The thermal mixing in a T-junction, which may result in cyclical thermal stresses and ultimately thermal fatigue on the solid walls, remains an ongoing interest in nuclear thermal-hydraulics research. Understanding and predicting these effects can advance the design and development process within the industry.

Numerous experimental and numerical campaigns have been reported in the literature studying thermal mixing between the fluids and thermal striping on the wall [1, 2, 3]. It has been reported that most practical engineering models such as Reynolds-Averaged Navier Stokes (RANS) and Wall-Modelled Large Eddy Simulation (WMLES) fail to capture the flow physics of a thermal mixing in a T-junction due to their inability to capture non-equilibrium turbulence. Numerical tools which can faithfully predict the turbulent thermal mixing, and thereby thermal fatigue, require extensive validation and verification. This necessary exercise require a high-resolution reference database.

Some recent works in the literature have reported high-fidelity numerical data for thermal mixing (c.f. thermal mixing in planar T-junction reported by Georgiou and Papalexandris [4]). However, some gaps in knowledge can clearly be seen in the literature. In that context, the present study reports a high-fidelity Direct Numerical Simulation (DNS) of thermal mixing in a T-junction geometry with a circular cross-section including the conjugate heat transfer with the solid walls. Past numerical studies have reported only near-unity or high-Prandtl number flows. The present DNS case, however, includes both unity- and low-Prandtl number fluids. Finally, the two fluids are employed in combination with two different thermal boundary conditions at the solid exterior boundary, representing the initial and final stages of a mixing transient.

COMPUTATIONAL MODEL

The present work considers a T-junction with equal inlet diameters with flow rates in each inlet. A preliminary calibration study to set up the DNS case was reported by Ajay Kumar et al. [5]. In order to reduce the high computational cost of a sharp corner at the junction, a revised shape with a radius of curvature, $r_c/D = 0.02$ is considered, where D is the pipe diameter. Fully-developed turbulent flow inlet condition is enforced by including $5D$ recirculating lengths upstream of the junction. Additional lengths of $3D$ are also added downstream of the recirculation lengths in order to avoid any effect of the junction on the recirculation. An outlet length of $13D$ is included in the domain. A solid wall of thickness $0.1D$ is included in the entire domain, along both inlet legs and the outlet leg.

The cold fluid temperature of T_c is imposed on the main inlet, while a hot fluid temperature of T_h is imposed in the branch inlet. The same bulk velocity of U_b is imposed on both inlets. A fully-developed turbulent flow is enforced at the junction, by recycling the velocity field in the initial $5D$ of each inlet pipe. A bulk Reynolds number in each inlet pipe is set as $Re_b = U_b D/\nu = 5300$, where ν is the constant fluid kinematic viscosity. The simulation is performed with four thermal fields within the passive scalar framework of the solver, along with the same set of momentum equations. Two different Prandtl numbers (unity and 0.025) are considered in combination with two different thermal conditions at the solid exterior boundaries (iso-temperature and adiabatic). The solid-to-fluid thermal conductivity ratio is set equal to 30 for $Pr = 1$ fluids, and equal to 1 for $Pr = 0.025$ fluids.

The high-fidelity simulations are performed using the open-source spectral element solver NekRS [6]. The flow is solved using the standard incompressible Navier-Stokes equations, assuming constant physical properties and no gravity. Temperature fields are solved as passive scalars. The governing equations are solved by approximating Lagrange interpolants to the Legendre polynomials of a specific order, using the Gauss-Lobatto-Legendre (GLL) node distribution. The velocity and the pressure fields are represented by the same polynomial degree in the spatial discretization (i.e., $P_N - P_N$ formulation). In order to avoid spurious pressure modes of the pressure-velocity collocated scheme, the solver employs a high-order splitting approach that has shown high-order accuracy in time and minimal mass and energy conservation errors. The equations are advanced in time using a third-order mixed Backward Difference/Extrapolation (BDF3/EXT3) scheme.

The estimate of Kolmogorov scales in the preliminary study [5] was used to design a computational grid for the present fully-resolved DNS. A structured grid of hexahedral macro-elements is generated in the domain. A two-dimensional section of this grid on a pipe cross-section is presented in Figure 1. The total number of macro-elements mapped in the fluid are

2.86×10^5, while that in the solid are 1.60×10^5. Each element is further resolved in space by the solver with a polynomial order, N. The present fully-resolved DNS is performed at N = 9, which results in a total of 4.46×10^8 GLL points. The mesh resolution is verified a posteriori using the Kolmogorov scale calculated from the resolved turbulent kinetic energy dissipation.

PRELIMINARY RESULTS

The distributions of instantaneous velocity magnitude and temperature across the pipe cross-section in the outlet leg $2D$ downstream of the junction are presented in Figures 2 and 3, respectively. The instantaneous flow will be elucidated using vortical structures near the junction. The major features of the flow physics like flow separation and recirculation will be discussed. The turbulent thermal mixing of the two fluids will also be analysed. The mean and high-order statistics for velocity and temperature will be presented.

The present high-resolution data provides access to temperature fluctuations in the fluid very close to the wall and within the solid wall. A comparison of the same will be presented revealing the degree to which the thermal fluctuations can penetrate inside the solid wall for different fluids and thermal boundary conditions. A power spectral density (PSD) analyses of the fluctuations in the solid will show the frequencies of fluctuation in the solid material. Such high-fidelity data is crucial for further development and validation of engineering models.

The DNS also provides crucial data in understanding of turbulent heat transfer and thermal mixing mechanisms for low-Prandtl fluids, experimental measurements for which are difficult to obtain and high-fidelity numerical data in the literature is scarce. Analyses on turbulent heat flux, turbulence anisotropy and budgets of turbulent kinetic energy will also be presented.

REFERENCES

[1]Smith, B.L., Mahaffy, J.H., Angele, K. : A CFD benchmarking exercise based on flow mixing in a T-junction, *Nucl. Eng. Des.*, **264**, 80-88 (2013).

[2]Howard, R.J.A., Serre, E. : Large-eddy simulation in a mixing tee junction: High-order turbulent statistics analysis, *Int. J. Heat Fluid Flow*, **51**, 65-77 (2015).

[3]Shams, A., Edh, N., Angele, K., Veber, P., Howard, R., Braillard, O., Niceno, B. : Synthesis of a CFD benchmarking exercise for a T-junction with wall, *Nucl. Eng. Des.*, **330**, 199-216 (2018).

[4]Georgiou, M., Papalexandris, M. V. : Direct numerical simulation of turbulent heat transfer in a T-junction, *J. Fluid Mech.*, **845**, 581-614 (2018).

[5]Ajay Kumar, A., Mathur, A., Gerritsma, M., Komen, E. : Design of a Direct numerical Simulation of flow and heat transfer in a T-junction , *Nucl. Eng. Des.*, **410**, 112403 (2023).

[6]Fischer, P., Kerkemeier, S., Min, M., Lan, Y.-H., Phillips, M., Rathnayake, T., Merzari, E., Tomboulides, A., Karakus, A., Chalmer, N., Warburton, T. : NekRS, a GPU-accelerated spectral element Navier–Stokes solver, *Parallel Computing*, **114**, 102982 (2022).

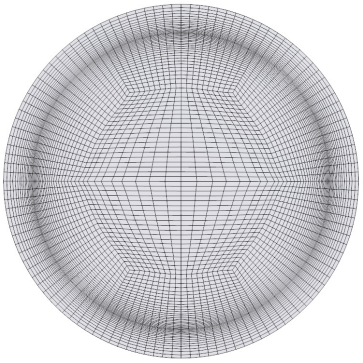

Figure 1: Base computational macro-elements in fluid and solid domains shown on a pipe branch cross-section

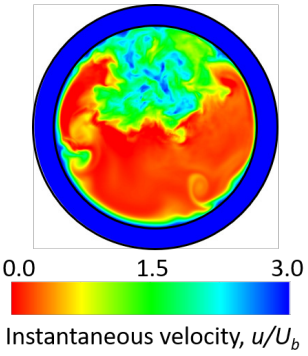

Figure 2: Instantaneous velocity distribution across the outlet pipe cross section

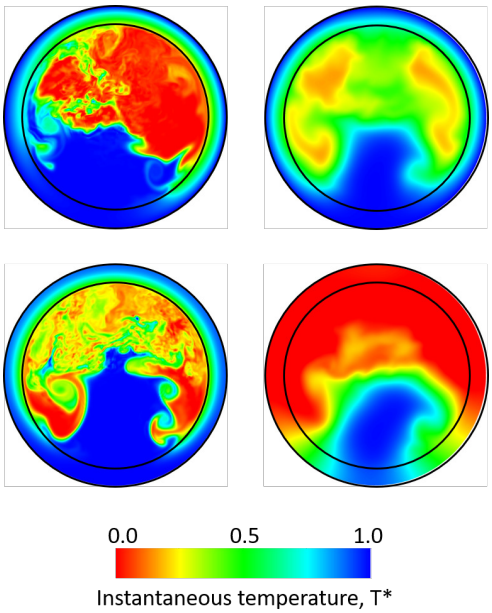

Figure 3: Instantaneous temperature distribution across the outlet pipe cross section for (left) $Pr = 1$ fluids, (right) $Pr = 0.025$ fluids, and (top) iso-temperature and (bottom) adiabatic conditions on the solid exterior boundary

WORKSHOP
Direct and Large-Eddy Simulation 14
April 10-12 2024, Erlangen, Germany

FRICTION AND HEAT TRANSFER PREDICTION IN FORCED-AIR CONVECTION

Davide Modesti[1] **and Sergio Pirozzoli**[2]
[1]Aeodynamics group, Faculty of Aerospace Engineering
Delft University of Technology, The Netherlands
[2]Dipartimento di Ingegneria Meccanica ed Aerospaziale
La Sapienza Università di Roma
d.modesti@tudelft.nl

INTRODUCTION

Forced thermal convection has countless applications in engineering, such as radiators, heat pumps, fuel cells, nuclear plants, and solar receivers. Most studies on forced thermal convection regard the temperature field as a passive scalar, neglecting its feedback effect on the velocity field through the variation of the transport properties of the fluid. Regarding the heat transfer prediction, the effect of variable-fluid properties is accounted for using empirical corrective factor $(\mu_b/\mu_w)^n$[1] applied to to the Nusselt number resulting from formulas obtained for the constant-property case where μ_m and μ_w are the viscosities of the fluid evaluated at the mean and wall temperatures, respectively. However, these corrections are fluid-dependent, are available only for a limited number of fluids, and their accuracy is often questionable. Although studies focusing on the effect of density and viscosity variations in forced thermal convection are available[1, 2], predictive formulas for the heat transfer and friction coefficients are invariably based on empirical fitting of experimental data, and the few numerical studies available did not discuss in detail the prediction of these coefficients. In this study, we aim to develop a more solid theoretical framework to estimate the mean friction drag and heat transfer in the presence of variation of the transport proo perties, limiting ourselves to the case of air as the working fluid. For that purpose, we use DNS data of plane turbulent channel flow at a moderate Reynolds number to evaluate the most common formulas used in engineering and develop improvements.

METHODOLOGY

We solve the compressible Navier–Stokes equations using our flow solver STREAmS [3]. Ten DNS have been carried out at bulk Mach number $M_b = u_b/c_w = 0.2$ (where c_w is the speed of sound at the wall temperature), and bulk Reynolds number $Re_b = 2\rho_b u_b h/\mu_m \approx 7600$–$37000$, where μ_m is the dynamic viscosity evaluated at the mixed mean temperature. The viscosity dependence on temperature is accounted for using Sutherland's law. We consider various mean-to-wall temperature ratios, namely $T_m/T_w = [0, 4, 0.5, 2, 3]$, resulting in friction Reynolds numbers in the range $Re_\tau = u_\tau h/\nu_w \approx 200$–$1000$, where ν_w is the kinematic viscosity at the wall. For each value of the mean-to-wall temperature ratio, we consider two flow cases denoted with the letter L or H, depending on whether the Reynolds number is comparatively 'low' or 'high'.

RESULTS

We begin our analysis by inspecting the instantaneous temperature field of flow cases H05 and H3, see figure 1. Both cases exhibit the qualitative features that characterize wall turbulence, with cold (or hot) flow structures protruding towards the walls, and hot (or cold) fluid regions protruding towards the channel center. Despite sharing the general features of wall turbulence, we also note a significant effect of the thermodynamic and fluid property variations between wall heating and wall cooling. These qualititive differences results in substantially altered heat transfer and friction drag compared to the constant-properties case, as shown in figure 2. In this work we borrow the theory of compressibility transformations, originally developed for high-speed turbulent boundary layer, and apply it to the case of variable propertoes fluid. We derive novel transformations that we use to predict the friction coefficient $C_f = 2\tau_w/(\rho_b u_b^2)$ and the Stanton number $St = q_w/[\rho_b C_p u_b (T_w - T_m)]$. The predictions obtained with this approach are compared to DNS data in figure 2 showing nearly perfect agreement for all the cooling and heating cases under scrutiny.

CONCLUSIONS

Prediction of heat transfer by forced convection in real fluids relies heavily on fitting experimental data with resulting uncertainties up to 20-30%. In contrast, we develop a more solid framework for computing these coefficients, that is based on the underlying mean flow equations, as routinely done in high-speed turbulent boundary layers. The results demonstrate that the method can predict heat transfer and friction coefficients with an accuracy within 1-2% compared to DNS data.

REFERENCES

[1]F. C. Yeh and F. S. Stepka. *Review and status of heat-transfer technology for internal passages of air-cooled turbine blades.* NASA Technical Paper 2232, NASA, 1984.

[2]A. Patel, B. J. Boersma, and R. Pecnik. Scalar statistics in variable property turbulent channel flows. *Phys. Rev. Fluids*, 2(8):084604, 2017.

[3]M. Bernardini, D. Modesti, F. Salvadore, and S. Pirozzoli. STREAmS: A high-fidelity accelerated solver for direct numerical simulation of compressible turbulent flows. *Comput. Phys. Commun.*, 263:107906, 2021.

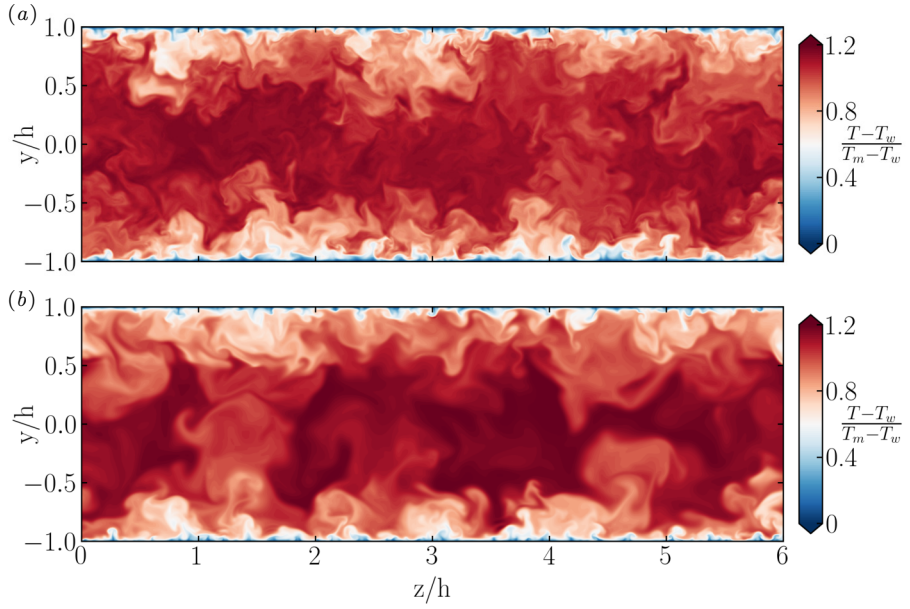

Figure 1: Instantaneous temperature field in a cross-stream plane, for flow case H05(a) and H3 (c)

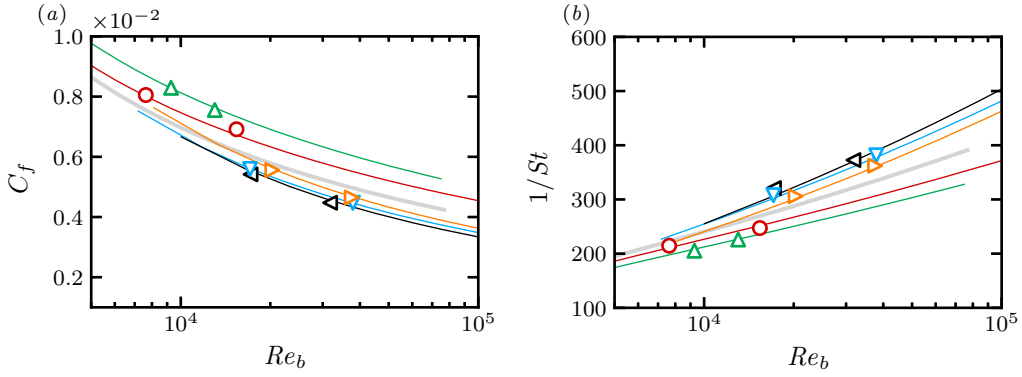

Figure 2: Friction coefficient (a) and Stanton number (b) as a function of the bulk Reynolds number $Re_b = 2h\rho_b u_b/\mu_m$. The gray line indicates the constant-properties case. Solid lines indicate predictions obtained inverting the present variable properties transformations, and symbols indicate DNS data for different mean-to-wall temperature ratios: $T_m/T_w = 0.4$, $T_w = 800K$ (left triangles), $T_m/T_w = 0.5$, $T_w = 220K$ (right triangles), $T_m/T_w = 0.5$, $T_w = 800K$ (downward triangles), $T_m/T_w = 2$, $T_w = 220K$ (circles), $T_m/T_w = 3$, $T_w = 220K$ (upward triangles).

WORKSHOP
Direct and Large-Eddy Simulation 14
April 10-12 2024, Erlangen, Germany

ENSTROPHY DYNAMICS IN A TURBULENT TEMPORAL PLUME

Elisabetta De Angelis[1], **Lorenzo Campana**[1], **Maarten van Reeuwijk** [2]
[1]Department of Industrial Engineering
Università of Bologna, Forlí, Italy
[2]Department of Civil and Environmental Engineering
mperial College, London, UK
e.deangelis@unibo.it

INTRODUCTION

In turbulent free shear flows such as jets, wakes and plumes, a sharp interface continually deformed over a wide range of scales separates the turbulent from the irrotational flow region: the turbulent/non-turbulent interface (TNTI) [1]. Near the TNTI, the exchanges of mass, momentum, and scalars (temperature) occur across this interface, making its study relevant to many engineering and geophysical flows, e.g., the dynamics near the TNTI govern the entrainment and mixing rates in turbulent reacting jets. Several previous works have focused on the role of vorticity or enstrophy in free shear flows, but they mainly concentrate on jets, wakes or mixing layers, as reviewed in [2]. Among these different flow configurations, a notable exception is the work in [3], which discussed aspects of the TNTI on a plane temporal plume. In line with this investigation, the present study aims to elucidate the role of enstrophy close to the sharp interface that separates the turbulent plume from the non-turbulent surroundings. The flow problem considered here is for a Reynolds number based on the initial conditions $Re = 200$ and Prandtl number $Pr = 1$. The domain is a cuboid of size $144H \times 144H \times 96H$ and has been discretized with $3240 \times 2880 \times 1920$ elements. From the initial conditions, the flow freely evolves in time. The data sets of the velocity fields, pressure and temperature are here analysed at three different time instant where we observe increasing Re_λ.

Temporal evolving flows do not show the typical shape of a jet or wake. Here the average interface is flat but instantaneously appears strongly convoluted with bulges and re-entrant zones as in Fig.1. Analysing the flow topology, two main classes of coherent tube-like vorticity structures are observed: the large vorticity structures (LVSs) and the intense vorticity structures (IVSs), consistent with what was observed in [4]. Visually the IVSs, identified by the λ_2-criterion, are smaller than the LVSs and exhibit no preferential orientation as in Fig 2. Conversely, the LVSs tend to be aligned in the spanwise or streamwise direction. Moreover, these structures show a striking correlation with the interface bulges confirming that they define its geometry.

Moving to the quantitative analysis of the enstrophy budget, the traditional averaging procedure regarding the global reference frame in the cross-flow direction turned out to be unsuitable for properly studying the enstrophy dynamics close to the interface. Thus, an analysis of the mean enstrophy budget conditioned to the instantaneous position of the TNTI has been performed. As customary in this type of study, the enstrophy threshold used for the conditional budget has been carefully considered, choosing a value in a range where the volume occupied by the turbulent region would be virtually independent from it.

The conditional budget confirms that the enstrophy dynamics is dominated by inviscid production and viscous destruction but highlights some interesting results. Like for the case of temporal jets and wakes, the viscous diffusion term is fundamental for the enstrophy increase close to the TNTI. Furthermore, in the conditional mean enstrophy budget, the convective term shows a different trend than that observed in jet flows [5]. Lastly, the baroclinic torque is essentially neg-

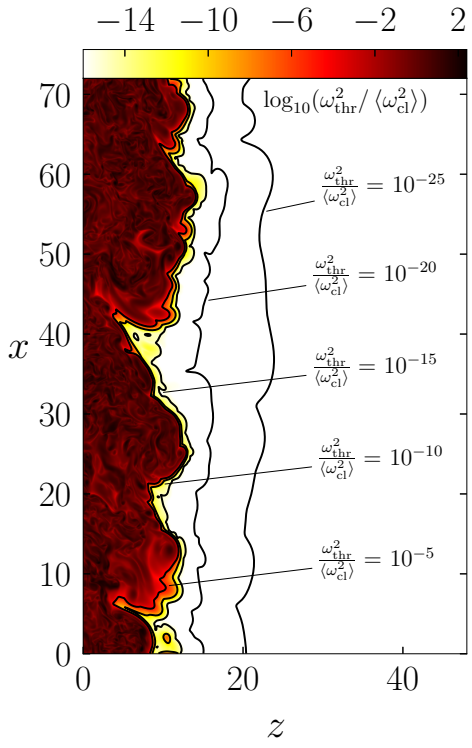

Figure 1: Cross-section showing logarithmic enstrophy contour normalised by the mean centre-line enstrophy, isolines of fixed threshold values, $\log_{10}(\omega_{\mathrm{thr}}/\langle\omega_{\mathrm{cl}}\rangle)$, are also shown.

ligible for almost all the cross-flow directions. However, at the interface location, it undergoes a relatively large increase in magnitude that nearly matches what was already observed [3], acquiring 16% of the net enstrophy budget balance.

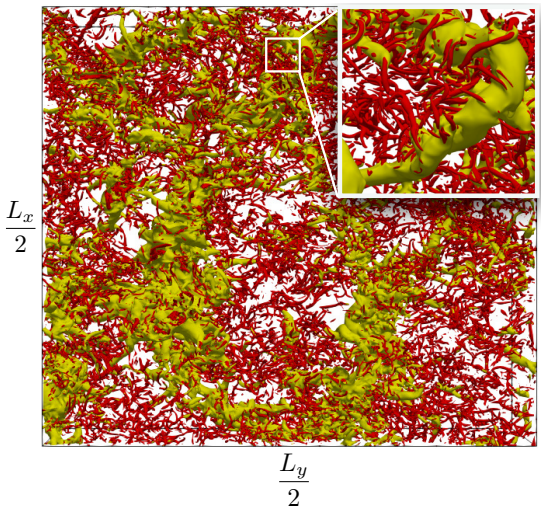

Figure 2: Large vorticity structures (LVSs) identified by a low pressure iso-surface (yellow) and intense vorticity structures (IVSs) identified by the λ_2-criteria (red).

REFERENCES

[1]Corrsin S. and Alan L. Kistler A. L., (1955), Free-stream boundaries of turbulent flows., *No. NACA-TR-1244.*

[2]da Silva, C. B. and Hunt J. CR. and Eames I. and Westerweel J., (2014), Interfacial layers between regions of different turbulence intensity., *Annual review of fluid mechanics, Vol. 46 pp. 567-590.*

[3]Krug D., Chung D., Philip J. and Marusic I., (2017) Global and local aspects of entrainment in temporal plumes., *Journal of Fluid Mechanics, Vol. 812, pp. 222–250.*

[4]da Silva C. B. and dos Reis Ricardo J. N., (2011), The role of coherent vortices near the turbulent/non-turbulent interface in a planar jet., *Philosophical Transactions of the Royal Society A: Mathematical, Physical and Engineering Sciences, Vol. 369, pp. 738–753.*

[5]Silva. T. S., Zecchetto M. and da Silva C. B., (2018), The scaling of the turbulent/non-turbulent interface at high Reynolds numbers. *Journal of Fluid Mechanics Vol. 843, pp. 156.*

WORKSHOP
Direct and Large-Eddy Simulation 14
April 10-12 2024, Erlangen, Germany

ON THE QUEST FOR THE ULTIMATE REGIME OF TURBULENT RAYLEIGH–BÉNARD CONVECTION

Adalberto Perez[1], Martin Karp[1], Niclas Jansson[1], Jörg Schumacher[3], Stefano Markidis[1], Philipp Schlatter[2]
[1]KTH Royal Institute of Technology, Stockholm, Sweden
[2]Friedrich–Alexander–Universität, Erlangen, Germany
[3]Technische Universität Ilmenau, Ilmenau, Germany

INTRODUCTION

Turbulent Rayleigh–Bénard convection (RBC) is the canonical flow in the study of buoyancy-driven flows. Over the years, a vast amount of research has been done on the topic [1, 2]. However, despite the great effort, concrete evidence of the predictions first made by Kraichnan [3] regarding an ultimate regime are still not available [4].

This ultimate regime is a conjecture in which it was hypothesised that as Ra increases, the Nusselt number diverges from the classical scaling $Nu \sim Ra^{1/3}$ and asymptotically converges to $Nu \sim Ra^{1/2}$ due to the laminar-turbulent transition of the boundary layers formed on the walls of the domain. Given the high Rayleigh numbers that are necessary for the manifestation of a possible ultimate regime, a number of challenges arise in experimental and numerical studies, such as a high sensitivity to non-Boussinesq behavior in experiments and limits on resolution and averaging time in previous direct numerical simulations [8].

We aim to provide high-quality numerical data that addresses some of these points. To ensure high resolution, we use the high-order spectral-element method (SEM) solver Neko [5] and the spectral error indicator (SEI) to evaluate the quality of the mesh. We collect proper statistics and perform uncertainty quantification using rigorous statistical tools.

GOVERNING EQUATIONS

In our simulations, the buoyancy-driven problem is simplified by the Oberbeck–Boussinesq (OB) approximation, in which the fluid density ρ is assumed to depend linearly on the temperature and where the fluid properties are constant. Under these assumptions, the temperature field is coupled to the momentum equation through a forcing term. Using the domain height H, the free-fall velocity U_f and the temperature difference between the top and bottom plate ΔT as scales for the non-dimensionalization (see e.g. [4] for more details), the OB equations are written as follows:

$$\begin{aligned} \nabla \cdot \mathbf{u} &= 0 \\ \frac{\partial \mathbf{u}}{\partial t} + (\mathbf{u}\cdot\nabla)\mathbf{u} &= -\nabla p + \sqrt{\frac{Pr}{Ra}}\nabla^2\mathbf{u} + T\mathbf{e}_z \\ \frac{\partial T}{\partial t} + (\mathbf{u}\cdot\nabla)T &= \frac{1}{\sqrt{RaPr}}\nabla^2 T \ , \end{aligned} \tag{1}$$

where T is the temperature field, $\mathbf{u}$, p the instantaneous velocity and pressure, and Pr the Prandtl number. With these definitions and assuming $Pr = 1$, Nu can be calculated by using multiple expressions; one such way is by calculating the heat flux trough the top and bottom plates, $Nu_{\langle A\rangle} = \langle|\partial T/\partial z|\rangle_{A,t}$. A second alternative is to integrate and properly scale the convective current over the whole domain, such that $Nu_{\langle V\rangle} = 1 + \sqrt{Ra}\langle u_z T\rangle_{V,t}$. In addition, the exact relations related to kinetic and thermal energy dissipation, ϵ_k and ϵ_t, respectively, can be used as a test for the heat transfer and convergence of the numerical grid.

NUMERICAL METHODS AND SIMULATION SET UP

For the numerical integration of the Navier–Stokes equation we use Neko [5], which implements the spectral-element method in modern object-oriented Fortran on diverse computer architectures such as GPUs; Neko was nominated to the ACM Gordon Bell Award 2023 due to its design and performance [6]. SEM is a high-order finite-element method, where the solutions are expressed as combinations of an orthogonal basis. High-order methods are essential for simulations of the magnitude undertaken in this study, as their fast convergence rate and favourable dispersion properties allow for reasonably refined meshes while keeping acceptable discretization errors. To assess the mesh quality, we rely on the spectral error indicator (SEI) which measures the error between the exact solution and its approximation of order N by decomposing it into the contribution of the truncation error due to using a finite number of coefficients in the high order expansion in SEM and the contribution of using a quadrature rule for integration [9].

Our initial study focus on simulations of cylindrical convection cells of aspect ratio $\Gamma = 0.1$ at $Ra = 10^8$ to $Ra = 10^{11}$ and $Pr = 1$. All cases ran with a mesh of 500 thousand elements of order 5 except the case with $Ra = 10^{11}$ which posses order 7. For all cases, precursor simulations were used to find initial conditions. The times at which these precursors where finalized are referred to as t_0.

RESULTS

The mesh selection process started by emulating the number of degrees of freedom of previous studies [8] and the spectral error indicators were calculated to supplement the analysis. Taking as an example the case with $Ra = 10^9$, we found that the magnitude of the errors is of order 10^{-8} for

most of the domain and has a peak of order 10^{-6} on particular elements at a wall distance of $0.31\delta_T$ from the bottom plate (considering $\delta_T = H/(2Nu)$ to be the thermal boundary layer thickness). A cross-section of the magnitude of the spectral error indicator can be seen in Figure 1, where one can notice that such errors are localized and, therefore deemed to not be significant. These error estimates can immediately provide a sense of the accuracy of results obtained that cannot be explicitly obtained by analyzing the fields.

Having assessed the mesh quality, the evolution of $Nu_{\langle A \rangle}$ for all cases can be observed in Figure 2. The dotted lines in the figures show the time instant in which we determine that the initial transient is over and a statistically stationary signal is achieved. We rely on robust statistical tools, i.e., the Augmented Dickey-Fuller (ADF) test to perform this calculation. This technique tests the null hypothesis that a unit root is present in the time series, which indicates that the time series is not stationary [7]. We note that the case with $Ra = 10^8$ has clearly converged to a quasi-steady stacked roll pattern for the slender cell configuration.

Discarding the initial portion of the data, we proceed to perform uncertainty quantification of the signals by using the Non-Overlapping Batch Means method (NOBM), which divides the data into subsections (batches), calculates the batch means and subsequently the sample mean estimator and confidence intervals. We test the lag-one auto-correlations of the samples in the batches to ensure statistical independence, which is crucial to get appropriate estimates of the variance. The averages and 95% confidence intervals are shown in Figure 3. We display the averages of $Nu_{\langle A \rangle}$, $Nu_{\langle V \rangle}$, $Nu_{\langle \epsilon_t \rangle}$ and $Nu_{\langle \epsilon_k \rangle}$ on top of the results reported in our reference study [8]. One can observe that Nu matches quite well in all cases. Larger differences were found for $Ra = 10^{11}$, but this case is obtained from a shorter time series. A longer simulation should aid in the convergence of the mean. $Ra = 10^8$ differs from our reference, which suggests that we converged to a different large-scale state. Additionally, considering that the comparison of the Nu calculations with the exact relations for ϵ_t and ϵ_k are typically used in the literature to determine mesh convergence, we can see that indeed obtaining a low spectral error indicator equally distributed across the domain is also a good measure of mesh convergence for spectral element codes.

Future work concerns similar analyses for simulations with $Ra \lesssim 10^{16}$ using up to 100 million elements, given that the relevant tools are in place. The present analysis using robust techniques to asses sources of uncertainty, paired with detailed investigation of the behaviour of the boundary layers and extended to higher Ra, will provide essential information on the nature and appearance of the ultimate regime.

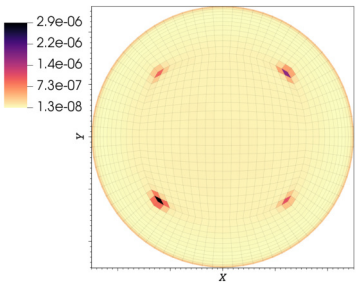

Figure 1: Cross section of the magnitude of the mean spectral error indicator at $z = 0.31\delta_T$ for $Ra = 10^9$.

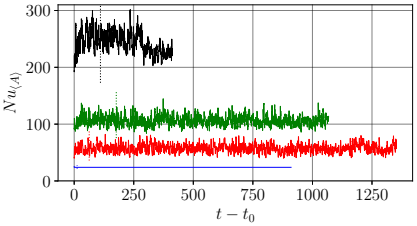

Figure 2: $Nu_{\langle A \rangle}$ as a function of time for $Ra = 10^8$ (—), $Ra = 10^9$ (—), $Ra = 10^{10}$ (—) and $Ra = 10^{11}$ (—). The vertical dotted lines in the same colors indicate the moment when the transient ends determined by the ADF test.

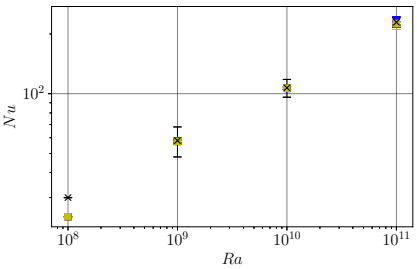

Figure 3: Scaling of Nu as a function of Ra. The black crosses indicate the results reported in [8]. The symbols correspond to different approaches on the calculations of Nu. $Nu_{\langle A \rangle}$ (■), $Nu_{\langle V \rangle}$ (■), $Nu_{\langle \epsilon_t \rangle}$ (■) and $Nu_{\langle \epsilon_k \rangle}$ (■).

REFERENCES

[1] Ahlers, G., Grossmann, S. & Lohse, D. Heat transfer and large scale dynamics in turbulent Rayleigh-Bénard convection. *Rev. Mod. Phys.*. **81**, 503-537 (2009)

[2] Chillà, F. and Schumacher, J. New perspectives in turbulent Rayleigh-Bénard convection, *European Physics Journal E.* **35**, 58 (2012)

[3] Kraichnan, R. Turbulent thermal convection at arbitrary Prandtl number. *The Physics Of Fluids.* **5**, 1374-1389 (1962)

[4] Lindborg, E. Scaling in Rayleigh–Bénard convection. *Journal Of Fluid Mechanics.* **956** pp. A34 (2023)

[5] Jansson, N., Karp, M., Podobas, A., Markidis, S. & Schlatter, P. Neko: A Modern, Portable, and Scalable Framework for High-Fidelity Computational Fluid Dynamics. (2021)

[6] Jansson, N., Karp, M., Perez, A., Mukha, T., Ju, Y., Liu, J., Páll, S., Laure, E., Weinkauf, T., Schumacher, J., Schlatter, P. & Markidis, S. Exploring the Ultimate Regime of Turbulent Rayleigh–Bénard Convection Through Unprecedented Spectral-Element Simulations. *Proceedings Of The International Conference For High Performance Computing, Networking, Storage And Analysis.* (2023)

[7] Xavier, D., Rezaeiravesh, S., Vinuesa, R. & Schlatter, P. Quantification of time-averaging uncertainties in turbulence simulations. *8th European Congress On Computational Methods In Applied Sciences And Engineering.* (2022)

[8] Iyer, K., Scheel, J., Schumacher, J. & K. R. Sreenivasan Classical 1/3 scaling of convection holds up to Ra=$10^1$5. *Proceedings Of The National Academy Of Sciences.* **117**, 7594-7598 (2020)

[9] Offermans, N., Massaro, D., Peplinski, A. & Schlatter, P. Error-driven adaptive mesh refinement for unsteady turbulent flows in spectral-element simulations. *Computers & Fluids.* **251** pp. 105736 (2023)

SESSION: Bubbly flow

Wednesday, April 10, 2024

14:50- 15:50

WORKSHOP
Direct and Large-Eddy Simulation 14
April 10-12 2024, Erlangen, Germany

MESCOSCALE LARGE EDDY SIMULATION (LES) OF BUBBLE COLUMN BUBBLY FLOWS BY CONSIDERING SGS TURBULENT DISPERSION AND ADDED MASS STRESS EFFECTS ON INTERFACIAL MASS TRANSFER

Xiaogang Yang[a*], Shanshan Long[a], Jie Yang[b], Martin Sommerfeld[c]
[a]Department of Mechanical, Materials and Manufacturing Engineering, The University of Nottingham Ningbo China, University Park, Ningbo 315100, PR China
[b]School of Natural Sciences, University of Hull, Hull HU6 7RX, UK
[c]Faculty of Process and Systems Engineering, Otto-von-Guericke-Universität Magdeburg, Zeppelinstraße 1, 06130 Halle, Magdeburg, Germany
*Corresponding author: xiaogang.yang@nottingham.edu.cn

INTRODUCTION

When applying two-fluid model Euler/Euler large eddy simulation (LES), the filtering process involves the use of a phasic 'function of presence' approach to the momentum equation, accounting for the co-sharing of a control volume by different phases. As a result, this leads to the terms denoting interfacial momentum forces, contributed by the dot product of the total stress term and gradient of the 'function of presence' term, which indicates the forces induced by the local flow perturbations at the interface of the second phase (bubbles). The subsequent spatial filtering for LES modelling of the momentum equation and the interfacial momentum terms leads to additional terms that can be attributed to drag and other parts that can be modelled as non-drag forces such as lift force and added mass force together with the sub-grid scale turbulent dispersion force (SGS-TDF) and added mass stress force (SGS-AMS). In the case of conducting two-phase LES, these interfacial momentum exchange terms need to be modelled in terms of the resolved quantities of the flow or filtered variables while taking into account the effect of unresolved fluctuations on the sub-grid scale (SGS). Most of the reported work on two-phase or three-phase LES has overlooked or neglected the unresolved SGS contributions. However, these terms play a crucial role in the prediction of the transverse bubble dispersion in bubbly flow. In the present study, the effects of adopting the spatial filtering for the interfacial momentum exchange terms on the turbulent dispersion and added mass stress in bubble column bubbly flows are studied as shown in Figure 1.

MATHEMATICAL MODELLING AND NUMERICAL METHODS

By taking both phase velocity fluctuations and bubble volume fraction fluctuations into account, the spatial filtering of the drag force and added mass force terms will give rise to the extra terms proportional to the area density slip velocity correlation, i.e., turbulent dispersion, and to the correlation of bubble volume fraction and gradient of SGS stress. In our modified SGS Smagorinsky model, the modified SGS eddy viscosity ν_T accounting for the bubble dynamic response to the turbulent eddies induced shear has also been implemented into the SGS-TDF term. The formulations of the filtered drag, lift and added mass forces employed in the Euler/Euler LES modelling, as shown by Equations (1) and (2), can be found in the study by Long et al. [1].

$$\mathbf{M}_{TD,L} = -\frac{3}{4}\rho_G \frac{C_D}{d_B}|\mathbf{u}_G - \mathbf{u_L}|\frac{\nu_{SGS}}{\sigma_{SGS}}\left(\frac{1}{\alpha_L}+\frac{1}{\alpha_G}\right)\nabla\alpha_G \quad (1)$$

$$\begin{aligned}\mathbf{M}_{AMS,L} = \alpha_G\rho_L C_{AM}\Bigg[&\frac{1}{\alpha_L\rho_L}\nabla\cdot(\alpha_L\rho_L\Omega)\\ &-\frac{1}{\alpha_G\rho_G}\nabla\cdot(\alpha_G\rho_L\Omega)\Bigg]\end{aligned} \quad (2)$$

Here,

$$\Omega = (1-\alpha_G)(C_S\Delta)^2|S_L|S_L\left(1+C_b\alpha_G\frac{\lambda}{d_B}\left(\frac{1}{1+St_{SGS}}\right)^{\frac{3}{2}}\right).$$

Since the modified SGS models have taken the turbulence kinetic energy contribution from BIT and bubble interaction with the turbulence eddies into account, the relative slip velocity between bubbles and liquid together with the local turbulent energy dissipation rate play significant roles in estimating the value of the interfacial mass transfer coefficient k_L. The eddy cell model proposed by Lamont and Scott indicated that the very small scale of the turbulent eddies plays an important role in the mass transfer and these motions lead to an extra contribution to the eddy viscosity [2]. They suggested that the surface renewal rate as the mass transfer indicator can be estimated as

$$k_L \propto \mu D_L^{\frac{1}{2}}\left(\frac{\epsilon_L}{\nu}\right)^{\frac{1}{4}}. \quad (3)$$

By considering the bubble-eddy interactions, it can be assumed that the local total turbulence dissipation rate is expressed as

$$\epsilon_L = \epsilon + \epsilon_B = \epsilon \left(1 + \frac{C_b(\overline{\alpha_G})\lambda}{d} \left(\frac{1}{1+St_{SGS}}\right)^{\frac{3}{2}}\right) = 2\nu \int_0^\infty \kappa^2 E(\kappa) d\kappa. \quad (4)$$

The influences of the bubbles' dynamic responses to the surrounding liquid and inclusion of the SGS-TDF and SGS-AMS models in the LES on the liquid turbulent kinetic energy spectrum and mass transfer can be evaluated using the following expression:

$$k_L \propto \mu D_L^{\frac{1}{2}} \left[\frac{\epsilon \left(1 + \frac{c_b \overline{\alpha_G} \lambda}{d} \left(\frac{1}{1+St_{SGS}}\right)^{\frac{3}{2}}\right)}{\nu}\right]^{\frac{1}{4}} \propto \mu D_L^{\frac{1}{2}} \left(\frac{2\nu \int_0^\infty \kappa^2 E(\kappa) d\kappa}{\nu}\right)^{\frac{1}{4}}. \quad (5)$$

It was revealed that ignoring the SGS-TDF and SGS-AMS results in the underestimation of the mass transfer coefficient. Figure 2 shows the volumetric mass transfer coefficient contours obtained at different heights with and without using both the SGS-TDF and SGS-AMS models.

CONCLUSIONS

This study highlights the importance of considering the SGS turbulent dispersion and added mass stress forces in Euler/Euler LES modelling of bubble column bubbly flow. It has been clearly demonstrated that by using Euler/Euler LES modelling and considering the effect of bubble-eddy interactions on the SGS turbulent dispersion and added mass stress models, the prediction of bubble dynamics can be improved significantly. This suggests that the modified SGS-TDF and SGS-AMS models may play an equivalent role in indicating the bubble fluctuating motion predicted by using the Euler/Lagrange LES modelling approach together with the stochastic dispersion model [3]. Finally, a correlation of the estimated mass transfer coefficient k_L to the local extra eddy has been proposed in this study.

ACKNOWLEDGEMENTS

This work was financially supported by the National Natural Science Foundation of China (Grant Nos. 21761132026, 91534118).

REFERENCES

[1]Long, S., Yang, X., Yang, J., Li, B.; Shi, W., Sommerfeld, M.: Euler-Euler LES of bubble column bubbly flows by considering sub-grid scale turbulent dispersion effect on modulating bubble transport, *Chemical Engineering Journal*, 477, 147239 (2023).

[2]Lamont J.C., Scott D.: An eddy cell model of mass transfer into the surface of a turbulent liquid, *AIChE Journal*, 16, 513-519 (1970).

[3]Sommerfeld, M., Muniz, M., Reichardt, T.: On the importance of modelling bubble dynamics for point-mass numerical calculations of bubble columns, *Journal of Chemical Engineering of Japan*, 51, 301-317 (2018).

FIGURES

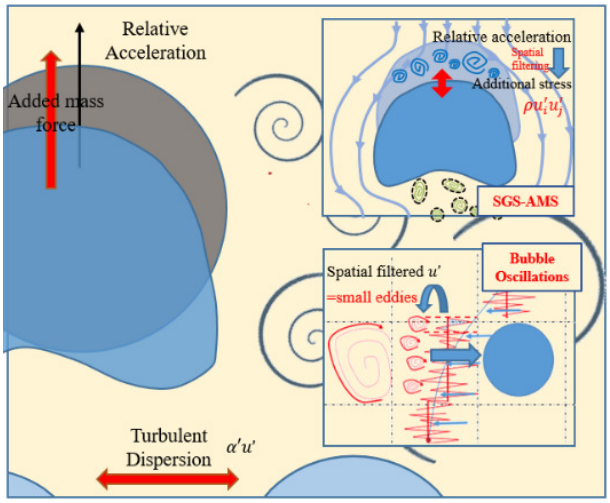

Figure 1: Schematic of contribution from SGS-TDF and SGS-AMS in bubbly flow.

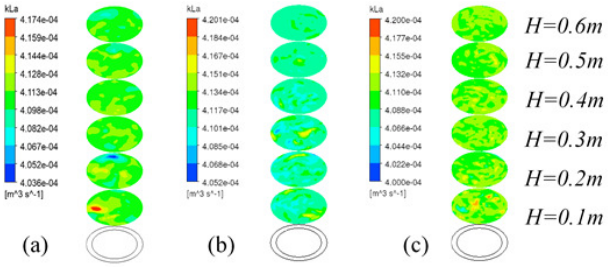

Figure 2: Contours of the simulated volumetric mass transfer coefficient, K_L, along the height of the bubble column by using (a) case 1: D+L+AM+TD; (b) case 2: D+L+AM+SGS-TDF; (c) case 3: D+L+AM+SGS-TDF+SGS-AMS.

WORKSHOP
Direct and Large-Eddy Simulation 14
April 10-12 2024, Erlangen, Germany

DNS OF BUBBLY TAYLOR-COUETTE FLOW TO PREDICT DRAG REDUCTION

B.J. Geurts[1,4], **A.D. Franken**[1], **S. R. Ephrati**[2], **A. Tyliszczak**[3]
[1] Mathematics of Multiscale Modeling and Simulation University of Twente, The Netherlands
[2] Department of Mathematical Sciences, Chalmers University of Technology, 412 96 Gothenburg, Sweden
[3] Department of Thermal Machinery, Czestochowa University of Technology, Poland
[4] Multiscale Physics, Center for Computational Energy Research, Department of Applied Physics, Eindhoven University of Technology, PO Box 513, 5600 MB Eindhoven, The Netherlands b.j.geurts@utwente.nl

INTRODUCTION

Direct numerical simulation (DNS) of the Navier-Stokes equations governing dispersed deformable bubbles in water shows clear modulation of turbulence properties. This paper adopts the volume-of-fluid method as implemented in the high-performance TBFSolver (https://github.com/cifanip/TBFsolver) to investigate the potential for drag reduction in Taylor-Couette flow. We simulate dispersed bubbly turbulence, at considerably higher gas volume fractions compared to literature and a range of Weber numbers to illustrate the effects of deformability on near wall turbulence modulation. Attention is given to (i) the fundamental resolution of bubble-bubble and bubble-wall interactions and (ii) the clustering of bubbles in Taylor-Couette turbulence.

The numerical technique used in the TBFsolver is based on the volume-of-fluid (VOF) method in which the one-fluid formulation is adopted, i.e., a single set of equations is solved on the entire domain. To describe the dispersed embedded flow, discontinuous material properties and interfacial terms associated with the bubbles are accounted for using a marker function f_i for each bubble i. Each bubble is given a marker which equals 1 in cells where the bubble fully occupies the cell, 0 where the fluid occupies the cell, and a value between 0 and 1 indicates that the cell contains a bubble interface. The value of the marker function is also referred to as the volume fraction. Given N bubbles, the marker functions are advected via

$$\frac{\partial f_i}{\partial t} + \mathbf{u}\cdot\nabla f_i = 0 \qquad \text{for } i = 1,\ldots,N. \tag{1}$$

The nondimensionalized incompressible Navier-Stokes equations and continuity equation are used to describe the flow:

$$\rho\frac{D\mathbf{u}}{Dt} = -\nabla p + \frac{1}{\mathrm{Fr}^2}\rho\hat{\mathbf{g}} + \frac{1}{\mathrm{Re}}\nabla\cdot(2\mu\mathbf{S}) + \frac{1}{\mathrm{We}}k\mathbf{n}\delta(n) \tag{2}$$

$$\nabla\cdot\mathbf{u} = 0 \tag{3}$$

Here $D\mathbf{u}/Dt$ is the material derivative of the velocity $\mathbf{u}$ with t the time. Moreover, p is the pressure, ρ the mass density, μ the viscosity, k is the curvature, $\hat{\mathbf{g}}$ is the normalized gravity vector, $\mathbf{S}$ the deformation tensor, and $\mathbf{n}$ is the normal vector to the interface. The dimensionless numbers are the Froude number $\mathrm{Fr} = U/\sqrt{gL}$, the Reynolds number $\mathrm{Re} = UL\rho_1/\mu_1$, and the Weber number $\mathrm{We} = LU^2\rho_1/\sigma$. Here L and U denote a characteristic length and a characteristic velocity, respectively. The subscript 1 denotes the continuous phase mass density.

The mass density and viscosity at a certain point follow from the marker functions and the properties of the continuous and dispersed phases. For instance, a cell with volume fraction c would have a density and a viscosity of

$$\rho = \rho_1\ (1-c) + \rho_2\ c, \tag{4}$$

$$\mu = \mu_1\ (1-c) + \mu_2\ c. \tag{5}$$

were $c = \max_i f_i$. The continuous surface force (CSF) method is used to model the surface tension term. This method replaces the delta function $\delta(n)\mathbf{n}$ by a smooth term, which is computationally easier but may induce spurious currents. Reducing such spurious currents can effectively be done by accurately computing the curvature of the interface for which a height function method is adopted.The advection of the dispersed phase is represented using the generalised height function method.

A three-dimensional uniform Cartesian grid is used to discretize the domain and a staggered arrangement of the variables was selected. The spatial discretization of the convective term is based on the finite volume approach. Additionally, the QUICK interpolation scheme is implemented to avoid unphysical oscillations that may occur as the spatial resolution is too low. A second-order finite difference scheme is employed for the diffusive term. Finally, a third-order Runge-Kutta scheme is used to discretize the convection and diffusion terms of the Navier-Stokes equations, while a Crank-Nicolson scheme is employed for the surface tension term.

RESOLVED BUBBLE COLLISIONS

The motion of a bubble impacting a solid wall was simulated in detail. In Figure 1 the energy dissipation in the vicinity of the bubble is plotted at various instances as the bubble rises under an angle of 45 degrees toward the wall and subsequently bounces back. Although the main features are well represented on a grid of 128^3 the findings at 256^3 convey a more precise capturing of the dynamics. This is also expressed by the evolution of the y-component of the centre of mass in Figure 2. The vertical line corresponds to the moment at which the distance between the bubble centre and the wall is reduced to four grid cells of the finest grid. Despite the modest spatial resolutions of these brief encounters, the overall capturing of the motion appears highly accurate.

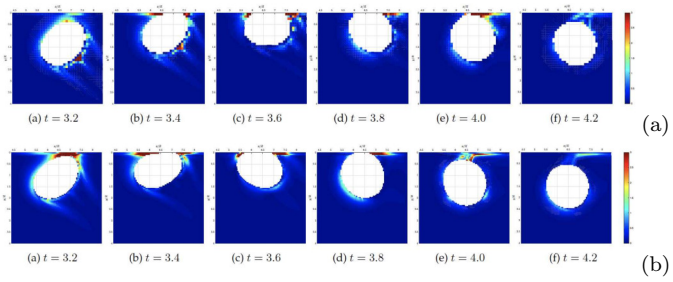

Figure 1: Energy dissipation in the vicinity of the bubble at different times using a grid with 128^3 (a) and 256^3 (b) grid cells.

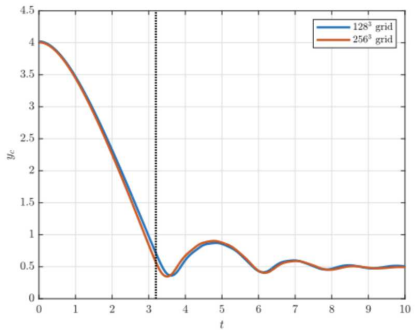

Figure 2: Vertical component of the center of mass motion at 128^3 and 256^3.

BUBBLY TAYLOR-COUETTE TURBULENCE

The numerical method in the TBFSolver can also be used to simulate a large number of bubbles. We concentrate on turbulence in Taylor-Couette flow as this presents a finite domain in which all conditions can be controlled with high fidelity. To simulate the turbulent flow in this configuration the TBFSolver was extended to cylindrical coordinates. We consider flow at $Re = 5 \times 10^3$ and a Froude number $Fr = 0.64$ and simulate a system with 120 bubbles of diameter $0.1d$ with d the distance between the outer and inner cylinder. This corresponds to a volume fraction of 1%. The grid was set to $[N_\theta, N_r, N_z] = [768, 192, 384]$ cells in the circumferential, radial and vertical directions which was verified to yield high-fidelity results following a number of probing simulations.

A snapshot of their spatial distribution is presented in Figure 3. We observe some degree of clustering in the bubble concentration, which is further quantified in Figure 4. These simulations allow us to study the effects of buoyancy and deformability of large bubbles in turbulent TC flow. An example of drag reduction as a result of the modification of the near wall turbulence is presented in Figure 5. Full DNS predictions are compared with an approximate computational model proposed in [1].

In the final presentation at the workshop, we expect to have further simulations of the Taylor-Couette flow and analysed the drag reduction phenomenon in more detail at different volume fractions and deformabilities.

REFERENCES

[1] V Spandan, R Verzicco, D Lohse : Physical mechanisms governing drag reduction in turbulent Taylor–Couette flow with finite-size deformable bubbles, *Journal of fluid mechanics*, **849**, R3 (2018).

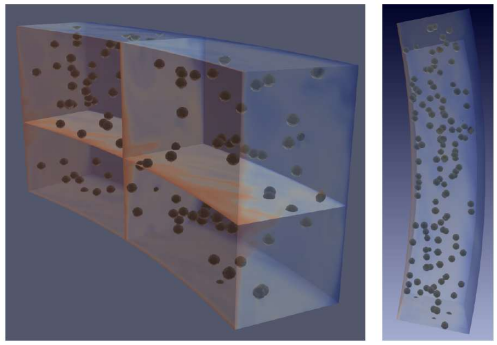

Figure 3: Snapshot of the velocity magnitude in two-phase TC flow - red/blue indicates high/low velocity. Bubbles are seen to cluster near the inner wall as seen clearly in the top-view (right figure).

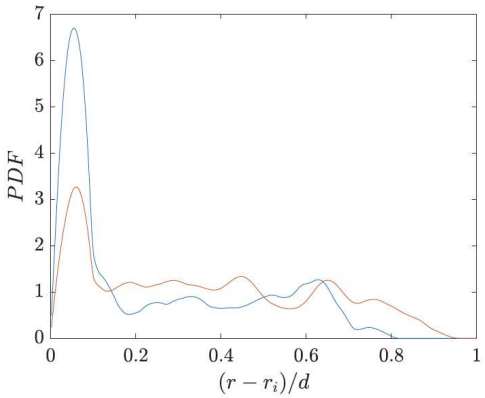

Figure 4: Probability distribution function of the radial coordinates of the gas phase. PDFs are based on averages over 2 flow-through times, taken after 18 (blue) and 48 (red) flow-through times.

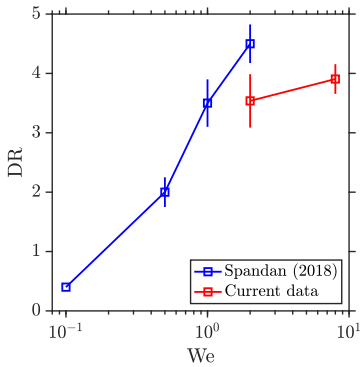

Figure 5: Drag reduction at large Weber numbers We using DNS - comparison with approximate model for low We [1].

WORKSHOP
Direct and Large-Eddy Simulation 14
April 10-12 2024, Erlangen, Germany

DNS OF MARANGONI MIGRATION OF A SUSPENSION OF DROPLETS IN MICROGRAVITY

Néstor Balcázar-Arciniega[1,*], Joaquim Rigola[1], Assensi Oliva[1]
[1,*] Heat and Mass Transfer Technological Center (CTTC),
Universitat Politècnica de Catalunya (UPC) - BarcelonaTech,
ESEIAAT, Colom 11, E-08222 Terrassa, Barcelona, Spain.
nestor.balcazar@upc.edu, nestorbalcazar@yahoo.es

INTRODUCTION

Interfacial phenomena induced by variable surface tension, e.g., thermocapillary or surfactants, are frequent in nature and industry. Beyond its scientific importance, thermocapillary migration play an essential role in microgravity environments [13] and micro-devices [11]. This work focuses on the Direct Numerical Simulation (DNS) of the Marangoni migration (Thermocapillarity) of droplets, using a multi-marker unstructured conservative level-set (UCLS) method [2, 5, 6, 7]. Validations, verifications and extensions of the UCLS solver have been reported in our previous works, for instance [1, 2, 5, 6, 8].

MATHEMATICAL MODEL AND NUMERICAL METHODS

The Navier-Stokes equations for the dispersed phase (Ω_d) and continuous phase (Ω_c) follow the one-fluid formulation,

$$\frac{\partial}{\partial t}(\rho\mathbf{v}) + \nabla\cdot(\rho\mathbf{v}\mathbf{v}) = -\nabla p + \nabla\cdot\mu\left(\nabla\mathbf{v} + (\nabla\mathbf{v})^T\right) + \rho\mathbf{g} + \mathbf{f}_\sigma, \quad \nabla\cdot\mathbf{v} = 0, \qquad (1)$$

where $\mathbf{v}$ is the fluid velocity, p is the pressure field, ρ is the fluid density, μ is the dynamic viscosity, $\mathbf{g}$ is the gravitational acceleration, $\mathbf{f}_\sigma$ is the surface tension force concentrated at the interface (Γ). Physical properties are constant at each fluid-phase with a jump discontinuity at Γ, $\beta = \beta_d H_d + \rho_c(1 - H_d), \beta = \{\rho, \mu, \lambda, c_p\}$ where H_d is the Heaviside step function that is one at fluid d and zero elsewhere. Regularization of physical properties is performed according to [5].

The UCLS method proposed by Balcazar et al. [1, 6] performs interface capturing, whereas the multi-marker approach [2, 5, 6, 7, 10] avoids the numerical coalescence of droplets. In this framework, the following advection and re-initialization equations are solved:

$$\frac{\partial\phi_i}{\partial t} + \nabla\cdot\phi_i\mathbf{v} = 0, \quad \frac{\partial\phi_i}{\partial\tau} + \nabla\cdot\phi_i(1-\phi_i)\mathbf{n}_i^0 = \nabla\cdot\varepsilon\nabla\phi_i, \quad (2)$$

$i = \{1, 2, ..., N_m - 1, N_m\}$, N_m is the number of UCLS markers, which equals the number of droplets, $\mathbf{n}_i^0$ is the interface normal unit vector calculated at $\tau = 0$. The curvature κ_i and normal vectors $\mathbf{n}_i$ are computed as follows [1, 2, 6]: $\kappa_i = -\nabla\cdot\mathbf{n}_i$, $\mathbf{n}_i = (||\nabla\phi_i||)^{-1}\nabla\phi_i$.

The Continuous Surface Force (CSF) model [9] is used for surface tension force ($\mathbf{f}_\sigma$, Eq.(1), as extended to the multi-marker UCLS method [2, 5, 6]: $\mathbf{f}_\sigma = \sum_{i=1}^{N_m}(\mathbf{f}_{\sigma,i}^{(n)} + \mathbf{f}_{\sigma,i}^{(t)})$. Here,

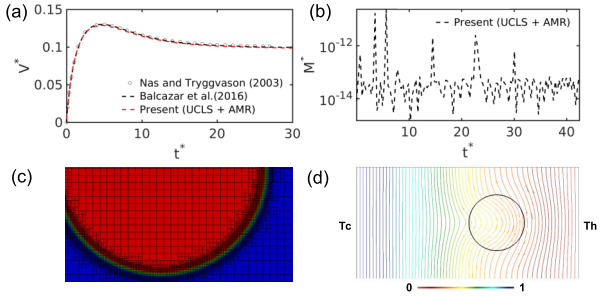

Figure 1: Thermocapillary migration of a single droplet, $\mathbf{g} = \mathbf{0}$. (a) Migration velocity $V^* = (\mathbf{e}_y\cdot\mathbf{v})U_r^{-1}$. Comparison against UCLS method on fixed meshes [5], and front-tracking method [12]. (b) Mass conservation $M^* = (M(t) - M(0))/M(0)$, $M(t) = \int_\Omega H_d^s dV$. (c) Adaptive mesh refinement around the droplet interface, with grid size $h_{max} = L_x/60$ and $h_{min} = h_{max}/2^4$. (d) Temperature isocontours.

$\mathbf{f}_{\sigma,i}^{(t)} = \nabla_{\Gamma_i}\sigma(T)\delta_{\Gamma,i}^s = (\nabla\sigma(T) - \mathbf{n}_i(\mathbf{n}_i\cdot\nabla\sigma(T)))\ \delta_{\Gamma,i}^s$ is the Marangoni force, $\nabla_{\Gamma_i} = \nabla - \mathbf{n}_i(\mathbf{n}_i\cdot\nabla)$, and $\delta_{\Gamma,i}^s = ||\nabla\phi_i||$ is the regularized Dirac delta function [1, 6]. On the other hand, $\mathbf{f}_{\sigma,i}^{(n)} = \sigma\kappa_i\mathbf{n}_i\delta_{\Gamma,i}^s = \sigma\kappa_i\nabla\phi_i$.

Transport equations are discretized by the finite-volume method on 3D collocated unstructured meshes [6]. The pressure-velocity coupling in fluid flow transport equation is solved by the fractional-step projection method. Unstructured flux limiters proposed by [1, 6] approximate the convective term of transport equations. Adaptive mesh refinement is introduced for the optimization of computational resources. Further details about the transport equations can be found in [5].

NUMERICAL EXPERIMENTS

The following dimensionless numbers characterize the thermocapillary migration of droplets: Ma $= \left(|\sigma_T|||\nabla T_\infty||d^2\rho_c c_{p,c}\right)(4\mu_c\lambda_c)^{-1}$, Re $= \left(|\sigma_T|||\nabla T_\infty||d^2\rho_c\right)(4\mu_c^2)^{-1}$, Ca $= (|\sigma_T|||\nabla T_\infty||d)\ (2\sigma_0)^{-1}$, $\eta_\beta = \beta_c\beta_d^{-1}$, $\beta = \{\rho, \mu, \lambda, c_p\}$, subindex c denotes the continuous phase and subindex d denotes the dispersed phase (droplet), Ma is the Marangoni number, Ca is the capillary number, Re is the Reynolds number, η_β denotes the physical property

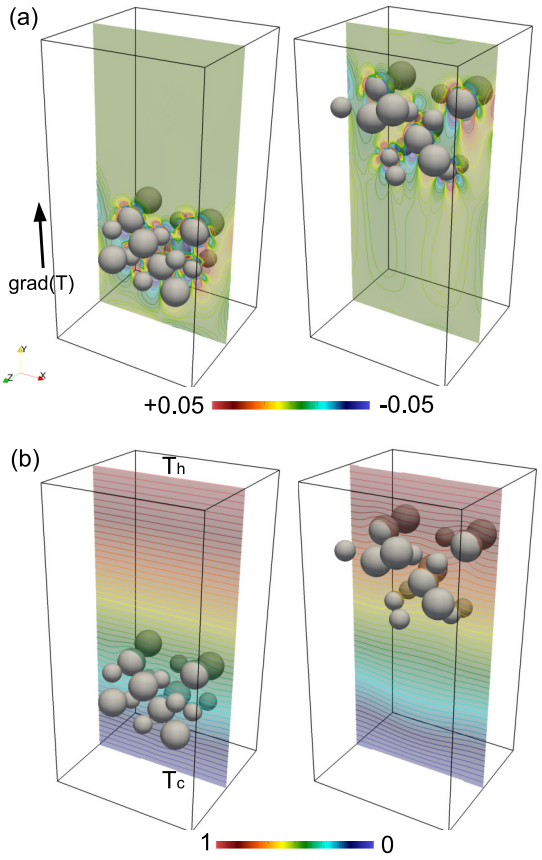

Figure 2: Thermocapillary migration of a bi-dispersed suspension of 18 droplets ($\mathbf{g} = \mathbf{0}$, is the gravity), $Re = 40$, $Ma = 50$, $Ca = 0.03$, $\eta_\rho = \eta_\mu = \eta_{c_p} = \eta_\lambda = 2$, $d/d^* = 1.5$, d is the equivalent diameter of bigger droplets and d^* is the equivalent diameter of smaller droplets. Ω a rectangular channel with extension $L_x = 5.33\,d$, $L_z = 5.33\,d$ and $L_y = 10.66\,d$. Uniform hexahedral mesh with grid size $h = d/48$, equivalent to 27648000 control volumes, distributed on 1536 CPU cores. (a) Vorticity contours ($(\nabla \times \mathbf{v}) \cdot \mathbf{e}_z$) at $t^* = t/t_r = \{35, 93\}$, $\mathbf{v}$ is the fluid velocity. (b) Temperature contours at $t^* = t/t_r = \{35, 93\}$.

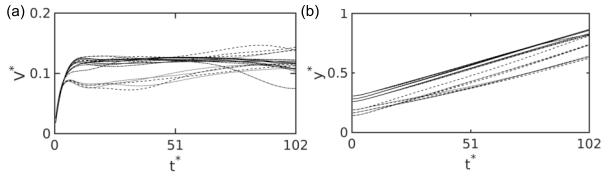

Figure 3: Thermocapillary migration of a bi-dispersed suspension of 18 droplets ($\mathbf{g} = \mathbf{0}$), $Re = 40$, $Ma = 50$, $Ca = 0.03$, $\eta_\rho = \eta_\mu = \eta_{c_p} = \eta_\lambda = 2$, $d/d^* = 1.5$. Uniform hexahedral mesh with grid size $h = d/48$, equivalent to 27648000 control volumes. Simulation performed on 1536 CPU cores. (a) Dimensionless migration velocity $V^* = \mathbf{e}_y \cdot \mathbf{v}_{c,i}/U_r$, $\mathbf{v}_{c,i}$ is the droplet velocity. (b) Dimensionless vertical position, $y^* = \mathbf{e}_y \cdot \mathbf{x}_{c,i}/L_y$, $\mathbf{x}_{c,i}$ is the droplet centroid.

ratio, ρ is the fluid density, μ is the viscosity, λ is thermal conductivity, $\sigma = \sigma(T) = \sigma_0 + \sigma_T\,(T - T_0)$ is the equation of state for surface tension coefficient, T is the temperature, $\nabla T_\infty = ((T_h - T_c)/L_y)\mathbf{e}_y$, $U_r = |\sigma_T|||\nabla T_\infty||(0.5d)/\mu_c$, $T_r = ||\nabla T_\infty||(0.5d)$, $t_r = 0.5d/U_r$, T_h is the temperature at the top boundary and $T_c < T_h$ is the temperature at the bottom boundary as depicted in Figure 2b. Numerical results for thermocapillary migration of a suspension of droplets in microgravity condition ($\mathbf{g} = \mathbf{0}$) are depicted in Fig.(2) and Fig.(3). Furthermore, simulation of thermocapillary migration of a single bubble is illustrated in Fig.(1). Present computations are in close agreement with front-tracking simulation reported by [12]. The effect of Marangoni number and $g \geq 0$ on the distribution of droplets will be reported in the full paper.

REFERENCES

[1]Balcázar, N., Jofre, L., Lehmkhul, O., Castro, J., Rigola, J. : A finite-volume/level-set method for simulating two-phase flows on unstructured grids. *International Journal of Multiphase Flow* **64**, 55-72 (2014).

[2]Balcázar, N., Lehmkhul, O., Rigola, J., Oliva, A. : A multiple marker level-set method for simulation of deformable fluid particles. *International Journal of Multiphase Flow* **74**, 125-142 (2015).

[3]Balcázar, N., Lemhkuhl, O., Jofre, L., Oliva, A. : Level-set simulations of buoyancy-driven motion of single and multiple bubbles. *International Journal of Heat and Fluid Flow* **56**, 91-107 (2015).

[4]Balcázar, N., Lehmkhul, O., Jofre, L., Rigola, J., Oliva, A. : A coupled volume-of-fluid/level-set method for simulation of two-phase flows on unstructured meshes. *Computers and Fluids* **124**, 12-29 (2016).

[5]Balcázar, N., Rigola, J., Castro, J., Oliva, A. : A level-set model for thermocapillary motion of deformable fluid particles. *International Journal of Heat and Fluid Flow* **62**, Part B, 324-343 (2016).

[6]Balcázar, N., Antepara, O., Rigola, J., Oliva, A. (2019) A level-set model for mass transfer in bubbly flows. *International Journal of Heat and Mass Transfer* 138. 335-356.

[7]Balcazar-Arciniega, N., Rigola, J., Oliva, A. (2024). DNS of Mass Transfer in Bi-dispersed Bubbly Flows in a Vertical Pipe. In: Marchioli, C., Salvetti, M.V., Garcia-Villalba, M., Schlatter, P. (eds) textitDirect and Large Eddy Simulation XIII. DLES 2023. ERCOFTAC Series, vol 31. Springer, Cham.

[8]Balcázar N., Antepara O., Rigola J., Oliva A. (2020). DNS of Drag-Force and Reactive Mass Transfer in Gravity-Driven Bubbly Flows. In: García-Villalba M., Kuerten H., Salvetti M. (eds) *Direct and Large Eddy Simulation XII. DLES 2019. ERCOFTAC Series*, vol 27. Springer, Cham.

[9]Brackbill, J.U., Kothe, D.B., Zemach, C. : A Continuum Method for Modeling Surface Tension, *J. Comput. Phys.* **100**, 335-354 (1992).

[10]Coyajee, E., Boersma, B.J. : Numerical simulation of drop impact on a liquid–liquid interface with a multiple marker front-capturing method. *J. Comput. Phys.* **228**, 4444-4467 (2009).

[11]Darhuber, A.A., Troian, S. M., Principles of microfluidic actuation by modulation of surface stresses. *Annual Review of Fluid Mechanics* **37**, 425–455. (2005)

[12]Nas, S., Tryggvason, G. Thermocapillary interaction of two bubbles or drops. *International Journal of Multiphase Flow* **29**, 1117–1135. (2003)

[13]Subramanian, R., Balasubramaniam, R., Clark, N., Motion of Bubbles and Drops in Reduced Gravity. *Applied Mechanics Reviews* **55**, B56–B57. (2002)

WORKSHOP
Direct and Large-Eddy Simulation 14
April 10-12 2024, Erlangen, Germany

DNS OF BUBBLE FRAGMENTATION BY TURBULENCE

A. Calado[1], **E. Balaras**[1]
[1]The George Washington University
Washington, D.C., USA
balaras@gwu.edu

INTRODUCTION

Bubble fragmentation due to turbulence is ubiquitous for two-phase flows in nature and engineering applications where the interfacial area is to be maximized. Predicting the bubble size distribution under different turbulent conditions is critical to have practical modeling tools for mass/momentum transfer. In the seminal work of Hinze [1], two main ideas are proposed: firstly as condition for breakup the local shear stress surrounding the bubble is sufficient to overcome the stabilizing surface tension and viscous forces; secondly that only the turbulent energy of eddies of similar size or smaller than the bubble diameter is used for breakup (larger eddies simply transport the bubble). Bubble formation in breaking wave events was studied in the experiments of Deane and Stokes [2], providing a connection between the bubble size spectrum and turbulent dissipation rate. The bubble sizes are statistically described, with size distribution found to follow a power law of $\beta = -10/3$ for bubbles larger than $\sim$ 1mm (driven by turbulent fragmentation), while smaller bubbles follow $\alpha = -3/2$ (stabilized by surface tension). The separating scale is attributed to the Hinze scale, D_H, whose work on breakup of droplets in turbulent flow led to the scaling relation between the largest stable drop size and turbulent dissipation rate ε, given in Eq. 1.

$$D_H = \left(\frac{We_c}{2}\right)^{3/5} \left(\frac{\sigma}{\rho}\right)^{3/5} \varepsilon^{-2/5} \tag{1}$$

This equation is valid above a critical Weber number We_c and Reynolds based on the bubble diameter, where σ is the surface tension coefficient, and ρ is the bulk/surrounding fluid density. Chan et al. [3] formalize an analogy between the bubble-mass cascade above the Hinze scale and the turbulent energy cascade attributed to Kolmogorov, known as the Kolmogorov-Hinze (KH) framework. The main assumption for such a cascade mechanism (beyond high Re and We) are that of locality, quasi-stationarity, and quasi-homogeneity, such that the bubble flux within an intermediate range of sizes is scale independent. These previous works considered the statistical characterization of breakups for high density bubbly flows. Other relevant studies focus on the physical mechanisms for breakup by studying a single bubble. Experiments by Risso and Fabre [5] in microgravity highlighted three distinct regimes based on the bubble We number with either no breakup, resonant breakup or sudden breakup. The number of daughter bubbles is also found to be strongly dependent on We. An improvement to the KH theory is proposed by including an efficiency parameter which depends on the bubble's residence time in turbulence, and the relation between eddy frequency and bubble's eigenfrequency. In the experimental work of Qi et al. [6], vortex-ring collisions are used to study single bubble breakup. Two distinct breakup mechanisms are identified: a primary mechanism where the bubble is interacting with the vortex length scale (close to bubble size D) and is stretched smoothly until eventually breaking up; the secondary mechanism stems from bubble interaction with the broken up smaller eddies of the vortex. This type of breakup has a smaller timescale and goes against the KH theory which assumes that eddies close to the bubble size are mainly responsible for breakup. The combined effect of large and small eddies seems to drive breakup, with eddies of size 0.74D being the most efficient (i.e. require less turbulent energy). In this model two necessary criteria are proposed for a bubble of equivalent diameter D to breakup due to turbulence. The first is the stress criterion, where the eddy inertia must be sufficient to break the interfacial forces. The eddy diameter D_e and velocity scale u_e thus defines the "eddy Weber" number that should be greater than unity (Eq. 2).

$$We_e = \frac{\rho u_e^2 D_e}{\sigma} > 1 \tag{2}$$

The second criterion is related to the eddy-bubble timescales, similar to the proposition of Risso and Fabre [5]: if the eddy turnover time ($\propto D_e/u_e$) is larger than the bubble relaxation time, the bubble tends to recover its spherical shape. This introduces a new dimensionless number, Ti,which should exceed a threshold value (Eq. 3).

$$Ti = \frac{\rho u_e^2 D^3/D_e^2}{\sigma} > \frac{96}{4\pi^2} \tag{3}$$

Using the above criteria, the minimum eddy velocity to break up a bubble can be computed and used in a probabilistic model. This model is found to give satisfactory statistical results when compared to experimental data relative to the classical KH framework. Since these experiments were conducted under Earth gravity, the buoyancy effects may not be negligible. Experiments conducted in microgravity report the critical Weber for breakup to be nearly 20 times larger to equivalent experiments done in normal gravity [5]. In a computational approach we can neglect gravity ($Fr = \infty$), isolating the effect of turbulent stresses and surface tension. We propose to look at the canonical case of how turbulence interacts with a single bubble and verify these criteria in a "local" sense. Experimentally this is extremely challenging, with DNS being an appealing alternative since all local flow

information is readily available. So far there have been no computational studies to support or refute this model. In the following section, a computational plan using DNS is presented to test this hypothesis.

METHODOLOGY

The computational experiments to be conducted must rely on high-fidelity DNS of incompressible two-phase turbulent flows. Our in-house DNS code has shown to be adequate and robust in simulating these types of flows with good parallel performance. The code uses a fractional step formulation, with a fast Poisson solver (FFT-based), conservative level-set to capture the interface, and Ghost Fluid Method (GFM) to model surface tension effects [7]. Application to turbulent free-surface interaction is shown in recent work [8], allowing the analysis of entrained and fragmenting air bubbles as seen in Fig. 1. Based on the bubble breakup criteria given in Qi et al.

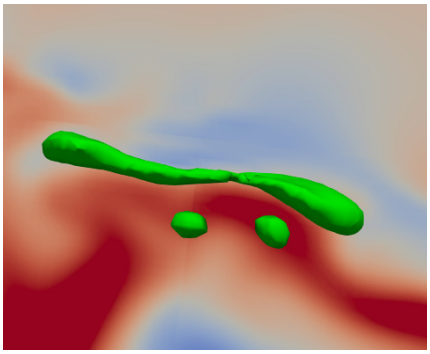

Figure 1: Turbulent bubble breakup: interface shown from level-set contour ($\phi = 0$), with background contour of velocity field.

[6], computational experiments are proposed to test the hypothesis by controlling the relevant dimensionless parameters independently. We propose to study the interaction of a single bubble in HIT. This can be achieved by first generating a HIT field in a triply periodic cubic domain in single-phase (water) at a specific Reynolds number. In the work of Rivière et al. [9] DNS of a single bubble break-up in HIT at $Re_\lambda = 38$, and different Weber was performed to investigate sub-Hinze bubble formation. However, the effects of relative bubble-to-eddy size, or relaxation time criteria has not been investigated, and the low Re has a limited range of eddy scales. In their computations forcing is kept active in the water phase. At time $t = 0$ when the bubble is introduced, the turbulence forcing shall be deactivated to see how the bubble deforms and breaks up from the decaying turbulence. This setup allows to start with the same initial velocity field and change the initial bubble diameter and surface tension independently. Varying these two parameters alone, we can investigate different bubble We and Ti numbers, and eddy-to-bubble ratios. Four different cases are considered and shown in Table 1 as part of the computational plan. Unless otherwise specified, the material properties of air and water (including surface tension) are used, with dimensionless numbers relative to the bulk/liquid phase.

The first case has both the We and Ti criterion satisfied for breakup, and the initial bubble diameter is larger than the integral scale. In the second case the initial bubble diameter is reduced such that bubble We is still greater than 1, however the time criterion is not satisfied. The hypothesis is that the eddy timescales are too large to allow breakup. The third case has an even smaller initial bubble diameter such that neither criterion is satisfied, and no breakup is expected according to the hypothesis. The fourth and last case mimics case 1, yet with an artificially lower surface tension than that of air-water. For this case we expect a violent breakup of the bubble given the large We and Ti numbers. Note that cases 2 and 3 have initial diameters $D < D_H$.

Parameter	Case 1	Case 2	Case 3	Case 4
Re_λ	125	125	125	125
$\frac{\lambda}{D}$	0.08	0.16	0.60	0.08
We_D	3.93	1.97	0.53	39.4
Ti	8.86	1.11	0.02	88.6
$\frac{D_H}{D}$	0.62	1.25	4.68	0.16

Table 1: Parametric space for DNS of bubble interaction with HIT

Based on previous studies the bubble should undergo first a "smooth" deformation phase, followed by a bulgy deformation phase and breakup. Breakup typically occurs within a few large eddy turnover times, such that the total simulation time can be relatively short (under large 5 eddy turnover times). Saving 10-20 snapshots per eddy turnover time can allow for post- processing and visualization of the dynamic breakup process. Beyond this visual or qualitative investigation, a more quantitative analysis can be performed by computing the local We number surrounding the bubbles and Ti number. The local We numbers can be based on the eigenvalues of the strain rate tensor or vorticity magnitude as in Qi et al. [6], as well as alternative approaches. The child bubble sizes can also be evaluated, with emphasis on how sub-Hinze bubbles are formed. Bubble statistics such as volume (or equivalent diameter), surface area and sphericity can be tracked during the transient break-up process and related to the local We and Re number.

REFERENCES

[1]J. Hinze. : Fundamentals of the hydrodynamic mechanism of splitting in dispersion processes, *A.I.Ch.E. Journal*, **1**, 289–295 (1955).

[2]G. Deane and M. Stokes : Scale dependence of bubble creation mechanisms in breaking waves, *Nature.*, **418**, 839–844 (2002).

[3]W. H. R. Chan, P. Johnson and P. Moin : The turbulent breakup cascade. Part 1. Theoretical developments, *Journal of Fluid Mechanics.*, **912**,(2021).

[4]X. Yu, K. Hendrickson and D. Yue : Scale separation and dependence of entrainment bubble-size distribution in free-surface turbulence, *Journal of Fluid Mechanics.*, **885**, (2019).

[5]F. Risso and J. Fabre : Oscillations and breakup of a bubble immersed in a turbulent field, *Journal of Fluid Mechanics.*, **372**, 323–355 (1998).

[6]Y. Qi, S. Tan, N. Corbitt, C. Urbanik, A. Salibindla and R. Ni : Fragmentation in turbulence by small eddies, *Nature communications.*, (2022).

[7]Dhruv, A., Balaras, E., Riaz, A., and Kim, J : A formulation for high-fidelity simulations of pool boiling in low gravity, *International Journal of Multiphase Flow*, **120**, (2019).

[8]A. Calado, I. Yildiran and E. Balaras : An interface capturing approach for turbulent, incompressible, two-phase flows based on fast pressure Poisson solvers, *submitted to International Journal of Multiphase Flow*, (2023).

[9]A. Rivière, W. Mostert, S. Perrard and L. Deike : Sub-Hinze scale bubble production in turbulent breakup, *Journal of Fluid Mechanics*, **917**, (2021).

SESSION: Numerics and methodology II

Wednesday, April 10, 2024

14:50- 15:50

WORKSHOP
Direct and Large-Eddy Simulation 14
April 10-12 2024, Erlangen, Germany

BEYOND CLASSICAL STABILITY ANALYSIS ON RUNGE-KUTTA SCHEMES: POSITIVITY AND PHASE PRESERVATION

J.Plana-Riu, F.X. Trias, A. Oliva
Heat and Mass Transfer Technological Centre
Technical University of Catalonia. ESEIAAT
Carrer de Colom 11, 08222 Terrassa (Barcelona), Spain.
josep.plana.riu@upc.edu

INTRODUCTION

In the numerical integration of an ordinary differential equation (ODE), the general concerns are performance, stability, and accuracy. All three are characterized by the method's coefficients as well as the step size. The former is usually not in the hands of the user once a scheme has been established, as coefficients are generally constant, while reducing the step size, which at the same time reduces the performance of the code; it will take longer to cover the desired domain. These generates a trade-off in which the user has to be aware of the pros and cons of using a larger or smaller step size given the requirements of the integration.

One of the different possibilities when integrating ODEs is the Runge-Kutta (RK) method, in which the value of the function that is being integrated, at the next step ϕ^{n+1}, is computed only considering the current step ϕ^n and intermediate approximate values, ϕ_i in the s stages of the scheme, so that

$$\phi_i = \phi^n + h\sum_{j=1}^{s} a_{ij} f(\phi_j), \tag{1a}$$

$$\phi^{n+1} = \phi^n + h\sum_{i=1}^{s} b_i f(\phi_i), \tag{1b}$$

where h is the step size and a_{ij}, b_i are the RK coefficients arranged in the so-called Butcher's tableau.

When the Navier-Stokes equations are semi-discretized,

$$M\mathbf{u} = 0, \tag{2a}$$

$$\Omega\frac{d\mathbf{u}}{dt} + C(\mathbf{u})\mathbf{u} = D\mathbf{u} - \Omega G\mathbf{p}, \tag{2b}$$

a differential algebraic equation (DAE) of order 2 is obtained. The solution of these equations using RK is developed by Sanderse and Koren [1] by means of a projection method.

Originally, the timestep Δt had been selected with the classical CFL condition, which estimates the eigenvalues of the method, and then the expected stable timestep is reduced with the so-called Courant number (or CFL number) to ensure the integration is stable. Later on, Trias and Lehmkuhl [2] used Gershgorin theorem to compute the eigenbounds of the predictor step in the projection method to use the largest possible timestep allowed by the stability region. This same technique can be applied to RK as the stability region is defined by the polynomial

$$R(z) = 1 + \sum_{k=1}^{s} \frac{1}{k!} z^k, \tag{3}$$

for $s \geq p$, being p the order of accuracy of the method. Hence, by the linear stability theory, in a general ODE,

$$\phi^{n+1} = R(h\lambda)\phi^n, \tag{4}$$

where $\lambda \in \mathbb{C}$ is the eigenbound of the system. Hence, stability will be obtained if $|R(h\lambda)| \leq 1$ holds.

Nonetheless, when this method was applied to a simulation with a timestep of 95% of the maximum stable value, some spurious modes appeared in the solution which were evident in the instantaneous fields, as seen in Fig. 1, and generated an overprediction of u_{rms} in the core of the channel. When 85% of the maximum stable timestep was used, then this instability was not present, and instead, the obtained fields were as expected. Trying to understand what generated these instabilities was the main motivation for the development of this work.

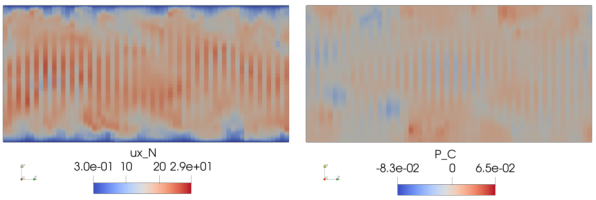

Figure 1: Spurious modes observed in the cross-stream plane at 95% of the maximum stable timestep for a coarse (64^3) $\mathrm{Re}_\tau = 180$ channel flow simulation for velocity (left) and pressure (right).

POSITIVITY-PRESERVING SOLUTIONS

Let us consider the following ODE,

$$\frac{d\phi}{dt} = \lambda\phi, \quad \lambda \in \mathbb{C}, \tag{5}$$

with $\phi(0) = 1$. Since it leads to $\phi(t) = e^{\lambda t}$ as an analytical solution, a monotonic solution is expected. In this first case, consider $\lambda = -1$, hence the stability polynomial $R(z)$ becomes

$$R(h) = 1 + \sum_{k=1}^{s} \frac{(-1)^k}{k!} h^k, \tag{6}$$

where, if $R(h) < 0$, ϕ^{n+1} will change sign and thus the obtained solution will not be monotonic. For instance, by using a third-order scheme, such as the strong-stability preserving third-order Runge-Kutta (SSPRK3) from Shu and Osher [3], $R(h) = 1 - h + \frac{1}{2}h^2 - \frac{1}{6}h^3$, the solution will not be monotonic for $h > 1.6$, as shown in Fig. 2 (left), even though it will be stable for step size values smaller than 2.5.

Nonetheless, in the case of having a complex eigenvalue, using this approach is not so straightforward. Hence, let $\lambda = -||\lambda||e^{-i\phi}$. Introducing it in the stability polynomial,

$$\begin{aligned} R(h\lambda) = 1 + \sum_{k=1}^{s} \frac{(-1)^k}{k!} (h||\lambda||)^k \cos(k\phi) \\ + i \sum_{k=1}^{s} \frac{(-1)^{k+1}}{k!} (h||\lambda||)^k \sin(k\phi), \end{aligned} \tag{7}$$

the polynomial can be split into a real and imaginary part, $R = R_r + iR_i$. By introducing it into the linear stability analysis equation, ϕ^n should be treated as complex so that $\phi^n = \phi_r^n + i\phi_i^n$. Expressed as a matrix equation,

$$\begin{pmatrix} \phi_r^{n+1} \\ \phi_i^{n+1} \end{pmatrix} = \underbrace{\begin{pmatrix} R_r & -R_i \\ R_i & R_r \end{pmatrix}}_{A} \begin{pmatrix} \phi_r^{n} \\ \phi_i^{n} \end{pmatrix}, \tag{8}$$

in which the oscillations will appear if and only if the matrix A fulfills $x^T Ax > 0$, $\forall x \in \mathbb{R}^2$. This will only hold if $R_r > 0$, being the same condition as for a purely diffusive case.

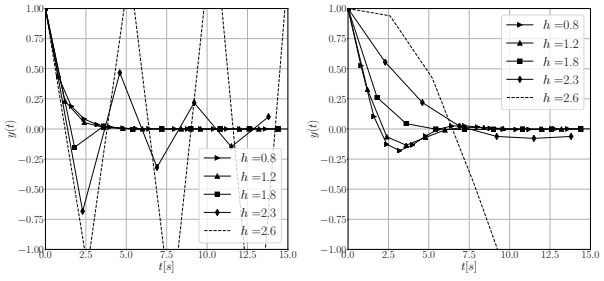

Figure 2: Numerical solutions for different h values for $d_t\phi = (-\cos(\alpha) + i\sin(\alpha))\phi$ with a SSPRK3 scheme, for $\alpha = 0$ (left) and $\alpha = 60^o$ (right)

PHASE-PRESERVING SOLUTIONS

In the previous section, the conditions for badly suited real contributions in the stability polynomial are presented. However, what happens when the imaginary contribution becomes negative? A sudden change of sign for the imaginary term will imply that the phase of this stability coefficient varies in π, which at the same time will transport the solution for half a period. Hence, having a negative imaginary contribution from the stability polynomial should also be avoided.

As shown in Fig. 2 (right), for $h > 2.5$, the phase of the solution has changed. In addition, an increase in magnitude can be observed as the solution is closer to the stability limit, which is surpassed for $h = 2.75$.

LIMITING THE STABILITY REGION FOR RUNGE-KUTTA SCHEMES

The observation of these phenomena generates the need to consider adding these conditions when setting the timestep of the numerical simulation. Hence, the "go-to" zone will be determined as follows,

$$\begin{cases} |R(h\lambda)| \leq 1, \\ R_r(h\lambda) > 0, \\ R_i(h\lambda) > 0, \end{cases} \tag{9}$$

so that both the sign and the phase of the solution are preserved, considering a stable integration in the first place. This will thus define two additional regions on top of the classical stability region: first of all, the positivity-preserving region will consist of all those combinations of $h\lambda$ such that $R_r > 0$ and thus, no synthetic change in the monotonicity of the solution should be observed. On the other hand, the phase-preserving region will be determined by the combinations of $h\lambda$ such that $R_i > 0$, and thus the phase is preserved throughout the integration.

By applying these conditions to the stability polynomial to limit the stability region of the scheme, the results from Fig. 3 are obtained for a third-order RK scheme. It can be observed that in integrations with eigenvalues with angles of approximately between 30 and 50 degrees, for a third-order scheme, the whole stability region can be exploited, as both the sign and as the phase will be preserved as long as the integration is stable. The applicability of these results to CFD in deeper detail is expected to be presented in the workshop.

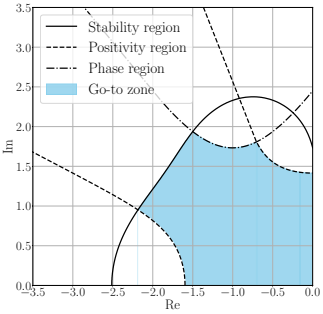

Figure 3: Stability region of a third-order Runge-Kutta scheme (black), with the positivity region (red) as well as the phase region (blue).

ACKNOWLEDGEMENTS

The investigations presented in this abstract are supported by the *Ministerio de Economía y Competitividad*, Spain, SIMEX project (PID2022-142174OB-I00). J. P-R. is also supported by the Catalan Agency for Management of University and Research Grants (AGAUR). The authors thankfully acknowledge these institutions.

REFERENCES

[1]Sanderse, B. and Koren, B. : Accuracy analysis of explicit Runge-Kutta method applied to the incompressible

[2]Trias, F.X. and Lehmkuhl, O. : A self-adaptive strategy fopr the time integration of Navier-Stokes equations, *Num. Heat Transfer, Part B: Fund.*, **60**, 116–134 (2011).

[3]Shu, C.-W.-. and Osher, S. : Efficient implementation of essentially non-oscillatory shock-capturing schemes, *J. Comp. Phys.*, **77**, 439–471 (1988)

WORKSHOP
Direct and Large-Eddy Simulation 14
April 10-12 2024, Erlangen, Germany

ON A CONSERVATIVE SOLUTION TO CHECKERBOARDING: ALLOWING NUMERICAL DISSIPATION ONLY WHEN AND WHERE NECESSARY

J.A. Hopman[1], **D. Santos**[1], **F.X. Trias**[1], **J. Rigola**[1]
[1] Heat and Mass Transfer Technological Center
Technical University of Catalonia, Carrer Colom 11, 08222 Terrassa (Barcelona), Spain.
jannes.hopman@upc.edu

INTRODUCTION

CFD codes with industrial applications commonly rely on a collocated grid arrangement, which handles complex geometries and unstructured meshes better than the staggered grid arrangement, with the added benefit of allowing a computationally more efficient data structure. If a central-differencing scheme is used to discretise the spatial differential operators, a set of wide-stencil operators is obtained. The gradient and divergence operator make use of a 3-wide stencil, creating a decoupling between the value of the central cell and its resulting differential value. The Laplacian operator in turn makes use of a 5-wide stencil, similarly disconnecting the central cell from its direct neighbours. In incompressible flows, this odd-even decoupling can lead to spurious pressure modes. These modes will persist because they are invisible to the gradient operator, offering no feedback onto the collocated velocity field. This problem is commonly known as the checkerboard problem.

The most widely used class of methods to solve this problem is through a weighted interpolation method (WIM), of which the pressure-weighted interpolation method, attributed to Rhie and Chow [1], is the most well-known example. This method establishes a coupling between directly neighbouring cells by adding a correction term which includes a cell-to-face pressure gradient. Usually this connection is constructed implicitly through a compact-stencil Laplacian operator, which additionally decreases computational complexity and cost. The application of these correction term leads to a non-zero discrete divergence at either the cell- or face-centered velocities. This, in turn, unavoidably introduces numerical dissipation to the evolution of kinetic energy, through the convective or pressure term [2].

When using symmetry-preserving methods for collocated grids, this numerical error remains as the largest source of numerical dissipation [3]. This error can at times be of the same magnitude as the applied LES models and therefore greatly interfere with turbulence modelling and high fidelity simulations [4]. To decrease the order of the pressure error introduced by the compact-stencil Laplacian, these works made use of a pressure predictor in the momentum prediction equation. Although greatly reducing the numerical dissipation, this adjustment makes the method more prone to checkerboarding, especially in case a small time-step is used or if the solution reaches a steady state.

The work of Hopman et al. [5] introduced a method that is able to dynamically change the pressure predictor, allowing more numerical dissipation if the solution starts showing oscillations. This was achieved by first answering a question that has been avoided in existing literature that discusses this topic: How should checkerboarding be quantified? By introducing a global, normalised, non-dimensional checkerboard coefficient, the pressure prediction could be regulated. This work explores other possible uses for this coefficient, whilst also introducing a local coefficient. By doing so, numerical dissipation can be limited, not only in when, but also in where it is allowed.

GLOBAL SCALAR ADJUSTMENT

In [5] the checkerboard coefficient was defined as:

$$C_{cb} = \frac{\mathbf{p}_c^T (L - L_c)\mathbf{p}_c}{\mathbf{p}_c^T L \mathbf{p}_c}, \tag{1}$$

where L_c and L denote the wide- and compact-stencil Laplacian, respectively. The coefficient ranges between 0 (smooth) and 1 (pure checkerboard). For this coefficient to regulate the strength of the coupling in the pressure field, there are two options (denoted with superscripts a and b) to apply C_{cb} to the projection method:

$$\mathbf{u}_c^p = \Delta t R\left(\mathbf{u}_c, \mathbf{u}_s\right) - \left(1 - C_{cb}^a\right) G_c \tilde{\mathbf{p}}_c^n, \tag{2}$$

$$L_c \tilde{\mathbf{p}}_c' - C_{cb}^b \left(L - L_c\right) \tilde{\mathbf{p}}_c' = M_c \mathbf{u}_c^p, \tag{3}$$

$$\mathbf{u}_c^{n+1} = \mathbf{u}_c^p - G_c \tilde{\mathbf{p}}_c', \tag{4}$$

$$\mathbf{u}_s^{n+1} = \Gamma_{cs} \mathbf{u}_c^{n+1} - C_{cb}^b \left(I - \Gamma_{cs}\Gamma_{sc}\right) G \tilde{\mathbf{p}}_c', \tag{5}$$

where the notation of [3] has been used. Option (a) was tested in [5] and gave good results, in which the pressure predictor was closer to $\tilde{\mathbf{p}}_c^n$ in the absence of checkerboarding and started to decrease in cases oscillations were detected in the domain. Option (b) involves solving a Poisson equation with a denser Laplacian which is usually avoided, however, equation (3) can be rewritten as:

$$L \tilde{\mathbf{p}}_c'^{(k+1)} = \frac{1}{C_{cb}^b} M_c \mathbf{u}_c^p - \frac{C_{cb}^b - 1}{C_{cb}^b} L_c \tilde{\mathbf{p}}_c'^{(k)}, \tag{6}$$

which finds the same solution but treats the wide-stencil Laplacian explicitly.

LOCAL SCALAR ADJUSTMENT

To apply a local adjustment to the projection method, which only acts in areas of the domain where oscillations are detected, a new definition for the checkerboard coefficient has to be used. Similar to equation (1), the local checkerboard coefficient is a vector with an entry per cell i given by:

$$[\gamma_{cb}]_i = \begin{cases} \frac{[(L-L_c)\mathbf{p}_c]_i}{[L\mathbf{p}_c]_i} & \text{if } [L\mathbf{p}_c]_i \neq 0, \\ 0 & \text{if } [L\mathbf{p}_c]_i = 0. \end{cases} \tag{7}$$

As before, this opens up two options (denoted with superscripts α and β) to adjust the projection method, which are less obvious than before. Option (α) regulates the inclusion of a pressure gradient in the momentum prediction equation:

$$\mathbf{u}_c^p = \Delta t R\left(\mathbf{u}_c, \mathbf{u}_s\right) - \left(I - \gamma_{cb}^{\alpha}\right) G_c \tilde{\mathbf{p}}_c^n. \tag{8}$$

Applying this coefficient directly to the pressure field instead, as $G_c\left(I - \gamma_{cb}^{\alpha}\right)\tilde{\mathbf{p}}_c^n$, will have the effect of an uneven predictor pressure with false gradients, decreasing the overall accuracy of the predictor velocity. However, applying the coefficient as done in equation (8) makes it difficult to calculate the instantaneous pressure field at time-step $n+1$, and a new variable ϕ_c is introduced which can be calculated as:

$$\phi_c^{n+1} = G_c \tilde{\mathbf{p}}_c^{n+1} = \left(I - \gamma_{cb}^{\alpha}\right) G_c \tilde{\mathbf{p}}_c^n + G_c \tilde{\mathbf{p}}_c'. \tag{9}$$

Some applications require the calculation of the instantaneous pressure field, in which case every few time-steps the algorithm has to update the fields without using option (α). Option (β), again, involves an adjustment through combining the compact- and wide-stencil Laplacian operators. This combination is not straight-forward, and to maintain the symmetry of the operator the adjustment has to be made as follows:

$$\mathcal{L} = \overline{L}_c + \overline{L} = -M\left(\overline{\Omega}_s + \Gamma_{cs}\overline{\Omega}\Gamma_{cs}^T\right) M^T \tag{10}$$

with:

$$\overline{\Omega}_s = diag(\Gamma_{cs}\gamma_{cb}^{\beta})\Omega_s, \tag{11}$$

$$\overline{\Omega} = \Omega - I_3 \otimes \left(diag(\gamma_{cb}^{\beta})\Omega_c\right). \tag{12}$$

Again, to avoid solving a Poisson equation with a wide-stencil Laplacian, the equation can also be solved as:

$$\overline{L}\tilde{\mathbf{p}}_c'^{(k+1)} = M_c \mathbf{u}_c^p - \overline{L}_c \tilde{\mathbf{p}}_c'^{(k)}, \tag{13}$$

reaching a solution to $\tilde{\mathbf{p}}_c'$ iteratively.

NUMERICAL TESTS

All together, four methods are described in this work, method (a), (b), (α) and (β). The latter three methods are newly introduced and are tested and compared to the results form method (a) given in [5]. To do so, a two-dimensional Taylor-Green vortex was used to test the numerical dissipation of each method, whereas a lid-driven cavity is used to test the checkerboard suppressing qualities of the solvers. Finally, a turbulent channel flow is used to test the solver in unsteady conditions by measuring the kinetic energy budgets. The results will be compared to method (a) to show if additional gains can be made in conservational properties, by dynamically regulating checkerboarding not only in time, but also in space.

ACKNOWLEDGEMENTS

This work is supported by the SIMEX project (PID2022-142174OB-I00) of *Ministerio de Ciencia e Innovación*, Spain and the RETOtwin project (PDC2021-120970-I00) of *Ministerio de Economía y Competitividad*, Spain. J.A.H. is supported by the predoctoral grant FI 2023 (2023 FI_B1 00204) of the *Catalan Agency for Management of University and Research Grants (AGAUR)*. D.S. is supported by the predoctoral grant FI 2022 (2022_FI_B_00173), extended and financed by *Universitat Politècnica de Catalunya and Banc Santander*.

REFERENCES

[1]Rhie, C. M., & Chow, W. L. (1983). Numerical study of the turbulent flow past an airfoil with trailing edge separation. AIAA journal, 21(11), 1525-1532.

[2]Felten, F. N., & Lund, T. S. (2006). Kinetic energy conservation issues associated with the collocated mesh scheme for incompressible flow. Journal of Computational Physics, 215(2), 465-484.

[3]Trias, F. X., Lehmkuhl, O., Oliva, A., Pérez-Segarra, C. D., & Verstappen, R. W. C. P. (2014). Symmetry-preserving discretization of Navier–Stokes equations on collocated unstructured grids. Journal of Computational Physics, 258, 246-267.

[4]Komen, E. M. J., Hopman, J. A., Frederix, E. M. A, Trias, F. X., Verstappen, R. W. C. P. (2021). A symmetry-preserving second-order time-accurate PISO-based method. Computers & Fluids, 225, 104979.

[5]Hopman, J. A., Alsalti-Baldellou, À., Trias, F. X. & Rigola, J. (2023). On a checkerboard-free, conservative method for turbulent flows. Proceedings of the Tenth International Symposium on Turbulence, Heat and Mass Transfer.

WORKSHOP
Direct and Large-Eddy Simulation 14
April 10-12 2024, Erlangen, Germany

ANALYSIS OF ENTROPY STABLE DG SCHEMES BASED ON ENERGY BALANCES FOR SCALE-RESOLVED SIMULATIONS.

Amaury Bilocq[1], **Nayan Levaux**[1], **Vincent E. Terrapon**[1], **Koen Hillewaert**[1]
[1]Aerospace and Mechanics Department, Université de Liège
Allée de la découverte 9, 4000 Liège, Belgium
amaury.bilocq@uliege.be

INTRODUCTION

High-order simulation methods like Discontinuous Galerkin (DG) have proven suitability for Direct Numerical Simulation (DNS) and (implicit) Large Eddy Simulations (LES) of subsonic flows [1]. In supersonic conditions, shock waves may develop. The discontinuity over the shock cannot be captured by polynomial interpolation and, therefore, both convergence and stability of the simulation deteriorate as Gibbs oscillations develop. In the extreme case, these oscillations lead to unphysical solutions and the failure of the computation. Shock capturing methods usually add artificial viscosity to smooth the shock such that it can be safely represented. However, this reduces accuracy and negatively impacts the turbulent kinetic energy budget. It is therefore desirable to reduce its action to a minimum.

The instability of high-order methods, caused by under-interpolation and integration, can be mitigated by leveraging a discrete equivalent of the entropy and its evolution equation, which introduces a discrete bound for the solution. Most of these entropy-consistent schemes are based on the use of entropy variables and the "summation-by-parts" (SBP) theorem, leading to the analogue to the integration-by-parts theorem at the discrete level. The vast majority rely on nodes that coincide with the Gauss-Legendre-Lobatto (GLL) quadrature points [2]. The presence of such nodes on the boundary greatly helps constructing SBP operators between two elements. However, the GLL quadrature has lower accuracy leading to the build-up of error. More recently, entropy stable schemes based on Gauss quadrature nodes, without points on the boundary, have been developed. While these methods improve greatly the accuracy of the solution, such SBP operators are numerically very costly since they introduce an "all-to-all" flux coupling between all degrees of freedom (Dofs) in the element and the need of the so-called *entropy projection* [3].

In the literature, the entropy stable Discontinuous Galerkin spectral element method (ESDGSEM) based on the GLL quadrature nodes and the entropy stable Discontinuous Galerkin method (ESDG) based on Gauss quadrature nodes have been compared based on their robustness and performance for compressible Euler and Navier-Stokes equations [4, 5] but not with a deep focus on turbulence. In the present work, a novel approach is introduced for the analysis of these schemes based on energy balances such as the budget of kinetic energy and moments of velocity weighted by the density. This work also compares a new hybrid DG solver for shock capturing, the so-called sensor-based scheme. To alleviate the computational cost associated with the ESDG scheme, the entropy stability is only activated in cells where shock stabilization is necessary or where the turbulence is under-resolved. Everywhere else, a standard DG formulation is applied.

NUMERICAL EXPERIMENTS

The comparison of the schemes is performed on the 3D Taylor-Green Vortex, a well-known test case consisting of a laminar-turbulent transition of a decaying vortex, at Re=1600 and M=1. In this configuration, shocklets interact with the small turbulent structures, making this test case a challenge for stabilization techniques.

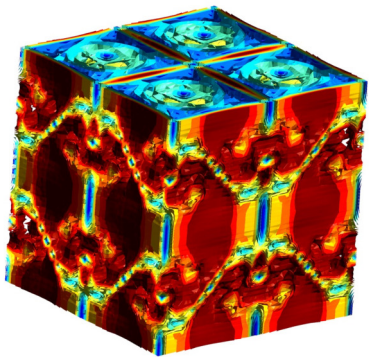

Figure 1: Magnitude of the velocity for the 3D Taylor-Green test case at convective time $T_c = 8$. The domain is a periodic box of length 2π.

First of all, the spatial convergence of each scheme has been computed based on the maximum error between the enstrophy obtained at different Dofs and the reference enstrophy from [6] (DNS of 512 Dofs per direction). Figure 2 shows that the convergence is better for the more complex ESDG scheme than for the ESDGSEM scheme but worse than for the sensor-based approach, which is an additional reason to introduce this method.

Then, the budget of kinetic energy as been investigated. In the case of a periodic domain, the conservative equation for the kinetic energy is given in its integral form by

$$\frac{d}{dt}\int_V \rho E_k dV = \int_V p\nabla\cdot\mathbf{v}dV - \int_V \tau : \nabla\mathbf{v}dV, \qquad (1)$$

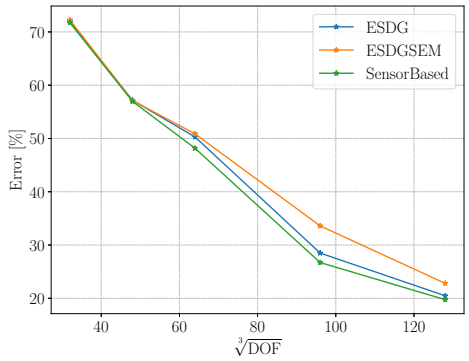

Figure 2: Convergence analysis based on the enstrophy from the reference solution [6] for the 3D Taylor-Green test case with respect to the number of degree of freedom for the two schemes.

where the first term is the variation of the kinetic energy, the second term is the pressure work and the third term is the viscous dissipation. The budget of kinetic energy is the difference between the measured variation (LHS of Eq. 1) and the theoretical variation (RHS of Eq. 1) of the kinetic energy. Figure 3 shows that, in this case, the convergence of the budget closure is the slowest for the ESDG scheme for a reduced number of Dofs. By looking to the terms constituting the budget of kinetic energy in Fig. 4 for the ESDG scheme and in Fig. 5 for the ESDGSEM, a difference in the pressure work can be spotted. This increase in the pressure work for the ESDG scheme can be explained due to presence of the *entropy projection* which improves the robustness of the method but induces a large numerical error for coarser mesh. The sensor based approach has a lower error and therefore seems interesting not only for efficiency but also for accuracy. The ESDGSEM scheme exhibits a slower convergence rate for finer mesh and tends to a constant error in the budget closure at convergence.

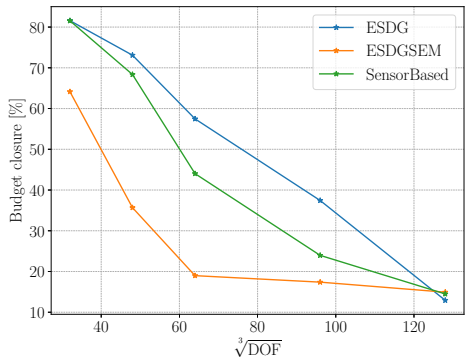

Figure 3: Budget closure of the kinetic energy for the 3D Taylor-Green test case with respect to the number of degree of freedom for the two schemes.

Therefore, the budget of kinetic energy highlights that even if the ESDG scheme is the more robust, it is adding unwanted numerical dissipation on hidden quantities such as the pressure work. Moreover, an other interest of the sensor based approach is the lower computational time compared to the

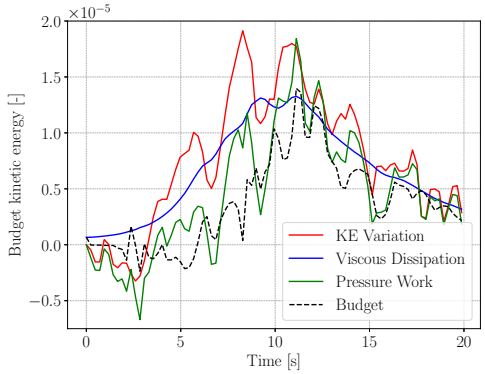

Figure 4: Variation of the terms constituting the budget of kinetic energy for the 3D Taylor-Green test case with 96 Dofs for the ESDG scheme.

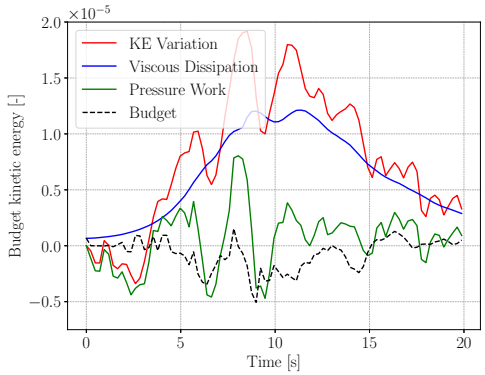

Figure 5: Variation of the terms constituting the budget of kinetic energy for the 3D Taylor-Green test case with 96 Dofs for the ESDGSEM scheme.

	ESDGSEM	ESDG	SensorBased
Cost	-	+47%	+7%

Table 1: Comparison of the cost of the method with respect to the less expensive ESDGSEM scheme to simulate the 3D Taylor-Green Vortex with 96 Dofs per direction.

ESDG scheme as shown in Tab.1.

REFERENCES

[1]Hillewaert, Koen : *Development of the discontinuous Galerkin method for high resolution, large scale CFD and acoustics in industrial geometries*. Université catholique de Louvain (2013).

[2]Gassner, Gregor : Split Form Nodal Discontinuous Galerkin Schemes with Summation-By-Parts Property for the Compressible Euler Equations, Journal of Comp. Phy. Vol. **327** (2016).

[3]Chan, Jess et al. : Efficient Entropy Stable Gauss Collocation Methods. *SIAM Journal on Scientific Computing* **41** (2019).

[4]Rojas, Diego et al. : On the Robustness and Performance of Entropy Stable Collocated Discontinuous Galerkin Methods . *Journal of Computational Physics*, **426** (2021).

[5]Chan, Jesse et al. : On the Entropy Projection and the Robustness of High Order Entropy Stable Discontinuous Galerkin Schemes for Under-Resolved FLows. *Frontiers in Physics*, **10** (2022).

[6]Lusher, David J., et Neil D. Sandham : Assessment of Low-Dissipative Shock-Capturing Schemes for the Compressible Taylor–Green Vortex. *AIAA Journal*, **59, n°2** (2021).

WORKSHOP
Direct and Large-Eddy Simulation 14
April 10-12 2024, Erlangen, Germany

DISCRETE ADJOINT SHAPE OPTIMIZATION OF A CURVED PIPE FOR MINIMAL VISCOUS DISSIPATION

Eman Bagheri, **Philipp Schlatter**, **Stefan Becker**
Institute of Fluid Mechanics (LSTM)
Friedrich–Alexander–Universität (FAU) Erlangen–Nürnberg, Germany
eman.m.bagheri@fau.de

INTRODUCTION

Curved pipes have a wide range of applications, such as in heat exchangers, chemical reactors, heat pipes and fluid transport systems. Various research has been conducted to shed light on the complex dynamics of the flow and turbulence in curved pipes. The curvature of the pipe causes a centripetal force at the bend and gives rise to the radial pressure gradient. This results in the acceleration of the velocity on the outer wall and deceleration on the inner wall. Consequently, this redistribution of the velocity field and skewing of the mean flow at the bend generates a Prandtl's secondary flow of the first kind. The skewing of the mean velocity and the emergence of the Dean vortices change the friction factor. The friction factor in curved pipes is a function of the Reynolds number and the curvature ratio. The experimental work from Cioncolini and Santini [1] showed that the friction factor in curved pipes is not necessarily higher than in the straight pipes at the same Reynolds number (substraight drag). Furthermore, for mildly curved pipes, the pressure loss could even be lower than the laminar correlation of the same curved pipe (sublaminar drag). Later the Direct Numerical Simulations (DNS) of Noorani et al. in [2] and [3] confirmed the existence of the substraight and sublaminar drag. Furthermore, the nature of turbulence transition for curved pipes is fundamentally different from straight pipes. For sufficiently high curvatures, curved pipes undergo a multistage supercritical transition. Canton et al. [4] thoroughly studied the supercritical transition in toroidal pipes using linear stability analysis. They identified the neutral curve separating stable and unstable regions associated with bifurcations.

Both the friction factor and the onset of the instabilities are dependent on the curvature ratio and Reynolds numbers. Therefore, to achieve a design with optimal pressure loss coefficient, both parameters must be locally determined along the axis of the curved pipe. This motivates the current work in which a free-form shape optimization of the curved pipe is performed. This optimization method enables us to locally modify the Reynolds number and the curvature ratio to minimize the total viscous losses.

PROBLEM DESCRIPTION

The baseline curved pipe to be optimized is shown in Fig. 1. This geometry is referred to as Ubend throughout this work. The turbulent flow at the inlet of the Ubend is fully developed at $Re_D = U_{bulk} D/\nu = 10000$. This corresponds to a friction Reynolds number of $Re_\tau = u_\tau R/\nu = 313$. The curvature ($\delta = \frac{D}{2R_c}$) of the baseline is 0.2, which is categorized as a strong curvature according to [1]. The red box shows the section subject to free-form shape optimization, while the regions outside of the red box remain unchanged.

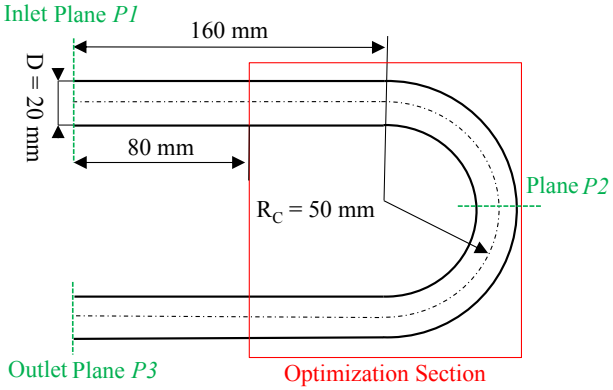

Figure 1: The geometry of the baseline Ubend to be shape-optimized for minimal viscous dissipation. The red box indicates the section of the pipe that is subject to optimization.

METHODOLOGY

The discrete optimization problem to be solved is formulated as follows:

$$\begin{aligned} &\min_S \; J(U(S), X(S)) \\ &s.t.\; U = G(U(S), X(S)) \\ &\quad X(S) = M(S) \end{aligned} \tag{1}$$

in which $J(U(S), X(S))$ is the discrete objective function that depends on the primal variables U, the computational grid X and the design vector S. The optimization problem must satisfy the discrete primal equation $U = G(U(S), X(S))$ as well as the mesh deformation equation $X(S) = M(S)$. The optimization is performed using the discrete adjoint solver in *SU2* (see [6]). Each design step starts with solving the primal equations (i.e. k-ω-SST RANS equations in our case). Following that, the corresponding adjoint equations are obtained with the help of the Algorithmic Differentiation package CodiPack [7]. The adjoint equations are solved, and sensitivities are calculated. In the next step, the gradient of the objective function is obtained and the mesh is deformed accordingly.

The objective function to be minimized is the total viscous dissipation over the entire domain:

$$J = \int_{\Omega} \left(\overline{\tau} : \nabla \overline{U} + \epsilon \right) dV \tag{2}$$

in which $\overline{\tau}$, $\overline{U}$ and ϵ are the mean viscous stress tensor, mean velocity and turbulent dissipation rate, respectively. The optimization outcome was validated a posteriori using DNS and experiments: DNS of both baseline and optimized geometries were performed to investigate the effect of optimization on turbulence. In the DNS, the outlet boundary was shifted by $16R$ downstream of *P3* to allow investigating the effect of the optimization on the turbulence farther downstream of the bend. We refer to the outlet boundary of the DNS domain as the extended outlet.

RESULTS

A local minimum is found after 50 design steps at which the objective function is reduced by 52 percent, and the pressure loss improves by 56 percent according to the k-ω-SST model used for the primal solution of the optimization. Fig. 2 shows the baseline and the optimized designs next to each other. The increased cross-sectional area of the optimized design leads to a smooth distribution of the radial pressure, thereby reducing the kinetic energy of secondary flow and the Dean vortices (see Fig. 3). The experiment shows that at $Re_D = 10000$, a pressure loss reduction of 62 percent is gained. This is in agreement with the predicted value of 64.5 percent from the DNS.

Fig. 4 shows an instantaneous non-dimensional vorticity field on the center plane of the baseline and optimized designs. The figure on the left shows that the turbulence intensifies at the bend, where Dean vortices are formed in the presence of a strong mean velocity gradient. On the contrary, the figure on the right shows that the optimization partially suppresses the turbulence near the bend and the vorticity field diminishes near the outlet. This effect can be seen in the Fanning friction factor along the streamwise direction of the optimized bend in Fig. 5. Initially, due to the redistribution of the velocity after the contraction region of the optimized shape, the friction factor rises to values associated with a fully developed flow at $Re_\tau = 708$. However, the friction factor rapidly drops from $z/R = 0$ to $z/R = 1$, then gradually decreases up to the extended outlet boundary. At a distance of $16R$ downstream of *P3*, the friction factor is reduced by 35 percent compared to that of the fully developed turbulent flow with the same Re_D at *P1*. The friction Reynolds number Re_τ drops to 252 as a result of turbulence suppression.

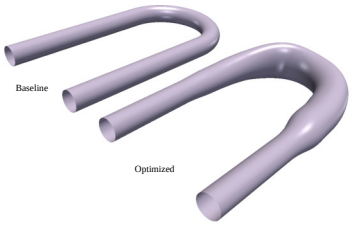

Figure 2: The geometry of the baseline and optimized Ubend.

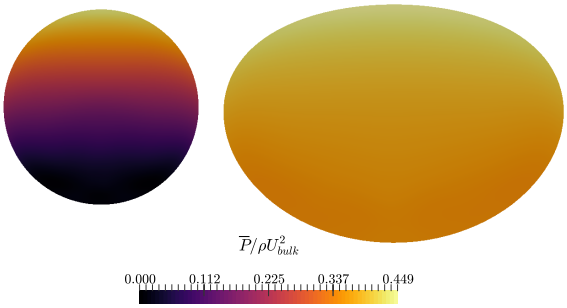

Figure 3: Comparison between the radial pressure distribution in baseline and optimized designs at plane *P2*.

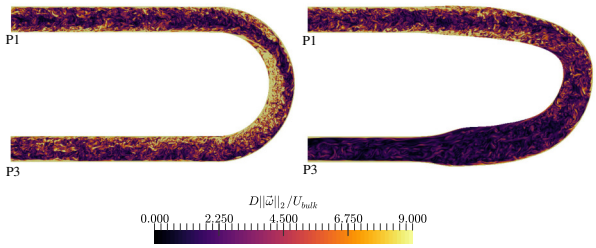

Figure 4: Instantaneous non-dimensional vorticity.

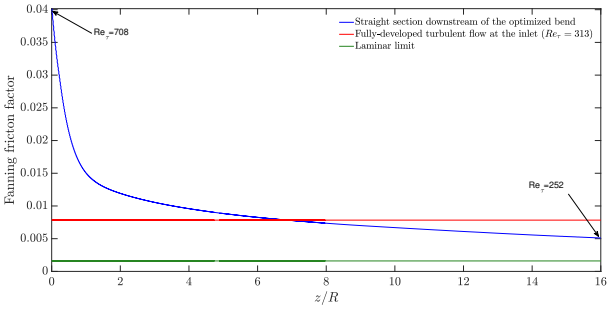

Figure 5: Fanning friction factor along the streamwise direction of the optimized bend starting at *P3* ($z/R = 0$) up to the extended outlet boundary ($z/R = 16$) located downstream of *P3*.

REFERENCES

[1]Cioncolini, A. and Santini, L. "An experimental investigation regarding the laminar to turbulent flow transition in helically coiled pipes", Experimental Thermal and Fluid Science, 2006.

[2]Noorani, A., El Khoury, G.K. and Schlatter, P., "Evolution of turbulence characteristics from straight to curved pipes". International Journal of Heat and Fluid Flow, 2013.

[3]Noorani, A. and Schlatter, P., "Evidence of sublaminar drag naturally occurring in a curved pipe", Physics of Fluids, 2015.

[4]Canton, J., Schlatter, P. and Örlü, R., "Modal instability of the flow in a toroidal pipe". JFM, 2016.

[5]Jovanovic, J. and Hillerbrand, R. "On peculiar property of the velocity fluctuations in wall-bounded flows", Thermal Science, 2005.

[6]Albring, T., Sagebaum, M. and Gauger, N. R., "Efficient Aerodynamic Design using the Discrete Adjoint Method in SU2", 17th AIAA/ISSMO Multidisciplinary Analysis and Optimization Conference, 2015.

[7]Sagebaum, M., Albring, T., Gauger, N. R., "High-Performance Derivative Computations using CoDiPack", ACM Transactions on Mathematical Software (TOMS), 2019.

[8]El Khoury, G. K., Schlatter, P., Noorani, A., Fischer, P. F., Brethouwer, G., Johansson, A. V., "Direct Numerical Simulation of Turbulent Pipe Flow at Moderately High Reynolds Numbers", Flow, Turbulence and Combustion, 2013.

SESSION: Combustion and reactive flows II

Wednesday, April 10, 2024

14:50- 15:50

WORKSHOP
Direct and Large-Eddy Simulation 14
April 10-12 2024, Erlangen, Germany

BEHAVIOUR OF TURBULENCE AT MULTIPLE SCALES DURING FLAME-WALL INTERACTION OF PREMIXED FLAMES WITHIN TURBULENT BOUNDARY LAYERS

Umair Ahmed[1] , **Sanjeev Kr. Ghai**[1], **Nilanjan Chakraborty**[1]
[1]School of Engineering, Newcastle University, Newcastle upon Tyne, United Kingdom, NE1 7RU
umair.ahmed@newcastle.ac.uk

INTRODUCTION

It is important from a modelling and engineering point of view to understand the different scales involved during the flame-wall interaction (FWI) process within turbulent boundary layers, as the vortex stretching phenomenon in turbulence is affected by different scales [1]. Computational Fluid Dynamics (CFD) relies on a multitude of methods ranging from Reynolds-averaged to Large Eddy Simulation techniques, and they address different ranges of scales of the turbulence kinetic energy spectrum. In the case of FWI it has been shown in the literature that the small scales of turbulence do not contribute to the straining of the flame when the flame is away form the wall, but when the flame starts to interact with the wall the contribution of the small scales of turbulence significantly increases [2]. To date no information is available about the behaviour of turbulent stresses at different scales in the case of FWI. In the present work Direct Numerical Simulation (DNS) data is used to investigate the behaviour of turbulent stresses at multiple scales for statistically planar flames propagating across a turbulent boundary layer at two different friction Reynolds numbers, $Re_\tau = 110$ and 180, and interacting with an isothermal inert wall. In this regard, the main objectives of this study are: (1) To perform a multiscale analysis of the anisotropy of the turbulent stress tensor for a large range of different filter sizes. (2) To compare the level of anisotropy for different wall normal distances and friction Reynolds numbers. (3) To provide detailed physical explanations for the observed behaviour.

DIRECT NUMERICAL SIMULATION DATA

For the purpose of the current analysis the simulations are performed using a three-dimensional compressible code called SENGA+ [2, 3, 4]. The code solves conservation equations for mass, momentum, energy and species mass fractions. The first and second-order spatial derivatives in SENGA+ are calculated using a 10^{th}-order finite difference central scheme for the internal grid points but the order of accuracy gradually reduces to the second order for the non-periodic boundaries. A third-order Runge-Kutta scheme is used for explicit time advancement. In the current simulations the combustion chemistry is represented by a single-step Arrhenius type chemical reaction for the sake of computational economy. As the present analysis focuses primarily on the fluid-dynamical aspects of FWI, it is expected that the findings of this study will not be affected by the choice of the chemical mechanism. Stoichiometric methane-air premixed flames under atmospheric conditions are considered for the current analysis. The Lewis number of all the species is taken to be unity and the unburned gas temperature T_R is taken to be 730K, which yields a Zeldovich parameter, $\beta = T_a(T_{ad} - T_R)/T_{ad}^2$ of 6.0 (where T_a, T_{ad}, T_R is the activation, adiabatic and reactant temperatures, respectively), and a heat release rate parameter of $\tau = (T_{ad} - T_R)/T_R = 2.3$. Standard values are taken for the Prandtl number, Pr, and the ratio of specific heat, γ (i.e., $Pr = 0.7$, γ=1.4).

The simulations in this analysis have been conducted in a configuration where turbulent boundary layers are formed on top of a chemically inert wall and the initial flow conditions for the reacting flow simulations have been generated using fully developed non-reacting turbulent channel flow solutions corresponding to $Re_\tau = \rho_R u_{\tau_{NR}} h \ / \ \mu_R$ =110 and 180, where $u_{\tau_{NR}} = \sqrt{|\tau_{w_{NR}}|/\rho_R}$ and $\tau_{w_{NR}}$ are the friction velocity and wall shear stress for the non-reacting channel flow, respectively, ρ_R and μ_R are the unburned gas density and dynamic viscosity respectively and h is the channel half height corresponding to the non-reacting fully developed channel flow solution. The computational domain size for both Re_τ =110 and 180 are taken to be $10.69h \times 1.33h \times 4h$ and equidistant cartesian grids of $1920 \times 240 \times 720$ and $3200 \times 400 \times 1200$ are used for Re_τ=110 and 180, respectively. These grids ensure that $y^+_{NR} = (\rho_R u_{\tau_{NR}} y) \ \ \mu_R$ for the wall adjacent grid points remained smaller than 0.6 and at least 8 grid points are accommodated within the thermal flame thickness $\delta_{th} = (T_{ad} - T_R) \ / \ \max|\nabla T|_L$ (where T is the instantaneous dimensional temperature).

In all simulations, periodic boundary conditions are used for both streamwise (i.e. x-direction) and spanwise (i.e. z-direction) and a pressure gradient (i.e., $-\partial p/\partial x = \rho u^2_{\tau_{NR}}/h$ where p is the pressure) has been imposed in the streamwise direction [3]. A no-slip impenetrable, inert wall boundary condition is implemented at $y = 0$, and an isothermal thermal wall boundary condition (i.e., $T_w = T_R$) is imposed at the wall. A partially non-reflecting boundary is specified at y/h=1.33. For both Re_τ =110 and 180 cases, the steady 1-D laminar flame simulation has been interpolated to the 3-D grid in such a manner that the reaction progress variable c=$(Y_{FR} - Y_F)/(Y_{FR} - Y_{FP})$ (where the subscripts R and P represent the fresh reactant and fully burned products, respectively) takes a value of 0.5, at $y/h \approx 0.85$ such that the

reactant side faces the wall, whereas the burned gas side faces the outflow side of the domain. The ratio of the laminar burning velocity S_L to non-reacting flow friction velocity $u_{\tau_{NR}}$ is taken to be 0.7 for all cases considered here. The simulations have been continued for a maximum of 2.0 flow through time based on the maximum streamwise mean velocity. The flames propagate towards the wall and eventually quench due to heat loss through the wall over the simulation time, but the boundary layer does not evolve significantly [3].

For the purpose of investigating multiple scales involved in turbulence, DNS data have been explicitly filtered by using a Gaussian filter kernel $G(r)$ such that the filtered values of a quantity Q can be expressed as follows:

$$\overline{Q(x)} = \int Q(x-r)G(r)dr. \quad (1)$$

The application of this low pass filter removes the high wavenumber content of the fluctuating velocity signal and an associated high pass filter (which removes the low wavenumber content) can be define as [4]: $\underline{Q} = Q - \overline{Q}$. Note that following Germano et al. [5] filtering operations in this work are only applied to the streamwise and spanwise directions.

RESULTS

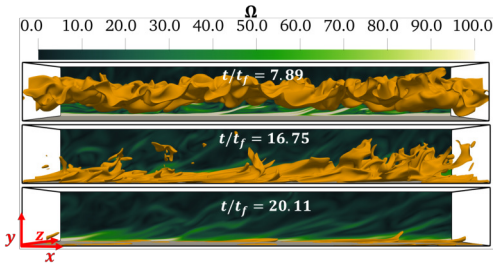

Figure 1: Head-on quenching for the premixed flame case with Re_τ=180 at different t/t_f. The isosurface coloured in yellow represents $c = 0.8$. The instantaneous normalised vorticity magnitude $\Omega = \sqrt{\omega_i\omega_i} \times h \ / \ u_{\tau,NR}$ is shown on the $x-y$ plane at $z/h = 4$. The grey surface denotes the wall.

The instantaneous views of $c = 0.8$ isosurface at different normalised times (e.g., $t \ \ t_f$=7.89, 16.75 and 20.11, where $t_f = \delta_{th}/S_L$ is the chemical time scale) for the Re_τ=180 case are shown in Fig. 1 where the distributions of the normalised vorticity magnitude $\Omega = \sqrt{\omega_i\omega_i} \times h \ / \ u_{\tau,NR}$ at $z \ \ h$=4.0 are also shown. The instantaneous views of $c = 0.8$ isosurface for the $Re_\tau = 110$ case show similar qualitative behaviour as that of the $Re_\tau = 180$ case and are not shown here for the sake of brevity. Figure 1 shows that the flame surface becomes wrinkled due to the interaction of turbulent shear and vortical motion within the boundary layer, but these wrinkles eventually quench when they come in the vicinity of the wall (i.e., the normalised minimum quenching distance is y_Q/δ_Z= 1.71 and 1.72 for Re_τ=110 and 180 turbulent cases, with $\delta_Z = \alpha_{T_0}/S_L$ and α_{T_0} being the Zeldovich flame thickness and thermal diffusivity in the unburned gas, respectively and y_Q is the wall-normal distance of the progress variable, c, isosurface) due to the heat loss. This quenching is reflected in the fragmented flame surface at later times in Fig. 1. The presence of the flame within turbulent boundary layers gives rise to a predominantly positive dilatation rate (i.e. $\partial u_i/\partial x_i > 0$), which in turn affects the turbulence statistics due to flame normal acceleration resulting from thermal expansion [3].

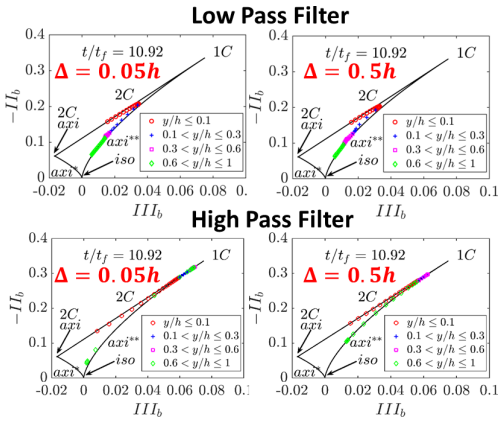

Figure 2: Plots of IIb versus $IIIb$ in the form of the Lumley triangle for Re_tau = 110 (1st and 3rd row) during flame-wall interaction for high and low pass filters at different filter widths . Note axi represents axisymmetric contraction and axi represents axisymmetric expansion.

The stress anisotropy tensor, b_{ij} is defined as: $b_{ij} = \tau_{ij}/\tau_{kk} - \delta_{ij}/3$, where $\tau_{ij} = \overline{u_iu_j} - \overline{u_i}\ \overline{u_j}$ for low pass filter and $\tau_{ij} = \underline{u_iu_j} - \underline{u_i}\ \underline{u_j}$ for high pass filter. The second and third invariants of b_{ij} are defined as $II_b = -b_{ij}b_{ji}/2$ and $III_b = b_{ij}b_{jk}b_{ki}/3$ respectively. Figure 2 shows the plots of II_b versus III_b using low and high pass filtering at different filter widths during flame wall interaction at $Re_\tau = 110$. It can be noticed that the behaviour not only changes with the filter width, but also with the change in the type of the filter used. This imples that sub-grid stresses have different behaviour at different scales and filter widths. The implications of this on modelling and more details of the behaviour during FWI will be presented in detail in the presentation.

REFERENCES

[1] A. Lozano-Durán, M. Holzner, and J. Jiménez, "Multiscale analysis of the topological invariants in the logarithmic region of turbulent channels at a friction Reynolds number of 932," *J. Fluid Mech.*, vol. 803, pp. 356–394, 2016.

[2] U. Ahmed, N. A. K. Doan, J. Lai, M. Klein, N. Chakraborty, and N. Swaminathan, "Multiscale analysis of head-on quenching premixed turbulent flames," *Phys. Fluids*, vol. 30, no. 10, p. 105102, 2018.

[3] U. Ahmed, N. Chakraborty, and M. Klein, "Influence of Flow Configuration and Thermal Wall Boundary Conditions on Turbulence During Premixed Flame-Wall Interaction within Low Reynolds Number Boundary Layers," *Flow, Turbul. Combust.*, vol. 111, pp. 825–866, sep 2023.

[4] M. Klein, T. Trummler, N. Urban, and N. Chakraborty, "Multiscale Analysis of Anisotropy of Reynolds Stresses, Subgrid Stresses and Dissipation in Statistically Planar Turbulent Premixed Flames," *Appl. Sci.*, vol. 12, no. 5, 2022.

[5] M. Germano, U. Piomelli, P. Moin, and W. H. Cabot, "A dynamic subgrid-scale eddy viscosity model," *Phys. Fluids A*, vol. 3, no. 7, pp. 1760–1765, 1991.

WORKSHOP
Direct and Large-Eddy Simulation 14
April 10-12 2024, Erlangen, Germany

LES STUDY OF SPARK IGNITION IN A COUNTER-CURRENT NOZZLE

A. Wawrzak[1], **A. Boguslawski**[1], **A. Tyliszczak**[1]
[1] Faculty of Mechanical Engineering and Computer Science
Czestochowa University of Technology, Poland
agnieszka.wawrzak@pcz.pl

INTRODUCTION

Numerous industrial applications are based on non-premixed systems and the combustion initiation through an externally introduced energy source as an electric spark. Undoubtedly, the ignition process possesses a stochastic nature that is largely conditioned by the flow regimes. Depending on the spark location with respect to vortical structures the initial scenario directly affects further flame development [1]. The size and strength of the turbulent structures that appear in the vicinity of the sparks are as important as the size and energy of the sparks [2].

The large vortical structures appearing with extreme regularity constitute a striking feature of the global instability that can emerge in the axisymmetric variable density jets [3] and in counter-current mixing layers established by applying suction to the periphery of an axisymmetric jet (counter-current jets) [4, 5]. The latter remains the least explored, and to the best authors' knowledge, there are no studies investigating the spark ignition in the counter-current nozzles. The present paper partially fills this gap. The potential of the global instability phenomenon to change the character of a combustion process has been recently demonstrated for auto-ignition events in counter-current hydrogen jets [6, 7]. The present paper extends that research and the one performed in [1, 2] offering a physical understanding of both the role of the global instability phenomenon in stabilizing the lifted flame and the mechanism of flame kernel development in vicinity of the vortical structures following the spark-ignition.

MODELLING

We consider a counter-current injection system in which a central jet nozzle ($D = 0.002$ m) providing a fuel (hydrogen/nitrogen in mass proportion 0.13/0.87) is surrounded by a co-axial nozzle ($D_{suc} = 2D = 0.004$ m) sucking the fluid. Outside of the annulus section, a stream of oxidizer (air) is supplied. The temperature of both the fuel and oxidizer is 300 K, and a flame is initiated with a spark. The analyzed counter-current configuration is presented schematically in Fig. 1. Sucking the fluid from the region surrounding the fuel jet produces a counter-current flow in the direct vicinity of the nozzle. To control its length we apply the velocity ratio $I = -U_{suc}/U_j$ (U_j - velocity of the jet, U_{suc} - velocity of the counter-current) equal to $I = 0.0$ (wall), $I = 0.1$ and 0.2. The composition/temperature of the fuel and oxidizer result in the density ratio $S = \rho_j/\rho_{cf} = 0.36$, which is below the critical one for the occurrence of global instability. Thus, the counter-flow is not required to induce the global mode. Nevertheless, it affects the flow structure significantly, determining further flame development.

We apply the Large Eddy Simulation (LES) with the laminar chemistry approach for the turbulence/flame interactions. The spark is modeled by the energy deposition (ED) model, where the source term $\dot{Q}$, possessing the Gaussian distribution in time and space, is added to the transport equation for the enthalpy [8]. We do not consider the inner geometry of the nozzles, and the computational domain is a rectangular box ($L_y = 30D, L_x = L_z = 15D$). The applied mesh counts of N_y=288, $N_x = N_z$=192 nodes in the axial and radial directions. The jet, suction, and co-flow are modeled through the instantaneous velocity profile for which the inlet mean velocity of the central jet is given by the Blasius profile. The LES solver used in this study is an in-house high-order solver based on the low Mach number approximation. The Navier-Stokes and continuity equations are discretised using the sixth order compact difference method on half-staggered meshes [9]. The chemical reactions are computed using the CHEMKIN interpreter with the help of a detailed mechanism of hydrogen oxidation [10] involving 9 species and 21 reactions.

RESULTS

Characteristic phenomena for global instability include the formation of large-scale structures and enhanced mixing. In Fig. 2, the former is identified by iso-surfaces of the Q-parameter, and the latter is captured with the mixture fraction contours shown in the central cross-section. The flow fields are presented at the time of the initiation of the spark ($t = t_0 - \Delta_t/2$, t_0 - the time moment when $\dot{Q}$ gets a maximum value; Δ_t - the time duration of the spark), along with the spark locations (the white circles at $x/D = z/D = 0.5$ and $y/D = 1.5$). Each spark has the total energy $\epsilon = \int \dot{Q} dV dt = 5$ mJ, char-

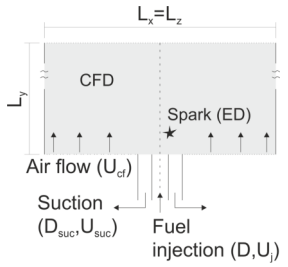

Figure 1: Simulation setup.

acteristics size $\Delta_s = 0.75D = 0.0015$ m and time duration $\Delta_t = 0.0005$ s. In the sparks regions, strong toroidal vortices emerge due to global instability. They are accompanied by the smaller longitudinal structures and side jets appearing as the streams of the fuel-rich mixture released from the fuel jet. The periodic shedding of large-scale structures in the regions of sparks is confirmed by the distinct peaks observed in the axial velocity spectra at heights $y/D = 1$ and $y/D = 2$. The localization of the peaks shifts toward higher non-dimensional frequencies ($St_D = fD/(U_j + U_{suc})$, f - frequency) with the increasing I and remains unchanged along the jet axis. Note that during the energy deposition, seven toroidal structures pass through the area where the spark is generated. We observe that for the higher I the more robust the vortical structures emerge, however, their shape becomes highly irregular and the flow seems more turbulent. The spatio-temporal locations of the vortices have a significant impact on the success/failure of the ignition and may lead to hysteresis in the flame position after the successful ignition. Depending on I and thus the frequency at which the vortices appear, the flame stabilizes as attached or lifted at various axial distances. This issue will be investigated within the present study. Additionally, we will consider the cases with the spark locations in the vicinity of the side jets at the axial distance where the vortical structures break down (see the red circle in Fig. 2).

The calculations performed so far reveal that with different velocity ratios, one can affect the flame kernel behavior after the spark initiation and change the final position of the flame. Figure 3 shows the temperature distributions for subsequent steps of the ignition and flame evolution. It can be seen that at the time instant $t = t_0$, at which the sparks reach the maximum energy, the flame kernel develops near its initial position. Subsequently, the formed flame is displaced, partially defragmentated, and stretched by the vortical structures. It propagates towards favorable mixture conditions and expands radially and axially. At $t = t_0 + \Delta_t$, one can observe that: (i) the temperature is the highest for $I = 0.0$, and the flame propagates towards the inlet along a thin shear layer; (ii) the flame rapidly expands in the radial direction due to intensified mixing of fuel and oxidizer immediately above the inlet plane both for $I = 0.1$ and 0.2. In subsequent time instants, the differences in the flame development become more pronounced.

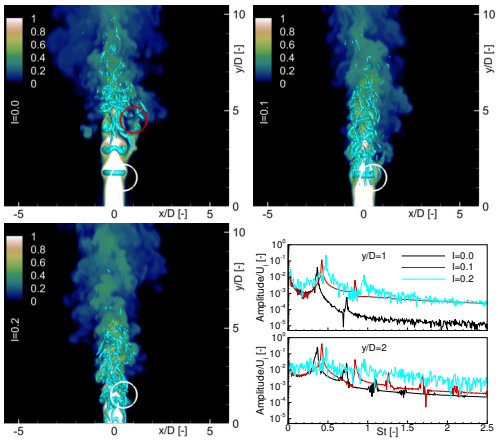

Figure 2: The flows (mixture fraction and Q-parameter, $Q = 5$ s^{-2}) prior to the spark ignition ($t = t_0 - \Delta_t/2$) along with the axial velocity spectra. Colored circles mark areas of sparks.

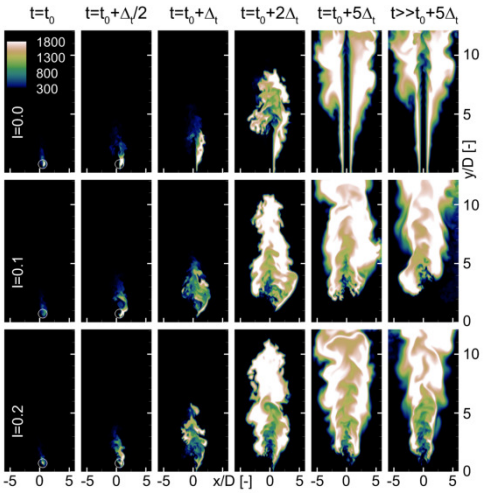

Figure 3: Spatio-temporal evolution of the flames (temperature contours) following the spark ignition.

For $I = 0.0$, the flame attaches to the nozzle, and the global instability and vortical structures are damped. In contrast, for $I = 0.1$ and 0.2, the flames are lifted and remain in this state until the end of the simulations. Worth noticing are two findings. First, the flame can expand spectacularly due to the presence of the side jets along which it initially propagates, as in the case with $I = 0.1$. Second, the flame may momentarily attach to the inlet plane and then detach to a lifted position if the structures are sufficiently robust, as in the case with $I = 0.2$.

REFERENCES

[1]Wawrzak A. and Tyliszczak A.: A spark ignition scenario in a temporally evolving mixing layer, *Combust. Flame*, **209**, 353–356 (2019).

[2]Wawrzak A. and Tyliszczak A.: Implicit LES study of spark parameters impact on ignition in a temporally evolving mixing layer between H2/N2 mixture and air, *Int. J. Hydrog. Energy*, **43**, 9815–9828 (2018).

[3]Monkewitz P.A., Bechert D.W, Barsikow B. and Lehmann B.: Self-excited oscillations and mixing in a heated round jet, *J. Fluid Mech.*, **213**, 611–639 (1990).

[4]Strykowski P. and Niccum D.: The stability of countercurrent mixing layers in circular jets, *J. Fluid Mech.*, **227**, 309–343 (1991).

[5]Wawrzak K., Boguslawski A. and Tyliszczak A.: A numerical study of the global instability in counter-current homogeneous density incompressible round jets, *Flow Turbul. Combust.*, **107**, 901–935 (2021).

[6]Wawrzak A., Wawrzak K., Boguslawski A., Tyliszczak A. and Geurts B.J.: Global instability phenomenon as a physical mechanism controlling dynamics of a nitrogen-diluted hydrogen flame, *Int. J. Heat Mass Transf.*, **213**, 124260 (2023).

[7]Wawrzak A., Wawrzak K., Boguslawski A., Tyliszczak A. and Geurts B.J.: Hydrogen jet flame control by global mode, *Flow Turbul. Combust.*, 1–23 (2023).

[8]Lacaze G., Richardson E. and Poinsot T.: Large eddy simulation of spark ignition in a turbulent methane jet, *Combust. Flame*, **156**, 1993–2009 (2009).

[9]Tyliszczak A.: High-order compact difference algorithm on half-staggered meshes for low Mach number flows, *Comput. Fluids*, **127**, 131–145 (2016).

[10]Mueller M., Kim T., Yetter R. and Dryer F.: Flow reactor studies and kinetic modeling of the H_2/O_2 reaction, *International Journal of Chemical Kinetics*, **31**, 113–125 (1999).

WORKSHOP
Direct and Large-Eddy Simulation 14
April 10-12 2024, Erlangen, Germany

HIGH FIDELITY SIMULATIONS OF HYDROGEN JET INJECTION INTO 3D TAYLOR GREEN VORTEX FOR DISI INTERNAL COMBUSTION ENGINE ANALYSIS

L.F. Rico Cortes[1,*], S.-J. Baik[1], A.Kempf[1]
[1]Institute for Energy and Materials Processes (EMPI) - Chair of Fluid Dynamics
University of Duisburg-Essen, Germany
*luis.ricocortes@uni-due.de

INTRODUCTION

Hydrogen-driven direct injection/spark-ignition (DISI) internal combustion engines are highly relevant in light of energy transition policies and environmental concerns. The introduction of hydrogen significantly affects the mixing process due to its high diffusivity. Additionally, the combustion properties of hydrogen, such as extended flammability limits, wide detonation range, high adiabatic flame temperature, and increased flame propagation speed, contribute to increased instabilities in engine operation. These instabilities, particularly cycle-to-cycle variations (CCV), hinder optimization and reliability in the design and production of hydrogen-driven engines. Experimental setups for understanding CCV production are limited, given the challenges in detecting, tracing, and measuring hydrogen [1]. Direct numerical simulations (DNS) provide a high-fidelity approach to thoroughly study the phenomenology in hydrogen engines. A preliminary step involves translating the engine operating conditions into a prescribed computational domain, simplifying the analysis by eliminating the complexities of the engine's geometry.

The Taylor Green Vortex (TGV) is a well-known flow configuration, notable for its prescribed vorticity decay, which can be solved analytically in terms of the Reynolds number [2]. By establishing a known reference for turbulent flow evolution, which encompasses the engine turbulent flow characteristics, it is possible to identify how hydrogen undergoes mixing. DNS, capable of resolving the smallest scales in the flow field, allows drawing conclusions on the formation and evolution of turbulent structures [3]. Hydrogen combustion in the TGV-based configuration has been investigated by [4, 5]; however, the present study introduces the novelty of incorporating hydrogen gas-injection. This work aims to represent the turbulent flow properties inside an internal combustion engine as an initial configuration of the TGV, to study the interaction of the flow field with the gas injection of hydrogen. The focus is centered on various phenomena, such as mixing, ignition, combustion, and flame propagation properties.

CASE DESCRIPTION

The Taylor Green Vortex is defined as a cubic domain with periodic boundary conditions. It is configured by defining a velocity field in terms of the following expressions,

$$\begin{aligned} u(x,y,z,t=0) &= V_0\ cos(x)sin(y)sin(z) \\ v(x,y,z,t=0) &= -V_0\ sin(x)cos(y)sin(z) \\ w(x,y,z,t=0) &= 0 \end{aligned} \tag{1}$$

where V_0 is the maximum velocity of the vortex. Pressure is set up in a corresponding manner but considering a P_0 coefficient factor. The characteristic length L_0 is defined as the diameter of the largest vortex; this length is equal to half of the computational domain. L_0 is then multiplied by π to extend the total domain length to match the frequency of the sinusoidal/cosinusoidal functions defining the velocity fields. The Reynolds number, defined in terms of L_0, V_0, and the kinematic viscosity ν, governs the turbulence behavior. Its value is intended to be representative of the engine conditions. The vorticity is prescribed in the TGV to increment and then decay up to a convective time scale of 25τ. This value is expected to change due to the effect of injection, ignition, and flame propagation. Properties such as pressure (P_0), density (ρ_0), and temperature (T_0) were set to represent the thermodynamic state inside the combustion chamber at the end of the compression stroke. The temperature definition enables obtaining values for viscosity and diffusivity. The mean molecular weight is influenced by the gaseous composition inside the domain, which is set to match atmospheric air.

Injection of 100% Hydrogen is performed by means of source terms S_ϕ for mass, momentum, and energy. This approach mitigates the moderately to highly characteristic underexpanded structure of the jet, enabling a focus on the pre-existing sub-sonic velocity profile. Thus, attention is directed towards the processes of mixing and hydrogen reaction within the combustion chamber rather than on expansion waves resulting from injection. In order to keep the inherently symmetric field configuration of the TGV, injection is configured by means of two opposing jets originating at the center of the cubic computational domain. The time evolution of the source terms is based on a ramp-up for the initial injection and a ramp-down to finalize it, representing the acceleration and deceleration of the jet.

Injection occurs over a span of 5 times the convective time scale (τ) of the TGV, concluding at the peak vorticity values for the TGV. The mass flow is prescribed so the total air to fuel ratio matches an equivalence ratio of 1.

Combustion is modeled by the *finite rate chemistry* approach, using the 11 species, 19 reactions hydrogen combustion mechanism of O'Connaire [6]. An Euler-Euler scheme for the different gaseous species transport is implemented, as read in equation 2,

$$\frac{\partial \rho Y_i}{\partial t} + \nabla.(\rho \vec{v} Y_i) = -\nabla.\vec{J_i} + w_i \tag{2}$$

where Y_i corresponds to the mass fraction, $\vec{J_i}$ is the diffusion flux, and w_i is the net rate production/consumption of species i. The diffusion term is computed based on a multicomponent model with a variable Lewis number. This is particularly relevant for hydrogen-based systems, as the high diffusivity of hydrogen cannot be accounted for with the unity Lewis number assumption.

Ignition is modeled as a sudden introduction of an energy source in the middle of the domain, equal to the prescribed minimum ignition energy and quenching distance to propagate the hydrogen flame under high pressure/high-temperature conditions. The simulation advances until combustion spreads over the whole domain, and the turbulence field completely decays up to the equilibrium state.

METHODS

All DNS simulations were performed using the in-house code *PsiPhi*, developed at Imperial College London and the University of Duisburg-Essen. The flow simulation is resolved with the finite volume method on an equidistant grid. A 7th Order Monotonicity Preserving Scheme (MP7) is applied for the convective terms of all transport equations. The solution is advanced in time by implementing an explicit low-storage third-order Runge-Kutta. Stability in time advancement is preserved by both implementing a CFL (< 0.1) and a diffusive stabilization (< 0.6) criteria. In order to parallelize computations, a domain decomposition approach is implemented using MPI (Message Passing Interface) communication.

To establish an independent mesh configuration for the smallest scales present both prior (Kolmogorov scale ~ 4 μm) and after combustion (flame thickness), the entire domain was discretized on different, highly resolved grids, including a 1024^3 resolution (~ 6 μm).

RESULTS

Figure 1 illustrates the time evolution of the double symmetrical injection in the TGV before ignition. The symmetrical structure is maintained at large scales, but small scales influence the perimeter of the hydrogen mass fraction field. Quantifying the wrinkling over the flame surface, particularly at the tip (1b) and the base of the jet, allows for an assessment of the impact of hydrogen's high diffusivity on the jet's morphology.

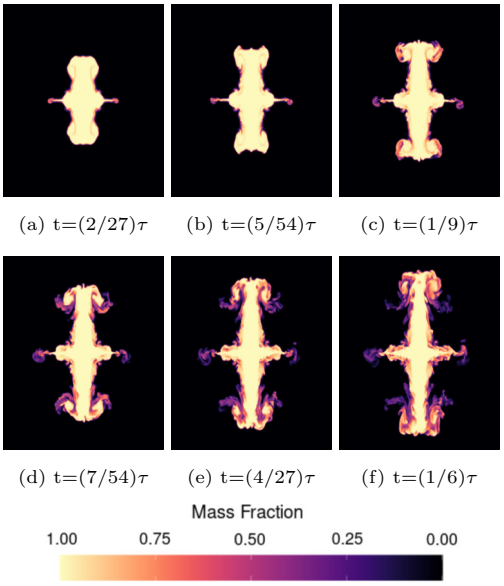

Figure 1: Hydrogen Mass Fraction Y_{H_2O} - Double Jet Development into TGV

Key flow properties, including turbulent kinetic energy, vorticity, and the Q-Criterion, are calculated during the simulation. Additionally, the quantification of heat release is monitored to identify reaction zones and track the development of flame propagation, ultimately leading to an estimation of flame speed. Following ignition, an analysis of flame propagation is conducted by examining the concentration of OH, heat release, and temperature. The ultimate goal is to quantify the duration of vorticity decay over time, coupled with a detailed examination of the composition of the turbulent energy spectrum in relation to the product species.

REFERENCES

[1]L. Engelmann, J. Laichter, P. Wollny, M. Klein, S. A. Kaiser, and A. M. Kempf, "Cyclic variations in the flame propagation in an spark-ignited engine: Multi cycle large eddy simulation supported by imaging diagnostics," Flow, Turbulence and Combustion, vol. 110, p. 91–104, Aug. 2022

[2]M. E. Brachet, "Direct simulation of three-dimensional turbulence in the taylor–green vortex," Fluid Dynamics Research, vol. 8, p. 1–8, Oct. 1991

[3]L. Engelmann, J. Hasslberger, S.-J. Baik, M. Klein, and A. Kempf, "Direct numerical simulation of an unsteady wall-bounded turbulent flow configuration for the assessment of large-eddy simulation models," Scientific Reports, vol. 13, July 2023.

[4]H. Zhou, J. You, S. Xiong, Y. Yang, D. Thévenin, and S. Chen, "Interactions between the premixed flame front and the threedimensional taylor–green vortex," Proceedings of the Combustion Institute, vol. 37, no. 2, p. 2461–2468, 2019.

[5]C. Z. X. Xu Yifan, "Direct numerical simulations of the taylor–green vortex interacting with a hydrogen diffusion flame: Reynolds number and non-unity-lewis number effects," Physics of Fluids, vol. 35, Apr. 2023.

[6]M. OĆonnaire, H. J. Curran, J. M. Simmie, W. J. Pitz, and C. K. Westbrook, "A comprehensive modeling study of hydrogen oxidation," International Journal of Chemical Kinetics, vol. 36, p. 603–622, Aug. 2004.

WORKSHOP
Direct and Large-Eddy Simulation 14
April 10-12 2024, Erlangen, Germany

MULTI-CYCLE DNS OF A LABORATORY SCALE ENGINE: IN-CYLINDER FLOW STRUCTURES AND TURBULENCE ANALYSIS

B.A. Danciu[1], **C.E. Frouzakis**[1], **G.K. Giannakopoulos**[1], **M. Bode**[2]
[1]CAPS Laboratory, Department of Mechanical and Process Engineering
ETH Zürich, 8092 Zürich, Switzerland
[2]Jülich Supercomputing Centre, Forschungszentrum Jülich GmbH
52425 Jülich, Germany
danciub@ethz.ch

INTRODUCTION

Understanding all the processes that take place in internal combustion engines (ICEs) is extremely challenging. The engine geometry can be complex and is important for the large flow scales. The flow field is usually highly turbulent, resulting in a very wide range of scales. The motion of the piston adds another layer of complexity.

ICEs have been studied experimentally for a long time. However, it is very difficult to sufficiently resolve all relevant phenomena. This problem is exacerbated in the study of combustion processes. Boundary layers are also challenging. To gain further insight into these complex processes, numerical simulations are used. These provide a very comprehensive view of all relevant areas, but are also challenging to compute. In particular, the large scale separation leads to simulations that require an extreme level of resolution. The latest generation of supercomputers makes it possible to perform direct numerical simulations (DNS). This is a huge step forward compared to classical reduced order approaches such as RANS and LES. It also has great potential to improve reduced order methods.

In this study, multi-cycle simulations of the compression and expansion strokes were carried out for the optical engine studied experimentally at TU Darmstadt [1]. Two operating conditions with 12 cycles each were computed on the supercomputer JUWELS Booster using the GPU-based CFD code nekRs and up to 3200 GPUs. These first-of-its-kind data provide a great insight into many engine-relevant processes. The focus of the analysis is on the in-cylinder flow structures and the development of turbulence.

NUMERICAL METHODS

This study is based on the high-order code nekRS [2]. It uses high-order spectral elements in which the solution, data, and test functions are represented as locally structured Nth-order tensor product polynomials on a set of E globally unstructured curvilinear hexahedral brick elements. This approach has two main advantages. First, for smooth functions such as solutions to the incompressible/low Mach Navier-Stokes equations, high-order polynomial expansions yield exponential convergence at the order of approximation, implying a significant reduction in the number of unknowns ($n \approx EN^3$) required to achieve engineering tolerances. Second, the locally structured forms allow for local lexicographic ordering with minimal indirect addressing and, crucially, the use of tensor product sum factorization to achieve low $\mathcal{O}(n)$ storage cost and $\mathcal{O}(nN)$ computational complexity. The time integration in nekRS is based on a semi-implicit splitting scheme using kth-order backward differences (BDFk) to approximate the time derivative, coupled with implicit treatment of the viscous and pressure terms and kth-order extrapolation (EXTk) for the remaining advection and forcing terms. This approach leads to independent elliptic subproblems consisting of a Poisson equation for the pressure, a coupled system of Helmholtz equations for the three velocity components, and an additional Helmholtz equation for the temperature.

CASE DESCRIPTION

An overview of the computed cases is given in Tab. 1. The non-reactive data have a size of 320 TB and required about 4.5 million core-hours computing time on nodes with four NVIDIA A100 GPUs each.

RESULTS AND CONCLUSIONS

In the following discussion, only the simulations for the 2500 rpm (OP E) case are used.

To quantitatively describe the flow dynamics in the cylinder, we calculate the tumble ratio, a global measure that characterizes the development of large-scale motion in the combustion chamber. The tumble ratio is defined as,

$$TR_i = \frac{\omega_i}{\omega_{cs}} \tag{1}$$

where ω_i represents the angular velocity of the solid-body flow rotating around the center of mass in the i-direction, and ω_{cs} denotes the angular velocity of the engine crankshaft. The angular velocity ω_i is determined by

$$\omega_i = \frac{L_i}{I_i} \tag{2}$$

Engine speed	Intake pressure	OP
1500 rpm	0.95 bar	C
2500 rpm	0.95 bar	E

Table 1: Engine operating conditions.

where L_i and I_i represent the angular momentum and the moment of inertia in relation to the center of mass in the i-direction.

The tumble ratio TR_y with respect to the y-axis is presented in Figure 1 for all simulated cycles. Tumble generation reaches its peak at maximum piston speed, which coincides with the largest mass flow rate, around 645 crank angle degree (CAD), after which it decreases steadily. The tumble ratios TR_x and TR_z with respect to the x-axis and z-axis are are close to zero, which is expected since the TU Darmstadt engine has an inlet duct designed to promote the formation of a clockwise tumble flow, which is the dominant large scale structure in this engine.

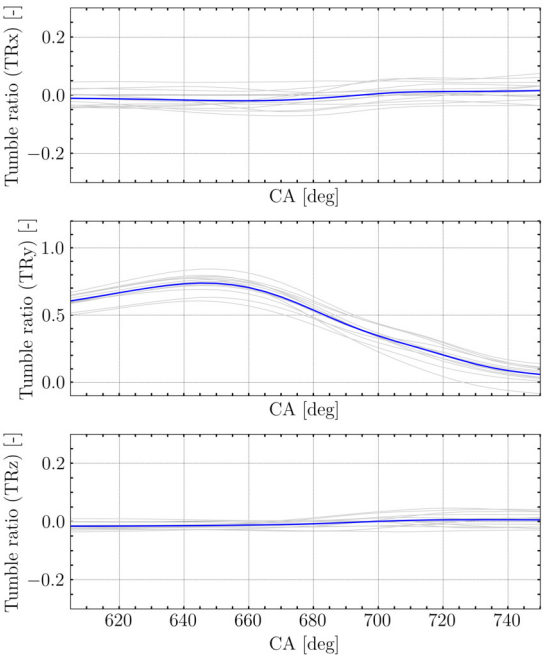

Figure 1: Tumble ratios around the center of mass with respect to the x-axis (top) y-axis (middle) and z-axis (bottom) for the compression and early expansion strokes (thin lines: individual cycles, thick blue line: mean values).

Understanding and controlling the tumble breakdown in internal combustion engines is crucial for optimizing combustion efficiency and emissions. In an attempt to quantify the tumble breakdown we analyze the evolution of the mean and turbulent kinetic energy, which are defined as,

$$MKE = \frac{1}{2}(\bar{u}^2 + \bar{v}^2 + \bar{w}^2), \tag{3}$$

$$TKE = \frac{1}{2}(u_{rms}^2 + v_{rms}^2 + w_{rms}^2) \tag{4}$$

Figure 2 shows the ratio between the total turbulent energy and the mean kinetic energy, which peaks around top dead center (TDC). This corresponds to the moment of tumble breakdown resulting in a transfer of kinetic energy from the large-scale tumbling motion to the small-scale turbulence, which promotes the mixing of air and fuel and facilitates the combustion process. After TDC the ratio decreases rapidly as the turbulence dissipates under the influence of viscous forces.

The distribution of local anisotropic Reynolds stress invariants is studied using the well-established anisotropic invariant

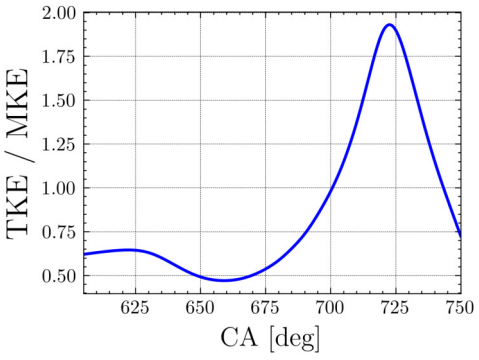

Figure 2: Ratio between the total turbulent and mean kinetic energy inside the cylinder throughout the compression and early expansion strokes.

map, commonly referred to as Lumley traingles. The second (I_2) and third (I_3) invariants obtained from the centre tumble plane are shown in Figure 3. During the early compression phase (630 CAD), the invariants show a significantly lower scatter compared to the TDC (720 CAD) and the flow has a higher tendancy towards 3D isotropy. Furthermore, during the tumble breakdown near the TDC, a significant number of data points can be seen in the region of axisymmetric expansion. For a reliable turbulence model, the anisotropy should be modeled correctly, as this can have a major impact on the correct prediction of the flow at different CAD and on the prediction of the tumble breakdown.

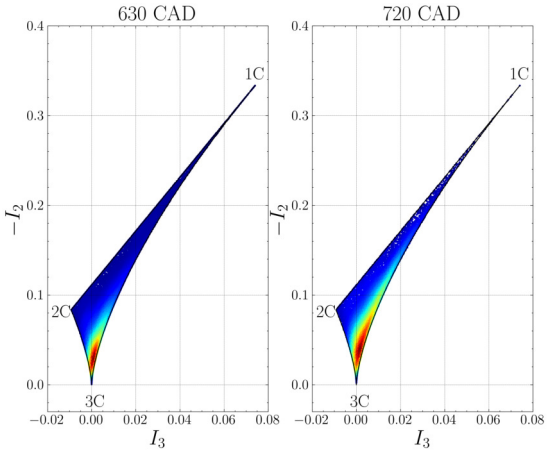

Figure 3: Lumley triangle visualized as scatter plot data at 630 CAD (left) and 720 CAD (right).

As a future step, reactive simulations will be performed in this engine to understand the complex interplay of turbulence and chemistry under real conditions.

REFERENCES

[1]E. Baum, B. Peterson, B. Böhm, and A. Dreizler: On The Validation of LES Applied to Internal Combustion Engine Flows: Part 1: Comprehensive Experimental Database, *Flow, Turbulence and Combustion*, vol. 92, 01 2014.

[2]P. Fischer, S. Kerkemeier, M. Min, Y.-H. Lan, M. Phillips, T. Rathnayake, E. Merzari, A. Tomboulides, A. Karakus, N. Chalmers, and T. Warburton : NekRS, a GPU-Accelerated Spectral Element Navier-Stokes Solver, *Parallel Computing*, vol. 114, p. 102982, 2022.

SESSION: Turbulent flows

Wednesday, April 10, 2024

16:20- 17:35

WORKSHOP
Direct and Large-Eddy Simulation 14
April 10-12 2024, Erlangen, Germany

INTEGRAL LENGTH AND TIME SCALES OF HIGHER ORDER MOMENTS

M. Klein[1]
[1]Department of Aerospace Engineering
University of the Bundeswehr Munich
markus.klein@unibw.de

INTRODUCTION

Integral length and time scales of velocity or scalar quantities play an important role for the modelling and analysis of turbulent flows. Integral scales are also important for quantifying statistical uncertainty, because, traditionally it is assumed that the decorrelation distance can be taken as twice the integral scale [1]. The confidence interval for a statistical quantity is typically proportional to the inverse of the square root of the number of independent samples N and the latter quantity is determined by dividing the measurement time or domain length (assuming statistical homogeneity in space or time) by the decorrelation distance. While every quantity has its own decorrelation distance, little seems to be known about integral scales of higher order moments. Such information might be particularly useful for DNS or LES simulations where the number of independent samples is often much more limited compared to experiments.

The probability distribution of the velocity field can often be reasonably approximated [2] by a Gaussian probability density function (PDF) e.g. for free shear flows or homogeneous turbulence. Under this assumption it is possible to express the covariance of higher order moments using the covariance of the variable themself. Hence, given a two point autocorrelation function, length scales of higher order moments can be calculated. As an example, the autocorrelation often has the shape of a decaying exponential [3] and in that case the integral scale of the variance of a signal has half the value of the integral scale of the signal itself. The theory outlined before has been applied recently [4] to analyse the autocorrelation and integral scales up to 4^{th} order moments in the case of synthetic turbulence and for the variance (i.e. 2^{nd} moment) using DNS data [5] of a plane turbulent jet.

The present work aims to first generalize this analysis using a DNS database of homogeneous isotropic turbulence (HIT) [6]. Subsequently the theory will be extended numerically for non-Gaussian distributions using appropriately generated synthetic turbulence [7]

ANALYSIS OF INTEGRAL SCALES OF HIGHER ORDER

If X, Y are two random variables and E denotes the expectation from time or space averaging, the covariance is given as $Cov(X,Y) = E(XY) - E(X)E(Y)$, while the variance is $Var(X) = E(X^2) - E(X)^2$. If we consider the velocity component u we can put $X = u(\mathbf{x})$ and $Y = u(\mathbf{x}+\mathbf{r})$ to obtain the two-point autocorrelation function $Corr(X,Y) = Cov(X,Y)/\sqrt{Var(X)Var(Y)}$. The integral scale $L_{u,u}(\mathbf{x},\mathbf{r})$ is usually defined as the integral of the normalised two point autocorrelation function with respect to $\mathbf{r}$. This can be generalised in a straightforward manner to integral scales L_{u^n,u^n} for the n^{th} moment by writing

$$R_{u^n,u^n}(\mathbf{r}) = Corr(X^n, Y^n) = \frac{Cov(X^n, Y^n)}{\sqrt{Var(X^n)Var(Y^n)}} \quad (1)$$

Now, considering two identically distributed random variable with Gaussian velocity PDF and $Cov(X,Y) = c$, it is possible to write Y as a linear combination of two independent Gaussian variables X, Z and as a result the covariance of higher order moments becomes a polynomial in c [4], e.g.

$$\begin{aligned} Cov(X^2,Y^2) &= 2Cov(X,Y)^2 \\ Cov(X^3,Y^3) &= 6Cov(X,Y)^3 + 9\sigma^4 Cov(X,Y) \\ Cov(X^4,Y^4) &= 24Cov(X,Y)^4 + 72\sigma^4 Cov(X,Y)^2 \end{aligned} \quad (2)$$

Figure 1 shows the autocorrelation functions for second and fourth order moments from a HIT database [6] in comparison with the theory outlined above. Despite the fact that the assumptions of the theory are not perfectly met and that the number of samples is finite, the agreement is quite satisfactory.

Close to walls or especially for bounded scalars the PDF cannot be expected to be Gaussian. Hence, in order to gain a better understanding of the behaviour of non-Gaussian statistics w.r.t. to their autocorrelations of higher order, a numerical analysis will be performed with special focus on bounded scalars. Let us start with the bimodal PDF $\alpha\delta(c) + \beta\delta(1-c)$, which is often used to express the PDF of mean reaction progress c in turbulent premixed flames. In other words the random variable c can only take the values 0 or 1 and as a result of this the same will holds true for c^2, more precisely we will have $c = c^2$. In this special case we find that the two-point autocorrelation function will be identically the same, independent of the moment order, and the same holds true for the integral scales. Apart from this trivial example it is difficult to obtain analytical results, because the above mentioned trick of expressing Y as a linear combination of two independent random variables works only because the sum of two Gaussians is again a Gaussian. Hence, it is difficult to generalize the same concept to other PDFs.

Alternatively, synthetic turbulence which follows not only a given autocorrelation function (e.g. [7, 8]) but in addition obeys a prescribed PDF distribution, can be used to get a first understanding. This can be achieved by combining a synthetic turbulence generator with the concept of inverse

transformation sampling [9]. We consider the two parameter Beta distribution P_β which is often used to parametrise the behaviour of bounded scalars:

$$P_\beta(c,\alpha,\beta) = \frac{\Gamma(\alpha+\beta)}{\Gamma(\alpha)\Gamma(\beta)} c^{\alpha-1}(1-c)^{\beta-1} \tag{3}$$

Figure 2 exemplarily, shows the synthetic signal, its PDF and autocorrelations functions. For the case shown here with parameters $\alpha = 20, \beta = 2$ the autocorrelation of the signal squared is nearly identical to the autocorrelation of the original signal. However, this is not in general the case for other choices of α, β. The full paper will explore a wide range of parameters α, β and will provide the details for the generation of the synthetic data.

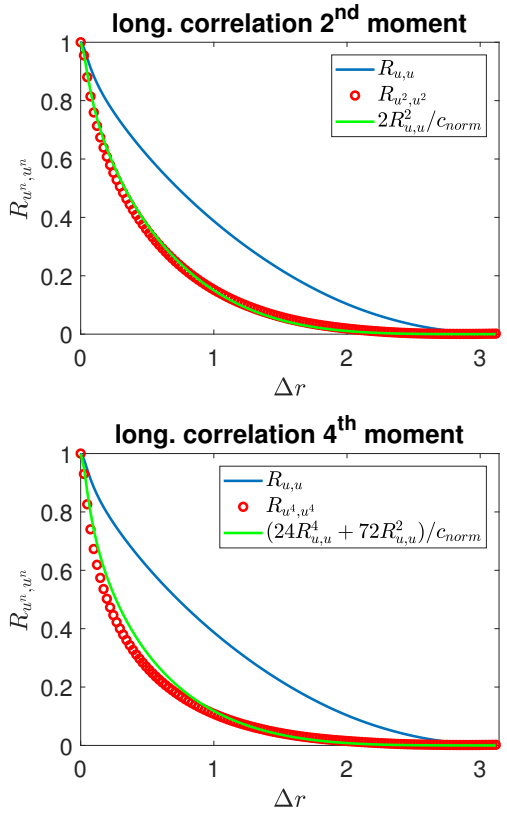

Figure 1: Autocorrelation functions $R_{u,u}$ and R_{u^n,u^n} $n = 2, 4$ obtained from the Madrid HIT database [6] and compared to the theoretical prediction in Eq. 2

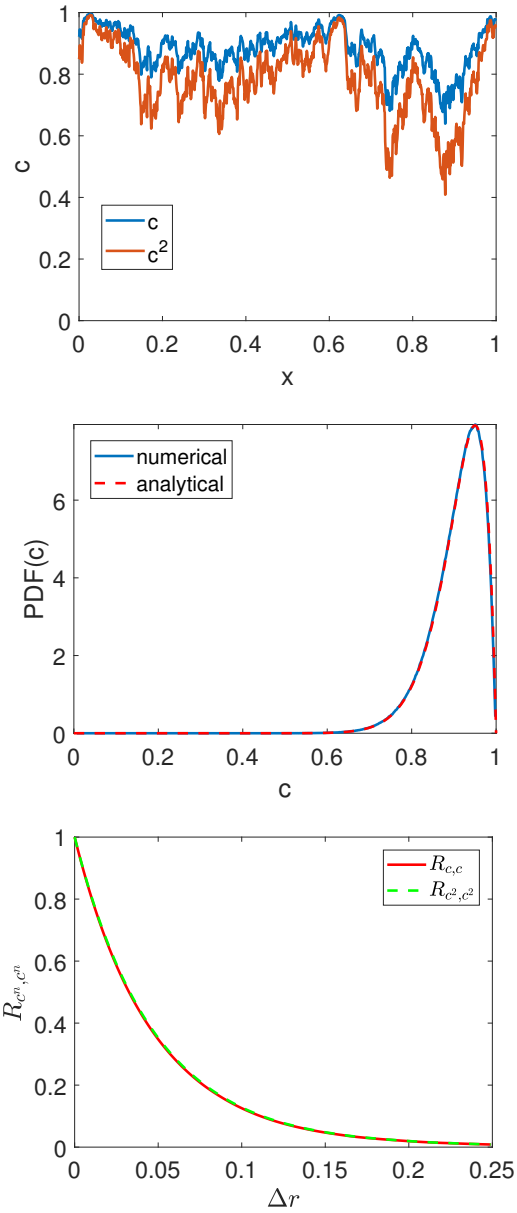

Figure 2: (Top) Excerpt of a synthetic turbulent signal c together with its squared value c^2, (Middle) Numerically obtained PDF of the signal and prescribed Beta PDF with the parameters $\alpha = 20, \beta = 2$, (Bottom) Autocorrelation function of c and c^2.

REFERENCES

[1]Benedict, L.H. and Gould, R.D.: Towards better uncertainty estimates for turbulence statistics, *Experiments in Fluids*, **22**, 129–136 (1996).

[2]She, Z.-S., Jackson, E. and Orszag, S.A.: Scale-dependent intermittency and coherence in turbulence, *Journal of Scientific Computing*, **3**, 407–434 (1988).

[3]Birch, A.D., Brown, D.R., Dodson, M.G. and Thomas, J.R.: The turbulent concentration field of a methane jet, *Journal of Fluid Mechanics*, **88**, 431–449 (1978).

[4]Klein, M.: Integral Turbulent Length and Time Scales of Higher Order Moments, *Flow Turbulence and Combustion*, (2022).

[5]Klein, M., Sadiki, A.and Janicka, J.: Investigation of the influence of the Reynolds number on a plane jet using direct numerical simulation, *International Journal of Heat Fluid Flow*, **24**, 785–794 (2003).

[6]Cardesa, J.I., Vela-Martín, A. and Jiménez, J.: The turbulent cascade in five dimensions, *Science*, **357**, 782–784 (2017).

[7]Klein, M., Sadiki, A. and Janicka, J.: A digital filter based generation of inflow data for spatially developing direct numerical or large eddy simulations, *Journal of Computational Physics*, **186**, 652–665 (2003).

[8]Trenberth, K.E.: Some effects of finite sample size and persistence on meteorological statistics. Part I: autocorrelations., *Monthly Weather Review*, **112** 2359–2368 (1984).

[9]Gentle, J.E.: Random Number Generation and Monte Carlo Methods, *Springer*, (2003).

WORKSHOP
Direct and Large-Eddy Simulation 14
April 10-12 2024, Erlangen, Germany

BREAKING THE REYNOLDS ANALOGY: DECOUPLING TURBULENT HEAT AND MOMENTUM TRANSPORT VIA SPANWISE WALL OSCILLATION IN WALL-BOUNDED FLOW

Lou Guérin [1], Cédric Flageul[1], Laurent Cordier [1], Stéphane Grieu [2], Lionel Agostini [1]
[1]Pprime institute, Curiosity Group, CNRS, Université de Poitiers, ISAE-ENSMA, Poitiers, France
[2]PROMES, University of Perpignan, Perpignan, France
lou.guerin@univ-poitiers.fr

KEYWORDS

Direct numerical simulation, turbulent channel flow, heat transfer, drag, spanwise wall oscillation

INTRODUCTION AND VALIDATION

This work investigates spanwise wall oscillation (SWO) [1, 2, 3, 4] as a method to preferentially enhance heat transfer over drag in turbulent channel flow. In the current formulation, the flow is considered incompressible and the temperature is set to a passive scalar with mixed boundary conditions [5]. This configuration is selected to induce a strong correlation between temperature and streamwise velocity, thereby increasing the challenge of achieving dissimilarity in drag and heat transfer enhancement.

Direct numerical simulations at $Re_\tau = 180$ and $Pr = 1$ are performed using spanwise wall oscillation of parameters T and W. This is achieved by specifying the time-dependent boundary condition for the spanwise velocity at the wall position (see Figure 1).

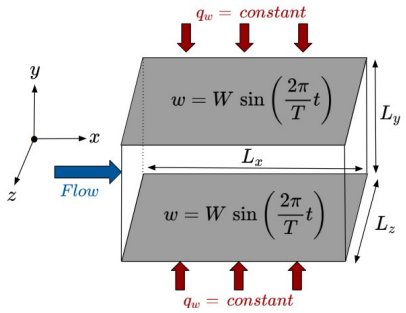

Figure 1: Schematic of the flow configuration.

Validation is performed using oscillation parameters $T^+ = 125$ and $W^+ = 18$ on a statistically steady flow at $Re_\tau = 180$. In Figure 2, the temporal evolution of the drag reduction is shown with the same actuation parameters, albeit at a marginally higher Reynolds number ($Re_\tau = 200$) than in the present work and is represented by the black line (data from [6]). The blue line depicts the analogous temporal drag variation acquired in the present study (see Equation 1), here represented by the friction coefficient C_f. The *nom* and *ac* subscript indicate quantities taken from the unactuated and actuated flow respectively, and the notation $^+_{nom}$ indicates normalisation with wall-units from the unactuated flow. The obtained trend closely resembles the referential data [6], with the drag reduction reaching $\sim 40\%$, validating the implemented wall actuation methodology.

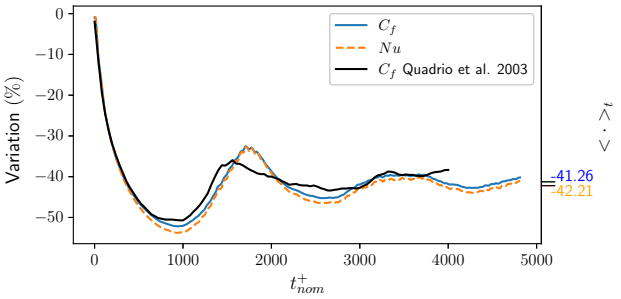

Figure 2: Temporal evolution of drag and heat transfer reduction at $Pr = 1$, subjected to spanwise oscillatory wall actuation, utilizing control parameters of $T^+_{nom} = 125$ and $W^+_{nom} = 18$. The black curve denotes data from [6] for reference.

In Figure 2, the temporal evolution of the Nusselt number is also shown, displaying strong agreement with the drag variation, and underscoring that SWO can also substantially reduce heat transfer.

$$\text{Variation} = \left(\frac{C_{f,ac}}{\langle C_{f,nom}\rangle_t} - 1\right) \times 100 \qquad (1)$$

ENHANCING HEAT TRANSFER

Direct numerical simulations at $Re_\tau = 180$ and $Pr = 1$ have shown a set of wall-oscillation parameters reducing drag and heat transfer similarly, maintaining coupled transport.

The temporal evolution of the spatially-averaged drag and heat transfer when applying spanwise wall oscillation with control parameters $T^+_{nom} = 500$ and $W^+_{nom} = 30$ is conveyed by Figure 3. Both heat transfer and skin friction exhibit substantial reduction over the first half oscillation cycle, decreasing by up to 25%. Thereafter, the heat transfer and friction exhibit periodic oscillation at the actuation frequency

of $T^+_{nom} = 500$. The friction drag varies between 5% below and 30% above the baseline, averaging 7.72% enhancement, as could be expected from the results of [7]. In contrast, the heat-transfer minima are marginally higher while the maxima surge to approximately 45% above baseline. This disproportionate heat-transport amplification yields 15% averaged thermal intensification, doubling the friction increase.

Overall, the results underscore the efficacy of spanwise wall oscillation in elevating turbulent heat convection. This Reynolds analogy breaking enables preferential elevation of heat transport over momentum.

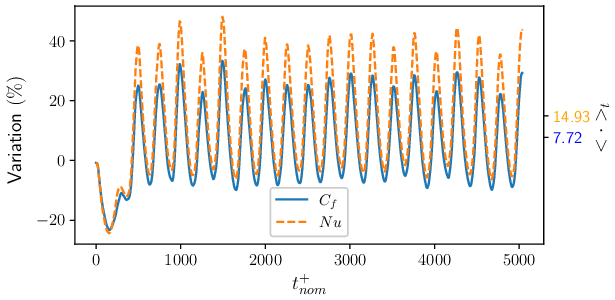

Figure 3: Temporal variation of friction coefficient C_f and Nusselt number Nu augmentation at $Pr = 1$, subjected to spanwise oscillatory wall actuation, utilizing control parameters of $T^+_{nom} = 500$ and $W^+_{nom} = 30$.

FIK IDENTITY

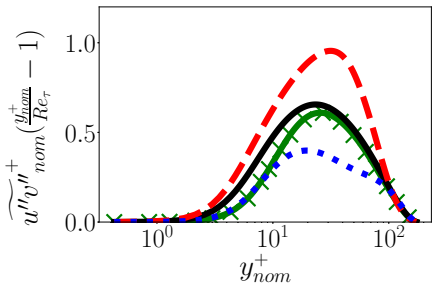

(a)

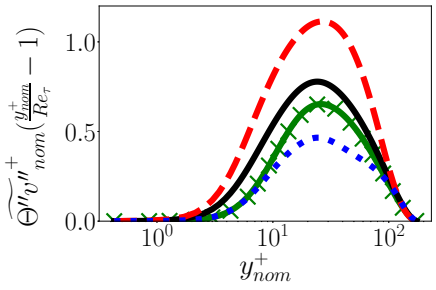

(b)

Figure 4: Wall normal distributions of (a): $\widetilde{u''v''}^+_{nom}(\frac{y^+_{nom}}{Re_\tau} - 1)$, (b): $\widetilde{\Theta''v''}^+_{nom}(\frac{y^+_{nom}}{Re_\tau} - 1)$. actuated stress on $C_{f,\min}$ phases, : on $C_{f,\max}$ phases, : actuated time wise stress, unactuated stress.

The FIK identity analysis [8, 9] allows a decomposition of the friction coefficient and Nusselt number into seperate components. This enables to directly link the turbulent shear stress to the friction coefficient and the turbulent heat flux to the Nusselt number. Moreover, this decomposition states the contribution of each source term towards both quantities. Details regarding these components and their quantification in the current study will be provided in the final article.

The FIK identity analysis hereby reveals a negligible impact of forcing terms on dissimilarity between heat transfer and drag actuation induced variations, as will be demonstrated in the final version of this article. Instead, differences arise from the solenoidal velocity and linearity of the temperature equation. Both the weighted turbulent shear stress and heat flux derived from the FIK identity turbulent components are amplified near the wall under oscillation (see Figure 4). However, the heat flux intensifies more substantially, especially at its peak. This preferential enhancement of the near-wall heat flux, exceeding the shear stress amplification, facilitates greater thermal transport augmentation relative to the friction increase.

Results therefore demonstrate spanwise oscillation can preferentially intensify heat transfer beyond drag, providing a promising technique for improving heat exchanger. Further work should optimize parameters and elucidate the underlying physics of this dissimilar heat transfer control.

REFERENCES

[1]K.S. Choi: Near-Wall Structure of Turbulent Boundary Layer with Spanwise-Wall Oscillation, *Physics of Fluids*, **12**(10), 2475–2482 (2000).

[2]P. Ricco, M. Skote and M.A. Leschziner: A review of turbulent skin-friction drag reduction by near-wall transverse forcing, *Progress in Aerospace Sciences*, **123**, 100713 (2021). doi: 10.1016/j.paerosci.2021.100713

[3]M. Quadrio: Drag Reduction in Turbulent Boundary Layers by In-Plane Wall Motion, *Philosophical Transactions of the Royal Society A: Mathematical, Physical and Engineering Sciences*, **369**(1940), 1428-1442, (2011).

[4]L. Agostini, E. Touber and M. Leschziner: The turbulence vorticity as a window to the physics of friction-drag reduction by oscillatory wall motion, *International Journal of Heat and Fluid Flow*, **51**, (2014). doi: 10.1016/j.ijheatfluidflow.2014.08.002

[5]G. F. Narváez Campo: Fluid-solid Thermal Coupling in Pipe and Channel Turbulent Flows Via a Dual Immersed Boundary Method, Ph.D. thesis, Universidade Federal do Rio Grande do Sul, (2019).

[6]M. Quadrio and P. Ricco: Initial response of a turbulent channel flow to spanwise oscillation of the walls, *Journal of Turbulence*, **4**, 1-23, (2003).

[7]W. Jung, N. Mangiavacchi and R. Akhavan: Suppression of turbulence in wall-bounded flows by high-frequency spanwise oscillations, *Physics of Fluids A Fluid Dynamics*, **4**, (1992). doi: 10.1063/1.858381

[8]T. Gomez, V. Flutet and P. Sagaut: Contribution of Reynolds stress distribution to the skin friction in compressible turbulent channel flows, *Phys. Rev. E*, **79**(3), 035301 (2009). doi: 10.1103/PhysRevE.79.035301

[9]Y. Hasegawa and N. Kasagi: Dissimilar control of momentum and heat transfer in a fully developed turbulent channel flow, *Journal of Fluid Mechanics*, **683**, 57–93 (2011). doi: 10.1017/jfm.2011.248

WORKSHOP
Direct and Large-Eddy Simulation 14
April 10-12 2024, Erlangen, Germany

SPECTRAL ANALYSIS OF THE REYNOLDS SHEAR STRESS TRANSPORT IN TURBULENT CHANNEL FLOWS

Myoungkyu Lee[1] **and Robert D. Moser**[2]

[1]Department of Mechanical Engineering, The University of Houston, Texas, USA
leemk@uh.edu

[2]Oden Institute for Computational Engineering and Sciences, The University of Texas at Austin, Texas, USA
rmoser@oden.utexas.edu

The Reynolds shear stress (RSS) characterizes the influence of turbulence on momentum transport in turbulent shear flows. As such, a comprehensive understanding of the dynamics of RSS is essential for insights into the dynamics of turbulence. Additionally, RSS is critical to reduced-order models for turbulent flow simulations, such as Reynolds-averaged Navier-Stokes and subgrid-scale models for large-eddy simulation. Because of its significance, RSS has been the target of extensive research. However, our current understanding remains incomplete, primarily due to the challenges associated with simultaneously measuring multiple velocity components and the cost of first-principle-based simulations (DNS), particularly for flows at high Reynolds numbers (Re).

To address this problem, We conduct a spectral analysis of the terms in the transport equation for RSS, $-\langle u'v'\rangle$, in high Re turbulent channel flows. Here, u' and v' represent velocity fluctuations in the streamwise (x) and wall-normal (y) directions, respectively. Additionally, $\langle\cdot\rangle$ denotes averaging in the streamwise and spanwise (z) directions, as well as over time. Our analysis technique is based on the approach introduced in [1]. The spectral transport equation is given by:

$$\frac{\partial E_{uv}}{\partial t} = E^{P}_{uv} + E^{T^{\perp}}_{uv} + E^{T^{\parallel}}_{uv} + E^{\nu}_{uv} + E^{\Pi}_{uv} \tag{1}$$

where E_{uv} is the u-v co-spectrum and $\int_0^\infty E_{uv}\mathrm{d}\mathbf{k} = -\langle u'v'\rangle$. The terms on the right-hand side of (1) represent the spectral densities of production (E^{P}_{uv}), wall-normal turbulent transport ($E^{T^{\perp}}_{uv}$), inter-scale transfer ($E^{T^{\parallel}}_{uv}$), viscous effects (E^{ν}_{uv}), and pressure effects (E^{Π}_{uv}), respectively.

Traditionally, the production of $-\langle u'v'\rangle$ is defined as $\langle v'^2\rangle\partial_y U$, where U is the mean velocity, as it describes the interaction between mean velocity and turbulent fluctuation. However, the pressure fluctuations in any turbulent shear flow also include the interaction between mean velocity and turbulent fluctuation. This interaction is mathematically represented by the rapid pressure [2], which arises from the decomposition:

$$\Pi = \Pi_{\mathrm{R}} + \Pi_{\mathrm{S}} + \Pi_{\mathrm{Stokes}} \tag{2}$$

where Π is the total static pressure, Π_{R} is the rapid pressure, Π_{S} is the slow pressure, and Π_{Stokes} is the Stokes pressure. Since the contribution of Π_{R} to the evolution of $-\langle u'v'\rangle$ is zero without a mean velocity gradient, we define the production of $-\langle u'v'\rangle$ as:

$$P_{uv} = \langle v'^2\rangle\partial_y U + \langle v'\partial_x\Pi'_{\mathrm{R}}\rangle + \langle u'\partial_y\Pi'_{\mathrm{R}}\rangle \tag{3}$$

The pressure term E^{Π}_{uv} thus includes only the effects of the slow and Stokes pressures (Π_{S} and Π_{Stokes}).

The preliminary findings from a spectral analysis, using data from the direct numerical simulation of turbulent channel flow at $Re_\tau \approx 5200$ [3], are illustrated in figures 1 to 6. For brevity, only the one-dimensional spectral density in z is presented here.

The spectrum E_{uv} exhibits two distinct peaks (Figure 1): one at $\lambda_z^+ = 100$, $y^+ = 25$ (inner peak), and another at $\lambda^+ = 5000$, $y^+ = 1000$ (outer peak). However, E^{P}_{uv} (Figure 2) has a solitary peak at $\lambda_z^+ = 100$, $y^+ = 25$, suggesting that a portion of the outer peak in E_{uv} is transported from elsewhere. Turning to $E^{T_\perp}_{uv}$ (Figure 3), the results indicate that turbulent wall-normal transport of Reynolds shear stress (RSS) occurs in both directions: toward the wall and the channel center. At $\lambda_z^+ = 100$, the direction changes at $y^+ = 25$, and the value of y^+ at which the direction of turbulent wall-normal transport changes increases linearly with λ_z^+. Additionally, some portion of the large-scale structure of RSS is directly transported to the near-wall region. Surprisingly, $E^{T_\parallel}_{uv}$ (Figure 4) suggests that inter-scale transfer occurs mostly from small-scale to large-scale, which is opposite to the direction of Richardson-Kolmogorov cascade. In summary, turbulence transports the RSS produced at the inner peak to the outer peak. As expected, the role of E^{ν}_{uv} (Figure 5) is mainly the destruction of RSS at relatively small scales. But, the pressure term E^{Π}_{uv} (Figure 6) dominates the destruction of RSS and is the primary mechanism removing large-scale RSS in the near-wall region (e.g. around $\lambda_z^+ = 1000$ and $y^+ = 10$).

While these initial findings provide valuable insights into the scale-by-scale budget of $\langle u'v'\rangle$ transport, they lack spectral information in the streamwise direction. In the forthcoming presentation, we will analyse the transport of $\langle u'v'\rangle$ using two-dimensional spectral densities, using the polar-log representation introduced in [1].

REFERENCES

[1]Lee, M and Moser, R.D. : Spectral analysis of the budget equation in turbulent channel flows at high Reynolds number, *J. Fluid. Mech.*, **860**, 886–938 (2019).

[2]Kim, J. : On the structure of pressure fluctuations in simulated turbulent channel flow, *J. Fluid. Mech.*, **205**, 421–451 (1988).

[3]Lee, M and Moser, R.D. : Direct numerical simulation of turbulent channel flow up to $Re_\tau \approx 5200$, *J. Fluid. Mech.*, **774**, 395–415 (2015).

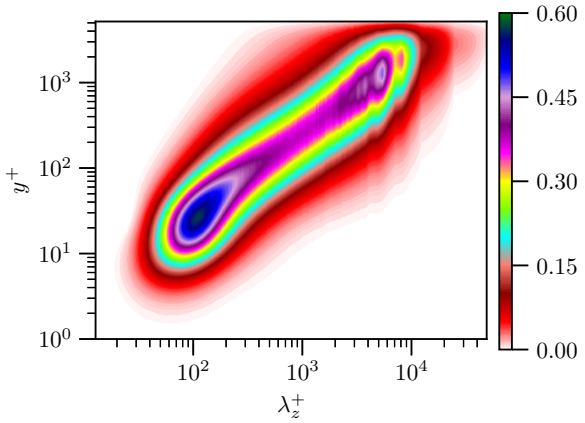

Figure 1: k_z-premultiplied spectral density of $\langle u'v' \rangle$, $k_z E_{uv}$

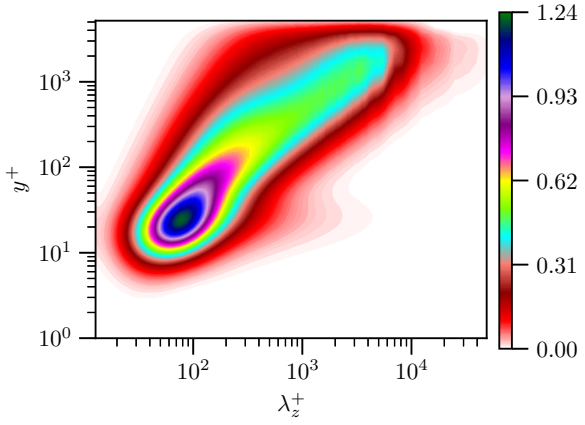

Figure 2: y- and k_z-premultiplied spectral density of $\langle u'v' \rangle$ production, $yk_z E_{uv}^P$

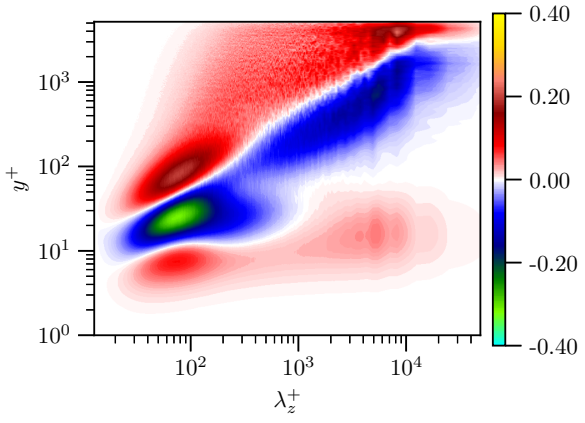

Figure 3: y- and k_z-premultiplied spectral density of wall-normal transport of $\langle u'v' \rangle$ by turbulence, $yk_z E_{uv}^{T^\perp}$

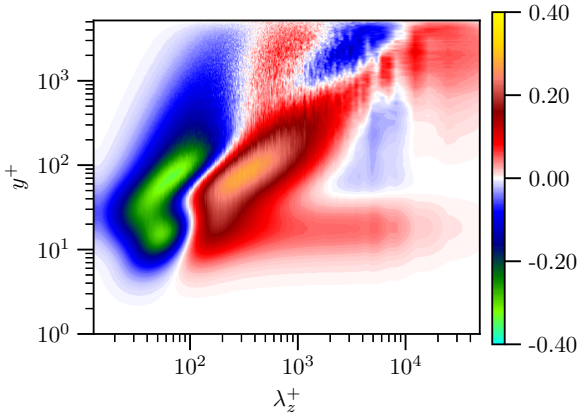

Figure 4: y- and k_z-premultiplied spectral density of inter-scale transfer of $\langle u'v' \rangle$, $yk_z E_{uv}^{T^\parallel}$

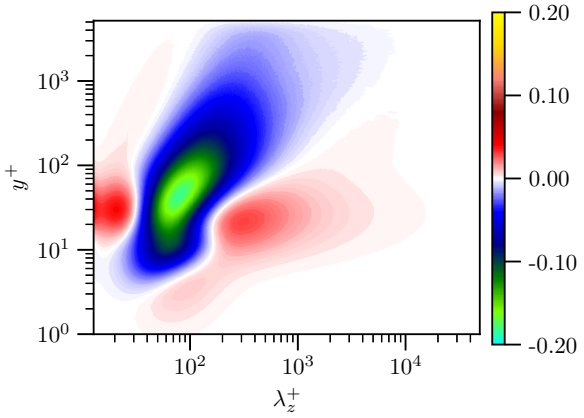

Figure 5: y- and k_z-premultiplied spectral density of transport of $\langle u'v' \rangle$ by molecular viscosity, $yk_z E_{uv}^\nu$

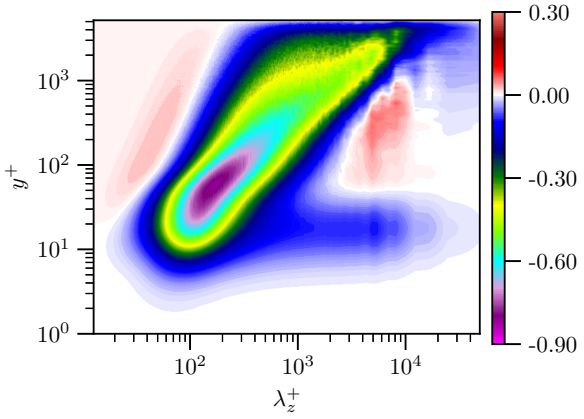

Figure 6: y- and k_z-premultiplied spectral density of transport of $\langle u'v' \rangle$ by pressure, $yk_z E_{uv}^\Pi$

WORKSHOP
Direct and Large-Eddy Simulation 14
April 10-12 2024, Erlangen, Germany

COMPONENTALITY OF THE REYNOLDS STRESS TENSOR SPECTRUM IN ANISOTROPIC TURBULENCE

Arthur Couteau[1,2], **Patrick Jenny**[1]
[1]Institute of Fluid Dynamics, ETH Zürich, 8092 Zürich, Switzerland
[2]Automotive Powertrain Technologies Laboratory, Swiss Federal Laboratories for Materials Science and Technology (Empa), CH-8600, Dübendorf, Switzerland
acouteau@ethz.ch

INTRODUCTION

Anisotropic turbulence remains a theoretical challenge, as the numbers of degrees of freedom in the system increase significantly. A recurring question, highly relevant for turbulence modeling approaches like LES, is the influence of anisotropy on the energy exchanges across scales.

In particular, it was shown in [1] that anisotropy induced at small scales can have an effect on the large scales. Considering the well-established global forward nature of the energy cascade, we are left to wonder how the anisotropic information is transported against it.

We present a study of the componentality of the Reynolds stress tensor (RST) in spectral space, that is, the distribution of energy between the different directions, and thus the difference of magnitude in the diagonal components of the tensor. To that end, we use a so-called "isotropic decomposition", effectively splitting the RST into several contributions, in particular into an isotropic 3D and an isotropic 2D states using DNS. As it is well known that in 2D turbulence the dynamics change and the energy cascade is reversed [2], we aim to link the emergence of isotropic 2D componental states in spectral space due to anisotropy to the inverse transport of anisotropic information.

NAVIER-STOKES EQUATIONS IN SPECTRAL SPACE

Since almost a century, the phenomenology of turbulent flows is built on the interactions of eddies of different sizes. It is then natural to look at the system in spectral space. The velocity field is expressed by a Fourier series as

$$\boldsymbol{u}(\boldsymbol{x},t) = \sum_{\boldsymbol{\kappa}} \hat{\boldsymbol{u}}(\boldsymbol{\kappa},t) e^{i\boldsymbol{\kappa}\cdot\boldsymbol{x}}. \tag{1}$$

The continuity and Navier-Stokes equations for the velocity modes $\hat{\boldsymbol{u}}(\boldsymbol{\kappa})$ read

$$i(\boldsymbol{\kappa}\cdot\hat{\boldsymbol{u}}) = 0, \tag{2}$$

$$\frac{\mathrm{d}}{\mathrm{d}t}\hat{u}_j(\boldsymbol{\kappa}) = -i\kappa_l \boldsymbol{P}_{jk} \sum_{\boldsymbol{\kappa}'} \hat{u}_k(\boldsymbol{\kappa}')\hat{u}_l(\boldsymbol{\kappa}-\boldsymbol{\kappa}') - \nu\kappa^2\hat{u}_j(\boldsymbol{\kappa}), \tag{3}$$

where $\boldsymbol{P}_{jk} = (\delta_{jk} - \frac{\kappa_j\kappa_k}{\kappa^2})$ is the "projection" tensor, ensuring that the velocity field remains divergence-free, Eq. (2).

Introducing the Reynolds averaging operator $\langle\cdot\rangle$, the energy and RST of mode $\boldsymbol{\kappa}$ are given by

$$\hat{E}(\boldsymbol{\kappa}) = \frac{1}{2}\langle\hat{u}_i(\boldsymbol{\kappa})\hat{u}_i^*(\boldsymbol{\kappa})\rangle, \tag{4}$$

$$\hat{R}_{ij}(\boldsymbol{\kappa}) = \langle\hat{u}_i(\boldsymbol{\kappa})\hat{u}_j^*(\boldsymbol{\kappa})\rangle. \tag{5}$$

The one-dimensional spectra of these quantities for wavenumber κ are computed by summing the contributions of all $\boldsymbol{\kappa}$ such that $\kappa - \kappa_0/2 \leq |\boldsymbol{\kappa}| < \kappa + \kappa_0/2$, with κ_0 the smallest wavenumber.

"ISOTROPIC DECOMPOSITION" OF THE REYNOLDS STRESS TENSOR

To study the componentality of the RST, we introduce the "isotropic decomposition" of the spectral quantity $\hat{R}_{ij}(\kappa)$. Since we simulate cases in which we have a base 3D isotropic flow and 2D anisotropy induced along the first two directions, we decompose $\hat{R}_{ij}(\kappa)$ as

$$\hat{R}_{ij}(\kappa) = \alpha(\kappa)\delta_{ij}^{3\mathrm{D}} + \beta(\kappa)\delta_{ij}^{2\mathrm{D}} + \hat{R}_{ij}^{\mathrm{res}}(\kappa), \tag{6}$$

where $\delta_{ij}^{3\mathrm{D}}$ is the identity 3x3 matrix, and $\delta_{ij,k}^{2\mathrm{D}}$ the identity matrix with δ_{33} set to zero. The residual 1D and non-zero off-diagonal components are gathered in the residual RST $\hat{R}_{ij}^{\mathrm{res}}$, which we observe to go to zero with sufficient time/ensemble averaging. This decomposition allows us to compute the amount of energy in associated 3D and 2D componental states, as

$$\hat{E}^{3\mathrm{D}}(\kappa) = \frac{3}{2}\alpha(\kappa), \tag{7}$$

$$\hat{E}^{2\mathrm{D}}(\kappa) = \beta(\kappa), \tag{8}$$

with the energy spectrum, Eq. (4), recovered as

$$\hat{E}(\kappa) = \hat{E}^{3\mathrm{D}}(\kappa) + \hat{E}^{2\mathrm{D}}(\kappa) \tag{9}$$

The time and spectral evolution of the 2D perturbations gives information on the transport of anisotropy across scales.

To illustrate the isotropic decomposition, we apply it to the case of Homogeneous Isotropic Turbulence (HIT), and obtain that small scales, unperturbed by the low-wavenumber forcing scheme [3], recover isotropy, as shown in Fig. 1. In terms of the isotropic decomposition, that means

$$\hat{E}^{3\mathrm{D}}(\kappa) \to \hat{E}(\kappa) \tag{10}$$

$$\hat{E}^{2\mathrm{D}}(\kappa) \to 0, \tag{11}$$

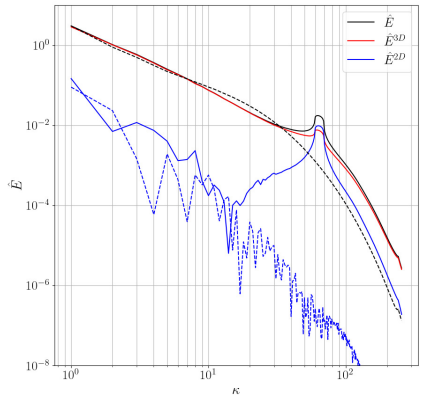

Figure 1: Energy spectra; dashed: HIT ($\hat{E}^{3D}$ is not shown since it coincides with the dashed black line $\hat{E}$); solid: HIT + 2D forcing. Note that the anisotropic influence of the low-wavenumber forcing scheme used to sustain turbulence decays as the wavenumber increases.

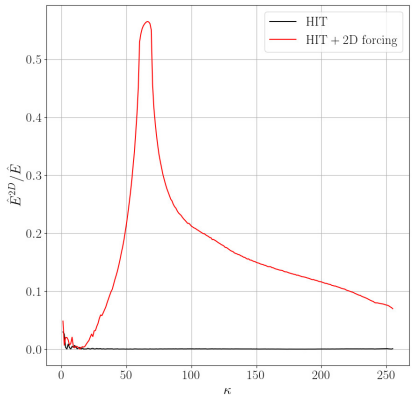

Figure 2: Ratio $\hat{E}^{2D}/\hat{E}$

ANISOTROPIC HOMOGENEOUS TURBULENCE

With the help of our decomposition, we aim to tackle the case of anisotropic turbulence, more precisely to study how anisotropic information is transported through scales. We introduce anisotropic perturbations in the HIT, in the form of forcing only 2 components in a given range of wavenumber, or by starting the simulation from 2D turbulence slices and letting the system relax towards 3D turbulence. We track information on the 3D and 2D spectra by applying the isotropic decomposition to Eq. (5).

The case of 2D forcing is setup as follows: first, an initial HIT flow is obtained using a low-wavenumber forcing. The 2D forcing is then introduced, acting on all modes in a chosen range of wavenumbers (e.g., $\kappa_1 \leq |\boldsymbol{\kappa}| < \kappa_2$), until the system reaches statistical equilibrium. It appears that the 2D perturbations have several effects on the energy spectrum and the componentality of the RST.

The introduction of 2D forcing gives rise to local inverse transfer of energy, essentially hindering the forward nature of the 3D cascade, however without changing the $-5/3$ scaling in the inertial range. This also leads to another equilibrium state, where the energy of the modes past the 2D forcing range is higher than in the HIT flow. As the energy dissipation is given by $2\nu\kappa^2\hat{E}(\kappa)$, the dissipation is higher and the system finds another statistical stationary state.

The study of the componentality of the RST spectrum in Fig. 1 also seems to indicate that the back-propagation of anisotropy is stopped at the inertial range, whereas 2D componental states past the 2D forcing range do not vanish, i.e., $\hat{E}^{2D}(\kappa)$ does not go to zero with $\kappa \to \kappa_{\max}$. While our setup only allows for a narrow inertial range ($N = 512$, $\mathrm{Re}_\lambda \approx 190$), which goes in the direction of non-vanishing anisotropy at small scales [4, 5]. This is better depicted in Fig. 2, where the ratio $\hat{E}^{2D}/\hat{E}$ decays with increasing wavenumber, but does not reach zero.

In the second case, the initial condition is built from repeated slices of developed 2D HIT and a small perturbation in the third direction. The system then relaxes towards 3D HIT. We focus here on the study of the effect of the pressure on the "return-to-(3D)-isotropy". It is well known that the pressure-rate-of-strain tensor Π_{ij} is responsible for the redistribution of energy among the RST diagonal components [6]. It is not feasible to directly compute the spectral contributions in a similar fashion to RST, Eq. (5), because it is a convolution in spectral space (though an expression for the pressure spectrum can be obtained using a quasi-normal approximation [7]). Nevertheless, the pressure acts in spectral space through the projection tensor. By projecting the convection term to the divergence-free plane, it changes its energy content and distribution between the different directions, thus affecting the componentality of the RST. We then aim to make use of the isotropic decomposition to assess the spectral effect of pressure during the return-to-isotropy.

CONCLUSION

We introduce an isotropic decomposition of the Reynolds stress tensor spectrum, aiming to study the interactions between 3D and 2D componental states present in anisotropic homogeneous turbulence. We show that introducing 2D perturbations in a range of wavenumbers changes the equilibrium of the system in the dissipation range. The perturbations do not back-propagate through the inertial range, but do not vanish at small scales past the perturbation range.

Furthermore, we aim to assess the effect of pressure in spectral space on the componentality of the Reynolds stress tensor. To that end, we aim to apply the isotropic decomposition to study a case of "return-to-isotropy" from initial 2D HIT.

REFERENCES

[1]Berning, H, : Effect of uniform anisotropic viscosity on turbulent flows, *Diss. ETH Zurich*, 2022

[2]Boffetta, G., Ecke, R.E. : Two-Dimensional Turbulence, *Annu. Rev. Fluid Mech.* 51, 427-451, 2012

[3]Eswaran V., Pope S.B. : An examination of forcing in direct numerical simulations of turbulence, *Comp. and Fluids* 16, 257-278, 1988

[4]Garg S., Warhaft Z. : On the small scale structure of simple shear flow, *Phys.of Fluids* 10:3, 1998

[5]Biferale L., Toschi F. : Anisotropic Homogeneous Turbulence: Hierarchy and Intermittency of Scaling Exponents in the Anisotropic Sectors, *Phys. Rev. Letters* 86:21, 2001

[6]Pope, S.B. : Turbulent Flows, *Camb. Univ. Press* 2000

[7]Lesieur M., Ossia S., Métais O. : Infrared pressure spectra in two- and three-dimensional isotropic incompressible turbulence, *Phys.of Fluids* 11:6, 1999

WORKSHOP
Direct and Large-Eddy Simulation 14
April 10-12 2024, Erlangen, Germany

ON SWIRL SWITCHING IN BENT PIPE FLOWS

V. Lupi[1], **D. Massaro**[1], **A. Peplinski**[1], **P. Schlatter**[1,2]
[1] FLOW/SimEx, Engineering Mechanics
KTH Royal Institute of Technology, Sweden
[2] Institute of Fluid Mechanics (LSTM)
Friedrich–Alexander–Universität (FAU) Erlangen–Nürnberg, Germany
lupi@mech.kth.se

INTRODUCTION

Curved pipes are ubiquitous in several biological systems and industrial applications. The two governing parameters for the flow in a curved pipe are the curvature δ, defined as the ratio between the radius of the cross-section of the pipe R_p and the radius of curvature of the bend R_c, and the bulk Reynolds number Re_b, based on the bulk velocity U_b, the diameter D and the kinematic viscosity ν.

Flows in curved pipes exhibit a secondary motion of Prandtl's first kind, present in both laminar and turbulent regimes, which increases the cross-plane mixing and heat transfer. Dean [1] derived an analytical solution for the fully developed laminar flow in toroidal pipes in the limit of low curvatures, showing that the secondary motion consists of two symmetric, counter-rotating vortices. Nevertheless, instantaneous asymmetry of the secondary flow has been observed by several authors in the turbulent regime [2, 3, 4]. This behaviour leads to a phenomenon referred to as *swirl switching*, defined by Brücker [2] as the quasi-periodic rotation of the plane of symmetry of the vortices around the geometric plane of symmetry of the bend. Swirl switching has detrimental effects on curved pipes since it brings about vibrations in the structure, leading, for example, to mechanical fatigue. Therefore, many efforts have been devoted by the scientific community to understand the origin of this phenomenon to mitigate it. Several causes have been suggested, including flow separation [3] and very large-scale structures arising in the upstream straight section [5]. However, since swirl switching also occurs in toroidal pipes [4], it has to be related to the effect of the curvature.

Despite many attempts, the origin of the swirl switching remains an unanswered question. In the current study, high-fidelity numerical simulations of the flow through spatially developing bent pipes are performed to understand the role of both the extent of the bend and the upstream turbulence on the phenomenon.

NUMERICAL FRAMEWORK

Direct numerical simulations (DNS) of the incompressible flow of a viscous, Newtonian fluid through both a 90°- and 180°-bend pipe are performed by numerically integrating the Navier–Stokes equations using the spectral element code `Nek5000` [6]. To finely resolve each region of the domain without prohibitively increasing the computational cost, an adaptive mesh refinement (AMR) technique based on the spectral error indicator (SEI) is employed in the simulations. For both bends, the curvature δ is equal to 1/3. This value is chosen since it is representative of sharper bends as well. Sketches of the two pipes considered in the study are shown in Figure 1, together with the adopted reference systems.

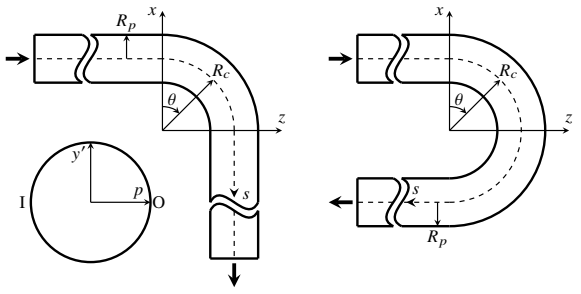

Figure 1: Sketch of the (*left*) 90°- and (*right*) 180°-bend pipe. The Cartesian reference system $\{x, y, z\}$ and the one used in the post-processing stage $\{s, p, y'\}$ are also displayed. The axis y' corresponds to the y-axis of the Cartesian coordinate system translated in the centre of the cross-section.

To understand the effect of the bending angle and upstream turbulence on the swirl switching, three distinct simulation setups are considered: 90°- (DNS-90T) and 180°-bend (DNS-180T) pipe flows with a turbulent inflow generated through the divergence-free synthetic eddy method (DFSyEM) proposed by Poletto [7], and the flow through a 180°-bend (DNS-180L) with a Hagen–Poiseuille (parabolic) velocity profile as inflow condition. No-slip and no-penetration conditions are imposed on the pipe walls, whereas a stress-free boundary condition is prescribed at the outlet of the domain.

RESULTS

The effect of both bending angle and inflow conditions on the swirl switching is studied by extracting spatially coherent structures. This is accomplished by applying proper orthogonal decomposition (POD) to the three-dimensional velocity fields obtained from DNS. For both DNS-90T and DNS-180T, the most energetic pair of modes represents an antisymmetric travelling structure, as shown in Figure 2. These modes break the symmetry of the flow with respect to the equatorial plane and thus are responsible for the swirl switching. The

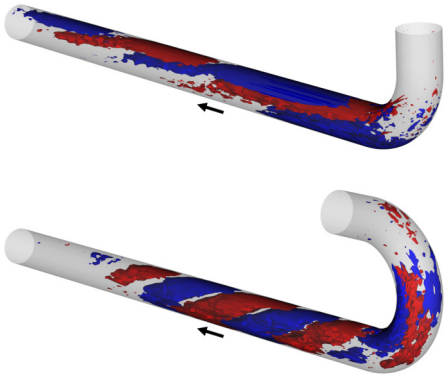

Figure 2: Isosurfaces of the velocity component normal to the equatorial plane (u_y) of POD mode 1 for (*top*) 90°-bend and (*bottom*) 180°-bend, both with turbulent inflow. Red surfaces indicate positive values, whereas blue surfaces represent negative ones. The black arrow indicates the flow direction.

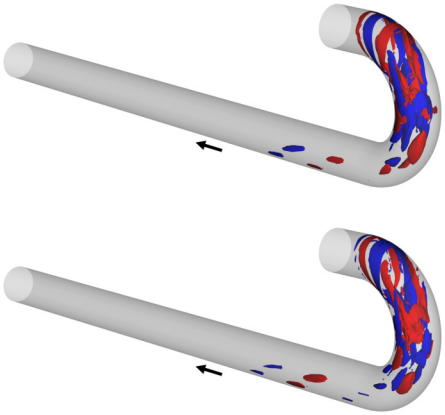

Figure 3: Isosurfaces of the streamwise velocity component (u_s) of (*top*) POD mode 1 and (*bottom*) POD mode 2 for 180°-bend with laminar inflow. Red surfaces indicate positive values, whereas blue surfaces represent negative ones. The black arrow indicates the flow direction.

flow reconstruction given by these modes and the mean field (POD mode 0) highlights, in fact, the oscillation of the vortices in the cross-section, similar to the behaviour described by Brücker [2]. It is then clear that the swirl switching occurs irrespective of the length of the bent section, although the bending angle affects its characteristics, e.g. the frequency of the dominant modes.

On the other hand, for a laminar inflow, the two most energetic modes are symmetric with respect to the equatorial plane, and they do not contribute to the swirl switching. Their spatial structure, shown in Figure 3, resembles the unstable eigenmode related to the supercritical Hopf bifurcation occurring at lower Reynolds number [8]. It is then argued that these modes are the footprints of such an instability mechanism. For DNS-180L, modes 17 and 18 represent the most energetic antisymmetric modes (see Figure 4) and account for the swirl switching. These findings highlight that the phenomenon is not primarily caused by large-scale structures originating in the straight section upstream of the bend. It is instead related to the curvature itself, as proposed by Noorani & Schlatter [4].

Time-averaged statistical quantities are computed from two sets of velocity fields reconstructed using only symmetric or antisymmetric POD modes. In the antisymmetric set, which is strictly linked to the swirl switching, the production of turbulent kinetic energy is substantial in the same regions where a large shear of the mean streamwise velocity component is detected. Based on the observation that symmetric POD modes are remnants of previous instabilities, it is argued that the antisymmetric modes responsible for the swirl switching arise because of a shear layer instability that breaks the symmetry of the flow and is part of the bifurcation cascade leading to the turbulent state. Verifying this hypothesis requires accurately tracking the transition process and investigating the stability properties of periodic and quasi-periodic flows.

Figure 4: Isosurfaces of the velocity component normal to the equatorial plane (u_y) of (*top*) POD mode 17 and (*bottom*) POD mode 18 for 180°-bend with laminar inflow. Red surfaces indicate positive values, whereas blue surfaces represent negative ones. The black arrow indicates the flow direction.

REFERENCES

[1]Dean, W.R. : Note on the motion of fluid in a curved pipe, *Lond. Edinb. Dubl. Philos. Mag. J. Sci.*, **4** (20), 208–223 (1927).

[2]Brücker, C. : A time-recording DPIV-study of the swirl switching effect in a 90° bend flow, *Proc. of* 8^{th} *International Symposium on Flow Visualization, September 1-4, Sorrento, Italy*, (1998).

[3]Tunstall, M.J. and Harvey, J.K. : On the effect of a sharp bend in a fully developed turbulent pipe-flow, *J. Fluid Mech.*, **34** (3), 595–608 (1968).

[4]Noorani, A. and Schlatter, P. : Swirl-switching phenomenon in turbulent flow through toroidal pipes, *Int. J. Heat Fluid Flow*, **61**, 108–116 (2016).

[5]Sakakibara, J. and Machida, N. : Measurement of turbulent flow upstream and downstream of a circular pipe bend, *Phys. Fluids*, **24** (4), 041702 (2012).

[6]Fischer, P.F., Lottes, J.W. and Kerkemeier, S.G. : Nek5000 web page, `https://nek5000.mcs.anl.gov` (accessed: 13 December 2023)

[7]Poletto, R. : Divergence free development of the synthetic eddy method in order to improve synthetic turbulence for embedded LES simulations, PhD thesis (2015).

[8]Massaro, D., Lupi, V., Peplinski, A. and Schlatter, P. : Global stability of 180°-bend pipe flow with mesh adaptivity, *Phys. Rev. Fluids*, **8** (11), 113903 (2023).

SESSION: Aerodynamics/Aeroacoustics I

Wednesday, April 10, 2024

16:20- 17:35

WORKSHOP
Direct and Large-Eddy Simulation 14
April 10-12 2024, Erlangen, Germany

NUMERICAL INVESTIGATION OF A TANDEM WING CONFIGURATION IN TRANSONIC FLOW REGIME

Marcel Blind[1]
Yannik Feldner[1]
Andrea Beck[1]
[1]Institute of Aerodynamics and Gas Dynamics
University of Stuttgart, Germany
blind@iag.uni-stuttgart.de

The simulation of unsteady, turbulent multiscale flows is an ongoing and challenging research topic. High-order methods are well suited for the simulation of such flows due to their low dispersion and dissipation errors. The open-source simulation framework FLEXI[1] is under active development in the Numerics Research Group at the IAG and in recent years has heavily been tuned towards large eddy simulation (LES).

One example of such unsteady and complex flows is the intricate interaction between two airfoils. In the framework of the DFG FOR 2895, a generic tandem wing configuration is introduced consisting of an OAT15A airfoil as the main wing and a NACA 64A-110 as the horizontal tail plane (HTP). A schematic of the tandem configuration is given in Fig. 1.

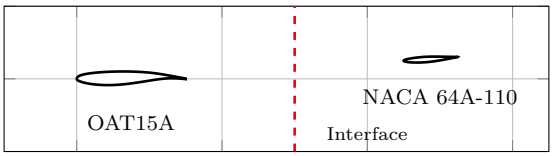

Figure 1: Overview of the tandem configuration consisting of two airfoils.

In the transonic flow regime, a shock forms on the main wing that exhibits an oscillatory movement, which is also referred to as *buffet*. The *buffet* induced effects on the boundary layer of the main wing propagate via the turbulent wake to the downstream HTP and interact there with the boundary layer. The *buffet* phenomenon has plenteous explanations. One of which is that the shock's oscillations cause an acoustic feedback loop that triggers the shock movement [6, 7, 9].

The interaction between the wing wake and the HTP under high-speed stall conditions has yet not been given much attention in the research community, neither experimentally nor numerically. Previous studies on different aircraft models observed buffet induced pressure fluctuations, and separations in the HTP area, yet the interaction between the wake and HTP boundary layer remains largely unexplored as those studies mainly relied on Reynolds-averaged Navier–Stokes (RANS) methods in the boundary layer region.

Fundamental experiments in controlled conditions have explored the influence of free stream turbulence on turbulent boundary layers, highlighting how large-scale disturbances affect boundary layer components, while smaller-scale components remain relatively unchanged [5].

To obtain insights into the physical effects that occur under such an interaction, a high-fidelity simulation of the tandem wing configuration is performed. Recently, Kleinert et al. [8] conducted a detached eddy simulation (DES) of the tandem wing setup, utilizing a RANS approach in the boundary layer that does not resolve the small-scale turbulence. Now, the unsteady wake data resulting from this simulation is used to perform an LES solely on the HTP using the discontinuous Galerkin framework FLEXI [1].

To achieve this, an interface is established to transfer the instantaneous wake data from the DES (TAU) to the FLEXI domain [2]. The zonal domain then only resolves the NACA 64A-110 airfoil, which has been previously studied both experimentally and numerically by Blind et al. [3]. The transfer of data is conducted using an interpolation method in both space and time, ensuring adequate spatial resolution at the FLEXI inflow to capture all turbulent structures from the TAU wake region. A detailed analysis of the interpolation process and associated errors can be found in Blind et al. [2].

The efficient computation of this simulation setup relies on creating optimized meshes. A method proposed by Blind et al. [4] involves using a deterministic residual determination algorithm for high-order methods to generate a multi-zone mesh. Each zone in this mesh has a distinct number of elements in

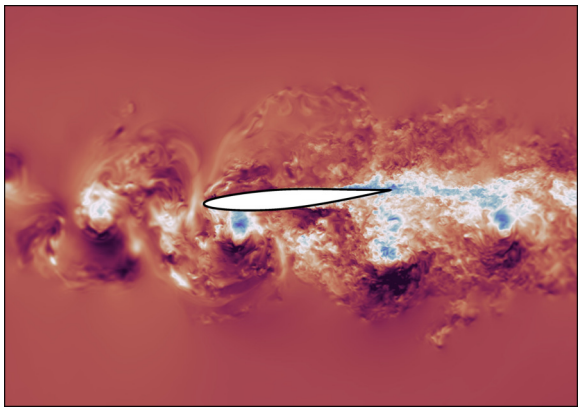

Figure 2: Instantaneous snapshot of the flow field.

[1] https://github.com/flexi-framework/flexi

the spanwise direction, interconnected via 2-to-1-interfaces to save elements while utilizing the unstructured capabilities of the FLEXI framework. By using 2-to-1-interfaces near the airfoil, the mesh design benefits from reduced resolution requirements in the wall-normal direction.

Using the previously introduced simulation setup, the impact of an OAT15A wake on the NACA 64A-110 HTP boundary layer can be analyzed. It is investigated whether scale-resolving wall-modeled large eddy simulations (WMLES) reveal a significant influence of the turbulent wake on the turbulent boundary layer of the NACA 64A-110 HTP airfoil. It could be shown that the wake leads to an increase in boundary layer thickness and drag while causing a decrease in lift. Large turbulent structures exhibit intense interaction with the airfoil, whereas smaller structures were prone to damping when interacting with the boundary layer. Furthermore, it is discussed if scale-resolving simulations enable a detailed investigation of physical effects in the boundary layer and evaluation of boundary layer properties that could not be studied using the precursor RANS simulation. Additionally, the admissibility of WMLES for strong wake-boundary layer interaction is investigated. In the study an equilibrium wall model based on Spalding's law of the wall is employed. The simulation results highlight that this wall model yields satisfactory results even for large wake structures interacting with the boundary layer on the HTP. Using WMLES for such problems thus is a reasonable choice, allowing for high-fidelity simulation while significantly reducing overall computational costs.

REFERENCES

[1]Krais, N., Beck, A., Bolemann, T., Frank, H., Flad, D., Gassner, G., Hindenlang, F., Hoffmann, M., Kuhn, T., Sonntag, M. & Munz, C. FLEXI: A high order discontinuous Galerkin framework for hyperbolic–parabolic conservation laws. *Computers & Mathematics With Applications*. **81** pp. 186-219 (2021), Development and Application of Open-source Software for Problems with Numerical PDEs

[2]Blind, M., Kleinert, J., Lutz, T. & Beck, A. A time-accurate inflow coupling for zonal LES. *CEAS Aeronautical Journal*. (2023)

[3]Blind, M., Schauerte, C., Schreyer, A. & Beck, A. Numerical and Experimental Investigation of a NACA 64A-110 Airfoil in Transonic Flow Regime. *ArXiv Preprint ArXiv:2303.10032*. (2023)

[4]Blind, M., Kahraman, A., Larsson, J. & Beck, A. Residual estimation for grid modification in wall-modeled large eddy simulation using unstructured high-order methods. *Computers & Fluids*. **254** (2023)

[5]Hancock, P. & Bradshaw, P. The Effect of Free-Stream Turbulence on Turbulent Boundary-Layers. *Journal Of Fluids Engineering-Transactions Of The ASME*. **105**, 284-289 (1983)

[6]Hartmann, A., Feldhusen, A. & Schröder, W. On the interaction of shock waves and sound waves in transonic buffet flow. *Physics Of Fluids*. **25** (2013)

[7]Jacquin, L., Molton, P., Deck, S., Maury, B. & Soulevant, D. Experimental Study of Shock Oscillation over a Transonic Supercritical Profile. *AIAA Journal*. **47**, 1985-1994 (2009)

[8]Kleinert, J., Ehrle, M., Waldmann, A. & Lutz, T. Wake tail plane interactions for a tandem wing configuration in high-speed stall conditions. *CEAS Aeronautical Journal*. (2023)

[9]Lee, B. Oscillatory Shock Motion Caused by Transonic Shock Boundary-Layer Interaction. *Aiaa Journal*. **28**, 941-944 (1990)

WORKSHOP
Direct and Large-Eddy Simulation 14
April 10-12 2024, Erlangen, Germany

ANALYSIS OF UPSTREAM TRAVELING WAVES ON TRANSONIC BUFFET

T. Lürkens[1], **M. Meinke**[1], **W. Schröder**[1,2]
[1]Institute of Aerodynamics and Chair of Fluid Mechanics (AIA), RWTH Aachen University, Germany
[2]JARA Center for Simulation and Data Science, Jülich, Germany
t.luerkens@aia.rwth-aachen.de

INTRODUCTION

In the transonic regime, the flow around supercritical airfoils is characterized by a supersonic region that is terminated by a shock wave. At certain combinations of freestream Mach number and angle of attack, the shock wave is subject to self-sustained oscillations at low frequencies on the order of $Sr \sim \mathcal{O}(10^{-2}) - \mathcal{O}(10^{-1})$ where the non-dimensional frequency is given by the Strouhal number $Sr = \frac{fc}{u_\infty}$. The impact of the buffet phenomenon on flight safety is severe. The alternating aerodynamic loads evoke a dynamical response of the wing structure commonly referred to as buffeting which can compromise its integrity and overall lifetime.

Although the phenomenon has been investigated for decades a comprehensive understanding of the underlying physical mechanisms of the self-sustained nature of the shock oscillation is still subject to ongoing scientific analyses. An often discussed model was introduced by Lee [1] and later modified by Hartmann et al. [2] proposing a closed feedback loop between the shock wave position, the vortices emerging from the shock wave/boundary layer interaction and the acoustic waves emerging from the trailing edge when these vortices pass over it. Therefore, the trailing edge flow and the resulting acoustics are of central interest for the thorough understanding of the phenomenon. In shear flows the dominant acoustic source term is the perturbed Lamb vector [3] given by

$$\boldsymbol{L'} = (\boldsymbol{\omega} \times \boldsymbol{u})'. \tag{1}$$

Since buffet and trailing edge pressure fluctuations are closely linked, the dynamical behavior of the Lamb vector is of particular interest in establishing a more thorough understanding of the physical principles underlying the buffet phenomenon. Therefore, in this work the influence of pressure perturbations onto the buffet phenomenon, and in particular the corresponding trailing edge flow with the resulting acoustic source term, i.e., the Lamb vector, are investigated with respect to the shock dynamics.

NUMERICAL SETUP

In this work highly resolved large-eddy simulations of the buffet phenomenon on the OAT15A airfoil are performed at an angle of attack $\alpha = 3.5°$, freestream Mach number $Ma = 0.73$, and chord-based Reynolds numbers Re_c in the range of $750\,000 - 3\,000\,000$. The simulations are performed using the hierarchical Cartesian solver of the simulation framework *multiphysiscs - Aerodynamics Institute Aachen* (m-AIA) solving the compressible Navier-Stokes equations by means of finite volume method.

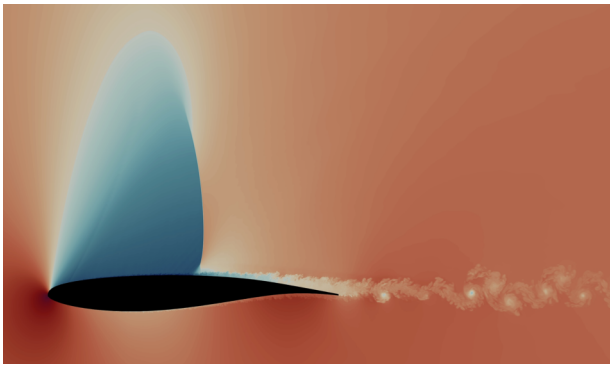

Figure 1: a) Instantaneous density contours of the buffet flow.

DYNAMIC MODE DECOMPOSITION

To analyze the flow structures the dynamic mode decomposition (DMD) is used. It is a data driven technique that allows the decomposition of the data field $\boldsymbol{q}(\boldsymbol{x}, t)$ into a series representation of spatio-temporal modes $\boldsymbol{\phi}_n$ characterized by a complex frequency λ_n, and the amplitude a_n [4]. The resulting series representation of the data field reads

$$\boldsymbol{q}(\boldsymbol{x}, t) = \sum_n a_n e^{\lambda_n t} \boldsymbol{\phi}_n(\boldsymbol{x}). \tag{2}$$

It corresponds to the projection of the flow field dynamics onto a linear system. Due to its ability to extract dynamic features at distinct frequencies from the flow field DMD is a well-established tool in investigating the buffet phenomenon [5]. A DMD performed on N snapshots results in a series representation of $N - 1$ modes given in complex pairs. Capturing low frequency phenomena like the buffet phenomenon while maintaining high frequency resolution results in a vast number of modes the individual assessment of which can be tedious. Therefore, the sparsity-promoting DMD (SP-DMD) algorithm by Jovanović [6] is used to isolate the dominating dynamics from the turbulent flow field while maintaining the number of resulting modes at a manageable level.

PRELIMINARY RESULTS

A first impression of the investigated flow features is given by the density contours shown in figure 1. The shock wave

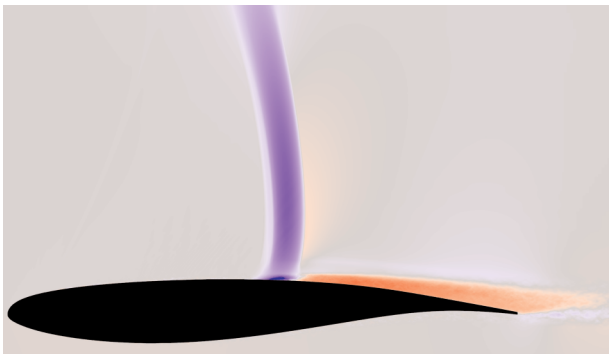

Figure 2: SP-DMD mode of the streamwise velocity component at the buffet frequency of $Sr = 0.072$

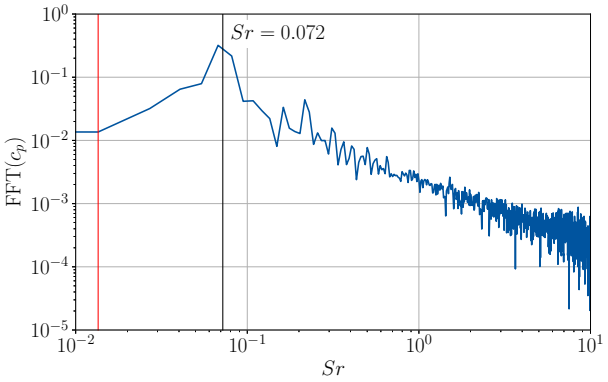

Figure 3: Frequency spectrum of the surface pressure signal at the mean shock position

and the resulting flow separation downstream of the shock are clearly visible. The dynamical coupling of these two flow features is illustrated in figure 2 by the first dominant mode extracted from the streamwise velocity field using SP-DMD. The frequency spectrum of the surface pressure signal at the mean shock position is given in figure 3. The peak found at $Sr = 0.072$ is in perfect agreement with the results from the SP-DMD. In figure 4 contours of the pressure fluctuations in the wall-bounded flow around the OAT15A are given. The oscillation of the shock wave and the trailing edge flow are identified as the main drivers of the pressure fluctuations. To understand the buffet phenomenon the communication path between the trailing edge flow and the shock wave is of major interest. It is obvious that there is a region of increased pressure fluctuations between the shock wave and the trailing edge that lies slightly off the airfoil surface and thus coincides with the temporarily separated region. This region of increased pressure fluctuations represents a potential path for the trailing edge acoustics to reach the shock wave and close the feedback loop proposed by Lee [1]. A detailed analysis of the propagation of trailing edge pressure fluctuations in the region between the shock wave and the trailing edge will be given in the conference contribution.

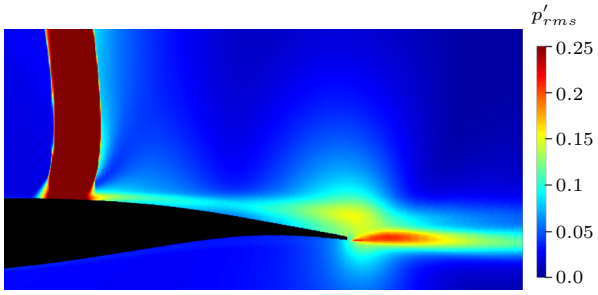

Figure 4: RMS values of pressure fluctuations near the trailing edge.

REFERENCES

[1]Lee, B. H. K. : Self-sustained shock oscillations on airfoils at transonic speeds, *Progress in Aerospace Sciences*, **37**, 147–196, (2001).

[2]Hartmann, A., and Feldhusen, A., and Schröder, W. : On the interaction of shock waves and sound waves in transonic buffet flow, *Physics of Fluids*, **25**, 026101, (2013).

[3]Ewert, R., and Schröder, W. : Acoustic perturbation equations based on flow decomposition via source filtering, *Journal of Computational Physics*, **188**, 365–398, (2003).

[4]Schmid, P. J. : Dynamic mode decomposition of numerical and experimental data, *Journal of Fluid Mechanics*, **656**, 5–28, (2010).

[5]Feldhusen-Hoffmann, A., and Lagemann, C., and Loosen, S., and Meysonnat, P., and Klaas, M., and Schröder, W. : Analysis of transonic buffet using dynamic mode decomposition, *Experiments in Fluids*, **62**, 66, (2021).

[6]Jovanović, M. R., and Schmid, P. J., and Nichols, J. W. : Sparsity-promoting dynamic mode decomposition, *Physics of Fluids*, **26**, 024103, (2014).

WORKSHOP
Direct and Large-Eddy Simulation 14
April 10-12 2024, Erlangen, Germany

DYNAMICS OF INCOMPRESSIBLE FLOW OVER A HIGH-LIFT AIRFOIL AT LOW REYNOLDS NUMBERS

Ming Teng[1], **Catherine Mavriplis**[1]
[1]Department of Mechanical Engineering
University of Ottawa
ming.teng@uottawa.ca

ABSTRACT

The present study explores the flow features of incompressible flow over an unswept airfoil in a high-lift configuration as it transitions to turbulence. With a fixed angle of attack $\alpha = 4.0°$, three low chordwise Reynolds numbers are considered: $Re_c = U_\infty c/\nu = 0.832\times10^4$, 1.270×10^4 and 1.830×10^4, where U_∞ represents the freestream velocity, c the stowed chord length of the multi-element (slat, main and flap) 30P30N airfoil, and ν the kinematic viscosity. A series of well-resolved three-dimensional direct numerical simulations are calculated via a high-order spectral element method. The study discusses the evolution of flow motions above the main element of the airfoil associated with increases in Re_c. Pairs of longitudinal counter-rotating vortices observed in the $Re_c = 0.832 \times 10^4$ case start to coexist with spanwise vortices at the initial stage of transition in the $Re_c = 1.270 \times 10^4$ case. As Re_c reaches 1.830×10^4, this phenomenon is no longer perceptible, indicating a major shift of dominating instability mechanisms. In the meantime, the shear-layer reattachment location shifts significantly upstream as Re_c increases from 0.832×10^4 to 1.270×10^4. For $Re_c = 1.830\times10^4$, the flow remains attached to the surface till it reaches the flap element. The present work investigates the flow dynamics, and aims to address the fundamental instability mechanisms that govern the transition route in three Re_c cases. Analysis incorporates both evolution of instantaneous coherent structures and mean flow statistics.

FLOW CONFIGURATION

Figure 1 shows the numerical setup of the computational domain along with the instantaneous spanwise vorticity, $\omega_z c/U_\infty$, for $Re_c = 1.830 \times 10^4$. Spanwise vorticity is written $\omega_z = \partial v/\partial x - \partial u/\partial y$, where x and y denote streamwise and wall-normal directions, and u and v are the corresponding instantaneous velocity components. The computational domain has a size of $x \times y \times z = 9c \times 5c \times 0.2c$ with z denoting the spanwise direction. A total of 332,050 elements is employed, yielding approximately 1.14×10^8 degrees of freedom using N=8 points in each direction within each element. The origin of the coordinate system is placed at the slat leading edge for $\alpha = 0°$ flow. Inflow boundary conditions are imposed as shown in red in Fig. 1 by prescribing a uniform velocity $(u, v, w) = (U_\infty\cos\alpha,\ U_\infty\sin\alpha,\ 0)$ where w signifies instantaneous velocity component in the $z-$direction and $\alpha = 4.0°$. A convective boundary-condition is applied at the two outflow boundaries, shown in blue in Fig. 1. No-slip conditions are imposed on the airfoil surface. The flow is assumed to be periodic in the $z-$direction. In the present work, no artificial disturbances are introduced. The flow, therefore, transitions to turbulence naturally from the instability of infinitesimal perturbations due to round-off or truncation errors.

GOVERNING EQUATIONS

The equations of conservation of mass and momentum for incompressible flow of a Newtonian fluid are:

$$\frac{\partial u_i}{\partial x_i} = 0, \tag{1}$$

$$\frac{\partial u_i}{\partial t} + \frac{\partial}{\partial x_j}u_i u_j = -\frac{1}{\rho}\frac{\partial p}{\partial x_i} + \nu\nabla^2 u_i. \tag{2}$$

The indices i and j on the velocity components $u_()$ refer to the spatial dimensions within the Einstein summation notation. ρ, ν and p denote fluid density, kinematic viscosity and hydrodynamic pressure respectively. Eqns. (1) and (2) are solved using NEK5000 [2], an open-source code based on a high-order spectral element method [4] which features highly scalable algorithms. $7^{th}-$order polynomials are used for spatial discretisation along with a $3^{rd}-$order temporal scheme.

RESULTS

Figure 2 presents instantaneous vortical structures visualized as isosurfaces of the λ_2 criterion [3], providing insight into the flow evolution in the three Re_c cases considered. The flow structures are coloured by the magnitude of the streamwise velocity, u/U_∞. Different values of the λ_2 are used to highlight the flow features in different regions.

Figure 2(a)(left) reveals the appearance of longitudinal counter-rotating vortices shortly downstream of the main-element leading edge in the $Re_c = 0.832 \times 10^4$ case. These coherent structures were also observed in Wang et al [5], conjectured to be Görtler vortices due to centrifugal instability. As flow separates, a Kelvin-Helmholtz (K-H) instability takes over and leads to the formation of quasi two-dimensional (2D) rollers. Roll-up vortices propagate downstream, appearing to interact with wake vortices. An increase in Re_c to $Re_c = 1.270 \times 10^4$ promotes the onset of quasi-2D vortices, and yields finer-scale structures in the wake region [see Fig. 2(b) (right)]. Longitudinal vortices now appear on top of spanwise vortices as they evolve downstream and break down into more complex structures. With a further increase in Re to

$Re_c = 1.830 \times 10^4$, the flow presents turbulent-like motions with a random distribution of hairpin vortices downstream of the slat trailing edge, as shown in Fig. 2(c).

The separation region over the main element reduces in size as Re_c increases. The shear layer, however, separates again as flow proceeds beyond the main element in all Re_c cases and does not reattach to the flap surface. The overall improvement of aerodynamic performance is observed with increasing Re_c and a corresponding reduced width of the wake region; lift and drag coefficients will be analyzed in the full paper. The impact of Re_c on the pressure coefficient distribution is most pronounced above the main element. One salient feature of a boundary-layer separation is its quasi constant-pressure region [1]. Absence of a reattachment to the surface is reflected by a constant-pressure region that extends to the trailing edge whereas transition in the separated shear layer is indicated by a slight rise in pressure beyond the constant-pressure region [6]. A detailed discussion of these features will be given in the full paper through analysis of the skin-friction coefficient and pressure-coefficient profiles.

REFERENCES

[1]Carmichael, B. H.: Low Reynolds number airfoil survey, *NASA-CR-165803-VOL-1.*, (1981).

[2]Fischer, P. F. and Lottes, J. W. and Kerkemeier, S. G.: NEK5000 Webpage, *http://nek5000.mcs.anl.gov*, (2008).

[3]Jeong, J. and Hussain, F.: On the identification of a vortex, *Journal of Fluid Mechanics*, **285**, 69–94 (1995).

[4]Patera, A. T.: A spectral element method for fluid dynamics: Laminar flow in a channel expansion, *Journal of Computational Physics*, **54**(3), 468–488 (1984).

[5]Wang, J. S. and Feng, L. H. and Wang, J. J. and Li, T.: Görtler vortices in low-Reynolds-number flow over multi-element airfoil, *Journal of Fluid Mechanics*, **835**, 898–935 (2018).

[6]Yarusevych, S. and Sullivan, P. E. and Kawall, J. G.: Coherent structures in an airfoil boundary layer and wake at low Reynolds numbers, *Physics of Fluids*, **18**(4), (2006).

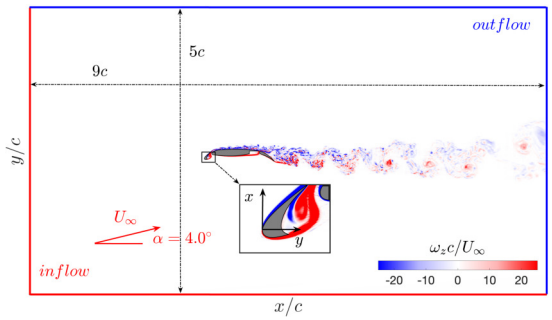

Figure 1: Sketch of the computational domain used for the calculations with instantaneous spanwise vorticity, $\omega_z c/U_\infty$, for $Re_c = 1.830 \times 10^4$ imposed on top. U_∞ and c stand for the freestream velocity and stowed chord length of the multi-element 30P30N airfoil, respectively. α denotes the angle of attack.

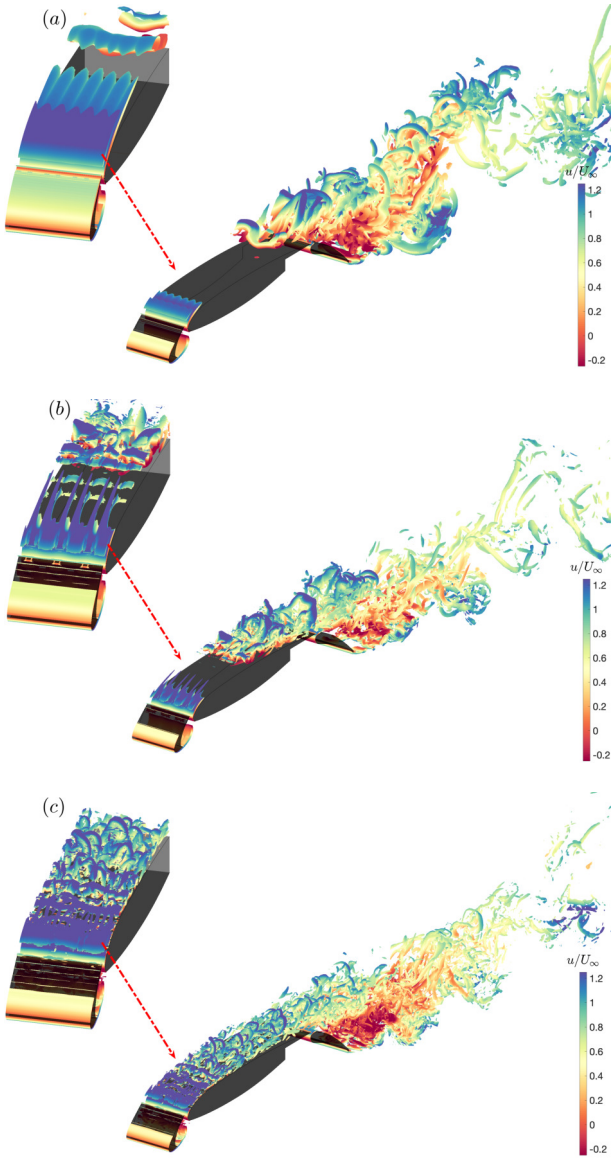

Figure 2: Iso-surfaces of the λ_2 (the middle eigenvalue of the strain-rate tensor), coloured by the magnitude of streamwise velocity, u/U_∞, for the three-dimensional $\alpha = 4.0°$ flow past a 30P30N airfoil of $0.2c$ span at (a) $Re_c = 0.832 \times 10^4$ at $tU_\infty/c = 10.80$ (t denotes time); (Left): $\lambda_2 = -10.0$, (Right): $\lambda_2 = -50.0$; (b) $Re_c = 1.270 \times 10^4$ at $tU_\infty/c = 23.70$; (Left): $\lambda_2 = -50.0$, (Right): $\lambda_2 = -100.0$; and (c) $Re_c = 1.830 \times 10^4$ at $tU_\infty/c = 23.88$; (Left): $\lambda_2 = -100.0$, (Right): $\lambda_2 = -150.0$.

WORKSHOP
Direct and Large-Eddy Simulation 14
April 10-12 2024, Erlangen, Germany

DIRECT NUMERICAL SIMULATIONS OF A FLAPPING WING IN TURBULENT FREE STREAMS AT MODERATE REYNOLDS NUMBER

Juan Manuel Catalán[1], Stefano Olivieri[1], Oscar Flores[1] and Manuel García-Villalba[2]
[1]Department of Aerospace Engineering, Universidad Carlos III de Madrid, Spain
[2]Institute of Fluid Mechanics and Heat Transfer, Technische Universität Wien, Austria
jcatalan@ing.uc3m.es

INTRODUCTION

The rapid advancement of micro-air vehicle (MAV) technology has garnered significant attention within the field of aerodynamics. As these small-scale aircraft find increasingly relevant applications in diverse sectors such as surveillance, environmental monitoring, and search-and-rescue missions, there is a growing need to deepen our comprehension of the flow physics involved in their flight. Notably, MAVs often operate at low speeds and low altitudes in the atmospheric boundary layer, exposing them to potentially intense turbulence conditions. Besides, in contrast to the typical conditions encountered by more conventional aircraft, the characteristic spatial and temporal scales of environmental flow perturbations can be closely comparable to those of these small aircraft. As a result, our current understanding of how atmospheric turbulence influences the aerodynamic performance of MAVs or similar devices remains incomplete.

Motivated by an interest in bio-inspired MAVs, here we present a high-fidelity, direct numerical simulation (DNS) framework tailored for investigating the aerodynamic interactions between a flapping wing and a turbulent free stream at low to moderate Reynolds numbers (fig. 1). We begin with a benchmark analysis on the generation of free-stream turbulence having well defined and controllable properties, comparing the flows obtained with two distinct approaches. Then, we delve into the characterization of a flapping wing subjected to fluctuations with high turbulence intensity and integral length-scale comparable to the chord, in order to reveal significant variations in the aerodynamic response with respect to the case of an unperturbed free stream.

METHODOLOGY

We consider the Navier-Stokes equations for an incompressible flow and Newtonian fluid,

$$\nabla \cdot \mathbf{u} = 0, \tag{1}$$

$$\frac{\partial \mathbf{u}}{\partial t} + (\mathbf{u} \cdot \nabla)\mathbf{u} = -\frac{1}{\rho}\nabla p + \nu \nabla^2 \mathbf{u} + \mathbf{f}_{\mathrm{st}} + \mathbf{f}_{\mathrm{ibm}}. \tag{2}$$

Here, $\mathbf{u}$ is the velocity, p the pressure, ρ the density and ν the kinematic viscosity. We include two external forcing terms: $\mathbf{f}_{\mathrm{st}}$ introduces synthetic turbulent fluctuations [1] and $\mathbf{f}_{\mathrm{ibm}}$ models the presence of solid bodies immersed in the flow [2]. Two approaches are considered for the generation of the free-stream turbulent fluctuations. The first approach is using a *synthetic turbulence* (ST) inflow generator based on digital filters [3]. Specifically, the flow is forced by means of the source term $\mathbf{f}_{\mathrm{st}}$ active in a relatively narrow region of influence [1]. This region of influence is located shortly after the inlet of the computational domain and centered around $x = 0$, see fig. 2 (top), so that the generated fluctuations are advected downstream by the mean flow. The fluctuations generated using this method are determined by the (input) turbulence intensity TI_0 and the (input) integral length-scale Λ_0, two parameters that are explicitly set in the algorithm.

The second approach consists of generating *grid-induced turbulence* (GT) by placing a solid passive grid (also centered at $x = 0$), as usually done in wind-tunnel experiments. For this method, the geometry of the grid implicitly determines the properties of the generated fluctuations. To achieve satisfactory flow properties (i.e., turbulence intensity, statistical homogeneity and isotropy), we choose the SSQ43 geometrical configuration of Djenidi et al. [4], corresponding to a monoplane grid made of rods with square cross-section of side d, evenly spaced by a distance $M = 4d$, see fig. 2 (bottom).

We investigate the impact of turbulence on a symmetrically flapping wing in an efficient thrust-producing configuration, which has been previously characterized in the case of an unperturbed free stream [5]. The wing undergoes a sinusoidal heaving and pitching motion. It is made of a NACA 0012 air-

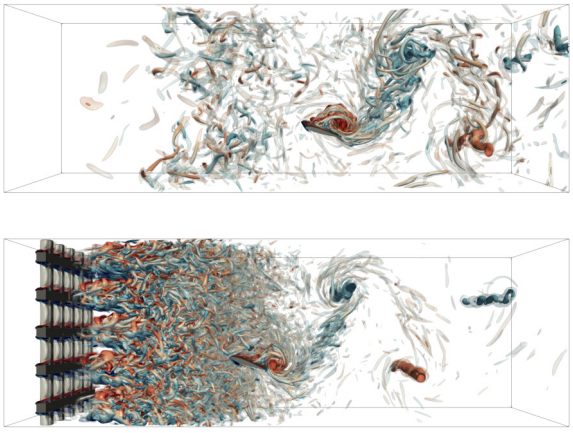

Figure 1: Snapshots from DNSs of a flapping wing in ST (top) and GT (bottom). Vortical structures are identified as Q-isosurfaces at $Qc^2/U_\infty^2 = 10$, coloured by the spanwise vorticity (from negative in blue to positive in red).

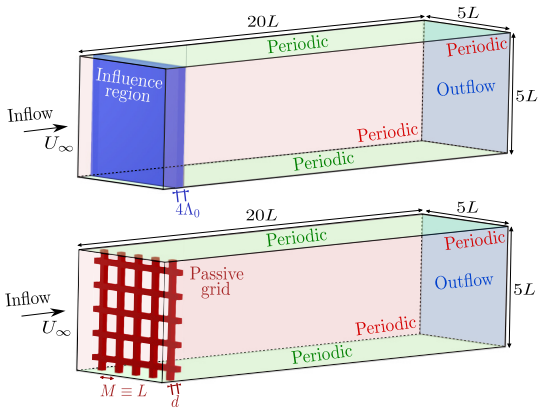

Figure 2: Sketches of the computational domain and boundary conditions, for ST (top) and GT (bottom) approach.

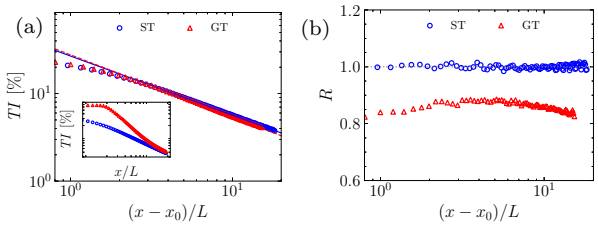

Figure 3: Large-scale properties of the turbulent flow generated in the ST case (blue circles) and GT case (red triangles): (a) turbulence intensity; (b) large-scale anisotropy.

foil and has an infinite aspect span to exclude tip effects. The Reynolds number based on the wing chord c is chosen to be $Re_c = U_\infty c/\nu = 1000$. For the sake of generality, we introduce a reference length-scale L that, in the present study, is set equal to the wing chord. Note that the spacing M in GT is also chosen equal to c, therefore having $L \equiv c \equiv M$.

Equations (1) and (2) are solved numerically using TUCAN, an extensively validated, parallel in-house solver, based on a fractional-step method on a staggered Cartesian grid [6]. We use centered (second-order) finite differences for the spatial discretization and a semi-implicit three-stage Runge-Kutta scheme for the time integration. The extent of the chosen computational domain, along with the prescribed boundary conditions, is illustrated in fig. 2. The domain is discretized using a uniform spatial resolution with two different grid spacings Δ deduced after a grid refinement study: (i) when comparatively analyzing the ST and GT approach (without the wing), we use $\Delta/L \approx 0.02$; (ii) when assessing the interaction between the flapping wing and the turbulent free stream, we refine the grid spacing to $\Delta/L \approx 0.01$.

RESULTS AND DISCUSSION

Comparison between ST and GT generation

After preliminary testing with the ST approach, we select a combination of the input parameters ($\Lambda_0 = 0.15L$, $TI_0 = 35\%$) such that the resulting flow has similar characteristics to that of the GT case.

Figure 3 shows the streamwise evolution of (a) the turbulence intensity TI and (b) the large-scale anisotropy R (defined as the ratio between the transverse and longitudinal velocity fluctuations). To properly compare the results, we account for the different length that the turbulent flow needs for full development (see inset of fig. 3a). We quantify this development length with a virtual origin x_0, that we obtain by fitting the data with respect to a power-lay decay. Once we account for this difference, the turbulence intensity TI evolves very similarly along the streamwise direction for the two cases (fig. 3a). On the other hand, we notice differences for the anisotropy R (fig. 3b): while the ST case achieves an almost perfect isotropy (i.e., $R = 1$), a remarkably higher degree of anisotropy is found for the GT case. Subsequently, we extend this analysis to the evolution of the characteristic length-scales and spectral energy distribution (not shown).

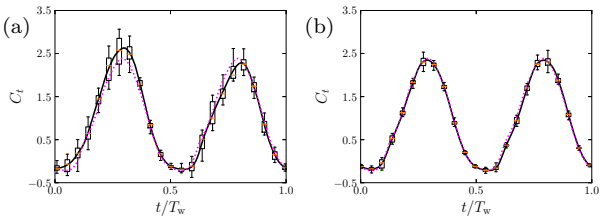

Figure 4: Time histories of the thrust coefficient over one flapping cycle: (a) ST case with $\Lambda_{LE} \approx 0.6c$; (b) GT case with $\Lambda_{LE} \approx 0.25c$. For both cases, $TI_{LE} \approx 20\%$. Boxes and whiskers indicate the fluctuations while the solid line indicates the average along the spanwise direction. The solution in the unperturbed case (i.e., $TI_{LE} = 0$) is indicated by the magenta dotted curve.

Wing-turbulence aerodynamic interactions

Figure 1 shows two representative cases where the flapping wing is immersed in a free stream generated with ST (top) or GT (bottom). For both cases, the turbulence intensity at the wing's leading edge (LE) is around 20%. In ST, however, we set $\Lambda_0 = 0.5c$ to have an integral length-scale at the LE, $\Lambda_{LE} \approx 0.6c$. In GT, $\Lambda_{LE} \approx 0.25c$. Qualitatively, it appears that the characteristic vortex pattern behind the flapping wing is much more affected in the ST case, where Λ_{LE} is approximately double compared to the GT case. We can quantify this effect in terms of the instantaneous thrust coefficient, reported in fig. 4: for larger Λ_{LE}, the spanwise fluctuations of the generated force are remarkably higher, along with a clearer departure of the spanwise average from the unperturbed case.

In this presentation, we will further deepen into what is the influence that free-stream turbulence (GT and ST) has on the aerodynamic performance of the case presented herein.

REFERENCES

[1]Schmidt, S. and Breuer, M. : Source term based synthetic turbulence inflow generator for eddy-resolving predictions of an airfoil flow including a laminar separation bubble, *Comput. Fluids*, **146**, 1–22 (2017).

[2]Uhlmann, M. : An immersed boundary method with direct forcing for the simulation of particulate flows, *J. Comput. Phys.*, **209**, 448–476 (2005).

[3]Klein, M., Sadiki, A. and Janicka, J. : A digital filter based generation of inflow data for spatially developing direct numerical or large eddy simulations, *J. Comput. Phys.*, **186**, 652–665 (2003).

[4]Djenidi, L., Kamruzzaman, Md. and Antonia, R. A. : Power-law exponent in the transition period of decay in grid turbulence, *J. Fluid Mech.*, **779**, 544–555 (2015).

[5]Moriche, M., Flores, O. and García-Villalba, M. : On the aerodynamic forces on heaving and pitching airfoils at low Reynolds number, *J. Fluid Mech.*, **828**, 395–423 (2017).

[6]Moriche, M. : A numerical study on the aerodynamic forces and the wake stability of flapping flight at low Reynolds number, *PhD thesis* (2017). Universidad Carlos III de Madrid.

WORKSHOP
Direct and Large-Eddy Simulation 14
April 10-12 2024, Erlangen, Germany

STATISTICAL ANALYSIS OF THE SEPARATED FLOW ABOUT A WING SECTION

R. Corsini, A. Cimarelli and E. Stalio
Dipartimento di Ingegneria "Enzo Ferrari"
Università degli studi di Modena e Reggio Emilia
enrico.stalio@unimore.it

INTRODUCTION

Aerodynamics studies on wings in subsonic conditions have a long history, dating back to the 19th century, but research in the field is still active. Possible applications are the design of more efficient aircraft and the production of wind energy. In the wind energy field, wind turbines operate over a wide range of flow conditions given that close to the ground winds are characterized by a high variability. In the design phase, a nominal operational range is determined, where optimum performance is achieved by a wind turbine. Outside this range, and for example for low wind speeds, the energy harvesting performance drops significantly. For this reason, an increasing effort is being spent, aiming at ensuring energy production during periods of low wind speeds.

In wind turbine design, an undesired aerodynamic effect is uncontrolled flow separation on the rotor blades [1]. Flow separation occurs on the airfoil geometries used for wind turbine blades when the boundary layer on the suction side is subjected to long and strong adverse pressure gradients, and separate before the trailing edge. Flows about wings are prone to separation at low-speeds and high angles of attack.

Airfoils operating in the low Reynolds number regime, i.e. at chord Reynolds number below 500 000, typically suffer from the presence of a laminar separation bubble [2, 3], very close to the leading edge. After laminar separation, reattachment occurs in turbulent flow conditions. Depending on the angle of attack of the unperturbed flow, a subsequent, final separation may also occur. The onset of turbulence in the boundary layer significantly affect conditions of a possible, final separation [4]. A useful categorization of different types of flow separation on airfoils is given by Gault [5].

Although high-fidelity numerical methods (DNS) are impractical for modelling complex systems such as a wind turbine, they represent a fundamental research tool to investigate the main physical phenomena occurring in the air flow on turbine blades. Up to the present time the only DNS solutions available in the literature deal with flow separation at the wing leading edge [6, 7] or with attached turbulent boundary layer on wing sections with low angle of attack [8].

In this work we investigate the flow about a wing section at a low Reynolds number ($Re = 66000$) and for an angle of attack ($\alpha = 15$ deg) which involves transition before a second, final separation. The geometry selected corresponds to the NACA 4412 airfoil. The above conditions, beside the presence of a separation bubble close to the leading-edge, give place to a turbulent, final separation on the suction side, at $x_S \approx 0.7c$.

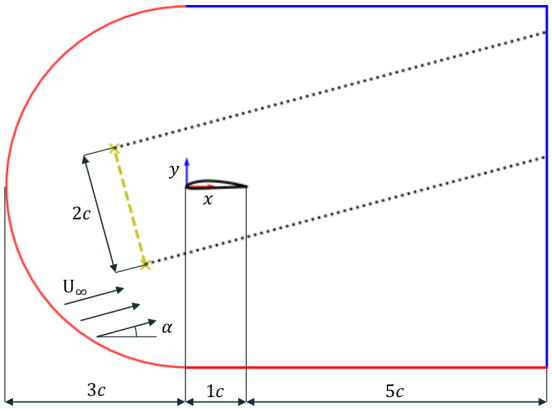

Figure 1: Scheme of the computational domain. Red lines indicate inflow conditions and blue lines indicate outflow conditions. Yellow dashed line denotes the location of the plane where free-stream turbulence is generated.

NUMERICAL METHODOLOGY

The direct numerical simulation of the turbulent flow about the NACA 4412 wing section has been performed with the code Nek5000.

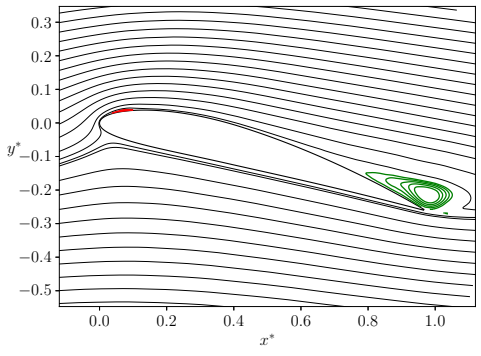

Figure 2: Streamlines of the mean velocity field.

The Reynolds number based on the chord length, c, and the free-stream velocity is $Re = 66000$. Figure 1 shows the outline of the C-type grid used for the simulation.

Dirichlet boundary conditions for velocity are imposed at the left and bottom boundaries to have an incoming flow at angle of attack, $\alpha = 15$ deg. A stabilized outflow condition is

used at the right and top boundaries, and periodic conditions are applied in the spanwise direction. In order to generate inflow turbulence, velocity fluctuations are induced on a plane placed $1c$ upstream of the leading edge of the wing and normal to the free-stream velocity, see figure 1. The magnitude of the source term is modulated to generate a turbulence intensity of Ti = 5% at the wing leading edge.

RESULTS

At the angle of attack investigated, two laminar boundary layers start to develop from the stagnation point on the lower surface, see figure 2. One is directed downstream and keeps laminar until the separation at the trailing edge. The other is directed towards the leading edge and separates close to the leading edge, under the action of the adverse pressure gradient on the upper surface. The laminar shear layer that is formed is highly unstable and becomes turbulent before reattaching. From the instantaneous reattachment line, a turbulent boundary layer evolves. This boundary layer finally separates at some distance downstream, before reaching the trailing edge, leading to the formation of a large recirculating region. Vortices shed from the separated region and the trailing edge give rise to a turbulent wake characterized by vortical structures with smaller length scale with respect to that typical of bluff bodies.

Two zones of recirculating fluid are identified in the mean flow field. A small and thin separation bubble is located close to the leading edge as a result of the laminar flow separation and reattachment. A second larger separation bubble is formed starting from $x = 0.68c$, due to flow separation in turbulent state. The most intense turbulent fluctuations are observed along the shear layer of the laminar separation bubble, where turbulence is triggered. The turbulent kinetic energy decreases in the boundary layer downstream until its final detachment. In the separated shear layer that is generated the turbulent fluctuations rise again under the action of high mean shears. Large turbulence intensities are also found in the shear layer developing from the trailing edge.

In figure 3, symbols indicate the starting and ending locations of the separated regions on the upper surface for the different combinations of Ti and α tested. By increasing the angle of attack, the laminar separation bubble originates at shorter distances from the leading edge and the location of turbulent separation significantly moves upstream along the upper surface. On the other hand, by increasing the turbulence intensity, the shear layer transition becomes more abrupt, causing the flow to reattach more rapidly after the laminar separation. In addition, the second separation is anticipated, leading to the formation of a larger recirculating region near the trailing edge.

CONCLUSIONS

The separated flow around a NACA 4412 wing section at $Re = 66000$ and $\alpha = 15$ deg is investigated by means of highly accurate DNS. Velocity fluctuations are induced in the incoming flow in order to trigger transition to turbulence. The main flow statistics, such as aerodynamic coefficients, mean velocity field, and turbulent kinetic energy, are examined to provide a description of the flow topology and the dynamics of the separated flow regions. The result of the present research are expected to be beneficial for the design of wind turbine blades and aircraft of increased aerodynamic efficiency.

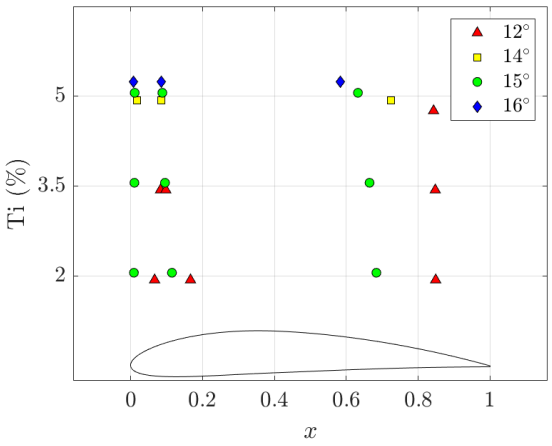

Figure 3: Mean positions of flow separation and reattachment as a function of angle of attack and turbulence intensity resulting from preliminary simulations.

ACKNOWLEDGEMENTS

This research is funded by NextGenerationEU- DD. 3277. Ecosystem For Sustainable Transition of Emilia-Romagna (ECOSISTER).

REFERENCES

[1]A. Yeznasni, R. Derdelinckx, and C. Hirsch, "Influence of dynamic stall in the aerodynamic study of hawts," *Journal of Wind Engineering and Industrial Aerodynamics*, vol. 39, no. 1, pp. 187–198, 1992.

[2]T. J. Mueller and S. M. Batill, "Experimental studies of separation on a two-dimensional airfoil at low reynolds numbers," *AIAA Journal*, vol. 20, no. 4, pp. 457–463, 1982.

[3]S. Wang, Y. Zhou, M. M. Alam, and H. Yang, "Turbulent intensity and reynolds number effects on an airfoil at low reynolds numbers," *Physics of Fluids*, vol. 26, no. 11, p. 115107, 2014.

[4]K. Koca, M. S. Genç, H. H. Açıkel, M. Çağdaş, and T. M. Bodur, "Identification of flow phenomena over naca 4412 wind turbine airfoil at low reynolds numbers and role of laminar separation bubble on flow evolution," *Energy*, vol. 144, pp. 750–764, 2018.

[5]D. E. Gault, "A correlation of low-speed, airfoil-section stalling characteristics with reynolds number and airfoil geometry," tech. rep., NACA TN No. 3963, 1957.

[6]I. Rodríguez, O. Lehmkuhl, R. Borrell, and A. Oliva, "Direct numerical simulation of a naca0012 in full stall," *International Journal of Heat and Fluid Flow*, vol. 43, pp. 194–203, 2013.

[7]W. Zhang, W. Cheng, W. Gao, A. Qamar, and R. Samtaney, "Geometrical effects on the airfoil flow separation and transition," *Computers & Fluids*, vol. 116, pp. 60–73, 2015.

[8]S. Hosseini, R. Vinuesa, P. Schlatter, A. Hanifi, and D. Henningson, "Direct numerical simulation of the flow around a wing section at moderate reynolds number," *International Journal of Heat and Fluid Flow*, vol. 61, pp. 117–128, 2016.

SESSION: Environmental and geophysical flows

Wednesday, April 10, 2024

16:20- 17:35

WORKSHOP
Direct and Large-Eddy Simulation 14
April 10-12 2024, Erlangen, Germany

DETAILED LES STUDY ON WIND GUSTS IMPACTING A HYPERBOLIC PARABOLOID STRUCTURE FROM DIFFERENT DIRECTIONS

G. De Nayer and M. Breuer
Professur für Strömungsmechanik,
Helmut-Schmidt-Universität, Hamburg, Germany
denayer@hsu-hh.de, breuer@hsu-hh.de

INTRODUCTION

Structures with hyperbolic paraboloid shapes were introduced in architecture by the lightweight pioneer Frei Otto [1] and are now widely used as large-span roofs for public facilities and eco-friendly buildings (Fig. 1). Immersed into the atmospheric boundary layer these *hypar* roofs are subject to gusty flows, which can lead to undesirable aerodynamic phenomena and in the worst case to structural damage and failure. Due to their specific shape the flow and the induced fluid forces highly depend on the wind direction as experimentally observed in [2]. The current paper presents a thorough LES investigation on discrete wind gusts of variable lengths and strengths impacting a hypar roof from three different wind directions. As a first step towards coupled fluid-structure interaction simulations, the roof is assumed to be rigid. The resulting flow structures and fluid forces are examined in detail.

Railway station roof in Warsaw.

Tent used as mobile roofing[1].

Figure 1: Examples of *hypar* roof structures.

RIGID HYPAR CASE

The geometry of the *hypar* case is composed of a four-corners roof with a square base of $L \times L = 6 \times 6$ m. The heights of the lower (B and D in Fig. 2) and higher (A and C) corners are $h = 2$ m and $2h = 4$ m, respectively. The hyperbolic paraboloid shape is symmetric with a shape parameter and a height-to-span ratio $\mathrm{SP} = \mathrm{HS} = h/(\sqrt{2}\ L) \approx 0.236$. The surface of the roof and the bottom ground wall, on which the structure is fixed, are considered to be ideally smooth.

In order to model the wind, the structure is immersed into a turbulent boundary layer characterized by a 1/7 power law. The thickness of the approaching boundary layer δ at the inlet of the computational domain is assumed to correspond to the height of the higher mast. The undisturbed flow above the boundary layer has a free-stream velocity of $u_\infty = 10$ m/s

[1] http://tensinet.com/index.php/component/tensinet/?view=project&id=4493

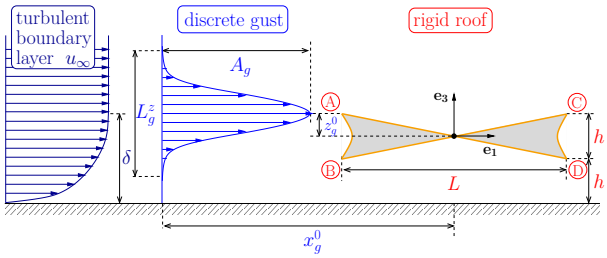

Figure 2: Description of the hypar case for $\alpha = 45°$.

(i.e., 36 km/h). Under standard atmospheric conditions ($\vartheta = 20°$ C), the Reynolds number based on the width of the roof and u_∞ is $\mathrm{Re}_L \approx 4$ million. The Mach number remains low ($\mathrm{Ma} \leq 0.03$), permitting the assumption of an incompressible flow. Furthermore, the fluid is considered to be isothermal.

The main flow direction is defined by the angle α between the wind direction and the straight line connecting the two low corners of the roof (B and D). In other words, $\alpha = 0°$ defines the case, where the wind direction is aligned with the two low corners. Contrarily, $\alpha = 90°$ fixes the wind direction along the two high corners (A and C). Presently, wind directions of $\alpha = 0°$, 45° and 90° are taken into account.

In the current study the assumed short-term highly dynamic wind events are described as deterministic discrete gusts using mathematical functions which represent its velocity over time. This procedure offers the advantage to have full control on the shape, amplitude and position of the gust during the injection phase and thus, on the impact on the structure. Following the IEC Standard (2002), the form of the gusts corresponds to the Extreme Coherent Gust (ECG) shape also known as 1-cosine gust. Three main parameters are used to vary the appearance of the gust. The first is the gust strength A_g. Since the gusts are injected in the same direction as the main wind direction, it means that the streamwise velocity in the region of the gust injection raises approximately according to $u_1^{max}/u_\infty = 1 + A_g/u_\infty$. In the present study gusts with values of $0.5 \leq A_g/u_\infty \leq 1.5$ corresponding to gust strength from *near gale* to *storm* are considered. The second main parameter is the size of the gust which varies in the interval $0.5 \leq L_g/L \leq 1.5$. The distance of the gust from the ground z_g^0 is the third main parameter of relevance for the structural response. Here, it is varied between $-1/6 \leq z_g^0/L \leq 1/3$.

COMPUTATIONAL FRAMEWORK AND SETUP

The turbulent flow is predicted by the large-eddy simulation (LES) technique using the finite-volume fluid solver FASTEST-3D [3]. The discretization is based on a curvilinear, block-structured body-fitted grid with a collocated variable arrangement. The filtered Navier-Stokes equations are solved by a semi-implicit predictor-corrector scheme. This projection method combined with standard discretization methods (midpoint rule and blended central scheme, 3% upwind) leads to a solver of second-order accuracy in time and space. A classical subgrid-scale model is applied to take the non-resolvable small scales into account, i.e., the standard Smagorinsky model with $C_s = 0.1$ and Van-Driest damping near solid walls. The discrete wind gusts are injected within the computational domain by adding a source term to the momentum equation following the technique introduced in [4].

Numerical predictions are carried out on a block-structured grid of 180 millions CVs following the wall-resolved LES recommendations. The grid was originally generated for the 45° case, since it was easier to obtain a high-quality grid for this configuration. In order to generate the computational grids for the two other wind directions, the roof structure is rotated by an angle of ±45°. The surrounding grid is then adapted using a hybrid mesh adaption technique combining inverse distance weighting and transfinite linear interpolation [5].

SOME FIRST RESULTS

Figure 3 depicts the key instantaneous flow characteristics for the three wind directions for the case without a gust. Using iso-surfaces of the dimensionless Q-criterion the different vortical structures are visible: In the 0° case, two conical vortices develop along the lower side of the roof from the lower corner at the front (B). No tip vortices are generated from both left and right corners. For the 45° configuration, the roof in the vicinity of each corner acts like an inclined airfoil on the flow and four tip vortices are formed. Astonishingly, these four tip vortices all rotate in the same direction. It should also be mentioned that both tip vortices induced at the front corners (A and B) are straight and less disturbed compared to those at the backside. The 90° setup presents conical vortices from the higher corner (A) at the front similar to the $\alpha = 0°$ case, but they develop on the upper side as visible in Fig. 3.

In civil engineering, the pressure distribution on the roof and the resulting fluid forces are particularly relevant. Figure 4 compares the time histories of the streamwise (c_x) and vertical (c_z) force coefficients for the three wind directions. In the 45° case, c_x is nearly constant. It increases about 10% and 18% for the 0° and 90° setups, respectively. c_z is close to 0 for the 45° case, which is due to the antisymmetry of the structure. However, for 0° the hypar shape leads to a strong increase of c_z up to 1.5. Due to the opposite shape, c_z is about -1.5 in the 90° configuration, which represents a strong downward directed force. Moreover, the force coefficients resulting from a strong gust with a strength of $A_g/u_\infty = 1.5$, a length of $L_g^x/L = 1$ and a cross-wise extension $L_g^y/L = L_g^z/L = 0.5$ are included in Fig. 4. For the three wind directions the gust is injected at $y_g^0 = 0$ and $z_g^0 = 0$, so that it impacts the middle of the roof. A rise up to 130% can be observed in c_x and c_z, with a remarkable change from downward to upward direction observed for the vertical force coefficient c_z.

The present work is a first step of ongoing investigations towards the fluid-structure interaction occurring on the flexible membranous counterpart of the *hypar* structure.

$\alpha = 0°$

Wind oriented from B to D.

$\alpha = 45°$

Wind perpendicular to AB.

$\alpha = 90°$

Wind oriented from A to C.

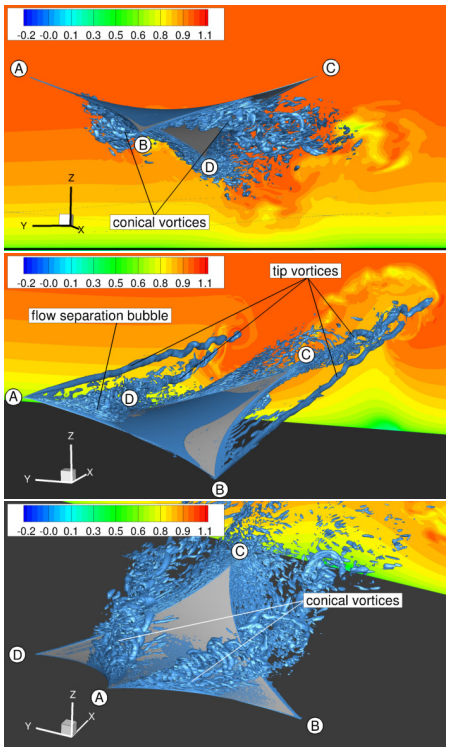

Figure 3: Key flow characteristics visualized by iso-surfaces (Q-criterion) and the dimensionless streamwise velocity in a crosswise y-z–plane for different wind directions without gust.

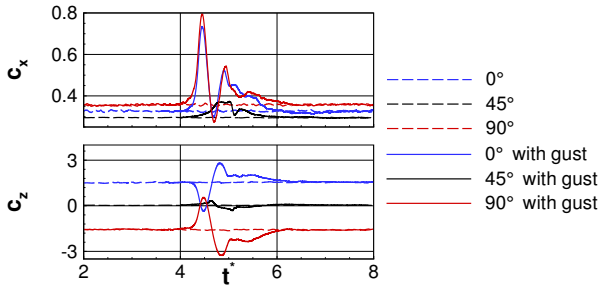

Figure 4: Streamwise c_x and vertical c_z force coefficients for the three different wind directions with and without gust.

REFERENCES

[1] Meissner, I.: Frei Otto – Forschen, Bauen, Inspirieren. München, Detail - Inst. für Internat. Architektur-Dokumentation, (2015).

[2] Dong, X. and Ye, J.: The point and area-averaged wind pressure influenced by conical vortices on saddle roofs. *J. Wind Eng. Indust. Aerodyn.* **101**, 67–84 (2012).

[3] Breuer, M., De Nayer, G., Münsch, M., Gallinger, T., Wüchner, R.: Fluid-structure interaction using a partitioned semi-implicit predictor-corrector coupling scheme for the application of large-eddy simulation. *J. Fluids Structures* **29**, 107–130 (2012).

[4] De Nayer, G. and Breuer, M.: A source-term formulation for injecting wind gusts in CFD simulations. *J. Wind Eng. Indust. Aerodyn.* **207**, 104405 (2020).

[5] Sen, S., De Nayer, G., Breuer, M.: A fast and robust hybrid method for block-structured mesh deformation with emphasis on FSI-LES applications. *Int. J. Numer. Methods Eng.* **111** (3), 273–300 (2017).

WORKSHOP
Direct and Large-Eddy Simulation 14
April 10-12 2024, Erlangen, Germany

INVESTIGATING THE FLOW OVER DIFFERENT CANOPIES CONSISTING OF HIGHLY FLEXIBLE BLADES

Bastian Löhrer, **Jochen Fröhlich**
Institute of Fluid Mechanics
Technische Universität Dresden, Germany
bastian.loehrer@tu-dresden.de

INTRODUCTION

A recently developed own numerical method is employed to investigate interactions between model vegetation canopies constituted of highly flexible elements and the surrounding turbulent channel flow. The densely arranged vegetation elements of a canopy form a body of low-momentum fluid, interacting with the surrounding flow. By varying the length of the canopy elements and the density of their positioning, the influence of these parameters is investigated.

PHYSICAL MODEL

Figure 1 gives an impression of the studied cases, where (a) features a model vegetation layer made up of relatively long blades, measuring $L = 1.6H$, where H is the height of the channel. In a second configuration (b) the blades are shorter, measuring $L = 0.64H$. The same blades are employed in a third case (c), but here the streamwise spacing ΔS_x between their points of fixation is reduced compared to (a) and (b), such that the foliage area of (c) is identical to that in the base configuration (a). The overall problem can be characterized by a set of dimensionless numbers. The Cauchy number (a) $Ca \approx$ 25,000, (b, c) $Ca \approx 1600$ and the buoyancy number (a) $B \approx$ 145, (b, c) $B \approx 9$ both indicate high flexibility of the blades, i.e., nominal drag and lift forces outweighing elastic restoring forces. The bulk-velocity Reynolds number is $Re_H \approx$ 20,064, based on the channel height H. The roughness density λ is defined as the ratio of the mean frontal area of a structure divided by its share of the bed area [1]. A value well above 0.1 indicates a dense canopy [2], which is met in the present cases, with $\lambda \approx 0.56$, 0.31 and 0.84, respectively.

NUMERICAL METHOD

The configurations were simulated using the in-house code PRIME developed at TU Dresden [3], [4]. It solves the Navier-Stokes equations for incompressible fluid employing a second-order finite volume approach on a staggered Cartesian grid and the Smagorinsky model to represent the sub-grid scale contribution. The motion of the flexible structures was computed with a finite-difference approach, using a geometrically exact Cosserat rod model [5]. Collisions were treated based on the model proposed in [6], with several technical enhancements. Coupling between fluid and structures was established with a dedicated Immersed-Boundary Method of [4].

The base configuration (a) was inspired by an experiment conducted at the University of Lyon [7]. The computational domain measures $L_x \times H \times L_z = 9.2\,H \times H \times 4H$, and contains (a,b) 672, (c) 1680 blades. Periodic boundary conditions were applied in the horizontal directions, a free-slip condition was imposed at $y = H$, and a no-slip condition was enforced at the bottom ($y = 0$) wall. The flow was driven by a spatially constant volume force which was adjusted in time to maintain the desired flow rate.

RESULTS

Characteristics of flow and canopy motion were extracted by means of time averages, including Reynolds stresses. Quadrant analyses give access to sweep and ejection events which are linked to low- and high-speed velocity streaks. The canopy envelope is constructed by projecting the Lagrangian information associated with the canopy blades onto a horizontal plane. In this framework, frequency and wavenumber spectra of the canopy envelope are readily computable, spatial and temporal correlations can be determined using the same tools as applied to the fluid data. The fluid-canopy interaction was studied through cross correlations between the two, and by collecting conditional fluid averages when following certain patterns in the canopy hull.

The contribution will shed light on the interplay of a vegetation canopy and the surrounding turbulent flow, building upon previous investigations [7], [8].

ACKNOWLEDGEMENTS

This work was funded by the French-German ANR-DFG project ESCaFlex (ANR-16-CE92-0020, DFG grant 634058).

The authors gratefully acknowledge the computing time provided to them at the NHR Center NHR4CES at RWTH Aachen University (project number p0020399) and at the Center for Information Services and HPC (ZIH) at TU Dresden. This is funded by the Federal Ministry of Education and Research, and the state governments participating on the basis of the resolutions of the GWK for national high performance computing at universities (`www.nhr-verein.de/unsere-partner`).

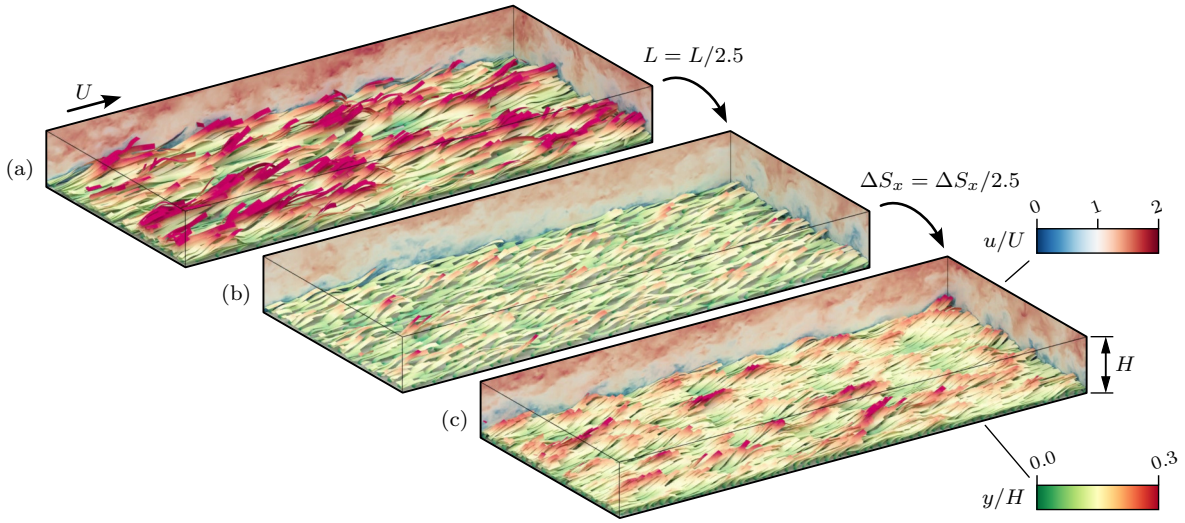

Figure 1: Illustration of the three physical models investigated, showing snapshots of the numerical solution. (a) Base configuration; (b) derived configuration with shorter blades; (c) derived configuration with shorter, but also more densely placed blades.

REFERENCES

[1] R. A. Wooding, E. F. Bradley, and J. K. Marshall, "Drag due to regular arrays of roughness elements of varying geometry," *Boundary-Layer Meteorology*, vol. 5, no. 3, pp. 285–308, 1973.

[2] H. M. Nepf, "Flow and Transport in Regions with Aquatic Vegetation," *Annual Review of Fluid Mechanics*, vol. 44, pp. 123–142, 2012.

[3] T. Kempe and J. Fröhlich, "An improved immersed boundary method with direct forcing for the simulation of particle laden flows," *Journal of Computational Physics*, vol. 231, no. 9, pp. 3663–3684, 2012.

[4] S. Tschisgale and J. Fröhlich, "An immersed boundary method for the fluid-structure interaction of slender flexible structures in viscous fluid," *Journal of Computational Physics*, vol. 423, p. 109 801, 2020.

[5] S. S. Antman, *Nonlinear Problems of Elasticity* (Applied Mathematical Sciences), red. by F. John, J. E. Marsden, and L. Sirovich. New York, NY: Springer New York, 1995, vol. 107.

[6] S. Tschisgale, L. Thiry, and J. Fröhlich, "A constraint-based collision model for Cosserat rods," *Archive of Applied Mechanics*, vol. 89, no. 2, pp. 167–193, 2019.

[7] B. Löhrer, L. G. de la Rochère, D. Doppler, S. Puijalon, and J. Fröhlich, "Simulation of the turbulent flow over a canopy of highly flexible blades," in *Proceedings of TSFP12*, Osaka, Japan (online), 2022.

[8] S. Tschisgale, B. Löhrer, R. Meller, and J. Fröhlich, "Large eddy simulation of the fluid–structure interaction in an abstracted aquatic canopy consisting of flexible blades," *Journal of Fluid Mechanics*, vol. 916, A43, 2021.

WORKSHOP
Direct and Large-Eddy Simulation 14
April 10-12 2024, Erlangen, Germany

BREAKDOWN OF OPTIMAL PERTURBATIONS IN THE HYDRO-MAGNETIC PIPE FLOW

Y. Velizhanina[1] **and B. Knaepen**[1]
[1]Physique des Systèmes Dynamiques, Faculté des Sciences
Université Libre de Bruxelles, 1050 Ixelles, Belgium
bernard.knaepen@ulb.be

INTRODUCTION

Stability of magnetohydrodynamic (MHD) flows is of major importance for various applications such as metallurgy, semiconductor crystal growth and fusion. For instance, in a tokamak fusion reactor, liquid metal blankets are strategically positioned behind the vessel's first wall. These blankets serve dual purposes: acting as a heat exchanger and producing tritium essential for sustaining the fusion reaction. Such blankets consist of an assembly of pipes and ducts where the liquid metal is circulated in the presence of a strong magnetic field. Instabilities and turbulence, contingent on flow parameters, can notably influence mass, momentum, and heat transfer in these MHD flows, thereby potentially altering the performance of the blanket system.

MECHANISMS OF INSTABILITY

Our study investigates the transition from laminar to turbulent flow in magnetohydrodynamic (MHD) pipes under the influence of a transverse magnetic field in the low magnetic Reynolds number regime. In this configuration, the magnetic field modifies the base flow by introducing inhomogeneities and thin boundary layers. In a previous work we have found that in the case of an electrically conducting pipe, this may lead to linear instabilities due to the presence of inflection points in the base velocity profile [1]. This is in contrast with the hydrodynamic pipe flow which is believed to be linearly unconditionally stable. Here we complement this study and investigate an alternative mechanism of transition to turbulence, focused on short-time amplification of initially small disturbances [2].

OPTIMAL TRANSIENT GROWTH

In the first part of the work presented here, we conduct a parametric study to identify the optimal perturbations of the flow. These are the perturbations leading to the largest transient growth at subcritical Reynolds numbers and are essential to shed light on the stability of parallel shear flows. They can be identified by computing the largest singular values of the propagator of the linearized system of MHD equations. Figure 1 presents an example of optimal perturbations, showcasing contours of axial velocity in a cross-sectional plane of the pipe. A comparison is made between the purely hydrodynamic and magnetohydrodynamic (MHD) cases at a Reynolds number of 5000. In the MHD case, the Hartmann number -

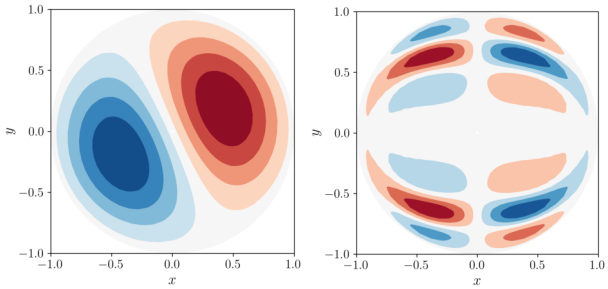

(a) $Ha = 0$ (b) $Ha = 10$

Figure 1: Contours of the axial velocity of the global optimal perturbation. a) Hydrodynamic case; b) MHD case.

which is proportional to the intensity of the magnetic field - is equal to 10. From this figure we observe that in the presence of the magnetic field, oriented in the x-direction, the perturbation's structure is significantly affected as it becomes elongated in the direction of the magnetic field and confined within the side layers of the flow.

NONLINEAR EVOLUTION OF OPTIMAL PERTURBATIONS

In the second part of this work we study the nonlinear evolution of the computed optimal perturbations. This is done by performing direct numerical simulations in which the initial conditions consist of the base laminar MHD velocity profile $U\mathbf{1}_z$ superposed with optimal perturbations $\mathbf{u}'$ of varying amplitudes,

$$\mathbf{u} = U(\mathbf{x})\mathbf{1}_z + \sqrt{\epsilon_0}\mathbf{u}'(\mathbf{x}, t) \tag{1}$$

where ϵ_0 is the initial kinetic energy of the perturbation. The objective of these simulations is to observe the non-linear deformation of the perturbations and the possible secondary instability mechanisms. By varying the initial kinetic energy of the perturbations we also determine the smallest values of ϵ_0 to trigger the transition to a turbulent flow. This is illustrated in figure 2 where we plot some sample results for the case $Re = 5000$ and $Ha = 5$. We observe that for $\epsilon_0 \lesssim 10^{-3}$ the flow returns to the laminar base state after an initial transient amplification of the perturbation except when some random 3D noise is added in the initial condition. For $\epsilon_0 \gtrsim 10^{-3}$ the flow transitions to a turbulent state that is maintained throughout the times considered.

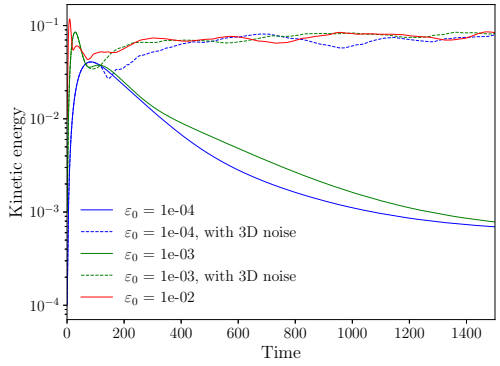

Figure 2: Nonlinear evolution of kinetic energy of the optimal perturbation for $Re = 5000$ and $Ha = 5$.

Our direct numerical simulations are performed using the non-linear finite volume solver YALES2 [3]. To avoid creating by hand a suitable grid tailored to capture the evolution of the optimal perturbations for each value of the parameters we use the dynamic grid adaptation capabilities provided in YALES2 through the mmg3d library described in [4].

REFERENCES

[1] Velizhanina, Y. and Knaepen, B. : On the instability of the magnetohydrodynamic pipe flow subject to a transverse magnetic field, *Phys. Fluids*, **35**, 044112 (2023).

[2] Trefethen, L. N. *et al* : Hydrodynamic Stability Without Eigenvalues. *Science*, **261**, 578–584 (1993).

[3] Moureau, V. and Domingo, P. and Vervisch, L. : Design of a massively parallel CFD code for complex geometries, *C. R. Méc.*, **339**, 141(2011).

[4] Dapogny C. and Dobrzynski C. and Frey P. : Three-dimensional adaptive domain remeshing, implicit domain meshing, and applications to free and moving boundary problems C. Dapogny, C. Dobrzynski and P. Frey, *J. Comput. Phys.*, **262**, 358–378 (2014).

WORKSHOP
Direct and Large-Eddy Simulation 14
April 10-12 2024, Erlangen, Germany

TRANSITIONAL AND TURBULENT FLOW AROUND A STEPPED CYLINDER

D. Massaro[1], A. Peplinski[1], P. Schlatter[1,2]
[1]SimEx/FLOW, Engineering Mechanics
KTH Royal Institute of Technology, Stockholm, Sweden
[2]Institute of Fluid Mechanics (LSTM)
Friedrich–Alexander–Universität (FAU) Erlangen–Nürnberg, Germany
dmassaro@kth.se

INTRODUCTION

The flow around a stepped cylinder, namely two cylinders with different diameters joined at one extremity, is investigated through direct numerical simulations at various Reynolds numbers. The adaptive mesh refinement technique is also employed to measure the committed error and automatically adapt the mesh. Indeed, the sharp junction discontinuity requires a very high resolution to capture the smallest scales and with, a conforming mesh, we would need to extend such a resolution in the far field. A global overview of the flow evolution is provided. First, we perform a global stability analysis for four different diameter ratios ($r = 1.1, 1.2, 2, 4$) to study the origin of the different wake cells. Then, we focus on a single ratio ($r = 2$) to investigate the turbulent regime with a stable and unstable cylinder shear layer.

Previous authors reported different vortex interaction modes defining a direct and indirect interaction for the range $1.14 < D/d < 1.76$ [1]. In the indirect interaction, the wake develops in three distinct regions labelled as the S and L cells behind the small and large cylinder [2], and the modulation cell N in the middle. The frequency hierarchy is as follows: $f_S > f_L > f_N$. However, the origin of the three cells remains unclear. Thus, a global stability analysis has been conducted and presented here.

Dunn and Tavoularis [2] not only classified the three wake cells at different Reynolds numbers (ranging from $Re_D = 63$ to $Re_D = 1100$) but also investigated their interaction at $D/d = 2$ and $Re_D = 150$. They identified a stable S-N cell boundary with a spanwise layer deflection toward the large cylinder and an unstable N-S interface, where the connection interruption occurred at a beat frequency of $f_S - f_N$. In the laminar regime, this has been confirmed by several studies. However, there is a growing need for investigations at higher Reynolds numbers to determine the validity of these laminar observations. To offer insights into the turbulent regime, our earlier simulation at $Re_D = 1000$ was the first to study a stable cylinder shear layer and a turbulent wake [5]. We focus on uncovering the origin of the modulation cell and understanding the downwash effect. These findings introduce a new perspective on the downwash phenomenon. Then, we extend our investigations by conducting a DNS at $Re_D = 5000$, entering a fully turbulent wake regime characterised by an unstable shear layer [6]. We analyse the coherent structures around the cylinder and describe the vortical eddies behind the junction. The results are in good agreement with the work by Tian et al. [10]. Employing proper orthogonal decomposition (POD), we decompose the flow into spatial and temporal dependencies, extracting the large-scale structures within the wake.

ADAPTIVE NUMERICAL FRAMEWORK

Direct numerical simulations are performed using the open-source code Nek5000 [3]. Nek5000 is a highly scalable and portable code based on the spectral element method (SEM) by Patera [9], offering minimal dissipation and dispersion. The SEM can be seen as a high–order finite element method (FEM) where the solution is represented by Lagrangian interpolants integrated over Gauss-Lobatto-Legendre points (GLL) and Gauss-Legendre (GL) points for the velocity and pressure field, respectively. The $P_N - P_{N-2}$ formulation is used. The time integration in Nek5000 relies on third-order backward differentiation (BDF), treating the advective term explicitly through an extrapolation (EXT) formula.

Our group implemented, validated and used the adaptive mesh refinement (AMR) technique in Nek5000 [4]. AMR incorporates two primary elements: error measurement and refinement strategy. Error estimation is evaluated through indicators derived from the current solution or estimators derived from alternative solutions, such as the adjoint problem. The refinement strategy consists of isotopically splitting the elements, h–type refinement. To identify the elements whose resolutions need to be improved, the spectral error indicator is used. The spectral error indicator (SEI) was introduced by Mavriplis [8]. For a 1D problem, where u is the exact solution to a system of partial differential equations and u_N is an approximate spectral-element solution with polynomial order N, the SEI is estimated as follows. Let expand $u(x)$ on a reference element in terms of the Legendre polynomials:

$$u(x) = \sum_{k=0}^{\infty} \hat{u}_k L_k(x) \tag{1}$$

where $\hat{u}_k$ are the associated spectral coefficients and $L_k(x)$ is the Legendre polynomial of order k. The error on $\|u - u_N\|_{L^2}$ consists of two contributions: a truncation error due to the finite number of coefficients in the spectral expansion and the quadrature error. The estimated ϵ results in:

$$\epsilon = \left(\int_{N+1}^{\infty} \frac{\hat{u}(k)^2}{\frac{2k+1}{2}} dk + \frac{\hat{u}_N^2}{\frac{2N+1}{2}} \right)^{\frac{1}{2}} \tag{2}$$

In the current study, the SEI is calculated for the different solution fields, according to the regime under investigation. For example, in the global stability analysis, the SEI is estimated for the linear direct and adjoint velocity perturbation fields. In this way, independent meshes can be designed, minimising the committed truncation and quadrature errors. In contrast, for the turbulent flow, the velocity field is used. The refinement process is stopped when the smallest spatial scales are captured.

GLOBAL STABILITY ANALYSIS

The global stability analysis of the three-dimensional flow around a stepped cylinder is presented here for the first time. We have studied the linear evolution for infinitesimal perturbations for the direct and dual problems in three different configurations: $r = 1.1, 1.2, 2, 4$. The AMR was used to design different meshes to reduce the committed truncation and quadrature errors. For the base flow, the linear direct and dual operators, we obtain three non-conforming and independent meshes. This is repeated for each Reynolds number and diameter ratio [7].

The global stability analysis reveals that independently of r, the first cell that undergoes a Hopf bifurcation is always the large cylinder (L). However, the sequence of their transitions depends on the parameter r. For $r = 1.1, 1.2$, the small cylinder (S cell) represents the second unstable mode, whereas, for $r > 1.2$, the modulation region gets unstable first. The three cells in the wake are observed for any r. The non-linear results support this finding, in contrast with the previous classification of the laminar vortex shedding in direct (L-S) and indirect (L-N-S) modes interaction based on r [1].

The unstable direct and dual eigenmodes are three-dimensional eigenvectors, resembling in the L cell the globally unstable mode found in flow past a circular cylinder at $Re_{D,cr} \approx 47$. The structural sensitivity analysis shows that the wavemaker region corresponds to two symmetrically placed lobes across the separation bubble. Furthermore, the angular frequencies of the eigenvalues closely match the oscillatory states observed in the non-linear DNS ($St \approx 0.11$).

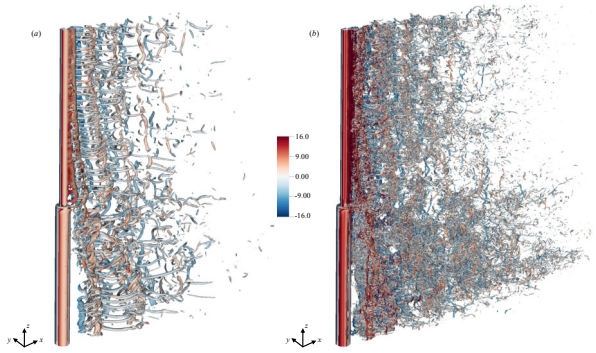

Figure 1: Instantaneous λ_2 structures coloured with the vertical vorticity component in the wake at (a) $Re_D = 1000$ ($\lambda_2 = -4\ U^2/D^2$) and (b) $Re_D = 5000$ ($\lambda_2 = -40\ U^2/D^2$). The figure is adapted from Massaro et al. [5].

INVESTIGATION OF THE TURBULENT REGIME

When Reynolds number increases, first, the wake gets turbulent, but with a stable shear layer ($Re_D = 1000$), and, then, the cylinder shear layer transitions as well ($Re_D = 5000$). These two different flow regimes are discussed here, highlighting their differences. In particular, for the subcritical regime ($Re_D = 1000$), the downwash mechanism and its connection with the modulation region (N) cell is explained [5].

The three-dimensional proper orthogonal decomposition (POD) is used for extracting the large-scale structures. The POD confirms the presence of 3 cells in the wake for both Reynolds numbers: the L, S and N with vortex shedding frequencies $f_L \approx 0.20, f_S \approx 0.41$ and $f_N \approx 0.18$ respectively. They correspond to the three most energetic travelling modes in the POD expansion. The analogy with the flow at the low Reynolds number is remarkable and allows us to claim that the three cells in the stepped cylinder wake are a general feature for a wide range of Reynolds numbers (at least up to $Re_D = 5000$). We expect that such a triad of structure is persistent even at higher Reynolds numbers. Indeed, the ratio between f_N/f_L, which are the shedding frequencies of the two cells coexisting behind the large cylinder, shows a diverging trend proportional to $\sim Re_D^{-0.031}$.

In contrast to the subcritical regime [5]: as Re_D increases, the downwash mode is less significant and the modulation region is more energetic. Overall, the three L, S and N travelling modes get more energetic and separate from all the other modes in the POD spectrum.

REFERENCES

[1]Lewis, C. G. and Gharib, M. : An exploration of the wake three dimensionalities caused by a local discontinuity in cylinder diameter, *Phys. Fluids*, **4**, 104-117, (1992)

[2]Dunn, W. and Tavoularis, S. : Experimental studies of vortices shed from cylinders with a step-change in diameter, *J. Fluid Mech.*, **555**, 409–437, (2006)

[3]Fischer, P. and Lottes, J. and Kerkemeier, S. : Nek5000: open source spectral element CFD solver diameter, *http://nek5000.mcs.anl.gov*, (2008)

[4]Offermans, N. and Massaro, D. and Peplinski, A. and Schlatter, P. : Error-driven adaptive mesh refinement for unsteady turbulent flows in spectral-element simulations, *Comput. Fluids*, **251**, 105736, (2023)

[5]Massaro, D. and Peplinski, A. and Schlatter, P. : The flow around a stepped cylinder with turbulent wake and stable shear layer, *J. Fluid Mech.*, **977**, A3, (2023)

[6]Massaro, D. and Peplinski, A. and Schlatter, P. : Coherent structures in the turbulent stepped cylinder flow at $Re_D = 5000$, *Int. J. Heat and Fluid Flow*, **102**, 109144, (2023)

[7]Massaro, D. and Schlatter, P. : Global stability of the flow past a stepped cylinder *(Under Review)*, (2023)

[8]Mavriplis, C. : Nonconforming Discretizations and a Posteriori Error Estimators for Adaptive Spectral Element Techniques, *PhD Thesis*, (1989)

[9]Patera, A. T. : A spectral element method for fluid dynamics: laminar flow in a channel expansion, *J. Comput. Physics*, **54**, 468-488, (1984)

[10]Tian, C. and Jiang, F. and Pettersen, B. and Andersson, H. I. : Vortex system around a step cylinder in a turbulent flow field, *Phys. Fluids*, **33**, 045112, (2021)

WORKSHOP
Direct and Large-Eddy Simulation 14
April 10-12 2024, Erlangen, Germany

EXPLORATION OF GEOSTROPHIC TURBULENCE ON A ROTATING SPHERE

A.D. Franken[1], E. Luesink[1], S.R. Ephrati[2], B.J. Geurts[1,3]
[1]Mathematics of Multiscale Modeling and Simulation University of Twente, The Netherlands
[2]Department of Mathematical Sciences, Chalmers University of Technology, 412 96 Gothenburg, Sweden
[3]Multiscale Physics, Center for Computational Energy Research, Department of Applied Physics, Eindhoven University of Technology, Eindhoven, The Netherlands
a.d.franken@utwente.nl

INTRODUCTION

In the fields of oceanography and meteorology, the primary dynamical framework for understanding large-scale flows is provided by geostrophic theory. Given the shallowness of the fluid domain compared to the horizontal length scales involved, planetary flows at macroscopic scales, are predominantly influenced by the Coriolis force due to rotation and hydrostatic pressure forces. This equilibrium, the geostrophic balance, forms the basis for understanding dominant flow structures on a planetary scale. When fluid dynamics on a rotating sphere are expressed as a perturbation around this balance, we find the quasigeostrophic equations (QGE).

The study of the QGE forms the basis for our understanding of mid-latitude oceanic and atmospheric dynamics. Typically, they are formulated on a midlatitude β-plane, representing a Cartesian tangent plane to the sphere where the Coriolis parameter is approximated to have a linear dependence on latitude. While this approach has been instrumental in identifying key dynamical features of planetary flows, it cannot take into account the influence of the equatorial region as the β-plane approach cannot be applied to the equator.

In 2009, a fully spherical version of the quasi-geostrophic theory was reintroduced into the scientific community independently by Verkley [1] and Schubert et al. [2]. These equations provide the global dynamics of a shallow fluid layer on a rotating sphere in terms of a single prognostic variable, called the potential vorticity (PV). In this formulation, not only is energy globally preserved, but any function of PV is globally conserved. However, simulating these equations poses challenges, as PV cascades to smaller scales. Typically, numerical schemes introduce (hyper-)viscosity to prevent the buildup of PV at the smallest resolved scales in simulations, thereby compromising the conservation of both energy and global PV.

Recently, a numerical scheme was developed for these equations [3] that conserves all resolved constants of motion by making use of the geometric structure of the equations. This allows for very long-time simulations of global geostrophic turbulence without the need for specific turbulence forcing or the additions of artificial dissipation. In this work, we analyse the energy spectrum of the resulting flow, as well as quantitatively investigate the emergence of strong zonal jets up to the critical latitude.

QUASI-GEOSTROPHIC EQUATIONS ON THE SPHERE

In its most general form, the QGE include the buoyancy force resulting from a small vertical density stratification. Since vertical velocities are neglected in the shallow water approximation, the effect of buoyancy appears as a PV source based on the local relative buoyancy difference. In the case of stable stratification, i.e., the density gradient is strictly negative, a finite difference approximation is usually taken in the radial direction, leading to the multilayer QGE. In this model, the fluid is assumed to be composed of several layers of uniform density that are each described by a two-dimensional PV field. When density gradients are sufficiently small, or one only considers a single layer on top of a deep basin, the model reduces to the single-layer QGE. This is the model we consider in this work, although the methodology can be extended to the multilayered model.

We consider a fluid layer of uniform density and average thickness H on a sphere of average radius a rotating with angular velocity Ω, with bottom topography given by $b(\mathbf{x})$. We assume the fluid layer to be shallow compared to the radius of the sphere. Under the additional assumption that the pressure is roughly hydrostatic, vertical motion is small compared to the horizontal velocity field, and the resulting horizontal velocity field $\mathbf{u}$ can be written in terms of a streamfunction ψ such that $\mathbf{u} = \mathbf{r} \times \nabla\psi$. The potential vorticity q is a Lagrangian invariant, so its evolution is given by

$$\dot{q} + \mathbf{u} \cdot \nabla q = 0 \tag{1}$$

where the PV is given by

$$q = f + \Delta\psi + \gamma f^2 \psi - f\frac{b}{H} \tag{2}$$

Here, $f = 2\Omega \sin\phi$ is the Coriolis parameter with ϕ the latitude, and $\gamma = 4a^2\Omega^2/gH$ is the Lamb parameter which measures the relative strength of the Coriolis term with g being the gravitational acceleration. Note that the velocity field can be calculated directly from the streamfunction, which in turn can be calculated by solving the inverse problem in equation (2). Since these equations include the full Coriolis parameter, the system can be solved on the sphere, which allows for global simulations of quasigeostrophic turbulence.

APPLICATION TO GEOSTROPHIC TURBULENCE

As mentioned in the introduction, in [3], a numerical method is presented for solving the QGE on the sphere. Building on the work for the two-dimensional Euler equations in [4]

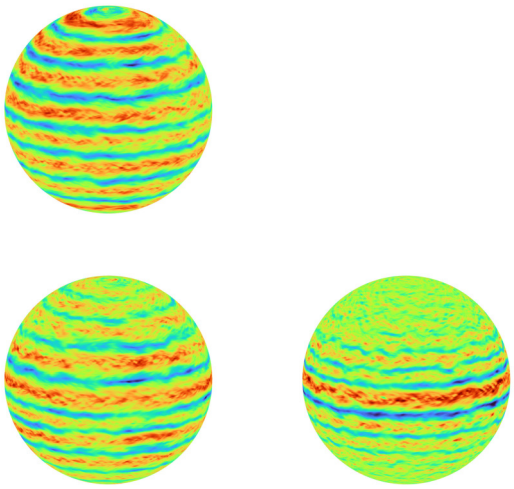

Figure 1: Zonal velocity of statistically stationary geostrophic turbulence at $\gamma = 0$ (top), $\gamma = 10^3$ (bottom left) and $\gamma = 10^4$ (bottom right)

and later for the two-dimensional Navier-Stokes equation in [5], this method exactly preserves integrated polynomials of PV, and it shows no drift in the Hamiltonian.

Additionally, to simulate turbulence on the sphere, we can introduce homogeneous forcing at small scales as well as dissipative terms. These both take the form of forces on the right-hand side of equation (1). By denoting the advection map with $\Phi_{adv,h}$ and employing a second-order Crank-Nicolson scheme with the map $\Phi_{CN,h}$ on a time interval h, we can use second-order Strang splitting to arrive at the time-stepping scheme:

$$q^{n+1} = \left(\Phi_{CN,h/2} \circ \Phi_{adv,h} \circ \Phi_{CN,h/2}\right) q^n, \qquad (3)$$

where n is the time level.

We simulate this flow on a unit sphere rotating at $\Omega = 500$ at several values of the Lamb parameter with the trivial bottom topography. Note that in the limit where this parameter vanishes, surface height variations vanish, and the two-dimensional rotating Navier-Stokes equations are recovered.

In Figure 1, the velocity component in the zonal direction is visualized at a time where the flow has developed into a statistically stationary state for the cases $\gamma = 0$ (two-dimensional rotating Navier-Stokes) and for $\gamma = 10^3$ and $\gamma = 10^4$. These visualizations clearly show the formation of strong jets in the zonal direction in all cases. However, only the two-dimensional Navier-Stokes equation produces these jets at the poles. In geostrophic turbulence, the amplitude of the jets is modulated near the poles. As the case for which $\gamma = 10^4$ shows, there is a qualitative change between equatorial flow and flow near the poles, as jets do not dominate beyond a certain critical latitude.

The associated kinetic energy spectrum for the case where $\gamma = 0$ is shown in Figure 2. In all cases, the external forcing is centred at modes with $l = 100$. The spectrum clearly shows the double cascade for two-dimensional turbulence as shown by the dashed and dash-dotted lines. This indicates that, at small scales, the energy spectrum closely resembles that of homogeneous isotropic turbulence in two dimensions. However,

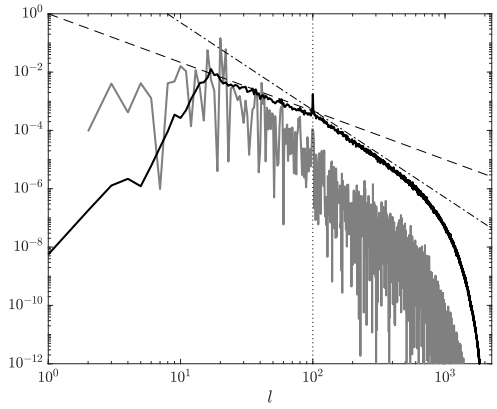

Figure 2: Kinetic energy spectra for the case $\gamma = 0$, corresponding to the rotating two-dimensional Navier-Stokes equations. The spectra are indexed using the spherical harmonics degree l and split into the zonal modes (for which $m = 0$) in gray and the non-zonal modes ($m \neq 0$) in black.

at large scales, rotation has a large influence on the spectrum. Most energy is contained in zonal modes, corresponding to zonal jet formation. For the geostrophic turbulence cases, similar spectra are available which clearly show that this model is fundamentally two-dimensional on small scales, as the same kinetic energy cascades are observed in the spectra. However, large-scale dynamics are strongly affected by the geostrophic balance, suggesting a qualitative transition in dynamics between the equatorial and polar regions. This also indicates that flow properties such as the energy spectrum or turbulent kinetic energy transfer rates should be computed locally, as global measures will not differentiate the large qualitative changes in flow structure over the domain.

OUTLOOK

In this work, a novel structure-preserving numerical method has been developed and employed to solve global planetary flow dynamics around the geostrophic balance. The results show that the single-layer quasi-geostrophic models show an energy spectrum closely related to two-dimensional turbulence. The geostrophic balance introduces a clear transition between equatorial and polar flow dynamics. With this global model, the critical latitude at which this transition occurs will be investigated further. Furthermore, this model can be extended to multiple layers. This allows us to include buoyancy effects, which will be the subject of further study.

REFERENCES

[1]Verkley, W. T. M.: A balanced approximation of the one-layer shallow-water equations on a sphere, *Journal of the atmospheric sciences*, **66(6)**, 1735-1748 (2009).

[2]Schubert, W. H., Taft, R. K., Silvers, L. G.: Shallow water quasi-geostrophic theory on the sphere, *Journal of Advances in Modeling Earth Systems*, **1(2)** (2009).

[3]Franken, A., Caliaro, M., Cifani, P., Geurts, B.: Zeitlin truncation of a Shallow Water Quasi-Geostrophic model for planetary flow. *arXiv preprint arXiv* **2306.15481** (2023)

[4]Modin, K., Viviani, M.: A Casimir preserving scheme for long-time simulation of spherical ideal hydrodynamics. *J. Fluid Mech.* **884**, A22 (2020)

[5]Cifani, P., Viviani, M., Modin, K.: An efficient geometric method for incompressible hydrodynamics on the sphere. *J. of Comp. Phys.* **472** 111772 (2023)

SESSION: Industrial and environmental applications I

Thursday, April 11, 2024

9:35- 10:50

WORKSHOP
Direct and Large-Eddy Simulation 14
April 10-12 2024, Erlangen, Germany

HIGH FIDELITY SIMULATIONS OF AIRBORNE VIRUS INACTIVATION IN A UV AIR PURIFIER: IMPACT OF VOLUMETRIC FLOW RATE AND UV RADIATION INTENSITY

S. Sankurantripati[1], **F. Duchaine**[1], **N. Francois**[2], **S. Marshall**[2]
[1]Computational Fluid Dynamics
CERFACS, France
[2]Computational Fluid Dynamics
VALEO, France
sankurantripati@cerfacs.fr

INTRODUCTION

The COVID-19 pandemic, caused by the pathogen Severe Acute Respiratory Syndrome Coronavirus-2 (SARS-CoV-2), emerged in 2019 and has spread globally. The virus is transmitted through three modes: surface/contact, droplet, and airborne. Airborne transmission is recognized as the dominant route [1]. Basic preventive measures like social distancing, sanitation, and face masks have reduced the spread of infection through contact and droplet transmission. To mitigate the infection risk due to the virus-laden droplets suspended in air, it is crucial to implement high-quality, scientifically peer-reviewed solutions. Ultraviolet Germicidal Irradiation (UVGI) stands as a proven and dependable technological solution for disinfecting microorganisms found in water or on surfaces. Introducing a portable UV air purifier (UVP) into an enclosed space represents a potential mitigation solution capable of enhancing the quality of the air. In this study, the disinfection properties of a UVP designed by VALEO to equip city buses are analyzed by numerical simulations. It is composed of axial fans, UV-C lamps, light traps and an electric tray as shown in 1. The research focuses on airborne virus inactivation using a multi-disciplinary solver, integrating Large Eddy Simulations (LES) for flow dynamics, Lagrangian particle tracking for airborne dispersion, and a UV radiation disinfection solver for assessing survival rates. The study explores varying purifier flow rates and UV lamp power to observe the survival rate of virus copies.

COMPUTATIONAL METHODOLOGY

Studying the survival rate of respiratory droplets inside an air purifier exposed to UV radiation and conducting a thorough evaluation entails extensive high fidelity computations over a prolonged physical time spanning from seconds to minutes leading to consumption of millions of computational hours. Therefore, air flow inside the purifier is first computed until the volume averaged kinetic energy is converged with time. As the impact of aerosol on the flow field is negligible, the resultant mean flow and turbulent characteristics are extracted and supplied to Lagrangian computations, where the mean air flow remains frozen, and only the particle dynamics are computed [2]. This one way Eulerian-Lagrangian approach is coupled with UV radiation and disinfection models that determine the survival of the viral copies. In the following sections, governing equations of each solver are detailed.

The in-house AVBP LES solver developed by CERFACS [3] that is used to solve the filtered compressible Navier-Stokes (NS) equations. This solver can run efficiently on massively parallel machines and could handle unstructured meshes. An explicit Lax Wendroff (LW) [4] numerical scheme, second order accurate in space and time, is used for convection terms and second order Galerkin scheme is used for diffusive terms in NS equations. The time step for the simulation depends on acoustic Courant Friedrichs Lewy number (CFL) which is set to $CFL = 0.9$. Wall adapting local eddy viscosity model (WALE) is selected to acquire sub-grid scale (SGS) viscosity. In Lagrangian framework, each respiratory droplet is modeled as an individual rigid sphere that consists of water, non-volatile matter (NA+, K+, Cl-, glycoprotein) along with virus copies. Interactions among particles are disregarded, but collisions between particles and walls are taken into account as inelastic collisions. From experimental studies on virus-laden droplets expelled due to sneezing and coughing, distribution of virus copies per droplet is modeled [5]. Abramzon-Sirignano (AS) model is elected to compute droplet evaporation process. Once the water mass is evaporated, the resulting matter is assumed to be spherical solid a.k.a droplet nucleus. Flow properties from Eulerian calculations are interpolated to the droplet's location and the forces acting on the droplet are computed. These forces are simplified to momentum transfer via drag forces using Schiller-Naumann correlation. Gravity forces on the particle are neglected. A simplified Langevin model is chosen to include the turbulent quantities into the Lagrangian calculations [2, 6]. The survival rate (S) of virus-laden aerosols when exposed to UV-radiation is determined using Chick-Watson model [7] which depends on susceptibility constant (k) of virus linked to the UV irradiation received by particles over time. For SARS-CoV-2, susceptibility constant in air medium is not available. Therefore, a decent estimate based on available data on airborne viruses [8], is considered for this current study ($k = 0.377 \pm 0.119 m^2/J$). Using thermal radiation view-factor model [9], UV irradiance received by a particle from a cylindrical UV lamp can be determined. To investigate the survival rate of virus copies within a single

respiratory droplet, the cumulative amount of UV radiation received by the droplet inside the purifier over it's exposure time is computed until it exits through the outlet fans.

NUMERICAL SETUP

An unstructured mesh comprising 49 million cells is used for computational investigations following mesh convergence studies. Three cases with volumetric flow rates (VFR) of 75, 100, and 150 m^3/hr are simulated by enforcing a constant mass flow rate at the inlet fans, maintaining a uniform temperature of 300 K, and setting the pressure outlet at the outlet fans to 1 atm. A body force approach is used to mimic swirl motion generated by axial fans. To take into account the temperature effects, the lamps are considered isothermal, no-slip conditions with a reference temperature of $T_{lamp} = 311$ K. The remaining walls are provided adiabatic, no-slip wall conditions. To mimic aerosols, injected particle size is assumed mono-disperse with a diameter of $50\mu m$ and viral load concentration of 2.35x10^9 copies/ml. Impact of UV lamp output power (W_l) on survival rate of virus copies is evaluated by changing $W_l = W_o$, $W_o/1.5$, $W_o/2$, $W_o/3$, $W_o/4$ and $W_o/6$ where $W_o = 13W$ for $k = 0.258, 0.377$ and $0.496 m^2/J$

RESULTS AND DISCUSSION

LES of UVP were conducted on the Irene-Rome supercomputers hosted at CEA under a GENCI allocation, requiring around 768,000 computational hours for flow field convergence and extraction of mean and turbulent quantities. In Figure 2, the instantaneous velocity distribution inside the purifier, along with particle dispersion, is presented. Upon entry through the inlet fans, the air undergoes swirling motion near the fan hub, forming a hollow disk-like stream profile with elevated transverse and axial velocities. The light traps near the inlet streamline the airflow towards the tray side, creating a recirculation zone on the opposite side, as indicated by iso-contour lines (u=0). These recirculation zones extend particle residence time, resulting in prolonged exposure to UV radiation. Figure 3 illustrates the virus inactivation rate over a 5-second interval achieved by the UVP under various UV radiation intensities and volumetric flow rates. As the VFR increases, more droplets undergo treatment within the 5-second interval, but their reduced residence time in the purifier results in a lower overall inactivation rate. A decrease in W_l from W_o to $W_o/6$ leads to an exponential reduction in the rate of inactivation. The susceptibility constant also exhibits a significant impact on the resulting inactivation rate. This parametric study facilitates the identification of an optimal configuration, where a higher number of particles can be treated within 5 seconds, using minimal UV lamp output power, aiming for a virus-inactivation rate of 95% for this UV air purifier.

REFERENCES

[1]R. Zhang, Y. Li, A. L. Zhang, Y. Wang, M. J. Molina, *Identifying airborne transmission as the dominant route for the spread of COVID-19*, *The COVID-19 Reader*, 2020, pp. 21–35, doi: 10.4324/9781003141402-3

[2]F. Duchaine, M. Cizeron, N. Odier, J. Dombard, S. Marshall, N. Francois, T. Poinsot, *High-performance CFD for respiratory droplet turbulent dispersion in a ventilated city bus*, *International Journal of Computational Fluid Dynamics*, 2021, **35**(9), pp. 758–777, doi: 10.1080/10618562.2021.1989421

[3]T. Schonfeld, M. Rudgyard, *Steady and unsteady flow simulations using the hybrid flow solver AVBP*, *AIAA Journal*, 1999, **37**(11), pp. 1378–1385, doi: 10.2514/2.636

[4]P. D. Lax, B. Wendroff, *Difference schemes for hyperbolic equations with high order of accuracy*, *Communications on pure and applied mathematics*, 1964, **17**(3), pp. 381–398, publisher: Wiley Online Library

[5]S. Anand, Y. S. Mayya, *Size distribution of virus-laden droplets from expiratory ejecta of infected subjects*, *Scientific reports*, 2020, **10**(1), p. 21174, publisher: Nature Publishing Group UK London

[6]P. Langevin, *Sur la théorie du mouvement brownien*, *C. R. Acad. Sci. Paris.*, 1908, **146**, pp. 530–533.

[7]H. Chick, *An investigation of the laws of disinfection*, *Journal of Hygiene*, 1908, **8**(1), pp. 92–158, doi: 10.1017/s0022172400006987

[8]C. B. Beggs, E. J. Avital, *Upper-room ultraviolet air disinfection might help to reduce COVID-19 transmission in buildings: A feasibility study*, *PeerJ*, 2020, **8**, doi: 10.7717/peerj.10196

[9]M. F. Modest, S. Mazumder, *Radiative heat transfer*, 2021, publisher: Academic Press

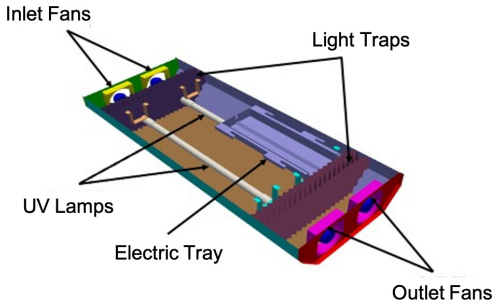

Figure 1: View of UV air purifier designed by VALEO.

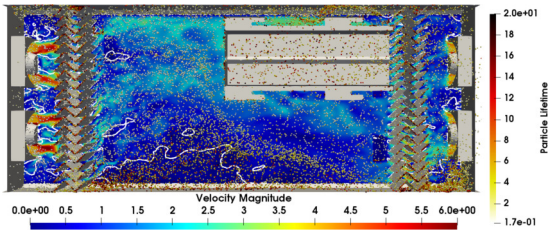

Figure 2: Instantaneous velocity magnitude contour on a longitudinal plane with iso-contour lines (u=0), accompanied by the dispersion of particles distinguished by their lifespan at a volumetric flow rate of 100 m^3/hr.

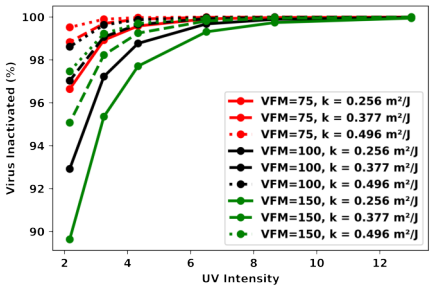

Figure 3: Overall Inactivation rate of this UVP in an interval of 5s by varying UV lamp power output and volumetric flow rate

WORKSHOP
Direct and Large-Eddy Simulation 14
April 10-12 2024, Erlangen, Germany

SCALE-RESOLVING SIMULATION OF MULTI-COMPONENT NOZZLE FLOWS

Philipp Oestringer[1]*, Dr. Steven Jöns[1], Prof. Andrea Beck[1]
[1]Institut für Aerodynamik und Gasdynamik (IAG)
Universität Stuttgart, Germany
* Corresponding author:
philipp.oestringer@iag.uni-stuttgart.de

INTRODUCTION

In this research project we aim to conduct scale-resolving simulations of hydrogen injection jets into air. In this way, an understanding and a capability to predict the complex physical properties of direct-injection of pressurized hydrogen gas into a volume of air, as it is required for a hydrogen combustion engine, shall be developed. The research is conducted and funded as part of DFG research unit FOR2687[1]. As such, it strives to investigate the multi-scale causal mechanisms that are at the origin of cyclic variations.
The particular challenge lies in the non-linear interaction of a number of physical mechanisms, namely shock waves, turbulent flow, combustion and acoustics, that act and interact across orders of spatial and temporal scales. This also leads to high computational demands and necessitates an identification of the relevant physical ingredients and efficient high-order numerical schemes.
As opposed to conventional liquid fuels such as gasoline, as a gaseous fuel, hydrogen is highly compressible. In order to achieve the hydrogen mass flow rate corresponding to a given engine power, hydrogen must be injected under high pressure, typically between 10-200 bars [2]. Gas dynamics theory stipulates that from a nozzle pressure ratio of 1.9 upwards, the injected gas will reach sonic speed and so-called choked conditions at the narrowest section of the injection nozzle. At the aforementioned higher injection pressures, the hydrogen gas will enter the combustion chamber at least at Mach 1 and over-pressure, expanding into the chamber volume and thereby usually accelerate further to several times the speed of sound. A supersonic under-expanded jet forms, which features so-called shock diamonds, an often repetitive pattern of compressive shocks and expansions.
Shock waves are dissipative processes, they generate entropy and as such, vorticity. The jet also naturally creates huge gradients in flow velocity and pressure, which also lead to shearing, backflows and vorticity. This generates eddies and turbulence, where the larger-scale flow pattern is imposed by the jet structure. On the other hand, from small eddies upwards, the turbulent flow directly influences the pressure field, which has a direct impact on the outer boundary shape of the jet and thus the reflections of characteristic curves, meaning expansion and compression waves, change and with them the shock diamond pattern. This again has drastic impacts on the jet's air penetrating properties, its shape and physical properties and will define the resulting air-hydrogen mixture. This in turn is highly relevant for the subsequent combustion.
The multi-scale nature of supersonic jet injection can thus be explained. Important, non-negligible interactions occur over huge ratios in physical sizes, between a jet length of tens of cm and a nozzle radius on the order of mm and overall jet structure, driving large eddies which decay chaotically into very tiny eddy structures, that in turn define the flow field that determines the jet shape.

[1] https://www.for-2687.de/

NUMERICAL IMPLEMENTATION

Due to the potentially significant and hardly predictable effect, that small parameter variations and numerical inaccuracies alike will have on the resulting flow field of multi-scale shock-turbulence interaction, numerical modeling of this system places strong emphasis on scale-resolving accurate schemes and high resolution (i.e. [4]). As this means high amounts of computations, it in turn requires these schemes to be computationally highly efficient. Large Eddy Simulations (LES) should therefore constitute the best numerical approach to unite the two opposing requirements of scale-resolving properties and efficient computation. We will conduct the simulations with the multiphase branch of *FLEXI*, a Discontinuous Galerkin Spectral Element (DGSEM) method using code. This code features the required additional abilities with respect to the standard *FLEXI* [3] code of real gas equations of state and can model flows with gases of several species, i.e. hydrogen and air.

A special focus needs to be placed on balancing the desirable low dissipation of the DGSEM method with the stability requirements for discontinuities such as shock waves in the flow field.
High-order numerical schemes are accurate and stable by themselves in relatively smooth zones of fluid flow, but the supersonic jet introduces discontinuities and potentially subgrid-scale turbulent structures. These flow features cause polynomial oscillations in the numerical discretization, the scheme therefore needs to be augmented by stabilizing methods.
Here, we will present our current approach to realizing a highly accurate LES of the above described complex hydrogen direct injection. Finite Volume sub-cell techniques with an indicator-based switching routine are used for shock capturing. The choice of indicator types, physical variables they act upon and parameter values will be discussed. Strong shocks also require

an adequate choice of Riemann solvers. Concerning aliasing errors from potentially under-resolved turbulence, we experienced favorable stabilizing properties on the jet of entropy or kinetic energy conserving split flux methods [1] computed on Gauß-Lobatto discrete integration nodes. Also employed is a sub-grid-scale turbulence model for additional viscosity, modeling the effect of the viscosity on the smallest eddy scales as an energy sink. The physical system under examination being a multi-species gas mixture, a double-flux method is employed to eliminate nonphysical oscillations at the species interface.

PHYSICAL PROPERTIES OF THE JET AND TURBULENT MIXTURE

With the aforementioned numerical tools, the simulations can be conducted and the results need to interpreted. We will explain the driving dynamics of the resulting jet and surrounding flow field. To this end, gas dynamic and turbulence theory can be employed to quantitatively and qualitatively evaluate the results and conclude on their physical relevance. Results in well-resolved 2D simulations and 3D-LES alike will be treated and differences will be pointed out. The general geometrical layout is that of an injection through a millimeter-sized nozzle-like inflow into a cylindrical combustion chamber. The confined nature of this device leads to a number of important aspects unique to this jet flow field.

The non-linear nature of the flow physics and the huge gradients involved in hydrogen direct injection lead to a rich variety of interesting physical effects, from evidence for an observation of characteristic theory to thermodynamics and diffusion or turbulent spectra.

The strongly non-stationary character of the flow also allows for the creation of insightful visualizations, such as Figure 1.

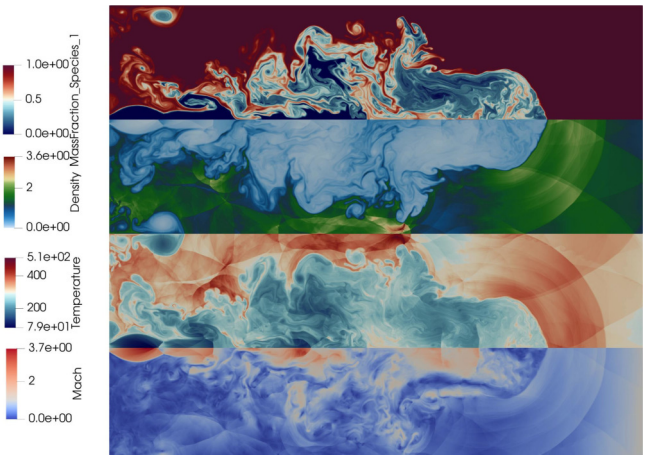

Figure 1: 2D simulation of hydrogen direct injection into air filled chamber. Nozzle pressure ratio of 10. Navier-Stokes equation, ideal gas equation of state, parabolic effects such as species diffusion, viscosity and heat conduction.

REFERENCES

[1] Gassner, G., Winters, A. and Kopriva, D. : Split Form Nodal Discontinuous Galerkin Schemes with Summation-By-Parts Property for the Compressible Euler Equations, Journal of Computational Physics. 327. (2016). 10.1016/j.jcp.2016.09.013.

[2] Hamzehloo, A. and Aleiferis, P. : Large Eddy Simulation of Near-Nozzle Shock Structure and Mixing Characteristics of Hydrogen Jets for Direct-Injection Spark-Ignition Engines, Conference Paper, 10th International Conference on Heat Transfer, Fluid Mechanics and Thermodynamics HEFAT2014, (2014). DOI: 10.13140/2.1.4978.0162.

[3] Krais, N., Beck, A., Bolemann, T., Frank, H., Flad, D., Gassner, G., Hindenlang, F., Hoffmann, M., Kuhn, T., Sonntag M. and Munz, C.D. : Flexi: A high order discontinuous Galerkin framework for hyperbolic-parabolic conservation laws, Computers & Mathematics with Applications 81, 186–219 (2020). DOI 10.1016/j.camwa.2020.05.004.

[4] Voisine, M., et al. : Spatio-temporal structure and cycle to cycle variations of an in-cylinder tumbling flow, Experiments in fluids 50.5: 1393-1407, (2011).

WORKSHOP
Direct and Large-Eddy Simulation 14
April 10-12 2024, Erlangen, Germany

A COMPARISON OF REYNOLDS-AVERAGED NAVIER-STOKES AND SCALE RESOLVING SIMULATION METHODS FOR A TIP CLEARANCE FLOW OF A LINEAR COMPRESSOR CASCADE

Johannes Deutsch[1], **Nima Fard Afshar**[1], **Stefan Henninger**[1], **Peter Jeschke**[1]
[1]Institute for Jet Propulsion and Turbomachinery
RWTH Aachen University, Germany
deutsch@ist.rwth-aachen.de

INTRODUCTION

Tip clearance flows have significant influence on the performance and stable operating range of axial compressors . Roughly, a third of all losses in axial compressors is attributed to tip clearance flows [1]. In case of tip critical designs, the blockage of the upper passage caused by the clearance flow can trigger flow instabilities ultimately leading to a compressor surge. In consequence, it is crucial to capture the effects of the tip clearance flow in the design phase of new turbomachinery components. Besides experimental investigations, numerical simulations provide insights in local flow phenomena. Due to run time restrictions for industrial applications, Reynolds-Averaged Navier-Stokes (RANS) simulations are used in the design phase although the limitations regarding the physical representation of the turbulent states are well-known. Large eddy simulations (LES) resolve the anisotropic large scale turbulent structures and reduce the modelling influence on the results significantly. However, LES simulations are computationally expensive and thus out of reach for their regular application in the design phase. Hybrid approaches RANS/LES like the Improved Delayed Detached Eddy Simulation (IDDES) proposed by Shur [2] reduce the resolution requirements in the boundary layers and could allow an application in the industry if they offer an improvement over RANS.
Within this study, we compare three different simulation methods, namely RANS, IDDES and LES as high fidelity reference, for a tip clearance flow of a linear compressor cascade. We identify differences of RANS and IDDES simulations to the LES and highlight potential modelling weaknesses.

TEST CASE

The investigated geometry is a purely numerical test case and is derived from the V103 compressor vane which has been extensively investigated both numerically and experimentally, see e.g. [3, 4]. Several modifications to the original geometry are made to allow a fair comparison of the different simulation methods. To reduce the computational costs for the test case, the Reynolds number is set to 1.8×10^5 while keeping the Mach number at 0.67. As shown in Figure 1, the leading edge is modified to a blunt geometry to ensure fully turbulent boundary layers on both sides of the vane.

The simulation domain extends 30 % chord (c) in the span (s) direction. At the lower endwall of the cascade, a gap with

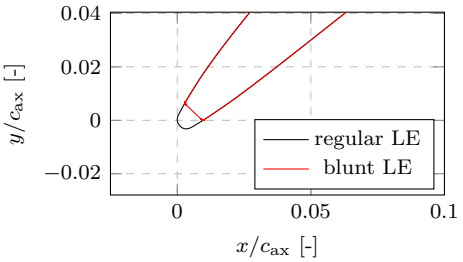

Figure 1: Modified V103 Compressor blade

a height h_{tip} of 1 % c is introduced, while the upper endwall is modelled as inviscid allowing a non-zero wall parallel velocity. Further details regarding the investigated operating point and the geometry are summarized in Tables 1 and 2.

Re_{in}	Ma_{in}	Tu_{LE}	α_{in}
1.8×10^5	0.67	3.3 %	47°

Table 1: Investigated operating point

c	h_{tip}	s	stagger angle β_s
0.12 m	1.2 mm	36 mm	22.5°

Table 2: Geometry of the modified V103 cascade

NUMERICAL METHODS

For all simulations, we used the flow solver TRACE[1] which is jointly developed by the Institute of Propulsion Technology of the German Aerospace Center (DLR) and MTU Aero Engines AG. We applied the finite volume solver of TRACE using structured multi-block grids. For spatial discretization in RANS, the upwind scheme of Roe with second-order accuracy for the convective fluxes is utilized while a central discretization is applied for the diffusive fluxes. LES requires to resolve fluctuations and uses a central scheme with 0.1 % of upwind flux to stabilize the solver. The IDDES is performed with a scheme supposed by Strelets [6] which blends between an upwind scheme in RANS regions and a central scheme in LES regions. At the inlet boundary

[1]**T**urbomachinery **R**esearch **A**erodynamic **C**omputational **E**nvironment

condition for the IDDES and LES simulations, a synthetic turbulence generator proposed by Shur et al. [5] is utilized to create realistic turbulent inflow conditions. The chosen turbulence models and applied fixes are listed in Table 3.

	Turbulence model	Turbulence model modifications
LES	WALE [7]	-
IDDES	k-ω [8]	Kato-Launder Limiter [9]
		Vorticity based
		IDDES length scale [10]
RANS	k-ω [8]	Kato-Launder Limiter [9]

Table 3: Simulation setups

The mesh for the LES contains 192×10^6 degree of freedoms (DoFs) and achieves a dimensionless resolution of $\Delta x^+ \leq 25$, $y^+ \leq 0.6$, and $\Delta z^+ \leq 20$ on the vane surface. For the IDDES, a slighlty coarser mesh with 75×10^6 DoFs is utilized with $\Delta x^+ \leq 40$, $y^+ \leq 0.6$, and $\Delta z^+ \leq 30$ on the vane surface. The dimensionless resolution for both simulations on the side wall is similar to the one on the vane surface in order to resolve the boundary layer properly. After reaching a statistical steady state, statistics have been collected over 8 throughflows of the blade passage for the LES and 12 throughflows of the IDDES.

RESULTS

The simulation results show significant differences in the shape of the tip clearance vortex as shown by the Mach number distribution downstream of the trailing edge in Figure 2.

In comparison to the IDDES and LES results, the spanwise extend of the tip clearance vortex in the RANS simulation is reduced while the extend in pitch direction is similar to the scale resolving simulation. The IDDES results match the LES results qualitatively. However, there are discrepancies in the prediction of the center of the tip clearance vortex and differences in the shape. In the further analysis, we compare the location of separation line of the tip clearance vortex on the endwall and the turbulent states in the tip clearance and on the side wall. For the IDDES, we find that the switch from modelled to resolved turbulence impacts the trajectory of the tip clearance vortex when comparing the results to the LES. The modelled turbulent kinetic energy is suddenly reduced in the boundary layer that emerges from the tip clearance on the suction side. As the resolved turbulent kinetic energy needs a certain development length, the boundary layer on the endwall separates. This leads to a different development of the tip clearance vortex. This highlights the need for further improvement of hybrid RANS/LES formulations.

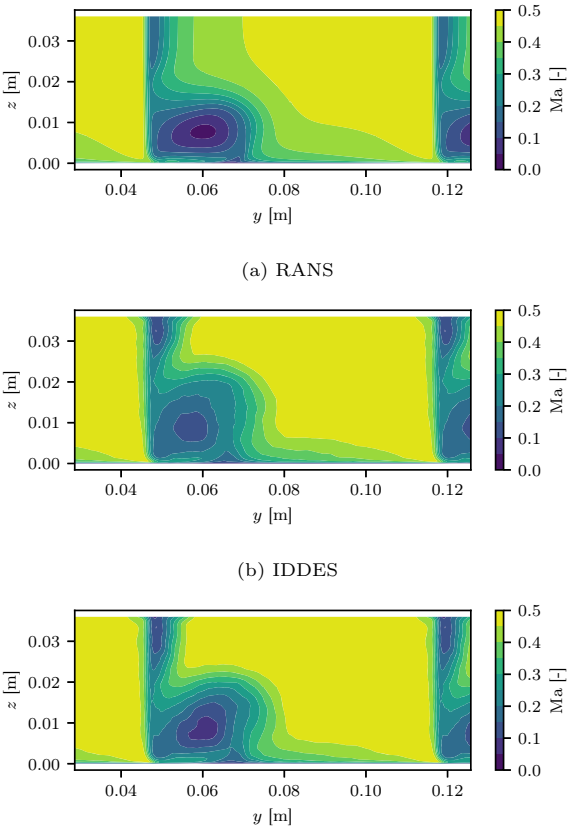

(a) RANS

(b) IDDES

(c) LES

Figure 2: Contours of Mach number at $x/c_{\mathrm{ax}} = 1.07$

REFERENCES

[1]Denton, J. D. : The 1993 IGTI Scholar Lecture: Loss Mechanisms in Turbomachines, *J. Turbomach.*, **115**, 621–656 (1993).

[2]Shur, M. L., Spalart, P. R., Strelets, M. Kh. and Travin, A. K. : A hybrid RANS-LES approach with delayed-DES and wall-modelled LES capabilities, *International Journal of Heat and Fluid Flow*, **29**, 1638–1649 (2008).

[3]Bell, R. M. and Fottner, L. : Investigations of Shock/Boundary-Layer Interaction in a Highly Loaded Compressor Cascade, *Proceedings of the ASME 1995 International Gas Turbine and Aeroengine Congress and Exposition. Volume 1: Turbomachinery, June 5-8, Houston, Texas, USA*, (1995).

[4]Zaki, T. and Durbin, P. and Wissink, J. and Rodi, W. : Direct Numerical Simulation of By-Pass and Separation-Induced Transition in a Linear Compressor Cascade, *Proceedings of the ASME Turbo Expo 2006: Power for Land, Sea, and Air. Volume 6: Turbomachinery, Parts A and B, May 8–11, Barcelona, Spain*, (2006).

[5]Shur, M.L., Spalart, P.R., Strelets, M.K and Travin, A. K: Synthetic Turbulence Generators for RANS-LES Interfaces in Zonal Simulations of Aerodynamic and Aeroacoustic Problems, *Flow Turbulence Combust*, **93**, 63–92 (2014).

[6]Strelets, M. : Detached eddy simulation of massively separated flows, *39th Aerospace Sciences Meeting and Exhibit, January 8-11, Reston, Virigina, USA*, (2001).

[7]Durcos, F., Nicoud, F. and Poinsot, T. : Wall-Adapting local eddy-viscosity models for simulations in complex geometries, *Numerical methods for fluid dynamics VI, March/April, Oxford, UK*, (1998).

[8]Wilcox, D. C. : Reassessment of the scale-determining equation for advanced turbulence models, *AIAA J.*, **26**, 11, 1299–1310 (1988).

[9]Kato, M. and Launder, B. E. : The Modelling of Turbulent Flow Around Stationary and Virbrating Square Cylinders, *9th Symposium on Turbulent Shear Flows, August 16–18, Kyoto, Japan*, (1993).

[10]Shur, M.L., Spalart, P.R., Strelets, M.K and Travin, A. K: An Enhanced Version of DES with Rapid Transition from RANS to LES in Separated Flows, *Flow Turbulence Combust*, **95**, 709–737 (2015).

WORKSHOP
Direct and Large-Eddy Simulation 14
April 10-12 2024, Erlangen, Germany

INFLUENCE OF INFLOW TURBULENCE ON THE LAMINAR SEPARATION BUBBLE OF A 3D LOW-PRESSURE TURBINE CASCADE USING LARGE EDDY SIMULATION

Nima Fard Afshar[1], Johannes Deutsch[1], Stefan Henninger[1], Peter Jeschke[1], Dragan Kozulovic[2]
[1]Institute of Jet Propulsion and Turbomachinery (IST), RWTH Aachen, Germany
[2]Institute of Jet Propulsion (ISA), University of the Bundeswehr, Munich, Germany
fard-afshar@ist.rwth-aachen.de

INTRODUCTION

The Low Pressure Turbine (LPT) design is still a challenging task due to increasing requirements on efficiency, weight, durability, manufacturability, maintainability, etc. One of the design trends is to decrease the LPT weight by reducing the number of stages. This results in the design principle of high-lift blades, which are subject to large adverse pressure gradients on the suction side. However, in the low Reynolds number regime, laminar boundary layer separation is likely and may be the primary cause of total pressure loss increase and corresponding efficiency decrease. In the case of open separation bubbles, the performance penalties are excessive, a situation which has to be prevented. In order to maximize the blade loading and to assure a reattachment of the flow, it is crucial that numerical design tools are sufficiently accurate to predict the correct physical behavior. Additionally, the numerical tools should be able to reproduce experimental conditions, such as the turbulence decay.
The MTU-T161 turbine cascade (described by [1]), considered in this work, is representative of high lift low pressure turbine airfoils used in modern jet engines. The cascade features diverging end walls, such that the flow cannot be studied using a simple spanwise periodic setup. Several publications [2], [3], [4] and [5] presented non-protected experimental and numerical studies of the MTU-T161 for Re=90,000 obtained by different solver and numerical approaches.
In this work, we investigate the influence of the inflow turbulence on the midspan flow of the three-dimensional LPT cascade MTU-T161 at a Reynolds number of 90,000 using Large Eddy Simulation (LES). For this purpose, two cases are considered. The first simulation exhibits free-stream turbulence as in the experimental campaign (FST case). The second case does not include any free-stream turbulence (Clean case). The effects of the free-stream turbulence on the profile pressure distribution and total pressure loss in wake are investigated. Additionally, the midspan flow of both cases is investigated regarding the entropy generation and turbulence anisotropy. The LES results are also held against conventional RANS methods to compare the capability of the RANS methods to capture the separation bubble and the corresponding losses. The results emphasize the need of synthetic turbulence in numerical tools to reproduce industrial relevant conditions.

NUMERICAL METHOD

The calculations of the MTU-T161 configuration were conducted using the solver TRACE, which is developed at the Institute of Propulsion Technology in the Department for Numerical Methods of the German Aerospace Center (DLR) and MTU AeroEngines AG. TRACE has been used for LES of LPT application in the past ([6], [7]). The LES calculations in TRACE solve the filtered compressible Navier-Stokes equations using a second-order accurate, density-based finite volume scheme applying MUSCL reconstruction. The subgrid-stresses are computed by the WALE model developed by [8]. A one-dimensional characteristic non-reflecting boundary condition implemented by [9] is used at the domain outlet to drive the time- and surface-averaged boundary state towards the prescribed values (static pressure). At domain inlet, a Riemann boundary condition is applied to set the stagnation pressure, stagnation temperature and flow angles. To reproduce realistic operating conditions, synthetic turbulent fluctuations in the inflow are introduced. The synthetic turbulence generator in TRACE uses the prescribed turbulent length scale and the Reynolds stress tensor components to represent the fluctuation field at the inlet based on superposition of Fourier modes ([10]).

RESULTS

The isentropic Mach number distribution in Figure 1 indicates, that the Clean case shows on both suction and pressure side considerably larger separation bubbles. The suction side flow, in the Clean case, does not reattach at the trailing edge causing an open separation bubble with a massive separation. On the other hand, the FST case, shows smaller separation bubbles on both suction and pressure surfaces. The difference in the separation bubble sizes is due to the influence of the free-stream turbulence on the boundary layer flow and the enhanced entrainment rate of the shear layer. In FST case, the free-stream turbulence enters the boundary layer, the velocity fluctuations grow up rapidly to produce the Reynolds stress, which in turn accelerates the transition to a fully turbulent state.
The momentum transfer from the mean flow toward the surface promotes the suppression of the separation bubble and a flow reattachment on the suction side. However, it should be noted that the FST is still classified as a "long separation

bubble" case.

The influence of the massive separation and the open separation bubble on the total pressure loss in the wake area (at $x/l_{ax} = 0.4$), is very clear in the Figure 2. We see much higher peak and wider loss values for the Clean case. It should be noted that the results (blade pressure distribution and total pressure wake loss) of the FST case have been validated against experimental results in the previous publications [3]

The anisotropy and entropy analysis show very different behavior for the two cases. Especially the passage flow is governed by different turbulent states. The FST case shows two-component turbulence state in the passage flow, while the Clean case is mostly governed by the one-component turbulence. When looking at the entropy contour (not shown in Abstract) we see a strong correlation between the separated shear layer and the generated losses. The entropy related to the turbulence production starts to rise along the separated shear layer and contributes the most to the overall entropy.

REFERENCES

[1]J. Gier, M. Franke, N. Hübner, and T. Schröder: Designing low pressure turbines for optimized airfoil lift, *Journal of Turbomachinery*, vol. 132, no. 3, p. 436 (2010).

[2]C. Müller-Schindewolffs, R.-D. Baier, J. R. Seume, and F. Herbst: Direct numerical simulation based analysis of rans predictions of a low-pressure turbine cascade, *Journal of Turbomachinery*, vol. 139, no. 8, p. 11, 2017.

[3]N. Fard Afshar, D. Kozulovic, S. Henninger, J. Deutsch, and P. Bechlars:Turbulence anisotropy analysis at the middle section of a highly loaded 3d linear turbine cascade using large eddy simulation, *Journal of the Global Power and Propulsion Society*, vol. 7, pp. 71–84, 2023.

[4]C. Morsbach, M. Bergmann, A. Tosun, B. F. Klose, E. Kügeler, and M. Franke: Large eddy simulation of a low-pressure turbine cascade with turbulent end wall boundary layers, *Flow, Turbulence and Combustion*, p. 28, 2023.

[5]M. Rosenzweig, M. Kozul, R. Sandberg, M. Marconcini, and R. Pacciani: High-fidelity simulations and rans analysis of a low-pressure turbine cascade in a spanwise-diverging gas path - end-wall flow analysis and loss generation mechanisms, *Volume 13B: Turbomachinery — Axial Flow Turbine Aerodynamics*, p. 10, American Society of Mechanical Engineers, 06262023.

[6]C. Morsbach and M. Bergmann: Critical analysis of the numerical setup for the large-eddy simulation of the low-pressure turbine profile t106c, *Direct and Large Eddy Simulation XII* (M. García-Villalba, ed.), vol. 27 of *ERCOFTAC Ser*, pp. 343–348, Cham: Springer International Publishing AG, 2020.

[7]S. Leyh and C. Morsbach: The coupling of a synthetic turbulence generator with turbomachinery boundary conditions, *Direct and Large Eddy Simulation XII* (M. García-Villalba, ed.), vol. 27 of *ERCOFTAC Ser*, pp. 349–355, Cham: Springer International Publishing AG, 2020.

[8]F. Nicoud and F. Ducros: Subgrid-scale stress modelling based on the square of the velocity gradient tensor, *Flow, Turbulence and Combustion*, vol. 62, no. 3, pp. 183–200, 1999.

[9]D. Schlüß, C. Frey, and G. Ashcroft: Consistent non-reflecting boundary conditions for both steady and unsteady flow simulations in turbomachinery applications, *Proceedings of the VII European Congress on Computational Methods in Applied Sciences and Engineering (ECCOMAS Congress 2016)* (M. Papadrakakis, ed.), (Athens), pp. 7403–7422, Institute of Structural Analysis and Antiseismic Research School of Civil Engineering National Technical University of Athens (NTUA) Greece, 2016.

[10]M. L. Shur, P. R. Spalart, M. K. Strelets, and A. K. Travin: Synthetic turbulence generators for rans-les interfaces in zonal simulations of aerodynamic and aeroacoustic problems, *Flow, Turbulence and Combustion*, vol. 93, no. 1, pp. 63–92, 2014.

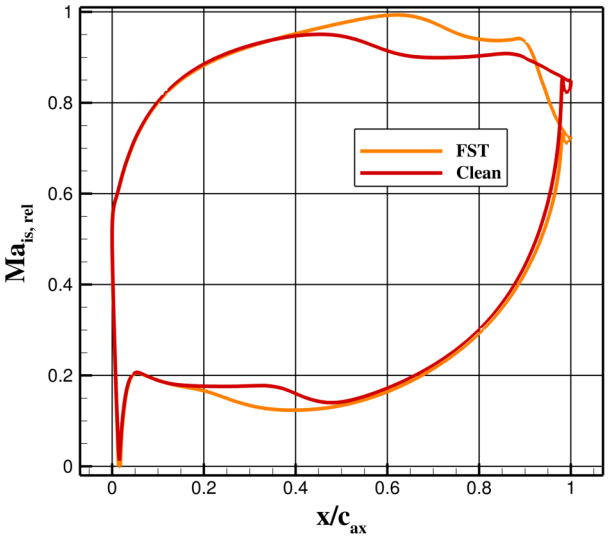

Figure 1: Relative isentropic Mach number distribution of LES for clean and FST cases at 50 % span

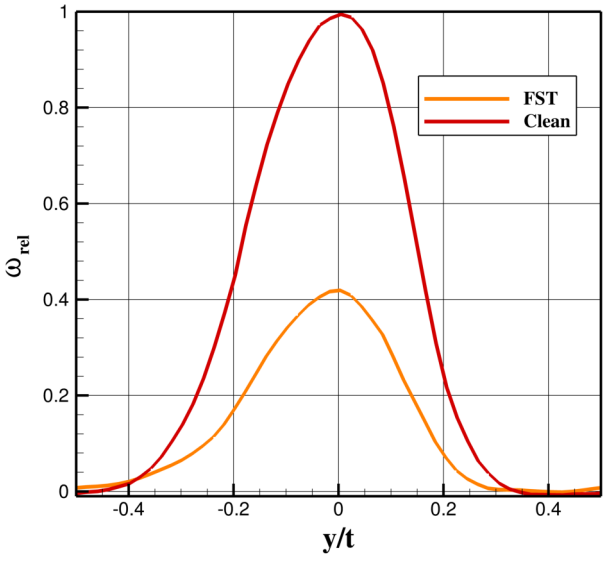

Figure 2: Relative Total pressure wake loss coefficient distribution of LES for clean and FST cases at 50 % span

WORKSHOP
Direct and Large-Eddy Simulation 14
April 10-12 2024, Erlangen, Germany

INVESTIGATION VIA LARGE-EDDY SIMULATIONS OF THE UNSTEADY AERODYNAMICS OF THE COMBINED CAPSULE-PARACHUTE SYSTEM DURING PLANETARY DESCENT

L.Placco[1], F. Dalla Barba[2], M. Bernardini[3] and F. Picano[1,2]
[1]Centro di Ateneo di Studi e Attività Spaziali 'Giuseppe Colombo' (CISAS)
Università degli Studi di Padova, Padova, Italy
luca.placco@unipd.it
[2]Department of Industrial Engineering
Università degli Studi di Padova, Padova, Italy
[3]Department of Mechanical and Aerospace Engineering
Sapienza Università di Roma, Roma, Italy

INTRODUCTION

The recent landings on Mars by the Chinese probe Tianwen-1, the U.S. rover 'Perseverance', and the upcoming European 'Rosalind Franklin' mission highlight the significance of in-situ exploration on Mars. However, in this context, recent and past failures underscore the critical nature of traversing the atmosphere. Indeed, the entry and descent phases of an interplanetary probe are characterised by complex aerodynamic phenomena [1]. Initially, these phenomena arise from the supersonic flow behaviour around the capsule. Subsequently, additional complexity emerges from the interaction between the existing flow instabilities and the deployed parachute, which is employed to decelerate the payload to the surface. Predicting these phenomena proves exceedingly challenging, given that they manifest in a compressible flow regime characterised by high Mach and Reynolds numbers. Conducting experimental campaigns faces difficulties due to the extreme environmental conditions to replicate and the prohibitive costs associated with suitable facilities. Standard computational approaches typically yield confined results, focusing solely on the general steady aerodynamic response of the system [2, 3]. Further work is then required with the use of a time-resolved representation of the fluid dynamics. As a result, the aim of this study is to address this demand by performing high-fidelity unsteady aerodynamics simulations through the recent advancements of the parallel computing scene, boosted by the promising ongoing development of GPU technology. We employ Large-Eddy Simulation to initially model the time-evolving flow around a Mars reentry capsule, examining flow behaviour at different configurations (0, 5, 10, and 15 degrees of angle-of-attack) prior parachute deployment (Ma = 2). Subsequently, a rigid decelerator representing a deployed parachute is introduced into the simulation to characterise the flow instabilities arising from the interaction of the turbulent wake of the capsule with the trailing decelerator. With multiple simulations we determine with high accuracy the supersonic flow around both the capsule and the parachute; special emphasis is placed on analysing the turbulent structures that contribute to the oscillatory and unsteady dynamics, as well as the 'breathing cycle' produced by the interaction of the two system together. Subsequently, the objective is to further describe these phenomena using low-order methodologies (e.g., POD) and modelling.

SIMULATIONS SETUP

Three-dimensional compressible Navier-Stokes equations are solved with the high-order finite difference solver STREAmS [4]. Turbulent structures are ultimately identified using the implicit Large-Eddy simulation (ILES) approach; in this way, conventional LES turbulence modelling has been omitted, using instead the numerical dissipation given by the domain discretisation as artificial viscosity acting at small scales. No-slip and no penetration wall boundary conditions on the body are enforced through an integrated Immersed-Boundary Method (IBM) algorithm. The domain employed for all the simulations has a size of $L_x = 20D$, $L_y = 10D$, $L_z = 10D$, where D is the maximum diameter of the capsule; parachute's diameter is set to $2.57D$. Two different computational grids have been employed, one for only the capsule and one for the capsule-parachute system, consisting of $N_x \cdot N_y \cdot N_z = 2048 \cdot 672 \cdot 672$ and $N_x \cdot N_y \cdot N_z = 2560 \cdot 840 \cdot 840$ nodes, respectively. The grid density changes in both axial and transverse directions, gaining resolution in the central portion of the domain; position of the capsule's nose is set at $[1D, 0, 0]$ while the parachute center lies at $[10D, 0, 0]$. Computations have been carried out on CINECA's Marconi100 cluster, employing GPU paralelisation. The simulation was performed at $Ma = 2$ and $Re = 10^6$ to simulate the beginning of the descent phase in the Mars' atmosphere.

RESULTS

Zoomed-in views of the instantaneous density ratio contours are presented in fig. 1, top, for the descent capsule in all the four cases. LES technique provides an high fidelity representation of the wake flow, solving precisely flow eddies from large to small scales. As expected, we observe a detached bow shock and the generation of an expansion fan at the shoulders of the probe; flow separation occurs causing a

suction effect on the surface of the backshield that forces the fluid to flow backward. This is connected to the high value of the drag coefficient generated by a typical blunt body. At the trailing end of the capsule a recompression shock then develops as the discontinuities progressively blend together to form a distinct shock. Comparing the four different cases, we observe how the recirculation region and the wake width at neck point reduce as the angle of attack of the capsule rises, as similarly observed by [5]. This is associated to the flow being slightly faster as it turns around the capsule, causing the recompression to appear early. Turbulent kinetic energy distributions reveals that most of the fluctuations in the flow field are concentrated at the back of the capsule, with a peak close to the overlap of the wake with the recompressive shock wave. The peak moves upstream together with the neck point as the angle of attack increases. To further characterize flow fluctuations, Discrete-Fourier-Transformation (DFT) analysis was applied to the time-oscillating lift force observed in all the three non-zero angle of attack configurations. All of them manifested a common low frequency content of about 30 Hz ($\approx$ 0.2 in the Strouhal number). Higher frequency contents ($\approx$ 0.4 and 0.6 in the Strouhal number) appear as the angle of attack increases from 5° to 15°; related futher details can be found in the reference paper [6].

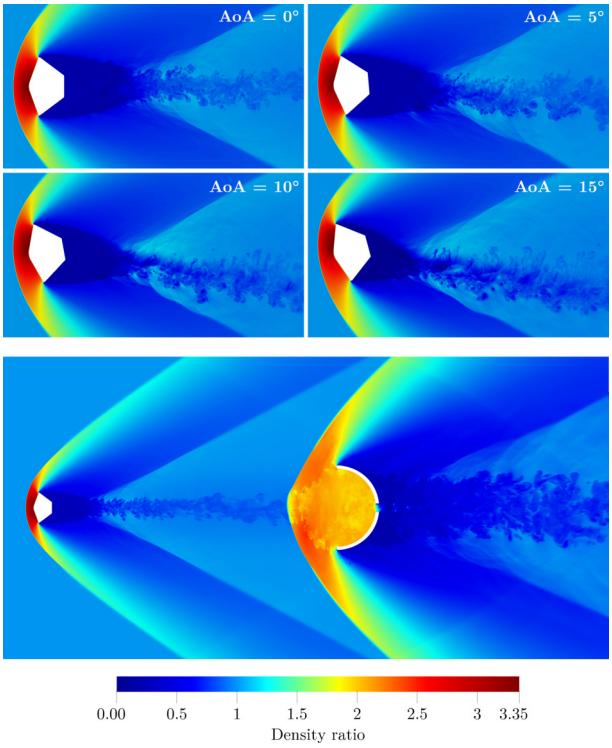

Figure 1: Top panel: instantaneous density ratio contours of the capsule at AoA = 0°, 5°,10°, 15° (y/D = 0 cross section, zoomed-in) - bottom: capsule-parachute system (y/D = 0 cross section, full view).

Full-view of the density ratio contour field of the capsule-parachute system case is given in figure 1, bottom. The capsule bow shock is steady, as well as the subsonic region between the shock and the capsule. On the contrary, the flow appears more unstable in the canopy region: the source of this instability is the turbulence shock interaction occurring due to the passage of the turbulent wake of the descent module through the bow shock of the parachute. The intensity of turbulence carried by the wake is amplified as the flow travel across the canopy bow shock (turbulence ingestion by the shock), leading to large fluctuations of momentum and pressure. In addition, being disrupted by the irregularities of the wake, the canopy bow shock does not reach a steady state and shows an oscillatory motion. This motion is related to the parachute 'breathing cycle', which is present regardless the parachute rigidity. The 'breathing' motion involves inhomogeneous pressure/density fluctuations, leading to large drag variations, despite the canopy area remaining constant. Main cause of the 'breathing' cycle seems to be the aerodynamic interaction between capsule wake and canopy bow shock. In real applications of flexible parachutes, canopy deformations couple with this interaction, amplifying drag variability [7].

CONCLUSIONS

The present work proposes high-fidelity time-evolving simulations of an entry capsule in a supersonic flight regime at different attitudes together with results of a simulation of the capsule interacting with a trailing parachute, employing LES and IBM techniques. The intent is to contribute to the understanding of the unsteady dynamics that arise in this critical situation, gaining insights on the optimal design choices to ensure a safe atmospheric entry and a successful landing procedure. Turbulent structures are effectively solved via ILES technique, allowing us to evaluate the flow properties and the capsule's response both in space and time. Relatively to the capsule-parachute interaction, we show how the critical 'breathing' instability associated to supersonic decelerators is intrinsically connected to the interaction of the turbulent wake flow of the descent module and the front bow shock produced by the parachute. To overcome the limitation of the current setup and further extended the representation of its dynamics, the implementation of a novel immersed boundary method technique is in progress, allowing the solution of flexible thin membranes. This will allow to proper represent both the entire deployment sequence and the system unsteadiness in all its components, thus providing the full representation of the 'breathing' dynamics.

REFERENCES

[1]C. D. Kazemba et al., Survey of blunt-body supersonic dynamic stability, *Journal of Spacecraft and Rockets*, **54**, 109-–127, (2017).

[2]J. F. Campbell et al., Experimental wake flow properties of a Viking '75 entry vehicle, *Journal of Spacecraft and Rockets*, **11**, 11-–15, (1974).

[3]S. M. Murman, Dynamic simulations of atmospheric-entry capsules, *Journal of Spacecraft and Rockets*, **46**, 829-–835, (2009).

[4]M. Bernardini et al., STREAmS: a high-fidelity accelerated solver for direct numerical simulation of compressible turbulent flows, *Comp. Phys. Comm.*, **263**, 107906, (2021).

[5]H. Kiritani et al., Transonic flow field analysis of a free flight capsule using ballistic range, *AIAA Scitech Forum*, (2020).

[6]L. Placco et al., Large-Eddy Simulation of the unsteady supersonic flow around a Mars entry capsule at different angles of attack, *Aerospace Science and Technology*, **143**, 108709, (2023)

[7]B. S. Sonneveldt et al., Summary of the Advanced Supersonic Parachute Inflation Research Experiments (ASPIRE) Sounding Rocket Tests with a Disk-Gap-Band Parachute, *AIAA* **3482**, (2019)

SESSION: Aerodynamics/Aeroacoustics II

Thursday, April 11, 2024

9:35- 10:50

WORKSHOP
Direct and Large-Eddy Simulation 14
April 10-12 2024, Erlangen, Germany

REQUIREMENTS & CURRENT CAPABILITIES FOR IMPLICIT LARGE EDDY SIMULATION OF THE IMPERIAL FRONT WING USING SPECTRAL H/P ELEMENT METHODS

Alexandra Liosi[1,2], Parv Khurana[1,2], Spencer Sherwin[1], Julien Hoessler[2], Adam Swift[2], Athanasios Chatzopoulos[2], Francesco Bottone[2]
[1]Department of Aeronautics
Imperial College London, London, U.K
[2]McLaren Racing Ltd, Woking, U.K
a.liosi22@imperial.ac.uk, p.khurana22@imperial.ac.uk,

INTRODUCTION

The requirements for performing Large Eddy Simulations (LES) using high-order spectral h/p element methods of the flow around complex geometries at high Reynolds (Re) numbers are investigated, focusing on the development and evolution of vortical systems. LES typically employs a model in the near-wall region or a filter to exclude small-scale information, which can be challenging to fine-tune in order to capture the load, transition mechanism, and formation of vortical structures. Spectral h/p element methods are a promising alternative for conducting wall-resolved LES without the necessity of a wall model or a filter. However, these methods introduce different concerns relevant to numerical accuracy, the influence of the stabilization on the flow resolution, and computational cost. To address these concerns, an industrial benchmark, the Imperial Front Wing (IFW), is examined. The IFW is a Formula 1 multi-element wing configuration, as seen in Figure 1, based on the McLaren 17D race car from 2003, which was never raced.

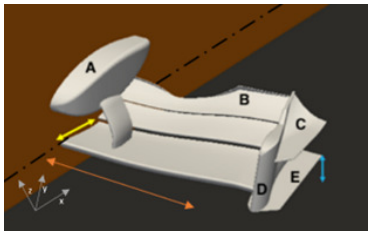

Figure 1: Imperial Front Wing [1] A: Nose Cone, B: Gurney Flap, C: Canard, D: Endplate, E: Footplate, Yellow Arrow: Mainplane Chord Length, Blue Arrow: Ride-Height (distance between footplate and ground), Dashed line: Symmetry Plane, Orange Arrow: Location of the slice y = -250 mm (distance from the symmetry plane)

Previous studies for this numerical configuration have primarily focused on the integral values such as lift and drag coefficients and the validation with available experimental results. Pegrum[5] introduced the IFW test case and conducted an experimental survey for the vortical system evolution emerging from the IFW, an isolated wheel, and their combination. Buscariolo et al.[1] repeated an experimental survey only on the IFW using high-frequency Particle Image Velocimetry (PIV). They simulated the IFW for the first time using the spectral h/p element method and reported good agreement with the updated experimental results. However, their study is limited to investigating the time-averaged fields. O'Sullivan[6] investigated different simulation methodologies from lower to higher fidelity and compared them against the information in [1] based on the integral values and the averaged shear-stress patterns. Slaughter[3] examined a simplified configuration of the IFW, which is a 2D slice across the spanwise location of y = -250 mm and includes the airfoil profiles of the three elements.

This study extends the data set supplied in Buscariolo et al.[1] by including the pressure and friction coefficient distribution, vortex path and intensity, quantitative measures for assessing convergence, and turbulence transition. The non-dimensional magnitudes are correlated against the shear-stress visualization figures to understand the flow dynamics, such as the transition mechanism and separation. A vortex tracking technique is deployed to monitor the development of the vortical system, vortex interactions, and core's path. Additionally, it provides guidelines for performing LES simulations using spectral h/p methods within an industrial environment for complex geometries at high Re.

NUMERICAL METHOD AND PROBLEM DESCRIPTION

The unsteady flow around the IFW at a $Re = 2.2 \times 10^5$ is described by the incompressible Navier-Stokes equations, which are non-dimensionalized and discretized using a continuous Galerkin projection. The characteristic time, or *Convective Time Unit*(CTU), is the needed time for the flow to travel one characteristic length with the free-stream velocity. The flow variables are approximated using high-order polynomials. The high-order velocity correction splitting scheme[2] is employed to decouple the pressure from the velocity while maintaining high-order accuracy in time via Nektar++[8]. Nektar++ is an open-source framework for solving unsteady partial differential equations using spectral h/p element method. An unstructured, conformal high-order mesh is created, including only prisms and tetrahedrons through *NekMesh* [7], the mesh-generation utility of Nektar++.

PRELIMINARY RESULTS & DISCUSSION

The simulation is initialized from another velocity field with lower fidelity, and the pressure is set to zero for $T = 0$. It has run until $T = 7.34CTUs$, and the flow fields have been averaged from $T = 4.64CTUs$ to $T = 7.34CTUs$. The averaging process for the integral values has started from $T = 1$ until the latest available time. The current mean and standard deviation values for the lift and drag coefficients are summarized in Table 1. The simulation has not run long enough for the moving averages to converge since the standard deviation of the lift coefficient is above 5%. Nevertheless, good agreement is observed with the reference case described in [1]. The results obtained from the fully converged simulation will be available in time for the conference.

Symbol	Reference	Current	Difference [%]
Mean C_L	-5.54	-5.49	0.90
Mean C_D	0.575	0.576	0.17
Std Deviation C_L[%]	N/A	11	N/A
Std Deviation C_D[%]	N/A	1	N/A

Table 1: Mean and Standard Deviation for the Lift and Drag Coefficients

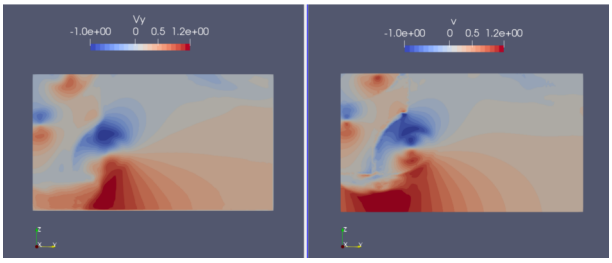

Figure 2: Full Scale Comparison of the Spanwise Velocity Component between Experiments(Left) and Nektar++(Right)

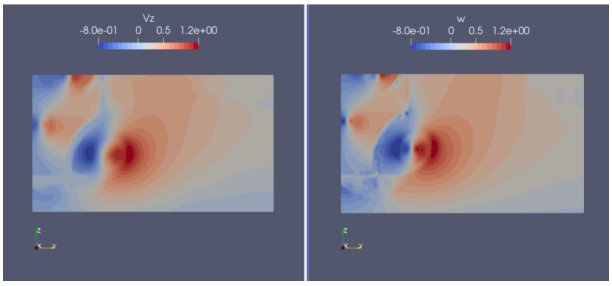

Figure 3: Full Scale Comparison of the Normal Velocity Component between Experiments(Left) and Nektar++(Right)

The preliminary averaged fields for pressure and velocity are compared against the averaged high-frequency PIV planes from the experimental survey in [1]. There are five planes available for validation. For one of these planes, the comparison between the experimental velocity fields and the numerical ones are presented in Figures 2 and 3 for the spanwise and normal components, respectively. The main vortical structures are captured in both figures and are in agreement with [5]. The location for each vortex core can be clearly seen in Figure 4, especially in the Total Pressure plot, where each vortex is

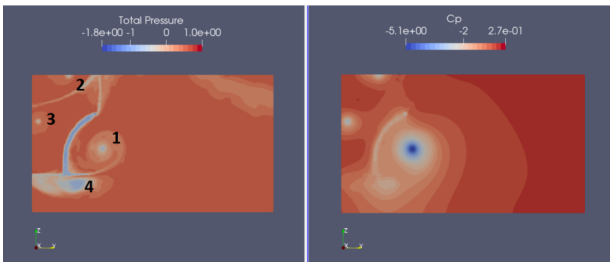

Figure 4: Total Pressure and Pressure Coefficient at X = -294 mm from Nektar++, 1: Main Vortex, 2: Endplate Vortex, 3: Canard Vortex, 4: Footplate Vortex

numbered and named. In detail, the footplate vortex(number 4) is formed of two vortices that have merged, leading to an elongated shape as seen in Figure 4. Its shape can be attributed to the evolution of this vortex with time. The large standard deviation of the lift coefficient can also be connected to the development of the footplate vortex. The shape and the strength of the vortex change with time, directly affecting the overall downforce produced by the IFW.

ACKNOWLEDGEMENTS

This project received funding from the European Union's Horizon 2020 research and innovation programme under the Marie Skłodowska-Curie grant agreement No 955923, and the current study was performed using the ARCHER2 UK National Supercomputing Service via the UK Turbulence Consortium (EP/R029326/1).

REFERENCES

[1]Buscariolo, F.F, Hoessler, J., Moxey, D., Jassim, A., Gouder, K., Basley, J., Murai, Y., Assi, G. R. S. and Sherwin, S. J.: Spectral/hp element simulation of flow past a Formula One front wing: validation against experiments, *J. Wind Eng. Ind. Aerodynamics*, **221**, 104832 (2022).

[2]Karniadakis, G. M. and Orszag, S. A.: High-Order Splitting Methods for the Incompressible Navier-Stokes Equations,*J. Computational Physics*, **97**, 414–443 (1991).

[3]Slaughter, J., Moxey, D. and Sherwin, S. J.: Large Eddy Simulation of an Inverted Multi-Element Wing in Ground Effect, *Flow Turbulence Combust*, **110**, 917—944 (2023).

[4]Karniadakis, G. M. and Sherwin, S. J.: Spectral/hp Element Methods for Computational Fluid Dynamics, *Oxford University Press* (2005).

[5]Pegrum, J. M. : Experimental study of the vortex system generated by a Formula 1 front wing, *Doctoral dissertation*, Imperial College London (2006).

[6]O'Sullivan, A., Puri, K. and Ferrer, E.: From RANS to LES: Comparison of Simulation Methodologies for the Imperial Front Wing, *AIAA AVIATION 2023 Forum* (2023).

[7]Green, M. D., Kirilov, K. S., Turner, M., Marcon, J., Eichstäedt, J., Laughton, E., Cantwell, C. D., Sherwin, S. J., Peiro, J. and Moxey, D.: Nekmesh: An Open-Source High-Order Mesh Generation Framework (2023).

[8]Moxey, D., Cantwell, C. D., Bao, Y., Cassinelli, A., Castiglioni, G., Chun, S., Juda, E., Kazemi, E., Lackhove, K., Marcon, J., Mengaldo, G., Serson, D., Turner, M. Xu, H., Peiró, J., Kirby, R. M. and Sherwin, S. J.: Nektar++: Enhancing the capability and application of high-fidelity spectral/hp element methods, *Computer Physics Communications*, **249**, 107–110 (2020).

WORKSHOP
Direct and Large-Eddy Simulation 14
April 10-12 2024, Erlangen, Germany

ACOUSTIC LINERS AND THEIR AERODYNAMIC IMPACT

H. Shahzad, S. Hickel, D. Modesti
Aerodynamics Group, Faculty of Aerospace Engineering, Delft University of Technology
Kluyverweg 2, 2629 HS Delft, The Netherlands
h.shahzad@tudelft.nl

INTRODUCTION

Aircraft engines are the primary source of noise during take-off and landing. In order to reduce noise, engine nacelles are equipped with noise control devices called acoustic liners. Acoustic liners consist of a porous facesheet and a solid backplate with a honeycomb core in between the two. Acoustic liners have a characteristic resonance frequency that can be tuned to the dominant frequency of the engine fan for noise reduction. Acoustic liners are widely used and represent the state of the art in engine noise reduction. However, they tend to increase aircraft drag. The increase in drag has always been accepted as a necessary compromise, and acoustic liners have primarily been studied and optimised from an acoustic perspective, so far. An in-depth understanding of how acoustic liners impact engine aerodynamics is, therefore, lacking.

Most numerical studies available in the literature are limited to isolated Helmholtz resonators [1], or the use of modelled boundary conditions [2]. Extending our previous fully resolved Direct Numerical Simulation (DNS) of realistic acoustic liner geometries in turbulent channel flows [3, 4], we present new DNS results of a turbulent boundary layer over fully resolved acoustic liners arrays, wherein the complexity of the geometry is handled using an immersed boundary method.

METHODOLOGY

We perform DNS of a turbulent boundary layer over acoustic liners using the solver STREAmS [5]. The simulation is performed in a rectangular box of size $L_x \times L_y \times L_z = 115\delta_0 \times (15 + k)\delta_0 \times 5\delta_0$, where δ_0 is the inflow boundary layer thickness, and k is the depth of the acoustic liner. The freestream Mach number is $M = u_\infty/c_\infty = 0.3$, where u_∞ is the freestream velocity and c_∞ is the speed of sound based on freestream conditions, and the friction Reynolds number varies in the range $Re_\tau \approx 1000$–2400. The domain consists of an initial smooth wall region of length $L_{x,s} = 45\delta_0$, followed by an acoustic liner array that extends from $x/\delta_0 = 45$ to the end of the domain, $x/\delta_0 = 115$. The compressible Navier–Stokes equations are discretized on a Cartesian grid with a mesh size $N_x \times N_y \times N_z = 21504 \times 672 \times 1120$. The geometry of the acoustic liner with a porosity $\sigma = 0.322$ is similar to the one considered by Shahzad *et al.* [3]. Figure 1 shows an instantaneous flow field from DNS of the acoustic liner, depicting the vortical structures visualised using the Q-Criterion. Figure 1 also shows a top view of the acoustic liners. We also study in the influence of the acoustic waves on the aerodynamic characteristics of acoustic liners by imposing an outflow pressure $p_o = A\sin(2\pi f_r t)$, where A is the amplitude of pressure wave, t is the time and f_r is the resonance frequency of the acoustic liner.

RESULTS

Figure 2 (a) shows the mean streamwise velocity comparison between the smooth wall region and the liner region, in the absence of incoming acoustic waves,. A clear downward shift, ΔU^+, of the viscous-scaled mean velocity profile with respect to the smooth wall is visible, which is a clear symptom of drag increase. However, the differences between the smooth wall velocity profile and that of the acoustic liner originate primarily near the wall and the velocity profiles are essentially parallel in the outer layer, indicating that Townsend's outer layer similarity hypothesis holds for the streamwise velocity. We find that the inverse of the viscous scaled wall-normal Forchheimer permeability, $1/\alpha_y^+$, is the relevant permeability for acoustic liners, which confirms the conclusions of Shahzad *et al.* [3]. Figure 2 (b) shows a comparison between the ΔU^+ of the boundary layer simulation and channel flow simulations [3]. The good match between the channel flow results and the boundary layer, despite the different cavity depth and resonance frequency, is because cavity resonance is significantly less important in the absence of tonal forcing due to an acoustic wave. Figure 3 shows an x-y plane of the instantaneous density field in the presence of acoustic waves of amplitude corresponding to a sound pressure level, SPL= 150dB at the outflow. This ongoing unprecedented fully resolved simulation with incoming acoustic waves will help us provide a complete picture of how acoustic liners interact with the flow, delineating the influence of acoustic waves and roughness.

REFERENCES

[1]Zhang, Q. and Bodony, D.J.: Numerical investigation of a honeycomb liner grazed by laminar and turbulent boundary layers, *J. Fluid Mech.*, **792**, 936 (2016).

[2]Scalo, C., Bodart, J. and Lele, S.K.: Compressible turbulent channel flow with impedance boundary conditions, *Phys. Fluids*, **27 (3)**, 035107 (2015).

[3]Shahzad, H., Hickel, S. and Modesti, D.: Turbulence and added drag over acoustic liners, *J. Fluid Mech.*, **965**, A10 (2023).

[4]Shahzad, H., Hickel, S. and Modesti, D.: Permeability and turbulence over perforated plates, *Flow Turb. Combust.*, **109 (4)**, 1241–1254 (2022).

[5]Bernardini, M., Modesti, D., Salvadore, F. Sathyanarayana, S., Posta, G.D. and Pirozzoli, S.: STREAmS-2.0: Supersonic turbulent accelerated Navier-Stokes solver version 2.0, *Comput. Phys. Commun.*, **285**, 108644 (2023).

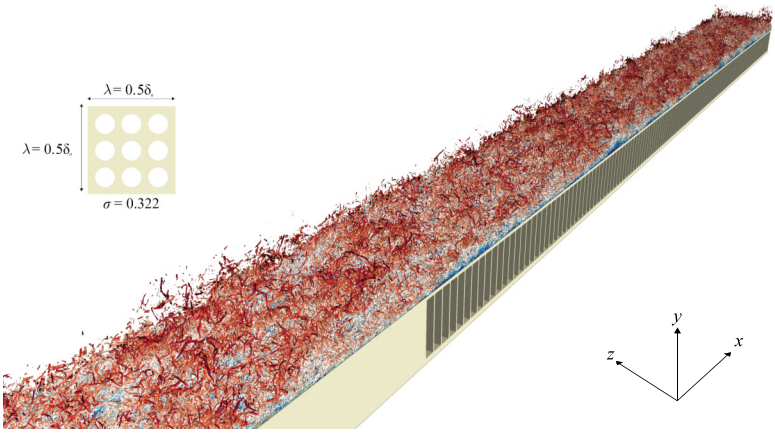

Figure 1: Instantaneous flow field of the boundary layer simulation. Orifice configurations within a single cavity are also shown at the top left. Vortical structures are visualised using the Q-Criterion, coloured by the streamwise velocity.

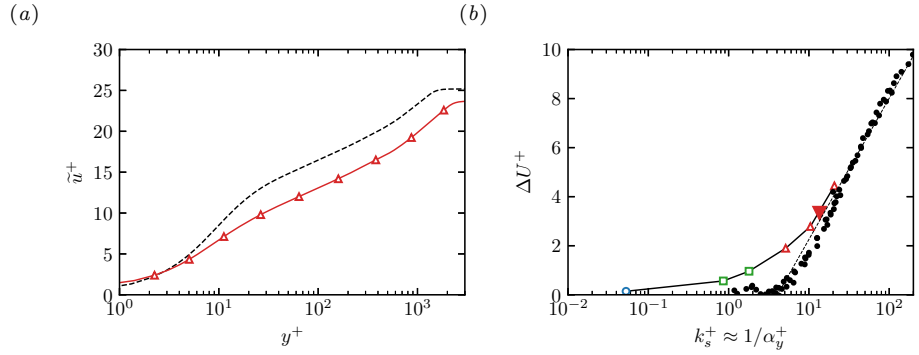

Figure 2: Mean streamwise velocity normalised by the friction velocity (a) as a function of the wall-normal coordinate. Different line types represent different streamwise locations in panel (a): triangles represent a region with liners after the smooth-rough transition point and dashed line represents a location within the smooth region. ΔU^+ (b) as a function of the viscous-scaled inverse of the Forchheimer coefficient. In (b), the filled inverted triangle represents ΔU^+ of the current simulation whereas the empty symbols represent data of channel flow simulations [3]. Filled circles are Nikuradse's data for sand-grain roughness.

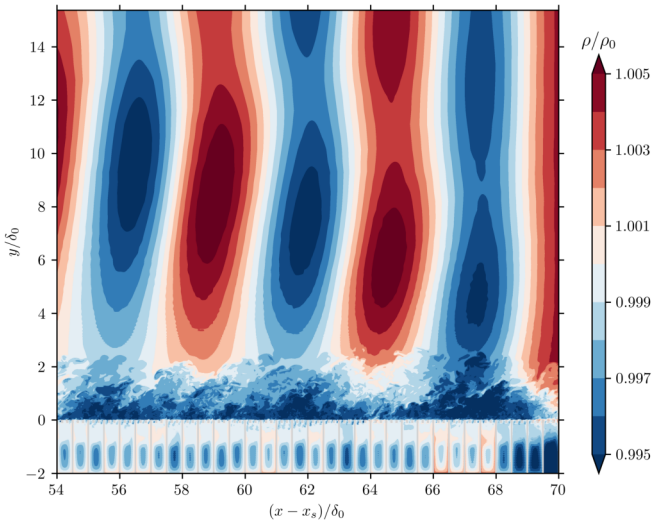

Figure 3: Instantaneous density field in an $x-y$ plane at $z/\delta_0 = 0.25$. Acoustic waves enter from the domain outflow at $(x-x_s) = 70$, where x_s is the location of the smooth-to-liner transition.

WORKSHOP
Direct and Large-Eddy Simulation 14
April 10-12 2024, Erlangen, Germany

A TOPOLOGICALLY CONSISTENT PROCEDURE FOR FINDING CRITICAL POINTS IN THE WALL SHEAR STRESS FIELD

L. Unglehrt[1], **M. Manhart**[1]
[1] Professorship of Hydromechanics
Technical University of Munich, Germany
lukas.unglehrt@tum.de, michael.manhart@tum.de

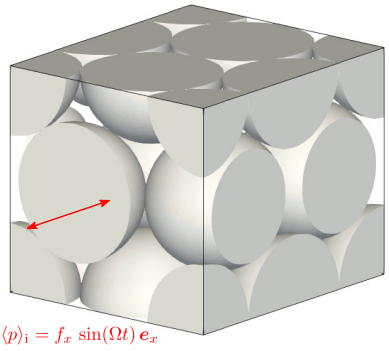

Figure 1: Hexagonal close-packing of spheres. The flow is driven by a sinusoidal pressure gradient and is triply periodic.

INTRODUCTION

In [14, 15] we investigated oscillatory flow through a sphere pack (figure 1) using direct numerical simulation. This case represents an idealisation of flow in regenerator-type cryocoolers [12], catalytic packed-bed chemical reactors [17] and wave-induced flow through coral reefs [10]. In such applications, one is often interested in the distribution of the heat or mass transfer rate over the pore walls [3], which is strongly influenced by the wall shear stress distribution (especially for high Prandtl or Schmidt numbers) [13]. Also, the wall shear stress field has been used to determine the flow topology in packed beds, especially to find recirculation zones [9].

In the analysis of the wall shear stress topology, one aim is to construct a topological skeleton consisting of critical points, where $\vec{\tau}_\mathrm{w} = 0$, and separatrices [6, 7, 11]. For curved walls, it is difficult to determine the critical points, since the tangential component of a piecewise linear wall shear stress field is discontinuous along the edges of the mesh; this may lead to multiple detection of critical points [16]. This has been partially addressed by Wang et al. [16], who proposed to use the Poincaré index to identify and classify critical points. A further complication in the present geometry is that the mesh contains holes near the contact points of the spheres.

The Poincaré index is defined for closed curves in a vector field and measures the number of rotations of the normalised vector $\vec{\tau}_\mathrm{w}/|\vec{\tau}_\mathrm{w}|$ as the curve is traversed in counterclockwise direction [1]. If a closed curve does not enclose a critical point, the Poincaré index is 0, if it encloses exactly one critical point,

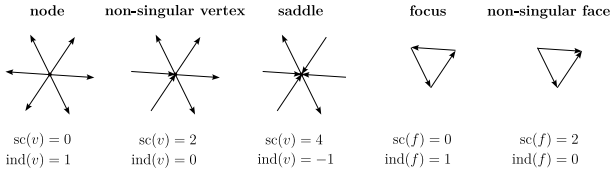

Figure 2: Different configurations of the sign change sc and index ind in a triangular mesh following Gortler et al. [5]. The arrows indicate the direction of the 1-form c_{ij}.

the Poincaré index is nonzero (-1 for saddles, $+1$ for nodes); and if it encloses multiple critical points, the Poincaré index is the sum of the indices of the enclosed critical points. The Poincaré-Hopf theorem states that the sum of the Poincaré indices of all critical points of a vector field is equal to the Euler characteristic χ of the manifold on which it is defined [4, 8]. For a closed manifold, this implies that the number of nodes N minus the number of saddles S is equal to the Euler characteristic $N - S = \chi$. The Euler characteristic of a polygonal mesh is defined as $\chi = V - E + F$ with the number of vertices V, edges E and faces F, and depends only on the topology of the manifold. The Poincaré-Hopf theorem can be used to check the consistency of vector fields obtained from experiments [4, 7].

In the present case, the wall shear stress field is considered on spherical meshes with 12 holes. Unfortunately, the method of Wang et al. [16] does not account for mesh boundaries, where critical points may occur in the wall shear stress component tangential [8] or normal [4] to the boundary, thus violating the Poincaré-Hopf theorem. Therefore, we present a method to identify critical points in the wall shear stress field for meshes with and without boundaries that is guaranteed to be consistent with the Poincaré-Hopf theorem.

A DISCRETE POINCARÉ-HOPF THEOREM

Our method is based on a discrete version of the Poincaré-Hopf theorem for closed meshes by Gortler et al. [5]. The vector field (wall shear stress) is encoded as a 1-form, which is an edge-based representation of the vector field [2]. For an edge between the points $\vec{P}_i$ and $\vec{P}_j$, the "discrete 1-form" is computed as [2]

$$c_{ij} = \frac{1}{2}\left(\vec{\tau}_{\mathrm{w},i} + \vec{\tau}_{\mathrm{w},j}\right) \cdot \left(\vec{P}_j - \vec{P}_i\right) . \tag{1}$$

Gortler et al. [5] defined the index of a vertex v and a face f

in terms of the sign changes $\mathrm{sc}(v)$ and $\mathrm{sc}(f)$ in the values of the 1-form as the adjacent sectors are traversed in order as

$$\mathrm{ind}(v) = \frac{2 - \mathrm{sc}(v)}{2}\,, \tag{2}$$

$$\mathrm{ind}(f) = \frac{2 - \mathrm{sc}(f)}{2}\,. \tag{3}$$

As can be seen from figure 2, the index is non-zero for singular vertices and faces, i.e. nodes, saddles and foci, and is zero for non-singular vertices and faces. For a non-zero 1-form on a closed oriented manifold mesh with vertices $\mathcal{V}$ and faces $\mathcal{F}$, the sum of the indices

$$\sum_{v\in\mathcal{V}} \mathrm{ind}(v) + \sum_{f\in\mathcal{F}} \mathrm{ind}(f) = \chi \tag{4}$$

is equal to the Euler characteristic of the mesh [5].

For meshes with boundary, we modified the index formula for vertices in the following manner

$$\mathrm{ind}(v) = \begin{cases} \frac{2-\mathrm{sc}(v)}{2} & \text{if } v \in \operatorname{int}\mathcal{V}\,, \\ \frac{1-\mathrm{sc}(v)}{2} & \text{if } v \in \partial\mathcal{V}\,, \end{cases} \tag{5}$$

where sign changes outside the mesh are not counted. The proof of an index formula analogous to equation (4) is based on the finding that $\mathrm{sc}(v)+\mathrm{sc}(f) = 1$ for any sector of the mesh and on the definition of the Euler characteristic.

METHODOLOGY

We apply the discrete Poincaré index to a direct numerical simulation dataset of oscillatory flow through a hexagonal sphere pack. We consider the case MF4 [14] which has a Reynolds number $Re = \langle u\rangle_\mathrm{s}\, d/\nu = 73$, where $\langle u\rangle_\mathrm{s}$ is the superficial volume-averaged velocity, d is the sphere diameter and ν is the kinematic viscosity, and a Womersley number $Wo = \sqrt{\Omega d^2/\nu} = 31.62$, where Ω is the frequency of oscillation. The wall shear stress is not available from the immersed boundary method employed for the simulations [15]. Hence, the instantaneous velocity fields were interpolated to spherical meshes of diameter $d + 2h$ and the wall shear stress was computed by the linear approximation. The wall shear stress is then projected onto the edges of the mesh according to equation (1) and the degenerate case $c_{ij} = 0$ is perturbed such that $c_{ij} > 0$ if $i < j$, giving each edge a well-defined direction.

RESULTS

Figure 3 shows the instantaneous wall shear stress at the maximum superficial velocity. The critical points are classified according to their discrete Poincaré index as saddles (-1), half-saddles $(-\frac{1}{2})$, half-nodes $(\frac{1}{2})$ and nodes $(+1)$. The positions and types of the critical points generally agree with the method of Wang et al. [16], but additional half-integer critical points are identified near the contact points and at the sections through the spheres. A separation region is found behind the contact points which has the same topology as described by Karabelas et al. [9] based on an experimental investigation.

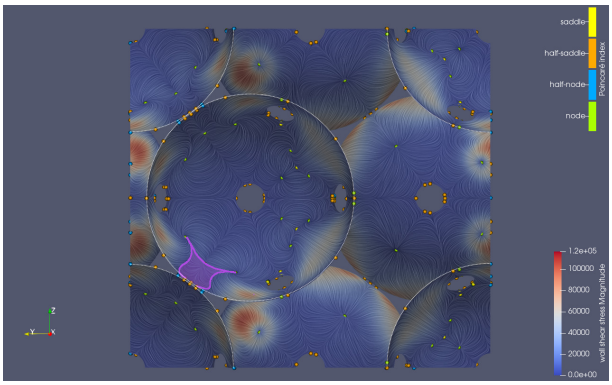

Figure 3: Line-integral convolution of the wall shear stress field of the case MF4 at the maximum superficial velocity coloured by the wall shear stress magnitude $|\vec{\tau}_\mathrm{w}|\, d^2/(\rho\nu^2)$. The flow goes into the plane. The critical points are coloured according to their discrete Poincaré index. The highlighted region indicates a separation region similar to those reported by [9].

REFERENCES

[1] Davis, H. & Commission, U. Introduction to Nonlinear Differential and Integral Equations. (Dover Publications, 1962)

[2] Do Goes, F., Desbrun, M. & Tong, Y. Vector Field Processing on Triangle Meshes. *SIGGRAPH Asia 2015 Courses*. pp. 1-48 (2015)

[3] Eigenberger, G. Fixed-Bed Reactors. *Ullmann's Encyclopedia Of Industrial Chemistry*. (2000)

[4] Foss, J., Hedden, M., Barros, J. & Christensen, K. A Topological Evaluation Procedure to Assess the Integrity of a PIV Vector Field. *Measurement Science And Technology*. **27**, 094007 (2016)

[5] Gortler, S., Gotsman, C. & Thurston, D. Discrete One-Forms on Meshes and Applications to 3D Mesh Parameterization. *Computer Aided Geometric Design*. **23**, 83-112 (2006)

[6] Helman, J. & Hesselink, L. Representation and Display of Vector Field Topology in Fluid Flow Data Sets. *Computer*. **22**, 27-36 (1989,8), https://doi.org/10.1109/2.35197

[7] Hunt, J., Abell, C., Peterka, J. & Woo, H. Kinematical Studies of the Flows around Free or Surface-Mounted Obstacles; Applying Topology to Flow Visualization. *Journal Of Fluid Mechanics*. **86**, 179-200 (1978)

[8] Jubin, B. A Generalized Poincaré-Hopf Index Theorem. (arXiv,2009)

[9] Karabelas, A., Wegner, T. & Hanratty, T. Flow Pattern in a Close Packed Cubic Array of Spheres near the Critical Reynolds Number. *Chemical Engineering Science*. **28**, 673-682 (1973)

[10] Lowe, R., Shavit, U., Falter, J., Koseff, J. & Monismith, S. Modeling Flow in Coral Communities with and without Waves: A Synthesis of Porous Media and Canopy Flow Approaches. *Limnology And Oceanography*. **53**, 2668-2680 (2008)

[11] Mazzi, V., Gallo, D., Calò, K., Najafi, M., Khan, M., De Nisco, G., Steinman, D. & Morbiducci, U. A Eulerian Method to Analyze Wall Shear Stress Fixed Points and Manifolds in Cardiovascular Flows. *Biomechanics And Modeling In Mechanobiology*. (2019)

[12] Pathak, M. Periodic Flow Physics in Porous Media of Regenerative Cryocoolers. (Georgia Institute of Technology, 2013)

[13] Rode, S., Midoux, N., Latifi, M., Storck, A. & Saatdjian, E. Hydrodynamics of Liquid Flow in Packed Beds: An Experimental Study Using Electrochemical Shear Rate Sensors. *Chemical Engineering Science*. **49**, 889-900 (1994)

[14] Unglehrt, L. & Manhart, M. Onset of Nonlinearity in Oscillatory Flow through a Hexagonal Sphere Pack. *Journal Of Fluid Mechanics*. **944** pp. A30 (2022)

[15] Unglehrt, L. & Manhart, M. Decomposition of the Drag Force in Steady and Oscillatory Flow through a Hexagonal Sphere Pack. *Journal Of Fluid Mechanics*. **974** pp. A32 (2023)

[16] Wang, W., Wang, W. & Li, S. Detection and Classification of Critical Points in Piecewise Linear Vector Fields. *Journal Of Visualization*. **21**, 147-161 (2018)

[17] Zagoruiko, A., Bobrova, L., Vernikovskaya, N. & Zazhigalov, S. Unsteady-State Operation of Reactors with Fixed Catalyst Beds. *Reviews In Chemical Engineering*. **37**, 193-225 (2021)

WORKSHOP
Direct and Large-Eddy Simulation 14
April 10-12 2024, Erlangen, Germany

LARGE EDDY SIMULATION AND DIRECT NOISE PREDICTION OF A FAN STAGE IN TRANSONIC REGIME

Allan Beurville[1], Jérôme Boudet[1], Vincent Clair[1], and Alexis Giauque[1]

[1]Laboratoire de Mécanique des Fluides et Acoustique, UMR5509,
36 Avenue Guy-de-Collongue, 69130 Écully, France

The broadband noise generated within a fan-OGV stage and partly caused by the interaction between shockwaves and turbulent structures cannot be easily modelled due to the stochastic nature of the flow. High fidelity numerical methods are able to simulate with sufficient accuracy the characteristics of the flow. LES of the ECL5 fan/OGV stage are performed using the AVBP solver developed by CERFACS. The purpose of those simulations is to locate and characterize broadband noise sources.

LES are performed on the ECL5 fan/OGV stage, an open test case designed at École Centrale de Lyon [1, 2, 3]. The stage is made of 16 rotor blades and 31 stator blades.

The computational cost of the LES is reduced by computing a periodic sector of the fan/OGV stage. In order to preserve the periodic extent for the rotor and the stator domains, the initial 31 vanes are adapted to 32 vanes. Fan stage performance is maintained by adjusting the chord length of the vanes [4]. The computational domain is represented in Figure 1.

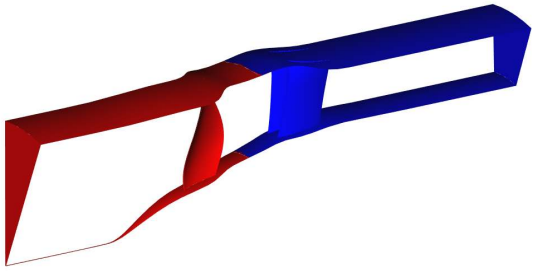

Figure 1: Computational domain of the ECL5 fan/OGV stage for the LES. Rotor domain is colored in red. Stator domain is colored in blue.

The present work is performed at the design point of the ECL5 at nominal speed ($\Omega = 11\,000$RPM). The corresponding inflow axial Mach number is 0.53 and the inlet relative Mach number at the fan blade tip is slightly above 1. The blade passage frequency is equal to 2933Hz.

Simulations of the ECL5 fan stage are performed using AVBP, an explicit unstructured fully compressible LES solver developed by CERFACS [5, 6, 7]. For turbomachinery applications, the resolution is performed over two domains: a rotating domain containing the rotor blade and a static domain containing the stator vanes. A third order interpolation is performed at every time-step to couple the domains. The coupling is ensured by the MISCOG methodology [8, 9]. Computational performance is preserved using the CWIPI library (ONERA) [10].

The computations are carried out using a third order Two-step Taylor Galerkin (TTGC) convection scheme [11]. Unresolved turbulent eddies are modelled using the SIGMA subgrid scale model [12]. Shockwaves are handled using Cook and Cabot hyperviscosity model [13]. Non-reflecting Navier-Stokes characteristic boundary conditions (NSCBC) are used both at the inlet and at the outlet [14]. A wall function (linear law below $y^+ = 11.45$, log law otherwise) is used near the walls in order to limit the computational cost [15, 16]. The time step for the simulation is slightly above $\Delta t = 1.6 \cdot 10^{-8}$s. The computational time is 200×10^3 CPUh for one rotation. The simulations are performed on a hybrid unstructured mesh. The mesh contains approximately 100 millions cells. It is designed to propagate acoustic waves one chord length upstream and downstream of the blade up to 15kHz [17]. The characteristic size of the elements is shown at 80% of the span in Figure 2. The dimensionless wall-normal distance y^+ of the first prismatic layer is under 35 on the blades skin.

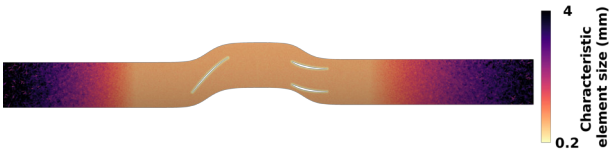

Figure 2: Characteristic size of the elements in millimeters. The reference value for the refined area is 0.8 mm. The mesh is progressively coarsened in order to limit acoustic reflections.

Three full rotations of the rotor have been performed. An iso-surface of the Q-criterion, colored by the relative Mach number is represented in Figure 3. The boundary layer in the supersonic region remains mainly laminar, and the transition is induced by the shockwave. A corner separation is noticed near the hub. Intense turbulent structures are found in the tip region. The average axial velocity at 80% of the span is shown in Figure 4 as well as the sonic line near the suction side of the rotor blade. The shockwave thickens the boundary layer, leading to wide rotor wakes.

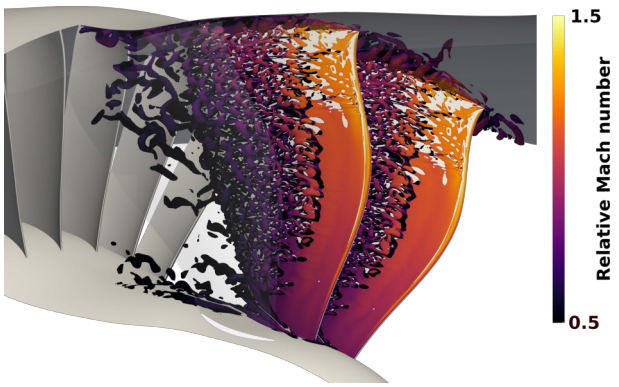

Figure 3: Isosurface of the Q-Criterion ($Qc^2/U^2 = 20$) colored by the relative Mach number.

Instantaneous pressure fluctuations at 80% of the span are shown in Figure 5 as well as the sonic line. Different noise sources are contributing to this acoustic field such as trailing edge noise, shockwave noise and interaction noise due to the rotor wakes interacting with the vanes leading edge. It can be observed that the acoustic waves propagating upstream, through the rotor, do not penetrate the supersonic regions and seem to be guided inbetween them.

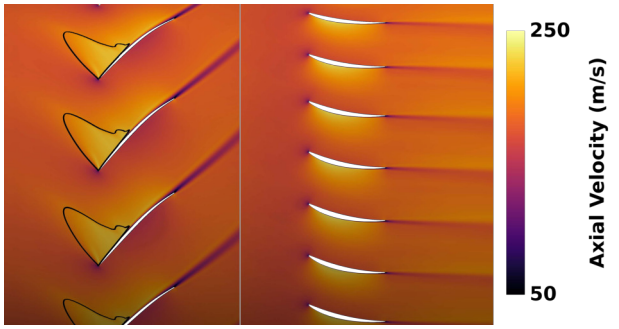

Figure 4: Average axial velocity at 80% of the span. The sonic line in the relative mean flow is represented in black.

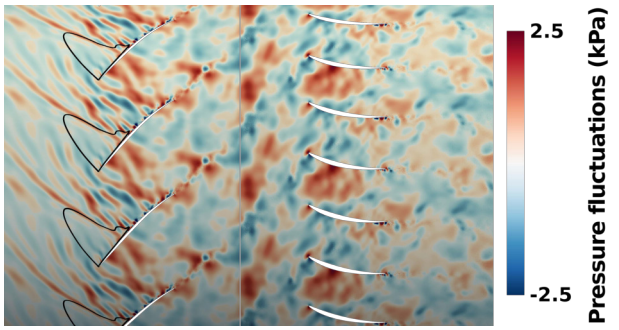

Figure 5: Instantaneous pressure fluctuations in both rotor and stator domains. Only a radial slice at 80% of the span is represented. The sonic line in the relative mean flow is represented in black.

Beyond the average and instantaneous fields, the simulation is monitored with over 4 000 unsteady probes recording thermodynamic and velocity variables with a sampling frequency around 97kHz. Those probes are located all over the blade skin, in the tip region, in the wakes, and in planes upstream the rotor blades, downstream the stator vanes and in the interstage.

The purpose of the study is to assess acoustics models using LES data and suggest modifications to take into account the presence of the shockwave. For this purpose, 8 full rotations of the ECL5 fan stage are planned. The resulting analysis including converged and well resolved acoustic spectra will be presented at the conference.

REFERENCES

[1]V. Pagès, P. Duquesne, S. Aubert, L. Blanc, P. Ferrand, X. Ottavy, and C. Brandstetter, "UHBR Open-Test-Case Fan ECL5/CATANA," *IJTPP*, May 2022.

[2]C. Brandstetter, V. Pagès, P. Duquesne, X. Ottavy, P. Ferrand, S. Aubert, and L. Blanc, "UHBR Open-test-case fan ECL5/Catana, Part 1: Geometry and aerodynamic performance," ETC, 2021.

[3]V. Pagès, P. Duquesne, X. Ottavy, P. Ferrand, S. Aubert, L. Blanc, and C. Brandstetter, "UHBR Open-test-case fan ECL5/Catana, Part 2: Mechanical and aeroelastic stability analysis," ETC, 2021.

[4]M. M. Rai and N. K. Madavan, "Multi-Airfoil NavierStokes Simulations of Turbine RotorStator Interaction," *Journal of Turbomachinery*, July 1990.

[5]T. Schonfeld and M. Rudgyard, "Steady and Unsteady Flow Simulations Using the Hybrid Flow Solver AVBP," *AIAA Journal*, Nov. 1999.

[6]S. Moreau, "Turbomachinery-related aeroacoustic modelling and simulation," Conference on Modelling Fluid Flow, Sept. 2018

[7]J. Al-Am, V. Clair, A. Giauque, J. Boudet, and F. Gea-Aguilera, "Direct noise predictions of fan broadband noise using LES and analytical models," AIAA, June 2022.

[8]G. Wang, F. Duchaine, D. Papadogiannis, I. Duran, S. Moreau, and L. Y. M. Gicquel, "An overset grid method for large eddy simulation of turbomachinery stages," *Journal of Computational Physics*, Oct. 2014.

[9]J. de Laborderie, F. Duchaine, L. Gicquel, O. Vermorel, G. Wang, and S. Moreau, "Numerical analysis of a high-order unstructured overset grid method for compressible LES of turbomachinery," *Journal of Computational Physics*, June 2018.

[10]F. Duchaine, S. Jauré, D. Poitou, E. Quémerais, G. Staffelbach, T. Morel, and L. Gicquel, "Analysis of high performance conjugate heat transfer with the OpenPALM coupler," *Comput. Sci. Discov.*, July 2015.

[11]O. Colin and M. Rudgyard, "Development of High-Order Taylor-Galerkin Schemes for LES," *Journal of Computational Physics*, Aug. 2000.

[12]F. Nicoud, H. B. Toda, O. Cabrit, S. Bose, and J. Lee, "Using singular values to build a subgrid-scale model for large eddy simulations," *Physics of Fluids*, Aug. 2011.

[13]A. W. Cook and W. H. Cabot, "Hyperviscosity for shock-turbulence interactions," *Journal of Computational Physics*, Mar. 2005.

[14]T. J. Poinsot and S. K. Lelef, "Boundary conditions for direct simulations of compressible viscous flows," *Journal of Computational Physics*, July 1992.

[15]P. Schmitt, T. Poinsot, B. Schuermans, and K. P. Geigle, "Large-eddy simulation and experimental study of heat transfer, nitric oxide emissions and combustion instability in a swirled turbulent high-pressure burner," *Journal of Fluid Mechanics*, Jan. 2007.

[16]F. Jaegle, O. Cabrit, S. Mendez, and T. Poinsot, "Implementation Methods of Wall Functions in Cell-vertex Numerical Solvers," *Flow Turbulence Combust*, Sept. 2010.

[17]J. Al-Am, V. Clair, A. Giauque, J. Boudet, and F. Gea-Aguilera, "A Parametric Study on the LES Numerical Setup to Investigate Fan/OGV Broadband Noise," *IJTPP*, May 2021.

WORKSHOP
Direct and Large-Eddy Simulation 14
April 10-12 2024, Erlangen, Germany

AEROELASTIC COUPLING BETWEEN A SHOCK-WAVE/TURBULENT BOUNDARY-LAYER INTERACTION AND A FLEXIBLE PANEL

L. Laguarda[1], **S. Hickel**[1], **F. F. J. Schrijer**[1], **B. W. van Oudheusden**[1]
[1]Department of Flow Physics and Technology, Faculty of Aerospace Engineering
Delft University of Technology, Kluyverweg 1, 2629HS Delft, The Netherlands
Email address for correspondence: L.LaguardaSanchez@tudelft.nl

Exposure to shock-wave/turbulent boundary-layer interactions (STBLIs) with substantial flow sepratation poses a significant risk of structural damage in high-speed flight [1]. Due to their characteristic low-frequency unsteadiness [2], STBLIs impose intermittent and high-amplitude loads on the surface that may excite resonant modes of lightweight skin-panels and induce high-cycle fatigue [3]. The few available studies of these complex fluid-structure interactions (FSIs) confirm that STBLIs can efficiently trigger low-order modes of panel vibration [4]; however, questions related to the coupling mechanism, the corresponding modulation of the STBLI dynamics as a result of the panel motion and the particular role of static and dynamic panel deformations remain still open.

Motivated by these questions, we conducted wall-resolved LES of a Mach 2.0 impinging STBLI over a flexible thin-panel to investigate the resulting dynamic coupling. A partitioned FSI approach, comprising a flnite-volume fluid solver and a finite-element structural solver, was employed for the calculations [5] and the solution has been integrated for a very long time to properly resolve low-frequency dynamics. The resulting mean panel deflection served as a rigid-wall geometry in a subsequent, long-integrated simulation aiming to discern effects caused by static surface displacements from those associated with the panel motion. Results are compared against the baseline configuration, an impinging STBLI flow over a flat-rigid wall.

An instantaneous impression of the flow field for the FSI case is provided in figure 1(a) and illustrates the investigated STBLI topology. Contours of zero streamwise velocity show the substantial flow separation, which is characteristic of strong interactions. The vertical displacement history of the quarter point location along the panel is shown in figure 1(b) and confirms the strong aeroelastic coupling over a broad frequency range. The resulting mean panel deformation is included in figure 2(a) and is consistent with the selected impingement location and the prescribed constant value of the cavity pressure, which corresponds to the average wall-pressure of the baseline STBLI over the region where the panel is located. The power spectral density (PSD) map of panel displacements in figure 2(b) provides an indication of the dominant vibration modes and their respective frequencies. We find that the first three bending modes of the panel oscillation contribute most to the unsteady panel response, and the corresponding frequencies appear in close agreement with natural oscillation frequencies of the pre-stressed panel (i.e., loaded with the mean wall-pressure field from the coupled STBLI) rather than those for the unloaded flat configuration. This highlights the importance of the mean panel deformation and the corresponding stiffening in the FSI dynamics.

Furthermore, statistics of wall-properties in figure 3 illustrate the impact of static and dynamic surface displacements on the flow. Skin-friction distributions in figures 3(a) show a clear increase in the streamwise extent of the recirculation region in presence of either the flexible or deformed-rigid panel, with no noticeable differences between the two. However, dynamic panel displacements significantly influence the separation-shock dynamics, evident from the higher wall-pressure fluctuation intensity at its foot in figure 3(b). This claim is further substantiated by spectral analysis of the separation-shock location signal, shown in figure 4, which reveals a dominant peak associated with the first bending mode of the panel oscillation that coexists with (rather than replaces) the characteristic low-frequency content of STBLI.

Based on the present results, unsteady FSIs involving STBLIs and flexible panels are likely to accentuate rather than mitigate the undesirable features of STBLIs. Even though results may vary depending on impingement location, interaction strength or cavity pressure, the use of flexible structural components as passive flow control devices (as hypothesized in literature) is not supported by the present findings.

REFERENCES

[1] McNamara, J. J. and Friedmann, P. P. : Aeroelastic and aerothermoelastic analysis in hypersonic flow: past, present, and future, *AIAA J.*, **49(6)**, 1089–1122 (2011).

[2] Clemens, N.T. and Narayanaswamy, V. : Low-frequency unsteadiness of shock wave/turbulent boundary layer interactions, *Annu. Rev. Fluid Mech.*, **46**, 469-492 (2014).

[3] Spottswood, S. M., Beberniss, T. J., Eason, T. G., Perez, R. A., Donbar, J. M., Ehrhardt, D. A. and Riley, Z. B. : Exploring the response of a thin, flexible panel to shock-turbulent boundary-layer interactions, *J. Sound Vib*, **443**, 74–89 (2019).

[4] D'Aguanno, A., Quesada Allerhand, P., Schrijer, F. F. J. and van Oudheusden, B. W. : Characterization of shock-induced panel flutter with simultaneous use of DIC and PIV, *Exp Fluids*, **64(1)**, 15 (2023).

[5] Laguarda, L., Hickel, S., Schrijer, F. F. J. and van Oudheusden, B. W. : Shock-wave/turbulent boundary-layer interaction over a flexible panel, *AIAA paper*, 2023-3884 (2023).

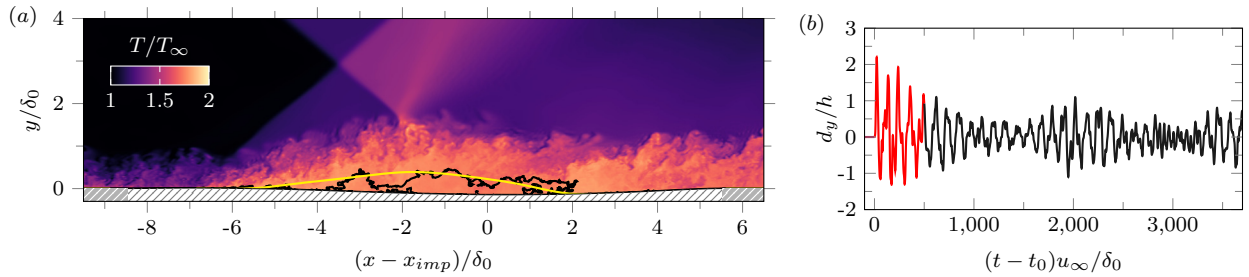

Figure 1: (a) Instantaneous STBLI flow over the flexible panel, and (b) vertical displacement history of the quarter point location along the panel length. Solid lines in (a) indicate instantaneous (black) and mean (yellow) isocontours of zero streamwise velocity, while hatching marks the rigid (gray) and flexible (white) segments of the surface. The corresponding friction Reynolds number at the inviscid impingement point x_{imp} in absence of the shock is $Re_\tau = 1226$, and x_{imp} is set at 60% of the panel length. The displacement signal in (b) is normalized with the panel thickness h, and the initial transient is shown in red.

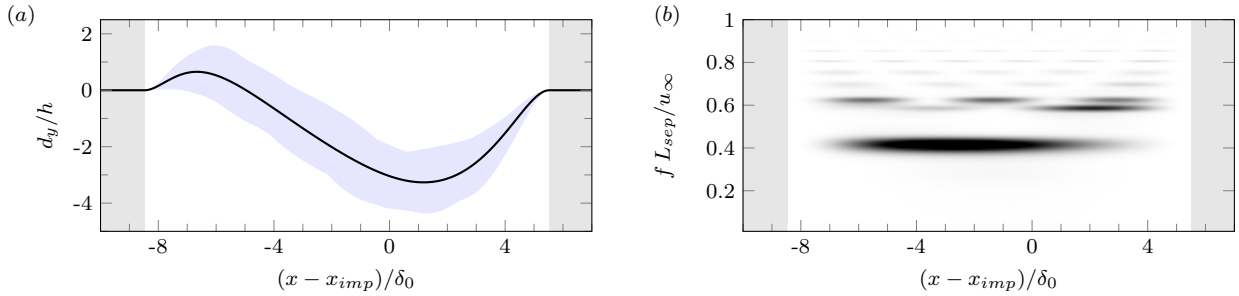

Figure 2: (a) Mean panel deflection (black) together with the envelope of all instantaneous deflection shapes (blue shade), and (b) pre-multiplied PSD map of displacement signals (the employed colormap increases linearly from white to black). The rigid segment of the surface is shaded in gray for reference.

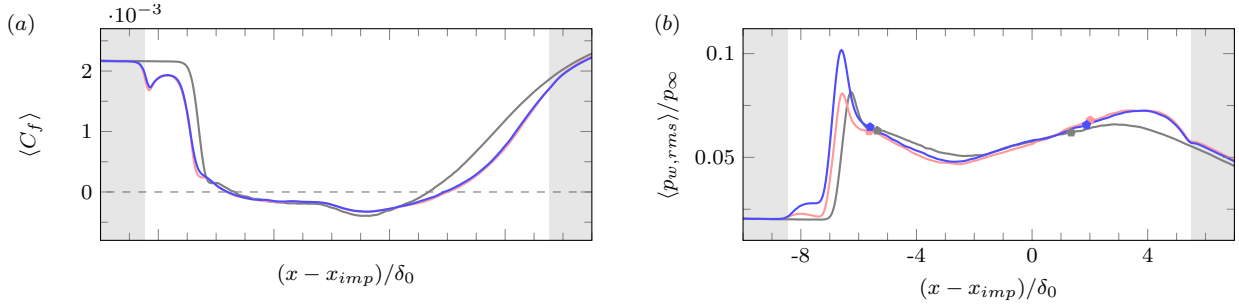

Figure 3: Time- and spanwise-averaged (a) skin-friction, and (b) wall-pressure RMS. Color legend: STBLI over (blue) a flat wall; (black) the deformed-rigid panel; (red) the flexible panel. Markers in (b) indicate the corresponding mean separation and reattachment points.

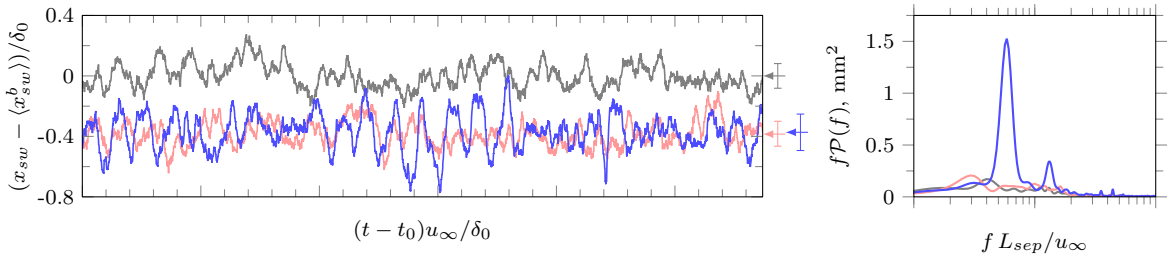

Figure 4: Time evolution of the spanwise-averaged separation-shock position referenced with respect to the mean shock position of the baseline STBLI. Arrows and vertical bars indicate the corresponding mean and standard deviation of each signal, and the panel on the right shows its associated pre-multiplied PSD. For the color legend, see the caption of figure 3.

SESSION: Numerical techniques

Thursday, April 11, 2024

9:35- 10:50

WORKSHOP
Direct and Large-Eddy Simulation 14
April 10-12 2024, Erlangen, Germany

STRUCTURED GRID-ADAPTATION FOR LES OF A SMOOTH RAMP FLOW

Johan Larsson and Nikhil Oberoi
Department of Mechanical Engineering
University of Maryland, College Park, MD, USA
jola@umd.edu

INTRODUCTION

The grid directly controls the accuracy, robustness and computational cost of most PDE solution techniques, yet it is often generated manually with decisions (grid-spacing, stretching functions, etc) based on user expertise. The overarching objective of the present work is to create a grid-adaptation methodology in which this entire process is performed by algorithms. The first step of this process is to estimate, from the result of a solution on a prior grid, what a more "optimal" grid resolution would be; this step requires the estimation of the residual (=source of error) and how this varies with the grid resolution in different directions. The resulting "optimal" grid resolution is then encoded in a Riemannian metric field $\mathbf{M}$, defined such that the optimal grid has elements of unity length in every direction, i.e., for which $l_i M_{ij} l_j = 1$ for every element edge l_i. The second step of a grid-adaptation process is to generate a new grid that satisfies, as best as possible, the grid-resolution encoded in the Riemannian metric field. This type of "metric-conforming" grid-generation has been done before for unstructured grids; the objective of the present work is to develop a method to achieve this for structured grids.

METHODOLOGY

A structured grid is defined by the coordinate mapping $\mathbf{x}(\mathbf{s})$. The size of an element in computational space is Δs_α in direction $\alpha = 1, 2, 3$; the vector defining the size and orientation of an element in physical space in this direction is $l_i^{(\alpha)} = \Delta s_\alpha \, \partial x_i / \partial s_\alpha$, with no summation on α. In this work, the grid is defined as the one that minimizes the functional

$$\int \left[\sum_{\alpha=1}^{3} m_\alpha^2 + \lambda \left(g_{12}^2 + g_{13}^2 + g_{23}^2 \right) \right] dV \qquad (1)$$

where the first term penalizes the resolution misfit

$$m_\alpha = \Delta s_\alpha^2 M_{ij} \frac{\partial x_i}{\partial s_\alpha} \frac{\partial x_j}{\partial s_\alpha} - 1, \;\; \alpha = 1, 2, 3,$$

and the second term penalizes non-orthogonality, with g_{ij} being the metric tensor of the coordinate mapping. The solution to this minimization problem is the Euler-Lagrange equation, which for this case becomes a nonlinear elliptic-like PDE. This is solved iteratively in Python for the present 2D geometry. Further details are provided in [1].

Some sample grids are shown in Fig. 1. The first has a perfectly Cartesian domain but with a non-Cartesian metric field defined as

$$\mathbf{M} = \begin{pmatrix} 1000 + a & 0 \\ 0 & 1000 - a \end{pmatrix},$$

with $a = 600 \sin(2\pi x_1) \sin(2\pi x_2)$. The figure shows clearly that the grid responds by twisting in order to better align with this prescribed non-Cartesian metric field.

The other two samples in Fig. 1 have non-Cartesian domains but with isotropic metric fields, and demonstrate how the grid aligns with the boundaries while preserving some degree of orthogonality due to the second term in the cost functional.

APPLICATION TO LES OF A SMOOTH RAMP

The method is applied to the separated flow over a backward-facing smooth ramp, which is one of the test cases of the High Fidelity CFD Verification workshop at the AIAA Scitech meeting in January 2024 [2]. The problem is solved here using the in-house *Tortuga* code framework, which solves the compressible Navier-Stokes equations with a Vreman subgrid model and a standard equilibrium wall-model. While most workshop participants use a standard set of human-designed grids, in the present study we instead use the grid-generation method described here. The initial grid is created by having the user define a metric field based on experience. In this case, this was specified to imply target grid-spacings of (in the streamwise, wall-normal and spanwise directions) $(0.12, 0.02, 0.08)\delta_{\text{ref}}$ at the lower wall and $(0.36, 0.32, 0.32)\delta_{\text{ref}}$ at the upper wall, with linear variation in between and where δ_{ref} is the nominal thickness of the incoming boundary layer. This was then used to create the initial "grid-0", which ended up having 40M cells.

A full simulation was then run on this grid, with solution snapshots saved after discarding the initial transient. The LES residual was then estimated from these snapshots using the method of Toosi and Larsson [3], from which the target metric field for the next grid was computed. This was then solved using the method described here, resulting in a "grid-1" with 87M cells. The process was repeated for "grid-2" with 193M cells. The sequence of grids is visualized in Fig. 2. Note how the adapted grids have finer wall-normal spacing in the incoming boundary layer and over the initial part of the bump, but then actually have coarser wall-normal spacing after the point of separation (about halfway down the ramp).

The High Fidelity CFD Verification workshop has reference DNS data computed, but with the majority of the results kept

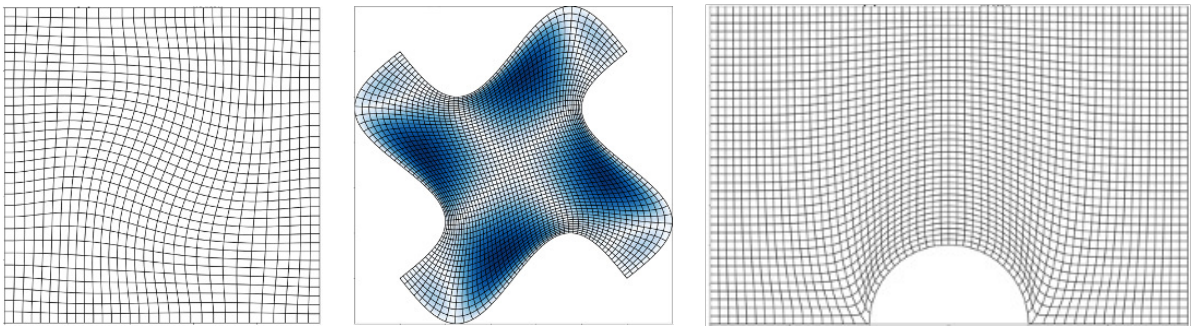

Figure 1: Sample grids, from metric fields that are non-uniform and non-isotropic metric field (left) and isotropic/uniform (middle and right).

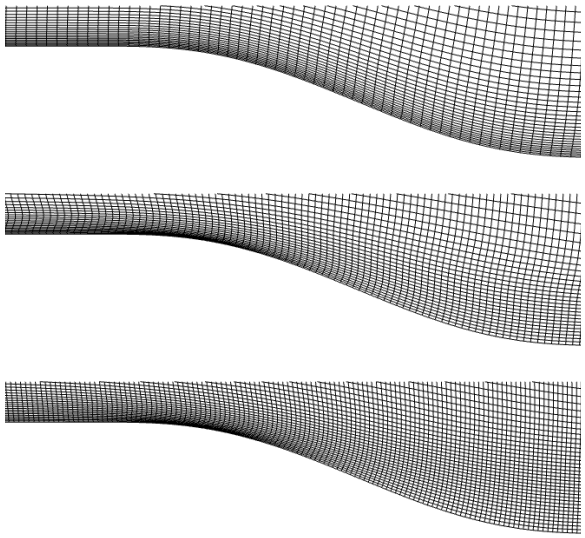

Figure 2: Sequence of adapted grids for the smooth ramp problem, showing every 5th grid line.

blind from participants until the time of the workshop. Before then, only some results in the incoming boundary layer are provided in order to allow participants to match their inflows to the DNS. The mean velocity profile in the incoming boundary layer is shown in Fig. 3, and is seen to converge to the DNS. The skin friction coefficient is shown in Fig. 4. It converges to the DNS results in the incoming boundary layer. In the remainder of the domain, the result is a blind prediction, with no ability to judge the accuracy of the results. The comparison with DNS will be available by the time of the DLES conference.

SUMMARY

A method for generating a structured grid that conforms, as well as possible, to a given Riemannian resolution-controlling metric field is proposed and tested. The method is meant to be paired with some method to estimate the residual of the PDE being solved. Future work is aimed at improving the balance between conforming to the metric and promoting an orthogonal grid, improving the near-boundary grid, and improving the general robustness of the method to solve the grid-generation PDEs which are highly nonlinear.

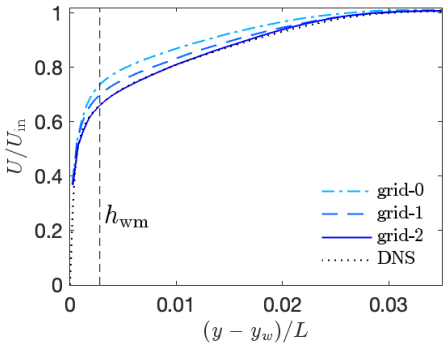

Figure 3: Mean velocity profile for the smooth ramp in the incoming boundary layer, compared to DNS data.

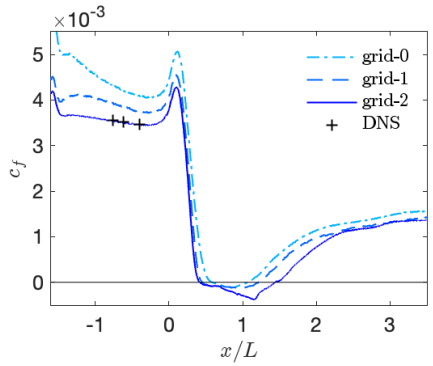

Figure 4: Skin friction coefficient for the smooth ramp, compared to DNS data in the incoming boundary layer only.

ACKNOWLEDGMENTS

This work was supported by the NNSA Predictive Science Academic Alliance Program (PSAAP; grant DE-NA0003993) and by the NASA Transformational Tools and Technologies project (grant 80NSSC22M0297).

REFERENCES

[1] N. Oberoi, M. K. Hasan, and J. Larsson, "Generation of metric-conforming structured grids with application to grid-adaptation for LES," *Int. J. CFD*, under review.

[2] J. Larsson, I. Bermejo-Moreno, and others, "Summary of the smooth body separation test case at the 2022 High Fidelity CFD Verification workshop," AIAA Paper 2023-1241, 2023.

[3] S. Toosi and J. Larsson, "Anisotropic grid-adaptation in large eddy simulations," *Comput. Fluids*, vol. 156, pp. 146–161, 2017.

WORKSHOP
Direct and Large-Eddy Simulation 14
April 10-12 2024, Erlangen, Germany

A FAST AND SCALABLE ALGORITHM FOR SPAN-WISE PERIODIC EXTERNAL FLOWS

Wei Hou[1], **Tim Colonius**[1]
[1]Division of Engineering and Applied Science (EAS)
Caltech, Pasadena, USA
whou@caltech.edu

INTRODUCTION

The immersed boundary (IB) method, the lattice Green's function (LGF), and adaptive mesh refinement (AMR) have been combined to conduct efficient simulations of 3D external flows on unbounded domains [4]. Together, the snug computational domain, restricted to vortical flow regions via the LGF [1] and the adaptive mesh refinement minimize [4**?**] the required number of cells while maintaining the versatility to define arbitrary immersed geometries [10]. The resulting IBLGF-AMR algorithm has been used to simulate flows around various immersed bodies at high Reynolds numbers, proving the efficacy and flexibility of this numerical framework [4].

While LGF formulations for both 2D and 3D unbounded domains have been derived and implemented, formulations for 3D spanwise periodic flows, despite their prevalence in theoretical and engineering applications (e.g. [5, 12, 13]), have not been reported. While other numerical methods have been used for spanwise periodic flows (e.g. [6, 7, 11]), we seek here to exploit the efficiencies of the LGF-AMR approach for such geometries.

In this presentation, we introduce a hybrid approach that combines a staggered finite-volume mesh with a Fourier spectral method for the periodic direction, prioritizing efficiency and scalability. The solver's validation involves simulating flow past a circular cylinder at Re = 300, with results demonstrating improved agreement with experimental data, especially in predicting RMS drag coefficients. Scaling the method to Re = 12,000, a level not previously attempted, our simulation shows an accurate prediction of experimentally measured mean drag coefficient and Strouhal number.

GOVERNING EQUATIONS

We solve the discretized Navier-Stokes equations with Fourier expansion in the spanwise direction. For k^{th} Fourier coefficient, the equations read:

$$\begin{aligned} \frac{d\tilde{\boldsymbol{u}}_k}{dt} + \mathcal{F}_k[\boldsymbol{N}(\boldsymbol{\omega},\boldsymbol{u})] &= -G_k\tilde{d}_k + \frac{1}{Re}L_k\tilde{\boldsymbol{u}}_k + P(t)^T\tilde{\boldsymbol{f}}_k \\ D_k\tilde{\boldsymbol{u}}_k &= 0 \\ P(t)\tilde{\boldsymbol{u}}_k &= \widetilde{\boldsymbol{u}}_{\Gamma,k} \end{aligned} \tag{1}$$

Here G_k, D_k, and L_k are the discretized and Fourier-transformed gradient operator, divergence operator, and Laplacian operator. $\boldsymbol{N}(\boldsymbol{\omega},\boldsymbol{u})$ is the nonlinear term in the physical variable space. $\mathcal{F}_k$ is the operator for the k^{th} Fourier coefficient. $P(t)$ is the projection operator mapping the velocity to the set of immersed boundary points.

In this formulation, except for the nonlinear terms, the evolution equations of every Fourier coefficient are decoupled, thus time-integrated independently once the nonlinear term is calculated. The full 3D computational mesh is constructed by extruding a 2D computational mesh in the spanwise direction. Each 2D slice houses the discretized values of a Fourier coefficient.

METHODOLOGY

The discretized governing equation is solved using the integrating factor of Laplacian and a half-explicit Runge-Kutta method [1, 2]. This time-stepping method involves solving a linear system in the following form:

$$\begin{bmatrix} (E_k^i)^{-1} & G_k & (P_n^{(i-1)})^T \\ G_k^* & 0 & 0 \\ P_n^i & 0 & 0 \end{bmatrix} \begin{bmatrix} \tilde{\boldsymbol{u}}_{k,n}^i \\ \tilde{d}_{k,n}^i \\ \tilde{f}_{k,n}^i \end{bmatrix} = \begin{bmatrix} \boldsymbol{r}_{k,n}^i \\ 0 \\ (\widetilde{\boldsymbol{u}}_{\Gamma,k})_n^i \end{bmatrix} \tag{2}$$

where E_k^i is the integrating factor of L_k [1]. This system is solved using a block LU decomposition:

$$\begin{aligned} \tilde{d}_k^* &= -L_k^{-1}G_k^*\boldsymbol{r}_{k,n}^i \\ S_{k,n}^i\tilde{f}_{k,n}^i &= P_k^iE_k^i[\boldsymbol{r}_{k,n}^i - G_k\tilde{d}_k^*] - (\boldsymbol{u_b})_{k,n}^i \\ \tilde{d}_{k,n}^i &= \tilde{d}_k^* + L_k^{-1}G_k^*(P_n^i)^T\tilde{f}_{k,n}^i \\ \tilde{\boldsymbol{u}}_{k,n}^i &= E_k^i[\boldsymbol{r}_{k,n}^i - G_k\tilde{d}_{k,n}^i - (P_n^{i-1})^T\tilde{f}_{k,n}^i] \end{aligned} \tag{3}$$

LATTICE GREEN'S FUNCTION (LGF)

Essential to this block LU decomposition is the L_k^{-1} operator. In free space, this operator is the lattice Green's function (LGF) [3]. The definition of the LGF is the analytical inverse of an elliptic operator. They can be written as numerical convolutions. Every entry in the corresponding kernels can be computed using a 1D integral [3]. Using the LGFs, the domain truncation error is only affected by the truncation of the source term [1].

ADAPTIVE MESH REFINEMENT

To efficiently resolve multiple scales, on the 2D slices, we employ an existing AMR algorithm compatible with LGFs

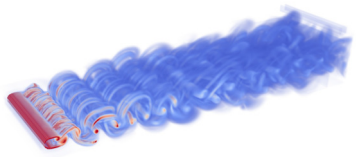

Figure 1: Flow past a cylinder at Re = 300.

Study	$\overline{C_D}$	$C_{L,rms}$	St
Kravchenko et al. (num.) [6]	1.28	0.40	0.203
Mittal and Balachandar (num.) [7]	1.26	0.38	0.203
Experimental [8, 9]	1.22	0.45	0.203
Present	1.25	0.44	0.203

Table 1: Comparison among the results from the present algorithm and previous studies.

Figure 2: $||\boldsymbol{\omega}||D/U_\infty = 10$ contour plots of the flow past a cylinder at $Re = 12000$.

Study	$\overline{C_D}$	$C_{L,rms}$	St
Norberg (exp.) [9]	-	0.435	0.199
Wieselsberger (exp.) [8]	1.15	-	-
Present	1.12	0.67	0.199

Table 2: Drag coefficient, lift coefficient, and Strouhal number comparison between present numerical method and experimental data for the flow past a cylinder at Re = 12,000.

[4]. In addition, we also created a compatible AMR method acting on the Fourier coefficient space. This method, as we'll detail in the presentation, can yield significant computational savings, and allows us to carry out high Reynolds number direct numerical simulations.

VALIDATION EXAMPLE

We simulated the flow past a cylinder at Reynolds number of 300 and compared our results with previous studies. The vorticity distribution of this flow is shown in Fig. 1 which illustrates the mode-B instability [5]. The comparison to previous experimental and numerical studies for the mean drag coefficients ($\overline{C_D}$), root mean squared lift coefficient ($C_{L,rms}$), and the Strouhal number St is shown in Table 1. We achieved excellent quantitative agreements in all three coefficients.

FLOW PAST A CYLINDER AT RE = 12,000

We also show a high Reynolds number direct numerical simulations for flow past a cylinder at Re = 12,000. The corresponding vorticity contour plot is shown in Fig. 2. The comparison with previous experimental data is shown in Table 2. To show the efficiency of the AMR algorithm, we show the comparison between the vorticity field and the mesh topology in Fig. 3. It shows that the AMR algorithm only refines the region with high vorticity distribution.

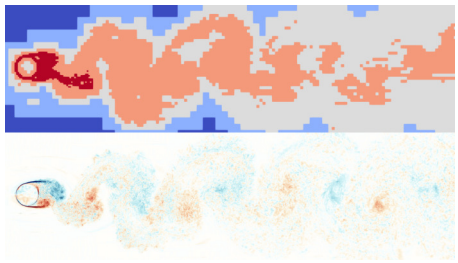

Figure 3: Grid topology (top) vs. span-wise averaged vorticity distribution (bottom) comparison for the simulation at Re = 12,000. Different colors on the grid topology figure represent different resolutions from coarse to fine in the order of deep blue, light blue, grey, orange, and red.

CONCLUSION

By combining the immersed boundary method, the lattice Green's function, and adaptive mesh refinement, we propose a new computational algorithm to conduct direct numerical simulations for spanwise periodic flow around immersed rigid bodies. We validated our algorithm by simulating the flow past a cylinder at Re = 300 and comparing our results to previous numerical and experimental studies. We also showcase the efficiency of our algorithm by simulating the flow past a cylinder at Re = 12,000.

REFERENCES

[1]Liska, Sebastian, and Tim Colonius. "A fast immersed boundary method for external incompressible viscous flows using lattice Green's functions." Journal of Computational Physics 331 (2017): 257-279.

[2]Brasey, Valérie, and Ernst Hairer. "Half-explicit Runge–Kutta methods for differential-algebraic systems of index 2." SIAM Journal on Numerical Analysis 30.2 (1993): 538-552.

[3]Martinsson, Per-Gunnar, and Gregory J. Rodin. "Asymptotic expansions of lattice Green's functions." Proceedings of the Royal Society of London. Series A: Mathematical, Physical and Engineering Sciences 458.2027 (2002): 2609-2622.

[4]Yu, Ke, Benedikt Dorschner, and Tim Colonius. "Multi-resolution lattice Green's function method for incompressible flows." Journal of Computational Physics 459 (2022): 110845.

[5]Williamson, Charles HK. "Vortex dynamics in the cylinder wake." Annual review of fluid mechanics 28.1 (1996): 477-539.

[6]Kravchenko, Arthur G., Parviz Moin, and Karim Shariff. "B-spline method and zonal grids for simulations of complex turbulent flows." Journal of Computational Physics 151.2 (1999): 757-789.

[7]Mittal, R., and S. Balachandar. "On the inclusion of three-dimensional effects in simulations of two-dimensional bluff-body wake flows." ASME fluids engineering division summer meeting. 1997.

[8]Wieselsberger, C. Further information on the laws of fluid resistance. No. NACA-TN-121. 1922.

[9]Norberg, Christoffer. "Fluctuating lift on a circular cylinder: review and new measurements." Journal of Fluids and Structures 17.1 (2003): 57-96.

[10]Peskin, Charles S. "The immersed boundary method." Acta numerica 11 (2002): 479-517.

[11]Rodríguez, Ivette, et al. "High performance computing of the flow past a circular cylinder at critical and supercritical Reynolds numbers." Procedia Engineering 61 (2013): 166-172.

[12]Berger, Eberhard, and Rudolf Wille. "Periodic flow phenomena." Annual Review of Fluid Mechanics 4.1 (1972): 313-340.

[13]Negi, Prabal Singh, et al. "Unsteady aerodynamic effects in small-amplitude pitch oscillations of an airfoil." International Journal of Heat and Fluid Flow 71 (2018): 378-391.

WORKSHOP
Direct and Large-Eddy Simulation 14
April 10-12 2024, Erlangen, Germany

SYSTEMATIC GRID DESIGN IN DIRECT NUMERICAL SIMULATION

S. Toosi[1], **P. Schlatter**[1]
[1]Institute of Fluid Mechanics (LSTM)
Friedrich–Alexander–Universität (FAU) Erlangen–Nürnberg, Germany
siavash.toosi@fau.de

INTRODUCTION

In direct numerical simulation (DNS) all relevant scales of a turbulent flow are directly and fully resolved on the computational grid used in the simulation. Due to the direct connection between the Kolmogorov length scale, η, and the smallest scales present in the flow, the resolution is usually set, characterized, and reported in terms of the ratio of the grid size Δ to the Kolmogorov length scale η. This is the correct measure for simple flows without significant variations in the structure of dissipative scales, and without large variations of η in space. However, any violations of these assumptions could lead to sub-optimal assessment of the resolution using η, leading to either more expensive simulations, or inaccurate results. Unfortunately, these assumptions break down in flows as simple as the canonical channel flow, where the dissipative structures change shape and size as a function of distance from the wall [cf. 1]. Given the recent concerns raised about the resolution of the current DNS datasets of channel and pipe flows (cf. [2]), it seems appropriate to investigate these concerns more closely and introduce a systematic method for designing the DNS grids.

ISSUES WITH THE CURRENT METHOD

The use of the Kolmogorov length scale η for grid design in DNS is motivated by the exponential decay of the amplitude of the spectral content of the turbulent fields at the dissipative range. While true, we should note that η is merely a non-dimensional number and is proportional to the dissipative scales with a constant of proportionality, say k_η, which can itself be a function of space. This variation of k_η in space means that a constant Δ/η, as usually used in grid design, is not necessarily the most meaningful criterion. Perhaps more importantly, assuming that the errors introduced at each location in space are proportional to the measure used for designing the grid (i.e., that a region with higher Δ/η, for instance, is associated with higher contribution to the error in the solution), it can be mathematically shown that the minimum solution error is not achieved for a uniform Δ/η throughout the domain, but instead for a uniform $\mathcal{V}_c\Delta/\eta$ (cf. [3, 4]), where $\mathcal{V}_c$ is the cell/element volume at that location. In addition, it is not straightforward to define the size of the dissipative scales in the non-homogeneous directions of the flow. Therefore, the current method of grid design for DNS appears far from optimal. and needs improvement. This need is magnified by the increasing cost of the simulations, as well as the expansion of the DNS range of applications to more complex flows.

ERROR ESTIMATION IN DNS

The heart of a systematic approach for grid design is a quantitative measure of errors introduced due to insufficient grid resolution. In general, there are many ways to define such a quantity, but the choice ultimately depends on the type of simulation and the quantities of interest from it. Here, we are interested in DNS, and on resolving all scales relevant to dissipation. As a result, we start by the governing equation for the velocity gradient, $A_{ij} = \partial u_i/\partial x_j$ (where u_i is the instantaneous velocity field), and define our quantitive measure of errors based on the errors in this equation due to finite resolution. Following the framework proposed in Toosi & Larsson [4, 5], we can define the residual in the governing equation of A_{ij} [6] as:

$$\begin{aligned}\mathcal{R}^{\Delta}_{ij}(\mathbf{x},\mathbf{n}) = \frac{\partial}{\partial x_k}\left(\overline{u_k A_{ij}}^{(\mathbf{n})} - \overline{u_k}^{(\mathbf{n})}\overline{A_{ij}}^{(\mathbf{n})}\right) \\ + \left(\overline{A_{ik}A_{kj}}^{(\mathbf{n})} - \overline{A_{ik}}^{(\mathbf{n})}\overline{A_{kj}}^{(\mathbf{n})}\right) \\ - \frac{1}{3}\left(\overline{A_{mk}A_{km}}^{(\mathbf{n})} - \overline{A_{mk}}^{(\mathbf{n})}\overline{A_{km}}^{(\mathbf{n})}\right),\end{aligned} \tag{1}$$

where $\overline{*}^{(\mathbf{n})}$ denotes a directional low-pass filtering oparation with a filter-width of $\Delta_{\mathbf{n}}$. The definition of such a filter is quite straightforward since two- and three-dimensional filters are often defined (on structured grids) as the subsequent application of uni-directional filters. Here we use the commutative filters defined in Ref. [7]. Note that $\mathcal{R}^{\Delta}_{ij}$ is a function of space $\mathbf{x} = x_i$, direction $\mathbf{n}$, and the component of velocity gradient.

The DNS error indicator $\mathcal{E}(\mathbf{x},\mathbf{n})$ can be defined (for simplification) as the modulus of the tensor $\mathcal{R}^{\Delta}_{ij}$, i.e.,

$$\mathcal{E}(\mathbf{x},\mathbf{n}) = \sqrt{\langle \mathcal{R}^{\Delta}_{ij}(\mathbf{x},\mathbf{n})\mathcal{R}^{\Delta}_{ij}(\mathbf{x},\mathbf{n})\rangle} \tag{2}$$

where $\langle * \rangle$ denotes averaging (if desired) over time and homogeneous directions of space. In general, the error indicator can be computed in any arbitrary direction $\mathbf{n}$; however, since the grid resolution can be adjusted in only a few directions, it is sufficient to compute $\mathcal{E}(\mathbf{x},\mathbf{n})$ only in those directions.

For the simple case of the channel flow with two homogeneous directions of space, with averaging in time and in the streamwise and spanwise directions, the error indicator will only be a function of the remaining spatial coordinate $x_2 = y$. For a Cartesian grid, $\mathcal{E}(\mathbf{x},\mathbf{n})$ needs to be computed in only the streamwise, wall-normal, and spanwise directions, leading to three independent functions of y. Figure 1 shows an example of this for a channel flow at a friction Reynolds number of $Re_\tau \approx 5200$. At every location, a higher value of $\mathcal{E}$ indicates a

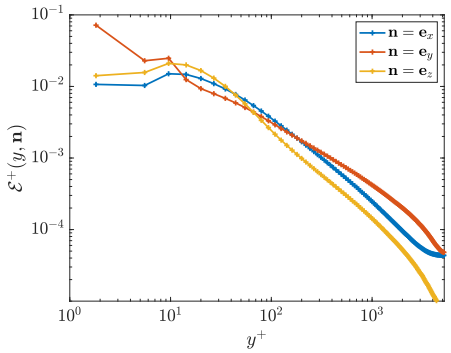

Figure 1: Error indicator of Eqn. 2 computed for a channel flow at $Re_\tau \approx 5200$ with a resolution of $(\Delta x^+, \Delta y_w^+/2, \Delta z^+) \approx (33, 1.8, 14)$ at the wall, with $\Delta y_c^+ \approx 77$ at the center.

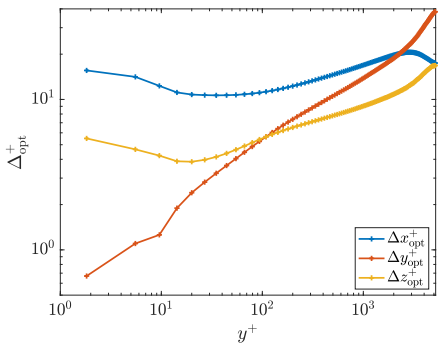

Figure 2: Optimal grid resolutions for the DNS of a channel flow at $Re_\tau \approx 5200$ for a grid that is of similar size (i.e., computational cost) the one used by Lee & Moser [8].

higher contribution to errors in the dissipation, and thus the solution.

GRID DESIGN

The optimal grid can be found by minimizing the volume integral of the error indicator over the computational domain Ω, with a constraint on the computational cost. This constraint is necessary to avoid a trivial solution where the grid spacing approaches zero and the cost approaches infinity. Taking the total number of grid points as a proxy for cost, this optimization problem can be mathematically stated as:

$$\text{minimize} \int_\Omega J(\mathbf{x}) \, \|\mathcal{E}(\mathbf{x},\mathbf{n})\| \, d\mathbf{x}, \text{such that} \int_\Omega \frac{d\mathbf{x}}{\mathcal{V}_c} = N_{\mathrm{tot}} \, ,$$

where $J(\mathbf{x})$ is a weight as a function of space (ideally, the adjoint field in output-based grid selection), $\|*\|$ is some form of summation over contributions from different directions $\mathbf{n}$ (e.g., a simple sum, or an L_2-norm), $\mathcal{V}_c = \mathcal{V}_c(\mathbf{x})$ is the local volume of the computational unit at location $\mathbf{x}$, and N_{tot} is the desired number of grid points.

It is relatively easy to show that for hexahedral computational units, and under relatively generic assumptions, this optimization problem can be solved mathematically (cf. [4]) with the following solution:

$$\begin{aligned} \mathcal{E}_{\mathrm{opt}}(\mathbf{x},\mathbf{n}_1) = \mathcal{E}_{\mathrm{opt}}(\mathbf{x},\mathbf{n}_2) = \mathcal{E}_{\mathrm{opt}}(\mathbf{x},\mathbf{n}_3) \\ J(\mathbf{x}) \, \|\mathcal{E}_{\mathrm{opt}}(\mathbf{x},\mathbf{n})\| \, \mathcal{V}_{c,\mathrm{opt}}(\mathbf{x}) = \text{const.} \, . \end{aligned} \tag{3}$$

Here, the first relation gives the shape of the cell and its relative resolutions in different directions (i.e., its aspect ratio or anisotropy) at any given location $\mathbf{x}$, while the second equation determines the spatial variation of the resolution, $\mathcal{V}_{c,\mathrm{opt}}$, as a function of space $\mathbf{x}$. Together, the two equations fully determine the optimal directional resolution [4]. In the absence of the adjoint fields for turbulent flows, one can take $J(\mathbf{x}) \equiv 1$ for a uniform weight.

Figure 2 shows the optimal resolutions predicted for the DNS of channel flow at $Re_\tau \approx 5200$ for a grid that is of the same size (i.e., similar computational cost) as the one used by Lee & Moser [8]. We note that the optimal resolutions predicted by the proposed method are quite similar to the one used in the DNS of Lee & Moser with $\Delta^+_{\mathrm{LM5200}} \approx (12.7, 0.5, 6.4)$ compared to $\Delta^+_{\mathrm{opt}} \approx (10.3, 0.33, 4.0)$. The wall-normal resolution predicted by the current method reaches a realtively high value of $\Delta y^+_{c,\mathrm{opt}} \approx 37$ at the center of the channel. This needs to be investigated further.

CONCLUSIONS AND OUTLOOK

This was a first attempt at proposing a systematic approach for grid design in DNS. The method appears quite promising given the similarity of the predicted grid to the one used by Lee & Moser (2015). However, more work is required to understand whether the differences are caused by missing physics in the proposed method, the relatively low resolution of the grid compared to the final DNS grid, or certain assumptions during grid generation process. It may also be that the predicted resolutions are in fact optimal and there is an underlying explanation for the discrepancies to the grid by Lee & Moser [8]. This will be discussed further in the final work. In addition, a more accurate investigation of the current DNS datasets and a more explicit connection between the error indicator and the flow physics will be provided, along with a more comprehensive assessment of the method's ability for generating DNS grids using *a posteriori* tests. The definition of the error indicator might be modified as well during this process.

REFERENCES

[1]Lee M., Moser R.D. : Spectral analysis of the budget equation in turbulent channel flows at high Reynolds number, J. Fluid Mech., **860**, 886–938, 2019.

[2]Monkewitz, P.A., Nagib, H.M. : The hunt for the Kármán 'constant' revisited. J. Fluid Mech., **967**, A15, 2023.

[3]Lapenta G.: Variational grid adaptation based on the minimization of local truncation error: time-independent problems, J. Comp. Phys., **193** (1), 159–179, 2004.

[4]Toosi, S., Larsson, J. : Towards systematic grid selection in LES: Identifying the optimal spatial resolution by minimizing the solution sensitivity, Comput. & Fluid., **201**, 104488, 2020.

[5]Toosi, S., Larsson, J. : The Germano identity error and the residual of the LES governing equation, J. Comp. Phys., **443**, 110544, 2021.

[6]Meneveau C. : Lagrangian dynamics and models of the velocity gradient tensor in turbulent flows, Annu. Rev. Fluid Mech., **43**, 219–245, 2011

[7]Vasilyev O.V., Lund, T.S., Moin P. : A general class of commutative filters for LES in complex geometries, J. Comp. Phys., **146**, 82–104, 1998.

[8]Lee M., Moser R.D. : Direct numerical simulation of turbulent channel flow up to $Re_\tau \approx 5200$. J. Fluid Mech., **774**, 395–415, 2015.

WORKSHOP
Direct and Large-Eddy Simulation 14
April 10-12 2024, Erlangen, Germany

DLES14: SYNTHETIC TURBULENCE GENERATION FOR SPECTRAL/HP ELEMENT METHODS

J. Isler[1], G. Vivarelli[1], C. Cantwell[1], F. Montomoli[1], S. Sherwin[1], Y. Frey[2], M. Meyer[3], R. Vazquez[2]
[1]Department of Aeronautics, Imperial College London, United Kingdom
[2]Rolls-Royce plc, Derby, United Kingdom
[3]Rolls-Royce Deutschland, Dahlewitz, Germany
j.isler20@imperial.ac.uk

INTRODUCTION

Advancements in the computing performance of modern hardware, along with improvements in numerical methods, have significantly enhanced the feasibility and frequency of using scale-resolving simulations, such as Direct Numerical Simulations (DNS), in industrial applications. However, to be effective as a tool, scale-resolving simulations must generate realistic incoming turbulence to provide reliable predictions of the flow field. The implementation of an inflow turbulence generation method is pivotal in this regard, offering enhanced predictions for critical aspects such as boundary layer transitions, flow separation, and reattachment. This is particularly crucial in the aerodynamic design of high- and low-pressure turbines, fans, and intakes, where precise modelling of these phenomena plays a significant role.

The challenge of introducing realistic turbulence in the computational domain will be addressed by the Synthetic Eddy Method (SEM) [1]. The source-term formulation of this method has been developed in the Nektar++ framework for the incompressible and compressible solvers [2, 3]. Nektar++ is a highly scalable spectral/*hp* element framework, which offers access to a wide range of spatial and temporal scales in turbulent flows [4, 5, 6]. In this work, the SEM is applied to an incompressible plane channel flow [7, 8] and to the low-pressure turbine T106A linear cascade [9]. Isotropic and anisotropic turbulence generation are employed in the numerical simulations. Also, unstructured meshes are used in order to verify the flexibility of the method to handle unstructured meshes.

SOURCE-TERM FORMULATION OF THE SYNTHETIC EDDY METHOD

Figure 1 shows a schematic diagram of the plane channel flow and synthetic eddy region. The synthetic eddy region is where the eddies are injected in the domain by adding a source-term to the conservation equation to drive the solution to the desired turbulent field. Since the SEM implemented here is based on the source-term formulation as described above, the synthetic region was placed, in this case, slightly downstream of the inlet boundary condition. It is worth mentioning that the synthetic region does not necessarily need to fill the whole domain in the y- and z-directions, but it can strategically be located in the region of interest. In the first time step, all the eddies are injected in random positions in

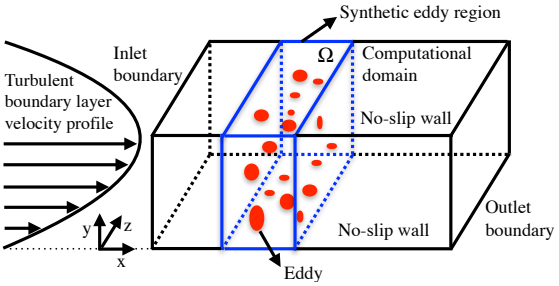

Figure 1: Schematic setup of the plane channel flow and synthetic eddy region (not to scale).

the synthetic region. Looking at the movement of a single eddy in the synthetic region as illustrated in figure 2. After its injection in the first time step, the eddy moves downstream generating fluctuations in the flow field. The movement of the eddy in the synthetic region (Ω) is given by the equation of motion as follows

$$x^n(t+\Delta t) = x^n(t) + U_b \Delta t, \tag{1}$$
$$y^n(t+\Delta t) = y^n(t), \tag{2}$$
$$z^n(t+\Delta t) = z^n(t), \tag{3}$$

where n represents the eddy number, Δt is the time step and U_b is the bulk velocity. The bulk velocity is assumed to be constant across the synthetic region and is calculated as

$$U_b = \frac{1}{\iint_{A^{in}} \rho \, dA} \iint_{A^{in}} \rho \vec{U} \cdot \vec{n} \, dA, \tag{4}$$

where ρ is the density, $\vec{U}$ is the mean velocity, $\vec{n}$ is the local unit normal and A^{in} is the inlet surface.

When the eddy leaves through the outlet plane of the synthetic region (figure 2), another eddy is randomly re-injected in the inlet plane. It is well represented by the expression below

$$\begin{bmatrix} x^n(t) \\ y^n(t) \\ z^n(t) \end{bmatrix} \xrightarrow{if\, x^n(t+\Delta t) > l_x} \begin{bmatrix} x^n(t+\Delta t) = -l_x \\ y^n(t+\Delta t) = random(y^n) \\ z^n(t+\Delta t) = random(z^n) \end{bmatrix}$$

Note that more than one eddy may leave the outlet plane per time step, so that all the eddies that left the synthetic region after a period of time Δt are going to be re-injected by the

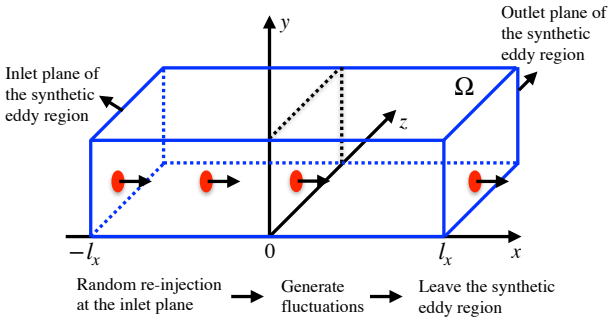

Figure 2: Displacement of an eddy n in the synthetic eddy region.

source-term. Thus, this is the mechanism that re-energises the system.

NUMERICAL METHOD

Incompressible and compressible flow simulations with synthetic turbulence generation are conducted in the Nektar++ framework. For the incompressible solver setup of the plane channel flow, the Continuous Galerkin (CG) method was employed for spatial discretisation. To solve the temporal discretisation, the velocity correction scheme was used. At the outflow boundary condition, we imposed a high-order outlet condition. Considering now the compressible solver setup for the low-pressure turbine, the Discontinuous Galerkin (DG) method is used for spatial discretisation. The diffusion terms are treated with the interior penalty method, and the advection terms are rewritten using a standard weak DG scheme, followed by the application of Roe's approximate Riemann solver. The set of ordinary differential equations obtained from the spatial discretization is integrated in time using a second-order singly diagonally implicit multi-stage Runge–Kutta (SDIRK2) method. At the inlet, we imposed an entropy-velocity compatible Riemann inflow boundary condition [10]. Also, a sponge layer is applied just upstream of the inflow boundary in order to damp the reflections from the outlet boundary condition, which is fully reflective. Here the synthetic eddy region, for the low-pressure turbine, is placed next to the sponge layer and upstream of the blade, as the source term formulation allows the synthetic eddy region to be placed in any part of the domain. In both cases, periodic boundary conditions were imposed in the span-wise direction.

RESULTS

The plane channel flow case, at Reynolds number $Re = 2767$ based on the bulk velocity, to investigate the incompressible implementation is shown in figure 3. It can be seen that the synthetic eddy region, where the eddies are injected, located close to the inlet region triggers the turbulent boundary layer.

ACKNOWLEDGEMENTS

The authors gratefully acknowledge the ARCHER2 UK National Supercomputing Service (https://www.archer2.ac.uk) and the Imperial College London Research Computing Service (DOI: 10.14469/hpc/2232) for the computational resources provided for this work. Financial support was provided by the

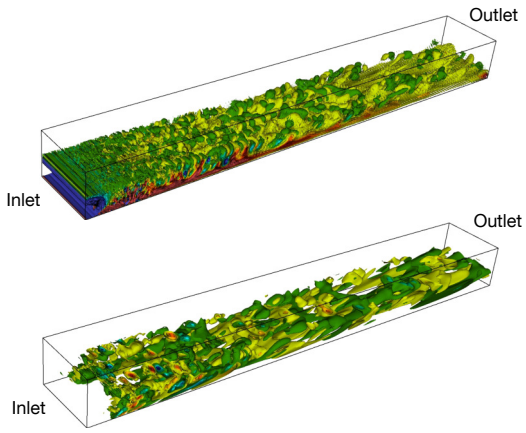

Figure 3: Fully three-dimensional incompressible turbulent channel flow. Iso-surfaces of Q-criterion at the top and iso-surface of the span-wise velocity at the bottom. Only the lower half of the channel is shown.

Aerospace Institute of Technology's FANFARE grant (number 113286).

REFERENCES

[1]Jarrin, N., Benhamadouche, S., Laurence, D., Prosser, R. : A synthetic-eddy-method for generating inflow conditions for large-eddy simulations, *International Journal of Heat and Fluid Flow*, **27**, 585–593 (2006).

[2]Schmidt, S. and Breuer, M. : Source term based synthetic turbulence inflow generator for eddy-resolving predictions of an airfoil flow including a laminar separation bubble, *Computers and Fluids*, **146**, 1–22 (2017).

[3]Giangaspero, G., Witherden, F. and Vincent, P. : Synthetic turbulence generation for high-order scale-resolving simulations on unstructured grids, *AIAA journal*, **60**(2), 1032–1051 (2022).

[4]Cantwell, C. D., Moxey, D., Comerford, A., Bolis, A., Rocco, G., Mengaldo, G., De Grazia, D., Yakovlev, S., Lombard, J. E., Ekelschot, D., Jordi, B., Xu, H., Mohamied, Y., Eskilsson, C., Nelson, B., Vos, P., Kirby, R. M., Sherwin, S. J. : Nektar++: An open-source spectral/hp element framework, *Computer Physics Communications*, **192**, 205–219 (2015).

[5]Moxey, D., Cantwell, C. D., Bao, Y., Cassinelli, A., Castiglioni, G., Chun, S., Juda, E., Kazemi, E., Lackhove, K., Marcon, J., Mengaldo, G., Serson, D., Turner, M., Xu, H., Peiró, J., Kirby, R. M., Sherwin, S. J. : Nektar ++: Enhancing the capability and application of high-fidelity spectral/hp element methods, *Computer Physics Communications*, **249**, 107110 (2020).

[6]Yan, Z.-Y., Pan, Y., Castiglioni, G., Hillewaert, K., Peiró, J., Moxey, D., Sherwin, S. J. : Nektar++: Design and implementation of an implicit, spectral/hp element, compressible flow solver using a Jacobian-free Newton Krylov approach, *Computers and Mathematics with Applications*, **81**, 351–372 (2021).

[7]Kim, J, Moin, P., Moser, R. : Turbulence statistics in fully developed channel flow at low Reynolds number, *Journal of Fluid Mechanics*, **177**, 133–166 (1986).

[8]Moser, R. D., Kim, J., Mansour, N. N. : Direct numerical simulation of turbulent channel flow up to Re_τ=590, *Physics of Fluids*, **11**(4), 943–945 (1999).

[9]Michelassi, V., Liwei, C., Pichler, R., Sandberg, R. D. : Compressible direct numerical simulation ofl low-pressure turbines - Part II: Effect of inflow disturbances, *Journal of Turbomachinery*, **137**, 071005 (2015).

[10]Lyu, G., Chen, C., Du, X., Sherwin, S. J. : Stable, entropy-pressure compatible sub- sonic riemann boundary condition for embedded dg compressible flow simulations, *Journal of Computational Physics*, **476**, 111896 (2023).

WORKSHOP
Direct and Large-Eddy Simulation 14
April 10-12 2024, Erlangen, Germany

MESH CONSTRAINTS FOR AN ENERGY PRESERVING UNCONDITIONALLY STABLE PROJECTION METHOD ON COLLOCATED UNSTRUCTURED GRIDS

D. Santos, F.X. Trias, J. Hopman, C.D. Pérez-Segarra
Heat and Mass Transfer Technological Center (CTTC)
Technical University of Catalonia, Terrassa, Spain
{daniel.santos.serrano, francesc.xavier.trias, jannes.hopman, cdavid.perez.segarra} @upc.edu

INTRODUCTION

The Navier-Stokes equations for Newtonian, incompressible flows in dimensionless primitive variables read:

$$\frac{\partial \boldsymbol{u}}{\partial t} + (\boldsymbol{u}\cdot\nabla)\,\boldsymbol{u} = \frac{1}{Re}\Delta\boldsymbol{u} - \nabla p, \tag{1a}$$

$$\nabla\cdot\boldsymbol{u} = 0, \tag{1b}$$

where Re represents the dimensionless Reynolds number. A fully-conservative finite-volume discretization, maintaining the symmetries of the differential operators for collocated unstructured meshes, was firstly introduced in [1]. Assuming there are n control volumes and m faces:

$$\Omega\frac{d\boldsymbol{u}_c}{dt} + \mathsf{C}\left(\boldsymbol{u}_s\right)\boldsymbol{u}_c + \mathsf{D}\boldsymbol{u}_c + \Omega\mathsf{G}_c\boldsymbol{p}_c = \boldsymbol{0}_c, \tag{2a}$$

$$\mathsf{M}\boldsymbol{u}_s = \boldsymbol{0}_c, \tag{2b}$$

where $\boldsymbol{p}_c = (p_1, p_2, \ldots, p_n)^T \in \mathbb{R}^n$ and $\boldsymbol{u}_c \in \mathbb{R}^{3n}$ are the cell-centered pressure and collocated velocity fields, respectively. The subindices c and s indicate if the variables are cell-centered or staggered at the faces. To verify mass conservation within each control volume, a velocity field is defined at the faces $\boldsymbol{u}_s = \left((u_s)_1, (u_s)_2, (u_s)_3, \ldots, (u_s)_m\right)^T \in \mathbb{R}^m$. Quantities defined at cells and at faces are related using an interpolator from cells to faces $\Gamma_{c\to s} \in \mathbb{R}^{m\times 3n}$:

$$\boldsymbol{u}_s \equiv \Gamma_{c\to s}\boldsymbol{u}_c. \tag{3}$$

The matrices $\Omega \in \mathbb{R}^{3n\times 3n}$, $\mathsf{C}\left(\boldsymbol{u}_s\right) \in \mathbb{R}^{3n\times 3n}$ and $\mathsf{D} \in \mathbb{R}^{3n\times 3n}$ are block diagonal matrices given by

$$\Omega = \mathsf{I}_3 \otimes \Omega_c, \qquad \mathsf{C}\left(\boldsymbol{u}_s\right) = \mathsf{I}_3 \otimes \mathsf{C}_c\left(\boldsymbol{u}_s\right), \qquad \mathsf{D} = \mathsf{I}_3 \otimes \mathsf{D}_c, \tag{4}$$

where $\mathsf{I}_3 \in \mathbb{R}^{3\times 3}$ is the identity matrix and $\Omega_c \in \mathbb{R}^{n\times n}$ is a diagonal matrix containing the cell-centered control volumes. $\mathsf{C}_c\left(\boldsymbol{u}_s\right) \in \mathbb{R}^{n\times n}$ and $\mathsf{D}_c \in \mathbb{R}^{n\times n}$ are the cell-centered convective and diffusive operators for a discrete scalar field, respectively. Finally, $\mathsf{G}_c \in \mathbb{R}^{3n\times n}$ is the discrete gradient operator, and the matrix $\mathsf{M} \in \mathbb{R}^{n\times m}$ is the face-to-center discrete divergence operator.

The 3−dimensional interpolator from cells to faces $\Gamma_{c\to s}$ is constructed as follows:

$$\Gamma_{c\to s} = N(\mathsf{I}_3 \otimes \Pi_{c\to s}), \tag{5}$$

where $\Pi_{c\to s} \in \mathbb{R}^{m\times n}$ is the scalar cell-to-face interpolator, and $N = (N_{s,x}N_{s,y}N_{s,z}) \in \mathbb{R}^{3m\times m}$, where $N_{s,i} \in \mathbb{R}^{m\times m}$ is a diagonal matrix containing the x_i spatial components of the face normal vectors.

Only five operators were needed to build this formulation: the cell-centered and staggered control volumes, Ω_c and Ω_s respectively, the face normal vectors N_s, the scalar cell-to-face interpolation operator $\Pi_{c\to s}$, and the cell-to-face divergence operator M. This simplicity not only eases the construction of the required operators but also improves the portability of a code developed within this framework, as demonstrated in [2]. The global kinetic energy $||\boldsymbol{u}_c||^2$ is conserved if [1]:

$$\mathsf{C}\left(\boldsymbol{u}_s\right) = -\mathsf{C}\left(\boldsymbol{u}_s\right)^T, \tag{6a}$$

$$-\left(\Omega\mathsf{G}_c\right)^T = \mathsf{M}\Gamma_{c\to s}, \tag{6b}$$

relating the gradient operator with the divergence operator and assuming the convective operator to be skew-symmetric. If $\mathsf{L}_c = \mathsf{M}_c\mathsf{G}_c$ is used to build the Poisson equation, the global kinetic energy is perfectly conserved. However, the well-known checkerboard problem is found with this approach. Alternatively, the use of $\mathsf{L} = \mathsf{MG}$ will be discussed in this work.

AN ENERGY-PRESERVING UNCONDITIONALLY STABLE PISO ALGORITHM

Assuming either explicit or implicit time integration, spatially discrete momentum equation (2a) can be rewritten as follows:

$$\mathbf{S}\boldsymbol{u}_c = \mathbf{r} - \mathsf{G}_c\boldsymbol{p}_c, \tag{7}$$

where $\mathbf{S} \in \mathbb{R}^{3n\times 3n}$ is the coefficient matrix after applying a discretization method (such as Finite Volume Method), and $\mathbf{r} \in \mathbb{R}^{3n\times 1}$ is a vector containing all the explicit terms apart from the pressure gradient. The coefficients are all known once the discretization procedure is selected.

By treating the pressure gradient as an explicit source and solving for the velocity, the momentum predictor is obtained:

$$\boldsymbol{u}_c^* = \mathbf{S}^{-1}\mathbf{r} - \mathbf{S}^{-1}\mathsf{G}_c\boldsymbol{p}_c^n. \tag{8}$$

Note that the momentum predictor $\boldsymbol{u}_c^*$ does not satisfy the continuity equation. To ensure so, a corrector step must be performed. The diagonal coefficients of $\mathbf{S}$ will be extracted in a diagonal matrix $\mathbf{A}$ (which will be easily invertible), and the off-diagonal coefficients will be keeped in a matrix $\mathbf{H}'$. Then, it is assumed that the diagonal matrix is acting on a new corrected velocity $\boldsymbol{u}_c^{**}$ while the off-diagonal part is acting on the predictor velocity $\boldsymbol{u}_c^*$.

The final algorithm reads [3]:

$$\begin{aligned} \boldsymbol{u}_c^* &= \mathbf{S}^{-1}\mathbf{r} - \mathbf{S}^{-1}\mathsf{G}_c\boldsymbol{p}_c, && \text{(9a)}\\ \mathsf{M}\tilde{\mathbf{A}}^{-1}\mathsf{G}\boldsymbol{p}_c^* &= \mathsf{M}\Gamma_{c\to s}\mathbf{A}^{-1}(\mathbf{r} - \mathbf{H}'\boldsymbol{u}_c^*) \longrightarrow \boldsymbol{p}_c^*, && \text{(9b)}\\ \boldsymbol{u}_c^{**} &= \mathbf{A}^{-1}(\mathbf{r} - \mathbf{H}'\boldsymbol{u}_c^*) - \mathbf{A}^{-1}\mathsf{G}_c\boldsymbol{p}_c^*, && \text{(9c)}\\ \boldsymbol{u}_s^{**} &= \Gamma_{c\to s}\mathbf{A}^{-1}(\mathbf{r} - \mathbf{H}'\boldsymbol{u}_c^*) - \tilde{\mathbf{A}}^{-1}\mathsf{G}\boldsymbol{p}_c^*. && \text{(9d)} \end{aligned}$$

Here, $\tilde{\mathbf{A}}^{-1} = diag(\Pi_{c\to s} vec(\mathbf{A}_c^{-1}))$ and and $\mathbf{A} = I_3 \otimes \mathbf{A}_c$ (the matrix $\mathbf{A}$ has three equal (diagonal) blocks). The PISO algorithm iterates through the corrector steps until the desired level of convergence is achieved. In this context, the utilization of the compact Laplacian operator L to mitigate checkerboard problems is assumed. Additionally, an (artificial) contribution to the kinetic energy will be introduced:

$$\boldsymbol{p}_c^T(\mathsf{M}\tilde{\mathbf{A}}^{-1}\mathsf{G} - \mathsf{M}_c\mathbf{A}^{-1}\mathsf{G}_c)\boldsymbol{p}_c = \boldsymbol{p}_c^T(\mathsf{L} - \mathsf{L}_c)\boldsymbol{p}_c. \qquad (10)$$

Ideally, the contribution of this term should be negative and maintained as small as possible to avoid introducing energy into our system, thereby preventing the simulation from destabilizing. At this point, note that each projection method that lead the equations to be solved in this way will encounter the same problem, for example, the classical Fractional Step Method [1], which is similar to the PISO algorithm but with no predictor step and corrector iterations.

GEOMETRICAL CONDITIONS OF THE PROJECTION METHOD IN ORDER TO BE UNCONDITIONALLY STABLE

Theorem.
Let us assume a general 2D or 3D mesh is constructed such that each control volume satisfies:

- **1.** $V_k = \sum_f \tilde{V}_{k,f} n_{i,f}^2, \forall k \in \{1, ..., n\}, i \in \{x, y, z\}$,
- **2.** $\sum_f \tilde{V}_{k,f} n_{i,f} n_{j,f} = 0, \forall k \in \{1, ..., n\}, i, j \in \{x, y, z\}, i \neq j$.

Then, $\mathsf{L} - \mathsf{L}_c$ is positive definite as long as the chosen interpolator is the volume weighted one (this is the unique possible choice of interpolator, for both $\mathsf{G}_c\boldsymbol{p}_c$ in the velocity correction equation and in the computation of $\tilde{\mathbf{A}}$). The converse is also true.

The volume weighted interpolator was introduced in [4], and can be constructed in any mesh as follows:

$$\Pi_{c\to s} = \Delta_s^{-1}\Delta_{sc}^T, \qquad (11)$$

where $\Delta_s \in \mathbb{R}^{m\times m}$ is a diagonal matrix containing the projected distances between two adjacent control volumes, and $\Delta_{sc} \in \mathbb{R}^{m\times n}$ is a matrix containing the projected distances between an adjacent cell node and its corresponding face. Fig.1 shows a representation of these distances.

Some consequences of the previous theorem are the following ones:

- Square and cubic meshes are stable when using the volume weighted interpolator even for highly distorted configurations.
- Triangular 2D meshes are stable when using the volume weighted interpolator and locating the cell-node at the circumcenter, even for highly distorted configurations, but tetrahedral meshes are not unconditionally stable.

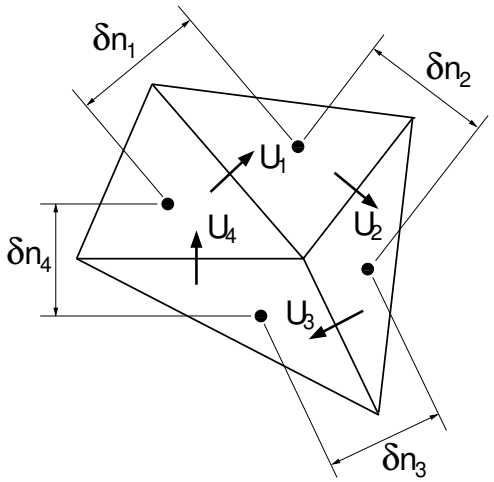

Figure 1: δn_i are the components of Δ_s, while the components of Δ_{sc} would be calculated in the same way but taking the distance between a control volume and their corresponding face centers.

CONCLUSIONS

Necessary and sufficient conditions in order to build an energy preserving unconditionally stable projection method on collocated unstructured grids are given in this work. Furthermore, different types of grids will be discussed in order to assess which are unconditionally stable even for highly distorted cases.

ACKNOWLEDGEMENT

This work is supported by the SIMEX project (PID2022-142174OB-I00) of *Ministerio de Ciencia e Innovación* and the RETOtwin project (PDC2021-120970-I00) of *Ministerio de Economía y Competitividad*, Spain. D. Santos acknowledges a *FI AGAUR-Generalitat de Catalunya* fellowship (2022FI_B_00173), extended and financed by *Universitat Politècnica de Catalunya and Banc Santander*. J.A.H. is supported by the predoctoral grant FI 2023 (2023 FI_B1 00204) of the *Catalan Agency for Management of University and Research Grants (AGAUR)*.

REFERENCES

[1]Trias, F. X. , Lehmkuhl, O. ,Oliva, A. , Pérez-Segarra, C.D. , Verstappen, R.W.C.P. : Symmetry-preserving discretization of Navier-Stokes equations on collocated unstructured meshes, *Journal of Computational Physics*, **258**, 246–267 (2014).

[2]Álvarez, X. , Gorobets A., Trias F.X. : A hierarchical parallel implementation for heterogeneous computing. Application to algebra-based CFD simulations on hybrid supercomputers, *Computers & Fluids*, **214** (2021).

[3]Issa, R.I. : Solution of the implicitly discretised fluid flow equations by operator-splitting, *Journal of Computational Physics*, **62** 40–65 (1986).

[4]Santos D., Muela J., Valle N., Trias F.X.: On the Interpolation Problem for the Poisson Equation on Collocated Meshes, *14th WCCM-ECCOMAS Congress 2020, 19–24 July, 2020 Paris, France*, (2021).

SESSION: Turbulent boundary layers/separation

Thursday, April 11, 2024

11:20- 12:50

WORKSHOP
Direct and Large-Eddy Simulation 14
April 10-12 2024, Erlangen, Germany

LES OF A TURBULENT BOUNDARY LAYER SUBJECTED TO ADVERSE AND ZERO PRESSURE GRADIENT IN A CHANNEL WITH A WAVY WALL

Piotr Kamiński[1], **Artur Tyliszczak**[1], **Witold Elsner**[1],
[1]Department of Thermal Machinery
Czestochowa University of Technology, Poland
piotr.kaminski@pcz.pl

INTRODUCTION

The turbulent boundary layer (TBL) exposed to the adverse pressure gradient (APG) condition occurs commonly in various flow configurations, e.g., over airfoils and turbine blades or inside diverging channels. TBL under APG conditions is usually accompanied by a separation, which occurs when the wall shear stresses reach zero ($\tau_w \approx 0$) [1]. This results in significant energy losses, and therefore research on the development of flow control methods aiming at delaying or eliminating the separation is crucial.

Techniques allowing for the TBL control are generally split into two categories. They can be active and passive. The former tend to be more effective although at a larger cost related to the complexity of the control devices and the need for an external energy source. For this reason, passive flow control methods are becoming favoured. These techniques usually involve some degree of wall modification such as grooves [2], herringbone riblets [4], bird feathers structure [3] or dimples [5]. The downside of these methods is that their effect diminishes as the Reynolds number increases [6]. A very recent passive flow control technique, which was proven successful in a postponement of the separation [7], is a spanwise two-dimensional wavy wall (WW) topology. As shown in [7], this method is effective for high Reynolds numbers for which the control by random structure rough surfaces fails.

In this work, we perform the Large Eddy Simulation (LES) analysis of the near-wall flow exposed to APG developing over WW identical as in experimental research of Drozdz et al. [7]. The use of the LES method gives us a very deep insight into the dynamics of the flow along WW. Additionally, we analyse whether the applied wall topology is effective in zero pressure gradient (ZPG) conditions. The goals of the research are the following: (i) to examine whether the local (in between waviness) or global APG exerts a more substantial influence on the TBL; (ii) to inspect changes in flow dynamics within successive waves, correlating with the escalating APG along the streamwise direction; (iii) to examine the impact of WW and pressure gradient on the wall shear stresses.

The research is performed for the Reynolds number based on the friction velocity and initial boundary layer thickness equal to $Re_\tau = 2500$. To correctly assess the influence of WW, the simulations of flow over the flat wall are performed to obtain a reference point. The obtained results are validated against experimental data.

NUMERICAL SETUP

The simulations are performed with the help of ANSYS Fluent code employing the WALE sub-grid model. A second-order bounded central differencing scheme is applied to discretize the Navier-Stokes equations. The SIMPLE algorithm is used for the pressure-velocity coupling with the second-order discretization of the pressure gradient term. An implicit second-order method is used for the time integration.

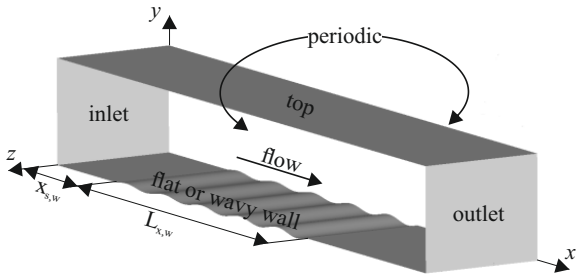

Figure 1: Computational domain.

The computational domain is shown in Fig. 1. In this configuration, the fluid (air) enters through the inlet (located at $x = -0.2$ m) and leaves through the outlet (located at $x = 1.1$ m). The bottom wall is either flat throughout a whole domain or wavy. The upper boundary (top), situated at a fixed height of $y = 0.2$ m, provides control over the pressure gradient ($dp/dx > 0$ (APG) or $dp/dx = 0$ (ZPG)) within the domain. The left and right boundaries, spaced by $z = 0.24$ m, are treated as periodic. The total length of the domain is equal to $L_x = 1.3$ m. The velocity profiles for the inlet and top boundary conditions were defined based on the experimental measurements. We note that for APG, the velocity on the top boundary is adjusted such that dp/dx increases along the streamwise direction. The waviness on the bottom wall starts at $x_{s,w} = 0.21$ m from the inlet and its length is equal to $L_{x,w} = 0.666$ m. The lengths of particular waves are the same and equal to $\lambda = 0.133$ m. This results in 5 periods. The amplitude $A(x)$ of the waviness increases along the streamwise direction according to the formula:

$$A(x) = A_0(0.00000366x^2 + 0.000614x + 3.351) \qquad (1)$$

for which the minimal and maximal values are $A(x = 0.01$ m$) = 0.0034$ m and $A(x = 0.676$ m$) = 0.0054$ m respectively.

In [7] this wall shape was found to be the most effective in enhancing the wall-shear stresses for the present flow regimes.

The simulations are performed on a series of block-structured hexahedral meshes consisting of 4.0×10^6 (mesh M1), 7.2×10^6 (M2), 18.3×10^6 (M3) and 41.1×10^6 (M4) nodes. Preliminary grid sensitivity studies have shown that starting from the mesh M4 the results differ only minimally. Hence, this mesh was used in the main computations.

RESULTS

The simulations of four test cases were performed, i.e., flat wall under ZPG (F-ZPG), flat wall under APG (F-APG), wavy wall under ZPG (W-ZPG) and wavy wall under APG (W-APG). The analysis of these configurations allows us for an in-depth examination of the effects of the local pressure gradients versus the global APG and ZPG conditions.

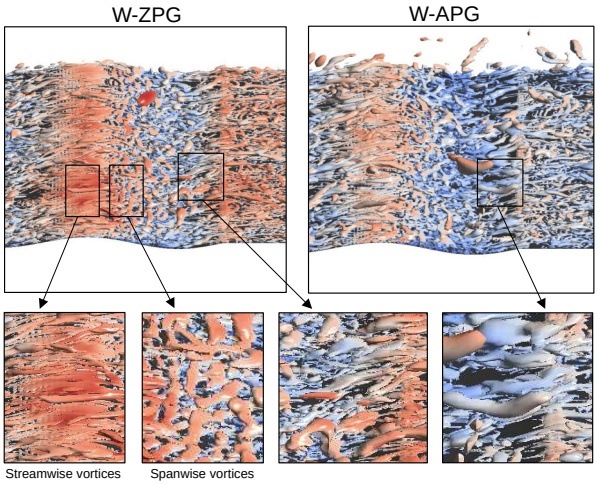

Figure 2: Q-parameter isosurfaces xxcoloured by instantaneous streamwise velocity. Last (5^{th}) waviness period of W-ZPG and W-APG case is presented.

Figure 2 presents Q-parameter isosurfaces for the last (5^{th}) WW period for cases W-ZPG and W-APG. It can be observed that, in general, WW causes the occurrence of two types of vertical structures. Longitudinal vortices exist on the hills of WW. They break down downstream and form spanwise structures on the downhill slopes. Scrutiny of the obtained results allows us to distinguish subtle differences in flow patterns between particular cases. Namely, on the uphill side of the 5^{th} period, the sizes of vortices for W-APG case are larger and more disorganised compared to W-ZPG configuration. This indicates that APG causes the growth of the vertical structure.

Figure 3 presents the points of separation and reattachment ($(x-x_n)/\lambda$, where x_n is the local beginning of $n-$th waviness period) within each consecutive wave marked on the $y-$axis. The black line represents the shape of the wave. It allows for an easy localisation of the separation/reattachment points on the wall. It can be seen that, for the W-APG case, both the separation and reattachment occur slightly earlier, i.e., more upstream than for the W-ZPG case. For waves 1-4, the length of the separation zone remains relatively constant for both cases. At 5th wave dp/dx is the strongest and leads notably larger separation length for W-APG. This means that if APG is strong enough its influence on TBL is larger than

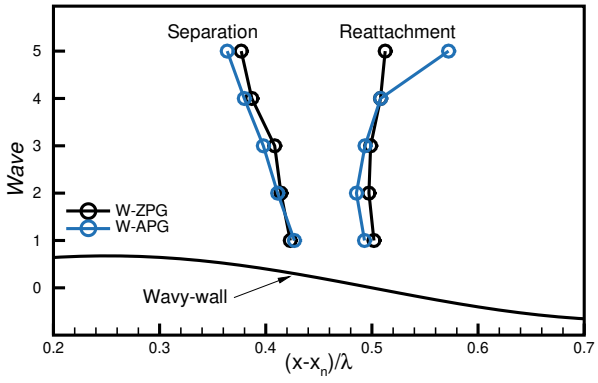

Figure 3: Locations of separation and reattachment points $(x-x_n)/\lambda$ on each consecutive wave ($y-$axis).

that caused by the local pressure gradients along the wavy wall.

CONCLUSIONS

In this abstract, we demonstrated the results of a preliminary study aiming at the assessment of the effect of the wavy wall topology on the near-wall flow dynamics in the APG and ZPG conditions.

It was shown that the presence of the wavy wall triggers the existence of two types of vortical structures, i.e. streamwise and spanwise. The former appear on the hills of the wavy wall and break down downstream which induces the formation of the spanwise vortices. The strong APG causes their growth, especially at the end of the wavy wall section.

The crests and troughs of the wavy wall cause the local APG conditions on the downhill slope. This results in the occurrence of separation bubbles. Up to 4^{th} period, their lengths are relatively the same both for W-ZPG and W-APG. However in the 5^{th} period, due to the growth of global APG, the separation bubble length is considerably larger for W-APG case.

REFERENCES

[1]Nagano, Y., Tagawa, M. and Tsuji, T. : Effects of adverse pressure gradients on mean flows and turbulence statistics in a boundary layer, *Turbulent Shear Flows 8: Selected Papers from the Eighth International Symposium on Turbulent Shear Flows, Munich, Germany, September*, no. 9–11, pp. 7-21 (1993).

[2]Lin, J. C. : Review of research on low-profile vortex generators to control boundary-layer separation, *Progress in aerospace sciences*, vol. 38, no. 4-5, pp. 389–420 (2002).

[3]Chen, H., Rao, F., Shang, X., Zhang, D. and Hagiwara, I. : Biomimetic drag reduction study on herringbone riblets of bird feather, *Journal of Bionic Engineering*, vol. 10, pp. 341–349 (2013).

[4]Benschop H. and Breugem W.-P. : Drag reduction by herringbone riblet texture in direct numerical simulations of turbulent channel flow, *Journal of Turbulence*, vol. 18, no. 8, pp. 717–759 (2017).

[5]Bearman P. W. and Harvey J. K. : Golf ball aerodynamics, *Aeronautical Quarterly*, vol. 27, no. 2, pp. 112–122 (1976).

[6]McMasters J. H. and Henderson M. L. : ow-speed single- element airfoil synthesis, *NASA. Langley Res. Center The Sci. and Technol. of Low Speed and Motorless Flight*, Pt. 1 (1979).

[7]Dróżdż A., Niegodajew P., Romańczyk M., Sokolenko V. and Elsner W. : Effective use of the streamwise waviness in the control of turbulent separation, *Experimental Thermal and Fluid Science*, vol. 121, p. 110291 (2021).

WORKSHOP
Direct and Large-Eddy Simulation 14
April 10-12 2024, Erlangen, Germany

DIRECT NUMERICAL SIMULATION OF TURBULENT BOUNDARY LAYERS WITH STREAMLINE CURVATURE AND PRESSURE GRADIENTS

Jason Appelbaum[1] **and Christoph Wenzel**[1]
[1]Institute of Aerodynamics and Gas Dynamics (IAG)
University of Stuttgart, Germany
appelbaum@iag.uni-stuttgart.de, wenzel@iag.uni-stuttgart.de

INTRODUCTION

The effects of streamline curvature on the structure of a turbulent boundary layer (TBL) will be presented, as investigated by means of direct numerical simulation (DNS). If the mean flow under which a TBL develops has a non-zero spatial gradient of the flow angle (in a Cartesian system), the flow is said to have 'streamline curvature'. Whereas convex curvature is known to stabilize a TBL flow, concave curvature tends have a destabilizing tendency, increasing turbulent transport in the local wall-normal direction. Because of this, curved TBL flows are considered 'complex' turbulent flows in that the flow is subject to rates of strain in addition to the classical mean shear $\partial\overline{u}/\partial y$, namely $\partial\overline{u_\xi}/\partial\eta = -\overline{u_\xi}/\partial r$, the local mean streamline curvature (calculated as the local wall-normal coordinate η derivative of the wall-tangential velocity component u_ξ). The resulting increase in turbulent kinetic energy is significant, being nearly an order of magnitude larger than those predicted by simple extension of calculation methods used for flat shear layers (see [1]). Furthermore, even for cases in which the curvature ratio $\delta/R < 1/100$, the effects of streamline curvature are significant [2].

Curved wall flows are accompanied by a radial pressure gradient to balance the apparent centrifugal force, in the conventional laminar incompressible case simplifying to $\partial p/\partial r = \rho u_\xi^2/r$. Pressure gradient along the streamwise direction is less well defined, and depends on the freestream condition and the wall geometry. In the special case in which streamlines run parallel to a concave wall, as in a duct / channel flow, the pressure is proportional to the inclination angle φ gradient along the streamwise path length coordinate s, i.e. ($p \propto 1/R = d\varphi/ds$ where R the local curvature radius). The boundary opposite the wall (convex) has a different sign of R. Accordingly, for a conventional bent constant height channel flow, increased pressure is found at the outer wall and reduced pressure at the inner wall in the bent region, meaning that a streamwise pressure gradient is present.

Therefore, for generalized curved wall flow, streamwise pressure gradients are present. Only the special case of axisymmetry or a specific far field condition will yield a curved wall flow free of streamwise wall pressure gradient. For these reasons, it is of great interest to examine not only the combined effect of streamwise pressure gradients, but to have a numerical case setup also capable of isolating each effect individually for adequate comparison.

NUMERICAL METHOD

All DNS have been run using the in-house code NS3D developed at the Institute of Aerodynamics and Gas Dynamics (IAG) at the University of Stuttgart. NS3D solves the 3D compressible fluid transport equations discretized on a structured curvilinear grid using high order finite differences. Simulations have been run on the Hawk HPC Platform at the High Performance Computing Center Stuttgart (HLRS) as part of the Gauss Computing Centre (GCS) Large-Scale Project "Investigation of Turbulence and Flow Control in Boundary Layers".

STUDY DESIGN

For clean inspection of the effects of streamwise pressure gradient (sPG) and streamline curvature (SC), a novel study design has been used which allows for the direct comparison of four cases, being [ZPG , sPG] × [SC , flat]. Such is the first dataset of its kind known to the authors, offering direct inspection of streamline curvature effects with and without a streamwise pressure gradient. Table 1 and Figure 1 provide a summary of the datasets. The first set of cases (1C & 1F) is

ID	Label	Description
1C	60° ZPG	**C**urved wall case with zero pressure gradient (ZPG) along wall
1F	flat ZPG	**F**lat wall case with zero pressure gradient (ZPG) along wall
2C	60°	**C**urved wall case with non-zero wall pressure gradient
2F	flat ∇p	**F**lat case with wall pressure matched to 2C

Table 1: DNS case summary

comprised of a curved wall ZPG case (1C) and a flat wall ZPG case (1F), the former being achieved through the modification of the domain top pressure profile such that nearly constant pressure is induced at the wall. Effectively, a streamline in the form of a nozzle / diffuser is induced in the potential flow outside of the TBL. Comparison of the these two datasets reveals effects of streamline curvature in absence of sPG at the wall. In the second set of cases (2C & 2F), the curved case (2C) has a top boundary condition which induces a wall-parallel freestream streamline, acting like an impermeable slip wall in terms of the averaged flow. A non-zero streamwise wall pressure gradient appears, similar to that of a curved channel flow. The flat case (2F) achieves the same wall pressure profile as 2C through the prescription of a specific pressure profile at the domain top boundary. Comparison of these two datasets allows the inspection of streamline curvature effects

in the presence of non-zero sPG at the wall. By comparing

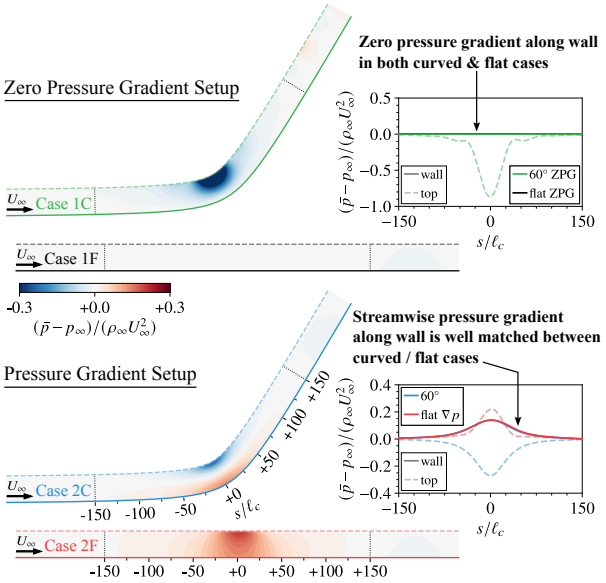

Figure 1: DNS visual case summary

the differences between each set of cases with one another, e.g. $\Delta[1C, 1F]$:$\Delta[2C, 2F]$ one may gain understanding about the relative prominence of the effects of streamline curvature and streamwise pressure gradient.

Finally, it should be noted that the study of streamline curvature itself is not new, indeed the dramatic effects of streamline curvature have been known and studied for >100 years. Early physical experiments on curved wall TBLs have laid the foundation on the topic (e.g. [3], [4] among others) and outstanding numerical studies (e.g. [5], [6]) have focused mainly on periodic, axisymetric duct flows, presumably due to the well-definedness of the boundary conditions, which are affected by interaction between the convex & concave walls. For the further improvement of turbulence models fit for complex shear flows, e.g. [7], it is crucial to acquire reliable canonical DNS datasets of curved wall TBLs in which the effects of streamwise pressure gradient are clearly identifiable.

TURBULENT BOUNDARY LAYERS WITH STREAMLINE CURVATURE AND PRESSURE GRADIENTS

The presentation will go into detailed comparisons of the datasets mentioned in Table 1. The flow may be visualized in Fig. 2 for the curved and flat domains. The destabilizing effect of concave wall curvature increases the magnitude of the wall-normal fluctuations.

The effect of streamline curvature on the friction coefficient c_f is illustrated in Fig. 3, where it is apparent that the enhanced sweeps of high speed fluid towards the wall in the concave curved cases increase c_f. The streamwise pressure gradient on the other hand reduces c_f in the adverse PG region s<0 before the point of maximal curvature s=0 and increases c_f in the favorable PG region s>0. Interestingly, when the envelope between the ZPG cases 1C & 1F ( ) is compared to that of the PG cases 2C & 2F ( ), the difference in skin friction coefficient (due to curvature) is seen to be very similar.

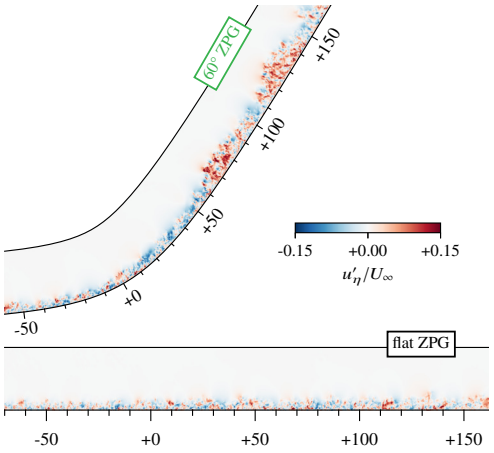

Figure 2: Snapshot of mean-removed wall-normal velocity u'_η

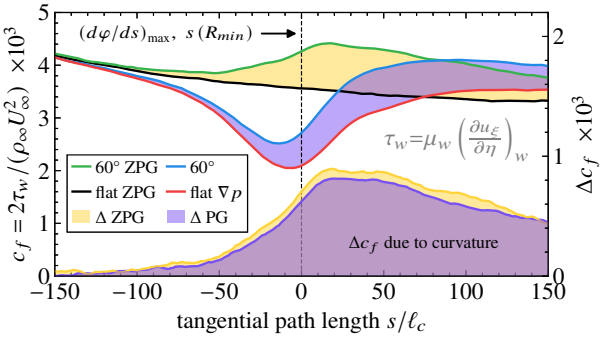

Figure 3: Friction coefficient c_f

REFERENCES

[1] P. Bradshaw and A. D. Young, "Effects of streamline curvature on turbulent flow," Tech. Rep. 169, Advisory Group for Aerospace Research & Development, 1973.

[2] P. H. Hoffmann, K. C. Muck, and P. Bradshaw, "The effect of concave surface curvature on turbulent boundary layers," *Journal of Fluid Mechanics*, vol. 161, pp. 371–403, 1985.

[3] H. Wilcken, "Turbulente Grenzschichten an gewölbten Flächen," *Ingenieur-Archiv*, vol. 1, pp. 357–376, 1930.

[4] V. C. Patel, "The Effects of Curvature on the Turbulent Boundary Layer," Tech. Rep. 3599, Ministry of Technology, 1969.

[5] R. D. Moser and P. Moin, "The effects of curvature in wall-bounded turbulent flows," *Journal of Fluid Mechanics*, vol. 175, pp. 479–510, 1987.

[6] G. Brethouwer, "Turbulent flow in curved channels," *Journal of Fluid Mechanics*, vol. 931, p. A21, 2022.

[7] P. E. Smirnov and F. R. Menter, "Sensitization of the SST Turbulence Model to Rotation and Curvature by Applying the Spalart-Shur Correction Term," *Journal of Turbomachinery*, vol. 131, p. 041010, 07 2009.

WORKSHOP
Direct and Large-Eddy Simulation 14
April 10-12 2024, Erlangen, Germany

INVESTIGATION OF TAYLOR'S HYPOTHESIS IN PRESSURE GRADIENT BOUNDARY LAYERS USING DIRECT NUMERICAL SIMULATION

Taygun R. Gungor[1]
[1]Department of Mechanical Engineering
Universite Laval, Canada
taygun-recep.gungor.1@ulaval.ca

Atalay Ak[2]
[2] Faculty of Aeronautics and Astronautics
Istanbul Technical University, Turkey
aka18@itu.edu.tr

Ali Yesildag[3]
[3] Faculty of Aeronautics and Astronautics
Istanbul Technical University, Turkey
yesildag18@itu.edu.tr

Yvan Maciel[4]
[4] Department of Mechanical Engineering
Universite Laval, Canada
yvan.maciel@gmc.ulaval.ca

Ayse G. Gungor[5]
[5] Faculty of Aeronautics and Astronautics
Istanbul Technical University, Turkey
ayse.gungor@itu.edu.tr

INTRODUCTION

In turbulent flows obtaining the two-point correlation tensor or spectral distribution of a quantity is of great importance due to the information they provide. However, this is not an easy task for experimental studies or spatially developing flows such as non-equilibrium turbulent boundary layers (TBLs) even if it is a numerical case. To obtain the spatial correlations, the temporal data are often utilized with the well-known Taylor's frozen turbulence hypothesis [4]. According to this hypothesis, the temporal information may be transformed into spatial information with a convection velocity, which is frequently the local mean velocity.

There are many studies in the literature addressing the use of the local mean velocity as the convection velocity. Del Álamo et al. [2] investigated the local mean velocity and found that small scales follow the local mean velocity but large scale structures have a more uniform convection velocity which is close to the bulk velocity. They suggested a new method in which each Fourier mode has its own convection velocity but this method relied on readily available spatial modes. Later, Renard and Deck [3] extensively analyzed various methods to evaluate the existing methods and also suggested a new method based on the method of Del Álamo et al. [2]. The new method, unlike Del Álamo et al.'s method, did not require any information about the spatial modes.

In this work, we employ the mean velocity as the convection velocity for individual structures and we compare the results that are obtained using spatial data and temporal data together with Taylor's frozen hypothesis. For individual structures, we consider vortex clusters for now but we will extend our analysis for the streaks and sweeps/ejections in the final paper. We employ a non-equilibrium pressure gradient TBL for this study.

DIRECT NUMERICAL SIMULATION

We employed a novel non-equilibrium TBL that evolves from a zero-pressure-gradient (ZPG) TBL to a TBL with a large velocity defect due to adverse pressure gradient (APG). But then later it is exposed to a favoruable pressure gradient (FPG). Therefore, the flow has two regions: the APG and FPG regions. The flow case is generated using a direct numerical simulation (DNS) code. The code uses a fractional step method to solve the three-dimensional incompressible Navier-Stokes equations in a three-dimensional rectangular volume. Regarding the computational specifics, the grid is structured and staggered. Spatial discretization is a fourth-order compact finite difference scheme for convective and viscous terms and a standard second-order discretization for the pressure term in both the streamwise and wall-normal directions. The spanwise direction employs a spectral expansion for discretization [6]. A semi-implicit three-step Runge-Kutta method is used for temporal discretization. More details of the DNS code and further particulars can be found in references [7] and [8]. The number of grids are $N_x, N_y, N_z = 12801, 770, 2700$ and the domain size is $(L_x, L_y, L_z)/\delta_e = 26.1, 3, 4.1$, where δ_e is the boundary layer thickness at the exit.

Figure 1 presents the spatial evolution of the the shape factor (H) and boundary layer (δ), displacement (δ^*), and momentum (θ) thicknesses. They demonstrate the highly non-equilbrium and spatially evolving nature of the flow. We choose three streamwise positions for our analysis: the small defect case of the APG region (P1, $H = 1.60$), the large defect region at the boundary of the two regions (P2, $H = 2.78$) and the small defect region of the FPG region (P3, $H = 1.60$).

We collect temporal data from these three positions, and also have instantaneous snapshots of the whole domain as the spatial data. The temporal data are taken at the exact loca-

tion. And the streamwise length of each structure is obtained using the mean velocity at the center of each structure. Therefore, we define a convective velocity for each structure. As for the spatial data, we use a box, the size of which is 2 local boundary layer thicknesses.

RESULTS

To evaluate the success of the mean streamwise velocity as the convective velocity for the Taylor's frozen turbulence hypothesis, we examine the streamwise length of the individual cluster. As stated in the introduction we focus on the vortex clusters for the moment. The vortex clusters are obtained using the Q criterion and are identified as the connected regions satisfying the following condition [1]

$$Q(x|t, y, z) > \alpha Q_{rms}(y) \tag{1}$$

where α is the threshold constant. After identifying the vortex clusters, we examine their aspect ratio for the position P1. Figure 2 presents the joint probability density function (pdf) of Δ_x/δ and Δ_y/δ, and Δ_x/δ and Δ_z/δ of vortex clusters where Δ_i is the length of a structure in the direction of i. We consider only P1 for the abstract but we will present the results for P2 and P3 in the final paper. The joint pdfs are presented for detached structures only. Here we consider detached struct ures as structures whose minimum wall-normal position is above 0.05δ. In addititon, only the structures whose center is between 0.3δ and 0.8δ are taken int account.

The joint pdfs show that using the Taylor's hypothesis with the local mean velocity is an accurate way of estimating the cluster's aspect ratios for detached structures. The results of temporal and spatial data for the detached structures coincide very well. The aspect ratio of structures are almost the same for both methods regardless of their size in any direction. Moreover, the levels are also very similar. The peak location of pdfs are almost same as well. These findings show the mean velocity is a good approximation as the convective velocity for detached vortex clusters.

We will present a more detailed analysis for the final paper. We will consider two additional defect positions and also examine Reynolds-stress-carrying structures too.

REFERENCES

[1]Del Alamo, Juan C., et al. Self-similar vortex clusters in the turbulent logarithmic region. *Journal of Fluid Mechanics* **561**, 329-358, (2006)

[2]Del Alamo, Juan C., and Javier Jiménez. Estimation of turbulent convection velocities and corrections to Taylor's approximation. *Journal of Fluid Mechanics* **640** 5-26, (2009)

[3]Renard, Nicolas, and Sébastien Deck. On the scale-dependent turbulent convection velocity in a spatially developing flat plate turbulent boundary layer at Reynolds number $Re_\theta = 13000$. *Journal of Fluid Mechanics* **775**, 105-148 (2015)

[4]Taylor, G.I. : The spectrum of turbulence, *Proceedings of the Royal Society of London. Series A-Mathematical and Physical Sciences*, **164(919)**, 476–490 (1938).

[5]Kim, J. and Moin, P. : Application of a fractional-step method to incompressible Navier-Stokes equations, *Journal of Computational Physics*, **59(2)**, 308–323 (1985).

[6]Lele, S.K : Compact finite difference schemes with spectral-like resolution, *Journal of Computational Physics*, **103(1)**, 16–42 (1992).

[7]Simens M.P., Jiménez J., Hoyas S., and Mizuno Y. : A high-resolution code for turbulent boundary layers, *Journal of Computational Physics*, **228(11)**, 4218–4231 (2009).

[8]Borrel G., Sillero J.A., and Jiménez J., : A code for direct numerical simulation of turbulent boundary layers at high Reynolds numbers in BG/P supercomputers, *Computers & Fluids*, **80(11)**, 37–43 (2013).

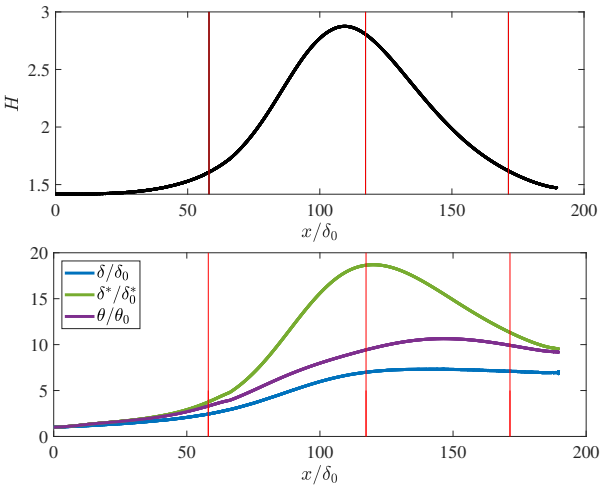

Figure 1: The spatial evolution of the shape factor (top) and δ, δ^*, and θ (bottom) as a function of x/δ_0. The sub-index 0 indicates the value at inlet.

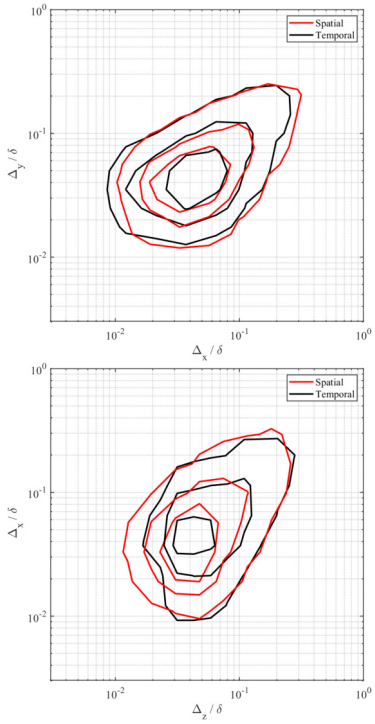

Figure 2: The joint pdfs of Δ_x/δ and Δ_y/δ (top), and Δ_x/δ and Δ_z/δ (bottom) for detached vortex clusters. The contours indicate the 30%, 60% and 90% of the total number of clusters. Only the clusters whose center is between 0.3δ and 0.8δ are considered.

WORKSHOP
Direct and Large-Eddy Simulation 14
April 10-12 2024, Erlangen, Germany

EFFECT OF CONVEX TRANSVERSE CURVATURE AND CONCAVE GROOVES ON THE TURBULENT BOUNDARY LAYER ALONG A CYLINDER IN AXIAL FLOW

Florian Wachter[1]
[1]Institute of Fluid Mechanics (LSTM)
Friedrich–Alexander–Universität (FAU) Erlangen–Nürnberg, Germany
flo.wachter@fau.de

INTRODUCTION

The present numerical study is a continuation of the work published in [1]. The focus of the investigation was on axisymmetric turbulent boundary layers (ATBL) that develop around streamwise oriented long cylindrical objects such as those found in applications like towed array sonars or marine seismic streamers. Such devices have, in a simplified view, a long tube-like geometry (circular cross-section) with several hydrophones embedded in its center and are typically towed underwater behind a vessel. Capable of sensing acoustic waves, they are widely used for navigation, communication, maritime surveillance and geophysical exploration. For these and many other applications, the turbulent fluctuations within the turbulent boundary layer (TBL) often have a negative impact compared with laminar flow. Turbulence in wall-bounded flows can excite vibrations in exposed solid structures and generally leads to increased wall shear stress. Furthermore, sound waves can be diffracted or absorbed when traveling through a region of turbulent flow, and turbulent fluctuations of velocity, wall shear stress and pressure can act as intense sound sources. Such sound sources induce the unwanted flow noise of the towed array sonar or marine seismic streamer which limits the performance of the acoustic pressure sensing device by decreasing the signal-to-noise ratio. With the motivation to improve the performance of these devices, the aim of the work in [1] was to design a surface modification that influences the turbulent boundary layer around a cylinder in axial flow to reduce the near-wall turbulent fluctuations.

The design of the surface modification was inspired by the findings of Krieger et al. [2] and Neves et al. [3]. Krieger et al. [2] carried out numerical investigations on the TBL along flat walls with streamwise-aligned grooves. They showed that within the longitudinal grooves there exists a strong damping of turbulence and a suppression of turbulent production. The near-wall turbulence in the grooves tends to approach the one-component state in the anisotropy-invariant map and therefore tends to stabilize the near-wall flow. However, the flat regions between the grooves experience a relative increase in velocity, and in some cases inflectional profiles that can induce turbulence. To improve the surface modification used in [2], the interspace region must be redesigned in a way that a stabilization of the turbulent flow is also possible in the area between the grooves. The design of the geometry in the intergroove region in [1] was inspired by the work of Neves et al. [3], who studied the effect of convex, transverse curvature on axisymmetric turbulent boundary layers around long cylinders in axial flow (see also [4] and [5]). Strong transverse curvature effects are present in ATBL flows around streamwise oriented cylinders when the boundary layer thickness δ considerably exceeds the radius of the cylinder a. The results in [3] reveal that turbulence is sensitive to convex transverse curvature. In [1], the data from Neves et al. [3] was analyzed within the anisotropy-invariant space. It was shown that with increasing curvature the anisotropy of the near-wall turbulence increases and tends to approach the one-component state of turbulence. According to [6] and [7], this suggests that an increase in transverse curvature may lead to flow stabilization. This observation is also supported in [3] where the velocity correlation coefficients appear to indicate a tendency towards flow stabilization in the simulation case with the strongest transverse curvature.

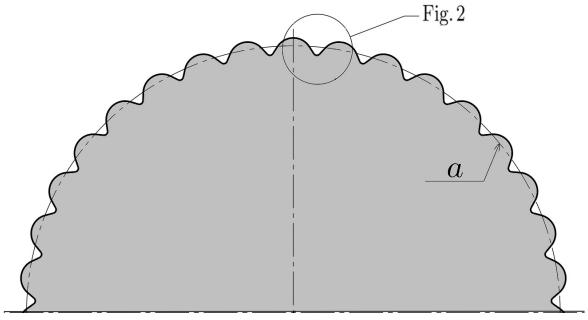

Figure 1: Cross-section of the modified cylinder (only top half shown). The streamwise flow direction is perpendicular to the image plane. The image section of Fig. 2 is indicated.

The design of the surface modification used in [1] is shown in Fig. 1 (only half of the modified cylinder is shown). Fig. 2 provides a closer look at the surface modification and reveals the groove-like regions (valley) and the interspace regions with their relatively strong, convex, transverse curvature (crest). Theoretically, both regions should increase the near-wall anisotropy of turbulence and force the turbulence towards its one-component state in the anisotropy-invariant map, thus leading to a stabilization of the flow.

The results in [1] showed that the surface modification resulted in a significant reduction in the overall wall shear stress. It was possible to considerably reduce the turbulent intensities, the Reynolds stress, the velocity spectra, and the turbulent dissipation in the valley regions (concave grooves). Furthermore, the analysis within the anisotropy-invariant space revealed a tendency towards flow relaminarization in the grooves. However, no tendency towards a flow stabilization could be observed in the crest regions (convex curvature). Furthermore, the pressure field could not be influenced by the modified cylinder surface in comparison to a reference cylinder with circular cross-section (dashed cylinder in Fig. 1). Suggestions to improve the surface modification are provided in [1]. The basic idea to improve the design is to apply stronger convex, transverse curvature in the regions between the grooves by reducing the crest radius a_c (see Fig. 2), or more precisely reducing the ratio of the crest radius to the viscous length scale a_c^+.

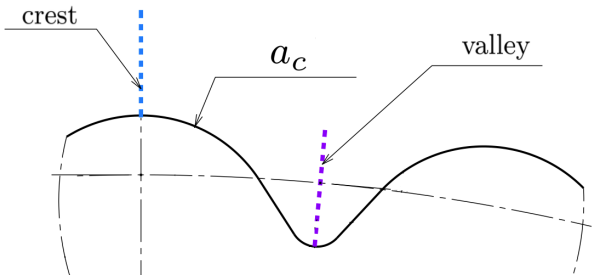

Figure 2: Enlarged detail view of the section highlighted in Fig. 1. The sample lines at the positions "crest" and "valley" are indicated as well as the convex, transverse curvature radius of the crest region a_c.

PRESENT INVESTIGATION

The suggestions from [1] to improve the surface modification are realized in the present numerical investigation. The surface modification shown in Fig. 1 is scaled down while keeping the mean radius of the cylinder $a = 11$ mm (dashed cylinder) so that the non-dimensional crest radius is reduced from $a_c^+ \approx 38$ (old surface modification from [1]) to $a_c^+ < 9$ in the present study. Furthermore, a new numerical setup is used, which leads to a better agreement of the reference cylinder (circular cross-section) results with recently obtained experimental data from Näger et al. [8].

The open-source code OpenFOAM is used to perform the computations using a finite volume method discretization. Wall-resolved large-eddy simulations in combination with the WALE (wall-adapting local eddy-viscosity) subgrid-scale model are applied to realize the incompressible flow simulations. The simulation domain has a length of twenty times the mean cylinder radius a and the outer farfield boundary has a radius of thirty times the radius a. Cyclic (periodic) boundary conditions are used in streamwise direction to resemble the flow over a long cylinder. A momentum source is used to drive the flow and to ensure that the desired volume-average velocity of 1 m/s is maintained. The temporal and spatial discretization schemes are of second order accuracy. The numerical grid is structured and of O-type character. The near-wall grid resolution in wall-units for the streamwise, radial and circumferential directions are $\Delta x^+ \approx 20$, $\Delta r^+ \approx 0.5$, and $\Delta\theta^+ \approx 2$, respectively.

The first results show that the surface modification of the present study is able to reduce the overall wall shear stress even more than the surface modification that was used in [1]. The analysis in the anisotropy-invariant map shows that the near-wall turbulence in the groove regions almost reaches the one-component state. The turbulent production, turbulent dissipation, and Reynolds stress profiles show a local relaminarization in the grooves. However, there is still no tendency for a flow stabilization observable in the crest region. Nevertheless, in addition to the improvement of the overall reduction in the wall shear stress and the local relaminarization in the grooved regions, the present surface modification was also able to influence the pressure field. A noticeable reduction in the root-mean-squared wall pressure fluctuations could be achieved in the valley regions while the crest regions showed no change in the wall pressure fluctuations in comparison to the reference cylinder. A similar tendency can be observed in the wall pressure spectra.

Simulations with a surface modification having $a_c^+ < 5$ (crest radius smaller than the viscous sublayer) are planned to extend the data that will be presented at the DLES14 workshop.

REFERENCES

[1]Wachter, F., Metelkin, A., Jovanović, J., Praß and J., Becker, S.: Numerical investigation of the effect of convex transverse curvature and concave grooves on the turbulent boundary layer along a cylinder in axial flow, *Int. J. Heat Fluid Flow*, **92**, 108855 (2021).

[2]Krieger, V., Perić, R., Jovanović, J., Lienhart, H., Delgado, A.: Toward design of the antiturbulence surface exhibiting maximum drag reduction effect, *J. Fluid Mech.*, **850**, 262–303 (2018).

[3]Neves, J., Moin, P., Moser, R. : Effects of convex transverse curvature on wall-bounded turbulence., *J.Technical Report Rep. TF-54, Dep. Mechanical Engineering, University Stanford, California*, (1992).

[4]Neves, J., Moin, P., Moser, R. : Effects of convex transverse curvature on wall-bounded turbulence. part 1. The velocity and vorticity, *J. Fluid Mech.*, **272**, 349-–382 (1994).

[5]Neves, J., Moin, P.: Effects of convex transverse curvature on wall-bounded turbulence. part 1. The pressure fluctuations, *J. Fluid Mech.*, **272**, 283-–406 (1994).

[6]Frohnapfel, B.: Flow Control of Near-Wall Turbulence: Strömungskontrolle Wandnaher Turbulenz, *Shaker Verlag*, (2007).

[7]Jovanović, J., Hillerbrand, R.: On peculiar property of the velocity fluctuations in wall-bounded flows, *J. Thermal Sci.*, **9**, 3–12 (2005).

[8]Näger, C., Wachter, F., Lienhart, H., Czwielong, F., Riedel, J., and Becker, S. : Boundary layer measurements of the flow along a streamwise-oriented circular cylinder using particle tracking velocimetry, *J. Int. J. Heat Fluid Flow*, **104**, 109225 (2023).

WORKSHOP
Direct and Large-Eddy Simulation 14
April 10-12 2024, Erlangen, Germany

ANALYSIS OF TURBULENT STATISTICS OVER THE BOEING SPEEDBUMP

Ronith Stanly[1], Timofey Mukha[2], Adam Peplinski[1], Stefano Markidis[1], Philipp Schlatter[1,4]
[1]FLOW Center and Swedish e-Science Research Center, KTH Royal Institute of Technology, Stockholm, Sweden
[2]Computer, Electrical and Mathematical Sciences and Engineering Division, King Abdullah University of Science and Technology (KAUST), Kingdom of Saudi Arabia
[3]Division of Computational Science and Technology, KTH Royal Institute of Technology, Stockholm, Sweden
[4]Institute of Fluid Mechanics (LSTM), Friedrich–Alexander–Universität (FAU) Erlangen–Nürnberg, Germany
ronith@kth.se

INTRODUCTION

The Boeing Speedbump is a set of test-cases, at different Reynolds numbers ranging from $Re_L = 1 \cdot 10^6 - 4 \cdot 10^6$ (based on the width of the bump model, L), proposed by the Boeing Company to improve the simulation accuracy of smooth-body separation using combined experimental and computational campaigns. The shape of the bump is a simplified version of the suction surface of a wing and hence can be used as a test problem to solve the challenges encountered while simulating wings; like an adverse pressure gradient quickly succeeding a region with a favourable pressure gradient, smooth body separation, reattachment of separated flow, etc.

MOTIVATION

As of now, two major experimental campaigns [1, 2] have characterized the flow at different Reynolds numbers. A few computational efforts [3, 4, 5] have been devoted to performing direct numerical simulation (DNS) over the hump at the lowest $Re_L = 1 \cdot 10^6$ although they did not study the complex boundary layer mechanisms that take place, in terms of how the boundary layer develops as it passes over the bump subjected to the changing pressure gradients. Several others have performed wall-resolved and wall-modelled large eddy simulation (LES) over the bump at higher Re_L. While the flow at the lower Re_L could be anticipated to be easier to predict at first, several flow features such as relaminarization of the initially turbulent boundary layer, an adverse pressure gradient following a region of favourable pressure gradient, and incipient separation behind the hump (very sensitive to mesh resolution), makes it a challenging problem. As such, we devote this work to analysing turbulent statistics over the Boeing Speedbump at $Re_L = 1 \cdot 10^6$.

CASE SETUP

The shape of the bump is described based on the width of the bump model, L. Although the case is fully 3D, owing to the computational costs associated with performing DNS, so far all DNS have been performed on a spanwise periodic section which corresponds to $\approx 0.04L$ spanwise extent about the centerline of the bump. In order to make it straightforward to have cross comparisons between experiments and computational simulations, the geometry is defined using a Gaussian shape as:

$$y(x) = h \exp\left(-\left(\frac{x}{x_0}\right)^2\right) \tag{1}$$

where x is the coordinate aligned with streamwise direction, $x_0/L = 0.195$. The height of the bump is $h/L = 0.085$. There are in fact two Reynolds numbers associated with this bump case, one is the Reynolds number based on L, which is $1 \cdot 10^6$ in this case; the second Reynolds number corresponds to the state of the boundary layer at some reference location upstream of the bump peak. For our case, we simulate a turbulent boundary layer at a momentum-loss thickness $Re_\theta = 1050$ at $x/L = -0.60$, where $x/L = 0$ corresponds to the location of the bump peak. This produces a boundary layer thickness at $x/L = -0.60$ which is $\frac{1}{8}$ the height of the bump, as what Balin and Jansen [3] had in their DNS.

METHOD

The high-order spectral element solver Nek5000 is used for this work. As described above, the inflow to the bump consists of a turbulent boundary layer, which poses its own challenges. In the current work, we use a precursor-based Dirichlet velocity condition at the inlet. Here, we first perform a precursor simulation of a turbulent boundary layer in SIMSON and extract 2D velocity slices from it to be imposed as Dirichlet condition to the simulation in Nek5000. We have extensively studied this specific inlet condition in comparison to other existing methods, like the synthetic eddy method and reduced-order methods based on POD, in recent work [6].

The inlet turbulent boundary layer is at a momentum-thickness based Reynolds number, $Re_\theta = 790$, and located at $x/L = -0.72$, which develops to $Re_\theta = 1050$ at $x/L = 0.60$. At the outlet, a stabilized stress-free outflow condition is applied to allow vortical structures to easily flow out of the domain without causing destabilizing pressure fluctuations. Periodic boundary conditions are applied at the spanwise boundaries, which are spaced at $\frac{\Delta Z}{L} = 0.04$ like in the other reference DNS of the bump. The no slip condition is applied at the bottom wall. Moreover, the top boundary is tilted along the streamwise direction according to a power law (as much as the displacement thickness of the boundary layer that would have developed in the wind tunnel), and a slip condition is applied in order to take the wind tunnel top wall into account without having to solve for the boundary layer using extra

computational effort.

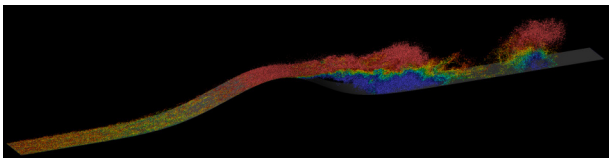

Figure 1: Flowfield over the Boeing Speedbump showing λ_2 structures over the bump colored by streamwise velocity

RESULTS

The flow has been simulated using three different grids leading up to DNS resolution. Figure 1 shows an instantaneous snapshot of the turbulent boundary layer passing over the Boeing Speedbump. Although the larger time-scales of the bigger structures behind the hump make it expensive to get a statistically steady solution across the whole domain for the DNS grid, more studies were performed on the coarser grids and their results are compared. Specifically, span and time averaged statistics have been used to validate the flow-field against other DNS in literature.

The mean and root-mean-square values of the velocity components converged quite well in the region ahead of the bump, although more time averaging is required to match those quantities behind the bump. More sensitive quantities like the distribution of skin-friction coefficient along the bump, as shown in Figure 2, match quite well in the region ahead of the hump. Here it is clear that our inflow condition quickly reaches the turbulent state as expected and shows similar behaviour to others in literature, only having a development length $< 10\delta_{99_0}$, where δ_{99_0} is the boundary layer thickness at the inlet. The C_f decreases initially as the turbulent boundary layer approaches the FPG side of the bump, where the flow accelerates and relaminarizes. At the peak of the bump, the flow now experiences a change from favourable to adverse pressure gradient, and then succession creates the formation of an internal layer which can be seen as a local dip in C_f right behind the hump. This local dip has been challenging to capture both in coarser grid simulations as well as in LES, however our DNS captures the dip quite well. Further behind the bump, the C_f continues to drop as the flow experiences incipient separation. Here, the flow structures get bigger in size and hence it takes longer to get converged results owing to larger time-scales, which manifests as oscillations in our C_f plot, which will be smoothened by running the simulation for longer in time.

OUTLOOK

At present, this DNS over the Boeing Speedbump has been validated against other work in literature and is being simulated for longer time to obtain a better time-averaged result; especially in the region behind the bump that have inherently larger time-scales. Although similar statistics have been reported in literature, no one has looked at more details of how the turbulent boundary layer evolves as it passes over the different sections of the bump ranging from favorable to adverse pressure gradients in comparison to canonical cases. Because, based on recent studies [7], it is known that an adverse pressure gradient region that succeeds a region of favourable pressure gradient behaves differently than if a flow experienced adverse pressure gradient right after a zero pressure gradient (which is what several canonical flows were studied on and used to derive scaling laws that fed into several models), hence this will be looked into in this work. Also, the region just after the hump where the internal layer forms has received less attention owing to the larger time scales associated with the flow that succeeds it. Considering the fact that this internal layer was not captured in coarse-grid simulations as well as in LES, understanding its mechanism is crucial to feed more information to build better turbulence and wall models.

In this study, we will perform more in-depth analysis of the turbulent statistics over the Boeing Speedbump at $Re_L = 1{\cdot}10^6$ by looking at how the pressure gradients affect the mean flow (as compared to canonical cases) and Reynolds stress distribution. We will also look at relevant 2D spectra to give more insights into the important mechanisms that drive the development of the boundary layer over the bump.

REFERENCES

[1]P. Gray, T. Corke, F. Thomas, I. Gluzman: Turbulence model validation through joint experimental / computational studies of separated flow over a three-dimensional tapered bump, *A Final Report*, (2023).

[2]O. Williams, M. Samuell, E. S. Sarwas and M. Robbins and A. Ferrante: Experimental Study of a CFD Validation Test Case for Turbulent Separated Flows, *AIAA SciTech Forum*, (2020).

[3]R. Balin and K. E. Jansen : Direct numerical simulation of a turbulent boundary layer over a bump with strong pressure gradients, *Journal of Fluid Mechanics.*, **918**, p. A14 (2021).

[4]A. Uzun and M.R. Malik : Simulaion of a Turbulent Flow Subjected to Favorable and Adverse Pressure Gradients, *AIAA Aviation Forum*, (2020).

[5]M. L. Shur, P. R. Spalart, M. K. Strelets, and An. K. Travin: Direct numerical simulation of the two-dimensional speed bump flow at increasing Reynolds numbers, *Intl. J. Heat and Fluid Flow*, **90**, p. 108840 (2021).

[6]S. Du, R. Stanly, D. Xavier, A. Perez, T. Mukha, S. Markidis, S. Razaeiravesh and P. Schlatter: Generating synthetic turbulence with vector autoregression of proper orthogonal decomposition time coefficients, *Manuscript*, (2023).

[7]P., Aadhy, and S., Theresa: A family of adverse pressure gradient turbulent boundary layers with upstream favourable pressure gradients, *Journal of Fluid Mechanics*, **996**, A11 (2023).

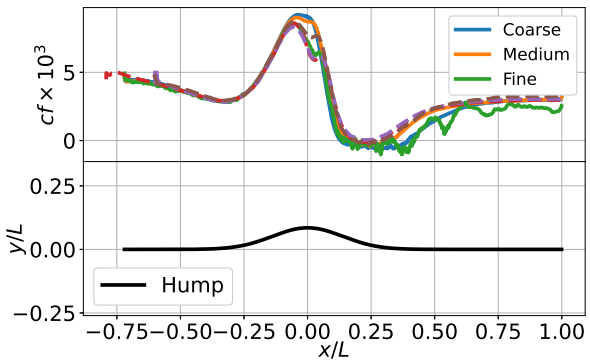

Figure 2: Validation of skin-friction coefficient, C_f, along the hump. The "Fine" grid case corresponds to DNS resolution. The dashed lines are other DNS in literature: yellow dashed line Uzun and Malik [4], green dashed line Balin and Jansen [3], red dashed line Shur et al. [5]

WORKSHOP
Direct and Large-Eddy Simulation 14
April 10-12 2024, Erlangen, Germany

BUILDING-BLOCK-FLOW MODEL FOR LARGE-EDDY SIMULATION: APPLICATION TO A SMOOTH BODY SEPARATED FLOW

G. Arranz[1], Y. Ling[1], S. Costa[1], M. Mani[1] and A. Lozano-Duran[1]
[1]Massachusetts Institute of Technology
77 Massachusetts Av., Cambridge, MA 02139, United States
garranz@mit.edu

INTRODUCTION

Computational fluid dynamics (CFD) plays a central role in the modern aerospace industry, serving as a tool for the design of hydro/aero-vehicles. However, closure models for CFD models are still unable to comply with the stringent accuracy requirements and computational efficiency demanded by the industry [1]. These limitations, imposed by the defiant ubiquity of turbulence and the necessity to capture key physical flow phenomena, call for the exploration of new venues to develop robust and accurate closure models for CFD.

In this talk, we introduce a machine-learning-based model for wall-model large-eddy simulation (WMLES), referred to as the building-block-flow model (BFM) to address these limitations. The foundation of the model rests on the premise that simple canonical flows contain the essential physics to provide accurate predictions in more complex scenarios. It is also envisaged to provide accurate results with coarse resolutions (affordable for industrial applications).

Previous versions of the BFM have been shown to improve predictions of both canonical and complex flow [2, 3]. In this talk, we will present the latest GPU-based version of the model and we will assess its performance in a complex flow with smooth body separation.

METHODOLOGY

The BFM is implemented in the finite volume solver charLES [4]. The solver integrates the filtered Navier-Stokes equations using a skew-symmetric finite volume formulation that has reduced dispersion error and is at least second-order accurate. The numerical discretization relies on a flux formulation that is approximately entropy preserving in the inviscid limit, thereby limiting the amount of numerical dissipation added into the calculation.

The BFM consists of 3 artificial neural networks (ANNs) trained with supervised learning. The first neural network is tasked with the prediction of the eddy-viscosity in the control volumes that are not in contact with a wall. The second and third networks predict the eddy-viscosity and the wall-shear stress in the control volumes attached to the wall, respectively. The inputs of the ANNs are the local value of the invariants of the velocity gradient tensor. In addition, the second and third networks use the parallel component of the relative velocity to the wall as input. These networks have been trained with LES simulation from simple canonical cases (denoted as *building blocks*) whose eddy viscosity has been adjusted to yield the correct velocity profile. These building blocks include channel flows at different Reynolds number, and Poiseuille-Couette flows with different pressure gradients.

RESULTS

To assess the performance of the BFM, we perform numerical simulations over the Gaussian Bump, proposed by Boeing and Williams et al. [5]. This geometry consists of a three-dimensional tapered bump, wider in the spanwise direction than the streamwise. The main idea of this test is to serve as a validation benchmark of smooth body separation for CFD models. The geometry of the bump is sketched in figure 1. The width of the bump is L and its maximum height is $0.085L$.

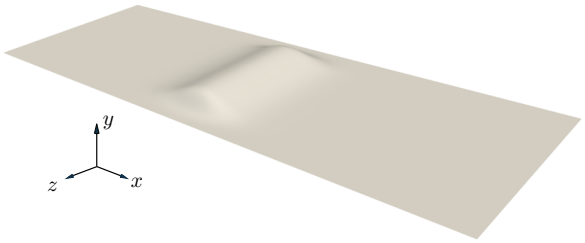

Figure 1: 3D view of the Gaussian Bump proposed by . The flow comes from left to right in the streamwise direction, x.

A uniform inflow of streamwise speed U is imposed upstream the bump. The simulations are performed at $Re_L = 3.6 \cdot 10^6$ (based on the bump width, L, and the free-stream velocity, U) and Mach number, $M = 0.17$. The grid size is $\Delta/L = 0.004$, which corresponds roughly to 5 to 10 points per boundary layer thickness, depending on the streamwise position [6].

To assess the performance of BFM, we compare the results from the simulations to those provided by experiments. In addition, using the same grid and the same solver (i.e,. charLES), we perform an additional simulation where the eddy-viscosity is provided by the Vreman model [7], and the wall-shear stress is predicted using and ODE-based equilibrium wall model (EQWM) [8].

Preliminary results using a previous version of the BFM have been obtained. Figure 2 shows the average velocity profile downstream the apex of the bump, where the separation bubble develops. We can observe that, with the present grid resolution, the Vreman model with the EQWM fails to pre-

dict the separation bubble. On the contrary, BFM captures the separation region, yielding a very good agreement with experimental results.

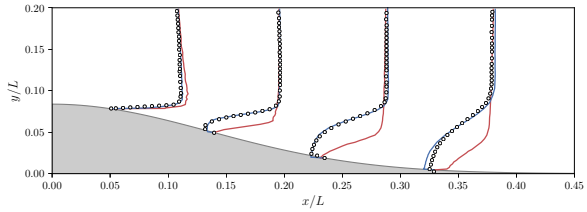

Figure 2: Average velocity profile downstream the apex of the Gaussian bump at $y/L = 0$. (white dots) Experimental measurements from Gray et al. [9]; (red) Vreman-EQWM; and (blue) BFM.

In the talk we will present the results obtained with the latest BFM version which will include a richer collection of building blocks.

REFERENCES

[1]J. Slotnick, A. Khodadoust, J. Alonso, D. Darmofal, W. Gropp, E. Lurie, and D. Mavriplis, "Cfd vision 2030 study: A path to revolutionary computational aerosciences," *Technical Report, NASA/CR-2014-218178, NF1676L-18332*, 2014.

[2]Y. Ling, G. Arranz., E. Williams., K. Goc, K. Griffin, and A. Lozano-Durán, "WMLES based on building block flows," *Proceedings of the Summer Program, Center for Turbulence Research , Stanford University*, 2022.

[3]G. Arranz, Y. Ling, and A. Lozano-Duran, *Wall-modeled LES based on building-block flows: Application to the Gaussian Bump*.

[4]L. Fu, M. Karp, S. T. Bose, P. Moin, and J. Urzay, "Shock-induced heating and transition to turbulence in a hypersonic boundary layer," *J. Fluid Mech.*, vol. 909, p. A8, 2021.

[5]O. Williams, M. Samuell, E. S. Sarwas, M. Robbins, and A. Ferrante, "Experimental study of a cfd validation test case for turbulent separated flows," in *AIAA Scitech 2020 Forum*, pp. 1–19, 2020.

[6]P. S. Iyer and M. R. Malik, "Wall-modeled les of flow over a gaussian bump," in *AIAA Scitech 2021 Forum*, pp. 1–18, 2021.

[7]A. W. Vreman, "An eddy-viscosity subgrid-scale model for turbulent shear flow: Algebraic theory and applications," *Phys. Fluids*, vol. 16, no. 10, pp. 3670–3681, 2004.

[8]J. Larsson, S. Kawai, J. Bodart, and I. Bermejo-Moreno, "Large eddy simulation with modeled wall-stress: recent progress and future directions," *Mech. Eng. Rev.*, vol. 3, no. 1, pp. 15–00418, 2016.

[9]P. D. Gray, I. Gluzman, F. O. Thomas, T. C. Corke, M. T. Lakebrink, and K. Mejia, "Characterization of separated flow over smooth gaussian bump," in *AIAA Aviation 2022 Forum*, 2022.

SESSION: Compressible flow

Thursday, April 11, 2024

11:20- 12:50

WORKSHOP
Direct and Large-Eddy Simulation 14
April 10-12 2024, Erlangen, Germany

FULLY COMPRESSIBLE, HIGHLY STRATIFIED CONVECTION: INSIGHTS FROM WELL-RESOLVED DIRECT NUMERICAL SIMULATIONS

John Panickacheril John [1] **and Jörg Schmacher**[1,2]
[1]Institut für Thermo- und Fluiddynamik, Technische Universität Ilmenau, Germany
[2]Tandon School of Engineering, New York University, USA
john.panickacheril-john@tu-ilmenau.de, joerg.schumacher@tu-ilmenau.de

INTRODUCTION

Turbulent convective flows driven by buoyancy due to temperature differences are ubiquitous in nature comprising both atmospheric and geophysical flows[1]. The incompressible Rayleigh-Bénard configuration governed by the Boussinesq equations can exemplify some of the complicated physics. In this setup, we have two infinitely long plates with the bottom plate kept at a higher temperature than the upper one. The incompressible Rayleigh-Bénard configuration has been extensively studied in the past.

However, in many scenarios, this thermal convection paradigm which is also known as the Oberbeck-Boussinesq (OB) limit is not adequate. Deviations from the OB limit are commonly termed as *non Oberbeck-Boussinesq* (NOB) effects. The NOB effects break the perfect statistical top-down symmetry observed in the conventional OB limit. NOB effects can occur due to several additional physical mechanisms including phase changes in the atmosphere [2], strong material properties and density dependence on temperature and pressure [3], and intrinsic compressibility effects. Here, we are focusing on genuine intrinsic compressibility effects attempting to isolate all the other possible routes to NOB effects. The latter will be studied here in direct numerical simulations (DNS).

Conventional incompressible Rayleigh-Bénard flows can be characterized by two governing parameters: the Rayleigh number, $Ra = C_p\langle\rho\rangle_B^2\Delta T g H^3/(\mu k T_B)$ and Prandtl number, $Pr = C_p\mu/k$. Here, C_p, g, ΔT, H, μ, k, $\langle\rho\rangle_B$ and T_B correspond to specific heat at constant pressure, acceleration due to gravity, temperature difference across the layer, depth of the convection layer, dynamic viscosity, thermal conductivity, mean density and temperature at bottom plate, respectively.

Additional parameters are required to characterize compressibility effects. The first parameter is the dissipation number, D defined as

$$D = \frac{gH}{C_p T_B}. \tag{1a}$$

This corresponds to an adiabatic equilibrium or temperature gradient across the depth if we have an isentropic process. The second parameter is the superadiabaticity,

$$\epsilon = \frac{\Delta T}{T_B}, \tag{1b}$$

which is the excess temperature gradient from the adiabatic equilibrium (see Fig.1). Superadiabaticity should be greater than one for instabilities to grow and thus convection to occur.

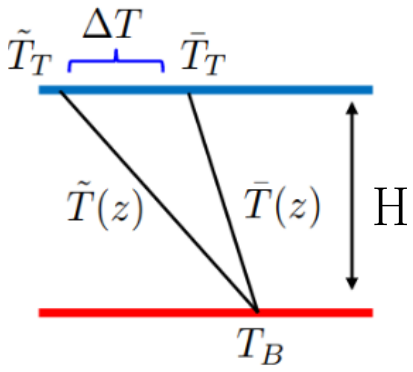

Figure 1: Simulation setup of the compressible turbulent convection flow. $\bar{T}(z)$ and $\tilde{T}(z)$ correspond to adiabatic and conductive equilibrium, respectively.

GOVERNING EQUATIONS AND DNS

The equations of motion for compressible convection are

$$\partial_t\rho + \partial_i(\rho u_i) = 0 \tag{2a}$$

$$\partial_t(\rho u_i) + \partial_j(\rho u_i u_j) = -\partial_i p + \partial_j\sigma_{ij} - \rho g\delta_{i,3} \tag{2b}$$

$$\partial_t(\rho e) + \partial_j(\rho e u_j) = -p\partial_i u_i + \partial_i(k\partial_i T) + \sigma_{ij}S_{ij} \tag{2c}$$

$$p = \rho RT \quad \text{where} \quad R = C_p - C_v. \tag{2d}$$

These equations correspond to mass, momentum and energy conservation laws along with the ideal gas equation of state. Here, ρ, ρu_i, p, ρe, T are the mass density, momentum density components, pressure, internal energy density, and temperature, respectively. The viscous stress tensor is $\boldsymbol{\sigma} = 2\mu\boldsymbol{S} + 2\mu\boldsymbol{I}(\boldsymbol{\nabla}\cdot\boldsymbol{u})/3$ with the Kronecker tensor $\boldsymbol{I}$ and the rate of strain tensor $\boldsymbol{S} = (\boldsymbol{\nabla u} + \boldsymbol{\nabla u}^T)/2$. The dynamic viscosity μ is assumed to be constant in these simulations. The thermal conductivity k is related to the viscosity through the Prandtl number, $k = \mu C_p/Pr$. In our DNS, $Pr = 0.7$. C_p and C_v correspond to specific heat at constant pressure and volume, respectively. Their ratio, $\gamma = C_p/C_v = 1.4$ for a diatomic gas is used and R is the gas constant. The internal energy is defined as $e = C_v T$.

A uniform grid is used in x– and y–directions along with periodic boundary conditions. In wall-normal z–direction, a non-uniform grid with a point clustering near the walls is

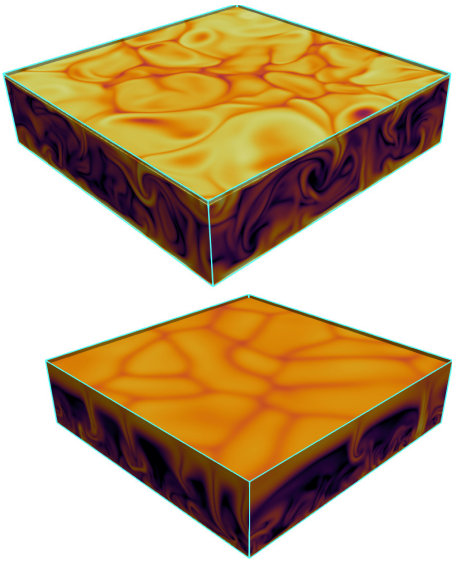

Figure 2: Visualization of the plume structure of the superadiabatic temperature field T_{sa}. Contours of $\ln|\boldsymbol{\nabla} T_{sa}|$ are shown at two instants, (a) for case 1 with $D = 0.1$ and (b) for case 8 with $D = 0.8$. Minimum/maximum contour levels correspond to -7.0/-2.4 in (a) and -9.5/-4.0 in (b). The top contour surface is slightly below $z = H$.

taken, which follows a hyperbolic tangent stretching function. Spatial derivatives are calculated by a 6th-order compact scheme for all points except near the walls [4, 5]; there 4th- and 3rd–order compact schemes are used at the last two grid points near the wall. No-slip, isothermal boundary conditions are applied at the top and bottom. The boundary condition for p is evaluated using the z-component of the momentum equation at $z = 0, H$, $\partial p/\partial z = \partial \sigma_{iz}/\partial x_i - \rho g$. The fields are advanced in time by a low storage 3rd-order Runge-Kutta with a Courant number of CFL = 0.5.

RESULTS

In the current work, we focus on moderate superadiabaticity $\epsilon \approx 0.1$ with the dissipation number ranging from $D = 0.1$—0.8. The dissipation number is a measure of the background stratification. The adiabatic background density profile defined as $\rho_a(z)/\rho_B = (1 - Dz/H)^{1/(\gamma-1)}$ [6] increases with D. For the highest D considered in our study, $\rho_B/\rho_T \approx 56$. In our recent work [7], we systematically analyzed the effect of stratification (by increasing D) at $\epsilon \approx 0.1$ for fixed Rayleigh number, $Ra \approx 10^6$ and Prandtl number, $Pr = 0.7$. The asymmetry in the superadiabatic temperature due to high D can be seen in Figure 2 comparing the lowest ($D = 0.1$) and highest ($D = 0.8$) compressibility cases respectively. The low compressibility case is similar to that of incompressible Rayleigh-Bénard convection with the plumes from the top and bottom more or less symmetric in frequency and magnitude. However considerable asymmetry is observed for the high compressibility case with slender plume structures from the top boundary although the top boundary layer thickness increases with D [8]. We showed that the transitional behaviour is due to significant compressibility effects near the top boundary resulting in considerable pressure fluctuations.

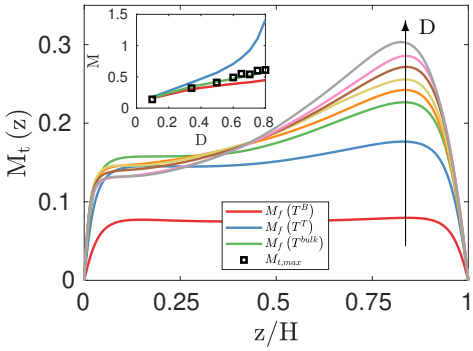

Figure 3: Turbulent Mach number for different cases.

We demonstrate this in Figure 3 by plotting the turbulent Mach number, $M_t(z) = u'(z)/\sqrt{\gamma R\langle T\rangle(z)}$. One finds that compressibility increases near the top boundary with D along with growing asymmetry between the boundaries. A characteristic Mach number, $M(T)$ can be defined in terms of ϵ and D as follows: $M = \sqrt{\epsilon D/(\gamma - 1)}$. From the inset of the figure, we observe that the maximum turbulent Mach number is comparable to the characteristic Mach number, $M(T_{bulk})$ defined using the bulk temperature.

Although we consider still an idealized flow, the sparse network of thin plume structures at top boundary at least qualitatively resembles the well-known granule network at the surface of the Sun. Higher Rayleigh number simulations would give further insights, thus in this work, we will present numerical simulations at $Ra \approx 10^7$. The new studies will include effects of compressibility on scaling of turbulent heat transfer with respect to Rayleigh numbers, a comprehensive analysis of the top boundary layer structure elucidating the formation and ejection of the slender plume like structures from the top boundary along with the compressibility effects on the mixing efficiency of the fluid falling from the top and rising from bottom into the bulk.

REFERENCES

[1]Chillà, F. and Schumacher, J.: New perspectives in turbulent Rayleigh-Bénard convection, *Eur. Phys. J. E*, **35**, 58 (2012).

[2]Stevens, B.: Atmospheric moist convection, *Annu. Rev. Earth Planet. Sci*, **33**, 605–643 (2005).

[3]Pandey, A., Schumacher, J. and Sreenivasan, K. R.: Non-Boussinesq low-Prandtl-number convection with a temperature-dependent thermal diffusivity, *Astrophys. J.*, **907**, 56 (2021).

[4]Lele, S.: Compact finite-difference schemes with spectral-like resolution, *J. Comp. Phys.*, **103**, 16–42 (1992).

[5]Baranwal, A., Donzis, D. A. and Bowersox, R. D. :Asymptotic behaviour at the wall in compressible turbulent channels, *J. Fluid Mech.*, **933**, A38 (2022).

[6]Jones, C., Mizerski, K. and Kessar, M.: Fully developed anelastic convection with no-slip boundaries, *J. Fluid Mech.*, **930**, A13 (2022).

[7]John, J. P. and Schumacher, J.: Compressible turbulent convection in highly stratified adiabatic background, *J. Fluid Mech.*, **972**, R4 (2023).

[8]John, J. P. and Schumacher, J.: Strongly superadiabatic and stratified limits of compressible convection, *Phys. Rev. Fluids*, **8**, 103505 (2023).

WORKSHOP
Direct and Large-Eddy Simulation 14
April 10-12 2024, Erlangen, Germany

IMPACT OF COMPRESSIBILITY ON DRAG REDUCTION BY SPANWISE TRAVELING TRANSVERSAL WAVES FOR TURBULENT FLAT PLATE FLOW

Xiao Shao[1], **Matthias Meinke**[1], **Wolfgang Schröder**[1 2]
[1]Institute of Aerodynamics and Chair of Fluid Mechanics(AIA)
RWTH Aachen University, Wüllnerstr. 5a, 52062 Aachen, Germany
[2]JARA Center for Simulation and Data Science
RWTH Aachen University, Seffenter Weg 23, 52074 Aachen, Germany
X.Shao@aia.rwth-aachen.de; m.meinke@aia.rwth-aachen.de; office@aia.rwth-aachen.de

INTRODUCTION

Turbulent boundary layer drag reduction plays a vital role in mitigating energy requirements in high Reynolds number flows. Various drag reduction techniques have been developed in the past to reduce friction drag. In addition to passive drag reduction techniques such as riblets, active techniques that involve control systems offer the advantage of adjustable actuation parameters according to the prevailing flow conditions. Since active methods require external energy input, they are not only evaluated based on drag reduction (DR) but also on net power savings (NPS), which is a crucial parameter for assessing flow control efficiency. One promising approach in active flow control is based on spanwise traveling transversal waves (STTW). Extensive research [1, 2, 3, 4, 5] has demonstrated the efficacy of STTW in controlling near-wall turbulent structures and reducing viscous and pressure drag. However, a majority of these investigations have been limited to incompressible or low Mach number turbulent boundary layers. In practical scenarios, transportation vehicles such as aircraft operate under compressible flow conditions. Therefore, this project is dedicated to analyzing and understanding the influence of compressibility on the efficiency of DR and NPS for compressible turbulent flat plate flow.

NUMERICAL SETUP

Turbulence scale-resolving numerical simulations for actively controlled turbulent boundary layer flow are conducted by the in-house flow solver m-AIA (multiphysics-Aerodynamisches Institut Aachen). A finite volume method (FVM) is used to solve the Navier-Stokes equations for three-dimensional unsteady compressible flow.

The turbulent boundary layer flow over a wall actuated by a sinusoidal wave motion is depicted in Figure 1. Two Mach numbers $M_1 = 0.2$ and $M_2 = 0.7$ are considered to investigate the effect of compressibility on DR and NPS, while the Reynolds number based on the momentum thickness of the reference case is $Re_\theta = \theta_{x_1} u_\infty/\nu = 1,000$, with $\theta = 1$ at location $x_1 = 160$. The domain sizes are defined by $L_x \times L_y = 361\theta \times 101\theta$ and $L_z/\theta = 21.65$, 32.47, 43.30, 54.19, and 64.94. In the x-direction, the configuration consists of a non-actuated region ($0 < x/\theta < 50$), a transition region ($50 < x/\theta < 125$) to ensure a smooth surface connecting the flat plate and wavy wall, a fully actuated region

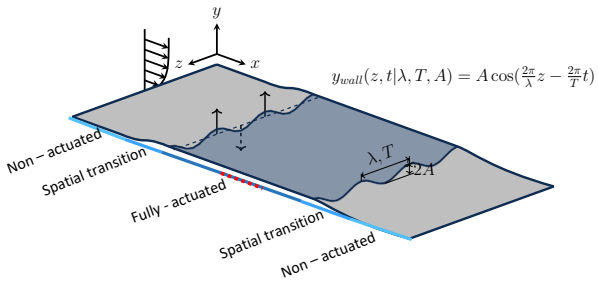

Figure 1: Schematic of spanwise traveling wave setup. The region corresponding to the dashed red line is used to calculate DR and NPS.

($125 < x/\theta < 235$), and finally, a transition to a non-actuated region. The grid resolution is $\Delta_x^+ \times \Delta_z^+ \approx 10.0 \times 4.0$, and $\Delta_y^+|_{wall} \approx 1.0$ with gradual coarsening along the y-coordinate yielding a maximum value of $\Delta_y^+ < 16.0$ inside the boundary layer. The near-wall grid resolution is chosen to be similar to that of a direct numerical simulation (DNS) to ensure an accurate solution for the impact of wall actuation on turbulent structures. The actuation parameters are specified by λ^+, T^+, A^+ in inner scaling based on the friction velocity u_τ and kinematic viscosity ν, as detailed in the table 1. Latin hypercube sampling is employed to obtain parameter settings within the predefined range of actuation parameters shown in table 1.

Further details on the numerical method, boundary conditions, and the validation for active control simulations can be found in the studies for flat plate TBL flows [2, 4] and turbulent airfoil flows [1, 3].

The efficiency of the actuation is assessed based on the drag coefficient for the actuated and non-actuated cases

$$\Delta c_d = \frac{c_{d,x,\mathrm{ref}} - c_{d,x,\mathrm{act}}}{c_{d,x,\mathrm{ref}}} \cdot 100 \tag{1}$$

$$c_d = \frac{F_{\mathrm{pressure}} + F_{\mathrm{friction}}}{\frac{1}{2}\rho u_\infty^2 A_{\mathrm{surf}}} \tag{2}$$

determined by pressure force $F_{\mathrm{pressure}} = \int_{A_{\mathrm{surf}}} -p\boldsymbol{n}dA$ and the friction force $F_{\mathrm{friction}} = \int_{A_{\mathrm{surf}}} \overline{\overline{\boldsymbol{\tau}}} \cdot \boldsymbol{n}dA$ acting on the wet-

ted surface A_{surf}. Furthermore, the NPS is defined by

$$\Delta P_{\text{net}} = \frac{P_{\text{ref}} - (P_{\text{act}} + P_{\text{control}})}{P_{\text{ref}}} \cdot 100 \qquad (3)$$

where $P_{\text{ref/act}} = F_{\text{ref/act}} u_\infty$ is the energy in the freestream, while $P_{\text{control}} = \int_{A_{\text{surf}}} [-p u_{\text{wall}} + \overline{\overline{\tau}} \cdot u_{\text{wall}}] \cdot \boldsymbol{n} dA$ is the required power to overcome the friction and pressure forces acting on the plate surface.

M	λ^+	T^+	A^+
0.2	$\{1000, 1500, 2000, 2500, 3000\}$	$[70, 160]$	$[10, 79]$
0.7	$\{1000, 1500, 2000, 2500, 3000\}$	$[70, 160]$	$[10, 79]$

Table 1: Dimensionless actuation parameters for the wavelength λ^+ the time period T^+, and amplitude A^+.

RESULTS

Figure 2(a, b) display the maps of DR as a function of wavelength and period at $M_1 = 0.2$ and $M_2 = 0.7$. At each Mach number, the solution of 36 cases is indicated by grey points. Cubic interpolation of these data onto an irregular grid over the parameter space $\lambda^+ = 1000, 1500, 2000, 2500, 3000$ and $70 \leq T^+ \leq 160$ was performed to generate the maps.

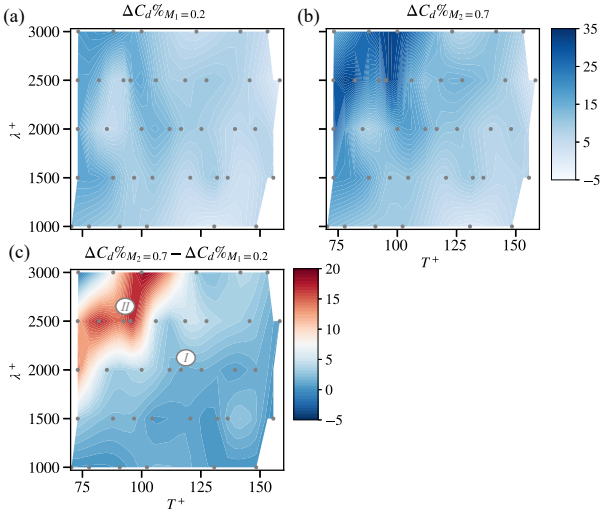

Figure 2: (a, b) Maps of DR at (a) $M_1 = 0.2$ and (b) $M_2 = 0.7$. (c) Map of the difference in DR between $M_1 = 0.2$ and $M_2 = 0.7$.

At $M_1 = 0.2$, the maximum DR of 19.2% at $(\lambda^+, T^+) = (3000, 88)$ is in close agreement with the incompressible case at $M = 0.1$ mentioned in [2], where a 16% drag reduction at $(\lambda^+, T^+) = (3000, 90)$ has been found. At $M_2 = 0.7$, the maximum DR increases to 27.5% at the actuation parameter setting $(\lambda^+, T^+) = (3000, 88)$. The drag reduction distribution at $M_2 = 0.7$ exhibits a similar pattern compared to $M_1 = 0.2$. Figure 2(c) shows the difference in DR as the Mach number changes from 0.2 to 0.7. In general, DR is higher at the higher Mach number. Depending on the disparity levels, the entire dataset can be decomposed into region$I$ and regionII. The dividing line of these regions is defined by the critical outer scale parameter, i.e., the phase speed $c = \lambda/T$.

The vortex topology based on λ_2 criteria and the pressure contour in the yz plane is shown in Figure 3. The isosurfaces of the vortex structures are generated by $\lambda_2 = -0.02$,

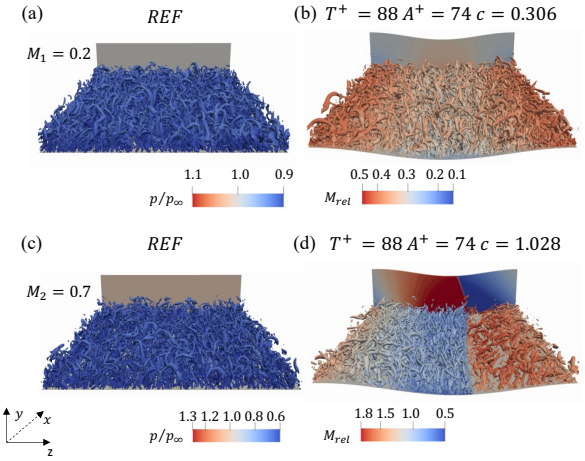

Figure 3: Instantaneous λ_2 criteria vortex topology and pressure contour of yz plane for (a, c) reference cases at (a) $M_1 = 0.2$ and (c) $M_2 = 0.7$; (b, d) actuated cases from regionII defined in Figure 2 at (b) $M_1 = 0.2$ and (d) $M_2 = 0.7$.

colored by the relative Mach number defined by $M_{\text{rel}} = \sqrt{u^2 + v^2 + (c - w)^2} / \sqrt{\gamma p / \rho}$. Compared to the reference flow field, the flow in the spanwise direction displays inhomogeneity. Both the pressure and velocity fields possess periodic behavior. The trough region exhibits a higher pressure distribution, while the crest zone features a larger velocity field. The phase speed c at $M_2 = 0.7$ is nearly 3.5 times greater than that at $M_1 = 0.2$, despite having the same inner actuation parameter setting. At $c = 1.028$ relative to the stagnation sound speed a shock wave shown in Figure 3(d) develops. The shock wave travels like the surface wave in the positive z direction. Within the shock wavefront, the vortices experience a reduction in number and size, influenced by the passing wave. Considering this phenomenon in connection with the increased drag reduction, it can be stated that the shock waves play a crucial role in enhancing friction drag reduction. However, shock waves do prevent any positive NPS.

The spanwise shock waves increase DR, but are detrimental to NPS. Detailed analyses of the turbulence statistics, turbulent flow structures, multivariate empirical mode decomposition, and skin-friction decomposition for compressible flow will be discussed in the conference presentation.

REFERENCES

[1]Albers M, Meysonnat P S, Schröder W. Actively reduced airfoil drag by transversal surface waves, *Flow, Turbulence and Combustion.*, **102**, 865–886 (2019).

[2]Albers M, Meysonnat P S, Fernex D, et al. Drag reduction and energy saving by spanwise traveling transversal surface waves for flat plate flow, *Flow, Turbulence and Combustion.*, **105(1)**, 125–157 (2020).

[3]Albers M, Schröder W. Lower drag and higher lift for turbulent airfoil flow by moving surfaces, *International Journal of Heat and Fluid Flow.*, **88**, 108770 (2021).

[4]Mäteling E, Albers M, Schröder W. How spanwise travelling transversal surface waves change the near-wall flow, *Journal of Fluid Mechanics.*, **957**, A30 (2023).

[5]Lagemann, E., Albers, M., Lagemann, C., Schröder, W. Impact of Reynolds Number on the Drag Reduction Mechanism of Spanwise Travelling Surface Waves, *Flow, Turbulence and Combustion.*, 1-14 (2023).

WORKSHOP
Direct and Large-Eddy Simulation 14
April 10-12 2024, Erlangen, Germany

GPU-ACCELERATED DNS OF DIABATIC TRANSITIONAL BOUNDARY LAYERS AT SUPERCRITICAL PRESSURES

P. C. Boldini[1], B. Bugeat[2], P. Costa[1], J. W. R. Peeters[1], R. Pecnik[1]
[1]Process & Energy Department, Delft University of Technology, The Netherlands
[2]School of Engineering, University of Leicester, United Kingdom
p.c.boldini@tudelft.nl

INTRODUCTION

In recent years, fluids at supercritical pressures have gained large interest in industrial applications to increase the efficiency of energy conversion systems, and to reduce the size of the equipment. In many of these applications, the fluid can operate in the vicinity of the critical point, where strong property variations occur across the pseudo-boiling (Widom) line. These property variations can cause heat-transfer deterioration or enhancement [1], and delay or promote transition to turbulence. Therefore, the location of the laminar-to-turbulent transition needs to be accurately predicted.
To investigate this, we recently performed the first-of-its-kind direct numerical simulation (DNS) of a transitional flat-plate boundary layer at supercritical pressure [2]. The controlled H-type transition scenario was investigated similar to the ideal-gas simulations of Sayadi et al. [3]. A much more abrupt breakdown to turbulence, with the appearance of secondary vortex systems, was observed in the transcritical regime. Here, due to the highly non-ideal thermodynamic behaviour, the numerical solution requires methods that: (i) conserve kinetic energy and entropy, (ii) preserve pressure equilibrium, and (iii) are stable and non-dissipative. Hence, the purpose of the present study is to discuss the numerical scheme and the GPU-porting of the in-house flow solver CUBENS (CUBic Equation of state Navier-Stokes), before applying it for the simulation of a transitional boundary layer at supercritical pressure.

METHODOLOGY

The CUBENS solver integrates the non-dimensional single-phase fully compressible Navier-Stokes (NS) equations (see Boldini et al. [2]) on a Cartesian coordinate system (x, y, z). In this formulation, the vector of conserved variables is defined as $\mathbf{Q} = [\rho, \rho u, \rho v, \rho w, \rho e]$. Consequently, the following non-dimensional numbers are obtained: Reynolds number $Re_\delta = \rho^*_\infty u^*_\infty L^*/\mu^*_\infty$, Mach number $M_\infty = u^*_\infty/a^*_\infty$, Prandtl number $Pr_\infty = C^*_{p,\infty}\mu^*_\infty/\kappa^*_\infty$, and an Eckert number $Ec_\infty = u^{*2}_\infty/(C^*_{p,\infty}T^*_\infty)$, where L^* is the local Blasius length scale $\delta^* = (\mu^*_\infty x^*/\rho^*_\infty/u^*_\infty)^{1/2}$. The system of equations is closed by a thermal and caloric equation of state (EoS) in reduced form [2]: (i) Van der Waals (VdW), less computationally expensive, or (ii) Peng-Robinson (PR) for a more accurate thermodynamic behaviour. With the reduced formulation, only the ratio C^*_v/R^* (i.e., the molecular degrees of freedom) needs to be specified beforehand. In addition, the transport properties are analytically evaluated, see Ref. [2].
The computational domain for boundary layer simulations is illustrated in Fig. 1. The inflow is located at x_0 and the outflow at x_e. The domain height is given by y_e. In the spanwise z-direction ($z = [0, z_e]$), periodicity is imposed. All dimensions are then re-scaled by the boundary-layer thickness at the domain inlet $\delta_{99,0}$. Non-reflecting boundary conditions, together with damping sponge layers, are applied at the inflow, free-stream, and outflow planes. At the wall, the no-slip and no-penetration conditions are prescribed, and it is isothermal. To achieve laminar-to-turbulent transition, disturbances are triggered by a wall-normal blowing and suction strip ($x_1 < x < x_2$) according to $v(x, y = 0, z, t) = f(x)\sum_{k=0}^{N} A_k \sin(\omega_k t)\cos(\beta_k z)$, with shape function $f(x)$, with amplitude A_k, frequency ω_k and spanwise wavenumber β_k of the considered N-modes [3].

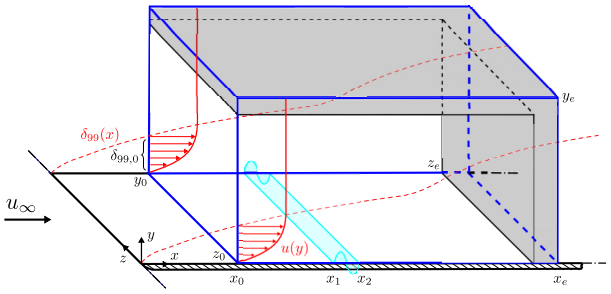

Figure 1: DNS computational domain.

In the context of a high-order spatio-temporal discretisation, sixth-order central finite-differences and an explicit third-order Runge-Kutta scheme are used, respectively. In order to minimise the dissipation errors, a split-convective form, which preserves kinetic energy and entropy (KEEP), is implemented [4]. However, this scheme does not maintain the pressure equilibrium (PE) due to the discretisation of the internal energy convective term [5]. Thus, based on the ideal-gas PE formulation of Shima et al. [5], its extension to an arbitrary EoS is introduced. In this way, no spurious pressure oscillations are generated without the need for any form of artificial diffusion [6]. Alongside MPI parallelisation, the solver is GPU-accelerated using OpenACC for computation offloading and CPU-GPU data transfer, along with CUDA-aware MPI for GPU-GPU communication. This allowed for significant gains in performance. For instance, for the same amount of supercomputer node hours, on a periodic computational box with 256^3 grid points yields: (a) for single CPU-node (128 AMD's Rome 7H12) vs. single GPU (1 NVIDIA's A100), a speed-up

of ×4.9; (b) for multi CPU-nodes (128 × 4) vs. multi GPUs (4), a speed-up of ×22.

RESULTS

Before dealing with transitional transcritical boundary layers, the performance of the KEEP-PE numerical scheme is assessed and verified. A 1-D inviscid advective test for supercritical N_2 is chosen as proposed by Ma et al. [6]. At a constant pressure of $p_0^* = 50\,\text{bar}$ and velocity of $u_0^* = 1\,\text{m/s}$, the smooth density profile is imposed as $\rho^* = 0.5(\rho_2^* + \rho_1^*) + 0.5(\rho_2^* - \rho_1^*)\sin(2\pi x^*)$, with $T_2^* = 300\,\text{K}$, $T_1^* = 100\,\text{K}$, and $T_{ref}^* = 200\,\text{K}$. Numerical results for CFL = 0.8 and at $t^* = 10\,\text{s}$ are presented in Fig. 2. Note that the crossing of the Widom line is located at $x^*/L^* \approx 0.55$–0.95.

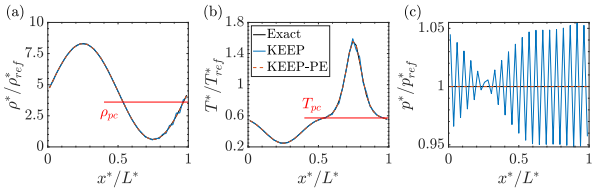

Figure 2: 1-D advection test comparing KEEP and KEEP-PE with the exact solution: (a) density, (b) temperature, (c) pressure. In red, pseudo-boiling properties ρ_{pc} and T_{pc}.

With the addition of the new PE discretisation, spurious oscillations are suppressed under transcritical conditions. Thus, in order to both conserve kinetic energy and entropy, while preserving the PE condition, the KEEP-PE scheme is adopted for the following investigation.

Next, the DNS of a transcritical transitional boundary-layer is computed using the in-house flow solver CUBENS. The controlled H-type breakdown is selected. The base-flow parameters are reported in Tab. 1.

p_r	$T_{r,\infty}$	M_∞	Pr_∞	C_v^*/R^*	$T_{r,w}$	T_w^*/T_∞^*
1.10	0.90	0.2	1.0	9/2	1.10	1.222

Table 1: Base-flow properties of the transcritical simulation. Note that the VdW-EoS is here chosen.

In Fig. 3, laminar boundary-layer profiles, which also serve as DNS initial condition, are displayed for the transcritical case of Tab. 1. A large wall-normal density stratification, i.e. $\rho_w^*/\rho_\infty^* = 0.328$, is noticeable.

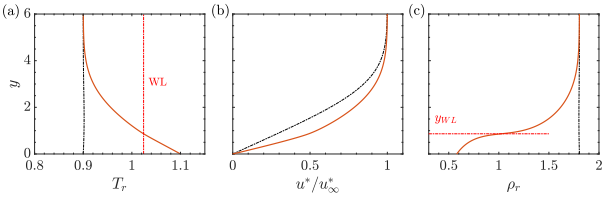

Figure 3: Self-similar base-flow profiles: (a) reduced temperature, (b) non-dimensional streamwise velocity, and (c) reduced density.

After performing a linear stability analysis of the laminar profiles, the DNS is set up such that a modal instability is triggered at the same primary frequency $\omega_{2\text{-D}}$ of the ideal-gas case of Ref. [3]. Therefore, in a disturbance strip at $Re_{\delta,mid} = 415$, a two-dimensional wave $(1, 0)$ and a pair of oblique subharmonic waves $(1/2, \pm 1)$ with $\omega_{3\text{-D}} = 0.5\omega_{2\text{-D}}$ and $A_{2\text{-D}}/A_{3\text{-D}} = 70$ are introduced (total number of modes is $N = 3$). Instantaneous flow structures are displayed in Fig. 4 by isocontours of the Q-criterion.

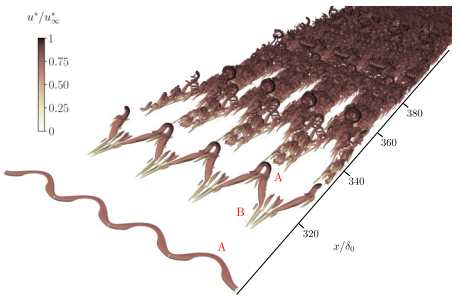

Figure 4: Visualisation of the instantaneous flow structures using isosurfaces of the Q-criterion ($Q = 0.025$), coloured by the streamwise velocity.

Clear, developed staggered patterns of Λ-structures (A) are not present. Instead, secondary vortex systems (B), inducing high-low-speed streaks with high-low-density fluid, are formed. A snapshot of the density inside the boundary layer (xy-plane) at a constant spanwise distance of $z/\delta_0 = 0$ is presented in Fig. 5.

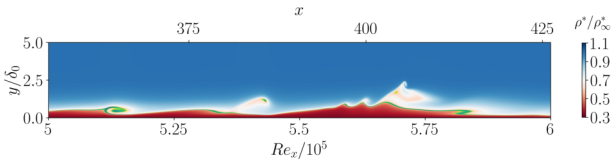

Figure 5: Instantaneous density contours (xy-plane). In green, pseudo-boiling regions with $\max(C_p)$.

The formation of Λ-vortices with hairpin vortices at their tips is characterised by strong vortical roll-up patterns between the liquid-like (free-stream) and gas-like (wall) region. Overall, a detailed flow analysis of all variables reveals an oscillation-free and stable flow field without the addition of any artificial diffusion, dissipation, or filtering.

ACKNOWLEDGMENTS

The European Research Council (grant no. ERC-2019-CoG-864660, Critical) has supported the investigations presented in this study. DNS were carried out on the Dutch National Supercomputer Snellius (SURF) (grant no. 2022/ENW/01251049).

REFERENCES

[1]Yoo, J. Y. : The Turbulent Flows of Supercritical Fluids with Heat Transfer, *Annu. Rev. Fluid Mech.*, 45, 495–525, (2013).

[2]Boldini, P. C., Bugeat, B., Costa, P., Peeters, J. W. R. and Pecnik, R. : Direct numerical simulation of H-type transition in a flat-plate boundary layer with supercritical fluids, *In Proceedings of 14th International ERCOFTAC Symposium on Engineering Turbulence Modelling and Measurements (ETMM14), Barcelona, Spain, September 6-8*, (2023).

[3]Sayadi, T., Hamman, C. and Moin, P. : Direct numerical simulation of complete H-type and K-type transitions with implications for the dynamics of turbulent boundary layers, *J. Fluid Mech.*, 724, 480–509, (2013).

[4]Kuya, Y. and Kawai, S. : High-order accurate kinetic-energy and entropy preserving (KEEP) schemes on curvilinear grids, *J. Comput. Phys.*, 442, 110482, (2021).

[5]Shima, N., Kuya, Y., Tamaki, Y. and Kawai, S. : Preventing spurious pressure oscillations in split convective form discretization for compressible flows, *J. Comput. Phys.*, 427, 110060, (2021).

[6]Ma, P. C., Lv, Y. and Ihme, M. : An entropy-stable hybrid scheme for simulations of transcritical real-fluid flows, *J. Comput. Phys.*, 340, 330–357, (2017).

WORKSHOP
Direct and Large-Eddy Simulation 14
April 10-12 2024, Erlangen, Germany

DIRECT NUMERICAL SIMULATION OF COMPRESSIBLE TURBULENT BOUNDARY LAYERS WITH HEAT TRANSFER AND PRESSURE GRADIENTS

Tobias Gibis[1] **and Christoph Wenzel**[1]
[1]Insitute of Aerodynamics and Gas Dynamics
University of Stuttgart, Stuttgart, Germany
gibis@iag.uni-stuttgart.de

INTRODUCTION

In contrast to incompressible boundary layers, compressible turbulent boundary layers can exhibit large temperature gradients in the wall normal direction even under adiabatic wall conditions, and the turbulent field also includes temperature, density, and total temperature fluctuations. Although considerable progress has been made in the description of compressible turbulent boundary layer flows in recent decades, their description is not nearly as complete as that of their incompressible counterpart. Open issues in compressible flows include fundamental principles such as the strong Reynolds analogy and the influence of compressibility on the quantities of the averaged flow field. For example, the Reynolds analogy is derived under the assumption of zero pressure gradient, so it is not readily apparent to what extent the results of the analogy hold for cases with pressure gradients.

This study aims to gain a deeper understanding of compressible turbulent boundary layers under the combined influence of pressure gradients and strong wall heat transfer. The essential problem of this case is the large number of influencing and interacting factors that have a significant impact on the resulting flow (such as the additional wall temperature condition), making their clear understanding inevitable. For example, in compressible flows with pressure gradients, the displacement effect observed in incompressible adverse pressure gradients is counteracted by compression due to the pressure gradient in the flow direction, depending on the Mach number and heat transfer conditions. Furthermore, when more than one parameter is changed simultaneously, it is often not possible to easily assign the resulting boundary layer behavior to the individual influences. Although the parameter space is more complex, the main research idea in understanding compressible boundary layers has been to transfer and apply incompressible knowledge using semi-empirical transformations that need to be transferred and improved to better handle these complex cases.

Since the intent of this study is to investigate strong heat transfer effects, it is necessary to first categorize what can be understood as such and what the implications are for case design. Subsequently, the case design and preliminary results of the pressure gradient cases are presented.

CLASSIFICATION OF HEAT TRANSFER EFFECTS

In the literature there is some variety in classifying the heat transfer strength, for example the wall temperature to recovery temperature ratio T_w/T_r, the inner scaled heat transfer $B_q = q_w/(\rho_w c_p T_w u_\tau)$, the diabatic parameter $\Theta = (T_w - T_e)/(T_r - T_e)$, the Eckert number $Ec = u_e^2/(c_p(T_w - T_r))$. The subscripts w and e denote wall and edge quantities of temperature T, velocity u, and density ρ; T_r is the recovery temperature, u_τ the friction velocity, q_w the wall heat flux and c_p the specific heat capacity. However, when comparing data at different Mach numbers, a simple T_w/T_r and B_q is not sufficient to classify the heat transfer strength that the boundary layer "feels". For this, quantities such as Θ and Ec have been claimed to be better comparison parameters [1, 2]. The reason for this is that in a compressible turbulent boundary layer the thermal boundary layer is determined by the balance of heat transfer and dissipation. As the Mach number increases, the dissipation increases. Therefore, to obtain a comparable heat transfer effect, the heat transfer must be stronger, which is included in both parameters. This is particularly problematic for cooled boundary layers, where the two effects counteract each other.

Extending this previous work, it can be shown that the Eckert number, in addition to the Reynolds and Prandtl numbers, determines the thermal boundary layer and, especially important for cooled boundary layers, the position of the temperature maximum.

To demonstrate this, DNS from zero pressure gradient simulations and a variety of reference data have been collected to show the effect of the Ec number and especially to classify the cooled conditions:

- Weak Cooling: Temperature peak in the viscous sublayer
- Moderate Cooling: Temperature peak in the buffer layer
- Strong Cooling: Temperature peak in the log-layer or above.

Using this classification allows to create cases with significantly different heat transfer behavior. As a consequence, a practical issue for moderately to highly cooled cases is that the stability of an SRA-based inflow condition for temperature fluctuation in digital filtering becomes much worse. This is because the temperature fluctuation is not negatively correlated with the velocity fluctuation as in the adiabatic cases. For the weak cooling regime, the temperature peak does not interact significantly with the turbulence.

COMPRESSIBLE TURBULENT BOUNDARY LAYERS WITH PRESSURE GRADIENTS

Combined with the pressure gradient, this would result in a large parameter space. To reduce the potential influence of Reynolds number effects, all cases of the study are designed to be self-similar in the flow direction, which controls the flow history and allows the most general conclusions; it also allows direct comparison with the adiabatic cases presented in [3, 4].

All cases considered are designed around a supersonic Mach number of $M_e \approx 2$ with a Rotta-Clauser kinematic parameter of $\beta_K \approx 0.65$ and wall temperature conditions that are heated, adiabatic, and moderately cooled. A strong cooling case is considered only for a reference zero pressure gradient. Other design criteria were to have some overlap in the Reynolds number range Re_τ to allow a meaningful comparison between the different cases, and a domain length long enough to prove self-similarity.

Since pressure gradients are an effect of the outer layer, it is shown that the self-similarity analysis [4] is still applicable. The present self-similar cases allow for a good database to start looking at what happens for heat transfer and pressure gradients for the flow structure, the thermal boundary layer (and the Reynolds analogy). For example, in figure 1 the turbulent heat flux and turbulent shear stress is shown. Showing the influence of pressure gradient on both profiles.

REFERENCES

[1] C. Wenzel, T. Gibis, and M. Kloker, "About the influences of compressibility, heat transfer and pressure gradients in compressible turbulent boundary layers," *Journal of Fluid Mechanics*, vol. 930, p. A1, Jan. 2022.

[2] M. Cogo, U. Baù, M. Chinappi, M. Bernardini, and F. Picano, "Assessment of heat transfer and Mach number effects on high-speed turbulent boundary layers," *Journal of Fluid Mechanics*, vol. 974, p. A10, Nov. 2023.

[3] C. Wenzel, T. Gibis, M. Kloker, and U. Rist, "Self-similar compressible turbulent boundary layers with pressure gradients. Part 1. Direct numerical simulation and assessment of Morkovin's hypothesis," *Journal of Fluid Mechanics*, vol. 880, pp. 239–283, Dec. 2019.

[4] T. Gibis, C. Wenzel, M. Kloker, and U. Rist, "Self-similar compressible turbulent boundary layers with pressure gradients. Part 2. Self-similarity analysis of the outer layer," *Journal of Fluid Mechanics*, vol. 880, pp. 284–325, Dec. 2019.

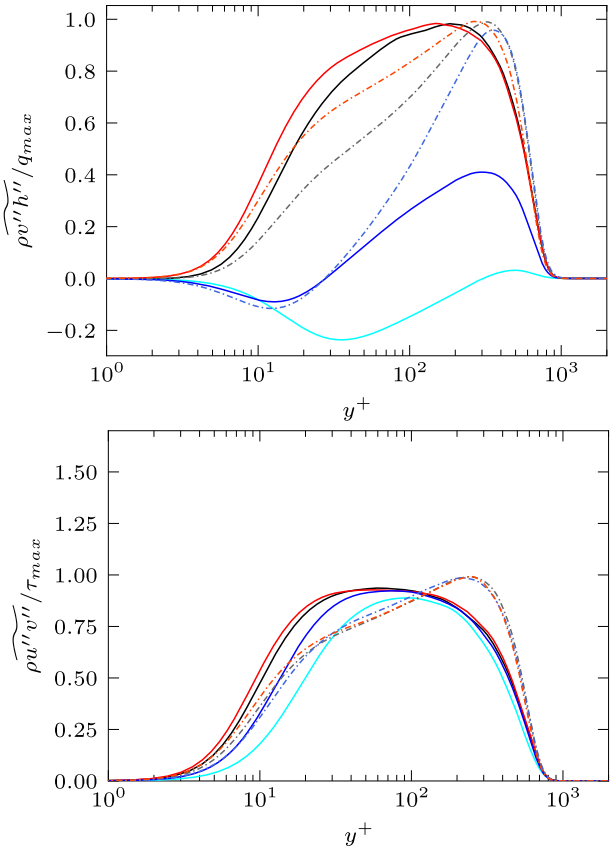

Figure 1: Turbulent heat flux profile (Top) and turbulent shear stress (bottom). Solid line: ZPG, Dash dotted lines: APG. Cyan/blue: cooled, black: adiabatic, red: heated

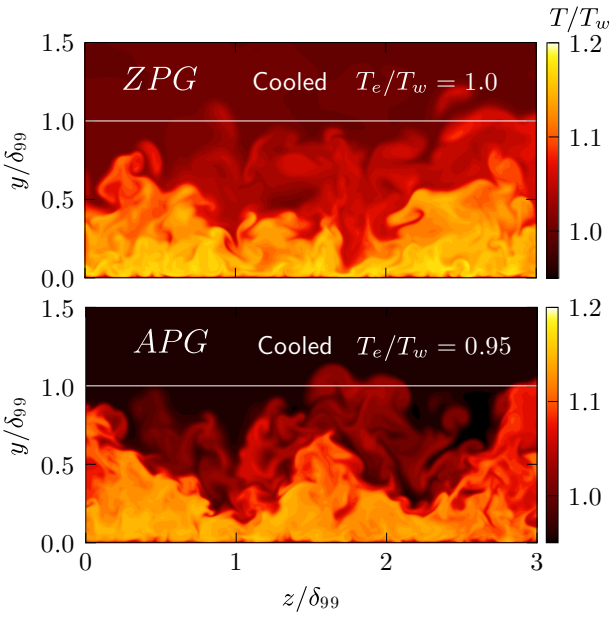

Figure 2: Comparison of a slice of instantaneous temperature normalized by wall temperature at a constant streamwise position of the temperature fields. Compared are two cooled cases, one with adverse and one with zero pressure gradient.

WORKSHOP
Direct and Large-Eddy Simulation 14
April 10-12 2024, Erlangen, Germany

REYNOLDS NUMBER EFFECTS ON HIGH-SPEED TURBULENT BOUNDARY LAYERS

G. Della Posta[1], M. Cogo[2], F. Picano[2], and M. Bernardini[1]
[1]Department of Mechanical and Aerospace Engineering (DIMA)
Sapienza University of Rome, Rome, Italy
[2]Centro di Ateneo di Studi e Attività Spaziali 'Giuseppe Colombo'
Università degli Studi di Padova, Padova, Italy
giacomo.dellaposta@uniroma1.it

INTRODUCTION

Given the renewed interest in sustained supersonic and hypersonic flight in the atmosphere, sub-orbital flights and planetary re-entry, a considerable effort has been recently devoted to a more in-depth understanding of high-speed wall-bounded flows. Recent research [1, 2] has thus focused on the study of compressible turbulent boundary layers in supersonic and hypersonic conditions exploiting the high fidelity offered by CFD methods like LES or DNS, which provides unrivalled accuracy and full access to the flow field.

However, given the relevant computational cost of such simulations, the existing literature typically considers flow cases at reduced Reynolds numbers, thus limiting the conceptual validity of the findings. In this study, we thus present a DNS database at Mach number $M_\infty = 2$ and friction Reynolds number $Re_\tau = \delta/\delta_v$ between 900 and 6000, where δ is the boundary layer thickness and $\delta_v = \nu_w/u_\tau$ is the viscous length scale. In addition to adiabatic wall conditions, we also consider an isothermal wall at the highest Reynolds number, representative of a boundary layer over a cold wall, to assess the relevance of thermal effects at high Reynolds numbers.

SETUP AND DISCUSSION

We simulated the cases in tab. 1 using our in-house high-fidelity solver STREAmS 2.0, which is an extensively validated finite-difference, CPU-GPU code for high-speed flows [3]. The domain is a box of length $L_x \approx 120\,\delta_{in}$, $L_y \approx 15\,\delta_{in}$, $L_z \approx 9\,\delta_{in}$, where δ_{in} is the boundary layer thickness at the inflow station. Periodic boundary conditions are enforced in the spanwise direction, purely non-reflecting boundary conditions at the outflow and top boundaries, unsteady characteristic boundary conditions at the bottom wall, and recycling–rescaling is applied at the inflow.

From fig. 1, we can observe that as expected, an extended region characterised by the standard law of the wall is noticeable for increasing Reynolds number. Fig. 2a confirms that peak streamwise turbulence intensity increases for larger Re_τ. The peak streamwise turbulence intensity $\widetilde{u''^2}_{pk}$ agrees well with the empirical fitting proposed by Pirozzoli and Bernardini [4]. Incompressible skin friction in fig.2b is instead consistent with the Kármán-Schoenherr fitting.

Finally, wall-normal distributions of the premultiplied velocity and temperature spectra for different wall conditions (fig. 3) show that for cold walls, the similarity between the velocity and the temperature fields is lost, with peak temperature fluctuations in the outer portion of the boundary layer.

M_∞	Re_τ	$\Theta = \frac{T_w - T_\infty}{T_r - T_\infty}$	$N_x \times N_y \times N_z$
2.0	850 - 2080	1.00	14336 × 768 × 1536
2.0	2390 - 5478	1.00	32768 × 1536 × 4096
2.0	2427 - 5920	0.25	32768 × 1536 × 4096

Table 1: Summary of computational cases considered.

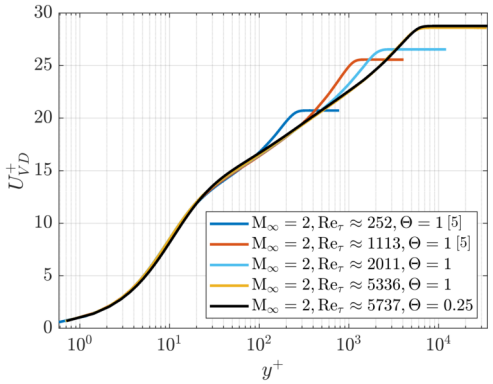

Figure 1: Van-Driest transformed streamwise velocity profiles.

REFERENCES

[1]Cogo, M., Salvadore, F., Picano, F., and Bernardini, M. : Direct numerical simulation of supersonic and hypersonic turbulent boundary layers at moderate-high Reynolds numbers and isothermal wall condition. *J. Fluid Mech.*, **945**, A30, (2022).

[2]Laguarda, L., Hickel, S., Schrijer, F.,and van Oudheusden, B. W.: Assessment of Reynolds number effects in supersonic turbulent boundary layers. *Int. J. Heat Fluid Flow*, **105**, 109234, (2024).

[3]Bernardini, M., Modesti, D., Salvadore, F., Sathyanarayana, S., Della Posta, G., and Pirozzoli, S. : STREAmS-2.0: Supersonic turbulent accelerated Navier-Stokes solver version 2.0. *Comput. Phys. Commun.*, **285**, 108644, (2023).

[4]Pirozzoli, S., and Bernardini, M. : Probing high-Reynolds-number effects in numerical boundary layers. *Phys. Fluids*, **25**(2), (2013).

[5]Pirozzoli, S. and Bernardini, M. Turbulence in supersonic boundary layers at moderate Reynolds number. *J. Fluid Mech.*, **688**, 120–168, (2011).

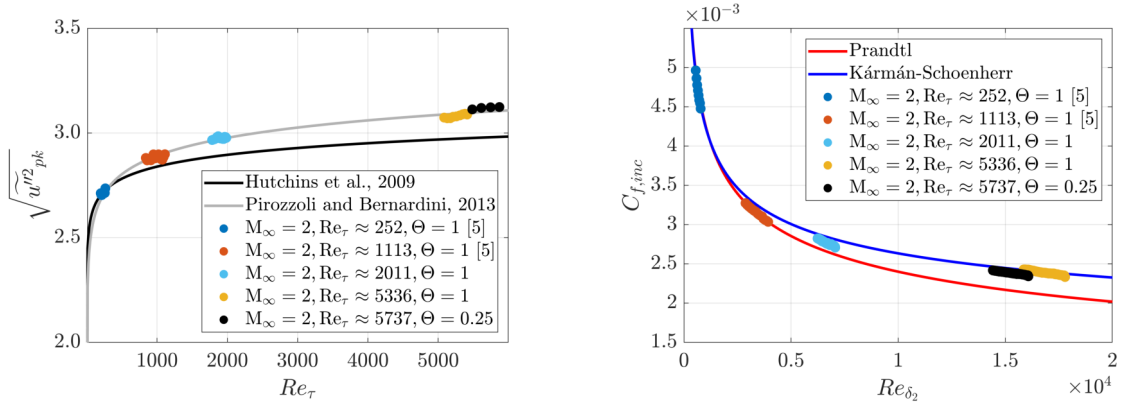

(a) (b)

Figure 2: Peak of streamwise turbulence intensity as a function of the friction Reynolds number (a); Incompressible skin friction as a function of $Re_{\delta_2} = \rho_\infty U_\infty \theta / \overline{\mu_w}$ (b).

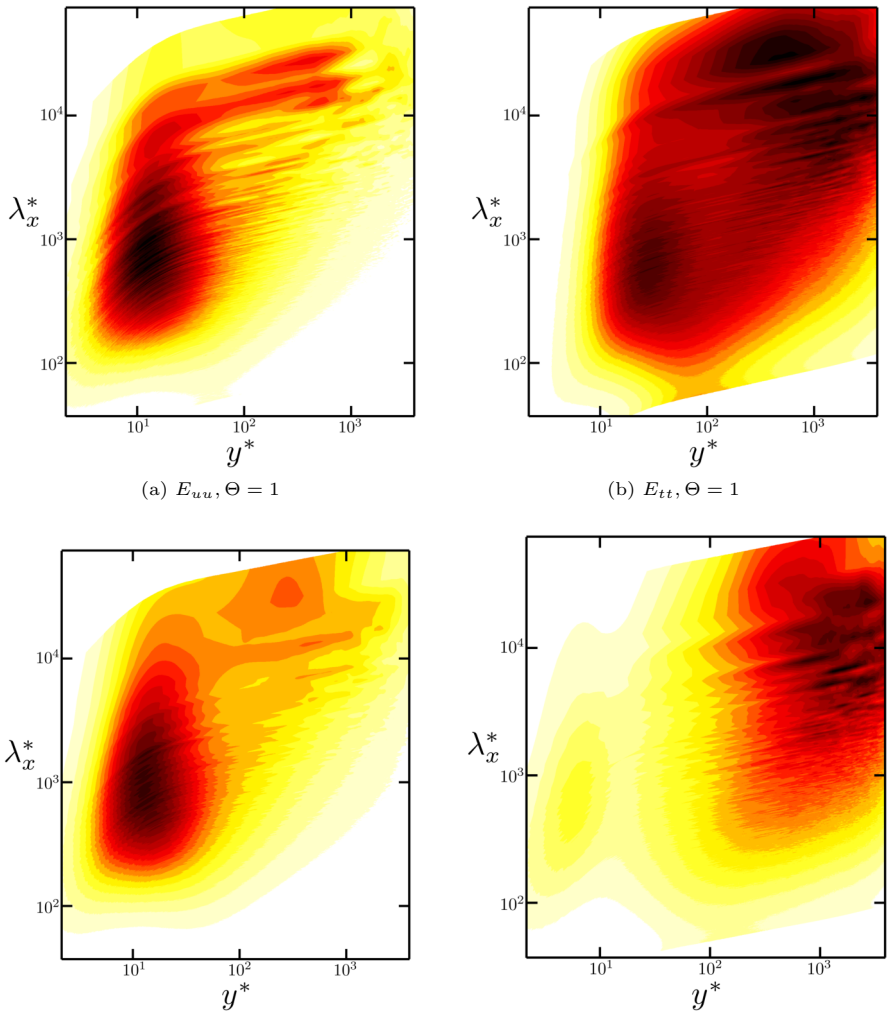

(a) $E_{uu}, \Theta = 1$ (b) $E_{tt}, \Theta = 1$

(c) $E_{uu}, \Theta = 0.25$ (d) $E_{tt}, \Theta = 0.25$

Figure 3: Wall-normal distribution of premultiplied velocity (left) and temperature (right) streamwise spectra at $Re_\tau \approx 5500$ for adiabatic (top) and cold (bottom) wall conditions.

WORKSHOP
Direct and Large-Eddy Simulation 14
April 10-12 2024, Erlangen, Germany

CONJUGATE HEAT TRANSFER IN CHANNEL FLOWS UP TO PRANDTL NUMBER 5

G. Cartland-Glover[1], **S. Rolfo**[1]
[1] Daresbury Laboratory
Science and Technology Facilities Council, UK Research and Innovation, United Kingdom
greg.glover@stfc.ac.uk

INTRODUCTION

Earlier studies on the conjugate heat transfer occurring in Target Station 2 of the ISIS Neutron and Muon Source at Rutherford Appleton Laboratory of the Science and Technology Facilities Council have indicated that thermal striping and low frequency oscillations may contribute to thermal stresses in the target station [1, 2]. The thermal stresses along-side phenomena such as pulsed heating, pressure waves, erosion, cavitation, radiolysis, radiation and material damage may cause the release of spallation products into the cooling water from the tantalum cladding of the target [1, 5]. The presence of spallation products in the cooling water is one of the key indicators of when the target should be replaced [5]. Apart from the current version of the target, all previous versions have had a shorter than desired operational lifespan [5].

We are concerned that the resolution of meshes we have used to simulate the cooling channels of Target Station 2 do not capture the turbulence fluctuations in the near-wall region [1, 2]. Therefore, as the size of the mesh could become significantly larger, i.e. up to ∼5B for each channel plus the solid, we are using canonical channel flow simulations to determine the required resolution. Flageul *et al.* [3] and Li *et al.* [7] based their configuration on the direct numerical database of heated channel flow of Kawamura *et al.* [6]. However, Flageul *et al.* [3] and Li *et al.* [7] studied fluids at Prandtl numbers of 0.71 and 1, while the cooling fluid in Target Station 2 has a Prandtl number of around 5.

NUMERICAL MODELS

Conjugate heat transfer was modelled using version 7 and 8 of *Code_Saturne* [4]. The flow is assumed incompressible and turbulent with Re_τ =395.0 with the application of four Prandtl numbers 0.71, 1.0, 2.0 and 5.0, which correspond to the cases in the DNS database reported by [6]. Wall-resolved Large Eddy Simulations were applied using the Smagorinsky sub-grid scale where the coefficient is 0.065.

The geometry modelled is consistent with [3] and [7], which is a channel flow of length 2π, height $2h$ (h is the half-height of the channel) and width of π (see Figure 1). The height of the walls above and below the channel, δ, was set as 3/8 [3].

Two materials were considered in resolving the heat transfer through the solid. These were stainless steel and treating the solid properties the same as the fluid. The solid properties were controlled through three related parameters, the ratios of fluid-solid thermal diffusivity, $G = \alpha_f/\alpha_s$, solid-fluid thermal conductivity, $G = k_s/k_f$ and the fluid-solid thermal effusivity, $K = 1/(G_2\sqrt{G})$. For the case where the solid properties were the same as the fluid, the value of the parameters were set to 1, while for stainless steel they were estimated from the Prandtl numbers of air and from water at different temperatures and pressures. The values of G, G_2 and K for all Prandtl numbers considered are given in Table 1.

Three mesh resolutions are detailed in Table 2, the wall normal distance of the first cell either side of the interface between the wall and the fluid was calculated according to the ratio $1/(RePr)$ with a hyperbolic tangent distribution of cell sizes. The remaining directions were specified with a uniform cell size distribution. The convergence of the averaged flow variables is assessed by checking that the change in the integral area of the variable profile (mean and variance of velocity and the scalar temperatures) is consistently below 1%.

RESULTS & DISCUSSION

The results presented here are the temperature scalar and its fluctuation for the coarse case in Figure 2 and 3, with initial calculations for the fine mesh presented in Figure 2. We will present further results at the conference.

The contours in Figure 2 depict cell values of the instantaneous, raw temperature scalar at $Pr = 5.0$ with stainless steel as the solid. Comparing the two images, we can clearly see that the fine mesh is capable of the capturing the smaller turbulent structures while the coarse mesh does not.

Figure 3 depicts the spatially and temporally averaged fluctuations of the thermal scalars in the near-wall region. The profiles on both sides of the fluid-solid interface are shown with the value at the interface determined by the gradient of the profile on either side of the interface. Note that for the case where the solid was treated as stainless steel and $Pr = 0.71$, a negative number was produced for the fluid side, therefore the value for the solid at the interface was used in the profile. On the solid side (left) the profiles are linear for both solid materials considered. On the fluid side (right), the profiles are linear up to $y^+ = 5$ for the case where the fluid and solid have the same properties, while the stainless steel profiles follow the DNS curves of Kawamura *et al.* [6]. Note that the temperature fluctuation deviates from the DNS solution at the interface with the value at the wall changes from ∼0.002 to just above 1 as Prandtl number increases. Therefore, for stainless steel, the higher the Prandtl number, the greater the fluctuation temperature. This could therefore impact on the

thermal stresses in target; however, this requires further investigation as the target materials (tungsten and tantalum) have smaller specific heat capacities and larger thermal conductivities than stainless steel giving smaller values of K and G while G_2 are larger.

REFERENCES

[1]G. Cartland-Glover, S. Rolfo, D. R. Emerson, D. Wilcox, D. Blanco-Lopez, L. G. Jones, D. M. Jenkins and S. Jago : Application of LES to the thermal-hydraulics of target station 2 of the ISIS Muon and Neutron Source, *Proc. of Direct and Large-Eddy Simulations 13, October 26-28, Udine, Italy*, (2022).

[2]G. Cartland-Glover, J. Gould, S. Rolfo, S. Jago, D. M. Jenkins, L.G. Jones, S. Gallimore, D. R. Emerson : Large Eddy Simulations of the cooling channels of ISIS Target Station 2, *8th High Power Targetry Workshop, November 6-10, Tokyo, Japan*, (2023).

[3]Flageul, C., Tiselj, I., Behamadouche, S. and Ferrand, M. : A correlation for the discontinuity of the temperature variance dissipation rate at the fluid-solid interface in Turbulent Channel Flows, *Flow, Turbul. Combust.*, **103**, 175–201 (2019).

[4]Fournier, Y., Bonelle, J., Moulinec, C., Shang, Z., Sunderland, A., and Uribe, J. : Optimizing Code_Saturne computations on petascale systems, *Comput. Fluids*, **45**, 103–108, (2011).

[5]L. G. Jones : ISIS Target Station 2 Update on Target Evolution, *8th High Power Targetry Workshop, November 6-10, Tokyo, Japan*, (2023).

[6]Kawamura, H., Ohsaka, K., Abe, H. and Kiyoshi Yamamoto, K. : DNS of turbulent heat transfer in channel flow with low to medium–high Prandtl number fluid, *International Journal of Heat and Fluid Flow*, **19**, 482–491 (1998).

[7]Li, Y., Ries, F., Nishad, K. and Sadiki, A. : Predictions of conjugate heat transfer in turbulent channel flow using advanced wall-modeled large eddy simulation techniques, *Entropy.* **23**, 725 (2021).

Pr	G	G_2	K
0.71	5.916	571.65	0.0007
1.00	0.047	21.94	0.2108
2.00	0.044	22.32	0.2133
5.00	0.040	24.21	0.2072

Table 1: Summary of the ratios to determine the properties of the solid for stainless steel.

Mesh	Coarse	Medium	Fine
N_x	128	256	512
$N_{y,fluid}$	64	128	256
$N_{y,solid}$	32	64	128
N_z	96	192	384
N_{fluid} (Millions)	0.8	6.3	50.3
N_{total} (Millions)	1.6	12.6	100.7

Table 2: Summary of computational meshes considered at $Re_{\delta_s} = 395$, $Re_\alpha = 1.4{\times}10^4$.

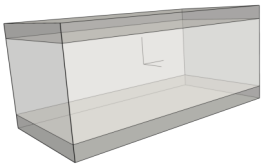

Figure 1: Geometry of the channel flow with conjugate heat transfer.

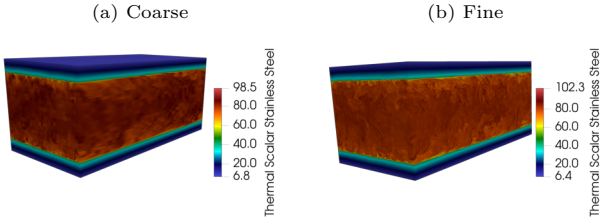

Figure 2: Contours of the instantaneous temperature scalar, where the solid is stainless steel at $Pr = 5.0$ for the coarse and fine mesh resolutions.

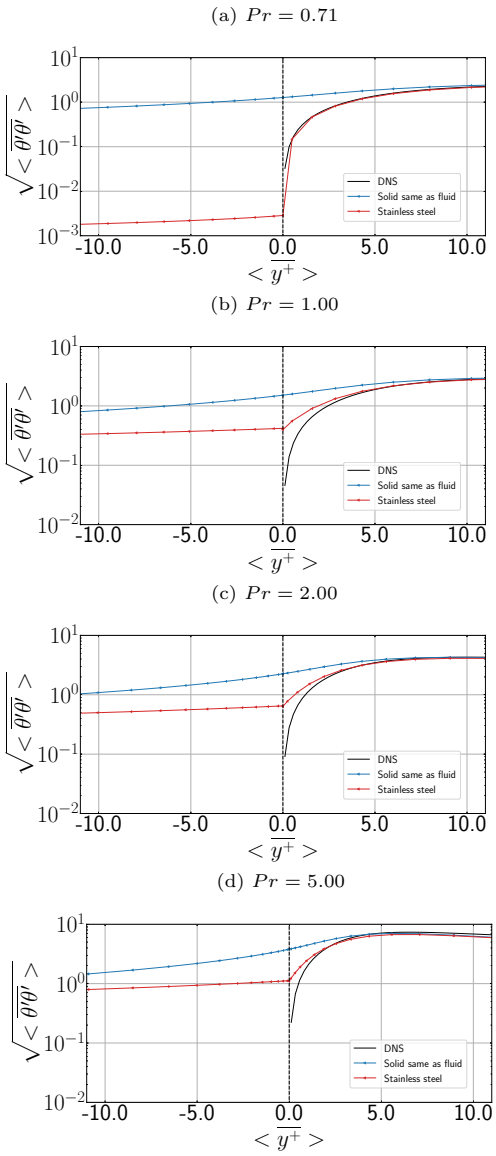

Figure 3: Profile of the fluctuations of the temperature scalar in the region of the solid-fluid interface at different Prandtl number.

SESSION: Bluff bodies

Thursday, April 11, 2024

11:20- 12:50

WORKSHOP
Direct and Large-Eddy Simulation 14
April 10-12 2024, Erlangen, Germany

EFFICIENT EULER-LAGRANGE LES OF AGGLOMERATE-LADEN FLOW IN A T-JUNCTION INCLUDING AN ANN-BASED COLLISIONAL BREAKAGE MODEL

A. Khalifa and M. Breuer
Professur für Strömungsmechanik
Helmut-Schmidt-Universität Hamburg, Germany
khalifa@hsu-hh.de, breuer@hsu-hh.de

INTRODUCTION

Turbulent flows that transport solid particles and agglomerates are of significance in various environmental (e.g., air pollution) and industrial (e.g., dry powder inhalers) applications. Particularly in dense flow systems, particle collisions drive particle dynamics and dictate the evolution of the particle size through agglomeration and breakup. Investigating such flows using particle-resolving direct numerical simulation and discrete element method (DNS-DEM) strategies is prohibitively expensive due to the wide spectrum of length and time scales that come into play. Recently, there has been a surge in employing multiscale data-driven modeling strategies to bridge the gap between expensive, direct methods and more cost-effective but less detailed approaches. By harnessing machine learning and high-resolution data, surrogate models for the description of certain physical phenomena can be developed to offer reliable predictions at manageable costs. This study demonstrates the effectiveness of an eddy-resolving multiscale Euler-Lagrange approach in forecasting particle-laden flows (e.g., the flow through a T-junction) applying a novel data-driven agglomerate collision model.

APPLIED METHODOLOGY

The prediction of the continuous phase is conducted within the Eulerian frame of reference utilizing the large-eddy simulation (LES) technique. The code employs the finite-volume method for block-structured grids as detailed in [1]. Additionally, an efficient Lagrangian tracking scheme is applied, enabling the deterministic identification of inter-particle collisions [2]. Collisions between individual primary particles are described based on an extended hard-sphere model that accounts for agglomeration. Furthermore, the method takes the effect of subgrid-scale motions on the particles into consideration. To enable cost-effective computations, agglomerates are tracked as spherical particles, which simplifies the detailed structures of agglomerates into single spheres with effective diameters. Consequently, the internal contact forces between the constituent particles within an agglomerate are not available. This limitation requires additional models to predict agglomerate breakage. Addressing this issue, efforts have been dedicated to develop models that describe deagglomeration due to fluid-induced stresses [3, 4], wall impacts [5, 6], and collisions [7]. All these models have been integrated into the described simulation methodology.

ANN-BASED AGGLOMERATE COLLISION MODEL

A data-driven modeling strategy is pursued to devise a model for predicting the outcome of collisions between agglomerates [7]. First, an extensive dataset of approximately 132,000 independent DEM simulations is generated, exploring a wide range of binary inter-agglomerate collision scenarios in a vacuum. The aim is to describe the collision-induced change in the number of particles and velocities of the collision partners in the absence of other external effects such as fluid flow.

For these DEM simulations, agglomerates composed of spherical, equally-sized, dry, and cohesive silica particles are prepared. Three primary particle sizes are individually considered to examine the influence of cohesion. Within each size category, 54 possible size combinations of collision partners are explored, consisting of a single primary particle as the smallest partner and 2000 particles as the largest partner. Additionally, both central and oblique collision cases are taken into account. Impact velocities are varied, typically comprising 41 different values, leading to diverse outcomes ranging from agglomeration to complete disintegration of both collision partners. To account for the heterogeneous nature of agglomerate structures, each collision event is repeated five times while adjusting the location of the collision point on the outer surface of one of the collision partners. The general setup of the DEM simulations carried out for generating the collision database is depicted in Fig. 1.

The analysis of the DEM results focuses on four key variables: The number of primary particles in the resulting fragments, and the three components of the post-collision velocity vector of each individual fragment. These values were directly used to train two feed-forward artificial neural networks (ANNs). The first ANN predicts the number of particles in each fragment, while the second network determines the post-collision velocity vector for each fragment. The division into two separate networks proves advantageous, as it allows for the customization of network settings to best align with the nature of the predicted outcome, i.e., the number of particles versus the velocity vector of the resulting fragments.

FLOW IN THE T-JUNCTION AND SOME RESULTS

The T-junction (see Fig. 2) consists of two square ducts that intersect at right angles, sharing the same hydraulic diameter of $D = 2$ mm. The horizontal ducts serve as the inlet on both ends, while the outlet is at the end of the vertical duct. The bulk velocity U_b is adjusted to achieve a Reynolds

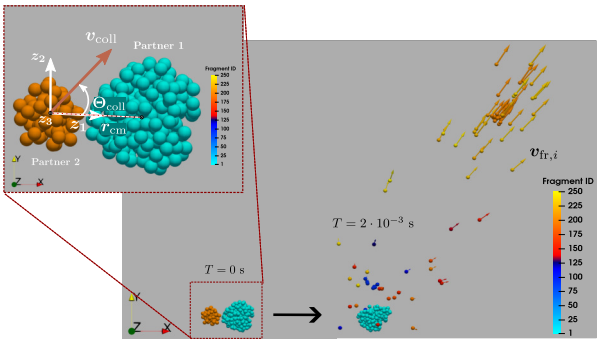

Figure 1: General setup of the DEM collision simulations [7].

number of Re = 8000 at which the flow is turbulent. At the junction, the merging of the two flow streams results in flow mixing and agglomerate collisions. Thus, the setup is particularly suitable for investigating breakage caused by collisions.

A statistically fully developed turbulent flow is assumed at both inlets, with three-dimensional inflow data obtained by supplementary straight duct simulations. A convective boundary condition is applied at the T-junction outlet. Additionally, no-slip and impermeability conditions are imposed on the solid smooth walls of the computational domain. The block-structured Cartesian grid is clustered towards the T-junction walls and the mixing region. It consists of approximately 8.5 million control volumes and fulfills the requirements of a wall-resolved large-eddy simulation.

The simulation starts with the initiation of the unladen fluid flow, continuing until a statistically steady state is reached. Subsequently, agglomerates comprising 500 silica primary particle are randomly released in two planes close to the inlets. Two powders, denoted **A** and **C**, differ only in the size of their primary particles ($d_p^A = 0.97$ μm, $d_p^C = 5.08$ μm), are investigated. The number and release frequency of agglomerates on each side of the junction are adjusted to achieve a total mass-flow rate of 0.1 mg/s.

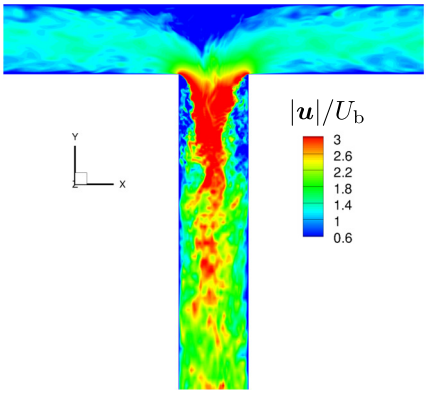

Figure 2: Snapshot of the instantaneous velocity magnitude in the T-junction.

A snapshot of the instantaneous flow field is depicted in Fig. 2. A detailed description of the turbulent flow including the Reynolds stresses will be provided in the paper. Here the focus is on the particulate phase.

The mass fractions of primary particles (FPP) determined at the T-junction outlet indicate a nearly complete deagglomeration for both powders (see Table 1). Powders **A** and **C** exhibit FPP values of 99.89% and 99.96%, respectively.

Table 1 also provides a comparison of the percentage contributions of the most important mechanisms responsible for agglomerate breakage of both powders. Remarkably, collision-induced breakage emerges as the predominant mechanism, accounting for 98.98% of the breakage events in the case of powder **C**. In contrast, other mechanisms like drag, rotary and turbulent stresses, as well as wall impacts, play marginal roles. These statistics are closely linked to the flow dynamics within the T-junction, where agglomerates released close to the inlets in a certain distance to the walls collide in the intersection zones before encountering regions of elevated fluid stresses such as the shear layers. Consequently, for the less breakage-resistant agglomerates of powder **C**, alternative deagglomeration mechanisms have a limited effect.

For powder **A**, collision-induced breakage remains dominant, but the contribution of the drag stress increases to 18% due to its greater resistance to breakage compared to powder **C**. Consequently, larger fragments persist after agglomerate-agglomerate collisions, and subsequent breakage is triggered by the drag force resulting from abrupt velocity changes due to the collisions.

Table 1: Summary of the most important breakage results.

Powder	Drag stress [%]	Collisions [%]	FPP [%]
A	18.12	81.03	99.89
C	0.945	98.98	99.96

The simulation for the case of powder **A** required approximately 72 hours of wall-clock time on 117 cores to simulate 12 dimensionless time units. Notably, the routine responsible for handling the collisions accounted for only about 5% of the CPU-time consumption, indicating its efficiency. Therefore, the proposed modeling strategy is especially beneficial for complex real-world flow scenarios involving millions of particles related to high mass loadings.

REFERENCES

[1] Breuer, M. A challenging test case for large–eddy simulation: High Reynolds number circular cylinder flow. *Int. J. Heat Fluid Flow* **21** (5), 648–654 (2000).

[2] Breuer, M. and Alletto, M. Efficient simulation of particle–laden turbulent flows with high mass loadings using LES. *Int. J. Heat Fluid Flow* **35**, 2–12 (2012).

[3] Breuer, M. and Khalifa, A. Revisiting and improving models for the breakup of compact dry powder agglomerates in turbulent flows within EulerianLagrangian simulations. *Powder Technology* **348**, 105–125 (2019).

[4] Breuer, M. and Khalifa, A. Refinement of breakup models for compact powder agglomerates exposed to turbulent flows considering relevant time scales. *Computers & Fluids* **194**, 104315 (2019).

[5] Khalifa, A. and Breuer, M. Data-driven model for the breakage of dry monodisperse agglomerates by wall impact applicable for multiphase flow simulations, *Powder Technology* **376**, 241–253 (2020).

[6] Khalifa, A., Breuer, M. and J. Gollwitzer Neural–network based approach for modeling wall–impact breakage of agglomerates in particle–laden flows applied in Euler–Lagrange LES, *Int. J. Heat Fluid Flow* **94**, 108897 (2022).

[7] Khalifa, A. and Breuer, M. Data-driven model for the outcome of binary agglomerate collisions including breakage and agglomeration based on artificial neural networks, *Chemical Engineering Research Design* **95**, 14–27 (2023).

WORKSHOP
Direct and Large-Eddy Simulation 14
April 10-12 2024, Erlangen, Germany

DNS AND LES SIMULATIONS OF THE FLOW OVER PERIODIC HILLS WITH A REMESHED VORTEX METHOD

Marthe de Crouy-Chanel[1], Chloé Mimeau[1], Iraj Mortazavi[1], Alessandro Mariotti[2] and Maria Vittoria Salvetti[2]
[1] Laboratoire M2N, Conservatoire National des Arts et Métiers, 2 rue Conté, 75003 Paris, France
[2] Dipartimento di Ingegneria Civile e Industriale, Università di Pisa, Largo Lucio Lazzarino 2, 56122 Pisa, Italia
marthe.de-crouy-chanel@lecnam.net

INTRODUCTION

Remeshed Vortex Methods (RVM) [1] are semi-Lagrangian approaches that address the Navier-Stokes equations in their vorticity-velocity formulation. The advection of the vorticity field is solved by discretizing the vorticity on numerical particles following the flow's dynamics. Subsequently, these particles are remeshed on an underlying Cartesian grid, allowing the incorporation of Eulerian methods in what was originally a Lagrangian approach.

These methods have proven to be stable and less dissipative alternatives to more traditional Eulerian methods. These characteristics make them well-suited for Large Eddy Simulation (LES) of turbulent flows. Particularly, the Variational Multiscale (VMS) [2] variant of the Smagorinsky model and the Spectral Vanishing Viscosity (SVV) [3] approach emerge as the most suitable for the present context, as they introduce diffusion only to the smallest scales of vorticity. The SVV approach is highly cost-effective due to its natural integration in the Spectral part of the present code. When tested on periodic isotropic homogeneous cases, both models demonstrated the absence of a need for coefficient adjustments when altering the Reynolds number or simulation resolution.

This study investigates the performance of these models in a more complex test case, i.e. the channel flow with periodic hills [5].

REMESHED VORTEX METHODS

Vortex methods are Lagrangian techniques, founded on the vorticity($\boldsymbol{\omega}$)-velocity($\mathbf{u}$) formulation of the incompressible Navier-Stokes equations:

$$\partial_t \boldsymbol{\omega} + (\mathbf{u}\cdot\nabla)\boldsymbol{\omega} - (\boldsymbol{\omega}\cdot\nabla)\mathbf{u} = \frac{1}{Re}\Delta\boldsymbol{\omega}\ ; \quad \Delta\mathbf{u} = -\nabla\times\boldsymbol{\omega}, \quad (1)$$

where $\boldsymbol{\omega} = \nabla\times\mathbf{u}$ and where $(\mathbf{u}\cdot\nabla)\boldsymbol{\omega}$ and $(\boldsymbol{\omega}\cdot\nabla)\mathbf{u}$ denote the advection and stretching terms, respectively. The Poisson equation $\Delta\mathbf{u} = -\nabla\times\boldsymbol{\omega}$ allows to recover the velocity field $\mathbf{u}$ from the vorticity field $\boldsymbol{\omega}$. The vorticity field is discretized on a set of numerical particles with position $\mathbf{x}_p$ and the solution of the governing equations is based on a fractional step algorithm. A single time step of this algorithm is decomposed as follows: initially, the particles carrying the vorticity field are convected in a Lagrangian manner. Subsequently, to prevent distortion of the vorticity field, the vorticity $\boldsymbol{\omega}_p$ associated with each particle p is distributed among the neighboring points of an underlying Cartesian mesh. At this point, the entire vorticity field has been redistributed on the mesh, and the stretching and diffusion terms, and Poisson equation are then solved on the grid using Eulerian schemes.

SUBGRID-SCALE MODELING

The filtered Navier-Stokes equations in their velocity-vorticity formulation can be expressed as:

$$\frac{\partial\bar{\boldsymbol{\omega}}}{\partial t} + \nabla\cdot(\bar{\boldsymbol{\omega}}\otimes\bar{\mathbf{u}} - \bar{\mathbf{u}}\otimes\bar{\boldsymbol{\omega}}) = \frac{1}{Re}\Delta\bar{\mathbf{u}} - \nabla\cdot\mathbf{R} \quad (2)$$

with $\bar{\boldsymbol{\omega}}$ and $\bar{\mathbf{u}}$ being the resolved (filtered) velocity and vorticity fields, respectively. Additionally, the term

$$\mathbf{R} = (\overline{\boldsymbol{\omega}\otimes\mathbf{u}} - \bar{\boldsymbol{\omega}}\otimes\bar{\mathbf{u}}) - (\overline{\mathbf{u}\otimes\boldsymbol{\omega}} - \bar{\mathbf{u}}\otimes\bar{\boldsymbol{\omega}}) \quad (3)$$

represents the subgrid-scale vorticity stress to be modeled.

Variational multiscale (VMS) models aim to mitigate the excessive dissipation of the largest scales present in classical artificial viscosity models by selectively applying artificial viscosity solely to the smallest of the resolved scales. This necessitates an additional explicit small-scale filtering. In the current approach, the eddy viscosity is computed across the entire range of scales in the velocity fields. The VMS-Smagorinsky model in vorticity-velocity writes

$$\mathbf{R}_{SGS} = \nu_{SGS}(\nabla\overline{\boldsymbol{\omega}}_S - (\nabla\overline{\boldsymbol{\omega}}_S)^T) \quad (4)$$

with $\nu_{SGS} = (C_S\Delta)^2|\overline{\mathbf{S}}|$ and where $\overline{\boldsymbol{\omega}}_S$ denotes the small scales of the resolved vorticity field. Furthermore, we explored Spectral Vanishing Viscosity (SVV) approaches, which serve as a form of regularization for spectral methods. This involves gradually introducing viscosity into the high-frequency end of the spectrum, where non-physical oscillations might arise. From a computational standpoint, SVV is seamlessly incorporated as a modified diffusion operator in the Fourier component of our solver, rendering it a more cost-effective alternative to traditional Large Eddy Simulation (LES) models.

PRELIMINARY UNCERTAINTY QUANTIFICATION STUDY

The models were first tested on the Taylor-Green Vortex (TGV) at $Re = 5000$ on a LES grid of resolution 96^3. To assess the sensitivity of both models to their parameters (specifically, the model coefficient and explicit filter order), we conducted

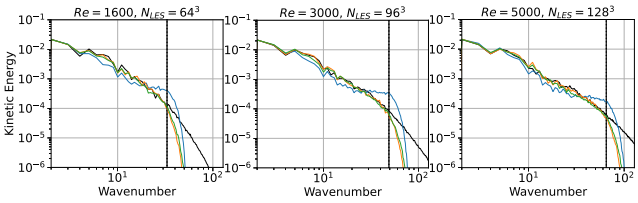

Figure 1: Kinetic energy spectrum at $t = 8.5$ for different configurations of the TGV test case, obtained with the optimal set of coefficients (blue - no model, green - VMS-Smag, orange - SVV, black - DNS).

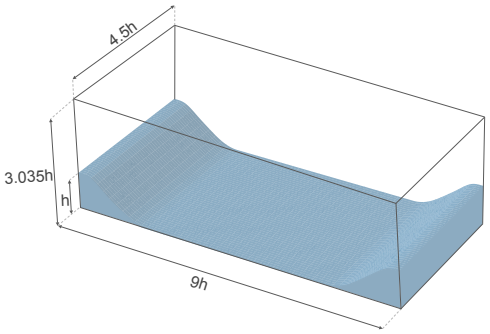

Figure 2: Periodic hills test case configuration

an uncertainty quantification analysis for both approaches, using the Polynomial Chaos Expansion (PCE) as a surrogate model [4]. PCE represents the model outputs as a combination of orthogonal polynomials depending on the model's parameters. This approach enabled us to evaluate the impact of parameter uncertainty on simulation results using a minimal number of simulations.

The study also aimed to identify regions of optimal coefficients, which were subsequently applied to different Reynolds numbers and grid resolutions, as well as on a new test case, the decay of Homogeneous Isotropic Turbulence (HIT), demonstrating the robustness of the models (refer to Figure 1 showing the results of LES with the VMS-Smagorinsky model and with SVV with the 'optimized' coefficients for different Reynolds numbers and resolutions of TGV).

THE PERIODIC HILLS TEST CASE

A test case involving walls is explored to assess the subgrid-scale models' capability. The configuration involves a channel flow over hills, following the classical setup introduced by [5] as depicted in Figure 2. This flow has been extensively studied in the literature through DNS, LES, and experimental investigations over various Reynolds numbers [6]. The domain size is $4.5h \times 3h \times 9h$, where h represents the height of the hills. Periodic boundary conditions are applied in the streamwise and spanwise directions. The flow undergoes perturbation with Gaussian noise, and a constant flow rate is enforced at the domain's entry. The wall treatment is implemented using a penalization method [7]. The Reynolds number is computed based on h and U_b, representing the bulk velocity at the crest of the hill.

Figures 3 and 4 show preliminary results from DNS with $Re = 2800$ and a resolution of $256 \times 192 \times 512$. Although the simulation at this resolution is not fully converged, it already exhibits promising outcomes. Further investigation will

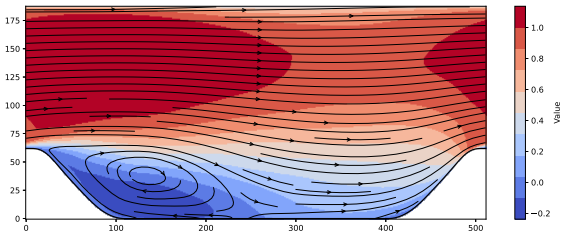

Figure 3: Time-averaged streamwise velocity field and streamlines for the periodic hills test case at $Re = 2800$.

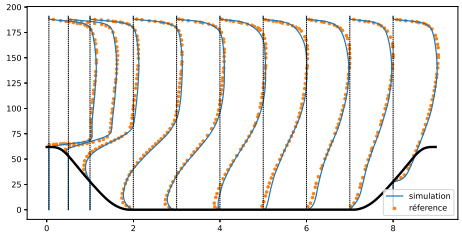

Figure 4: Comparison of time-averaged streamwise velocity profiles with reference [6] for the periodic hills test case at $Re = 2800$.

involve a higher Reynolds number of $Re = 10595$ to assess the performance of the presented turbulence models, alongside other classical models such as WALE.

REFERENCES

[1]G.-H. Cottet and P. Koumoutsakos, *Vortex Methods - theory and practice.*, Cambridge University Press, 2000.

[2]J.R.T. Hughes, L. Mazzei, A.A. Oberai and A.A. Wray, The multiscale formulation of large eddy simulation: Decay of homogeneous isotropic turbulence, *Physics of Fluids*, Vol. **13**, pp. 505–512, 2001.

[3]E.Tadmor, Convergence of Spectral Methods for Nonlinear Conservation Laws, *SIAM Journal on Numerical Analysis*, Vol. **26**, pp. 30–44, 1989.

[4]D. Xiu, G.E. Karniadakis, The Wiener–Askey Polynomial Chaos for Stochastic Differential Equations, *SIAM Journal on Scientific Computing*, Vol. **24**, pp. 619–644, 2002.

[5]C.P. Mellen, J. Fröhlich, W. Rodi, Large eddy simulation of the flow over periodic hills, *Proc. 16th IMACS World Congress*, 2000.

[6]M. Breuer, N. Peller, C. Rapp and M. Manhart, Flow over periodic hills – Numerical and experimental study in a wide range of Reynolds numbers, *Computers & Fluids*, Vol. **38**, pp. 433–457, 2009.

[7]C. Mimeau, F. Gallizio, G.-H. Cottet and I. Mortazavi, Vortex penalization method for bluff body flows, *International Journal for Numerical Methods in Fluids*, Vol. **79**, pp. 55–83, 2015.

WORKSHOP
Direct and Large-Eddy Simulation 14
April 10-12 2024, Erlangen, Germany

EFFECT OF INFLOW UNSTEADINESS ON ELONGATED RECTANGULAR CYLINDERS

A. Mariotti[1], G. Lunghi[1], M. Morello[1], S. Brusco[2], M.V. Salvetti[1]
[1]Department of Civil and Industrial Engineering, University of Pisa, Pisa, Italy
[2]Faculty of Engineering, Western University, London, Canada
alessandro.mariotti@unipi.it

INTRODUCTION

The present work investigates the unsteady high-Reynolds flow around two rectangular cylinders with a chord-to-depth ratio of 3:1 and 5:1. These flows can be considered as paradigmatic cases of practical interest in the field of wind engineering, such as tall buildings and bridge sections. The flow dynamics around the cylinder strongly depend on the chord-to-depth ratio. In both geometries, the shear layers separate at the upstream edges, rolling up to form vortical structures (Kelvin-Helmholtz instability). These structures are then convected downstream and eventually interact with other vortical structures forming from the separated shear layers. A mean-flow reattachment occurs on the lateral side of the 5:1 rectangular cylinder, resulting in a closed separated-flow region characterizing the mean flow. Further downstream, a second shear-layer separation at the trailing edge leads to Von Karman vortex shedding in the near wake. On the other hand, the 3:1 rectangular cylinder appears to be in an intermediate condition between flows with and without mean-flow reattachment. For these geometries, reattachment is not ensured for the entire duration of the vortex-shedding cycle. Figures 1a and 1b show the mean flow streamlines and a snapshot of the instantaneous vortex-indicator λ_2 from LES simulations conducted under constant inflow velocity at $Re = 40000$ (based on the freestream velocity, u_∞, and the cylinder depth, D) for the 3:1 and 5:1 rectangular cylinders.

Although the stationary flows around rectangular cylinders with various chord-to-depth ratios have been the subject of several studies (see, for instance, [1] for the 5:1 rectangular cylinder), only recently has attention been paid to unsteady inflow conditions. These non-constant flows can be due to intense and sudden thunderstorm phenomena, which can cause catastrophic damage to buildings, potentially resulting in significant economic and human losses. The accelerating flows cause a sudden variation in mean and fluctuating loads, affecting the flow dynamics and surface pressures [2]. The nature of flow modifications in unsteady flows was observed in [3] to depend on the chord-to-depth ratio and appears to be governed by the separated shear-layer response to changing flow conditions. These modifications induced by accelerated motion can affect the oscillating loads acting on the cylinder's lateral surface: the existence of constant-frequency time cells in the evolution of alternate vortex shedding around a square cylinder during accelerated motion was demonstrated in [4], and LES simulations are validated accordingly [5].

This research activity aims to further investigate the flow dynamics over elongated rectangular cylinders under unsteady inflow conditions representative of thunderstorm conditions. The focus is on exploring characteristic frequencies and their dependence on inflow acceleration intensity and the chord-to-depth ratio. The key questions include: (i) does the vortex shedding frequency exhibit a stepwise time behavior as observed for the square cylinder? (ii) Is the impact of these changes in vortex shedding frequency on the fluctuations of aerodynamic loads as significant as observed for the square cylinder? The second question arises due to the different topology of the mean flow on the cylinder surface. Finally, targeted studies will focus on shedding light on the evolution of topological features on the sides of the cylinders, as this significantly affects the near-wake and bulk quantities. Despite the simplicity of the geometries, this study may contribute to expanding our understanding of the dynamic loads on civil buildings caused by thunderstorm outflows.

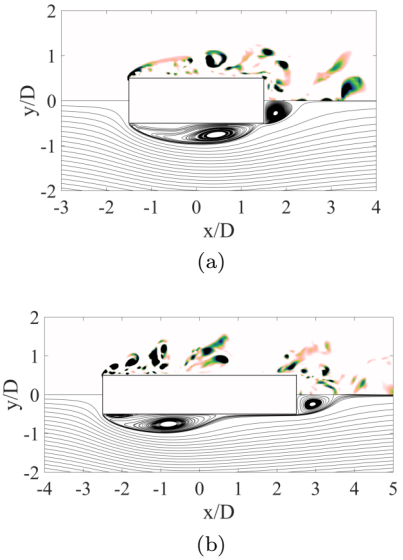

Figure 1: Instantaneous vortex-indicator λ_2 (top) and mean flow streamlines (bottom) at $Re = 40000$ for (a) the 3:1 and (b) the 5:1 rectangular cylinder.

NUMERICAL METHOD AND PROBLEM DEFINITION

The incompressible flow around a 3:1 and a 5:1 rectan-

gular cylinder at zero angles of attack is investigated herein. Large-Eddy Simulations (LES) are carried out by employing the open-source code Nek5000, based on a high-order spectral-element method. Each spectral element is rectangular or a suitable coordinate mapping of a rectangle. The basis functions inside the elements are Legendre polynomials of order N for velocity and $N-2$ for pressure in each direction; $N=6$ has been used in this work, as in [5]. A third-order backward finite-difference scheme based on the high-order splitting method is used for time advancing. The computational domains are sketched in Fig. 2. The cylinder center is located at $x/D = y/D = 0$, being D the width of the 3:1 or the 5:1 rectangular cylinder, and the computational domain spans the following dimensions $-75 \leq x/D \leq 125$, $-75 \leq y/D \leq 75$ and $0 \leq z/D \leq 5$.

A uniform unsteady velocity profile with no turbulence is imposed at the inlet, traction-free boundary conditions are used for the outflow and for the upper and lower boundaries of the domain, and no-slip is imposed at the body surface; periodicity boundary conditions are applied in the spanwise direction. The spectral element size and distribution are the same used in [5]. In particular, the element size in the streamwise and crossflow directions is $\Delta x/D = \Delta y/D = 0.125$ near the cylinder, while in the spanwise direction the element size is uniform $\Delta z/D = 0.558$ as done in [5]. A low-pass filter is applied to the velocity field in the modal space as in [5] because the grid resolution is not fine enough to resolve all turbulent scales at the considered Reynolds number. Since the filter introduces dissipation of the highest resolved modes only, this can be considered as a subgrid-scale dissipation.

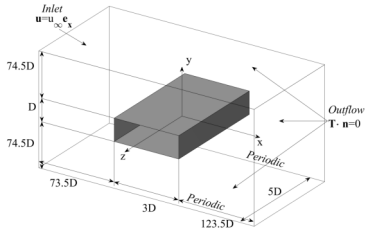

(a)

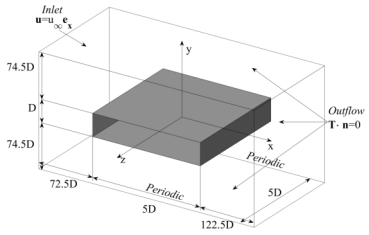

(b)

Figure 2: Sketch of the computational domains for the 3:1 and the 5:1 rectangular cylinder.

The time evolutions of the Reynolds number and the acceleration, normalized by the inflow instantaneous velocity, are depicted in Fig. 3. The reference case (black line) replicates the time histories analyzed experimentally in [4] and numerically in [5] around a square cylinder. It involves a Reynolds number varying from $Re = 17200$ to $Re = 65360$, with a maximum non-dimensional acceleration of $aD/u_\infty^2 = 0.0076$. Similar to the study on the square cylinder [5], the variations in the transients are investigated using time-frequency analysis. Additionally, different acceleration intensities are reproduced as part of a parametric study, aiming to mimic those induced by full-scale thunderstorm outflows.

The final presentation will focus on the impact of inflow-acceleration intensities on the 3:1 and 5:1 rectangular cylinders. We will discuss the mean and fluctuating force coefficients and wake frequencies under unsteady inflow conditions. As an illustrative result, the time behavior of the vortex shedding frequency for the 5:1 rectangular cylinder is shown in Fig. 4. This information holds significance in predicting potential aeroelastic phenomena arising from vortex shedding induced by the varying flow conditions typical of thunderstorm outflows.

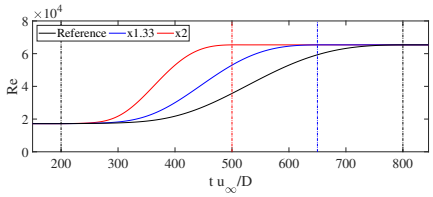

(a)

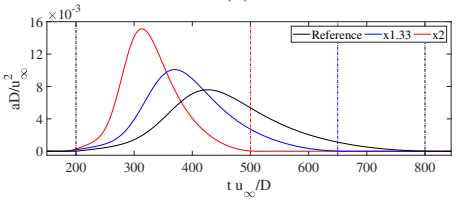

(b)

Figure 3: Time history of (a) the inflow Reynolds number and (b) the non-dimensional acceleration.

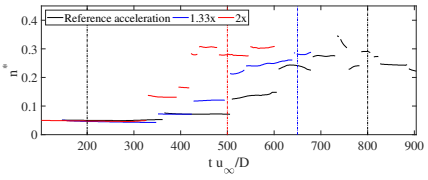

Figure 4: Time behavior of the vortex shedding frequency for the 5:1 rectangular cylinder.

REFERENCES

[1]Bruno, L., Salvetti, M.V. and Ricciardelli, F. : Benchmark on the aerodynamics of a rectangular 5:1 cylinder: and overview after the first four years of activity, *J. Wind Eng. Ind. Aerod.*, **126**, 87–106 (2014).

[2]Li, X., Li, S., Su, Y., Peng, L., Cao, S. and Liu, M. : Study on the time-varying extreme value characteristics of the transient loads on a 5:1 rectangular cylinder subjected to a thunderstorm-like wind, *J. Wind Eng. Ind. Aerod.*, **229**, 105161 (2022).

[3]Yang, T. and Mason, M. S. : Aerodynamic characteristics of rectangular cylinders in steady and accelerating wind flow, *J. Fluids Struct.*, **90**, 246–262 (2019).

[4]Brusco, S., Buresti, G., Lo, Y.-L., Piccardo, G. : Constant-frequency time cells in the vortex-shedding from a square cylinder in accelerating flows, *J. Wind Eng. Ind. Aerod.*, **230**, 105182 (2022).

[5]Mariotti, A., Brusco, S., Lunghi, G., Piccardo, G. and Salvetti, M.V. : Large-Eddy Simulations of the accelerating flow around a square cylinder, *Marchioli, C., Salvetti, M.V., Garcia-Villalba, M., Schlatter, P. (eds) Direct and Large Eddy Simulation XIII. ERCOFTAC Series*, **31** 23–28 (2024).

WORKSHOP
Direct and Large-Eddy Simulation 14
April 10-12 2024, Erlangen, Germany

THREE-DIMENSIONAL DIRECT NUMERICAL SIMULATIONS OF SHOCK-WAVE BOUNDARY LAYER INTERACTIONS FOR A COMPRESSION RAMP AND IMPINGING-REFLECTING SHOCK WAVE

Pushpender K. Sharma[1], Mariadebora Mauriello[2], Neil Sandham[1], Lionel Larchevêque[2]
[1]Aerodynamics and Flight Mechanics Research Group
University of Southampton, United Kingdom
[2] IUSTI Laboratory
Aix-Marseille University, France
p.k.sharma@soton.ac.uk

INTRODUCTION

Shock wave boundary layer interactions (SWBLI) can cause significant concerns when travelling in the trans-, super-, and hypersonic regimes, resulting in flow separation, unsteadiness, and transition to turbulence, which result in increased drag, high aerodynamic loads, and engine inlet performance losses, to name a few. Different configurations, such as impinging-reflecting or compression-ramp SWBLIs, can be used to study these effects. Pagella et al. [1] compared two-dimensional (2D) simulations for a compression ramp (CR) versus an impinging-reflecting (IR) shock wave at Mach=4.8. The pressure and skin-friction profiles showed good agreement between the two cases. They further investigated the linear growth regime using DNS with small-perturbation and linear stability theory and found that the growth of disturbances also showed a good agreement with each other. However, this 2D study omitted some important flow physics, so the present work aims to identify subtle but potentially important differences between the two flow configurations when non-linear breakdown to turbulence and low-frequency unsteadiness are present.

NUMERICAL METHODS AND NUMERICAL SETUP

The 3D Navier-Stokes equations are solved in conservative form. The `OpenSBLI` solver, which is an open-source finite-difference-based solver, is used on structured Cartesian (for shock-reflection setup) and curvilinear (for ramp setup) coordinates systems. Two sets of flux reconstruction schemes, i.e., WENO and TENO, are available to compute the inviscid fluxes. It is noted that the TENO scheme is less dissipative compared to the WENO scheme. The viscous fluxes are computed using the 4^{th} order central differences. 3^{rd} order Runge-Kutta scheme is used for time integration.

Figure 1(a) shows a 3D view of the IR SWBLI setup for flow at Mach 1.5 over a flat plate. The IR case has the following domain extents and the number of points in x-, y-, and z-directions: $0 \leq x \leq 375$, $0 \leq y \leq 140$, $0 \leq z \leq 27.32$, and (N_x, N_y, N_z) = (2050, 325, 200), respectively. The CR case setup (not shown here) is tested using two grids; one is an analytical grid based on log-cosh variation with control parameters to adjust the curvature of the corner and the top boundary, while the second grid is created using Pointwise software, but using the same bottom-wall streamwise profile as that of the analytical grid. In both analytical and Pointwise CR grids, the domain extents and the number of points in x-, y-, and z-directions are $0 \leq x \leq 375$, $0 \leq y \leq 158$, $0 \leq z \leq 27.32$, and (N_x, N_y, N_z) = (2050, 365, 200), respectively. All the distances are scaled with the displacement thickness $\delta_0^* = 7.5\times10^{-5}$ m at the inflow plane, which is initialized using a similarity solution for a unit Reynolds number of 10^{-7} m^{-1}. Hence, the simulation Reynolds number based on this δ_0^* is $Re_{\delta_0^*} = 750$. No-slip and isothermal boundary conditions are used at the wall, while the extrapolation method is used at the inflow (for pressure) and outflow, while the span is periodic.

Two sets of deterministic forcing are used to trigger flow transition based on Sansica et al. [2]. The first contains two opposite oblique modes with a single spanwise wavenumber but having two different frequencies with a very small difference between them, i.e., $e^{i(\beta z-\omega_1 t)}+e^{i(-\beta z-\omega_2 t)}$. The second case contains two parallel oblique modes, i.e., $e^{i(\beta z-\omega_1 t)} + e^{i(\beta z-\omega_2 t)}$. Here, $\beta = 0.23$ is the spanwise wavenumber, and $\omega_1 = 0.100$ and $\omega_2 = 0.104$, such that the difference frequency is $\Delta\omega$=0.004, which is chosen to excite the difference mode corresponding to the low-frequency unsteadiness/breathing of the separation bubble [2]. The wall pressure data is collected over a cycle of this difference frequency (i.e., $T = 2\pi/\Delta\omega$) to evaluate the frequency spectrum.

RESULTS AND DISCUSSION

Before finalizing the grids for 3D simulations, a detailed 2D laminar flow study was performed to check the wall-pressure variation and skin friction comparison among various cases. Figure 1(b) compares the wall-pressure variation of the 2D IR case (with the top shock generated using 2.5° wedge-angle) against the CR cases after the flow is fully developed. After initial tests, it was found out that to have a match, the corner of the ramp should be placed at $x = 154$, and the ramp angle to get the same pressure rise across the bubble should be 5.1° for the analytical grid while a slightly higher ramp angle of 5.2° is required for the Pointwise grid. The deviation noted towards the end of the domain for the IR case is due to the shock reflection from the top boundary hitting the wall and is not of concern as it doesn't affect the bubble region.

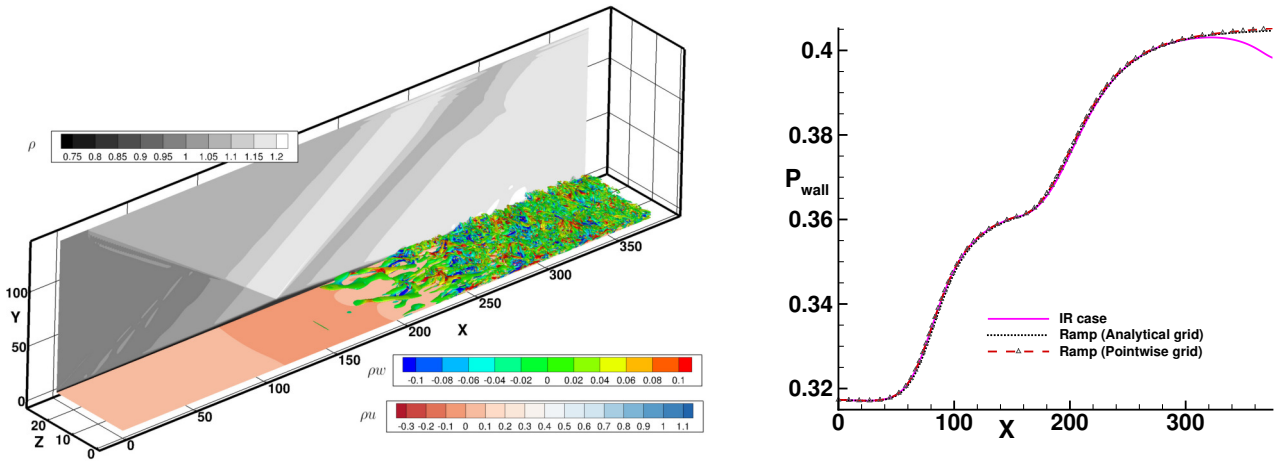

(a) (b)

Figure 1: (a) 3D view of IR flat-plate SWBLI, with Q-isosurfaces, and (b) wall-pressure comparison among three different cases showing good agreement over the separation bubble.

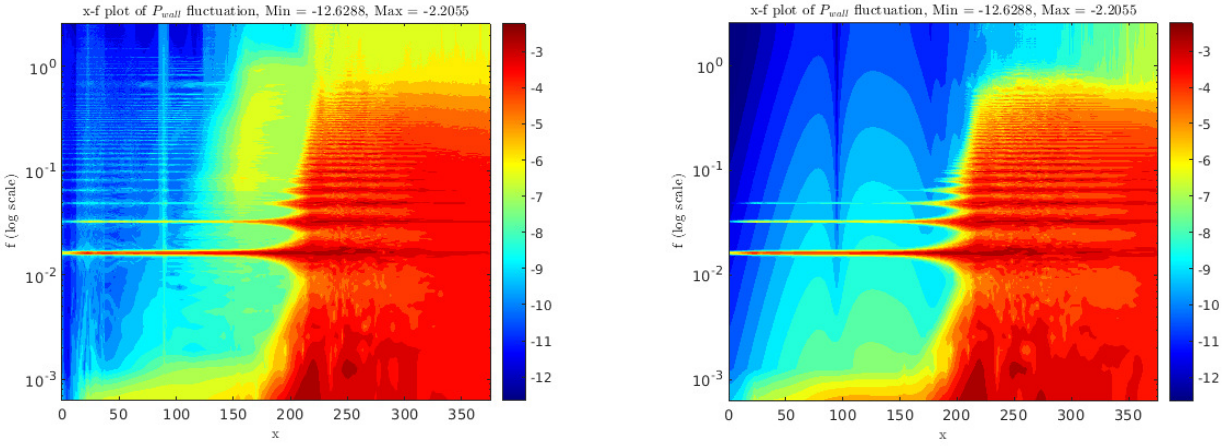

(a) (b)

Figure 2: Wall-pressure fluctuations spectrum (span-averaged) in x-f plane (frequency versus streamwise-distance) for (a) impinging-reflecting SWBLI, and (b) compression-ramp SWBLI.

Figure 2 shows a power spectrum comparison of wall-pressure functions for the 3D cases in the streamwise distance (x) versus frequency (f) plane, i.e., x-f plane, IR case on the left and CR case on the right. It is noted that the wall pressure data shows periodicity in the separation bubble region over a time period of the difference frequency (i.e., $T = 2\pi/\Delta\omega$). The two cases look similar in terms of the forcing frequency response, including the cascade of higher frequency scales, and the vortex shedding response at the reattachment point at $x \approx 210$. However, subtle differences can be noted in terms of the high-frequency patch between $150 \leq x \leq 200$ that is noted for the IR case, while this is missing for the CR case. The final detailed flow physics and comparisons of results for the other parallel-waves cases will be presented at the conference. Also, we will show more results with respect to the non-linear analysis ([3]) for these cases during the conference.

CONCLUSIONS

We have noted that the CR cases produce more pronounced low-frequency content at the separation point and this is not dependent on the grid generation method. We also note that the IR case shows an intermediate frequency patch inside the bubble close to the inviscid shock-impingement location, while it is absent in the CR case.

REFERENCES

[1]Pagella, A., Babucke, A. and Rist, U. : Two-dimensional numerical investigations of small-amplitude disturbances in a boundary layer at Ma= 4.8: Compression corner versus impinging shock wave, *Phys. Fluids*, **16**, 2272–2281 (2004).

[2]Sansica, A., Sandham, N. D. and Hu, Z. : Instability and low-frequency unsteadiness in a shock-induced laminar separation bubble, *J. Fluid Mech.*, **798**, 5–26 (2016).

[3]Mauriello, M., Larchevêque, L. and Dupont, P. : Non-linearities in transitional shock wave/boundary layer interactions, *Proc. of 12th International Symposium on Turbulence and Shear Flow Phenomena, July 19-22, Osaka, Japan*, (2022).

WORKSHOP
Direct and Large-Eddy Simulation 14
April 10-12 2024, Erlangen, Germany

DNS, LES AND EXPERIMENTAL ANALYSIS OF THE FLOW AROUND A 5:1 RECTANGULAR CYLINDER AT MODERATE REYNOLDS NUMBER

M.V. Salvetti[1], G. Lunghi[1], A. Mariotti[1], R. Corsini[2], A. Cimarelli[2], E. Stalio[2]
[1]DICI, University of Pisa, Pisa, Italy
[2]DIEF, University of Modena and Reggio Emilia, Modena, Italy
maria.vittoria.salvetti@unipi.it

INTRODUCTION

Elongated rectangular cylinders of infinite span are simplified geometries relevant for real civil structures, e.g., tall buildings and bridge decks. In particular, the flow around the 5:1 rectangular is the object of the international Benchmark on the Aerodynamic of a Rectangular 5:1 Cylinder (BARC), which is a blind benchmark, i.e., with no *a priori* selected reference measurements. The flow is characterized by shear-layer separation at the upstream edges, followed by the roll up of these layers in which vortical structures form (Kelvin-Helmholtz instability), and their subsequent convection downstream and interaction with other vortical structures. A second separation occurs at the cylinder rear edges with the classical Von Karman vortex shedding in the near wake (Fig. 1 bottom). The mean flow topology is characterized by a closed separated region on the cylinder lateral side with flow reattachment occurring downstream (Fig. 1 top).

From the various contributions to the BARC benchmark, a significant dispersion emerged in the mean-flow topology aside the cylinder; that, in turn, translates in high discrepancies in some quantities of interest, as, for instance, the distribution of mean and fluctuating pressure on the cylinder side [1]. Experiments carried out in different facilities are available in the literature [1, 2, 3]. These experiments are carried out at Reynolds numbers, based on the cylinder depth, D, and on the freestream velocity, ranging from 20000 to 110000. On the other hand, Direct Numerical Simulations (DNS) were carried out at $Re = 3000$ [4, 5] and more recently at $Re = 8000$ and 14000 [6].

We compare, herein, for the first time, DNS and experimental results at the same Reynolds number, i.e., $Re = 14000$. This provides cross-validation and can highlight the effects of differences in the setup, as, e.g., of the freestream turbulence present in the experiments. Furthermore, experimental and DNS data will be used to asses the accuracy and reliability of large-eddy simulations with varying setup.

EXPERIMENTAL SETUP AND METHODOLOGY

The experimental campaign is carried out in a closed-return subsonic wind tunnel, characterized by a circular open test section 1.1 m in diameter and 1.42 m in length, and 0.9% freestream turbulence level. The 5:1 aluminium-alloy hollow model is 200 × 40 × 800 mm in the streamwise, crossflow and spanwise directions, respectively. Two end plates are located at the spanwise ends ($z/D = \pm 10$) to mitigate three-dimensional effects. The model is equipped with 540 pressure taps, 72 of which on the spanwise centreline $z/D = 0$. Experiments are carried out at a Reynolds number based on the free-stream velocity and the cylinder thickness equal to 14000.

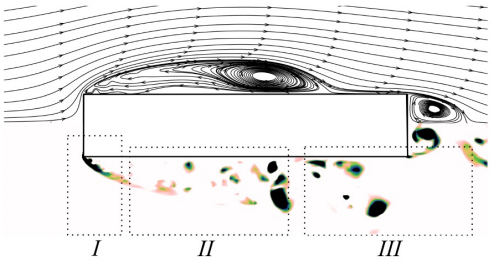

Figure 1: Qualitative behavior of the BARC flow. Top part: mean streamlines; bottom part: instantaneous vorticity.

Differential pressures are measured through two Pressure Systems ESP-16HD miniature electronic pressure scanners, directly housed inside the model. Velocity measurements are obtained by using an IFA AN 1003 A.A. Lab System hot-wire anemometry module with Dantec 55P11 probes, which can be moved in all directions with an accuracy of 0.1 mm. For each realization, the sampling frequency is set to 16000 Hz and the acquisition time is 32.768 seconds. The manufacturing curvature radius of the upstream edges is evaluated by using the digital microscope RS PRO.

DIRECT NUMERICAL SIMULATION SET-UP

The numerical simulation of the turbulent flow around the $5:1$ rectangular cylinder has been performed with the open-source code Nek5000. This solver is based on a high-order spectral element method where, within each element, the velocity components and the pressure are expanded in terms of tensor product of Legendre polynomials of order N and $N-2$, respectively. For the present DNS, the polynomial order is $N = 7$. Time integration is carried out by a second-order backward differentiation scheme combined with a second-order extrapolation scheme for the treatment of the nonlinear term. The non-dimensional time step is kept fixed at $\Delta t = 2.6 \cdot 10^{-4}$ during the simulation to fulfill CFL < 0.5 in each point of the domain.

Concerning the boundary conditions, a constant streamwise velocity profile is imposed at the inflow (no turbulence), homogeneous Dirichlet condition for pressure and homogeneous

Neumann condition for velocity are used at the outflow and in the cross-stream direction, and no-slip condition is set at the surfaces of the cylinder. Spanwise boundaries are periodic.

The Reynolds number is the same as in experiments. The dimensions of the computational domain are $80D \times 31D \times 5D$ in the streamwise, cross-stream and spanwise direction, respectively. The upstream face of the cylinder is located at $20D$ from the inflow and centred in the cross-stream direction. The number of elements is $N_e = 8988000$, which corresponds approximately to 3 billion of degrees of freedom per time step and per unknown. The element distribution is homogeneous in the spanwise direction, whereas it is refined in the wall-normal directions approaching the cylinder surfaces. The smallest grid spacing is obtained at the edges of the cylinder, $(\delta x_{\min}, \delta y_{\min}, \delta z) = (0.0021, 0.0021, 0.007)$. These grid spacings are computed as the distance between $N + 1$ evenly spaced nodes within the spectral element. In the near-wall region the spatial resolution meets the following characteristics $(\delta x^+, \delta y_w^+, \delta z^+)_{\max} = (4.1, 0.66, 5.1)$, where the superscript $+$ denotes the normalization in viscous units and Δy_w is the distance from the wall of the second computational node. In turbulent regions, the ratio between the grid spacings and the Kolmogorov scale η is at most $(\delta x/\eta, \delta y/\eta, \delta z/\eta)_{\max} = (4.2, 4.6, 6.3)$. Statistics are collected over a period of $250D/U_\infty$ while the flow is statistically stationary and then averaged in the spanwise direction and with respect to the xz symmetry plane.

A first comparison between experiments and DNS is given in Fig, 2 showing the distribution on the cylinder lateral side of the time-averaged pressure coefficient and of its standard deviation. A perfect agreement is found for the mean pressure, while some differences are present in the standard deviation. As expected, the effect of the inflow turbulence is visible in the experiments on the front face. Moreover, the peak of the pressure fluctuations has the same location but a higher intensity in DNS than in experiments. The reasons of this discrepancy will be analyzed in the final presentation.

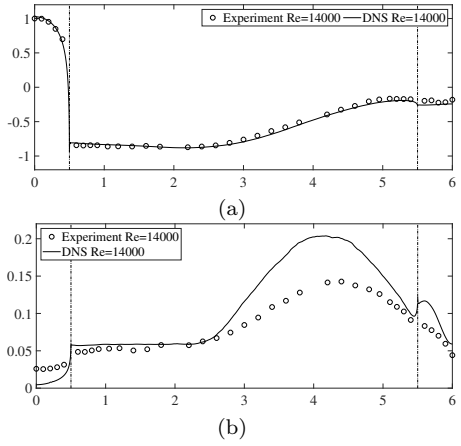

Figure 2: (a) Time-averaged pressure coefficient and (b) its standard deviation on the cylinder surface.

LES SETUP AND METHODOLOGY

Large-Eddy Simulations are carried out by adopting the open-source code Nek5000, as for DNS. The basic setup is the same as in [7]. The order of basis functions inside the elements is $N = 6$ and a third-order backward finite-difference scheme based on the high-order splitting method is used for time advancing. The computational domain spans the following dimensions $-75 \leq x/D \leq 125$, $-75 \leq y/D \leq 75$ and $0 \leq z/D \leq 5$, the cylinder center being located at $x/D = y/D = 0$. The computational domain is thus larger than in DNS.

A uniform velocity profile with no turbulence (smooth flow) is imposed at the inlet, traction-free boundary conditions are used for the outflow and for the upper and lower boundaries of the domain, and no-slip is imposed at the body surface; periodicity is applied in the spanwise direction. The spectral element size and distribution are the same used in [7]. In particular, the element size in the streamwise and cross-flow directions is $\Delta x/D = \Delta y/D = 0.125$ near the cylinder, while in the spanwise direction the element size is uniform $\Delta z/D = 0.558$. A low-pass filter is applied to the velocity field in the modal space because the grid resolution is not fine enough to resolve all turbulent scales at the considered Reynolds number. Since the filter introduces dissipation of the highest resolved modes only, this can be considered as a subgrid-scale dissipation. Two LES are performed at $Re = 14000$ on the flow around the rectangular cylinder having two different upstream-edge treatments.

We plan to carry out sensitivity analysis to grid refinement, upstream edge rounding and possibly to the domain size.

REFERENCES

[1]Bruno, L., Salvetti, M.V. and Ricciardelli, F. : Benchmark on the aerodynamics of a rectangular 5:1 cylinder: and overview after the first four years of activity, *J. Wind Eng. Ind. Aerod.*, **126**, 87–106 (2014).

[2]Mannini, C., Marra, A.M., Pigolotti, L., Bartoli, G.: The effects of free-stream turbulence and angle of attack on the aerodynamics of a cylinder with rectangular 5:1 cross section. *J. Wind Eng. Ind. Aerod.*, **161**, 42–58 (2017).

[3]Pasqualetto, E., Lunghi, G., Rocchio, B., Mariotti, A. and Salvetti, M.V. : Experimental characterization of the lateral and near-wake flow for the BARC configuration, *Wind Struct.*, **34**(1), 101–113 (2022).

[4]Cimarelli, A., Leonforte, A. and Angeli, D. : Direct numerical simulation of the flow around a rectangular cylinder at a moderately high Reynolds number, *J. Wind Eng. Ind. Aerod.*, **174**, 39–49 (2018).

[5]A. Chiarini and M. Quadrio: The Turbulent Flow over the BARC Rectangular Cylinder: A DNS Study. *Flow Turbulence Combust* (2021).

[6]Corsini, R., Cimarelli, A. and Stalio, E. : DNS of the flow about a 5:1 rectangular cylinder with sharp corners, *Marchioli, C., Salvetti, M.V., Garcia-Villalba, M., Schlatter, P. (eds) Direct and Large Eddy Simulation XIII. DLES 2023. ERCOFTAC Series*, **31**, 9–16 (2024).

[7]Rocchio, B., Mariotti, A. and Salvetti, M.V. : Flow around a 5:1 rectangular cylinder: Effects of upstream-edge rounding, *J. Wind Eng. Ind. Aerod.*, **204**, 104237 (2020).

WORKSHOP
Direct and Large-Eddy Simulation 14
April 10-12 2024, Erlangen, Germany

BUDGET OF TURBULENT KINETIC ENERGY AND TEMPERATURE VARIANCE ON THE 5:1 RECTANGULAR BODY

R. Corsini, A. Cimarelli and E. Stalio
Dipartimento di Ingegneria "Enzo Ferrari"
Università degli studi di Modena e Reggio Emilia
roberto.corsini@unimore.it

INTRODUCTION

The turbulent flow about blunt, rectangular bodies is often encountered in civil and wind engineering applications as well as in land transport aerodynamics. Relevant examples include deck slabs of long-span bridges and high-rise buildings of rectangular section and the problem of the aerodynamics of vehicles of simple shape like trucks. The flow about an elongated rectangular cylinder with sharp corners involves several critical aerodynamics features like fixed-position separation in laminar conditions, reattachment and vortex shedding in the wake. In the applications, this gives place to vortex-induced vibration effects, promotes convective heat transfer between the atmospheric air and simple shaped, high-rise buildings and affects pollutant dispersion in the urban environment.

A considerable research effort has been expended since the past 20 years in the investigation of the aerodynamics of a two-dimensional rectangular cylinder with aspect ratio 5:1, especially by research groups based in Europe [1, 2, 3, 4] and this in turn has made this aerodynamics case a canonical case, of acronym BARC, which stands for "Benchmark on the Aerodynamics of a two-dimensional Rectangular Cylinder". Despite the context of abundance of research and publications, both numerical predictions and experimental data about this flow configuration are characterized by a strong dependency upon the details of the setup and the quest for the "correct solution" at different Reynolds numbers is still underway [5].

Turbulent kinetic energy budget for the flow around a 5:1 rectangular cylinder was recently documented in several works [4, 6, 7, 8]. The production of turbulent kinetic energy in the leading-edge shear layer is addressed in the experimental studies by Moore et al. [4] and Rocchio et al. [7]. In the latter the authors investigate the effects of upstream-edge rounding. Chiarini and Quadrio [8] presented and discussed in detail the budget equations for the tensor of the Reynolds stresses based on DNS data at $Re = 3000$. Cimarelli et al. [6] reported the existence of negative production phenomena in the shear layer, i.e. a reversal of flow energy from the mean field to the fluctuating field. To the best of our knowledge, no results can be found in the literature about the transport equation of turbulent heat fluxes and temperature variance for this flow.

In this work we present results from three Direct Numerical Simulations around the BARC body at different Reynolds number, including passive scalar transport. The Reynolds numbers investigated are 3000, 8000 and 14000 respectively while the Prandtl number is fixed at $Pr = 0.71$. Simulations are carried out using the code NEK5000 [9]. The discussion includes a description of the main terms of the transport equations of the turbulent kinetic energy and scalar variance. The Reynolds number effect on these budget terms is also discussed.

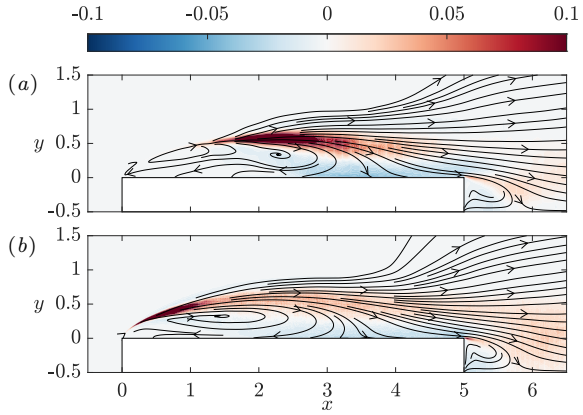

Figure 1: Distribution of $P^k - \langle\varepsilon\rangle^k$ superimposed with field lines of energy flux ϕ^k at $Re = 3000$ (a) and 14000 (b).

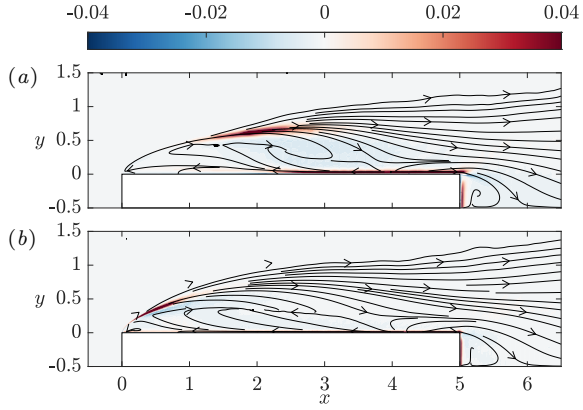

Figure 2: Distribution of $P^\theta - \langle\varepsilon\rangle^\theta$ superimposed with field lines of scalar variance flux ϕ^θ at $Re = 3000$ (a) and 14000 (b).

RESULTS

The flow configuration consists in the laminar flow separation at the upstream corner, a transition process occurring in

the separated shear-layer and the reattachment of the turbulent flow. Two boundary layers are formed starting from the reattachment position: one which leads to the final separation at the downstream corner and the shedding of vortices in the wake, and a second boundary layer developing upstream which finally generates a smaller, counter-rotating spanwise vortex of the mean flow.

The terms of the transport equation of the turbulent kinetic energy $\langle k \rangle$ and passive scalar variance $\langle \theta' \theta' \rangle$ are analysed to provide insight into the production, dissipation, and transport of turbulent and scalar fluctuations. The influence of the Reynolds number on these terms is also considered. For a statistically steady flow, the transport equations for $\langle k \rangle$ and $\langle \theta' \theta' \rangle$ can be suitably expressed as follows:

$$\frac{\partial \phi_j^k}{\partial x_j} = P^k - \langle \varepsilon \rangle^k \tag{1}$$

$$\frac{\partial \phi_j^\theta}{\partial x_j} = P^\theta - \langle \varepsilon \rangle^\theta, \tag{2}$$

where P is the production term, $\langle \varepsilon \rangle$ is the dissipation term, and ϕ_j are the fluxes of turbulent kinetic energy or scalar variance taking into account the contributions by the mean, turbulent, diffusive, and pressure transports.

The production of turbulent kinetic energy is active along the leading-edge shear layer, in the region where Kelvin-Helmholtz instabilities are amplified under the action of high mean shears and transitional process occurs. As the Reynolds number increases, the region of maximum production of turbulent kinetic energy moves upstream along the shear layer centreline, in accordance with the anticipation of transition to turbulence with Re, and reaches higher values because of more intense mean velocity gradients. The viscous dissipation mainly acts in the shear layer region. The effects of the Reynolds number on the dissipation term $\langle \varepsilon \rangle^k$ mainly concern the location and the magnitude of its largest values. As for P_k, while Re increases, higher dissipation values are observed at more upstream positions along the shear layer. Figure 1 shows the net production of $\langle k \rangle$ together with the mean path of energy fluxes given by turbulent, pressure, diffusive and convective mechanisms, for the cases at $Re = 3000$ and 14000. The excess of production of turbulent energy in the shear layer is partially carried downstream towards the wake while the other part is transported towards the cylinder wall, where it is dissipated. For increasing Re, a higher fraction of energy is redistributed in the upstream part of the primary recirculating region.

With regard to the scalar variance, high production values of $\langle \theta' \theta' \rangle$ are observed in the outer region of the shear layer and in the near-wall region. The extension of the latter increases toward the leading edge with the growth of Re due to the enhancement of turbulence mixing over a wider region of the cylinder surface. The net production and transport of scalar variance differs from that of turbulent energy to their distribution and mean path above the cylinder, as shown in figure 2. In this case, lines of scalar variance flux also originate from the wall and contribute to the transport of $\langle \theta' \theta' \rangle$ in the core of the primary vortex, for $x < x_r$, and in the wake, for $x > x_r$, where x_r is the mean reattachment line.

CONCLUSIONS

The phenomena of generation, dissipation and transport of turbulent kinetic energy and scalar variance in the separating and reattaching flow around a 5:1 rectangular cylinder are investigated. The analysis is based on high accurate DNS data generated at different Reynolds numbers ($3000 < Re < 14000$) and $Pr = 0.71$. The effects of the Reynolds number on the budget terms are evaluated, the most noticeable being the triggering of production and dissipation processes at shorter distances from the leading edge and the different energy (and scalar variance) redistribution within the recirculating region. These results constitute a valuable base of information that might improve our current understanding of separating and reattaching flows, and lead to the development of turbulence models of greater accuracy and wider applicability in bluff bodies aerodynamics.

ACKNOWLEDGEMENTS

This research is funded by NextGenerationEU- DD. 3277. Ecosystem For Sustainable Transition of Emilia-Romagna (ECOSISTER).

REFERENCES

[1]L. Bruno, D. Fransos, N. Coste, and A. Bosco, "3d flow around a rectangular cylinder: A computational study," *Journal of Wind Engineering and Industrial Aerodynamics*, vol. 98, no. 6-7, pp. 263–276, 2010.

[2]D. Nguyen, D. Hargreaves, and J. Owen, "Vortex-induced vibration of a 5:1 rectangular cylinder: A comparison of wind tunnel sectional model tests and computational simulations," *Journal of Wind Engineering and Industrial Aerodynamics*, vol. 175, pp. 1–16, 2018.

[3]A. Cimarelli, A. Leonforte, and D. Angeli, "On the structure of the self-sustaining cycle in separating and reattaching flows," *J. Fluid Mech.*, vol. 857, pp. 907–936, 2018.

[4]D. Moore, C. Letchford, and M. Amitay, "Energetic scales in a bluff body shear layer," *J. Fluid Mech.*, vol. 875, pp. 543–575, 2019.

[5]R. Corsini, D. Angeli, E. Stalio, S. Chibbaro, and A. Cimarelli, "Flow solutions around rectangular cylinders: The question of spatial discretization," *Wind and Structures, An International Journal*, 2022.

[6]A. Cimarelli, A. Leonforte, E. De Angelis, A. Crivellini, and D. Angeli, "On negative turbulence production phenomena in the shear layer of separating and reattaching flows," *Physics Letters A*, vol. 383, pp. 1019–1026, 2019.

[7]B. Rocchio, A. Mariotti, and M. Salvetti, "Flow around a 5:1 rectangular cylinder: Effects of upstream-edge rounding," *J. Wind Eng. Ind. Aerodyn.*, vol. 404, p. 104237, 2020.

[8]A. Chiarini and M. Quadrio, "The turbulent flow over the barc rectangular cylinder: a dns study," *Flow, Turbulence and Combustion*, 2021.

[9]P. F. Fischer, J. W. Lottes, and S. G. Kerkemeier, "nek5000 web page." `http://nek5000.mcs.anl.gov`, 2008.

SESSION: Industrial and environmental applications II

Thursday, April 11, 2024

14:50- 16:05

WORKSHOP
Direct and Large-Eddy Simulation 14
April 10-12 2024, Erlangen, Germany

INFLUENCE OF ATMOSPHERIC STABILITY ON WIND AND THERMAL CONDITIONS IN AN URBAN CANYON

Ximeng Kang[1], Alistair Revell[1], Saleh Rezaeiravesh[1], David Topping[1], Martin Ferrand[2], Charles Moulinec[3]
[1]The University of Manchester (UoM) Manchester, UK
[2]Électricité de France (EDF) Paris, France
[3]Science and Technology Facilities Council (STFC), Daresbury Laboratory, Warrington, UK
ximeng.kang@postgrad.manchester.ac.uk

INTRODUCTION

Atmospheric stability is recognized as an important factor influencing urban airflow patterns and air temperature distribution. Understanding buoyancy effects on urban ventilation is important for mitigating extreme heat conditions and improving climate resilience. However, the underlying flow mechanisms in those buoyancy-driven scenarios are not well understood yet. In this project, the numerical simulations for a building array with different Richardson numbers were conducted using LES with Smagorinsky model. The results are rigorously validated against wind tunnel experiment. Additionally, detailed flow structures are presented to illustrate the effect of atmospheric stability.

METHODOLOGY

The energy equation in terms of temperature:

$$\frac{\partial T}{\partial t} + \nabla \cdot (VT) = \nabla \cdot (\alpha_{th} \nabla T) \ , \tag{1}$$

where α_{th} is the thermal diffusivity.

The flow is considered incompressible with the momentum equations written as,

$$\rho \left(\frac{\partial V}{\partial t} + V \cdot \nabla V \right) = -\nabla P + \mu \nabla^2 V + \rho g - \rho \beta \left(T - T_{ref} \right) g \ , \tag{2}$$

where β is thermal expansion coefficient, T_H, T_0 are the temperature boundary conditions at the height of canyon top and floor.U_H is the velocity at the canyon top surface. The term $\rho g - \rho \beta \left(T - T_{ref} \right) g$ is the buoyancy based on the Boussinesq approximation. This approximation allows for the density variation caused by temperature differences to be neglected, except for the buoyancy force term in the momentum equation. The buoyancy force can be approximated as a linear function of the temperature difference:

$$\rho = \rho_0 \left[1 - \beta \left(T - T_{ref} \right) \right] \tag{3}$$

The configurations of the CFD cases have been adjusted to be identical to those used in wind tunnel experiment conducted by Uehara et al. in 2000[1], see Fig. 1 . The inlet velocity U_{ref} is set as uniform 1.5m/s, resulting in a model building Reynolds number of $Re_H = U_H H/\mu = 10135$, and a roughness Reynolds number of $Re^* = u^* Z_0/\mu = 26.8$. The numerical simulations were conducted using LES without wall model on Code_Saturne 7.0 for a building array with various Richardson numbers, ranging from -0.21 to 0.78, based on different temperature differences between the ambient and the ground. The mesh used for the simulation was generated using the trimmed mesh technique in STAR CCM+ V2019, resulting in approximately 59 million mesh cells with a first-layer height of around 0.0015m. The y^+ along the canyon boundaries is between 2 and 5.

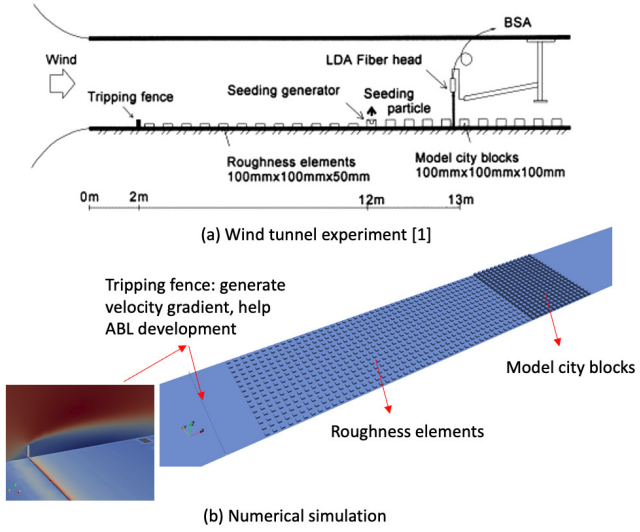

Figure 1: Arrangement of the roughness elements and modeled city blocks.

VALIDATION

A mesh resolution study was initially conducted. Results associated to the meshes with 32 million, 59 million, and 91.4 million cells (with uniform cells within the canyon) were compared. The mesh with 59 million cells was chosen due to the minimal difference observed compared to the 91.4 million mesh resolution.

The results are rigorously validated against wind tunnel test. The time-averaged velocity and temperature profiles as well as Reynolds shear stress at the centerline of street canyon agree well with experimental results in Fig. 2, demonstrating the accuracy of the current CFD model.

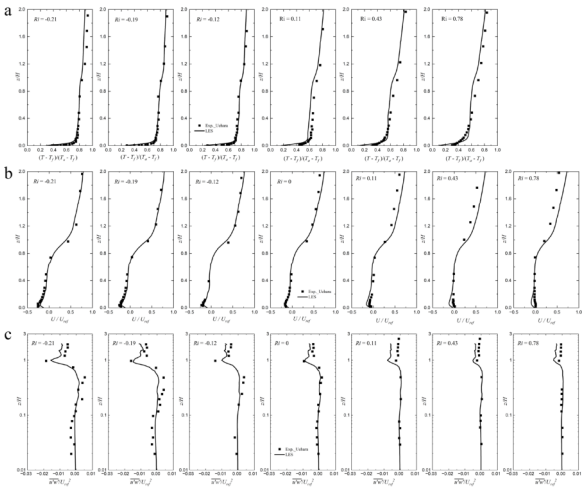

Figure 2: Comparisons between vertical profiles of normalised time-averaged a) temperature b) horizontally velocity c) Reynolds shear stress at the vertical centreline of street canyon obtained from simulations and experiments.

RESULTS ANALYSIS

Profiles, contours and streamlines are obtained at different atmospheric stability conditions to investigate the flow mechanisms. The wind direction is marked in Fig. 3. In the neutral case, the original circulation is clockwise. In unstable conditions, where the ground temperature surpasses the ambient temperature, an upward buoyancy force is generated. This, combined with the clockwise circulation, results in higher upward vertical velocity near the leeward wall. Consequently, this enhances the original circulation and leads to a higher magnitude of Reynolds shear stresses near the top of the canyon. Conversely, in stable cases where the ground temperature is lower than ambient temperature, a downward trend in vertical velocity occurs, resulting in lower vertical velocity. This, in turn, weakens the original circulation and leads to a lower Reynolds shear stress magnitude at the top of the canyon. These conclusions can also be observed with profiles in Fig. 4. Additionally, regarding eddy heat flux (Fig. 4 (d)), positive values are observed under unstable conditions, indicating cooling effects within the canyon. In contrast, stable conditions exhibit negative values, hindering heat dissipation. Finally, Three-dimensional effects are evident in the flow streamlines, Fig. 3 (d).

CONCLUSIONS AND FUTURE WORKS

- Buoyancy effects enhance the circulation within the canyon under unstable conditions, while weaken the circulation under stable conditions. As a result, there is higher Reynolds shear stress (magnitude) at the top of canyon under unstable conditions and a lower Reynolds shear stress under stable conditions. Strong three-dimensional effect can be observed in the flow structures.
- Future work will focus on different buildings arrangements and heating pattern to establish a comprehensive parameter database.

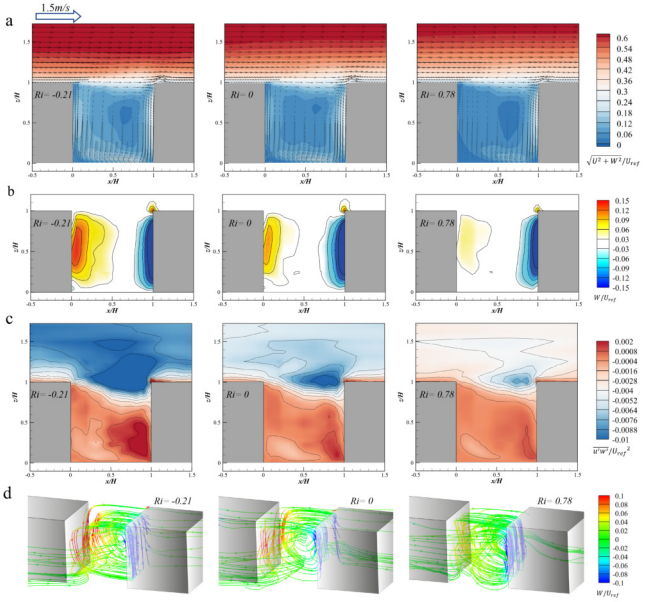

Figure 3: Contours of a) Composite velocity distributions b) Vertical velocity distributions c) Reynolds shear stress distributions and and d) 3D streamlines streamlines within the street canyon.

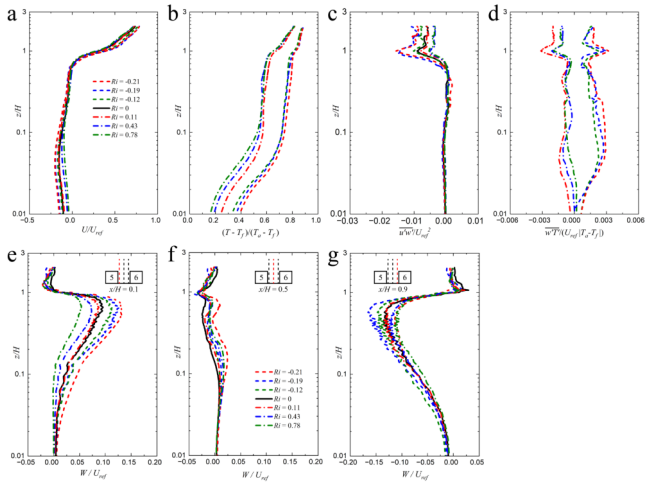

Figure 4: Comparisons of vertical profiles of normalised time-averaged a) horizontally velocity b) temperature c) Reynolds shear stress d) eddy heat flux e-g) vertical velocity at different x/H positions at the vertical centreline of street canyon for cases with different Richardson numbers from -0.21 to 0.78.

REFERENCES

[1]Uehara, K., Murakami, S., Oikawa, S. and Wakamatsu, S. : Wind tunnel experiments on how thermal stratification affects flow in and above urban street canyons, *Atmos. Environ.*, **34**, 1553–1562 (2000).

WORKSHOP
Direct and Large-Eddy Simulation 14
April 10-12 2024, Erlangen, Germany

APPLICATION OF LAGRANGIAN STOCHASTIC METHODS FOR INDOOR AIR QUALITY

Harriet Jones[1], Gregory Cartland-Glover[1], Ashish Kumar[2], Terry Dillon[2] and Stefano Rolfo [1]
[1]Science and Technology Facilities Council (Scientific Computing Department)
Daresbury Laboratory, UK
harriet.e.jones@outlook.com

INTRODUCTION

Particulate matter of 2.5 µm or less in diameter ($PM_{2.5}$) poses a serious health hazard. Exposure to elevated concentrations causes the premature loss of millions of lives every year, from ailments including coronary heart disease, stroke and lung cancer [1]. While indoor exposure in workplaces and public areas is now better characterised, much remains to be done in terms of understanding the exposure risks to individuals within domestic settings [2] Cooking is a significant source of $PM_{2.5}$ in the home [3], and it is critical, for the improvement of domestic air quality, that this source be properly characterised and mitigated. Historically, the RANS approach has been used for such scenarios, due to the high computational demands of LES, but this may well come at a cost to the accuracy of the results [4]. The aim of this work is to utilise high-fidelity computational fluid dynamics (CFD) modelling and Stochastic Lagrangian Particle Tracking to simulate $PM_{2.5}$ dispersion during stir frying in a typical UK kitchen. Results are validated using experimental data gained from the DOMestic Systems Technology InCubator (DOMESTIC), based at the University of York in the UK.

METHODOLOGY

DOMESTIC is a controlled environment measuring 5.80 x 2.20 x 2.30 m, and contains a full-scale kitchen equipped with a cooker and a range of $PM_{2.5}$ and temperature sensors, along with sonic anemometers, for full spatial resolution of the data (see Figure 1). High-emission dishes such as stir-fries are primarily studied. For the results shown below, cooking duration was 12 minutes with a pan temperature of 180 °C, after which the cooking pan was covered and removed from the test house. Experiments were conducted in airtight conditions. The geometry and meshing of the DOMESTIC model was performed in SALOME, with mesh sizes being between 40 -170 million cells. The open-source, finite volume solver used was *code_saturne*, which is developed and maintained by EDF R&D. Boundaries were set to a temperature of 10°C to match the experimental data. A standard Eulerian single phase incompressible flow model was used, along with the Boussinesq approximation in the buoyancy term. Second order accurate discretisation in space and time was used for both momentum and heat transfer. WALE and Dynamic Smagorinsky SGS models were tested and compared with a RANS (EBRSM) approach. The fry pan was modelled as a solid cylinder with

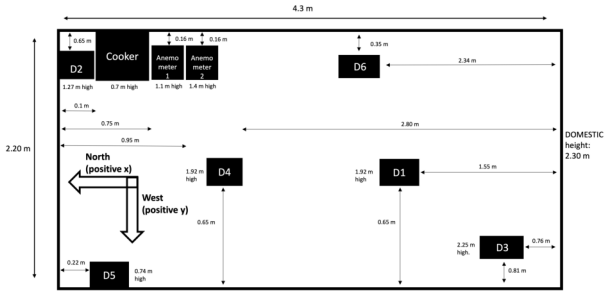

Figure 1: Layout of DOMESTIC test house showing location of of anemometers and $PM_{2.5}$ sensors (D1-6).

a surface temperature of 180°C, with $PM_{2.5}$ particles being injected at a rate of 3.5 mg/min just above this heat source (from the experimental data and O'Learey et al.,[5]). One-way fluid-particle coupling was used. Cases were run for an in-simulation time of 12 minutes on an HPE Cray EX system (ARCHER2).

RESULTS AND DISCUSSION

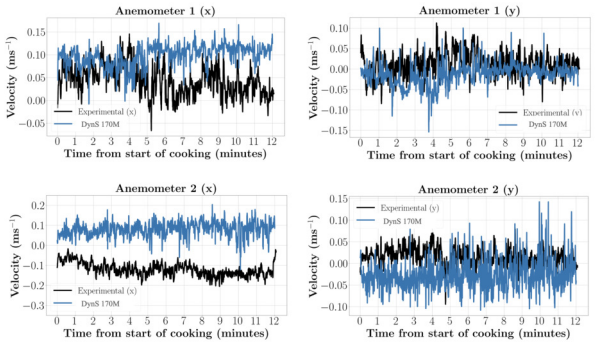

Figure 2: Velocities at anemometers 1 and 2 in the x and y direction - results for 170 million cell Dynamic Smagorinsky case compared against experimental results.

The experimental hydrodynamics were fairly well captured by the model, as seen in Figure 2 (for clarity, only the most successful case, the 170 million cell Dynamic Smagorinsky, is shown). The slight discrepancies are attributed to exper-

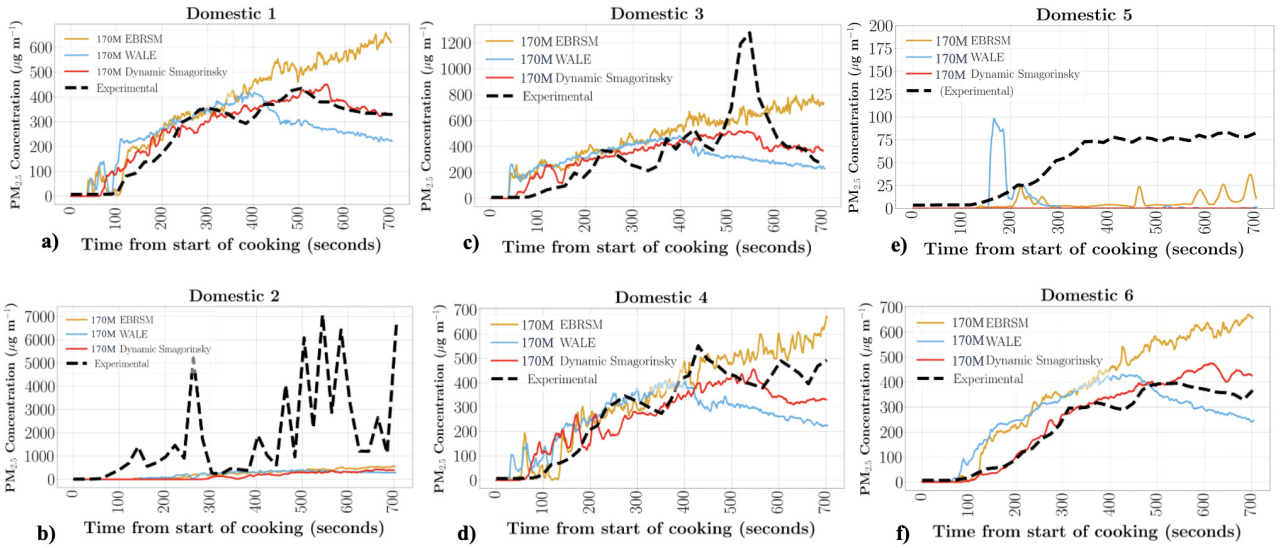

Figure 3: Experimental vs simulated results from $PM_{2.5}$ sensors (D1-6).

imenter movement and the current lack of steam within the model.

Despite rigorous standardisation protocols there was considerable variability in the experimental $PM_{2.5}$ concentrations between runs. Results shown here are the averages of all four runs. The experimental results (see Figure 3) indicate that, in unventilated conditions, dishes such as stir fries may produce local concentrations of $PM_{2.5}$ of over 40 times the World Health Organisation recommended 24 hour maximum exposure of 15 µg m^{-3} [6]. As Figure 3 shows, the LES approach appeared to be the most successful, with the overall best fit to the experimental results given by the 170 million cell mesh Dynamic Smagorinsky model. All models underpredicted concentrations at D2, the sensor in close proximity to the cooking source. Again, this is likely to be due to the absence of steam and experimenter movement from the model – note the alternations between peaks as high as 7000 µg m^{-3} and troughs of under 600 µg m^{-3} seen in the experimental data at this sensor (Figure 3 (b)) which suggest that the sensor is being subjected to intermittent gusts of particle-laden air. All models also under predicted the concentrations of $PM_{2.5}$ at D5, the table-height sensor (Figure 3, (e)), with the 170M WALE also showing a short but intense peak in concentration early on in the simulations, not seen in the experimental results. The currently used assumption that the container is perfectly sealed is unlikely to reflect the real-life air leakage into and out of the domain, and including this into the model would likely improve the mixing currently observed.

CONCLUSIONS

In this work, Lagrangian stochastic methods were used to simulate $PM_{2.5}$ dispersion in a typical UK kitchen, with validation data being supplied from the DOMESTIC test house. The use of two LES SGS models (Dynamic Smagorinsky and WALE) were compared with a RANS model (EBRSM). The LES approach outperformed the RANS approach, with the Dynamic Smagorinsky providing the best fit to the experimental results overall. The incorporation of material particles of a range of different radii, along with the effects of steam, is currently under development, the results of which will be presented at the conference.

ACKNOWLEDGEMENTS

STFC acknowledges the funding for this project through the STFC Air Quality Network (SAQN) [grant number ST/S005366/1]. Compute time on ARCHER2 provided via an Engineering and Physical Sciences Research Council (EPSRC) “Access to High Performance Computing” grant.
The DOMESTIC installation was supported by the EPSRC [grant number EP/T014490/1].

REFERENCES

[1]COMEAP (Committee on the Medical Effects of Air Pollutants): *Long-term exposure to air pollution: effect on mortality*, London, UK: Health Protection Agency (2009).

[2]Lewis, A. C., Jenkins, D., and Whitty, C. J. M: Hidden harms of indoor air pollution — five steps to expose them, *Nature*, **614**, 220–223 (2023).

[3]Healy, R.M., et al. : Quantitative determination of carbonaceous particle mixing state in Paris using single-particle mass spectrometer and aerosol mass spectrometer measurements, *Atmos. Chem. Phys.*, **13**, 9479–9496 (2013).

[4]Blocken, B. : LES over RANS in building simulation for outdoor and indoor applications: A foregone conclusion? *Build. Simul.* **11**, 821–870 (2018).

[5]O’Leary, C., Kluizenaar, Y., Jacobs, P., Borsboom, W., Hall, I., and Jones, B. : Investigating measurements of fine particle (PM2.5) emissions from the cooking of meals and mitigating exposure using a cooker hood, *Indoor Air*, **29**(3), 423–438 (2019).

[6]World Health Organization. *WHO global air quality guidelines: particulate matter (PM2.5 and PM10), ozone, nitrogen dioxide, sulfur dioxide and carbon monoxide*, Bonn, Germany: WHO European Centre for Environment and Health (2021).

WORKSHOP
Direct and Large-Eddy Simulation 14
April 10-12 2024, Erlangen, Germany

INFLUENCE OF FREE-STREAM TURBULENCE ON REAL-GAS FLOWS THROUGH A SUPERSONIC TURBINE CASCADE

C. Matar[1], X. Gloerfelt[2], P. Cinnella[1]
[1]Jean le Rond d'Alembert Institute
Sorbonne University, Paris, France
[2]DynFluid Laboratory
Arts et Métiers Institute of Technology, Paris, France
camille.matar@dalembert.upmc.fr

INTRODUCTION

In low-cost, small-size power systems, it is advantageous to use single-stage turbine designs leading to high pressure ratios and high Mach number conditions at stator outlet. This favors supersonic regimes where shock waves constitute one of the main sources of performance loss. This is particularly critical in Organic Rankine Cycle (ORC) turbines, which use molecularly complex organic vapors as the working fluid. Such fluids do not obey the ideal gas equation of state, which strongly influences the expansion, and more specifically the flow around the trailing edge (TE) [1] and the back pressure.
The very high pressure ratios achieved in supersonic turbine stator vanes induce strongly favorable pressure gradients that delay boundary layer transition on the blade surface. As a consequence, the latter may remain laminar until reaching the TE even at moderately high Reynolds numbers [2]. In the case of supersonic flow, the shock waves generated at the TE impinge on the laminar boundary layer at the suction side of the neighboring blade, thus causing separation and abrupt boundary layer transition to turbulence. In practice, due to the presence of incoming free-stream turbulence, transition is triggered upstream of the shock wave/boundary layer interaction (SWBLI). The extent and intensity of the latter is then expected to be highly dependent on the inlet turbulence level, finally influencing the boundary layer state upstream of the TE, the back pressure, and the turbine losses.
To shed light onto the interplay among freestream turbulence, boundary layer transition under highly favorable pressure gradients, and turbine losses, we perform Large Eddy Simulations (LES) for both air and an organic vapor R134a behaving like a dense gas, under varying levels of inlet turbulence intensity. Initial comparisons between the air and R134a flows highlight the effect of the gas thermodynamic behavior on the stator vane performance. Then, an in-depth analysis is carried out on the effect of varying the free-stream turbulence level on the flow around the blade, with a focus on boundary layer development and performance loss mechanisms.

CASE STUDY AND NUMERICAL METHODS

The present configuration is a supersonic stator vane designed by Baumgärtner et al. [3]. The outlet isentropic Mach number is $M_{is} = 1.5$ for both air and R134a, corresponding to pressure ratios of $\Pi = 3.67; 3.20$, respectively, and the exit flow angle is $\theta = 76^o$. The Reynolds numbers based on blade chord ($c = 16$mm) and outflow conditions are $Re_{air} \approx 1.7 \times 10^6$ and $Re_{R134a} \approx 2.4 \times 10^6$. Two levels of inlet turbulence intensity are investigated: $Tu = 2.7\%; 3.4\%$. Additional LES are ongoing and will showcase higher turbulence levels. Free-stream disturbances are injected at the computational domain inlet plane by superimposing random Fourier modes with the inlet boundary treatment, which relies on Riemann invariants.
Compressible LES are carried out using the in-house MUSICAA high-order finite-difference solver for multiblock structured grids. The code is equipped with several thermodynamic and transport law models. In this study, the ideal gas model is used for air, while the thermodynamic behavior of the molecularly complex vapor R134a is modeled with the Peng-Robinson-Stryjeck-Vera equation of state [5], although in the present simulations we consider thermodynamic operating conditions in the so-called diluted gas region, where deviations with respect to the ideal gas behavior are mild. The inviscid fluxes are discretized by means of 10th-order centered differences whereas 4th-order is used for viscous fluxes. High-order coordinate transforms are used to account for mesh deformations. The scheme is supplemented with a 10th-order selective filter to eliminate grid-to-grid oscillations, along with a low-order shock capturing term activated locally by a combination of Jameson's shock sensor and Ducros' dilatation/vorticity sensor. A four-stage Runge-Kutta algorithm is used for time integration and high-order Implicit Residual Smoothing is applied to relax stability constraints on the time step. This allows CFL numbers up to 5 in the present computations. The filter also acts as a regularization term draining energy at subgrid scales, so that no explicit subgrid-scale model is used (implicit LES). More details about the numerical methodology can be found in [4]
The computational domain extends from $-1c$ to $2c$ and $0.1c$ in the streamwise and spanwise directions respectively. The blade surface is discretized by 2 000 points, and the span by 200 points, with a total of 212M grid points. The resulting resolution in wall units is $n^+ \leq 2$, $t^+_{avg} \approx 50$ and $z^+_{avg} \approx 20$ in the wall normal, tangential and spanwise directions respectively.

PRELIMINARY RESULTS

A global view of the flow around the blade is given in Figure 1 for the case $Tu = 2.7\%$, featuring a wide spectrum of in-

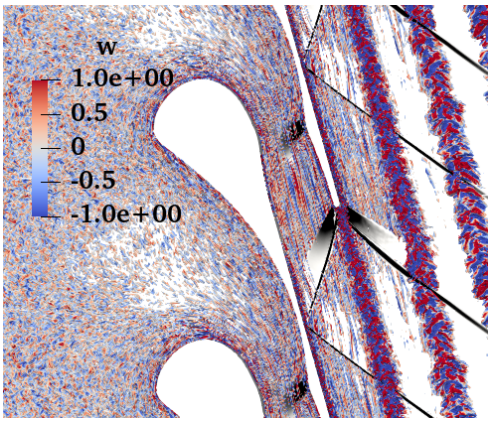

Figure 1: Instantaneous $Q-$criterion contour colored by spanwise velocity w, and density gradient magnitude in the background.

coming vortical structures which eventually wrap around the leading edge and stretch as they enter the vane passage. Moreover, shock waves generated at the TE impinge on the blade suction side, as indicated by the strong local density gradients, forming a SWBLI region. Finally, an unsteady wake develops downstream of the TE featuring highly three-dimensional structures with no apparent vortex shedding.
Further details of the flow near the wall are obtained by inspecting mean boundary layer velocity and Reynolds shear stress profiles in Figure 2. These are extracted from 0% and 2.7% inlet turbulence levels LES, at two positions on the blade suction side: just upstream *pre* and downstream *post* of the SWBLI. For $Tu = 0\%$, the *pre* boundary layer corresponds to a laminar profile while strong deviations are found for $Tu = 2.7\%$. Moreover, the corresponding cross-correlation profiles feature non-zero content only for the latter case, showing that the boundary layer is not laminar just upstream of the SWBLI only in the case where free-stream disturbances are injected. Finally, the velocity profiles across the *post* boundary layer collapse to a somewhat turbulent state that is not in equilibrium (large deviations from the log-law), but features similar shear stress profiles.

While there is strong evidence that transition is triggered in the SWBLI region in the $Tu = 0\%$ case, a different mechanism appears to disturb the boundary layer prior the SWBLI when turbulence is injected. In Fig. 3 we show carpet plots of the instantaneous friction coefficient on the suction side. The graph focuses only on the region around the SWBLI and the TE. For $Tu = 2.7\%$, the characteristics of free-stream turbulence induced transition are observed, with the generation of turbulent spots that contaminate the rest of the flow at the wall. This results in a smaller SWBLI region (thin against large recirculation region), leading in turn to a modified boundary layer state and shock wave pattern at the TE.

CONCLUSION AND WORK IN PROGRESS

A detailed investigation of the effect of gas behavior and free-stream turbulence on the flow through the supersonic stator vane is in progress and will be presented at the conference, with a focus on boundary layer development and loss generating mechanisms. The ongoing additional LES will feature

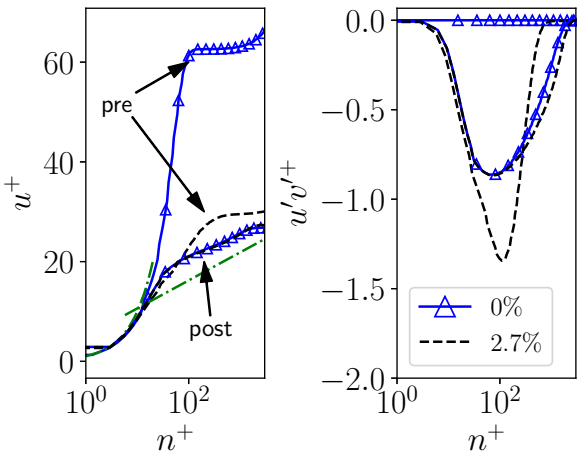

Figure 2: Boundary layer profiles just upstream (*pre*) and downstream (*post*) of the SWBLI. Left: tangential velocity. Right: Reynolds shear stress $u'v'^+ = \overline{u'v'}/u_\tau^2$.

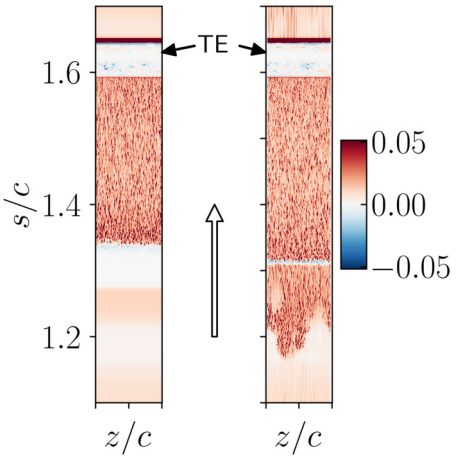

Figure 3: Carpet plot of instantaneous friction coefficient on blade suction side. Left: $0\%Tu$. Right: $2.7\%Tu$. The arrow indicates the flow direction

higher inlet disturbance levels, as well as higher grid refinement.

REFERENCES

[1]Galiana, F. J. Dura, Wheeler, A. P. S., Ong, J. : A study of trailing-edge losses in Organic Rankine Cycle turbines, *Journal of Turbomachinery*, **138**, 1–9 (2016).

[2]Zhao, Y., Sandberg, R. D. : Bypass transition in boundary layers subject to strong pressure gradient and curvature effects, *Journal of Fluid Mechanics*, **888**, (2020).

[3]Baumgärtner, D., Otter, J., Wheeler, A. P. S. : The effect of isentropic exponent on transonic turbine performance, *Journal of Turbomachinery*, **142**, 1–13 (2020).

[4]Bienner, A., Gloerfelt, X., Cinnella, P., Multiblock parallel high-order implicit residual smoothing time scheme for compressible Navier–Stokes equations, *Computers & Fluids*, Vol. 269, 106138 (2023).

[5]Stryjek, R., Vera, J. H. : PRSV: An improved Peng–Robinson equation of state for pure compounds and mixtures, *The Canadian Journal of Chemical Engineering*, **64**, 323–333 (1986).

WORKSHOP
Direct and Large-Eddy Simulation 14
April 10-12 2024, Erlangen, Germany

BOUNDARY LAYER STABILITY AND SHOCK INTERACTIONS IN A HIGH-SPEED LOW PRESSURE TURBINE CASCADE

Maxime Borbouse[1], Gustavo Lopes[2], Sergio Lavagnoli[2], Michel Rasquin[3], Koen Hillewaert[1,3]
[1]Aerospace and Mechanics Department, Université de Liège
Allée de la découverte 9, 4000 Liège, Belgium
[2]Turbomachinery and Propulsion Department, von Kàrmàn Institute for Fluid Dynamics
Chaussée de Waterloo 72, 1640 Rhode-St-Genèse, Belgium
[3]Cenaero, Rue des frères Wright 29, 6041 Gosselies, Belgium
koen.hillewaert@uliege.be

INTRODUCTION

In the last few decades, turbofan engines have garnered considerable attention in aeronautical research, especially in the pursuit of improving fuel efficiency. The goal has been to boost engine efficiency by improving both thermodynamic and propulsive efficiency. The latter can be enhanced by increasing the engine bypass ratio. The size of the fan presents a significant constraint: with the increase of fan diameter, the rotation speed needs to decrease to maintain transonic conditions at the tip. In a classical turbofan engine, the fan is directly coupled to the low-pressure spool which limits its speed. The Geared Turbofan (GTF) concept allows to bypass this compromise. It involves separating the fan rotation from that of the turbine using a gearbox such that the turbine can reach higher speeds. This results in the development of high-speed low-pressure turbines, in which the typical low Reynolds numbers are now obtained at high/transonic Mach numbers. Loss mechanisms and the aerodynamics of blades are therefore significantly altered by compressibility effects. Under low Reynolds numbers, there is a risk of separation on the suction side, leading to a notable increase in losses. To prevent large separation, researchers have investigated utilizing new blade geometries as well as turbulence and wake-induced transition. Separation that occurs can manifest either as an open separation leading to high losses without reattachment or as a closed bubble adopting different modes. The transition allows for reattachment, giving rise to separation bubbles. If reattachment occurs prior the TE, the portion of turbulent wetted area contributing to skin friction losses is actually reduced. However, if it occurs to late, the outlet BL momentum and displacement thicknesses are large and losses increase. These regimes may be significantly altered due to choking of the passage, or due to the interaction with shocks.

By examining the aerodynamics of the blades, the primary objective is to comprehend the boundary layer condition at separation to discern the specific mode of the resulting separation bubble. From a numerical perspective, addressing this subject poses significant challenges. Both steady and unsteady Reynolds averaged Navier Stokes simulations (RANS and URANS, respectively) encounter difficulties in accurately resolving transition. To comprehensively understand and characterize transition, shocks, and other complex mechanisms within the flow, high-fidelity simulations must be employed. Direct numerical simulation (DNS) stands out as the most reliable approach, enabling the capture of all flow length scales, albeit at a considerably higher computational cost. One method that is particularly suited for high accuracy DNS on generic geometries is the discontinuous Galerkin method (DGM). In this work, the solver ArgoDG (see [1, 2]) is used.

The primary focus of interest in this study lies in studying the aerodynamics of the blades, particularly in the conditions encountered during both on-design and off-design scenarios in a Geared Turbofan (GTF), notably during cruise and take-off conditions. The results obtained aim to facilitate the development of low-order models for profile and secondary losses, as well as turbulence and transition models, by providing extensive and very accurate statistical data bases. Furthermore, this work serves to validate the methodology employed in studying flows within high-speed LPTs by comparing experimental and DNS data. It is essential to note that this work primarily focuses on analyzing the behavior and effects of the blades themselves, excluding any consideration of inlet turbulence.

NUMERICAL SETUP

The computational domain and mesh are depicted in Figure 1. The mesh was constructed using Gmsh 4.5.6 [5]. The geometric parameters and flow conditions are respectively

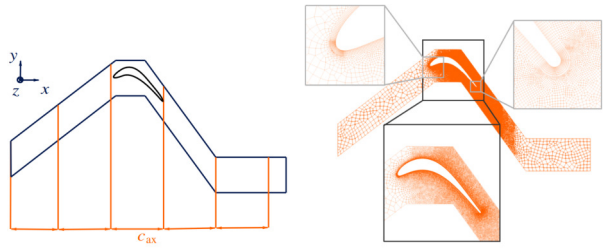

Figure 1: Domain and mesh definition in the periodic plane.

given in Tables 1 and 2. The spatial discretization combines discontinuous Galerkin with the symmetric interior penalty discontinuous Galerkin (SIPDG), which leads to a 4th order

Parameter	Symbol	Value
Pitch to chord ratio [-]	g/c	0.63
Throat to chord ratio [-]	o/c	0.37
TE radius to chord ratio [-]	$d_{\mathrm{TE}}/(2c)$	0.008

Table 1: Cascade geometric parameters.

Quantity	Value				
$\mathrm{Re}_{s,\mathrm{out}}$ [-]	70×10^3			120×10^3	
$M_{s,\mathrm{out}}$ [-]	0.70	0.90	0.95	0.9	0.96
p_{out} [Pa]	7771.16	5617.12	5213.22	9629.34	8806.7
T_{in}° [K]	300				
α [°]	36.3				

Table 2: Flow conditions.

spatial discretisation. It is important to note that no shock capturing strategies were employed. The computational domain includes five boundaries: inlet, outlet, top, bottom, and the blade. Periodic BCs were employed at the top and bottom boundaries as well as in the spanwise direction with a relative span of 0.35% of the chord c. Total conditions and flow angles are imposed at the inlet, while at the outlet, only static pressure is fixed. A sponge layer is added near the outlet, with spatially varying strength,

$$\sigma = \tan(x - 1.55) \cdot \mathrm{step}(1.55), \tag{1}$$

which penalises the instantaneous flow u with respect to the time average $\overline{u}$ by adding the source term

$$S = \sigma(u - \overline{u}) \tag{2}$$

to the equations in order to prevent outgoing waves and perturbations from reflecting back into the domain.

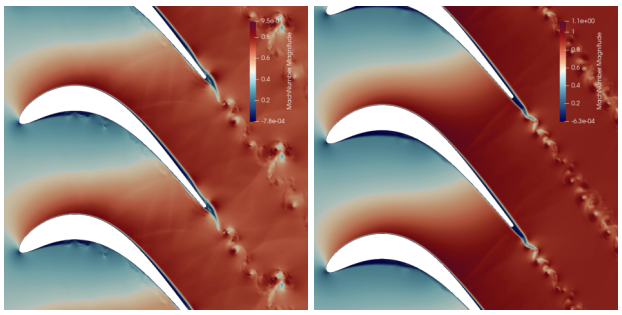

(a) (b)

Figure 2: Mach number contours for $\mathrm{Re}_{s,\mathrm{out}} = 70 \times 10^3$ and $M_{s,\mathrm{out}} = 0.7$ (a) and $M_{s,\mathrm{out}} = 0.9$ (b).

DISCUSSION OF RESULTS

Figures 2, 3, 4 illustrate the flow, its turbulent and compressible behaviors, for the low Reynolds / high Mach number case. Separation bubble appears on the pressure side (PS) for each case and turbulent reattachment is observed. A separation is observed on the suction side (SS) as well with periodic reattachment for low Reynolds number case and reattachment for the high Reynolds number case. Eddies detachment at the trailing edge (TE) produces acoustic waves propagating upstream. These waves are blocked for high Mach number cases, the higher ones showing a choked passage. This behavior impacts separation and transition over both sides of the blade. The boundary layer (BL) state was characterized with statistics and integral parameters, revealing that the shock prevent separation in the low Reynolds number case.

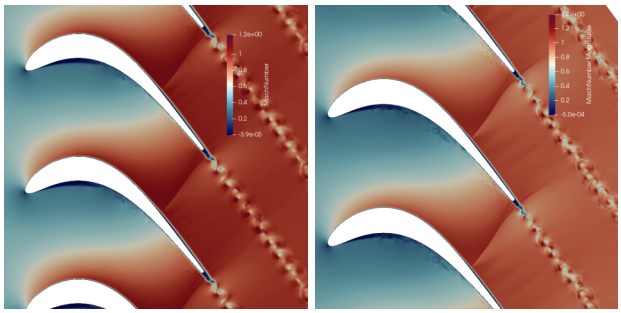

(a) (b)

Figure 3: Mach number contours for $\mathrm{Re}_{s,\mathrm{out}} = 70 \times 10^3$ and $M_{s,\mathrm{out}} = 0.95$ (a) and $\mathrm{Re}_{s,\mathrm{out}} = 120 \times 10^3$ and $M_{s,\mathrm{out}} = 0.96$ (b).

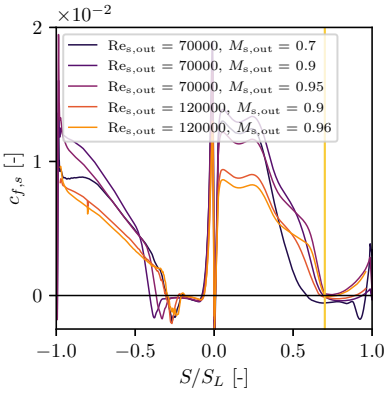

Figure 4: Skin friction distributions along blade PS and SS for $\mathrm{Re}_{s,\mathrm{out}} = 70 \times 10^3$, 120×10^3 and $M_{s,\mathrm{out}} = 0.7$,0.9,0.95 resp. 0.96.

REFERENCES

[1]Hillewaert, Koen: *Development of the discontinuous Galerkin method for high resolution, large scale CFD and acoustics in industrial geometries.* Université catholique de Louvain (2013).

[2]Carton De Wiart, Corentin: *Towards a Discontinuous Galerkin Solver for Scale-resolving Simulations of Moderate Reynolds Number Flows, and Application to Industrial Cases.* Université catholique de Louvain (2014).

[3]Loris Simonassi et al.: An experimental test case for transonic low-pressure turbines - part I : Rig Design, instrumentation and experimental methodology. In: *Volume 10B : Turbomachinery - Axial Flow Turbine Aerodynamics ; Deposition, Erosion, Fouling, and Icing ; Radial Turbomachinery Aerodynamics (2022).*

[4]Loris Simonassi et al.: An experimental test case for transonic low-pressure turbines - part 2 : Cascade aerodynamics at on- and off-design Reynolds and Mach numbers. In: *Volume 10B : Turbomachinery - Axial Flow Turbine Aerodynamics ; Deposition, Erosion, Fouling, and Icing ; Radial Turbomachinery Aerodynamics (2022).*

[5]C. Geuzaine and J.-F. Remacle.: Gmsh: a three-dimensional finite element mesh generator with built-in pre- and post-processing facilities. International Journal for Numerical Methods in Engineering 79(11), pp. 1309-1331 (2009).

WORKSHOP
Direct and Large-Eddy Simulation 14
April 10-12 2024, Erlangen, Germany

LAGRANGIAN FDF MODELING OF NANOPARTICLE SYNTHESIS IN TURBULENT SPRAY FLAMES

S.-J. Baik[1,2], A. Karimi Noughabi[1], I. Wlokas[1,2], A. Kempf[1,2]
[1]Chair of Fluid Dynamics, Institute for Energy and Materials Processes (EMPI),
University of Duisburg–Essen, Germany
[2]Center for Nanointegration Duisburg-Essen (CENIDE), University of Duisburg–Essen, Germany
seung.baik@uni-due.de

INTRODUCTION

Gas-phase nanoparticle synthesis is a popular method for producing powders with diverse compositions and size properties. Flames are a stable source of thermal conditions for nanoparticle formation, making flame-based methods the norm in the production of nanoparticles. At the laboratory scale, nanoparticle synthesis is mostly laminar with moderate Reynolds numbers and low pressure. However, achieving these conditions in pilot-scale operations can be challenging, and turbulent flows are expected. The resulting nanoparticles are impacted not only by coagulation and sintering but also by turbulence's effects on local particle number concentration and morphology.

The present study discusses the numerical modeling of the spray flame synthesis of iron oxide nanoparticles in the SpraySyn burner [1] using the Lagrangian filtered probability density function (FDF) method in large eddy simulation (LES). The aim is to compare the results of this LES-FDF approach with conventional simulations, evaluating the impact of fine structure on nanoparticle synthesis.

NUMERICAL METHOD

This investigation utilizes LES to address the low-Mach formulation of the Favre-filtered Navier-Stokes equation. Large eddies are resolved, and subgrid turbulence is modeled. Primary and secondary breakup processes of the spray are assumed near the burner surface, representing droplets as Lagrangian spherical particles. Gas-phase combustion is modeled using the Premixed Flamelet Generated Manifold (PFGM) approach [2], involving computing flamelets in advance with the Cantera library. The results are organized into a manifold accessed by a progress variable and two mixture fractions. The study employs a combined reaction mechanism for iron compounds and a surrogate mechanism for the solvent mixture (ethanol/2EHA). The surrogate mechanism is formulated by combining a lumped fuel pyrolysis model with a C2 reaction mechanism, as described by Nanjaiah [3]. This formulation results in a comprehensive reaction scheme comprising 59 species and 294 reactions. Estimation of iron oxide nanoparticle formation and growth relies on the sectional approach, as proposed by Gelbard [4]. This method discretizes the particle property space into N_S sections, with each section representing a particle number concentration Q_k associated with a specific particle size v_k. The nucleation source term is assumed to impact only the first section, where monomer particles form from the gas phase. Subsequently, particles are growing through coagulation with particles from both the same or other sections. In this study, the nanoparticle sections are represented by the transport of the filtered mass density function (FMDF) F rather than the conventional Eulerian way. The transport equation of FMDF for nanoparticle sections can be derived as:

$$\frac{\partial}{\partial t}F + \frac{\partial}{\partial x_i}\widetilde{u}_i F = -\frac{\partial}{\partial x_i}([\overline{u_i|\Psi} - \widetilde{u}_i]F) + \frac{\partial}{\partial \psi_Q}\left[\overline{\frac{1}{\rho}\frac{\partial J_i^Q}{\partial x_i}\middle|\Psi}\, F\right] - \frac{\partial}{\partial \psi_Q} S_Q F \quad (1)$$

Where ψ_Q, J_i^Q, and S_Q denote particle number concentration (Q) sample space vector, the diffusive flux of component Q, and the source term of component Q respectively. The transport equation (1) of FMDF is solved by stochastic Lagrangian particles with IEM (Interaction by Exchange with the Mean) mixing model which represents conditional subgrid diffusion effect. The mixing constant C_m for the nanoparticle subgrid interaction (IEM mixing) is estimated based on highly resolved simulation data [5] as shown in Fig. 1. The value of C_m is smaller for heavier nanoparticles, indicating that the conventional C_m typically used for the gas phase is not applicable for nanoparticle synthesis.

EXPERIMENTAL AND NUMERICAL SETUP

The SpraySyn burner is composed of a slender tube ($D_{in/out} = 0.4/0.7$ mm) for the precursor solution and a nozzle for the dispersion gas ($D = 1.5$ mm), followed by a broad sinter matrix ($D = 70$ mm) that provides hot pilot flame products and sheath gas. The precursor solution consists of 0.05 ml of iron(III)-nitrate nonahydrate per liter of a mixture of ethanol and 2-ethyl hexanoic acid and is injected at a volume flow rate of 2 ml/min at ambient pressure. For further details on the SpraySyn burner, the previous experiment works [1, 6] should be referred to.

The numerical simulations were carried out utilizing the large eddy simulation (LES) code, PsiPhi [7], which has been successfully validated in various LES studies. The computational domain 120x35x35 mm^3 was used for the simulations, consisting of a cartesian grid with an equidistant spacing of

Δ =0.5 mm and a total of 240x70x70 grid nodes, comprising approximately 1.17 million cells. All simulations used 24 sections. Around 2.1M stochastic particles are used and the simulation requires approximately 57.6K core hours.

RESULTS

As depicted in Fig. 2 (top), the mean values of nanoparticle sections were determined by averaging over all stochastic particles within each LES cell. Figure 3 shows a comparison between the mass-weighted particle size distribution obtained from the simulations with various mixing constants, and assumed normalized particle number distributions based on measured (PMS [6]) count median diameters and geometric standard deviation at the different heights above the burner. It is important to emphasize that the simulations show wider size distributions than the self-preserving distribution expected in a perfectly homogeneous scenario. This observation is expected, given the notable inhomogeneity and fluctuations in the scalar fields caused by turbulence and turbulent mixing as shown in Fig. 3.

ACKNOWLEDGMENTS

The authors gratefully acknowledge the financial support by DFG in the scope of SPP 1980 (project No. 375220870 and 375857243).

REFERENCES

[1]Schneider, F., Suleiman, S., Menser, J., Borukhovich, E., Wlokas, I., Kempf, A., Wiggers, H., Schulz, C., *Rev. Sci. Instrum.*, (2019).
[2]J. A. van Oijen, L. P. H. de Goey, *Combust. Sci. Technol.*, (2000).
[3]M. Nanjaiah, S.-J. Baik, B. Kunstmann, M. Kohns, H. Hasse, A. Kempf, I. Wlokas, *11th European Combustion Meeting*, (2023).
[4]F. Gelbard, Y. Tambour, J. H. Seinfeld, *J. Colloid Interface Sci.*, (1980).
[5]S.-J. Baik, P. Wollny, M. Nanjaiah, I. Wlokas, A. Kempf, *Appl. Energy Combust. Sci.*, (2023).
[6]M. Nanjaiah, I. Skenderovic, T. Rosenberger, F. Kunze, I. Wlokas, F. E. Kruis, H. Wiggers, C. Schulz, *J. Aerosol Sci.*, (2021).
[7]Proch, F., Kempf, A.M., *Comb. Flame*, **161**, 2627–2646 (2014).

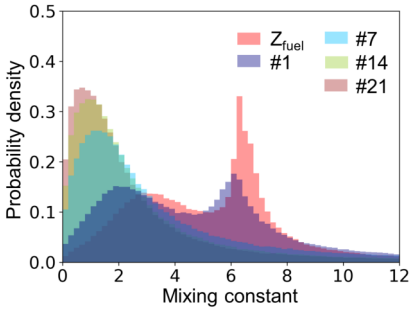

Figure 1: The distribution of the estimated mixing constant, obtained through artificial filtering from highly resolved simulation data [5], is presented for particles with diameters of 0.45 nm (#1), 1.46 nm (#7), 5.75 nm (#14), 22.6 nm (#21), and the fuel mixture fraction (Z_{fuel}).

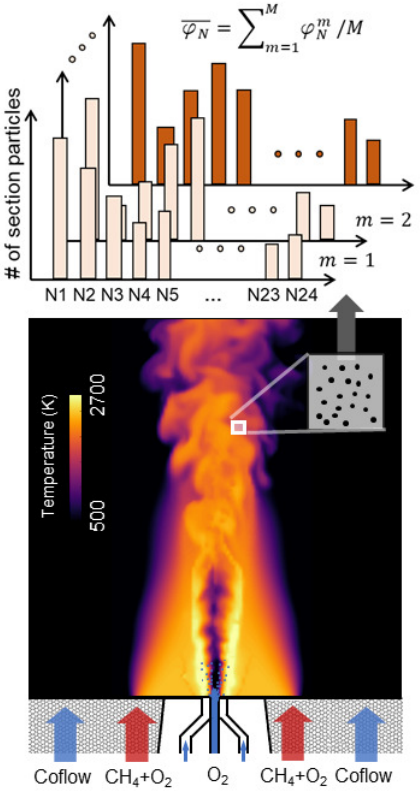

Figure 2: A schematic drawing of the burner inlet and instantaneous gas temperature (bottom), and the procedure of constructing the mean particle number concentration of each section from stochastic particles in a cell (top).

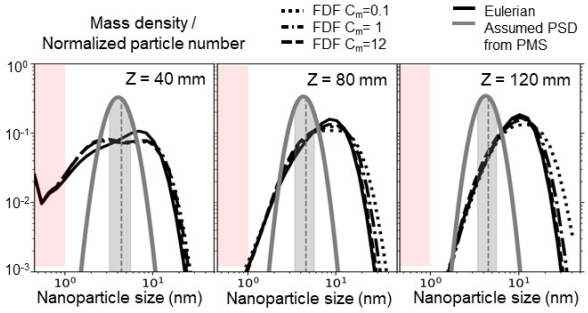

Figure 3: Comparison between the particle size distribution (mass-weighted) obtained from the simulations, and assumed distributions (normalized particles number) based on measured count median diameters and geometric standard deviation (PMS) [6] at the different heights above the burner, along the centerline of the flame. The vertical line and grey filled area indicate count median diameters and geometric standard deviation from the experiment respectively.

SESSION: Wall modelling

Thursday, April 11, 2024

14:50- 16:05

WORKSHOP
Direct and Large-Eddy Simulation 14
April 10-12 2024, Erlangen, Germany

THERMAL DIFFUSIVITY WALL-FUNCTION IN SIMULATIONS OF TURBULENT CHANNEL FLOW WITH DROPLET CONDENSATION

P. Bahavar[1], **C. Wagner**[1,2]
[1]Institute of Aerodynamics and Flow Technology
German Aerospace Center (DLR)
[2]Institute for Thermo- and Fluid Dynamics
Technische Universität Ilmenau
philipp.bahavar@dlr.de

INTRODUCTION

The latent heat of the phase transition provides an intrinsic link between heat and mass transfer in flows with condensation. In many of these flows, from heat exchangers to large-scale atmospheric convection, the heat transfer rates are modified due to phase change effects. In an automotive context, the accurate prediction of dropwise surface condensation is necessary to ensure the reliability of the sensors used by driver support systems.

However, including especially dropwise condensation in numerical flow simulations remains challenging, with insufficient accuracy in simplified models on one end of the spectrum [1], and high computational costs in fully resolved direct numerical simulations (DNS) on the other end [2].

In this work, we investigate a condensation wall model using a scaled thermal diffusivity regarding its predictive capabilities in DNS of turbulent channel flow in comparison to the super-droplet approach recently published in [3].

NUMERICAL SETUP

Turbulent flow through a vertical, differentially heated channel is described via the incompressible Navier–Stokes equations,

$$\nabla \cdot \boldsymbol{u} = 0, \tag{1}$$

$$\frac{\partial \boldsymbol{u}}{\partial t} + (\boldsymbol{u} \cdot \nabla)\boldsymbol{u} = -\frac{1}{\rho}\nabla p + \nu \nabla^2 \boldsymbol{u} + \boldsymbol{B}. \tag{2}$$

The Boussinesq approximation is employed to include buoyancy as a function of both temperature T and vapor concentration c,

$$\boldsymbol{B} = -\beta_T (T - T\_ref)\, \boldsymbol{g} - \beta_c (c - c\_ref)\, \boldsymbol{g}, \tag{3}$$

where β is the expansion coefficient of the fluid around the reference values, and $\boldsymbol{g}$ is the gravitational acceleration. Coupled convection–diffusion equations describe the active scalars,

$$\frac{\partial T}{\partial t} = \kappa \nabla^2 T - \boldsymbol{u} \cdot \nabla T + S_{PT,T} \tag{4}$$

$$\frac{\partial c}{\partial t} = D \nabla^2 c - \boldsymbol{u} \cdot \nabla c + S_{PT,c} \tag{5}$$

with the thermal diffusivity κ, the binary mass diffusion coefficient D, and the phase change source terms S_{PT} to account for the change in vapor concentration due to condensation, and the associated absorption or release of latent heat. Condensation is triggered on a cell-by-cell basis depending on local oversaturation, and treated as an instantaneous process.

The investigation domain is a channel with half-height δ and length $6\pi\delta$, set up in an inlet–outlet configuration with flow along the direction of gravity. The spanwise direction is periodic, while no-slip and impermeability conditions are applied to the wall, along with fixed temperatures. One wall is cooled with respect to the inlet temperature of the fluid, $T_c < T_{in}$, while $T_h = T_{in}$ ensures that no heat transfer occurs at the heated wall. The bulk velocity u_b is chosen to give $Re = u_b \delta / \nu = 2000$, and a Richardson number of $Ri = 0.01$. The working fluid is humid air, with $Pr = 0.73$ and $Sc = 0.65$.

The DNS is performed using a custom solver implemented in OpenFOAM, with second-order central differencing for the spatial discretization, a second-order accurate explicit leapfrog-Euler time integrations scheme, and the projection method for pressure–velocity coupling [4].

DROPLET-INDUCED HEAT TRANSFER ENHANCEMENT

Based on average condensation rates at the cooled surface, the locally available condensate mass can be extrapolated across the time scale necessary to grow macroscopic droplets. Since the resolution requirements for DNS including droplets spanning a realistic size distribution incurs prohibitive computational costs when investigating larger geometries, the condensate is instead consolidated into super-droplets [5] of a pre-determined length scale given by the mean droplet height $\langle h \rangle$, comparable to the turbulent scales [3]. These super-droplets are then included into the simulation as static wall deformations, and their effect on the flow throughout the channel recorded. Based on the bulk temperature of the fluid at the channel outlet, the enhancement of the total heat flux at the cooled wall can be calculated.

As the increase of the heat transfer originates from the wall-near modifications introduced by the droplets, an alternative approach to capturing the effect is to directly alter the thermal properties of the fluid close to the wall. For the condensation wall model, we set

$$\kappa = \begin{cases} f \cdot \kappa_0 & \text{for } y^+ \leq \langle h^+ \rangle \\ \kappa_0 \left(1 + (f-1)\, \exp\left(-5 y^+ / h^+\right)\right) & \text{else,} \end{cases} \tag{6}$$

which blends the scaled value $f \cdot \kappa_0$ for $y^+ \leq \langle h^+$ with the original value κ_0 using a steep exponential transition.

The value of the scaling factor f was calibrated using the DNS with condensate super-droplets with $\langle h^+ \rangle = 6.5$ to achieve a matching bulk temperature evolution. Figure 1 shows the dimensionless bulk temperature $\theta = (T - T_c) / (T_{in} - T_c)$ along the streamwise length of the channel. The successful calibration of the scaling factor leads to an adequate match in temperature profiles, capturing the enhancement of the heat transfer obtained from the DNS with super-droplets. However, the resulting profile is more shallow near the inlet and steeper near the outlet in comparison.

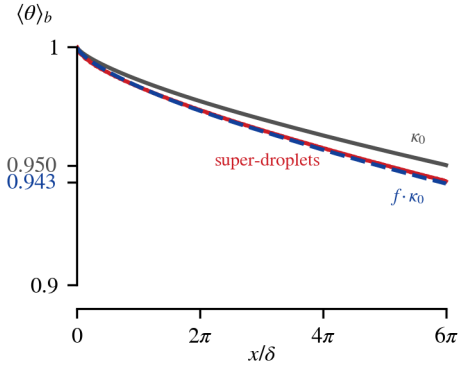

Figure 1: Streamwise profiles of the bulk temperature θ_b for the DNS with unscaled κ_0, scaled κ, and super-droplets.

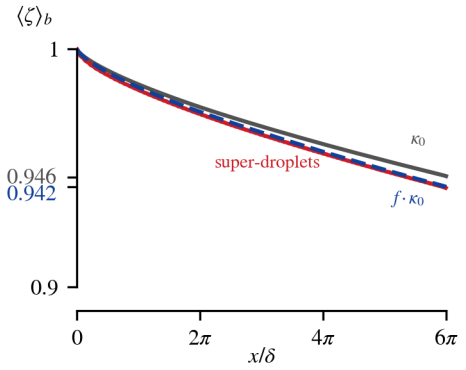

Figure 2: Streamwise profiles of the bulk humidity ζ_b for the DNS with unscaled κ_0, scaled κ, and super-droplets.

Similarly to the bulk temperature, the averaged dimensionless bulk humidity $\zeta = (c - c_{sat}(T_c)) / (c_{in} - c_{sat}(T_c))$ of the fluid can be compared across the three different simulations. Figure 2 shows the corresponding profiles along the channel. Although the scaling factor f was calibrated using only the bulk temperature, the predicted bulk humidity matches the result of the DNS with super-droplets, thus capturing the enhanced mass transfer caused by the droplets on the surface. Again, the profile progresses more shallow near the inlet and steeper near the outlet compared to the super-droplet DNS, mirroring the behavior of the bulk temperature.

To further investigate the different mechanisms by which the flow through the channel is influenced by the wall model as opposed to the super-droplets, we evaluate the wall-normal profile of the turbulent kinetic energy k. Comparing these

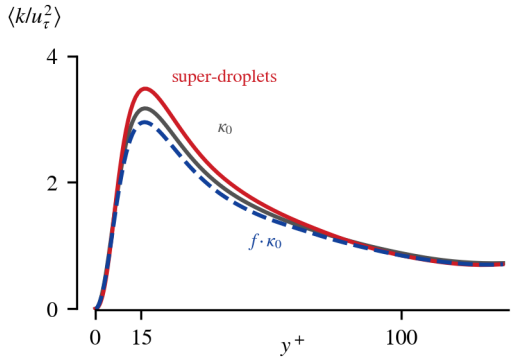

Figure 3: Wall-normal profiles of the turbulent kinetic energy k for the DNS with unscaled κ_0, scaled κ, and super-droplets.

profiles shows that turbulence is enhanced by the presence of the super-droplets. The surface deformations at the wall present obstacles to the flow and induce both wall-normal and spanwise flow, contributing to additional turbulent mixing and thereby increasing the heat transfer at the cooled surface. In contrast, scaling κ causes lower temperatures near the wall without introducing fluctuations, leading to increased aiding buoyancy and consequently attenuated turbulence [6].

CONCLUSION

The results from the DNS with a condensation wall model based on scaling the thermal diffusivity near the channel wall show that because of the strong connection between heat and mass transfer in flows with condensation, calibration with respect to the bulk temperature is sufficient to accurately predict the bulk humidity. However, the resulting flow fields are fundamentally different, underlining the necessity to account for the direct interaction between fluid flow and droplet surfaces to ensure accurate simulations of flows with dropwise surface condensation.

REFERENCES

[1]Leriche, M., Roessner, W., Reister, H. and Weigand, B. : Numerical Investigation of Droplets Condensation on a Windshield: Prediction of Fogging Behavior, *SAE Technical Paper* (2015)

[2]Kuerten, J. G. M : Point-Particle DNS and LES of Particle-Laden Turbulent flow - a state-of-the-art review, *Flow, Turbulence and Combustion*, **97**, 3, 689–713

[3]Bahavar, P. and Wagner, C. : Sessile super-droplets as quasi-static wall deformations in direct numerical simulation of turbulent channel flow, *Computers & Fluids*, **269**, 106135 (2024).

[4]Kath, C. and Wagner, C. : Highly Resolved Simulations of Turbulent Mixed Convection in a Vertical Plane Channel, *Notes on Numerical Fluid Mechanics and Multidisciplinary Design*, **132**, 515–524 (2016)

[5]Shima, S., Kusano, K., Kawano, A., Sugiyama, T. and Kawahara, S. : The super-droplet method for the numerical simulation of clouds and precipitation: a particle-based and probabilistic microphysics model coupled with a non-hydrostatic model, *Q.J.R. Meteorol. Soc.*, **135**, 1307–1320 (2009).

[6]Kasagi, N. and Nishimura, M. : Direct numerical simulation of combined forced and natural turbulent convection in a vertical plane channel, *Int. Journal of Heat and Fluid Flow*, **18**, 1 88–99 (1997).

WORKSHOP
Direct and Large-Eddy Simulation 14
April 10th-12th 2024, Erlangen, Germany

Formulation of an algebraic Wall-Modelled LES Formulation Suitable for Laminar-Turbulent Transition Prediction

F. Menter[1*], A. Stabnikov[2], A. Matushenko[2], E. Guseva[1] and A. Garbaruk[2]
[1] ANSYS Germany GmbH
[2] St. Petersburg Polytechnic University, 29, Polytechnicheskaya Str., 195251, St.-Petersburg, Russia
[1*] florian.menter@ansys.com

INTRODUCTION

The current group has recently proposed an algebraic hybrid RANS-LES Wall-Modeled LES (aWMLES) formulation which allows to combine a near-wall Prandtl mixing length model with any algebraic LES mode [1]. LES models using this near wall 'extension' enable an integration of the Navier-Stokes equations through the viscous sublayer without providing the stringent mesh resolution required for a Wall-Resolved LES (WRLES) on the wall-parallel directions.

In principle, the RANS treatment in the inner layer is beneficial in almost all scenarios and helps to reduce mesh sensitivities of LES for wall bounded flows, making it an attractive default for industrial codes. The main area, where the near-wall RANS layer can have a negative impact on the simulation is however for flows with laminar-turbulent transition. In such scenarios, the RANS model can be activated in the laminar boundary layer upstream of transition and thereby prevent the formation of a correct laminar boundary layer. This in turn can have a strong and negative effect on the transition dynamics (onset, length etc.).

Considering that the WMLES formulation is algebraic, it would be desirable to identify an indicator which would allow to deactivate the RANS model in the laminar boundary layer, without any negative impact on the fully turbulent model characteristics. Several such indicators were tested, but none could be identified which satisfies both these requirements. This leaves two options. The first would be to use non-local indicators connecting the outer part of the boundary layer with the inner RANS layer. However, such an approach is not attractive from an implementation and HPC performance standpoint, as it introduces non-local operations and parallel data exchange into the solver.

The alternative is to use a transport equation to transport the information of the status of the outer layer into the inner layer RANS region. This approach is taken in this paper.

aWMLES – Basic Formulation

The aWMLES formulation uses a blend of a RANS and an LES model $\nu_t = f_{sw}\nu_{t,RANS} + (1 - f_{sw})\nu_{t,LES}$, where $\nu_{t,LES}$ can be any algebraic LES model. The RANS model is given by $\nu_{t,RANS} = f_{wd}(0.41d_w)^2 S$, where d_w is the wall distance and S is the strain rate. The two functions involved are the switching function f_{sw} and the sublayer damping function f_{wd}. The switching function $f_{sw} = e^{-\left(\frac{C_{w1}d_w}{h_{max}}\right)^{C_{w2}}}$ (h_{max} is the generalized maximum edge length of the cell) has two parameters $C_{w1} = 2.45$ and $C_{w2} = 2.0$, which have been optimized to reproduce the correct logarithmic layer (Fig.1).

To prevent activating of the RANS layer in the laminar part of transitional flows, one could in principle ensure using a mesh that is fine enough to push the RANS model into the sublayer. The mesh requirement for this is $h_{max} < \frac{C}{\sqrt{Re_\delta}}\delta$, where δ is the boundary layer thickness and C is a coefficient which depends on the model coefficients. Such fine meshes can typically not be achieved and one needs to find a way to turn off the RANS model in the laminar region. This indicator (I_{LT}) can then be used to multiply the RANS part of the aWMLES: $\nu_t = \nu_{t,RANS} f_{sw} I_{LT} + \nu_{t,LES}(1 - f_{sw})$. The indicator is based on two elements. The first is the primary indicator, which can distinguish between laminar and turbulence flow in the outer part of the boundary layer. Two such measures are tested. The first is the Vortex Tilting Measure (VTM) parameter which detects three-dimensional disturbances of the flow: $VTM = \frac{\sqrt{6}\cdot|\varepsilon_{ijk}S_{ji}\Omega_j\Omega_k|}{(\Omega_l\Omega_l\cdot\sqrt{3\cdot S_{ij}S_{ij} - S_{ii}S_{jj}})}$, where S_{ij} components of the strain rate tensor and Ω_i components of the vorticity vector. For the second version (aWM-σ-TVR) the turbulent viscosity ratio in the 'LES' region as computed

by the σ-LES model is used: $TVR = \frac{(C_\sigma h_{max})^2 D_\sigma}{\nu}$, where D_σ is the differential operator and $C_\sigma = 1.35$ of the σ model [2] and ν – molecular kinematic viscosity. While both indicators can distinguish between laminar (I_{LT} zero) and turbulent flow (I_{LT} non-zero) in outer part of the boundary layer, they both go to zero in the RANS regions of high Reynolds number flows and thereby switch to 'laminar'. A method is therefore required to 'transport' the information from the LES to the RANS region. This is achieved through a transport equation: $\frac{\partial \rho\phi}{\partial t} + \frac{\partial}{\partial x_i}\left(\rho u_i \phi - 10(\nu_t + \nu)\frac{\partial \rho\phi}{\partial x_i}\right) = \left(arg_\phi - \phi\right)(1.0 - f_{sw,\phi})$S. Details of that formulation will be given in the final paper, but the main characteristic is that the large diffusion term is used to transfer the outer boundary layer information to the RANS layer.

Test Cases and Results

Three cases are considered. The first one is fully turbulent periodic channel flow at two Reynolds numbers based on the friction velocity, $Re_\tau = 395$ and $Re_\tau = 18\,000$. This is the basic testcase set for the aWM-LES models and needs to remain unchanged. The results for the periodic channel flow (Fig 1) illustrate that the LT indicator does not negatively affect the fully turbulent solution of the baseline aWM-σ model.

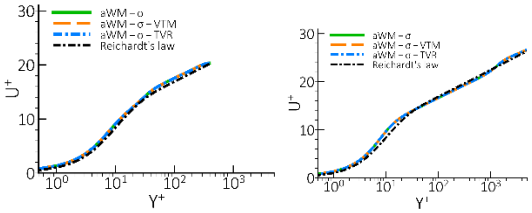

Figure 1. Velocity profiles in log-scale for aWM-σ model with activated and deactivated laminar turbulent indicator for the periodic channel flow at $Re_\tau = 395$ (left) and $Re_\tau = 18\,000$ (right).

The other two cases represent flows with separation induced transition, where so-called laminar separation bubble is formed. In the experiments of Hultgren and Volino [3], a flat plate boundary layer was subjected to a streamwise pressure gradient causing laminar separation and turbulent reattachment. Activating the indicator equation results in the proper prediction of the laminar flow and significantly improves transition behavior in the Volino case (Fig 2.) for both VTM and TVR LT indicator. The baseline aWM-σ model fails to predict laminar boundary layer and delays reattachment of the laminar separation bubble due to 'RANS' mesh resolution.

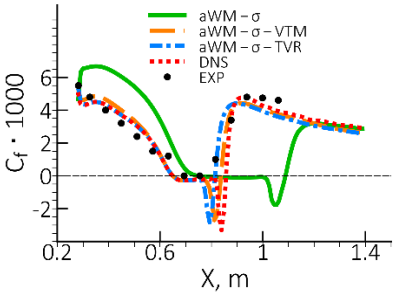

Figure 2. Skin friction coefficient for the aWM-σ model with activated and deactivated laminar turbulent indicator for the Volino

The final testcase is the flow around an Eppler-387 airfoil at $Re_c = 10^5$ and zero angle of attack. The considered flow regime is characterized by large laminar separation bubble (~$0.5c$) on the upper side and laminar boundary layer along the lower side of the airfoil. For all the cases the 'RANS' mesh resolution is used in laminar part of the flow.

For this case aWM-σ model fails to predict laminar boundary especially on the lower side of the airfoil where boundary layer should be laminar (see Fig. 3). The use of the VTM based LTT indicator improves prediction of the laminar flow, but the solution has some region of the disturbed laminar boundary layer in the lower side of the airfoil. The aWM-σ-TVR predicts proper laminar boundary layer and provides slightly better agreement with the experimental pressure distribution in the laminar separation bubble ($0.5 < x/c < 0.9$).

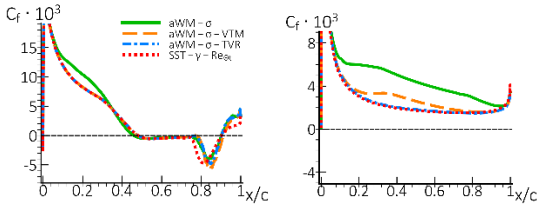

Figure 3. Skin friction coefficient on the upper (left) and lower (right) side of the airfoil for the aWM-σ model with activated and deactivated laminar turbulent indicator for the Eppler-387 airfoil.

REFERENCES

[1] Menter F. et al. A Family of Wall-Modeled Large Eddy Simulation Formulations // 14th International ERCOFTAC Symposium on Engineering Turbulence Modelling and Measurements. 2023, Barcelona, Spain

[2] Nicoud, F., Toda, H.B., Cabrit, O., Bose, S., Lee, J.: Using singular values to build a subgrid-scale model for large eddy simulations. Physics of Fluids. 23, (2011)

[3] Volino R.J., Hultgren L.S. Measurements in Separated and Transitional Boundary Layers Under Low-Pressure Turbine Airfoil Conditions // Journal of Turbomachinery, Vol. 123, 2001. pp. 189–197

WORKSHOP
Direct and Large-Eddy Simulation 14
April 10-12 2024, Erlangen, Germany

TOWARDS INVESTIGATION OF AIRFOILS NEAR STALL USING SPECTRAL ELEMENT-BASED WALL-MODELED LARGE-EDDY SIMULATION

T. Mukha[1], **P. Schlatter**[2], **M. Parsani**[1]
[1]Computer, Electrical and Mathematical Sciences and Engineering Division, King Abdullah University of Science and Technology (KAUST), Kingdom of Saudi Arabia
[2]Institute of Fluid Mechanics (LSTM), Friedrich–Alexander–Universität (FAU) Erlangen–Nürnberg, Germany
timofey.mukha@kaust.edu.sa, philipp.schlatter@fau.de, matteo.parsani@kaust.edu.sa

INTRODUCTION

In this work, we present results from high-order simulations of turbulent boundary layers (TBLs) using wall-modeled LES (WMLES). This contribution is a continuation of the work previously presented at DLES13, where we explored the selection of boundary conditions suitable for WMLES conducted using the spectral-element method (SEM) [3]. Here, we demonstrate state-of-the-art accuracy in simulations of flat-plate turbulent boundary layers using SEM-based WMLES, which represents an important milestone for this simulation approach. As the next step, we consider the flow around the Aerospatiale A-airfoil at a near-stall condition. At this stage, an a priori analysis of WMLES accuracy has been conducted, with a simulation campaign currently ongoing.

COMPUTATIONAL METHODOLOGY

The simulations are performed using Nek5000, which is a solver for the incompressible Navier-Stokes equations, based on the spectral-element method. Here, we formally solve the spatially filtered form of the equations, augmented by the Vreman subgrid scale model [9] for closure. Algebraic wall stress modeling based on Spalding's law [6] is applied, in order to avoid capturing the inner layer dynamics.

SIMULATIONS OF A FLAT PLATE BOUNDARY LAYER

The first presented case is that of a zero-pressure-gradient turbulent boundary layer (TBL) developing on a flat plate. The inflow conditions are generated using a precursor simulation with the pseudo-spectral code SIMSON [1]. The inflow Reynolds number is $Re_\theta^{in} = 790$, and the data is interpolated onto the WMLES meshes as a pre-processing step. During the WMLES, the inflow data is read from disc, and cubic temporal interpolation is used to get values at any given time within the range of the dataset. The sampling point distance for the wall model is set to $0.2\delta_{99}(x)$, with the distribution of the thickness pre-computed using a power-law estimate. The order of the polynomial basis is set to 7.

The mesh size is adapted to follow the growth of the TBL in the wall-normal and streamwise direction, such that there are always ≈ 4 elements per $\delta_{99}(x)$. For the spanwise direction, the resolution is fixed, so that the mesh is structured. Simulations on 3 meshes (M1, M2, M3) are conducted corresponding to, respectively, 1, 2, and 4 elements per δ_{99} and the inflow.

The predicted skin friction coefficient is shown in Figure 1 together with reference data from DNS and wall-resolved LES found in the literature [2, 4, 5]. The dashed lines show relative errors with respect to the LES of Eitel-Amor et al. [2]. Improvement with spanwise mesh refinement is observed, with the results on the M3 mesh in excellent agreement with the reference data: The relative errors do not exceed 2%.

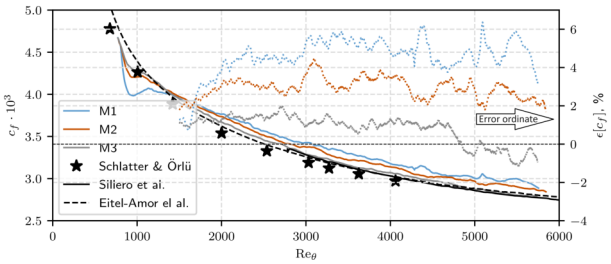

Figure 1: Obtained skin friction coefficient profiles, c_f, corresponding relative error curves (see ordinate axis on the right), $\epsilon[c_f]$, and reference data [2, 4, 5].

The mean velocity profiles in outer scaling are shown in Figure 2. Similar to c_f, the results improve with mesh refinement, and the M3 curves are very accurate, particularly at larger Re_θ. On the coarser grids, the WMLES profiles tend to over-predict the reference data over a portion of the outer layer. This is, in fact, the main cause of the corresponding over-prediction in the wall stress observed via the c_f curves.

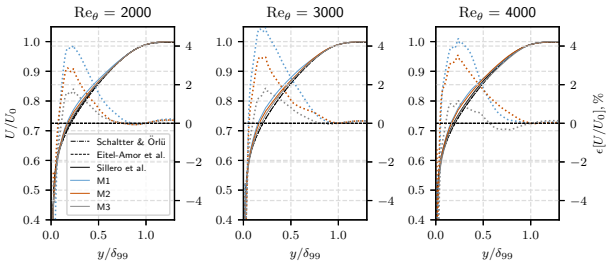

Figure 2: Outer-scaled mean streamwise velocity profiles, U/U_0, corresponding relative error curves, $\epsilon[U/U_0]$, and reference data [2, 4, 5].

SIMULATIONS OF AN AIRFOIL NEAR STALL

Following the setup of the wall-resolved LES in [8], we consider the Aerospatiale A-airfoil at the angle of attack 13.3°and cord Reynolds number $Re_c = 10^7$. The focus of the simulation is on the suction side of the foil, where the TBL experiences the effect of an adverse pressure gradient (APG). According to the reference data, the transition of the TBL occurs without a laminar separation bubble, and there is no (mean) separation in the region of the APG either. The case can therefore be considered somewhat easier to predict with WMLES compared to those with separation regions. The high Reynolds number also lends well to demonstrate the savings that can be achieved by WMLES. For reference, the wall resolved simulation in [8] requires a grid with 38 billion degrees of freedom.

We intend to adopt a similar meshing strategy as for the TBL, however the thickness of the boundary layer varies much stronger in the streamwise direction, compared to the flat plate case. The ratio of δ_{99} at the trailing edge and at $x/c = 0.1$ is ≈ 100. This entails that the spanwise resolution will have to be based on a compromise between the need to capture the transition of the TBL and limiting the anisotropy of the mesh downstream. This will likely prove to be biggest challenge in terms of the simulation setup. We may also consider using an unstructured quad mesh for the surface of the foil, which will allow to adapt the resolution in the spanwise direction at the cost of poorer numerical properties of the grid.

As a first step to evaluating the accuracy of WMLES for this flow, an a priori analysis is conducted based on the available LES data [8]. As demonstrated in Figure 3, Spalding's law can, in principle, give accurate stress predictions between $x/c \approx 0.2$ and $x/c \approx 0.8$. Further downstream the APG makes the log-law region very short and vertically shifts it downwards.

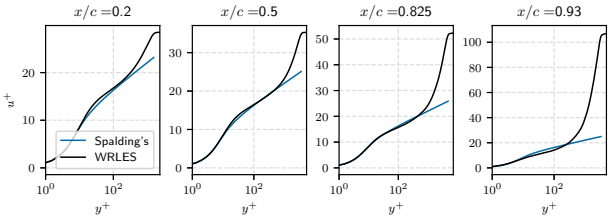

Figure 3: Inner-scaled velocity profiles on the suction side of the airfoil. The blue line shows the Spalding's law and black line the wall-resolved LES of Tamaki and Kawai [8].

In Figure 4, the relative error in the wall stress predicted by Spalding's law based on the reference LES data is shown. The accuracy is quite sensitive to the distance to the sampling point, and the results in the figure are for distance $\approx 0.1\delta_{99}$. In line with Figure 3, the predictions are within acceptable accuracy when the TBL is in a state close to the canonical flat-plate TBL. The poor predictions near the trailing edge are, perhaps, not of strong concern since the boundary layer growth is mainly determined by the APG in that region. However, the lack of accuracy near the transition region is an issue since poor prediction of c_f will entail an incorrect TBL thickness as it approaches the APG region, causing it to remain poor downstream. The reasoning here is based on the discussion in [7], where the integral momentum equation has been used to study the influence of c_f and the APG on the development of θ.

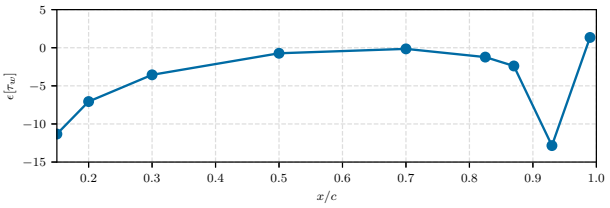

Figure 4: Relative error in the wall shear stress predicted by Spalding's law based on velocity profiles available in the LES database of Tamaki and Kawai [8].

CONCLUSIONS AND OUTLOOK

We present results from WMLES of two attached TBL flows, using an SEM-based solver, Nek5000. For the flat-plate TBL, results show excellent agreement with reference data at sufficient grid resolution. In light of its computational efficiency, this makes SEM a very strong candidate for high-order WMLES of flows at large Reynolds numbers. As the next step, we consider the Aerospatiale A-airfoil at a near-stall condition. Simulations are currently ongoing, and we are confident to have at least preliminary results at the time of the conference. A priori analysis shows that equilibrium wall models adequately predict the wall stress some distance away from the leading and trailing edges. At the same time, it is difficult to fulfill best-practice guidelines for WMLES mesh construction using a structured grid, and alternative meshing strategies are worth exploring. A successful WMLES of this case would be an important milestone towards simulating industrial flows. In particular, we are interested in applying the developed methodology to racing boat hydrofoils. In parallel, we are working on a GPU implementation of the wall models to further decrease the time-to-solution.

REFERENCES

[1]Chevalier, M., Schlatter, P., Lundbladh, A. and Henningson, D. S. : SIMSON: A pseudo-spectral solver for incompressible boundary layer flows, *TRITA-MEK 2007:07, Royal Institute of Technology, Sweden* (2007).

[2]Eitel-Amor, G., Örlü, R. and Schlatter P. : Simulation and validation of a spatially evolving turbulent boundary layer up to $Re_\theta = 8300$, *International Journal of Heat and Fluid Flow*, **47**, 57–69 (2014).

[3]Mukha, T., Brethouwer, G., and Schlatter, P. : Boundary conditions for wall-modelled large-eddy simulation using spectral element discretization, *Proc. of Direct and Large-Eddy Simulations 13, October 26-28, Udine, Italy*, (2022).

[4]Schlatter, P. and Örlü, R. : Assessment of direct numerical simulation data of turbulent boundary layers, *Journal of Fluid Mechanics*, **659**, 116–126 (2010).

[5]Sillero, J. A., Jiménez, J. and Moser R. D. : One-point statistics for turbulent wall-bounded flows at Reynolds numbers up to $\delta^+ \approx 2000$, *Physics of Fluids*, **25:10**, p. 105102 (2013).

[6]Spalding, D. B. : A single formula for the 'law of the wall', *Journal of Applied Mechanics*, **28:3**, 455–458 (1961).

[7]Tamaki, Y., Fukushima, Y. Kuya, Y. and Kawai, S. : Physics and modeling of trailing-edge stall phenomena for wall-modeled large-eddy simulation, *Physical Review Fluids*, **5:7**, 074602 (2020).

[8]Tamaki, Y., Kawai, S. : Wall-resolved large-eddy simulation of near-Stall airfoil flow at $Re_c = 10^7$, *AIAA Journal* **61:2**, 698–711 (2023).

[9]Vreman, A. W. : An eddy-viscosity subgrid-scale model for turbulent shear flow: Algebraic theory and applications, *Physics of Fluids*, **16:10**, 3670–3681 (2004).

WORKSHOP
Direct and Large-Eddy Simulation 14
April 10-12 2024, Erlangen, Germany

GALEXI: SCALE-RESOLVING SIMULATIONS OF COMPRESSIBLE TURBULENCE ON GPU-ACCELERATED SYSTEMS

Marius Kurz[1], **Daniel Kempf, Marcel Blind, Andrea Beck**
Institute of Aerodynamics and Gas Dynamics
University of Stuttgart, Germany
[1]marius.kurz@iag.uni-stuttgart.de

INTRODUCTION

The application of scale-resolving simulations such as LES and DNS is still elusive for many engineering applications due to the required computational effort and the limited computational resources. It was thoroughly demonstrated in the last decade that high-order numerical methods show significant advantages in terms of computational cost required for given accuracy for DNS and LES and that they can be implemented efficiently on traditional CPU-based system architectures. However, the improvements in performance for CPU-based systems has slowed down significantly over the last years. Consequently, more specialized architectures such as GPUs have become increasingly popular in the last decade as they still promise considerable performance improvements per generation and thus allow to tackle more complex flow cases, while also yielding better performance per invested amount of energy. However, CPU codes cannot be easily run on GPU hardware, since they exhibit a distinctly different architecture and require different programming languages. Hence, existing codebases have to be translated efficiently to GPU hardware, both in terms of implementation effort and computational performance. In this study, we demonstrate such an effort for GALEXI, a GPU-accelerated implementation of the FLEXI [1] solver. Hence, we demonstrate how an unstructured DG code can be implemented efficiently for GPU architectures and demonstrate that GALEXI is capable of tackling challenging large-scale problems with complex geometries by computing an LES of an OAT-T15A airfoil with shock buffeting inducing complex shock-turbulence interactions.

IMPLEMENTATION

GALEXI is a GPU implementation of the FLEXI code with the compute kernels implemented using the CUDA Fortran framework provided by Nvidia. Consequently, GALEXI also solves the compressible Navier–Stokes equations using the discontinuous Galerkin spectral Element Method (DGSEM). A split-flux approach [2] is used to counter aliasing errors in underresolved simulations and a shock-capturing scheme based on the blending approach by Hennemann *et al.* [3] is used to handle shocks within the domain. The parallelization of GALEXI is based on CUDA-aware MPI and employs the latency hiding strategy of the CPU baseline to overlap the necessary communication with local computations. The required compute kernels are implemented with respect to the following design principles:

- All routines called during time-stepping run on the GPU to avoid any data transfer to main memory.
- Order of computations are reorganized to allow for the maximum degree of parallelization at the cost of repeating computations in some places.
- Small, individual kernels are fused if this allows to perform more operations on the loaded amount of data.
- Kernels are organized in parallel streams to hide the starting latency and reduce the impact of tail effects.

Following these design principles allows to yield a scalable and efficient implementation of the described numerical methods, as is demonstrated in the following.

APPLICATION

In this study, the GALEXI code is applied to two different flow cases. First, the compressible Taylor–Green vortex (TGV) [4], which serves as a validation test case that is well examined in the literature. For the TGV case, a Cartesian mesh with periodic boundary conditions is initialized with analytically prescribed velocity fluctuations, which evolve into turbulent flow over time. In the compressible case, these fluctuations are set at transsonic and supersonic levels which then yields intricate shock-turbulence interactions constituting an excellent test case for compressible turbulence. Here, GALEXI shows good agreement with the references from the literature. Since the computational effort of this case can be easily scaled due to the Cartesian mesh, the TGV is also used for scaling tests to assess the scaling abilities of the code. For this, GALEXI was used to compute the compressible TGV with varying resolution (10^6 to 10^9 DOF) and using up to 128 A100 GPUs. The tests were performed on the HAWK-AI partition of the HAWK system at the HLRS in Stuttgart, which comprises a total of 24 GPU nodes each equipped with 8 Nvidia A100 GPUs, which yields a total of 192 A100 GPUs on the system. The Performance Index (PID) is used to quantify the performance of the code and measures the time it requires a single compute unit (a single CPU core or a single GPU) to update a single degree of freedom (DOF) for a single time stage of the integration scheme. The results in Fig. 1 show the results of the scaling tests for GALEXI (*left*) as well as for the basline CPU implementation FLEXI (*right*). The results

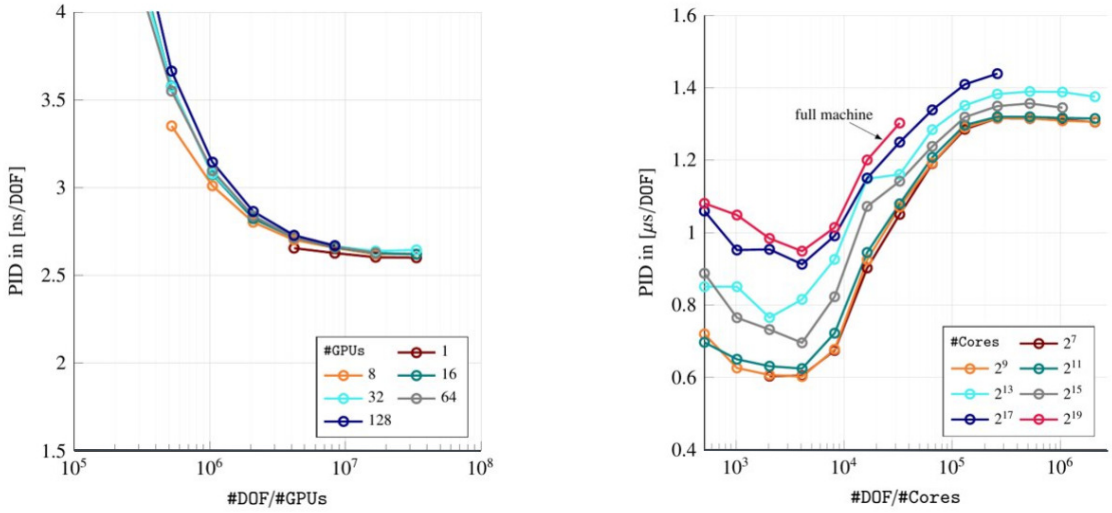

Figure 1: Scaling results for the GPU (*left*) and CPU (*right*) implementation. Please note that the y-axis is scaled differently with the PID in the GPU case given as nanoseconds per DOF and in the CPU case as microseconds per DOF.

show that using GALEXI, the computational power on a single A100 corresponds to the performance achieved on 256 to 512 CPU cores using the CPU implementation. Moreover, the results show almost perfect weak scaling at high loads (DOF per GPU) for up to 128 GPUs, while loads below 10^6 DOF per GPU cannot provide sufficient work for the GPUs causing a significant drop in performance. These results underline the excellent performance of the employed implementation strategy and the applied numerical methods.

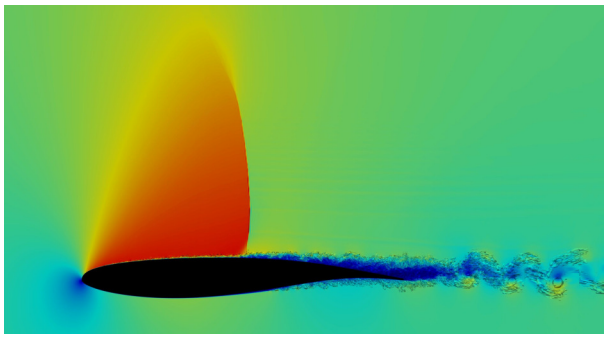

Figure 2: Instantaneous flow field around the OAT-T15A airfoil at transonic conditions showing the buffeting shock on the suction side.

In a second step, the validated code is applied to compute an LES of an OAT-T15A airfoil at transsonic conditions, where it exhibits a shock buffet on the suction side, as shown in Fig. 2. In this study is demonstrated that GALEXI can be applied to challenging computations of compressible turbulence with shock-turbulence interactions also for complex geometries, where unstructured meshes are highly beneficial. Moreover, it is shown that the application of GPUs can significantly accelerate the computation and improve the required Watt-to-solution considerably in comparison to the CPU implementation.

*

REFERENCES

[1] N. Krais, A. Beck, T. Bolemann, H. Frank, D. Flad, G. Gassner, F. Hindenlang, M. Hoffmann, T. Kuhn, M. Sonntag, and C.-D. Munz, "FLEXI: A high order discontinuous Galerkin framework for hyperbolic–parabolic conservation laws," *Computers & Mathematics with Applications*, vol. 81, pp. 186–219, 2021.

[2] G. J. Gassner, A. R. Winters, and D. A. Kopriva, "Split form nodal discontinuous Galerkin schemes with summation-by-parts property for the compressible Euler equations," *Journal of Computational Physics*, vol. 327, pp. 39–66, 2016.

[3] S. Hennemann, A. M. Rueda-Ramírez, F. J. Hindenlang, and G. J. Gassner, "A provably entropy stable subcell shock capturing approach for high order split form dg for the compressible euler equations," *Journal of Computational Physics*, vol. 426, p. 109935, 2021.

[4] J. R. Bull and A. Jameson, "Simulation of the compressible taylor green vortex using high-order flux reconstruction schemes," in *7th AIAA Theoretical Fluid Mechanics Conference*, p. 3210, 2014.

WORKSHOP
Direct and Large-Eddy Simulation 14
April 10-12 2024, Erlangen, Germany

ON THE WALL-MODELED LARGE EDDY SIMULATIONS OF THE WINDSOR BODY AT DIFFERENT YAW ANGLES

B. Eiximeno [1,2], I. Rodríguez [2], O. Lehmkuhl [1]
[1]Barcelona Supercomputing Center (BSC)
Barcelona, Spain
[2]Turbulence and Aerodynamics Research Group (TUAREG)
Universitat Politècnica de Catalunya (UPC) Terrassa, Spain
benet.eiximeno@bsc.es

INTRODUCTION

Wall-modeled large eddy simulations have been used successfully on industrial flows as an aircraft in landing conditions [1], however, the results submitted to AutoCFD3 [2] show that they are not popular yet for studies in the automotive industry. Among the 101 data entries in the workshop, only 8 studies, 4 of the Windsor body without wheels at 2.5° of yaw and 4 of the notchback configuration of the DrivAer, were performed employing wall-modeled large eddy simulations.

Be that as it may, Figure 1 shows that for the Windsor body case in the AutoCFD3 workshop, wall-modeled LES is the only methodology that contains the reference experimental value of the drag coefficient inside the 95% confidence interval of the data.

The Windsor body is a bluff body that mimics a simplified square-back car. As in any other square-back vehicle, e.g. sport utility vehicles (SUVs), buses, and trucks, the dominant contributor to the drag force is the forced separation at the abrupt rear end of the model [3]. This separation creates a recirculation area behind the vehicle, resulting in a powerful suction effect on its back face which is only predicted correctly by LES turbulence models.

Most of the studies in the literature about square-back vehicles are experiments focused on the characterization of the wake bi-stability for the case of an inlet flow without a yaw angle [3]. The few studies that analyze the flow at different yaw angles are experiments focused on drag reduction by modifying the rear-end edges. Furthermore, there are no studies that talk about the compressibility effects on the flow. Despite the typical Mach number in the automotive industry being below $M_0 < 0.2$, all the results submitted to AutoCFD3 were obtained under the incompressibility hypothesis and failed to predict the value for the lift coefficient of the Windsor body.

This work aims to present a full characterization of the turbulent flow in Windsor body using wall-modeled LES at several yaw angles and elucidate whether the differences with the experimens reported were due to local compressibility effects.

NUMERICAL METHODOLOGY

The filtered compressible and incompressible Navier-Stokes equations are numerically solved using SOD2D (Spectral high-Order coDe 2 solve partial Differential equations) [4], a low-

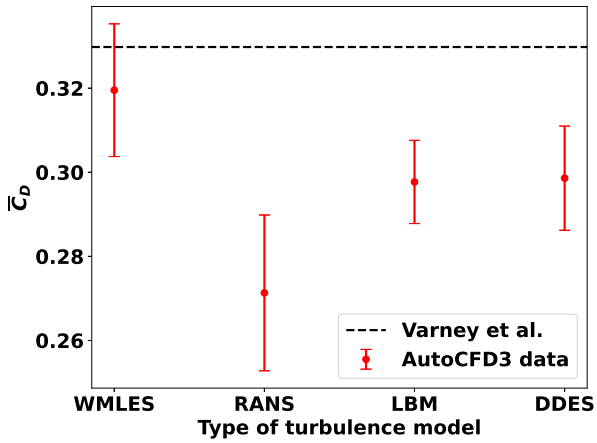

Figure 1: Drag coefficient (with the 95% confidence interval) of all the submissions for the Windsor body case of AutoCFD3 [2] ($\delta = 2.5°$) grouped according to the type of turbulence model

dissipation spectral element method (SEM) code. SOD2D is based on a spectral-element version of Galerkin's finite element-method continuous model with a modified version of Guermond's entropy viscosity stabilization [5]. The aliasing effects of the reduced order integration caused by employing SEM integration for convective terms are countered with the skew-symmetric splitting presented by Kennedy and Gruber [6]. In the case of the compressible solver, the time-advancement algorithm is based on an explicit fourth-order Runge-Kutta method. For the incompressible solver, an explicit second-order Adams-Bashforth for the convection terms and an implicit second-order Crank-Nicolson for the diffusion terms are used. Additionally in the incompressible case, the fractional step method is used to solve the coupled velocity pressure system, by means of a conjugate gradient solver as an iterative solver of the final linear system.

The chosen SGS viscosity model is the local formulation of the integral length-scale approximation (ILSA) as in Lehmkuhl et al. [7]. The near wall region is modeled using the Reichardt wall law [8] with an exchange location in the 5th node.

To study the turbulent flow topology different yaw angles

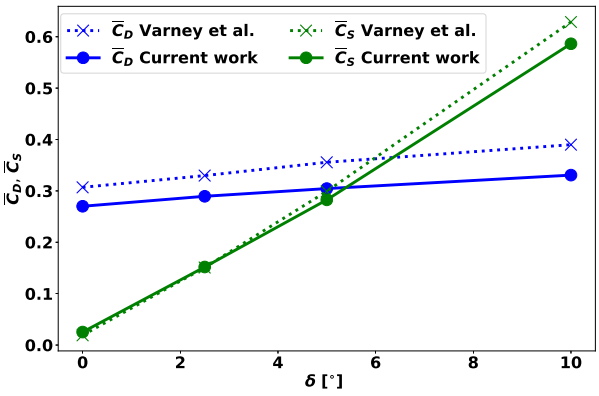

Figure 2: Comparison of the obtained drag $\overline{C}_D$ and side $\overline{C}_S$ force coefficients for all yaw angles with the experimental results from Varney et al. [9]

of $\delta = 0°, 2.5°, 5°, 10°$ at Reynolds number $Re = UL_{ref}/\nu = 2.9 \times 10^6$ are computed. Here the Reynolds number is defined in terms of the length of the model, L_{ref}. Additionally, in order to analyse the local compressibility effects, two additional numerical simulations are performed at yaw angle $\delta = 2.5°$ at $M_0 = 0.2$ and assuming incompressible flow.

Two domains are used in the present study. The first one, for the characterization of the yaw angle extends from $-4.5 \leq x/L_{ref} \leq 6.5$, $-2 \leq y/L_{ref} \leq 2$ and $0 \leq z/L_{ref} \leq 2.5$ with the nose of the car centered at the origin of the coordinates. The second domain, aimed to the study of the compressibility effects is equivalent to the wind tunnel used by Varney et al. [9]. The computational grids are made of 4th-order hexahedra. The grid used for the yaw angle characterization has 135.2 million grid points and the grid for the compressibility effects has 108.1 million grid points.

RESULTS

Figure 2 compares the obtained variation of the drag and side force coefficients with the yaw angle with the results from the experiments made by Varney et al. [9]. Both forces exhibit the same increasing trend as in the experiments, however, the drag values are slightly lower because the blockage ratio of the used computational domain is smaller than the one of the wind tunnel used by Varney et al. [9]. On the other hand, the lift force coefficient remains constant at $\overline{C}_L = -0.15$ at all yaw angles while its mean experimental value is $\overline{C}_L = -0.035$.

The drag and side force coefficients at $M_0 = 0.2$ exhibit similar behavior, but contrary to what happened for the incompressible cases, the lift force coefficient raises to $\overline{C}_L = -0.056$, which is more consistent with the experimental values. One of the possible causes can be attributed to the fact that in the areas where the flow is accelerated, as the beginning of the roof and the ground clearance zone, the local Mach number gets higher than $M = 0.3$, as can be seen in Figure 3. As a consequence, changes in the pressure distribution (not depicted here) are observed in these zones, impacting the lift force. Interestingly, these zones were previously identified as having the least accurate predictions in the studies reported in AutoCFD3 [2].

A more thorough discussion about the flow configuration at different yaw angles and the compressibility effects will be included in the final version of the manuscript.

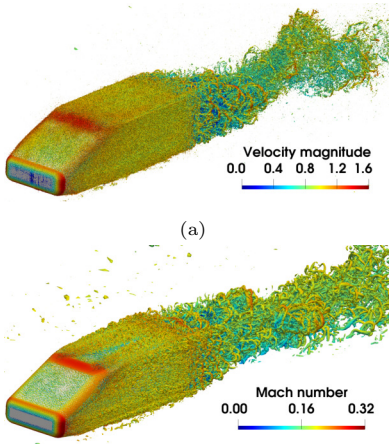

Figure 3: Instantaneous flow field representation using $Q^* = 700$ for the case at $\delta = 2.5°$ when running under incompressible conditions (a) and at $M_0 = 0.2$ (b)

REFERENCES

[1] K. A. Goc, O. Lehmkuhl, G. I. Park, S. T. Bose, and P. Moin, "Large eddy simulation of aircraft at affordable cost: a milestone in computational fluid dynamics," *Flow*, vol. 1, p. E14, 2021.

[2] "3rd edition of the AutoCFD, the Automotive industry CFD workshop." Workshop, 2022. Available online: `https://autocfd.eng.ox.ac.uk/`.

[3] M. Grandemange, M. Gohlke, and O. Cadot, "Turbulent wake past a three-dimensional blunt body. part 1. global modes and bi-stability," *Journal of Fluid Mechanics*, vol. 722, pp. 51–84, 2013.

[4] L. Gasparino Ferreira da Silva, F. Spiga, and O. Lehmkuhl, "Sod2d: A Gpu-Enabled Spectral Finite Elements Method for Compressible Scale-Resolving Simulations." `https://ssrn.com/abstract=4519596`, 2023. Available at SSRN.

[5] J.-L. Guermond, R. Pasquetti, and B. Popov, "Entropy viscosity method for nonlinear conservation laws," *Journal of Computational Physics*, vol. 230, no. 11, pp. 4248–4267, 2011.

[6] C. A. Kennedy and A. Gruber, "Reduced aliasing formulations of the convective terms within the Navier-Stokes equations for a compressible fluid," *Journal of Computational Physics*, vol. 227, no. 3, pp. 1676–1700, 2008.

[7] O. Lehmkuhl, U. Piomelli, and G. Houzeaux, "On the extension of the integral length-scale approximation model to complex geometries," *International Journal of Heat and Fluid Flow*, vol. 78, p. 108422, 2019.

[8] H. Reichardt, "Vollständige darstellung der turbulenten geschwindigkeitsverteilung in glatten leitungen," *ZAMM-Journal of Applied Mathematics and Mechanics*, vol. 31, no. 7, pp. 208–219, 1951.

[9] M. Varney, G. Pavia, M. Passmore, and C. Crickmore, "Windsor model experimental aerodynamic dataset." `https://doi.org/10.17028/rd.lboro.13161284`, 2020.

SESSION: Immersed boundary methods

Thursday, April 11, 2024

14:50- 16:05

WORKSHOP
Direct and Large-Eddy Simulation 14
April 10-12 2024, Erlangen, Germany

APPLICATION OF AN IMMERSED BOUNDARY METHOD TO PREDICT THE FLOW IN AN EXPERIMENTAL WIND GUST GENERATOR: AN LES STUDY

K. Boulbrachene and M. Breuer
Professur für Strömungsmechanik,
Helmut-Schmidt-Universität, Hamburg, Germany
boulbrak@hsu-hh.de, breuer@hsu-hh.de

INTRODUCTION

A wind gust is a short-term but strong phenomenon naturally appearing in the atmospheric boundary layer, which can lead to severe damages of civil engineering constructions. This is especially the case for modern lightweight membranous structures such as tents or large-span roofs. Therefore, there is the need to study the fluid-structure interaction of such buildings preferably in a wind tunnel under controlled conditions. However, generating wind gusts in an experimental setup is not a trivial task. Recently, Wood et al. [1] developed a new wind gust generator denoted the "Paddle". The working principle relies on the partial blocking of the outlet of the wind tunnel nozzle by a plate that vertically moves into the free-stream. This device leads to a rising velocity of the jet leaving the nozzle. The kinematics of the paddle determines the characteristics of the horizontal gust. In order to get a deeper insight into the paddle-flow interaction and the arising flow field, large-eddy simulations (LES) of the process were carried out. The predicted results were analyzed in detail and compared with the available experimental measurement data.

COMPUTATIONAL FRAMEWORK AND SETUP

The motion of the paddle is described as a moving boundary employing the immersed boundary method with a direct forcing approach [2]. The presence of the immersed boundary is incorporated into the Navier-Stokes equations for an incompressible fluid by adding a forcing term to the right-hand side which represents the influence of the solid object on the surrounding fluid. The immersed boundary is described by Lagrangian points. In the direct forcing scheme proposed by Uhlmann [2], the force term is evaluated at the Lagrangian force points. To couple the fluid and the solid phases, certain quantities have to be transferred between the Eulerian and the Lagrangian frames of reference. For this purpose, a bounded continuous approximation of the Dirac delta function is employed as introduced by Peskin [3]. The discrete analogues of the basic properties of the Dirac delta function ensure the integral conservation of the force and moment leading to smooth flow fields without any pressure disturbances. A uniform and a non-uniform distribution of the Lagrangian markers were investigated on a non-uniform Eulerian grid by applying modified window functions according to Pinelli et al. [4]. The latter was found to be significantly more efficient.

The turbulent flow is predicted by the LES technique using the finite-volume solver FASTEST-3D [5, 6]. The discretization is based on a curvilinear, block-structured grid with a collocated variable arrangement. However, for the present configuration solely Cartesian grids are applied. The filtered Navier-Stokes equations are solved by a semi-implicit predictor-corrector scheme. This projection method combined with standard discretization methods (mid-point rule and blended central scheme, 3% upwind) leads to a solver of second-order accuracy in time and space. The standard Smagorinsky model ($C_s = 0.1$) with Van-Driest damping near solid walls is applied.

To set up a numerical counterpart of the experimental wind gust generator [1], the wind tunnel geometry is represented by a long rectangular duct with the same cross-section as the outlet of the nozzle of the wind tunnel (0.375 m $\times$ 0.5 m). The flow leaving the nozzle enters a large cuboid room (2 m $\times$ 4.375 m $\times$ 4.5 m in which the ground plate and the moving paddle are installed. A uniform horizontal velocity is defined at the inlet patch. The flow and especially the boundary layers at the walls develop within the duct achieving a free-stream velocity of $u_\infty = 5.14$ m/s at its outlet. No-slip and impermeability boundary conditions are applied on the walls of the duct, the far-field walls and the ground plate. A convective boundary condition is defined at the outlet.

The Eulerian grid is a block-structured Cartesian grid consisting of 36.6 $\times 10^6$ control volumes. The geometric block-structure consisting of 10 blocks is split up into a parallel block-structure with 340 blocks leading to an optimal load balancing efficiency. Grid refinement near relevant rigid walls (i.e., duct walls and ground plate) is essential to capture the significant viscous effects leading to the formation of thin boundary layers. The maximum first cell size is chosen within the viscous sublayer in order to fulfill the recommendations for wall-resolved LES.

The geometry of the thin moving paddle (thickness 3 $\times 10^{-3}$ m) is simplified by a parallelepiped of right angles. Two distributions of the Lagrangian markers are used for the description of the paddle. A uniform distribution leads to about 6.7 million markers, since the spacing between the Lagrangian markers is defined according to the minimum local Eulerian grid spacing. Alternatively, a one-dimensional non-uniform distribution in spanwise direction allows to reduce the number to about 0.76 million. A smooth analytical function is fitted to the vertical velocity curve describing the paddle motion in the experiment. This paddle motion pattern imitates the standard 1-cosine symmetric gust shape defined in the IEC-Standard (2002). To mimic the undershooting of the

streamwise velocity below the free-stream velocity observed at the nozzle's outlet in the experiment during and after the paddle encounter, a time-dependent inlet boundary condition is defined.

SOME FIRST RESULTS

Here only a first insight into the dynamic flow field during and after the gust generation can be given. For this purpose, Fig. 1 depicts an isometric view on the setup and the arising flow based on iso-surfaces of the streamwise velocity (u/u_∞ = 1.38) at four different characteristic instants in time. At instant 1, the paddle is still at is idle position (not depicted here). At instant 2, the flow starts to deviate from its original stream as the paddle blocks 15.8% of the nozzle's outlet. This causes the streamwise velocity to accelerate and the vertical velocity to build up negative values below the paddle. A strong vortical structure with a pressure minimum in its center starts to form at the backside of the paddle. At instant 3 (not depicted here), the paddle continues its downstroke leading to a higher streamwise velocity extending to the ground plate. Furthermore, the size of the strong vortex originating from the bottom edge of the paddle increases. At instant 4 shown in Fig. 1, the paddle arrives at its maximum blocking ratio of 38.3%. In the remaining outlet region above the ground plate high streamwise velocities are observed characterizing the resulting strong horizontal gust. At instant 5, the paddle starts traveling back to its idle position and the large vortical structure hits the ground plate. At this instant the strength of the generated gust already decreases again resulting in highly transient velocity fields due to the shear layer developing at the bottom edge of the paddle. At instant 6, the paddle leaves the nozzle's outlet and the process of flow recovery to the initial state starts. More details of the flow field will be provided in the paper.

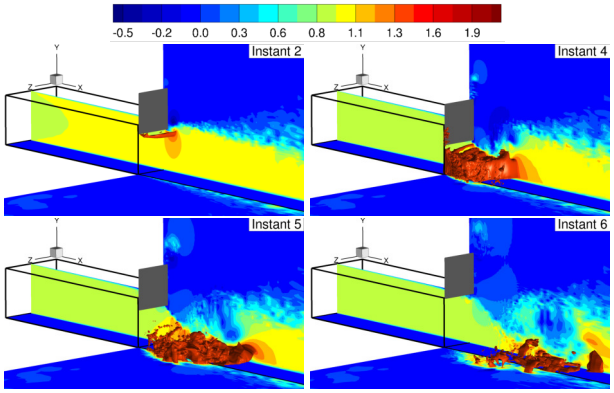

Figure 1: An isometric view of the generated gust at instant 2 (15.8% blocking ratio, instant 4 (max. blocking ratio of 38.3%), instant 5 (22.0 % blocking ratio), and instant 6 (paddle just left the nozzle's outlet). All planes depict the streamwise velocity and the gust structure is highlighted by iso-surfaces of $u/u_\infty = 1.38$.

In the following a comparison between the predicted data and the laser Doppler anemometer measurements by Wood et al. [1] is presented based on the streamwise velocity at seven streamwise positions (see Fig. 2). These are located in the region in which a wind tunnel model is typically placed in. Since the flow generated by the paddle's motion is dependent on the state of the flow at which the paddle is entering the nozzle's outlet, an ensemble averaging of the data is carried out. The numerical results are based on 10 initial conditions, whereas in the experiment the ensemble-averaged data are determined using 25 realizations. The time history at a single point possesses a bell-shaped pattern which is consistent with the displacement curve of the paddle. According to the mass conservation principle, the flow beneath the paddle is forced to accelerate when the paddle starts to block the nozzle's outlet. The flow acceleration continues until the maximum displacement of the paddle is reached. When the paddle starts traveling back to its idle position, the streamwise velocity decelerates. Obviously, it even drops below the free-stream velocity which is attributed to the paddle acting as a bluff body blocking the fluid flow and thus causing high pressure losses. Later on, the free-stream velocity is recovered. The numerical results are found to be in reasonable agreement with the experimental data, taking the difference in the ensemble averaging into account. For the first three locations, the streamwise velocity curves closely agree with the measurements. Moreover, both results consistently illustrate the increase in the maximum streamwise velocity along the downstream direction. At the last three locations, the streamwise velocity exhibits a chaotic and turbulent character at the descending slope. These velocity fluctuations are attributed to the free shear layer and the vortices shed from the bottom edge of the paddle. Increasing the number of realizations for the ensemble averaging reduces this phenomenon as visible in the experimental data. Further discussions of the results will be provided in the paper.

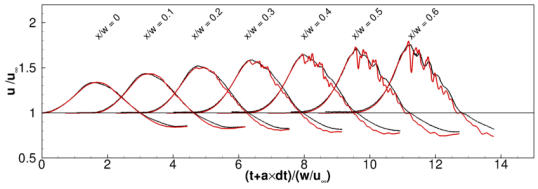

Figure 2: Comparison between the ensemble-averaged experimental streamwise velocity u/u_∞ (black) [1] and the numerical predictions (red) at seven points.

REFERENCES

[1] Wood, J. N., Breuer, M., Neumann, T.: A novel approach for artificially generating horizontal wind gusts based on a movable plate: The Paddle. *J. of Wind Eng. Indust. Aerodyn.* **230**, 105170 (2022).

[2] Uhlmann, M.: An immersed boundary method with direct forcing for the simulation of particulate flows. *J. Comput. Physics* **209**(2), 448–476 (2005).

[3] Peskin, C. S.: The immersed boundary method. *Acta Numerica* **11**, 479–517 (2002).

[4] Pinelli, A., Naqavi, I., Piomelli, U., Favier, J.: Immersed-boundary methods for general finite-difference and finite-volume Navier-Stokes solvers. *J. Comput. Physics* **229**(24), 9073–9091. (2010).

[5] Durst, F. and Schäfer, M.: A parallel block-structured multigrid method for the prediction of incompressible flows. *Int. J. Numer. Methods Fluids* **22**(6), 549–565 (1996).

[6] Breuer, M., De Nayer, G., Münsch, M., Gallinger, T., Wüchner, R.: Fluid-structure interaction using a partitioned semi-implicit predictor-corrector coupling scheme for the application of large-eddy simulation. *J. Fluids Structures* **29**, 107–130 (2012).

WORKSHOP
Direct and Large-Eddy Simulation 14
April 10-12 2024, Erlangen, Germany

TOWARDS NOVEL INSIGHTS IN GAS TURBINE AEROTHERMODYNAMICS WITH WALL-MODELED LES AND IMMERSED BOUNDARY METHOD

G. Baldan[1], F. De Vanna[2,*], E. Benini[2]
[1] Dipartimento di Scienze e Tecnologie Aerospaziali del Politecnico di Milano, Politecnico di Milano, Italy
[2] Dipartimento di Ingegneria Industriale, University of Padova, Italy
[*]corresponding: francesco.devanna@unipd.it

INTRODUCTION

Gas turbine aerodynamics represent a salient and contemporary engineering challenge. One of the most notable problems associated with the operation of gas turbine vanes at high speed is the potential for the flow to reach transonic regimes, thereby introducing many intricate aerodynamic phenomena, including boundary layer separation and Shock-wave/Boundary-Layer Interactions (SBLIs). In addressing these issues, Direct Numerical Simulations (DNS) are recognized as the most accurate approach; however, they often prove unfeasible in practical scenarios due to their computational demands. As a promising alternative, Large Eddy Simulation (LES) has emerged, surpassing conventional Reynolds Averaged Navier-Stokes (RANS) strategies by directly resolving the dynamics of energy-dominant, flow-dependent large eddies on the computational grid, as opposed to modeling them [1]. Nonetheless, the computational requirements of Wall-Resolved LES (WRLES), primarily driven by the necessity for high-resolution near solid boundaries, still render it unsuitable for real-world operating conditions. This is because the number of grid points required for a WRLES arrangement scales approximatively with the second power of the Reynolds number, making computation infeasible on standard architectures. Consequently, various approaches seeking to merge the LES framework with RANS methods have emerged in recent years. Among these, the Wall-Modelled LES (WMLES) approach has obtained significant attention. The method combines conventional LES techniques for resolving the most significant flow structures with a wall-stress/heat-flux model to address near-wall dynamics, demonstrating superior accuracy compared to other hybrid/zonal numerical discretizations [2].

In addition to these challenges, efficiently handling the complex geometries inherent to gas turbine technologies and combining complex geometries with highly efficient and massive parallel solvers presents another significant computational obstacle. The Immersed Boundary Method (IBM) has emerged as a promising strategy in this path. IBM, in fact, allows the body surface to intersect computational cells, enabling the use of a Cartesian mesh, regardless of geometric complexity; thus, making the solver structure prone to scale over thousands of computational units. However, IBM faces difficulty accurately resolving near-wall regions due to local mismatches between the mesh and the physical body. Our receipt is to provide a robust combination of WMLES, a method designed to set the first off-the-wall point as far as possible from the body surface, with the IBM strategy. This integrated approach provides an efficient computational framework for tackling the challenging conditions of high Reynolds/high-Mach number flows. Moreover, the overall framework seamlessly integrates with contemporary Graphics Processing Units (GPUs) architectures, offering simulation cost advantages and enhanced system physics description.

In light of these challenges, the present study applies such an innovative IBM+WMLES technique in analyzing the aerothermodynamics of a gas turbine vane. To the best of our knowledge, no prior research in this direction has been documented in the literature, marking this as a pioneering effort to elucidate the intricate physics of these systems. In particular, the present research aims at reproducing numerically the well-established experimental activity of a transonic turbine vane by Arts et al. [3]. Following a detailed comparison between the experimental and numerical arrangements, the full potential of the proposed method will be harnessed by examining the time-dependent behavior of the system. This critical phase of the study will shed light on the dynamic aspects of gas turbine aerothermodynamics, providing insights that are challenging to explore with standard CFD approaches, thus offering an alternative to overcome the limitations often associated with conventional RANS in capturing the intricate transient behaviors inherent to gas turbine systems.

GOVERNING EQUATION AND NUMERICAL METHODS

The present study is carried out with URANOS (Unsteady Robust All-around Navier-Stokes Solver), a well-established fully compressible Navier-Stokes solver developed at the Industrial Engineering Department of the University of Padova [4]. The solver deals with the filtered Navier-Stokes system of equations in a conservative formulation which, introducing both the Reynolds ($\phi = \bar{\phi} + \phi'$) and Favre ($\phi = \tilde{\phi} + \phi'', \tilde{\phi} = \overline{\rho\phi}/\bar{\rho}$) decompositions, reads as:

$$\frac{\partial \bar{\rho}}{\partial t} = -\frac{\partial \bar{\rho}\tilde{u}_j}{\partial x_j} \tag{1a}$$

$$\frac{\partial \bar{\rho}\tilde{u}_i}{\partial t} + \frac{\partial \bar{\rho}\tilde{u}_i\tilde{u}_j}{\partial x_j} = -\frac{\partial \bar{p}_i\delta_{ij}}{\partial x_j} + \frac{\partial \bar{\tau}_{ij}}{\partial x_j} - \frac{\partial T_{ij}^{SGS}}{\partial x_j} \tag{1b}$$

$$\frac{\partial \bar{\rho}\tilde{E}}{\partial t} + \frac{\partial \bar{\rho}\tilde{u}_j\tilde{E}}{\partial x_j} = -\frac{\partial \bar{p}\tilde{u}_j}{\partial x_j} + \frac{\partial \tilde{u}_j\bar{\tau}_{ij}}{\partial x_j} - \frac{\partial \bar{\mathcal{J}}_j}{\partial x_j} - \frac{\partial E_j^{SGS}}{\partial x_j} \tag{1c}$$

The SubGrid-Scale (SGS) terms are modelled via the canonical Boussinesq's hypothesis evaluating the turbulent viscosity,

μ_{SGS} through the Wall-Adaptive Large-Eddy (WALE) viscosity model [5]. As far as the wall model, the one proposed by Kawai t al. [2] is employed so that the wall shear-stress value, $\tau_{w,wm}$, and the wall heat flux, $q_{w,wm}$, are fed as boundary conditions for the external flow according to the procedure reported by De Vanna et al. [6] is used.

RESULTS

Figure 1 showcases a specific flow instance obtained through the proposed IBM+WMLES approach. This analysis is centered on modeling the three-dimensional behavior of a Mach 2.91 high-angle-turning supersonic boundary layer over a compression ramp replicating the available DNS database, as documented by Priebe and Martín [7]. To tackle the inherent complexity of this high-Reynolds and high-Mach flow, a non-uniform Cartesian grid is employed, thus exploiting high-order numerical methods over the computational power offered by several GPUs. In particular, the ramp is treated as an immersed body, and the near-wall dynamics are addressed through the wall-modeling approach. Notably, the immersed boundary block within this framework plays a pivotal role by driving all velocity components to zero, ensuring the desired wall temperature, and accurately enforcing the wall shear stress and heat flux. This thorough analysis unveils a noteworthy outcome: the proposed IBM+WMLES method excels in accurately representing the intricate, time-dependent, and non-linear dynamics of SBLIs, a fundamental attribute for a numerical method intended to faithfully capture the complexities of high-Reynolds and high-Mach flows, such as those in gas turbine applications.

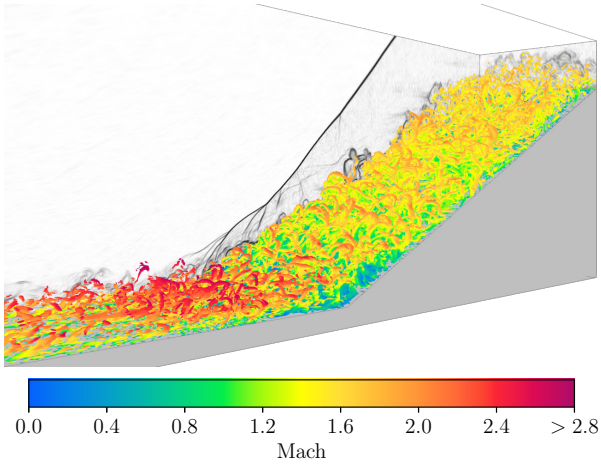

Figure 1: Instantaneous Schlieren density and Q-criterion contours for a supersonic ramp.

Figure 2 provides an insightful visualization of the ongoing activities about the flow dynamics analysis of gas turbine vane. The geometrical configuration accurately mirrors the experimental setup by Art et al. [3]. In this arrangement, the freestream Mach number is fixed to 0.15, while the chord Reynolds number is set at 2.31e+5. These specific conditions, coupled with the flow acceleration through the vane, culminate in achieving a Mach number at the vane outlet that closely approximates unity, thus giving rise to the formation of a shockwaves trains over the vane trailing edge. Again, a non-uniform Cartesian grid is adopted that clusters grid points around the blade region. This approach enables the utilization of advanced high-order hybrid-central/shock-capturing numerical schemes, striking a balance between computational efficiency and numerical precision. Notably, these methods significantly reduce numerical diffusivity, facilitating a comprehensive exploration of shock physics and their interaction with diffusive phenomena. Additionally, our fully explicit numerical framework is highly compatible with GPU computing architectures, unlocking a vast array of opportunities for advancing gas turbine technology. This includes the integration of optimization strategies informed by LES databases, ushering in new horizons for gas turbine design.

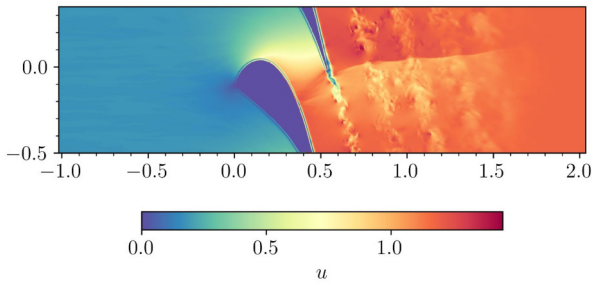

Figure 2: Instantaneous freestream-scaled velocity contours for a transonic the gas turbine vane by Art et al. [3]

Further details will be shared during the conference presentation and in the final paper.

REFERENCES

[1] S. T. Bose and P. Moin, "A dynamic slip boundary condition for wall-modeled large-eddy simulation," *Physics of Fluids*, vol. 26, no. 1, 2014.

[2] S. Kawai and J. Larsson, "Wall-modeling in large eddy simulation: Length scales, grid resolution, and accuracy," *Physics of Fluids*, vol. 24, no. 1, 2012.

[3] T. Arts, M. Lambertderouvroit, and A. W. Rutherford, "Aero-thermal investigation of a highly loaded transonic linear turbine guide vane cascade. a test case for inviscid and viscous flow computations," *NASA STI/Recon Technical Report N*, vol. 91, p. 23437, 1990.

[4] F. De Vanna, F. Avanzi, M. Cogo, S. Sandrin, M. Bettencourt, F. Picano, and E. Benini, "URANOS: A GPU accelerated Navier-Stokes solver for compressible wall-bounded flows," *Comput. Phys. Commun.*, vol. 287, p. 108717, 2023.

[5] F. Nicoud and F. Ducros, "Subgrid-scale stress modelling based on the square of the velocity gradient tensor," *Flow Turbul. Combust.*, vol. 62, no. 3, pp. 183–200, 1999.

[6] F. De Vanna, G. Baldan, F. Picano, and E. Benini, "On the coupling between wall-modeled LES and immersed boundary method towards applicative compressible flow simulations," *Comput. Fluids*, vol. 266, p. 106058, 2023.

[7] S. Priebe and M. P. Martín, "Low-frequency unsteadiness in shock wave–turbulent boundary layer interaction," *J. Fluid Mech.*, vol. 699, pp. 1–49, 2012.

WORKSHOP
Direct and Large-Eddy Simulation 14
April 10-12 2024, Erlangen, Germany

A DATA-DRIVEN IBM METHOD FOR THE ANALYSIS OF WALL-BOUNDED TURBULENT FLOWS

M. Meldi[1] **and M. M. Valero**[1]
[1]Univ. Lille, CNRS, ONERA, Arts et Métiers ParisTech, Centrale Lille, UMR 9014 - LMFL Laboratoire de Mécanique des fluides de Lille
Kampé de Feriet, F-59000 Lille, France
marcello.meldi@ensam.eu

INTRODUCTION

The development of reliable, efficient, and cost-effective numerical tools for the accurate prediction of multi-physics problems is a timely key challenge in Computational Fluid Dynamics (CFD). In fact, the development of predictive tools to investigate flow configurations including several complex aspects (turbulence, compressibility effects, fluid-structure interaction, transport of active and passive scalars) must take into account requirements exhibiting goal rivalry. Future paradigms in the numerical development of flow solvers strive for increased accuracy of the predictive computational strategies while reducing the computational resources required. Therefore, efficient numerical modeling in fluid mechanics is essential for progress in fundamental studies as well as industrial applications. Among the flow problems previously introduced, the accurate numerical representation of near-wall flow features for bodies immersed in turbulent flows needs key advancement. The prediction of numerous flow features of unstationary flows, such as aerodynamic forces, is driven by the precise representation of localized near-wall dynamics. This aspect is particularly relevant and, at the same time, challenging for the flow prediction around complex geometries. In this case, classical body-fitted approaches may have to deal with high deformation of the mesh elements, possibly leading to poor numerical prediction. Additionally, the simulation of moving bodies may require prohibitively expensive mesh updates. In the last decades, several numerical strategies have been proposed to handle these two problematic aspects. Among these proposals, the Immersed Boundary Method (IBM) [1] has emerged as one of the most popular approaches. State-of-the-art IBM methods can account for body movement and deformation with reduced computational cost. However, the complete resolution of near-wall features, in particular for high Reynolds regimes, is a challenging issue. In fact, owing to the regularity of the grid and the difficulties in applying arbitrary local directional stretching, a larger number of mesh elements is usually required in IBM to obtain similar accuracy of body-fitted tools [2].

In the present work, a *physics informed* data-driven strategy based on Data Assimilation [3, 4] and Machine Learning [5] is proposed to improve the accuracy of a classical IBM, namely the penalization model [6]. More precisely, an Ensemble Kalman Filter (EnKF) [4] is used to infer an optimized parametric description of the IBM penalization model, using available physical information. The results obtained with this data-driven procedure are then used to feed a Random Forest algorithm [7], which produces a black-box IBM model, which is then integrated into the numerical CFD solver. DA and ML tools exhibit complementary features. On the one hand, DA approaches can produce large amounts of data needed to train the ML tools, which may be difficult to obtain, particularly in realistic applications. On the other hand, ML strategies can infer the functional behavior of models, which is a task often too expensive for DA based approaches. The analysis is performed for the turbulent flow in a plane channel, $Re \approx 550$, for which results from a Direct Numerical Simulation (DNS) [8] are available to the research team.

METHODOLOGY

The EnKF strategy relies on the combination of two sources of information:

- The *model*, which provides a quasi-continuous representation of the physical phenomena at play. In this case, an ensemble of $N_e = 40$ coarse-grained DNS runs are performed using the open-source code OpenFOAM.
- The *observation*, which represents available data that can be sparse in space and time. In this analysis, synthetic sensors are generated at the wall to enforce a non-slip condition at the wall (see Figure 1).

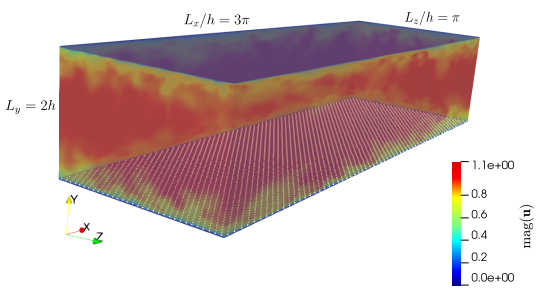

Figure 1: Test case of investigation and synthetic sensors positioned at the wall.

The DA algorithm relies on a forecast step, where the solution is advanced in time via the model, and an analysis step, where model prediction and observation are combined to obtain an augmented prediction. This prediction is used to infer the coefficients of the tensor $\mathbf{D}$ which controls the IBM volume forcing integrated into the Navier–Stokes equations:

$$\mathbf{f}_P = \begin{cases} \mathbf{0} & \text{if } \mathbf{x} \in \Omega_f \\ -\nu\,\mathbf{D}\,(\mathbf{u} - \mathbf{u_{ib}}) & \text{if } \mathbf{x} \in (\Sigma_b \cup \Omega_b) \end{cases} \quad (1)$$

where $\mathbf{u_{ib}}$ is the target wall velocity, Σ_b is the fluid-solid interface region and Ω_f and Ω_b are the fluid and solid regions, respectively. The value of the volume forcing $\mathbf{f}_P$ and the predicted velocity field $\mathbf{u}$ are then used as input-output information to train the black box IBM model.

The DA and ML operations are sequentially performed on the fly thanks to the C++ platform *Coupling OpenFOAM with Numerical EnvironmentS* (CONES) [9], which is able to connect the numerical simulations with the DA and ML codes without the need to stop the numerical simulations. This is an important advantage in particular in the case of numerous DA analysis phases and ML training, because the time required to start/end the simulation may be significantly larger than the time advancement of the CFD solution between two data-driven steps.

RESULTS

First, the results obtained via DA applications are presented in Figure 2. In particular, the compensated time-averaged streamwise velocity $\langle U \rangle^+ = \langle u_x \rangle / u_\tau$ is shown. Here x is the streamwise direction, and u_τ is the streamwise velocity. One can see that the dark-grey line corresponding to the DA prediction almost superposes with the red line of the reference high-fidelity DNS. On the other hand, all the other results, which are obtained using different classical IBM, including the penalization method, do not provide an accurate prediction of the flow. The discrepancies observed are mainly due to a poor prediction of u_τ (see Table 1), which is strictly connected to the accurate representation of the wall shear stress. One interesting result is that the DA-optimized penalization method obtains a good approximation of the no-slip condition for the velocity at the wall, which is not obtained by the classical penalization IBM (grey dotted line).

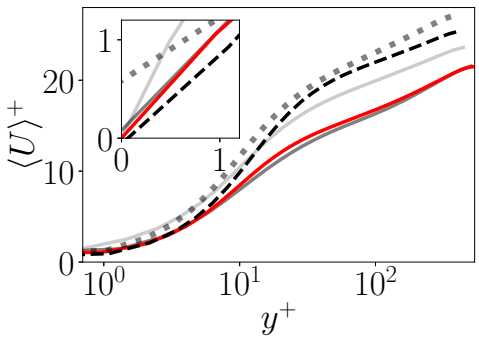

Figure 2: Mean streamwise velocity. Red: reference DNS. Continuous dark-grey: DA solution (state estimation + IBM optimization). Others: classical IBM approaches.

The field prediction generated by the DA algorithm is used on the fly to train a Random Forest Regression tool which, integrated into the CFD calculation algorithm, is able to make satisfactory predictions up to second-order statistics based on the instantaneous flow information. The results shown in Figure 3 indicate that the ML model trained with the IBM model obtained with DA is able to obtain a very similar prediction of the flow field when used with the same grid and for the same Re_τ of the DA investigation. Undergoing analyses by the team, which will be presented at the conference, aim to assess the predictive performance of the DA-ML IBM model outside of the training conditions, i.e., using different meshes and considering different values for Re_τ.

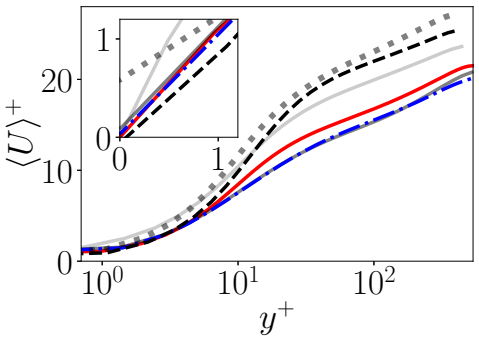

Figure 3: Mean streamwise velocity. Red: reference DNS. Dark-grey: DA solution (IBM optimization). Dashed-dotted blue: Random Forest ML model. Others: classical IBM approaches.

Overall, as shown in Table 1, both data-driven procedures are capable of better predicting the flow by reducing the number of computational resources $C.C$ required (the reported results are adimensionalized with respect to $C.C$ from the penalization IBM).

Case	calculated Re_τ	$C.C^\star$
Reference DNS	536	$\approx 12k$
DA solution	545	830.9
Random Forest IBM	577	5.7
IBM - Penalization	419	1

Table 1: Summary of computational resources required for test cases considered.

REFERENCES

[1]Peskin, C.S: Flow Patterns Around Heart Valves, *J. Comp Phys.*, **10**, 252–271 (1972).

[2]Verzicco, R.: Immersed boundary methods: Historical perspective and future outlook, *An. Rev. Fluid Mech.*, **55**, 129–155 (2022).

[3]Daley, S. B. : Atmospheric Data Analysis, *Cambridge University Press* (1991).

[4]Asch, M., Bocquet, M. and Nodet, M.: Data Assimilation: Methods and Applications, *SIAM* (2016).

[5]Burkov A.: The Hundred-Page Machine Learning Book (2019).

[6]Angot, P., Bruneau, CH. and Fabrie, P.: A penalization method to take into account obstacles in incompressible viscous flows, *Numerische Mathematik*, **81**, 497–520 (1999).

[7]Breiman, L.: Random Forests, *Machine Learning*, **45**, 5–32 (2001).

[8]Valero, M.M. and Meldi, M.: A physics-infused Immersed Boundary Method using online sequential Data Assimilation, *arXiv:2310.09087* (2023).

[9]Villanueva, L., Valero, M.M., Sarkic Glumac, A. and Meldi, M.: Augmented state estimation of urban settings using on-the-fly sequential Data Assimilation, *Comp. & Fluids*, 106118 (2024).

WORKSHOP
Direct and Large-Eddy Simulation 14
April 10-12 2024, Erlangen, Germany

FEEDBACK-FORCING IMMERSED BOUNDARIES IN SPECTRAL ELEMENT METHODS: CAPABILITIES AND LIMITATIONS

L. Weber[1,3], F. Secchi[2], D. Gatti[2], B. Frohnapfel[2], P. Schlatter[3,4]
[1]Institute of Thermal Energy Technology and Safety (ITES)
Karlsruhe Institute of Technology (KIT), Germany
[2]Institute of Fluid Mechanics (ISTM)
Karlsruhe Institute of Technology (KIT), Germany
[3]FLOW, Department of Engineering Mechanics
KTH Royal Institute of Technology Stockholm, Sweden
[4]Institute of Fluid Mechanics (LSTM)
Friedrich–Alexander–Universität (FAU) Erlangen–Nürnberg, Germany
lorenz.weber@kit.edu

INTRODUCTION

This study presents an assessment of a feedback-forcing immersed boundary method (IBM) in the framework of a spectral element flow solver. No-slip and no-penetration boundary conditions for the velocity field are enforced by the action of a volume force field which is specified inside the immersed object. The resulting volume force distribution is discontinuous across the fluid–solid interface, leading to challenges when the method is coupled with a spectral discretization. The discontinuity is often eliminated by using a smooth kernel function to distribute the forcing field across the fluid–solid interface [1, 5]. Nevertheless, several works in the literature avoid such a remedy and report reliable estimation of mean flow quantities in complex flow problems, e.g. [4, 6, 7].

In the present study, the results based on such an IBM formulation are assessed through the comparison with a body-conforming mesh. The flow under investigation is a fully-developed turbulent channel flow over random surface roughness at friction Reynolds number $Re_\tau = 240$ (as in [2]). The used surface topography taken from [3] is shown in Figure 1.

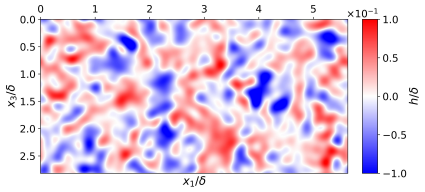

Figure 1: Surface scan from [3]. The reference point for the roughness height h is placed at the mean location of the surface topography.

METHOD

The flow is governed by the incompressible Navier–Stokes equations which, in non-dimensional form, read:

$$\frac{\partial u_i}{\partial x_i} = 0, \tag{1}$$

$$\frac{\partial u_i}{\partial t} + u_j \frac{\partial u_i}{\partial x_j} = -\frac{\partial p}{\partial x_i} + \frac{1}{Re}\frac{\partial^2 u_i}{\partial x_j \partial x_j} + f_i. \tag{2}$$

In the equations, indices $i, j = 1, 2, 3$ and summation is implied over repeated indices. The action of the immersed boundary is introduced in the momentum equation (2) through the volume force field f_i. Evidently, for body-conforming cases, $f_i = 0$, $i = 1, 2, 3$.

Following the work of [1], the volume force field used to model no-slip boundary conditions for the velocity field on the stationary rough wall surfaces of the channel is

$$f_i = -\alpha \int_0^t u_i \mathrm{d}t' - \beta u_i, \qquad i = 1, 2, 3. \tag{3}$$

The volume force defined in equation (3) can be interpreted as a closed-loop control system with an integral and a proportional term. Here the feedback-error for the local forcing is defined as the difference between the target boundary velocity (zero for fixed walls) and the local fluid velocity.

Differently from the method discussed by [1], in the present work, the volume force field acts at every grid location inside the solid walls of the channel. This scenario is depicted in the sketch of Figure 2, where the boundary surface is drawn as a continuous red line and all grid-points of the solid region are marked with thick black symbols. In the literature (e.g. in [4]) this approach is chosen for its simplicity: (a) it does not require Lagrangian surface marker points and, therefore, no interpolation of forces onto the Eulerian grid and (b) no smoothing kernel is used for the discontinuities in the force field.

SIMULATION

The mean channel half-height δ is chosen as characteristic length. For the IBM simulation, the height of the computational box equal to $L_2 = 2.33\delta$ to fully accommodate the surface topography such that the average net channel height is 2δ. In consequence, the mean height of the bottom rough wall is located at $x_2 = 0$, whereas the top one is located at

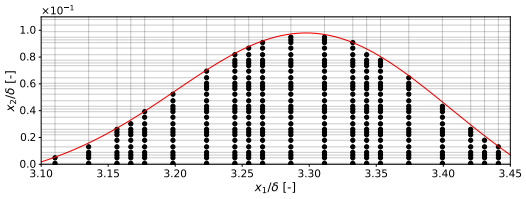

Figure 2: Representation of the virtual surface by GLL points of the spectral element method at the location $z/\delta = 0.8$.

$x_2 = 2\delta$. A schematic visualization of the simulation setup is depicted in Figure 3.

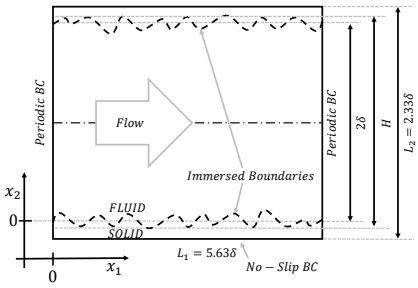

Figure 3: Schematic setup of IBM simulation.

Note that the body-conforming computational mesh is obtained by deforming the spectral elements of the computational box of a channel with plane walls in the x_2-direction. This procedure is a standard functionality offered by the spectral element code *Nek5000* [8].

RESULTS

Wall-normal profiles of mean velocity and single point correlations of velocity fluctuations (*i.e.* Reynolds stresses) often represent the essential data that a DNS should be able to provide accurately. One part of this analysis are the mean velocity profiles as shown in Figure 4. A good agreement is seen between the two cases, especially towards the channel centerline. In the inner and buffer regions the IBM mean velocity profile deviates slightly from the body-conforming one.

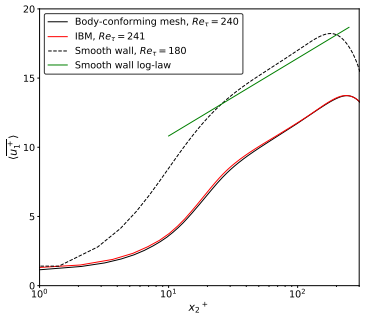

Figure 4: Comparison of $\langle \overline{u_1^+} \rangle$ for $Re_\tau = 240$.

In contrast, local quantities near the immersed surface, are, as expected, affected by oscillations caused by the spectral representation of discontinuities across the solid-fluid interface. We compare local (time-averaged) velocity profiles, the pressure distribution and the shear stress acting locally on the wall. One example is the local pressure distribution $\overline{p^+_{wall}}$ (in viscous units). A representative close-up of the rough surface is chosen for visualization in Figure 5. It can be seen that the magnitude and the location of local extrema in the distribution of $\overline{p^+_{wall}}$ agree between both cases. However, the IBM case exhibits oscillations on a smaller scale around the pressure distribution of $\overline{p^+_{wall}}$ that are not observed in the body-conforming mesh case and, clearly, are non-physical.

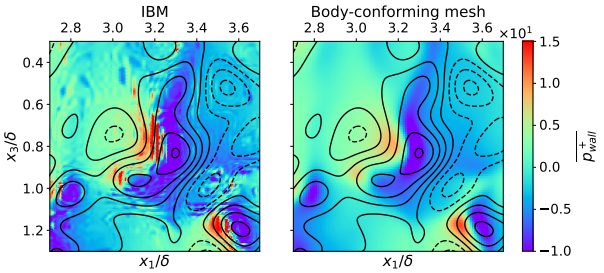

Figure 5: Time-averaged pressure distribution at $Re_\tau = 240$ in comparison to results with body-conforming mesh. Contour lines represent the local height of the geometry.

CONCLUSION

The study shows that accurate predictions of global flow properties seem not to be affected by the unavoidable oscillations associated with the representation of a discontinuous force field within a spectral framework. All deviations from the body-conforming mesh case for the global time-averaged drag and velocity are on the order of less than 1%.

In contrast, the evaluation of local quantities at the fluid-solid interface remains challenging or not possible at all. In particular, significant discrepancies are observed for the near-wall velocity gradients and local stresses acting on the wall. This observation marks an important limitation of the applicability of feedback-forcing IBM in spectral solvers.

REFERENCES

[1] D. Goldstein, R. Handler, and L. Sirovich, "Modeling a no-slip flow boundary with an external force field," *J. Comp. Phys.*, vol. 105, no. 2, pp. 354–366, 1993.

[2] M. Thakkar, A. Busse, and N. Sandham, "Direct numerical simulation of turbulent channel flow over a surrogate for nikuradse-type roughness," *J. Fluid Mech.*, vol. 837, 02 2018.

[3] M. Thakkar, A. Busse, and N. Sandham, "Dataset for investigation of turbulent flow over irregular rough surfaces using direct numerical simulations," 2017.

[4] F. Secchi, D. Gatti, and B. Frohnapfel, "The wall-jet region of a turbulent jet impinging on smooth and rough plates," *Flow Turb. Combust.*, vol. 110, no. 2, p. 275–299, 2022.

[5] C.S. Peskin, "Flow patterns around heart valves: A numerical method", *J. Comp. Phys.*, Vol. 10, no. 2, p. 252-271, 1972.

[6] A. Perez, R. Örlü, A. Talamelli, and P. Schlatter, "Appraisal of cavity hot-wire probes for wall-shear-stress measurements", *Exp. Fluids*, Vol. 63, 2022.

[7] P. Forooghi, A. Stroh, P. Schlatter and B. Frohnapfel, "Direct numerical simulation of flow over dissimilar, randomly distributed roughness elements: A systematic study on the effect of surface morphology on turbulence", *Phys. Rev. Fluids*, Vol. 3, p. 044605, 2018.

[8] P. Fisher, J. Lottes, and S. Kerkemeier, "NEK5000 Version 19.0.." `https://nek5000.mcs.anl.gov/`, 2008-2020. Argonne National Laboratory, Illinois.

WORKSHOP
Direct and Large-Eddy Simulation 14
April 10-12 2024, Erlangen, Germany

AN IMMERSED BOUNDARY METHOD FOR NEUTRALLY-BUOYANT PARTICLES OF ARBITRARY SHAPE

Maximilian Schenk[1], **Manuel García-Villalba**[1], **Markus Uhlmann**[2], **Manuel Moriche**[1]
[1]Institute of Fluid Mechanics and Heat Transfer, TU Wien, Vienna, Austria
[2]Institute for Hydromechanics, Karlsruhe Institute of Technology, Karlsruhe, Germany
maximilian.schenk@tuwien.ac.at

INTRODUCTION

Particle-laden flows are present in many important natural and industrial processes, such as environmental transport, material science and many other fields. These flows are governed by the complex interaction between fluid and particle motion. Optimizing designs and process efficiency and upscale industrial facilities, like fluidised beds, is many times limited by the lack of accurate predictive models. Currently, the available reduced order models are still not precise enough. To tackle the difficulties imposed by such intricate and complex fluid-particle problems by numerical simulation, the Immersed Boundary Method (IBM) is often the method of choice because of its high-computational efficiency and the capacity of handling arbitrary shaped bodies.

METHODOLOGY

We solve the Navier-Stokes equation for an incompressible flow around a particle of arbitrary shape whose motion is governed by the Newton-Euler equations. For the flow solver we use second-order finite differences on a staggered grid and a 3-stage Runge-Kutta scheme, in which linear terms are treated implicitly and non-linear terms are treated explicitly. The presence of the particle is modeled with an IBM originally proposed by Uhlmann [8], later modified by García-Villalba et al. [2] to handle neutrally-buoyant and moderately light particles, and now extended for non-spherical particles (of arbitrary shape). We maintain the advantages presented in [2], for example the extra effort of forcing throughout the volume of the particle is compensated because the same distribution of markers is used to compute volume integrals and apply the direct forcing term. Recall that forcing in the interior of the particle has shown to be superior compared to only forcing on the surface of the particle [5, 6].

The modifications of the algorithm can be summarized in: i) tracking the rotation of the particle by means of a quaternion-based formulation and ii) solving the angular momentum equation of the particle in a body-fixed reference frame [5]. One of the main advantages of the new algorithm compared to existing methods is its simplicity, namely, the new formulation uses no extra term needed for the possible non-overlapping of the center of gravity of the particle and its surface shell [7]. We also need to generate uniform distribution of Lagrangian markers inside the volume of non-spherical particles. For that purpose we generate a 3D Voronoï tessellation and iterate their coordinates using Lloyd's algorithm until a uniform distribution is obtained [5].

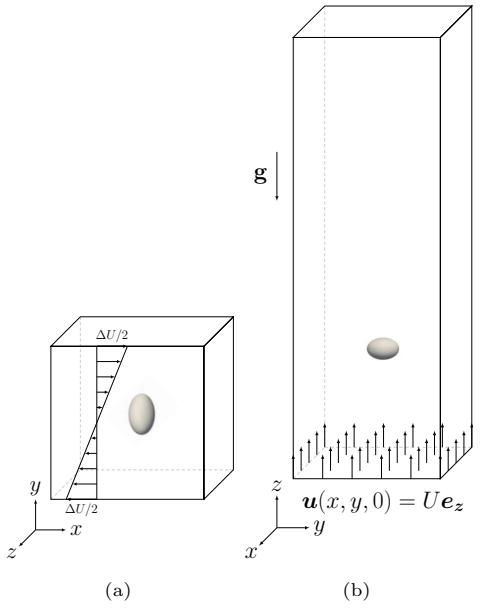

Figure 1: Sketch of a) the Jeffery orbit problem and b) the settling particle in the steady-oblique regime.

VALIDATION

In this section we present preliminary results of the ongoing validation process of the proposed algorithm. For both presented cases, there is an incompressible Newtonian fluid with a constant density, ρ_f, a kinematic viscosity, ν. Furthermore, in both shown cases the aspect ratio of the ellipsoid is $\chi = d/a$, where d is the equatorial diameter and a is the symmetry axis length. Last but not least, D_{eq} corresponds to the equivalent diameter and describes the diameter of a sphere, which occupies the same volume as the arbitrary shaped body itself.

Motion of a spheroid in shear flow

We analyse the motion of a neutrally-buoyant prolate spheroid in the well-known Jeffery orbit configuration [4], as shown figure (1a). The domain used is a cube of side-length $L = 6.4D_{eq}$ and we use a resolution of $D_{eq}/\Delta x = 20$, which results in a grid size of 128^3. The aspect ratio of the prolate

is set to $\chi = 0.5$. We impose the velocity at the bottom and top walls, so that the shear Reynolds number is

$$Re_{\dot{\gamma}} = \frac{\dot{\gamma} D_{eq}^2}{\nu} = 6.4 \tag{1}$$

and periodicity in the streamwise and lateral directions (x and z). We initialize the flow with the velocity profile that would take place in the absence of the particle. Please note that the prolate is free to translate and rotate. When the symmetry axis of the spheroid is contained in a plane parallel to streamwise and vertical direction the kinematic of the spheroid are unique defined by the angle, ϕ, and its time derivative, $\dot{\phi}$. Exact solutions of this case, when the Reynolds number is zero, were derived by [4] and can also be found in [3]. The resulting motion is periodic with period, $T\dot{\gamma} = 2\pi\,(\chi + 1/\chi)$, and the motion is given by:

$$\phi = \arctan\left(\frac{1}{\chi}\tan\left(\frac{\dot{\gamma} t}{\chi + \frac{1}{\chi}}\right)\right) \tag{2}$$

$$\dot{\phi} = \frac{\dot{\gamma}}{1+\chi^2}\left(\chi^2 \sin^2\phi + \cos^2\phi\right) \tag{3}$$

The obtained results are in agreement with the solution presented in figure (2):

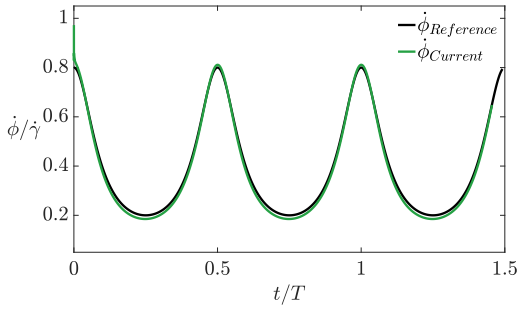

Figure 2: Time history of $\dot{\phi}$ obtained in this work and exact solution for Stokes regime [3]

Settling of an oblate spheroid in ambient fluid

Let us now analyse the settling of a single oblate in an unbounded domain. We consider a spheroid of aspect ratio $\chi = 1.5$ and density ratio $\tilde{\rho} = 2.14$, at a Galileo number $Ga = U_g D_{eq}/\nu = 152$, where $U_g = \sqrt{|\tilde{\rho} - 1| g D_{eq}}$ is a gravitationally scaled velocity. For this combination of (χ, $\tilde{\rho}$, Ga) the resultant regime is called steady-oblique. [5] The computational domain is a cuboid with side lengths $L_x = L_y = 5.34 D_{eq}$ and $L_z = 16 D_{eq}$ with a resolution of $D_{eq}/\Delta x = 24$, similar to the cases presented in [5] (see Figure 1b). At the bottom boundary we impose a vertical velocity $\boldsymbol{u}(x, y, 0) = U\boldsymbol{e}_z$, where $\boldsymbol{U}$ is an estimate of the settling velocity of the particle. An advective boundary condition is imposed at the top of the domain to extract flow structures minimizing the impact of any reflections of the boundary on the solution. In addition, periodicity is imposed in the lateral directions (x and y). We compare our results with the reference data from [5] generated with a highly accurate Spectral Element Method [1]. The obtained particle Reynolds number is $Re_p = |\boldsymbol{u}_p| D_{eq}/\nu = 165.9$ and deviates with an error of 2.4%. The same error is found for the vertical particle velocity and slightly higher for the horizontal component, please note that the horizontal component is an order of magnitude smaller than the vertical one. Next, we can compare the tilting angle, ϕ, between the symmetry axis of the particle and the vertical axis, where $\phi = 5.683°$ and the obtained error is 6.8%, which is in comparison to [5, table7, page15] a noticeable improvement. Finally, the trajectory angle, α, where the error is 4.8% and the trajectory angle itself is $\alpha = 4.03°$. In conclusion, the new methodology captures the steady oblique regime satisfactorily. At the time of writing we are running additional test cases. In the talk we will show these and additional cases from the ongoing validation process.

REFERENCES

[1]Chrust, Bouchet, G., & Dušek, J. (2013). Numerical simulation of the dynamics of freely falling discs. Physics of Fluids (1994), 25(4), 44102–44102. https://doi.org/10.1063/1.4799179

[2]García-Villalba, Fuentes, B., Dušek, J., Moriche, M., & Uhlmann, M. (2023). An efficient method for particle-resolved simulations of neutrally buoyant spheres. Computers & Fluids, 263, 105936. https://doi.org/10.1016/j.compfluid.2023.105936

[3]Guazzelli, Morris, J. F., & Pic, S. (2012). A physical introduction to suspension dynamics. Cambridge University Press.

[4]Jeffery. (1922). The motion of ellipsoidal particles immersed in a viscous fluid. Proceedings of the Royal Society of London. Series A, Containing Papers of a Mathematical and Physical Character, 102(715), 161–179. https://doi.org/10.1098/rspa.1922.0078

[5]Moriche, Uhlmann, M., & Dušek, J. (2021). A single oblate spheroid settling in unbounded ambient fluid: A benchmark for simulations in steady and unsteady wake regimes. International Journal of Multiphase Flow, 136(3), 103519. https://doi.org/10.1016/j.ijmultiphaseflow.2020.103519

[6]Yu, & Shao, X. (2007). A direct-forcing fictitious domain method for particulate flows. Journal of Computational Physics, 227(1), 292–314. https://doi.org/10.1016/j.jcp.2007.07.027

[7]Tschisgale, Kempe, T., & Fröhlich, J. (2018). A general implicit direct forcing immersed boundary method for rigid particles. Computers & Fluids, 170, 285–298. https://doi.org/10.1016/j.compfluid.2018.04.008

[8]Uhlmann. (2005). An immersed boundary method with direct forcing for the simulation of particulate flows. Journal of Computational Physics, 209(2), 448–476. https://doi.org/10.1016/j.jcp.2005.03.017

SESSION: LES fundamentals and modelling

Friday, April 12, 2024

11:00- 12:30

WORKSHOP
Direct and Large-Eddy Simulation 14
April 10-12 2024, Erlangen, Germany

TEMPORAL LARGE-EDDY SIMULATION BASED ON DIRECT DECONVOLUTION

D. Oberle[1], C. D. Pruett[2], and P. Jenny[1]
[1]Institute of Fluid Dynamics, ETH Zurich, Switzerland
[2]Department of Mathematics and Statistics, James Madison University (Retired), USA
doberle@ethz.ch

INTRODUCTION

The fundamental goals of an effective Large-Eddy Simulation (LES) include approximating the exact residual-stress for the chosen filter and preventing numerical instability. Despite the historical adoption of conventional models like the Smagorinsky model, they often exhibit excessive dissipation and poor correlation with exact residual-stresses. LES methodology significantly advanced with the introduction of the Approximate Deconvolution Model (ADM)[1], which considers residual-stress approximation and stabilization independently.

A derivative of the ADM, based on Eulerian time-domain filtering, was first introduced by Pruett *et al.* [2]. Termed the temporal approximate deconvolution model (TADM), this laid the foundation for Temporal LES (TLES). As Pruett stated in 2008, temporal filtering in the context of LES has not received the expected attention, even though he showed that none of the offered concerns such as Galilean invariance or the requirement of the time-filter being causal are significant.[3] Just recently, Corrêa *et al.*[4] have shown that TADM can lead to better results than conventional LES in simulations of a lid-driven cavity. Furthermore, TLES bridges the gap between DNS and RANS by accommodating an internally consistent spectrum of approaches within computational fluid dynamics.

We propose a new TLES model, termed the Temporal Direct Deconvolution Model (TDDM). It is based on the same causal filter kernel as used for TADM, but the non-filtered fields are recovered using the differential form of the exponential filter rather than a truncated series expansion of the inverse filter operator. Another major difference is that the temporal residual-stress is closed by an additional ODE, which is analytically derived. This allows for a direct recovery of the deconvolved fields, provided that all relevant length and time scales are sufficiently resolved.

GOVERNING EQUATIONS

The equation for the Eulerian temporal filtering operator reads

$$\bar{f}(t;T) = \frac{1}{T}\int_{-\infty}^{t} \exp\left(\frac{t'-t}{T}\right) f(t')dt', \tag{1}$$

where T is the filter width, $f(t)$ a function dependent on time, and the overbar denotes a filtered quantity. The integral of the filter contains an exponential function, referred to as the "kernel". The selection of an exponential kernel is beneficial, as it leads to an equivalent differential form of the filter given by Leibniz's rule as

$$\frac{d}{dt}\bar{f}(t;T) = \frac{f(t)-\bar{f}(t;T)}{T}. \tag{2}$$

This linear ODE is pivotal to the closure of the residual-stress model, which will be discussed later. Applying temporal filtering to the incompressible Navier-Stokes (NS) equations results in

$$\frac{\partial \bar{u}_i}{\partial t} + \frac{\partial \bar{u}_i\bar{u}_j}{\partial x_j} = -\frac{1}{\rho}\frac{\partial \bar{p}}{\partial x_i} + \nu\frac{\partial^2 \bar{u}_i}{\partial x_j \partial x_j} - \frac{\partial \tau_{ij}}{\partial x_j}. \tag{3}$$

The temporal residual-stress tensor τ_{ij} is defined as

$$\tau_{ij} = \overline{u_i u_j} - \bar{u}_i\bar{u}_j. \tag{4}$$

The system is closed using the exact deconvolution, which is based on the rearrangement of Eq. (2) to describe the non-filtered quantity f as a function of the filtered quantity $\bar{f}$ and its derivative with respect to time

$$f = \bar{f} + T\frac{d\bar{f}}{dt}. \tag{5}$$

By applying the differential filter operation to the velocity product $u_i u_j$ and subsequently rearranging, we get the closure equation. Note that this results in an ordinary differential equation that only involves t as the independent variable, i.e.,

$$\frac{\partial \tau_{ij}}{\partial t} = -\frac{\tau_{ij}}{T} + T\frac{\partial \bar{u}_i}{\partial t}\frac{\partial \bar{u}_j}{\partial t}. \tag{6}$$

Equation (6) provides an analytical closure to the governing system by defining the temporal evolution of the temporal residual-stress tensor. As such, the TDDM mirrors DNS when no regularization term is employed, with the sole difference being that filtered equations are solved instead.

The TDDM solution algorithm is such that first the time derivative of the filtered velocity is computed by solving the temporally filtered NS equations. Afterwards the temporal residual-stress τ_{ij} is computed, which will then be used in the momentum equation of the next time step. Initially the stress is set to zero, and the filtered and unfiltered velocities are identical.

SUMMARY OF THE MAIN FINDINGS

For a first proof of concept, the TDDM was implemented in the spectral element code Nek5000 [5] to simulate two canonical incompressible flows as three test cases: an *a priori* test case of Homogeneous Isotropic Turbulence (HIT) with a Reynolds number of $Re_\lambda = 50$, a greatly coarsened *a posteriori* HIT case with $Re_\lambda = 190$, and an *a posteriori* highly anisotropic turbulent channel flow with $Re_\tau = 180$. Deconvolution models can be viewed as generalizations of the scale-similarity model of Bardina[6], well-known to be insufficiently dissipative without artificial damping. Indeed, this has been the experience for both the ADM and the TADM. In both cases the deficiency was overcome by the introduction of a secondary-regularization term on the right-hand side of the momentum equation. In our preliminary iteration, we used a regularization term based on selective frequency damping, introduced by Åkervik *et al.*[7]. We analyzed the energy spectra, the mean flow, the root-mean-square of the velocity fluctuations, and the Reynolds stresses. The results demonstrate a significant improvement compared to no-model solutions regarding the mean flow in the turbulent channel and the energy spectrum in the HIT case, while the computational cost is reduced dramatically compared to direct numerical simulation. Furthermore, it can be shown that with adequate temporal and spatial resolution, the unfiltered fields can be fully restored using Eq. (5). [8]

The underlying premise of TLES is that attenuation of high-frequency content also attenuates high-wavenumber content. Yet, to date, the effect in wavenumber space of removing high-frequency oscillations by time-domain filtering is not well understood. We numerically investigated the relationship between frequency and wavenumber with particular attention to the role of the temporal residual-stress in TLES. Since under-resolved simulations that use high-order, non-dissipative numerical methods require some measure of artificial dissipation for stabilization the regularization term is of practical relevance to under-resolved applications of TLES. Specifically, we analyzed the effects of Eulerian time-domain filtering with a causal exponential filter on homogeneous isotropic turbulence. The data are generated by direct numerical simulation of the Navier-Stokes equations, which are driven to maintain an average Reynolds number (Re_λ) of 200. *A priori*, Fourier transformations of the velocity fields were performed in order to compute the unfiltered and filtered energy and dissipation spectra in both wavenumber space and wavenumber-frequency space. Furthermore, the amount of unresolved dissipation of an insufficiently resolved simulation was approximated in an attempt to estimate the required additional artificial dissipation. The results indicate that the numerically motivated stabilization term can be reduced due to temporal filtering, as shown in Fig. 1. Moreover, it has been shown that a sharp cutoff in the frequency domain does not translate into a sharp cutoff in the wavenumber space. Thus, a hybrid model that combines temporal filtering for the residual-stress and spatial filtering for stabilization might be advantageous. [9]

Following up on these findings, we performed a numerical examination of two different spatial regularization terms in conjunction with TDDM: a spatial variant of selective frequency damping, functioning as a relaxation term that gradually drifts the velocity towards the filtered velocity, and the dynamic Smagorinsky model incorporating a prefactor. Furthermore, the hypothesis that the temporal residual-stress

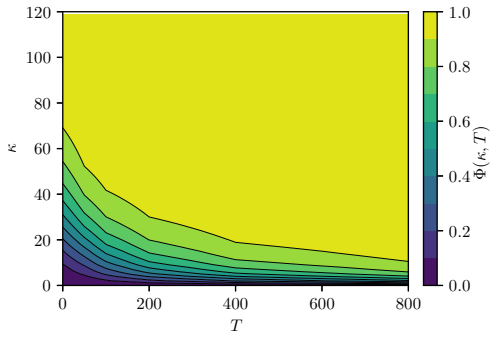

Figure 1: Fraction of the resolved dissipation ϕ; this figure illustrates how larger filter widths can resolve a larger fraction of the total dissipation with reduced resolution.

leads to a reduction of the required artificial dissipation in under-resolved simulations was tested. We also corroborated earlier discoveries with *a posteriori* results and tested various cases, including the Taylor-Green vortex flow with a Reynolds number of $Re = 3000$, forced homogeneous isotropic turbulence with $Re_\lambda = 200$, turbulent channel flow at $Re_\tau = 590$, and the flow over a periodic hill with $Re = 10,935$. Additionally, we also analyzed the various dissipation contributions in TDDM, as well as their interrelations. We also discussed grid artifacts and energy budget errors, to compare the different models. Our results confirm the hypothesis that residual-stress dissipation reduces the necessary artificial dissipation. Because of the numerical ill-conditioning of deconvolution, whether temporal or spatial, there are practical limitations in the size of the filter width T. Due to these limitations, the impact remains relatively minor. The *a posteriori* results of the new spatial regularization term show it to be effective in eliminating energy from the high wavenumber range.

REFERENCES

[1]Stolz, S., Adams, N.A. : An approximate deconvolution procedure for large-eddy simulation, *Physics of Fluids*, vol. 11, no. 7, 1699-1701, (1999).

[2]Pruett, C.D., Gatski, T.B., Grosch, C.E., Thacker, W.D.. : The temporally filtered Navier–Stokes equations: Properties of the residual stress, *Physics of Fluids*, vol. 15, no. 8, 2127-2140, (2003).

[3]Pruett, C.D. : Temporal large-eddy simulation: Theory and implementation: Properties of the residual stress, *Theoretical and Computational Fluid Dynamics*, vol. 22, no. 3-4, 275-304, (2008).

[4]Corrêa, L., Mompean, G., Kurokawa, F.A., Sousa, F.S. : Temporal large-eddy simulations of the lid-driven cavity by finite volume method, *Journal of the Brazilian Society of Mechanical Sciences and Engineering*, vol. 40, no. 9, (2018).

[5]Argonne National Laboratory : Nek5000 Version 19.0, https://nek5000.mcs.anl.gov, (2023).

[6]Bardina, J., Ferziger, J., Reynolds, W. : Improved subgrid-scale models for large-eddy simulation, *13th fluid and plasmadynamics conference*, 1357, (1980).

[7]Åkervik, E., Brandt, L., Hennigson, D.S., Hœpffner, J., Marxen, O., Schlatter, P. : Steady solutions of the navier-stokes equations by selective frequency damping, *Physics of Fluids*, vol. 18, no. 6, 068102, (2006).

[8]Oberle, D., Pruett, C.D., Jenny, P. : Temporal large-eddy simulation based on direct deconvolution, *Physics of Fluids*, vol. 32, no. 6, 065112, (2020).

[9]Oberle, D., Pruett, C.D., Jenny, P. : Effects of time-filtering the Navier–Stokes equations, *Physics of Fluids*, vol. 35, no. 6, 065112, (2023).

WORKSHOP
Direct and Large-Eddy Simulation 14
April 10-12 2024, Erlangen, Germany

HIGH-ORDER NUMERICAL SCHEMES BASED ON APPROXIMATE DECONVOLUTION DISCRETISATION

A. Boguslawski [1], K. Wawrzak [1], A. Tyliszczak [1], B. J. Geurts [2]
[1] Department of Thermal Machinery
Czestochowa University of Technology, Poland
[2] Mathematics of Multiscale Modeling and Simulation
University of Twente, Netherlands
artur.tyliszczak@pcz.pl

INTRODUCTION

It has been shown recently [1] that low-order finite differencing schemes can easily be transformed into high-order methods by approximate deconvolution of the filters implied by the original low-order schemes. The approximately inverted filter is applied to the function to be differentiated, before the low-order scheme is applied. This can lead to an overall more accurate method. We discuss new discretizations arrived at in detail and apply the new schemes to a number of canonical flow problems.

The inversion of the filter implied by the basic spatial discretization was called Approximate Deconvolution Discretisation (ADD) and analysed in [1] using trapezoidal, Simpson, and spectral quadratures to define the discrete form of the implied filters. It was shown analytically and via numerical experiments that the order of the ADD scheme is determined by the accuracy with which the inversion of the implied filter kernel can be realized, and not by the order of the original scheme. This opens up new possibilities to create schemes of an arbitrary order based on, for example, second-order central differencing. A range of central and asymmetric schemes can be developed. The new high-order schemes will be tested on canonical fluid dynamics testcases like the double-jet and Taylor-Green flows.

APPROXIMATE DECONVOLUTION OF INDUCED FILTERS

Consider a general finite difference method for numerically approximating the first-order partial derivative of a function u in one spatial dimension given by

$$\delta_x u(x_i) = \frac{1}{h} \sum_{j=-n}^{m} a_j u_{i+j} \tag{1}$$

where we denoted $u_{i+j} = u(x_{i+j})$, i.e., the solution in the point x_{i+j} of the grid $\{x_k\}$. For convenience we restrict to discretization on a uniform grid with a grid spacing h, and adopt a general stencil of $m + n + 1$ nodes, denoted by $[-n, m]$.

The implied filter L can be related to the discretization weights and expressed in terms of a series of explicit top-hat filters [2]. It can be expressed as a weighted average of skewed top-hat filters of width h

$$L(u(x_i)) = \sum_{j=-n+1}^{m} b_j \left(\frac{1}{h} \int_{x_i+(j-1)h}^{x_i+jh} u(\eta) d\eta \right) \tag{2}$$

where

$$b_j = \sum_{i=j}^{m} a_i, \quad j = -n+1, \ldots, m \tag{3}$$

Using Lagrange interpolation in the ADD procedure

$$\begin{aligned} L_{n,m}^{N^L,M^L}\left[u\left(x_i\right)\right] &= \frac{1}{h} \sum_{j=-n+1}^{m} b_j \int_{x_i+(j-1)h}^{x_i+jh} u\left(\eta\right) d\eta \\ &\approx \frac{1}{h} \sum_{j=-n+1}^{m} b_j \int_{(j-1)h}^{jh} L\left(\xi\right) d\xi \end{aligned} \tag{4}$$

where $L(\eta)$ is the Lagrange polynomial of degree $d^L = N^L + M^L$, with

$$N^L \geqq n \quad \text{and} \quad M^L \geqq \ m \tag{5}$$

The Lagrange polynomial is defined as

$$L(y) = \sum_{l=-N^L}^{M^L} u_{i+l} l_l(y) \tag{6}$$

where $y = x - x_i$, and the Lagrange basis polynomials are

$$l_l(y) = \prod_{\substack{N^L \leqq m \leqq M^L \\ m \neq l}} \frac{y - y_m}{y_l - y_m} = Q_l^L \sum_{q=0}^{d^L} A_q^l y^q \tag{7}$$

where

$$Q_j^L = \prod_{\substack{-N^L \leqq m \leqq M^L \\ m \neq j}} \frac{1}{y_l - y_m} \tag{8}$$

Here, the coefficients A_q^l are established by a recurrence procedure. Finally, using Lagrange interpolation the discrete form of the implied filtration is

$$L_{n,m}^{(N^L,M^L)}[u(x_i)] = \tag{9}$$
$$= \frac{1}{h} \sum_{j=-n+1}^{m} b_j \sum_{l=-N^L}^{M^L} u_{i+l} \times$$
$$\times Q_l^L \sum_{q=0}^{d^L} A_q^l \frac{[(l+1)h]^{q+1} - (lh)^{q+1}}{q+1}$$

and consequently the discrete form of the filter kernel reads

$$G_l^{(n,m),(N^L,M^L)} =$$
$$= \frac{1}{h} \sum_{j=-n+1}^{m} b_j \sum_{q=0}^{d^L} A_q^j \frac{[(l+1)^{q+1} - l^{q+1}]h^{q+1}}{q+1}$$
for $l = -N^L, \ldots, M^L$

Figure 1 shows the differentiation errors as a function of the mesh size in case fourth-order Lagrange interpolation is applied to a smooth function $u(x) = \sin(x) + \cos(x)$. Limiting our attention to periodic boundary conditions, the inversion of the discretised implied filter was performed by the Wiener procedure.

The central scheme, where $N^L = M^L = 2$, is compared to asymmetric interpolation ($N^L = 1, M^L = 3$,$N^L = 3, M^L = 1$). It can be seen that the central interpolation leads to a sixth-order scheme while in the case of asymmetric interpolation, the accuracy

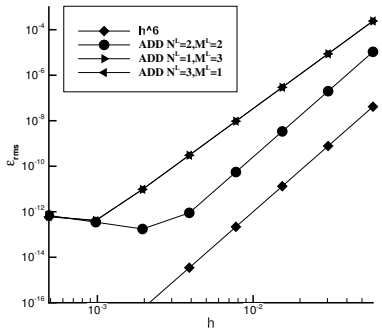

Figure 1: Error of differentiation for the first derivative. The integral is calculated using the Lagrange polynomial of degree four and a comparison is made with central and asymmetric interpolation.

is reduced to fifth order. The asymmetric interpolation could be considered as upwinding and the stability properties of these schemes for the first and second derivatives will be studied.

New high-order ADD schemes will be tested using canonical flow problems such as Taylor-Green and double jet flows. Sample results for the double jet flow are shown in Fig. 2 where vorticity contours obtained with ADD-spectral differentiation [1] are presented.

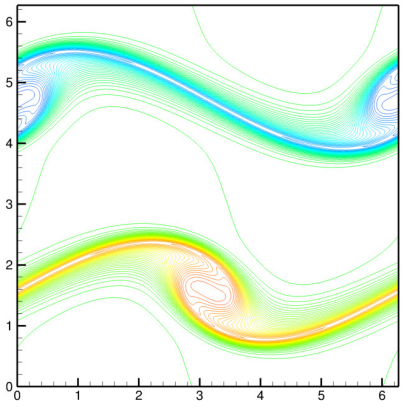

Figure 2: Vorticity contours in the double jet flow.

REFERENCES

[1]Boguslawski, A., Tyliszczak, A. and Geurts, B. J. : Approximate deconvolution discretisation, Comput. Math. Appl., **154**, 175–198 (2024).

[2]Geurts B. J., van der Bos F.: Numerically induced high-pass dynamics in large-eddy simulation, Phys. Fluids, **17**, 125103-12 (2005).

WORKSHOP
Direct and Large-Eddy Simulation 14
April 10-12 2024, Erlangen, Germany

IMPROVING THE APPROXIMATE DECONVOLUTION METHOD FOR LARGE EDDY SIMULATIONS THROUGH THE USE OF INDUCED FILTERS

L. Caban[1], A. Tyliszczak [1], B.J. Geurts[2] and J.A. Domaradzki[3]
[1]Department of Thermal Machinery, Czestochowa University of Technology, Poland
[2]Mathematics of Multiscale Modeling and Simulation, University of Twente, The Netherlands
[3]Department of Aerospace and Mechanical Engineering, University of Southern California, USA
lena.caban@pcz.pl

INTRODUCTION

The LES approach has undergone over 50 years of development, during which significant efforts have been dedicated to various aspects, including filtering techniques, commutation errors, sub-grid models, and addressing interactions with numerically induced errors. This extensive work has contributed to the current maturity of the LES approach, establishing it as a reliable tool in computational fluid dynamics (CFD) simulations. Among these aspects, modeling sub-grid terms has received the most attention due to its substantial impact on simulation accuracy.

The sub-grid stress tensor, denoted as $\tau_{ij} = \overline{u_i u_j} - \overline{u}_i \overline{u}_j$, emerges from the filtering of the advective term in the Navier-Stokes equations. The filtering, represented by the bar symbol, is associated with some kernel G such that $\int G \mathrm{d}\Omega = 1$. Numerous papers have been dedicated to models for τ_{ij}, generally falling into two categories: those developed based on physical principles and those data-driven. Among the latter, the Approximate Deconvolution Method (ADM) stands out as the most popular, boasting a strong theoretical foundation. Introduced by Stoltz and Adams [1], the ADM approach for LES involves approximating u from the filtered variables ($\overline{u} \to u^*$) and utilizing it directly in $\tau_{ij} = \overline{u_i^* u_j^*} - \overline{u}_i \overline{u}_j$. The 'recovered' variables u^* are obtained by the van Cittert iterative deconvolution method defined as

$$u^* = \underbrace{\sum_{n=0}^{N} (I - G)^n}_{Q_{N_{\mathrm{ADM}}}} \overline{u} \tag{1}$$

The approximate character of the ADM approach comes not only from the limited number of terms N_{ADM} in (1). Primarily, ADM does not result in $u^* \to u$, as sometimes misleadingly inferred. In practice, the filtering stems from assuming a computational mesh on which the equations are solved. The mesh implicitly excludes (or filters out, in LES terminology) from the solution all scales smaller than a grid spacing h. The way how this is done is unknown, and hence, the form of G is unknown. It has to be assumed, but even then the formula (1) will not generate the flow scales smaller than h, they remain unrecoverable. So, the question arises "What does ADM actually do?".

The role of ADM is to 'recover' part of the solution in the range of the smallest resolved flow scales (RFS), where significant computational distortions occur from solving the filtered equations on a numerical mesh using discretization methods [3]. Such an ADM-improved solution, when applied in $\overline{u_i^* u_j^*}$, will approximate $\overline{u_i u_j}$ accurately provided that G employed in (1) is chosen properly. There is, however, no univocal recipe how G should be selected. It can be assumed *ad hoc* or tuned to reflect the level of distortion of $\overline{u}$ in the RFS range.

In this paper, we focus on this issue of selecting the filter kernel G in the ADM approach, comparing the accuracy of LES-ADM applied to modelling the Taylor-Green vortex flow (TGV), which is an important canonical problem in turbulence. Achilles' heel of most benchmark cases are initial and boundary conditions of which different assumptions and implementations often lead to differences between results larger than those resulting from the use of different models or methods being actually compared. In TGV, analytically defined initial conditions and assumed 3D periodicity of the solution exclude these uncertainties. Beside these simplifications, TGV serves as an excellent test case to validate turbulent flow models. It is characterised by a laminar-turbulent transition that leads to fully developed turbulent flow transforming into decaying homogenous isotropic turbulence.

NUMERICALLY INDUCED FILTERS

Because of discretization of the LES equations (and DNS as well) on a numerical mesh, the partial derivatives (e.g., $\partial_x, \partial_{xx}$) at the PDE level are not equal to their discrete counterparts ($\partial_x \neq \delta_x$, $\partial_{xx} \neq \delta_{xx}$). This can be expressed as $\delta_x \overline{u} = \partial_x \breve{\overline{u}}$ where the $\breve{(\cdot)}$ symbol denotes a numerically induced filter [2] with an associated filter kernel G_I. For a general form of the finite/compact difference (FD/CD) approximation, spanned on the stencils M, N and given as

$$u'_i + \sum_{k=1}^{M} a_k \left(u'_{i-k} + u'_{i+k} \right) = \frac{1}{h} \sum_{j=1}^{N} b_j \left(u_{i+j} - u_{i-j} \right) \tag{2}$$

the induced filter can be defined as a linear combination of local top-hat filters [4]. The transfer function of G_I in spectral space in terms of the scaled wave number $\omega_n = 2\pi n/K$ (K - number of grid points; $\omega_n \in [0, \pi]$) is defined as

$$\widehat{G}_I(\omega) = \frac{\omega'(\omega)}{\omega} \tag{3}$$

where $\omega'(\omega)$ is a modified wave-number associated with a particular discretization method [5]. Assuming that G in (1) differs from G_I, for instance G is taken as finite or compact difference type filter (FDF, CDF) with general formula

$$\bar{f}_i + \sum_{k=1}^{M_f} a_k \left(\bar{f}_{i+k} + \bar{f}_{i-k}\right) = \frac{1}{2}\sum_{j=0}^{N_f} b_j \left(f_{i+j} + f_{i-j}\right) \qquad (4)$$

their transfer functions differ and the mismatch can be significant. Figure 1 shows transfer functions of the 2nd-10th order FDF and CDF filters compared with $\widehat{G}_I(\omega)$ induced by a 6th order CD approximation ($M = 1$, $N = 2$ in (2)). Additionally, in some LES studies an explicit filtering is applied (G_E), which acts on $\overline{u}$ at each time step [2]. The form and width $\Delta \geq h$ of G_E are known and its use intends to reduce numerical errors for the small scales in the RFS through the chosen separation of scales between π/Δ and the cut-off wave-number π/h. In total, the effective filter acting on $\overline{u}$ is the superposition of G_E and G_I. Denoting it as $H = G_E G_I$ the result of the deconvolution can be written as [6]

$$Q_{N_{\mathrm{ADM}}}(H\overline{u}) = \frac{I - (I - G)^{N_{\mathrm{ADM}}+1}}{G} H\overline{u} \qquad (5)$$

To illustrate the impact of using different G and H, in Fig. 2 we show the transfer function of the convolution $\widehat{Q_5 * H} = \widehat{Q_5}\widehat{H}$. When Q_5 is based on H (blue lines), the deconvolution effectively removes the effect of filtering. If Q_5 is computed based on a filter G of lower order than H (black lines), the deconvolution is not able to recover the RFS of the unfiltered solution. On the other hand, if the order of G is higher than that of H an overshoot occurs. In this case the deconvolved field u^* would contain more energy than $\overline{u}$.

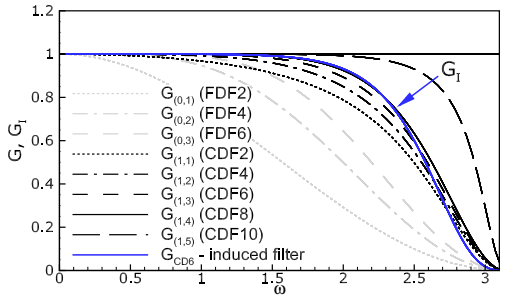

Figure 1: Transfer functions of several FDF and CDF schemes along with the filter induced by the 6th order CD scheme. Subscripts (M_f, N_f) are the stencils used in (4)

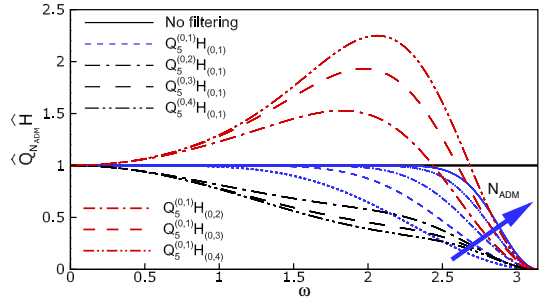

Figure 2: Effect of deconvolution using various order filters.

TAYLOR-GREEN VORTEX SIMULATION

Figure 3 shows the evolution of the energy dissipation for TGV at $Re = 400$ and $Re = 1600$ obtained using the 6th order CD scheme. The red lines correspond to the present DNS results obtained on two different meshes. It can be seen that the agreement with DNS data from Brachet et al. [7] and Van Rees et al. [8] obtained using a pseudo-spectral method is excellent. The grey and black lines with circles denote the LES-ADM results on the grid with 64^3 nodes employing Q_5 computed with two assumed kernels. We compare Q_5 based on the 2nd order FD filter, whose transfer function $\widehat{G}$ significantly differs from $\widehat{G}_I$ (see Fig. 1), and 6th order FD filter, whose $\widehat{G}$ approximates $\widehat{G}_I$ quite well. Evidently, in the latter case the results are more accurate, especially for $Re = 400$. During the conference we will present a detailed analysis of LES-ADM for various combination of filters and discretization schemes, including a comparison of the evolution of higher order moments (skewness and flatness). We will consider dissipative and non-dissipative discretizations. The simulations will cover both the initial phase of the TGV evolution as well as the later stages of energy decay resembling homogenous isotropic turbulence.

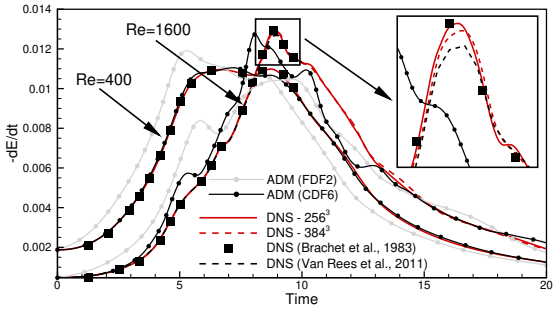

Figure 3: TGV: Rate of energy dissipation for DNS at $Re = 400$ and $Re = 1600$.

REFERENCES

[1]Stolz S., Adams N. A.: An approximate deconvolution procedure for large-eddy simulation, *Physics of Fluids*, **11**(7), 1699–1701, 1999.

[2]Lund, T. S. : The use of explicit filters in large eddy simulation, *Computers & Mathematics with Applications*, **46**(4), 603–616 (2003).

[3]Carati, D., Winckelmans, G. S. and Jeanmart, H. : On the modelling of the subgrid-scale and filtered-scale stress tensors in large-eddy simulation, *Journal of Fluid Mechanics*, **441**, 119–138 (2001).

[4]Geurts, B.J. and van der Bos, F. : Numerically induced high-pass dynamics in large-eddy simulation, *Physics of Fluids*, **17**(12), 125103 (2005).

[5]Caban, L. and Tyliszczak, A.: High-order compact difference schemes on wide computational stencils with a spectral-like accuracy, *Computers & Mathematics with Applications*, **108**(4), 123–140 (2022).

[6]Tantikul, T. Domaradzki, J.A: Large eddy simulation using truncated Navier-Stokes equations with the automating filtering criterion, *Journal of Turbulence*, **11**(21),1–24 (2010).

[7]Brachet, M. E., Meiron, D. I., Orszag, S. A., Nickel, B. G., Morf, R. H. and Frisch, U. : Small-scale structure of the Taylor–Green vortex, *Journal of Fluid Mechanics*, **130**(1), 411–452 (1983).

[8]Van Rees, W. M., Leonard, A., Pullin, D. I. and Koumoutsakos, P. : A comparison of vortex and pseudo-spectral methods for the simulation of periodic vortical flows at high Reynolds numbers, *Journal of Computational Physics*, **230**(8), 2794–2805 (2011).

WORKSHOP
Direct and Large-Eddy Simulation 14
April 10-12 2024, Erlangen, Germany

A STABLE REGULARIZATION OF THE GRADIENT MODEL

F.X. Trias[1], **A. Gorobets**[2], **A. Oliva**[1]
[1] Heat and Mass Transfer Technological Center, Technical University of Catalonia
C/Colom 11, 08222 Terrassa (Barcelona) E-mail: francesc.xavier.trias@upc.edu
[2] Keldysh Institute of Applied Mathematics, 4A, Miusskaya Sq., Moscow 125047, Russia

INTRODUCTION

In the last decades, many engineering/scientific applications have benefited from the advances in the field of Computational Fluid Dynamics (CFD). Unfortunately, most of practical turbulent flows cannot be directly computed from the Navier–Stokes equations because not enough resolution is available to resolve all the relevant scales of motion. Therefore, practical numerical simulations have to resort to turbulence modeling. We may therefore turn to large-eddy simulation (LES) to predict the large-scale behavior of turbulent flows. In LES, the large scales of motions are explicitly computed, whereas effects of small scale motions are modeled. Since the advent of CFD many subgrid-scale models have been proposed and successfully applied to a wide range of flows. Eddy-viscosity models for LES is probably the most popular example thereof. Then, for problems with the presence of active/passive scalars (*e.g.* heat transfer problems, transport of species in combustion, dispersion of contaminants,...) the (linear) eddy-diffusivity assumption is usually chosen. However, this type of approximation systematically fails to provide a reasonable approximation of the actual SGS flux because they are strongly misaligned [1, 2]. This was clearly shown in our previous works [3, 4] where SGS features were studied *a priori* for a RBC at Ra-number up to 10^{11} (see $\boldsymbol{q}^{eddy}$ in Figure 1). This leads to the conclusion that nonlinear (or tensorial) models are necessary to provide good approximations of the actual SGS heat flux (see $\boldsymbol{q}$ in Figure 1). In this regard, the nonlinear Leonard model [5] or gradient model, which is the leading term of the Taylor series of the SGS flux, provides a very accurate *a priori* approximation (see $\boldsymbol{q}^{nl}$ in Figure 1). However, the local dissipation introduced by the model can take negative values; therefore, the Leonard model cannot be used as a standalone SGS flux model, since it produces a finite-time blow-up. In this context, we aim to shed light to the following research question: *can we a simple approach to reconcile accuracy and stability for the gradient model?*

DECONSTRUCTING THE GRADIENT MODEL

Let us firstly consider the following transport equation

$$\partial_t \phi + \mathcal{C}(\boldsymbol{u},\phi) = \mathcal{D}\phi, \tag{1}$$

where $\boldsymbol{u}$ denotes the advective velocity and ϕ represents a generic (transported) scalar field. The non-linear convective term is given by $\mathcal{C}(\boldsymbol{u},\phi) \equiv (\boldsymbol{u}\cdot\nabla)\phi$ whereas the diffusive terms reads $\mathcal{D}\phi \equiv \Gamma\nabla^2\phi$. Shortly, LES equations arises from

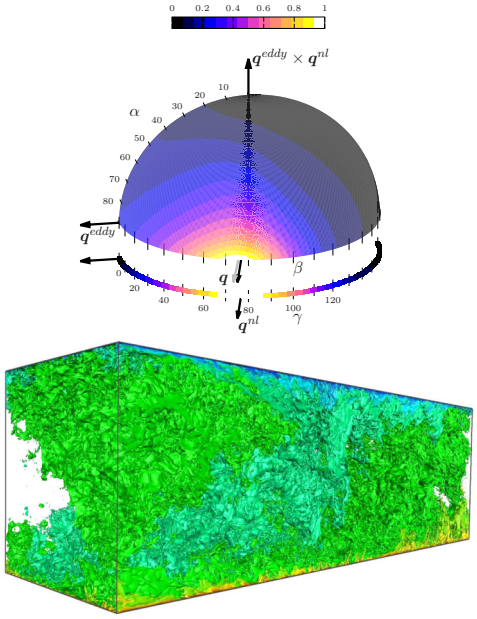

Figure 1: Left: alignment trends of the actual SGS heat flux. For details the reader is referred to our work [3]. Right: DNS of the air-filled RBC at $Ra = 10^{10}$ studied in Refs. [3, 6].

applying a spatial commutative filter, $\overline{(\cdot)}$, with filter length, δ,

$$\partial_t \overline{\phi} + \mathcal{C}(\overline{\boldsymbol{u}},\overline{\phi}) = \mathcal{D}\overline{\phi} - \nabla\cdot\tau_\phi, \tag{2}$$

where $\tau_\phi \equiv \overline{\boldsymbol{u}\phi} - \overline{\boldsymbol{u}}\,\overline{\phi}$ is the subgrid scalar flux. Then, the gradient model follows from considering a Taylor-series expansion of the filter

$$\phi = \overline{\phi} + \phi' = \overline{\phi} - \frac{\delta^2}{24}\nabla^2\phi + \mathcal{O}(\delta^4), \tag{3}$$

where ϕ' is the filter residual. Then, applying this to $\overline{\boldsymbol{u}\phi}$ and $\overline{\boldsymbol{u}}\,\overline{\phi}$ leads to

$$\begin{aligned}\overline{\boldsymbol{u}\phi} &\approx \boldsymbol{u}\phi + \frac{\delta^2}{24}\nabla^2(\boldsymbol{u}\phi)\\ &= \boldsymbol{u}\phi + \frac{\delta^2}{24}(\nabla^2\boldsymbol{u})\phi + \frac{\delta^2}{12}\nabla\boldsymbol{u}\nabla\phi + \frac{\delta^2}{24}\boldsymbol{u}\nabla^2\phi, \qquad (4)\\ \overline{\boldsymbol{u}}\,\overline{\phi} &\approx \left(\boldsymbol{u} + \frac{\delta^2}{24}\nabla^2\boldsymbol{u}\right)\left(\phi + \frac{\delta^2}{24}\nabla^2\phi\right)\\ &= \boldsymbol{u}\phi + \frac{\delta^2}{24}(\nabla^2\boldsymbol{u})\phi + \frac{\delta^2}{24}\boldsymbol{u}\nabla^2\phi + \frac{\delta^4}{24^2}\nabla^2\boldsymbol{u}\nabla^2\phi. \qquad (5)\end{aligned}$$

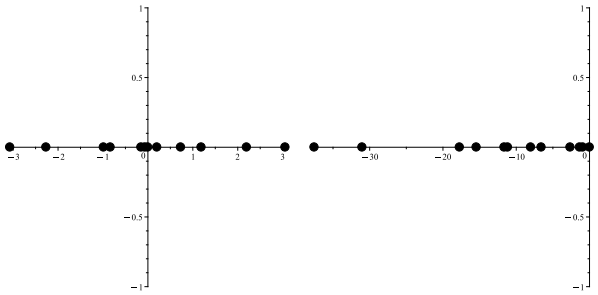

Figure 2: Location of the eigenvalues for the matrix $\mathsf{CF}-\mathsf{FC}$ (left) and $\mathsf{C}^{UP}\mathsf{F}-\mathsf{FC}^{UP}$ (right). Results correspond to a 4×3 Cartesian with a random divergence-free velocity field.

Finally, plugging this into the definition of τ_ϕ and discarding high-order terms leads to the standard form of the gradient model

$$\tau_\phi \approx \tau_\phi^{grad} = \frac{\delta^2}{12}\nabla\boldsymbol{u}\nabla\phi. \tag{6}$$

Alternatively, it can be expressed in terms of regularized (smoother) forms of the convective operator as follows

$$\nabla\cdot\tau_\phi^{grad} = \mathcal{C}(\boldsymbol{u},\phi) + \overline{\mathcal{C}(\boldsymbol{u},\phi)} - \mathcal{C}(\overline{\boldsymbol{u}},\phi) - \mathcal{C}(\boldsymbol{u},\overline{\phi}), \tag{7}$$

where

$$\overline{\mathcal{C}(\boldsymbol{u},\phi)} - \mathcal{C}(\boldsymbol{u},\phi) = \frac{\delta^2}{24}\nabla^2\nabla\cdot(\boldsymbol{u}\phi) = \frac{\delta^2}{24}\nabla\cdot(\nabla^2(\boldsymbol{u}\phi)), \tag{8}$$

$$\mathcal{C}(\overline{\boldsymbol{u}},\phi) - \mathcal{C}(\boldsymbol{u},\phi) = \frac{\delta^2}{24}\nabla\cdot((\nabla^2\boldsymbol{u})\phi), \tag{9}$$

$$\mathcal{C}(\boldsymbol{u},\overline{\phi}) - \mathcal{C}(\boldsymbol{u},\phi) = \frac{\delta^2}{24}\nabla\cdot(\boldsymbol{u}\nabla^2\phi). \tag{10}$$

The alternative form given in Eq.(7) is simply based on the non-linear convective operator and the linear filter; therefore, its implementation is straightforward. Moreover, it avoids the interpolations required if the standard gradient model given in Eq.(6) is directly implemented. Finally, it facilitates the analysis of the gradient model, neatly identifying those terms that may cause numerical instabilities. This is addressed in the next section.

STABILIZING THE GRADIENT MODEL

Following the notation used in Ref. [7], the novel form of the gradient model given in Eq.(7) would be discretized as follows

$$\mathsf{M}\boldsymbol{\tau}_{\phi,h}^{grad} = \mathsf{C}(\boldsymbol{u}_s)\,\boldsymbol{\phi}_c + \mathsf{FC}(\boldsymbol{u}_s)\,\boldsymbol{\phi}_c - \mathsf{C}(\mathsf{F}\boldsymbol{u}_s)\,\boldsymbol{\phi}_c - \mathsf{C}(\boldsymbol{u}_s)\,\mathsf{F}\boldsymbol{\phi}_c, \tag{11}$$

where $\boldsymbol{u}_s$ and $\boldsymbol{\phi}_c$ are respectively the discrete velocity field defined at the faces and the cell-centered scalar field. Moreover, M, $\mathsf{C}(\boldsymbol{u}_s)$ and F are matrices representing the discrete divergence, convective and filter operators. For details, the reader is referred to Ref. [7]. This discrete form of τ_ϕ^{grad} can be expressed in matrix-vector form as follows

$$\mathsf{M}\boldsymbol{\tau}_{\phi,h}^{grad} = \begin{pmatrix}\mathsf{I}\\ \mathsf{F}\end{pmatrix}^T \begin{pmatrix}\mathsf{C}(\boldsymbol{u}_s)-\mathsf{C}(\mathsf{F}\boldsymbol{u}_s) & -\mathsf{C}(\boldsymbol{u}_s)\\ \mathsf{C}(\boldsymbol{u}_s) & 0\end{pmatrix}\begin{pmatrix}\mathsf{I}\\ \mathsf{F}\end{pmatrix}\boldsymbol{\phi}_c. \tag{12}$$

Recalling that the discrete convective and filter operator should be respectively represented by a skew-symmetric matrix, $\mathsf{C}=-\mathsf{C}^T$, and a symmetric matrix, $\mathsf{F}=\mathsf{F}^T$, the contribution of the gradient model to the time-evolution of the L2-norm of $\boldsymbol{\phi}_c$ is given by

$$-\boldsymbol{\phi}_c\cdot\mathsf{M}\boldsymbol{\tau}_{\phi,h}^{grad} = \boldsymbol{\phi}_c\cdot(\mathsf{CF}-\mathsf{FC})\,\boldsymbol{\phi}_c. \tag{13}$$

Hereafter, for simplicity, $\mathsf{C}=\mathsf{C}(\boldsymbol{u}_s)$. Therefore, stability of the gradient model is determined by the sign of the Rayleigh quotient of the matrix $\mathsf{CF}-\mathsf{FC}$. Therefore, if $\mathsf{C}=-\mathsf{C}^T$, as it should be from a physical point-of-view,

$$\boldsymbol{\phi}_c\cdot\mathsf{CF}\boldsymbol{\phi}_c = \boldsymbol{\phi}_c\cdot(\mathsf{CF})^T\boldsymbol{\phi}_c = \boldsymbol{\phi}_c\cdot\mathsf{F}^T\mathsf{C}^T\boldsymbol{\phi}_c = -\boldsymbol{\phi}_c\cdot\mathsf{FC}\boldsymbol{\phi}_c. \tag{14}$$

In this case, there is no guarantee that the eigenvalues of the matrix $\mathsf{CF}-\mathsf{FC}$ will lie on stable half-side and, therefore, the gradient model will be eventually unstable. This is clearly shown in Figure 2 (left) where the locations of the eigenvalues is displayed for a 3×4 Cartesian mesh with a random divergence-free velocity field.

Nevertheless, at this point, we have neatly identified the discrete operators that lead to unstable modes. Hence, they must be modified if we aim to solve the problem. A very simple solution consists on using an upwind for the convective terms in Eq.(13); namely, replacing C by C^{UP} in the off-diagonal terms in Eq.(12), leading to an overall contribution to the time-evolution of the L2-norm of $\boldsymbol{\phi}_c$ given by

$$-\boldsymbol{\phi}_c\cdot\mathsf{M}\boldsymbol{\tau}_{\phi,h}^{grad} = \boldsymbol{\phi}_c\cdot\left(\mathsf{C}^{\mathsf{UP}}\mathsf{F}-\mathsf{FC}^{\mathsf{UP}}\right)\boldsymbol{\phi}_c, \tag{15}$$

where C^{UP} corresponds to a first-order upwind discretization of the convective term. In this way, all the eigenvalues lie on the stable half-side (see Figure 2, right). A formal proof together with both *a priori* and *a posteriori* tests will be presented.

ACKNOWLEDGMENTS

F.X.T. and A.O. are supported by SIMEX project (PID2022-142174OB-I00) of *Ministerio de Ciencia e Innovación* and the RETOtwin project (PDC2021-120970-I00) of *Ministerio de Economía y Competitividad*, Spain. Calculations were carried out on MareNostrum 4 supercomputer at BSC. The authors thankfully acknowledge these institutions.

REFERENCES

[1] C. W. Higgins, M. B. Parlange, and C. Meneveau. The heat flux and the temperature gradient in the lower atmosphere. *Geophysical Research Letter*, 31:L22105, 2004.

[2] S. G. Chumakov. "*A priori* study of subgrid-scale flux of a passive scalar in isotropic homogeneous turbulence. *Physical Review E*, 78:036313, 2008.

[3] F. Dabbagh, F. X. Trias, A. Gorobets, and A. Oliva. A priori study of subgrid-scale features in turbulent Rayleigh-Bénard convection. *Physics of Fluids*, 29:105103, 2017.

[4] F. Dabbagh, F. X. Trias, A. Gorobets, and A. Oliva. Flow topology dynamics in a three-dimensional phase space for turbulent Rayleigh-Bénard convection. *Physical Review Fluids*, 5:024603, 2020.

[5] A. Leonard. Large-eddy simulation of chaotic convection and beyond. *AIAA paper*, 97-0304, 1997.

[6] F.X. Trias, F.Dabbagh, A.Gorobets, and C.Oliet. On a proper tensor-diffusivity model for large-eddy simulation of buoyancy-driven turbulence. *Flow, Turbulence and Combustion*, 105:393–414, 2020.

[7] F. X. Trias, O. Lehmkuhl, A. Oliva, C.D. Pérez-Segarra, and R.W.C.P. Verstappen. Symmetry-preserving discretization of Navier-Stokes equations on collocated unstructured meshes. *Journal of Computational Physics*, 258:246–267, 2014.

WORKSHOP
Direct and Large-Eddy Simulation 14
April 10-12 2024, Erlangen, Germany

HOW TO MODEL DISTANT TRIAD INTERACTIONS TO SUPPLEMENT IMPLICIT LES?

E. Lamballais[1], R. Vicente Cruz[1] & R. Perrin[2]
[1] Curiosity Group, Pprime Institute, CNRS - Univ-Poitiers - ENSMA, France
[2] Department of Mechanical Engineering, Faculty of Engineering, Kasetsart University Sriracha, Thailand
eric.lamballais@univ-poitiers.fr

INTRODUCTION

In the closure problem associated to large-eddy simulation (LES), the strategy of subgrid-scale modelling can be developed regardless numerics through the definition of a low-pass filtering operator disconnected from the numerical errors (commutation, differentiation, aliasing). This formal approach has stimulated research on the interactions between large and small-scale motions in turbulence, especially those through a separation length Δ used to define the low-pass filter. Even if this way of thinking subgrid-scale modelling is elegant, it is widely recognized that the contribution of numerical errors can become pervasive, making practical LES weakly connected to this type of research except when spectral Fourier methods can be used. This mismatch between theory and practice may be one of the reasons of the development of a more empirical approach of LES where the subgrid-scale modelling is entrusted to numerics, leading to the concept of implicit LES.

The present authors have proposed a very simple strategy of implicit subgrid-scale modelling which consists in boosting artificially the dissipation at small scale. This effect can be obtained through the differentiation of the viscous term [1] or by solution filtering [2, 3]. Both techniques are virtually identical while being an implicit counterpart of spectral vanishing viscosity, with the advantage that the governing equations are not modified as well as their boundary conditions. The corresponding operators are essentially linear making the approach Galilean invariant and very flexible. Concerning the second feature, a very simplified spectral closure can be used for *a priori* calibration [1].

This strategy has been extensively used with success [1, 2, 3, 4]. However, it has to be recognized that the numerical consistency of the implicit operator leads to a modelling inconsistency through its lack of activity at large scale [4]. Expressed in terms of triad interactions in the spectral space, this inconsistency means that distant interactions are completely missed by implicit modelling. It could be thought that local interactions are better represented through the application of artificial dissipation at small scale, but this feature is more connected to the scale selectivity of the expected low-pass filtering than to the intensification of triad interactions at the smallest computed scales. Referring to the physical/numerical duality of subgrid-scale modelling as discussed in [4], the numerical component could be entrusted to an implicit model, only active at small-scale, whereas the physical component would be assigned to an explicit model, mainly active at large-scale. This idea to combine two models to better control their resulting scale selectivity is not new, even in the context of implicit LES (see for instance [5]). Here, the goal is to assess such a combination while considering the explicit model as a supplementation to restore the modelling of triad distant interactions. More precisely, the questions are how this specific modelling can be accurately ensured and to what extent it is actually beneficial.

RESULTS

As challenging flow configuration, the 3D Taylor-Green vortex problem is mainly addressed. This problem is very demanding for subgrid-scale modelling which has to handle transition from laminarity with a strong breakdown followed by developed turbulence. Because of these very different states, it seems illusory to design a subgrid-scale model assuming turbulence in equilibrium. In this study, our methodology is to extensively use the database of a DNS performed at the high Reynolds number $Re = 40\,000$ with a computational mesh of 5400^3 nodes. The assessment of the subrid-scale modelling is based on LES carried out at various resolutions $(1080^3, 540^3, 300^3, 216^3)$ corresponding to ratios $k_d/k_c = (5, 10, 18, 25)$ where k_d and k_c are the cutoff wavenumber of the DNS and LES mesh respectively. For all the calculations, the finite-difference and sixth-order accurate code Xcompact3d is used. The investigation is based on both *a priori* and *a posteriori* analyses. As low-pass filter of reference, we use a super-Gaussian transfer function $T_f(k) = \exp(-k^6\Delta^6/256)$ which closely mimics the influence of the numerical dissipation related to the implicit modelling part of the approach [4].

In preliminary mixed subgrid-scale modelling tests presented in [4], the explicit part is ensured by the Smagorinsky model as a way to represent distant triad interactions in an implicit LES. Even if interesting features are observed, especially a compensation mechanism between explicit and implicit dissipation, no clear benefit of this supplementation was observed with a lack of consistency in the scaling of the resulting spectral viscosity at large scale. The purpose of the study is to examine to what extent the Smagorinsky model fails to fulfill this role while developing more accurate models. Writing the subgrid-scale tensor $\sigma_{ij} = \overline{u_i^* u_j^*} - \overline{u_i^*}\,\overline{u_j^*}$, its exact expression is given by $u_i^* = u_i|_{k_d}$ where $u_i|_{k_d}$ is the full DNS solution. The scale-similarity Bardina model is the approximation $u_i^* = \bar{u}_i$

whereas an idealized perfect deconvolution model can be written as $u_i^* = u_i|_{k_c}$ where $u_i|_{k_c}$ is the DNS solution projected on the LES mesh. Another option is to disconnect the LES cell size $\Delta x = \pi/k_c$ from the separation length Δ with for instance $\Delta x = \Delta/2$, i.e. $k_c = 2k_\Delta$, enabling the approximation $u_i^* = u_i|_{2k_\Delta}$ as an idealized perfect deconvolution model based on a twice refined LES mesh.

To exemplify these different approximations, their associated spectral viscosities are compared in figure 1 at the critical time $t = 10$ of the turbulent breakdown for $k_d/k_c = 18$ (see also figure 2 for an illustration of the instantaneous flow state at this time). Even if a non-zero plateau value is provided for the Smagorinsky model at small k, i.e. as a potential modelling of distant triad interactions, its level is only about 25% of the exact value. This exact plateau value corresponds to distant triad interactions that are, by construction, completely missed in implicit LES, and poorly mimicked by the Smagorinsky model as shown in figure 1. Note that this result is expected in the sense that it is well known that the Smagorinsky stresses are weakly correlated to their exact counterparts because of the eddy viscosity assumption. Despite the lack of this assumption in the structural Bardina model, its plateau value is even smaller than that of the Smagorinsky model (see figure 1), suggesting that it is not a good candidate for modelling distant triad interactions. Note that the exact as well as the modelled spectral viscosities exhibit a rise when $k \to k_\Delta$. This behaviour should not be viewed as the footprint of the local triad interactions but more as the signature of the super-Gaussian filter. In particular, this behaviour is not observed with the Smagorinsky model when a Gaussian filter is used.

The spectral viscosities obtained for a perfect deconvolution model are also presented in figure 1. When the deconvolution is restricted to the spectral range $[0, k_\Delta]$, the plateau value reaches about 50% of the exact value, which is a significant improvement. The extension of the deconvolution up to $2k_\Delta$ enables to recover remarkably well the expected plateau value. This observation suggests that an approximate deconvolution model [6] should be based on a more refined mesh than Δ, which is not technically easy in the context of implicit LES for which the numerical dissipation scales on Δx. Another option is to find a rescaling of the predicted plateau value to avoid the disconnection between Δ and Δx. The purpose of this study is to establish this rescaling to make it valuable at any LES resolution and any time for the present 3D Taylor-Green flow. To illustrate this challenging task, the time evolution of the averaged value $\nu_{s<k_\Delta/4}$, as an estimation of the plateau value, is presented in figure 3. The option to rely on a dynamic procedure will be addressed. Once this stage is successfully completed, *a posteriori* tests will be performed to observe whether the present type of supplementation is beneficial for implicit LES. The near-wall behaviour of the resulting mixed subgrid-scale modelling will also be assessed through LES of turbulent pipe and boundary layer flows.

REFERENCES

[1]T. Dairay, E. Lamballais, S. Laizet, and C. Vassilicos, "Numerical dissipation vs. subgrid-scale modelling for large eddy simulation," *J. Comp. Phys.*, vol. 337, pp. 252–274, 2017.

[2]E. Lamballais, R. Vicente Cruz, and R. Perrin, "Viscous and hyperviscous filtering for direct and large-eddy simulation," *J. Comp. Phys.*, vol. 431, p. 110115, 2021.

[3]R. Perrin and E. Lamballais, "High-order finite-difference schemes for (hyper-)viscous filtering on non-uniform meshes," *Flow Turb. Combust.*, vol. https://doi.org/10.1007/s10494-023-00503-5, pp. 1–30, 2023.

[4]R. V. Cruz and E. Lamballais, "Physical/numerical duality of explicit/implicit subgrid-scale modelling," *J. Turbulence*, vol. 24, no. 6-7, pp. 235–279, 2023.

[5]S. Hickel, N. A. Adams, and J. A. Domaradzki, "An adaptive local deconvolution method for implicit LES," *J. Comp. Phys.*, vol. 213, no. 1, pp. 413–436, 2006.

[6]C. Stolz and N. A. Adams, "An approximate deconvolution procedure for large-eddy simulation," *Phys. Fluids*, vol. 11, no. 7, pp. 1699–1701, 1999.

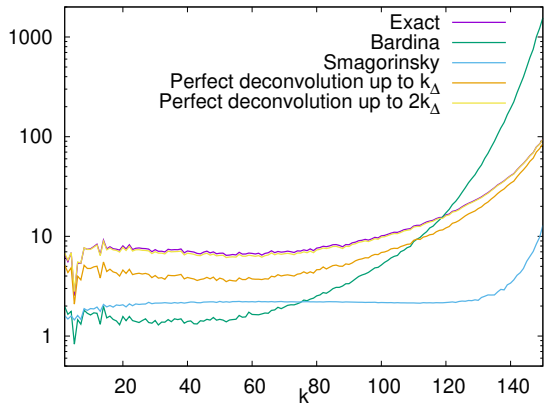

Figure 1: Exact and modelled spectral viscosities $\nu_s(k,t)$ at $t = 10$ for $k_d/k_c = 18$. *A priori* testing.

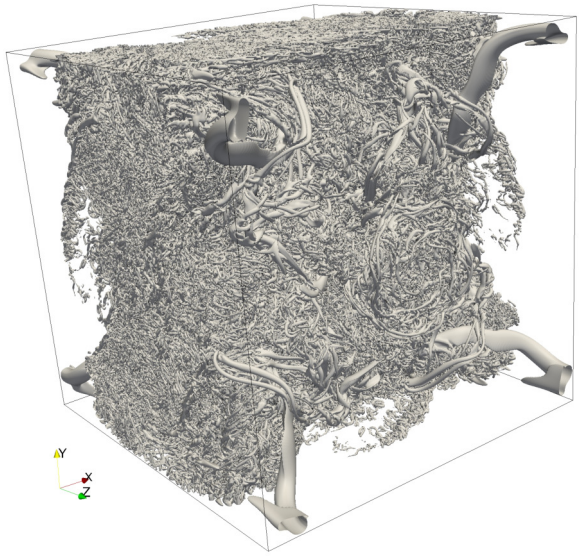

Figure 2: Isosurface of Q-criterion at $t = 10$ from DNS data.

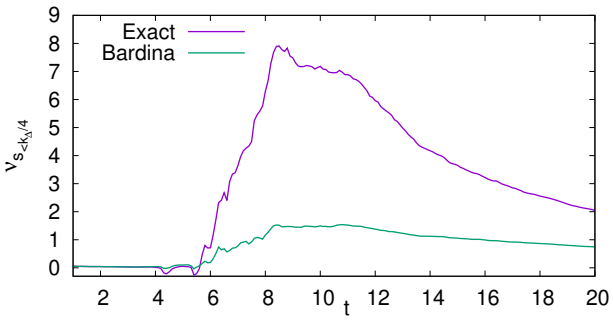

Figure 3: Time evolution of averaged value $\nu_{s<k_\Delta/4}$.

WORKSHOP
Direct and Large-Eddy Simulation 14
April 10-12 2024, Erlangen, Germany

EVALUATION OF DYNAMIC σ SUB-GRID SCALE MODELS

M. Münsch[1], J. Wendler[2], P. Schlatter[1]
[1]Institute of Fluid Mechanics (LSTM),
Friedrich–Alexander–Universität (FAU) Erlangen–Nürnberg, Germany
[2]Institute of Software Methods for Product Virtualization,
Deutsches Zentrum für Luft- und Raumfahrt (DLR), Germany
manuel.muensch@fau.de

INTRODUCTION

The ambition of the CEEC project (https://ceec-coe.eu/) is to enable the use of exascale computers for CFD applications and to demonstrate their capabilities through light-house cases, like the flow around a Japanese Bulk Carrier (JBC). These configurations are characterized by curved surfaces, potential flow separation from adverse pressure gradients or fluid-structure-interaction. Despite exascale computing there is still a need for turbulence modeling and LES [1]. Furthermore the light-house cases will require wall-modeled LES (WMLES) in which machine-learning enriched wall-models are in the focus to tackle complex flow scenarios.

In this regards, in contrast to the classical Smagorinsky model or dynamics model by Germano, advanced sub-grid scale models, like the σ-model, are the route of choice [2, 3]. Within this contribution two slightly different variants of the dynamics σ sub-grid scale model, the GSIG [2] and the GsvsSIG [4] model, are investigated for a channel flow ($Re_\tau = 590$), the flow around a cylinder ($Re_\tau = 3900$) and a periodic hill case ($Re_h = 10595$).

NUMERICAL METHOD AND MODELING

Here the incompressible formulation of the filtered conservation equations are considered:

$$\frac{\partial \overline{u}_i}{\partial x_i} = 0 \tag{1}$$

$$\frac{\partial \overline{u}_i}{\partial t} + \frac{\partial}{\partial x_j}(\overline{u}_i\ \overline{u}_j) = -\frac{1}{\rho}\frac{\partial \overline{p}}{\partial x_i} + (\nu + \nu_t)\frac{\partial}{\partial x_j}\left(\frac{\partial \overline{u}_i}{\partial x_j} + \frac{\partial \overline{u}_j}{\partial x_i}\right). \tag{2}$$

The turbulent viscosity ν_t is computed via the σ-model [2], i.e., basing on the analysis of the singular values σ_1, σ_2 and σ_3 of the resolved velocity gradient tensor $\overline{g}_{ij} = \frac{\partial \overline{u}_i}{\partial x_j}$:

$$\nu_t = (C_\sigma \Delta)^2 D_\sigma \quad \text{with} \quad D_\sigma = \frac{\sigma_3(\sigma_1 - \sigma_2)(\sigma_2 - \sigma_3)}{\sigma_1^2}. \tag{3}$$

To adapt for different flow scenarios the model constant C_σ can be estimated by a a dynamic procedure in the fashion of Germano [5] with modifications by Lilly [6]. According to [2], the dynamic approach reads as follows:

$$(C_\sigma \Delta)^2 = -\frac{1}{2}\frac{<L_{ij}\mathcal{M}_{ij}>_{vol}}{<\mathcal{M}_{ij}\mathcal{M}_{ij}>_{vol}} \quad \text{with} \tag{4}$$

$$M_{ij} = \widetilde{\Delta^2 D_\sigma \overline{S}_{ij}} - \Delta^2 D_\sigma \widetilde{\overline{S}_{ij}} \tag{5}$$

which is called the GSIG approach. Here $< . >_{vol}$ denotes volume averaging over the whole domain.

In addition, Baya Toda [4] suggested an additional dimensionless shear and vortex sensor (SVS) to detect pure shear as a measure for the vicinity of a wall, inspired by the WALE [7] operator, leading to the so called GsvsSig version of the dynamic approach:

$$SVS = \frac{(\mathcal{S}^d_{ij}\mathcal{S}^d_{ij})^{\frac{3}{2}}}{(\overline{S}_{ij}\ \overline{S}_{ij})^{\frac{5}{2}} + (\mathcal{S}^d_{ij}\mathcal{S}^d_{ij})^{\frac{5}{4}}}\ . \tag{6}$$

Here $\mathcal{S}^d_{ij}$ is the traceless, symmetric part of the squared velocity-gradient tensor.

The upper equations and models are solved via the second-order, finite volume code FASTEST-3D which relies on co-located variable arrangement. An explicit low storage Runge-Kutta approach is used to advance the momentum equation in time within the predictor step. In the corrector step a Poisson equation is solved to obtain the pressure and divergence free velocity field at the new time step.

FIRST RESULTS

For the channel case both models produce satisfying results with no significant difference compared to the Smagorinsky model [8] or the static σ-model in terms of the velocity profile and the secondary moments. For example Figure 1 shows the relative error of the inner-scaled velocity u^+ of the models considered with respect to DNS data [9].

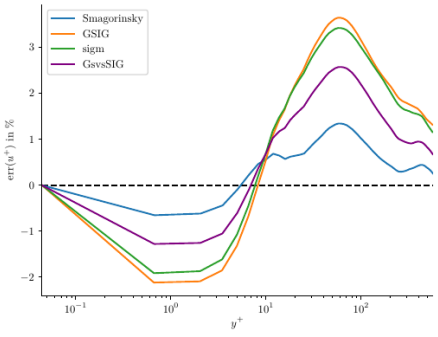

Figure 1: Relative error of the inner-scaled velocity u^+ of the SGS-models with respect to DNS data.

For the cylinder case Figure 2 shows the profiles in comparison to data from Lourenco&Shih (according to [10]). Here the values of the recirculation length with $L_r = 1.311\ D$ for GSIG and $L_r = 1.366\ D$ for GsvsSIG are overpredicted compared to the the experimental data and the Smagorinsky model. The Strouhal numbers are identical with 0.210 for the Smagorinsky-, the static σ-, and the GSIG-model. The GsvsSIG approach delivers a slightly higher values with 0.215. Both of the models models predict a slightly lower mean drag coefficient $\overline{c_d}$ compared to the Smagorinsky or static σ-model with: 1.020 (GSIG), 1.011 (GsvsSIG), 1.107 (Smagorinsky) and 1.118 (static σ).

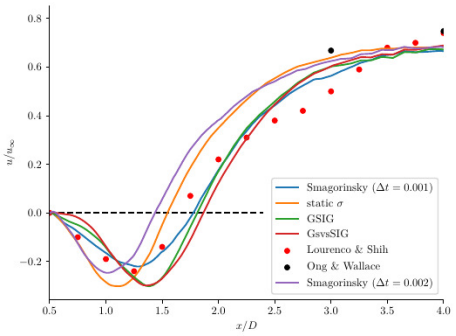

Figure 2: Profiles of the streamwise velocity in the wake of the cylinder.

The top and bottom separation angles and the error in respect to an extrapolation equation by Jiang [11] are shown in the following tabular:

Case	θ_t	error [%]	θ_b	error [%]
Smagorinsky	88.031	1.32	87.896	1.16
Static σ-model	88.250	1.57	87.924	1.19
GSIG	87.139	0.29	87.246	0.41
GsvsSIG	87.154	0.31	87.151	0.30

Table 1: Time averaged separation angles for the different models and their error with respect to the reference extrapolation.

Here the predictions of the separations angles fit very well to the reference data. This motivates the test of the models on the periodic hill case ($Re_h = 10595$) to check on the prediction of the flow separation in this scenario. Since computations are currently ongoing the final results will be presented at a later stage within the conference presentation.

OUTLOOK

As an outlook perspective, the experience gained from the periodic hill case will serve as an input for the construction of wall-models enriched by multi-agent reinforcement learning in the future. The results will be compared to reference data as provided by Breuer [12] for example.

REFERENCES

[1]M. A. Sprague, S. Boldyrev, P. Fischer, R. Grout, W. I. Gustafson Jr, and R. Moser, *Turbulent Flow Simulation at the Exascale: Opportunities and Challenges Workshop: August 4-5, 2015, Washington, DC*. National Renewable Energy Lab.(NREL), Golden, CO (United States), 2017.

[2]F. Nicoud, H. Baya Toda, O. Cabrit, S. Bose, and J. Lee, "Using singular values to build a subgrid-scale model for large eddy simulations," *Physics of Fluids*, vol. 23, no. 8, 2011.

[3]H. Baya Toda, O. Cabrit, G. Balarac, S. Bose, J. Lee, H. Choi, and F. Nicoud, "A subgrid-scale model based on singular values for les in complex geometries," in *Proc. of the Summer Program 2010*, pp. 193–202, Center for Turbulence Research, 2010.

[4]H. Baya Toda, O. Cabrit, K. Truffin, B. Gilles, and F. Nicoud, "A dynamic procedure for advanced subgrid-scale models and wall-bounded flows," in *7th International Symposium On Turbulence and Shear Flow Phenomena*, 2011.

[5]M. Germano, U. Piomelli, P. Moin, and W. Cabot, "A dynamic subgrid-scale eddy viscosity model," *Physics of Fluids A: Fluid Dynamics*, vol. 3, no. 7, pp. 1760–1765, 1991.

[6]D. Lilly, "A proposed modification of the germano subgrid-scale closure method," *Physics of Fluids A: Fluid Dynamics*, vol. 4, no. 3, pp. 633–635, 1992.

[7]F. Ducros, F. Nicoud, and T. Poinsot, "Wall-adapting local eddy-viscosity models for simulations in complex geometries," in *Numerical Methods for Fluid Dynamics VI* (M. Baines, ed.), pp. 293–299, 1998.

[8]J. Smagorinsky, "General circulation experiments with the primitive equations," *Monthly Weather Review*, vol. 91, no. 3, pp. 99–164, 1963.

[9]R. Moser, "Dns data for turbulent channel flow", *http://turbulence.ices.utexas.edu/MKM_1999.html*, May 2015.

[10]P. Beudan and P. Moin, "Numerical experiments on the flow past a circular cylinder at a sub-critical reynolds number, report no. tf-62, department of mechanical engineering," tech. rep., Stanford University, 1994.

[11]H. Jiang, "Separation angle for flow past a circular cylinder in the subcritical regime," *Physics of Fluids*, vol. 32, no. 1, 2020.

[12]M. Breuer, B. Kniazev, and M. Abel, "Development of wall models for les of separated flows using statistical evaluations," *Computers & Fluids*, vol. 36, no. 5, pp. 817–837, 2007.

SESSION: Roughness

Friday, April 12, 2024

11:00- 12:30

WORKSHOP
Direct and Large-Eddy Simulation 14
April 10-12 2024, Erlangen, Germany

DNS OF SUPERSONIC TURBULENT BOUNDARY LAYERS OVER ROUGH SURFACES

M. Cogo[1], D. Modesti[2], M. Bernardini[3] and F. Picano[1,4]
[1]Centro di Ateneo di Studi e Attività Spaziali "Giuseppe Colombo", Università degli Studi di Padova, Padova, Italy
[2]Faculty of Aerospace Engineering, Delft University of Technology, Delft, Netherlands
[3]Department of Mechanical and Aerospace Engineering, Sapienza University of Rome, Rome, Italy
[4]Department of Industrial Engineering, Università degli Studi di Padova, Padova, Italy
michele.cogo.1@phd.unipd.it

INTRODUCTION

The study of supersonic and hypersonic boundary layers is essential to determine drag and heat transfer on flight vehicles, but the predicted flow dynamics is vulnerable to the onset of surface roughness. For example, thermal protection systems (TPSs), which are typically required to endure high-temperature conditions, present gaps between the tiles that can be though as a structured roughness pattern. Regular or irregular roughness topologies can also arise from random pitting, spallation or ablation. At the present time only experimental studies have tackled this problem for turbulent boundary layers (TBLs) [1], while a few numerical studies have been recently performed for turbulent channels [2]. In this context, the study of TBLs is essential to characterize the streamwise development of the flow statistics, which can be heavily influenced by roughness-generated shock waves.

In this study, we propose to leverage the compressible solver STREAmS [3] to perform a series of direct numerical simulations of compressible turbulent boundary layers over rough walls. This high fidelity dataset will be instrumental to derive predictive formulas for friction and heat transfer and compare them to the smooth wall counterparts. Particular attention is paid to the relation between the roughness height k, the local boundary layer thickness δ_{99} and the viscous length $\delta_\nu = \nu_w/u_\tau$, where u_τ is the friction velocity, τ_w is the mean wall shear stress and ν_w is the kinematic viscosity at the wall. The ratio between these scales indicates the level of scale separation, which is targeted to be representative of the fully-rough regime as described by [5].

NUMERICAL METHODS

The Navier–Stokes equations are solved using STREAmS [3], an open-source numerical solver for compressible flows oriented to modern HPC platforms using MPI parallelization and supporting multi-GPU architectures under the CUDA paradigm. In shock-free regions, the convective terms are evaluated using high-order energy preserving schemes, while a shock capturing formulation is activated with a Ducros sensor. The diffusive terms are discretized using a locally conservative scheme expanded to standard Laplacian formulation. The complexity of the roughness geometry is handled using a ghost-point-forcing immersed boundary method to treat arbitrarily complex geometries [2].

PRELIMINARY RESULTS

We have performed preliminary simulations at freestream Mach number $M_\infty = 2$ and friction Reynolds number up to $Re_\tau = \delta_{99}/\delta_\nu \approx 1700$. The domain has a total length of $135\delta_{in}$ which is composed of a smooth portion (up to $50\delta_{in}$) followed by a rough wall, being δ_{in} the boundary layer thickness at the inflow. Turbulence at the inflow is generated by means of the recycling-rescaling procedure, with the recycling plane located at $x_{rec} = 40\delta_{in}$.

For these tests we have used 3D cubical roughness elements with height $k/\delta_{in} = 0.01$, with a streamwise and spanwise spacing of $\lambda = 2k$, similarly to [2]. Note that these tests are already full scale simulations as they features about 16 billion mesh points, achieving a resolution of at least 20 points per element along each direction. This translates in a resolution that corresponds approximately to $\Delta x^+ = \Delta z^+ = 3$ and $\Delta y^+ = 0.5$ at the selected stations. In order to have a first assessment of the effect of different roughness patterns, we considered a geometry in which cubical elements are aligned with each other (CB-A), and another in which they are staggered (CB-S). Figures 1 and 2 report the instantaneous contours of streamwise velocity in a wall-parallel plane below the roughness crest ($y_{slice} = 0.08k$). Both figures show the smooth-to-rough transition in the flow domain, in which a sudden decrease in velocity is visible. The near-wall streaks visible in the smooth portion breaks down when roughness starts. Moreover, in the rough wall region the flow recovers the free-stream conditions at a higher distance from the wall, meaning that the boundary layer thickness increases.

Cases CB-A and CB-S exhibit clearly different streamwise evolution of the friction Reynolds number, which is matched between the two cases at different locations downstream. This is visible in Table 1, which also reports the roughness Reynolds number k^+ and the ratio k/δ_{99}. Figure 3 reports profiles of the inner-scaled streamwise velocity $u^+ = \tilde{u}/u_\tau$ as function of the wall-normal coordinate $y^+ = y/\delta_\nu$ at the selected stations reported in Table 1. In a similar fashion of [2], rough profiles are shifted accounting for a virtual origin located at $d = 0.9k$. Moreover, the smooth wall profile of [4] at the same Re_τ is reported for comparison. Here, it is apparent that the staggered case CB-S exhibits a negative mismatch com-

pared to the CB-A case, indicative of an increased drag. We attribute this behavior to the larger frontal area exposed to the incoming flow, which also generates a more intense shock wave at the smooth-rough transition. Both cases do not show a clear log-layer region, which could be due to the fact that the fully-rough regime is still not yet achieved given the computed properties of Table 1.

CONCLUSIONS

We conducted a preliminary assessment of the effect of different roughness patters on supersonic turbulent boundary layers at $M_\infty = 2$ and friction Reynolds number of $Re_\tau \approx 1700$. The roughness surface is composed of 3D cubical elements disposed in two different patters: aligned and staggered. We first investigated the instantaneous flow dynamics, noticing the breakdown of near-wall streaks due to the onset of roughness, with clear differences between cases CB-A and CB-S.

The increased drag of the rough plate is visible on the mean velocity profiles for both cases. However, the staggered cases, CB-S, reports the biggest downshift compared to the smooth wall profile due to the larger frontal area.

Both cases do not exhibit a clear log layer in the present configuration, which may be caused by the still relatively low separation of scales.

Additional analysis are necessary to shed light to the present results, and additional cases will be presented at the workshop.

REFERENCES

[1] Bowersox, R. Survey of high-speed rough wall boundary layers: Invited presentation. *37th AIAA Fluid Dynamics Conference And Exhibit*. pp. 3998 (2007)

[2] Modesti, D., Sathyanarayana, S., Salvadore, F. & Bernardini, M. Direct numerical simulation of supersonic turbulent flows over rough surfaces. *Journal Of Fluid Mechanics*. **942** pp. A44 (2022)

[3] Bernardini, M., Modesti, D., Salvadore, F., Sathyanarayana, S., Della Posta, G. & Pirozzoli, S. STREAmS-2.0: Supersonic turbulent accelerated Navier-Stokes solver version 2.0. *Computer Physics Communications*. **285** pp. 108644 (2023)

[4] Cogo, M., Salvadore, F., Picano, F. & Bernardini, M. Direct numerical simulation of supersonic and hypersonic turbulent boundary layers at moderate-high Reynolds numbers and isothermal wall condition. *Journal Of Fluid Mechanics*. **945** pp. A30 (2022)

[5] Jiménez, J. Turbulent flows over rough walls. *Annu. Rev. Fluid Mech.*. **36** pp. 173-196 (2004)

Case	x/δ_i	k^+	δ_{99}/k	Re_τ
CB-A	128	57	29	1714
CB-S	87	67	25	1712

Table 1: Flow and roughness properties at selected stations.

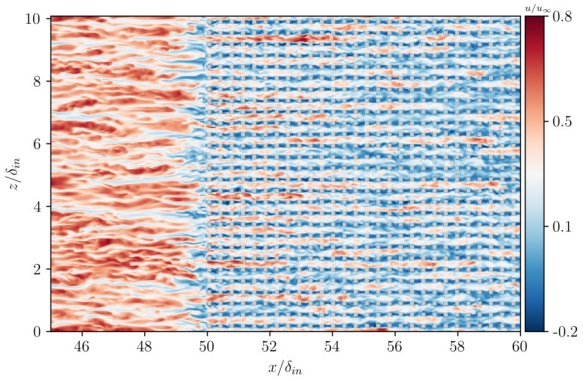

Figure 1: Streamwise velocity contours in a wall-parallel plane below the roughness crest. Here, cubes are aligned (case CB-A).

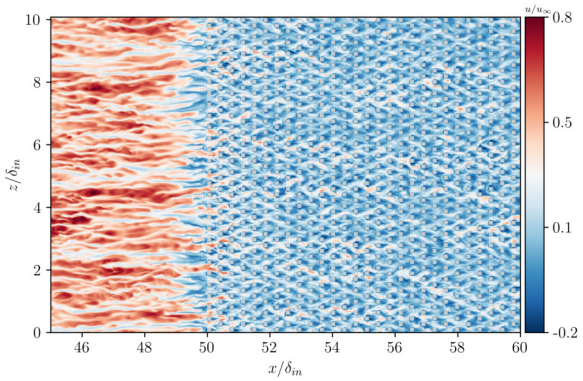

Figure 2: Streamwise velocity contours in a wall-parallel plane below the roughness crest. Here, cubes are staggered (case CB-S).

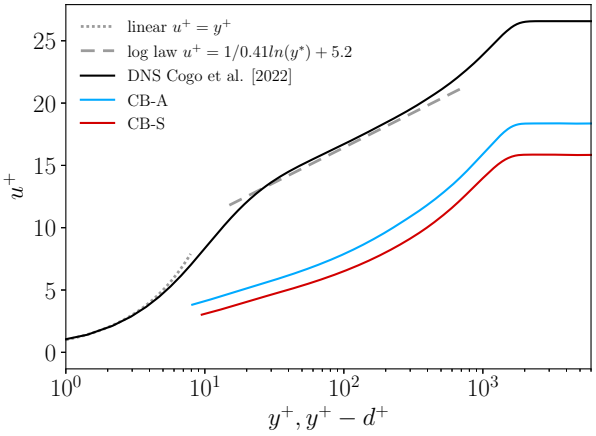

Figure 3: Inner-scaled streamwise velocity profiles u^+ as function of the wall-normal coordinate y^+. Cases CB-A and CB-S are compared to DNS data from [4].

WORKSHOP
Direct and Large-Eddy Simulation 14
April 10-12 2024, Erlangen, Germany

DIRECT NUMERICAL SIMULATION OF A ROUGH PIPE USING BODY-FITTED GRID

Venkatesh Pulletikurthi and Philipp Schlatter
[1]Institute of Fluid Mechanics (LSTM)
Friedrich–Alexander–Universität (FAU) Erlangen–Nürnberg, Germany
venkatesh.pulletikurthi@fau.de

INTRODUCTION

Surface roughness effects on the wall-bounded flows are extensively studied for their ubiquitous applications [1, 2, 3]. Numerical techniques like immersed boundary methods [4] and body-fitted grid methods [2] are used to resolve the heterogeneous and homogeneous roughness. However, the numerical studies are predominantly focused on turbulent channel flows because of the ease in implementation and simulation in those Cartesian frameworks. Direct Numerical Simulations were conducted in a turbulent pipe with cosine roughness by Ref. [5] using a second order finite volume solver on a body fitted grid. However, the pipe flows poses unique challenges to resolve heterogeneous roughness using body-fitted grids and low-order numerical solvers.

In this study, we use high-order spectral method to simulate heterogeneous roughness in a pipe for the first time, using Nek5000, a spectral code for a better accuracy. We will discuss the first order and second order statistics with a heterogenous roughness in comparison with channel flows for $Re_b = 11700$ which corresponds to $Re_\tau \approx 361$ for a smooth pipe [6].

METHODOLOGY

A high-order spectral code, NEK 5000 [7], is used to integrate in time the non-dimensionalized incompressible Navier–Stokes equations. The velocity and pressure are discretized using Legendre polynomial basis on Gauss–Lobatto–Legendre (GLL) points generated on a body fitted grid using Pn-Pn formulation. A O-grid mesh is generated for a pipe of Radius, R_0, and length $6R_0$. The GLL points are modified based on the surface topology to adjust to the body fitted grid. In figure 1, a preliminary mesh is shown for a varying surface generated using sine and cosine function,

$$R_{new} = R_0 - k_s * \| \cos(\kappa_\theta R_0 \theta) \cdot \sin(\kappa_z z) \| \qquad (1)$$

where κ_θ and κ_z are the wavenumbers in azimuthal and axial directions. It can be noted that unlike in channel flow, the characteristic radius remains the same as the pipe radius, R_0. The crest to trough height, k_s, is considered as 0.03 in the transitionally rough regime, $k_s^+ \approx 11$ for Re_τ of 361. The GLL points are moved radially to accommodate the surface topology and the radial displacement is reduced towards the center by using ratio, r/R_0, where r is the radial location of the GLL points.

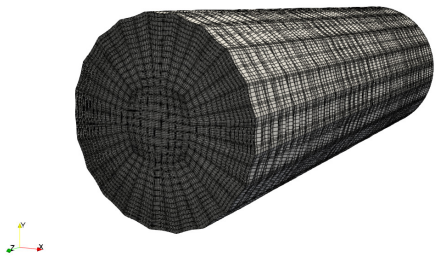

Figure 1: Bodyfitted grid of a surface topology of surface given in Eq. 1.

Roughness Profile

Figure 2 shows the heterogenous roughness profile generated with peak to trough height, k/R, 0.03, and a maximum wavelength (λ_{max}/R), 0.8 and minimum wavelength λ_{min} of 0.4 with Gaussian distribution extracted from the machine learning model created by Ref. [8].

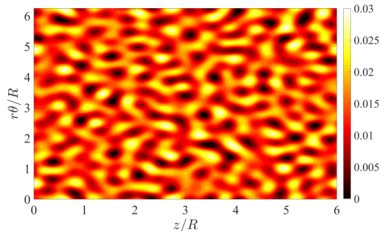

Figure 2: Heterogeneous surface roughness profile of crest to trough height, k_s/R_0, 0.03 and maximum wavelength (λ_{max}/R_0) of 0.8 and minimum wavelength, λ_{min}/R_0, 0.4 created by Ref. [8].

RESULTS

Figure 3 shows the normalized instantaneous axial velocity (u_z) contours and mean velocity profiles. It can be observed that the wavenumber in axial direction is chosen high to include smaller wavelengths, 0.3 in both axial and azimuthal directions. This is applicable for pipe flows to simulate using existing high order spectral codes. Figure 3(c) shows the mean velocity profiles normalized with local maximum velocity and it can be seen that although the k_s/R_0, is relatively low in

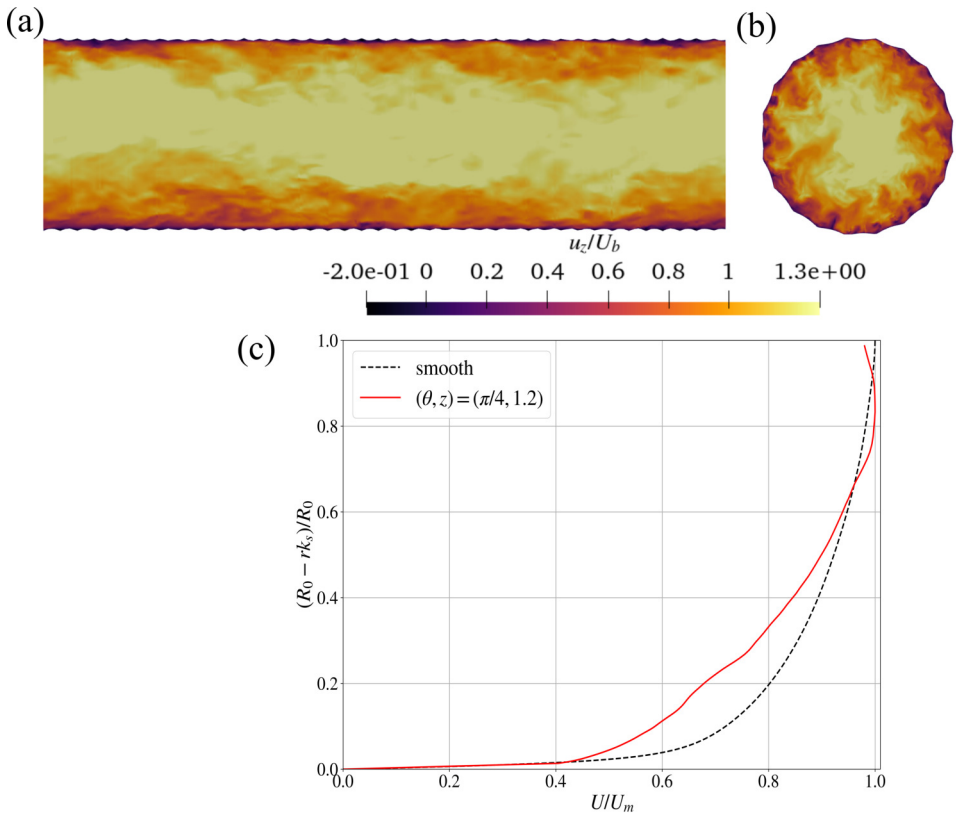

Figure 3: Instantaneous axial velocity contours (a) YZ plane (b) XY plane, and (c) mean axial velocity profiles of systemic roughness described in Eq 1 normalized with maximum velocity, U_m, and the radial distance, r, is defined from $0 - R_0$ and k_s is the roughness height.

the transitionally rough regime, it significantly changes mean velocity profile compared to smooth pipe.

FUTURE WORK

A varying surface based on cosine and sine function is simulated in a pipe flow using high order spectral code on a body fitted grid. At the conference, results for hetergeneous roughness shown in figure 2 will be discussed and compared with smooth pipe and roughness in pipes using finite volume methods. We will also further compare our results with roughness in channel flows using immersed boundary methods and overlapping methods based on spectral methods.

REFERENCES

[1] A. Ashrafian and H. I. Andersson, "Roughness effects in turbulent channel flow," *Progress in Computational Fluid Dynamics, an International Journal*, vol. 6, no. 1-3, pp. 1–20, 2006.

[2] S. Leonardi, P. Orlandi, and R. A. Antonia, "Properties of d-and k-type roughness in a turbulent channel flow," *Physics of Fluids*, vol. 19, no. 12, 2007.

[3] J. Kussin and M. Sommerfeld, "Experimental studies on particle behaviour and turbulence modification in horizontal channel flow with different wall roughness," *Experiments in Fluids*, vol. 33, no. 1, pp. 143–159, 2002.

[4] A. Busse, M. Lützner, and N. D. Sandham, "Direct numerical simulation of turbulent flow over a rough surface based on a surface scan," *Computers & Fluids*, vol. 116, pp. 129–147, 2015.

[5] L. Chan, M. MacDonald, D. Chung, N. Hutchins, and A. Ooi, "A systematic investigation of roughness height and wavelength in turbulent pipe flow in the transitionally rough regime," *Journal of Fluid Mechanics*, vol. 771, pp. 743–777, 2015.

[6] G. K. El Khoury, P. Schlatter, A. Noorani, P. F. Fischer, G. Brethouwer, and A. V. Johansson, "Direct numerical simulation of turbulent pipe flow at moderately high reynolds numbers," *Flow, Turbulence and Combustion*, vol. 91, pp. 475–495, 2013.

[7] J. W. L. Paul F. Fischer and S. G. Kerkemeier, "nek5000 Web page," 2008. http://nek5000.mcs.anl.gov.

[8] F. Pérez-Ràfols and A. Almqvist, "Generating randomly rough surfaces with given height probability distribution and power spectrum," *Tribology International*, vol. 131, pp. 591–604, 2019.

WORKSHOP
Direct and Large-Eddy Simulation 14
April 10-12 2024, Erlangen, Germany

DNS OF TURBULENT FLOW OVER RANDOM SPHERE PACKS – INSIGHT FROM TURBULENT KINETIC ENERGY BUDGETS

S. v. Wenczowski[1], **M. Manhart**[1]
[1] Professorship of Hydromechanics
Technical University of Munich (TUM), Germany
simon.wenczowski@tum.de, michael.manhart@tum.de

INTRODUCTION

The exchange of mass and momentum across the interface between a porous medium and a turbulent flow is of high relevance for both natural systems and industrial processes: Examples for technical applications span from food drying to fuel cells. In nature, a prominent example is the hyporheic zone, which comprises the bio-geo-chemically active topmost layers of a river bed, where the water is in permanent interaction with the overlying turbulent flow. Using the hyporheic zone as an example, our research provides insight into the near-interface hydrodynamics, which is likely transferrable to comparable flow cases.

In the present study, we (i) evaluate the budget of turbulent kinetic energy (TKE), (ii) connect the observations to visualizations of the turbulence structure, and (iii) investigate the impact of the interface definition. In the scope of single-domain Direct Numerical Simulation (DNS), the porous medium is represented by a static mono-disperse random sphere pack. All spatial and temporal scales of turbulent motion are resolved, both in the pore space of the porous medium and in the overlying free flow region. Eight cases were simulated to systematically sample a parameter space spanned by Reynolds numbers of $Re_\tau \in [150, 500]$ and permeability Reynolds numbers of $Re_K \in [0.4, 2.8]$. By considering ratios of flow depth h to sphere diameter D up to $h/D = 10$, we reduce the blocking effect of individual grains.

Statistics are analysed within a time-space double-averaging framework [1]. Additionally, instantaneous flow fields allow us to visualize vortices and typical structures within the turbulent flow. From both perspectives, Re_K is observed to drastically change the flow conditions near the surface of the sphere pack. Irrespective of Re_K, cases with similar Re_τ were found to exhibit a high degree of similarity in the outer-layer. The similarity appears most clearly if a kinetic interface definition is chosen and a consistent normalization is applied.

DISCRETISATION AND SOLUTION

Our in-house code MGLET [2] solves the incompressible Navier-Stokes equations based on a Cartesian Finite-Volume discretization. The code resorts to a third order Runge-Kutta scheme for explicit time integration and targets strongly MPI-parallel LES and DNS of turbulent flows with complex geometries. In the present study, an Immersed Boundary Method (IBM) of second order [3] was employed to represent the porous medium. The multi-grid design of MGLET allows embedded grids, such that a local near-interface refinement of $\Delta x^+ = \Delta y^+ = \Delta z^+ < 1$ could be achieved. Due to optimized I/O routines [4], simulations with more than 10^9 cells can be conducted efficiently. A VTK-based functionality for runtime visualization has been added recently.

BOUNDARY CONDITIONS

To represent the granular porous medium, mono-disperse random sphere packs have been generated. During the simulation, the spheres remain static and a no-slip boundary condition is imposed on their surface. In the bed-parallel x- and y-directions, the domain has periodic boundary conditions. A volume force is imposed to drive the flow in x-direction. To approximate the free water surface, a slip boundary condition is applied at the top of the domain. Figure 1 shows the case configuration together with a visualization of vortex structures.

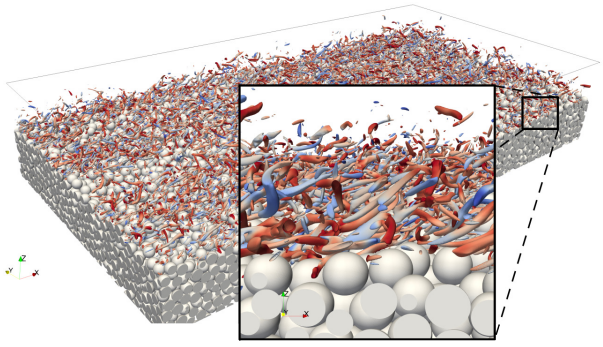

Figure 1: Instantaneous flow field with vortex structures.

ANALYSIS FRAMEWORK

The complex and strongly three-dimensional flow situation is analysed within a double averaging framework [1]. First, an arbitrary quantity ϕ is averaged in time.

$$\phi_{(\boldsymbol{x},t)} = \overline{\phi}_{(\boldsymbol{x})} + \phi'_{(\boldsymbol{x},t)} \ , \qquad \overline{\phi}_{(\boldsymbol{x})} = \frac{1}{T}\int_0^T \phi_{(\boldsymbol{x},t)}\,\mathrm{d}t \tag{1}$$

Consecutively, the temporal mean is decomposed into a spatial average and a spatial variance.

$$\overline{\phi}_{(\boldsymbol{x})} = \langle\overline{\phi}\rangle_{(z)} + \widetilde{\overline{\phi}}_{(\boldsymbol{x})} \ , \qquad \langle\overline{\phi}\rangle_{(z)} = \frac{1}{A_f}\iint_{A_f} \overline{\phi}_{(\boldsymbol{x})}\,\mathrm{d}x\,\mathrm{d}y \tag{2}$$

In equation (2), $\langle\overline{\phi}\rangle$ represents the intrinsic average over the fluid-filled area A_f within a horizontal averaging plane, while in-plane spatial variations are marked by a tilde.

PRELIMINARY RESULTS

Within the double-averaging framework, the TKE budget equation can be formulated as follows:

$$\frac{\partial}{\partial t}\left\langle \frac{1}{2}\overline{u'_\alpha u'_\alpha}\right\rangle = \Pi + T - \varepsilon \tag{3a}$$

$$\Pi = -\left\langle \overline{u'_\alpha u'_j}\right\rangle \frac{\partial\,\langle\overline{u}_\alpha\rangle}{\partial x_j} - \left\langle \overline{u'_\alpha u'_j}\,\frac{\partial\,\widetilde{\overline{u}}_\alpha}{\partial x_j}\right\rangle \tag{3b}$$

$$\begin{aligned} T = &-\left\langle \frac{1}{2}\,\widetilde{\overline{u}}_j\,\frac{\partial\,\overline{u'_\alpha u'_\alpha}}{\partial x_j}\right\rangle - \left\langle \frac{1}{2}\,\frac{\partial\,\overline{u'_\alpha u'_\alpha u'_j}}{\partial x_j}\right\rangle - \left\langle \frac{1}{\rho}\,\overline{\frac{\partial\,p' u'_\alpha}{\partial x_\alpha}}\right\rangle \\ &+\left\langle \nu\frac{\partial}{\partial x_j}\left(\overline{u'_\alpha\frac{\partial u'_\alpha}{\partial x_j}} + \overline{u'_\alpha\frac{\partial u'_j}{\partial x_\alpha}}\right)\right\rangle \end{aligned} \tag{3c}$$

$$\varepsilon = \nu\left\langle \overline{\frac{\partial u'_\alpha}{\partial x_j}\frac{\partial u'_\alpha}{\partial x_j}} + \overline{\frac{\partial u'_\alpha}{\partial x_j}\frac{\partial u'_j}{\partial x_\alpha}}\right\rangle \tag{3d}$$

In equation (3b), the production Π is further decomposed. The second term represent the work of Reynolds stresses against in-plane velocity gradients, such that TKE is produced, while the spatial variance of the velocity field is reduced [5]. In equation (3c), T summarizes different types of TKE transport. Finally, equation (3d) provides the TKE dissipation rate ε.

An evaluation of cases with different Re_K but similar Re_τ shows that the combined effect of roughness and permeability reduces the near-wall peak in TKE production (figure 2). The lower shear intensity provides a plausible explanation. While most of the produced TKE is dissipated at the same height, a minor amount is transported into the topmost layers of the sediment bed by advective, turbulent and viscous transport. Only the pressure diffusion (third term in equation (3c)) propagates small amounts of TKE into deeper regions.

Various interface definitions are possible. We define the interface at $z = \mu_z$ at the centroid of the momentum absorption by the porous medium. This interface definition yields an adapted flow depth of $(h - \mu_z)$ and a consistent friction velocity u_τ^μ, which can be used to normalize the budget components Π, T and ε. For groups of cases with similar Re_τ, figure 2 demonstrates that this normalization recovers a high degree of similarity in the far-wall region.

SUMMARY

Based on a single-domain DNS, we evaluated double-averaged TKE budgets for turbulent flow over a mono-disperse random sphere pack. With increasing Re_K, the combined effect of roughness and permeability lowers the near-wall shear intensity, changes the structure of turbulence, and reduces the near-wall peak in TKE production. Despite the drastic impact of Re_K near the interface, a consistent interface definition reveals a high degree of outer-layer similarity for cases with similar Re_τ.

ACKNOWLEDGEMENTS

We gratefully acknowledge the financial support of the DFG in the scope of grant no. MA2062/15-1. Computing time for the project is granted by the Leibniz Supercomputing Centre on SuperMUC-NG under project `pn68vo`.

REFERENCES

[1]Raupach M. R. and Shaw R. H., "Averaging procedures for flow within vegetation canopies", *Boundary-Layer Meteorology*, vol. 22, no. 1, p. 79–90, 1982.

[2]Manhart, M., Tremblay, F & Friedrich, R. : MGLET: A Parallel Code for Efficient DNS and LES of Complex Geometries. *Parallel Computational Fluid Dynamics 2000*. 449–456, (2001)

[3]Peller, N. Numerische Simulation Turbulenter Strömungen Mit Immersed Boundaries. (Technische Universität München, 2010)

[4]Sakai Y., Mendez S., Strandenes H., Ohlerich M., Pasichnyk I., Allalen M., and Manhart H., "Performance optimisation of the parallel CFD code MGLET across different HPC platforms", in *Proceedings of the Platform for Advanced Scientific Computing Conference*, PASC '19, (New York, NY, USA), Association for Computing Machinery, 2019.

[5]Ghodke C. D. and Apte, S. V., "Roughness effects on the second-order turbulence statistics in oscillatory flows", *Computers & Fluids*, vol. 162, p. 160–170, 2018.

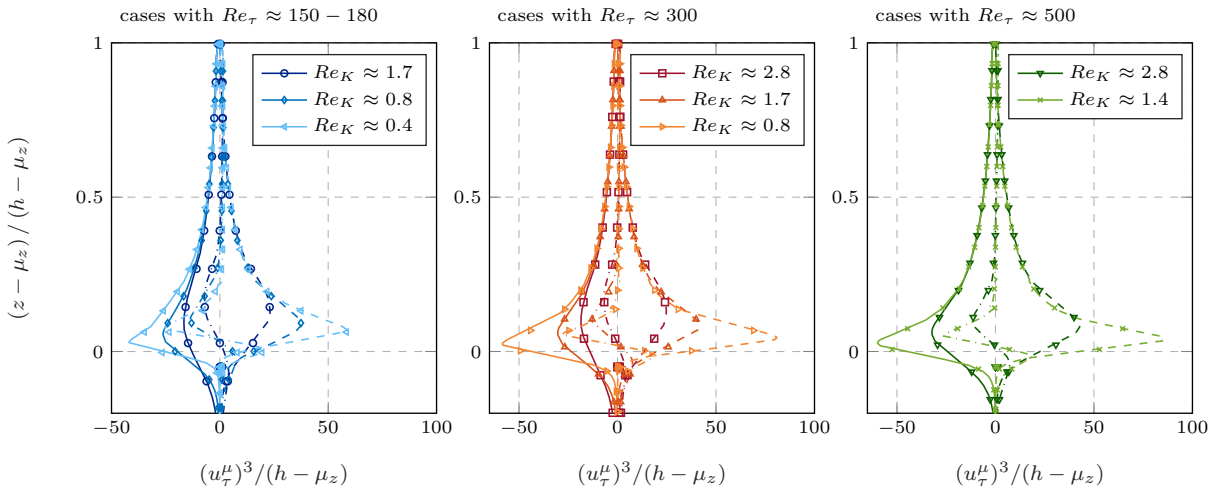

Figure 2: TKE budget terms for production (Π, - - -), total transport (T, -·-·-), and dissipation (ε, ——). Plots show groups of cases with similar Re_τ, but different Re_K. The interface position is considered by $(h - \mu_z)$ and the consistent friction velocity u_τ^μ.

WORKSHOP
Direct and Large-Eddy Simulation 14
April 10-12 2024, Erlangen, Germany

EFFECTS OF SPANWISE HETEROGENEOUS ROUGHNESS ON SHOCK-WAVE/TURBULENT BOUNDARY LAYER INTERACTIONS

Wencan Wu, Luis Laguarda, Davide Modesti, Stefan Hickel
Aerospace Engineering Faculty
Delft University of Technology, Delft, The Netherlands
w.wu-3@tudelft.nl

ABSTRACT

A novel passive flow-control method for shock-wave/turbulent boundary-layer interactions (STBLI), consisting of a rough wall with ridges aligned in the streamwise direction as shown in Fig.1, is investigated with wall-resolved large-eddy simulation (LES). The working mechanism is that this rough surface induces large-scale secondary streamwise vortices because of the imbalance between local production and viscous dissipation of turbulent kinetic energy. The induced vortices bring high-speed fluid closer to the wall thus energizing the boundary layer.

We consider an oblique shock (shock angle 40°) impinging on a turbulent boundary layer at free-stream Mach number $M_\infty = 2.0$ and friction Reynolds number $Re_\tau = 355$ based on the boundary layer thickness at the inviscid impingement point x_{imp}. The shape of the rough wall is composed of sinusoidal ridges and flat valleys between them, see Fig.1(b). A parametric study is performed to investigate the effect of the non-dimensional spacing between the ridges, namely $D/\delta_0 = \{0.125, 0.25, 0.50, 1.0, 2.0\}$, where δ_0 is the boundary layer thickness at the inlet. The non-dimensional height H/δ_0 and wavelength (width) λ/δ_0 of the ridges are 0.1 and 0.2 respectively for all simulations. The roughness, fully resolved by a cut-cell-based immersed boundary method, covers the entire computation domain. Simulation results are compared with a smooth wall STBLI at the same flow condition.

Fig.2 shows that streamwise vortices are induced by the spanwise heterogeneous roughness in the turbulent boundary layer, i.e., upwash over the ridges and downwash in the valleys. The secondary flow vortices increase in size with D/δ_0 and reach a maximum height of 0.57 δ_0 for $D/\delta_0 = 1.0$. The subsonic area of the incoming boundary layer, which is represented by the spanwise-averaged height of the sonic line, reaches a maximum value of 43% larger at $D/\delta_0 = 0.25$ than the counterpart in the smooth wall case. From Fig.3(a), we note that before the interaction, the friction coefficient C_f is a non-monotonic function of the spacing D/δ_0 and that it reaches a maximum for the intermediate value $D/\delta_0 = 0.5$. The separation region is divided into a secondary separation zone and a primary separation zone in cases with $D/\delta_0 = 2.0, 1.0, 0.5$. The extension of the separation region decreases with increasing D/δ_0 from 0.25 to 1.0. Fig.3(b) shows that when D/δ_0 decreases, the location of the onset of the interaction migrates upstream until $D/\delta_0 = 0.25$, then moves downstream in $D/\delta_0 = 0.125$. At the same time, the maximum wall pressure near the reattachment point first drops then rises with decreasing D/δ_0. Among all cases, the non-monotonic trend is evident, with the case $D/\delta_0 = 0.25$ exhibiting the longest interaction length yet the smallest pressure increase, resulting in the most gradual pressure rise. Regarding the pressure fluctuation shown in Fig.3(c), we observe that the peak value in the $D/\delta_0 = 0.25$ case is 12% lower than that in the smooth wall case, suggesting an attenuated footprint of the separation shock unsteadiness on the rough surface. The location of the peak pressure fluctuation moves similarly to the onset of the interaction, with case $D/\delta_0 = 0.25$ exhibiting the most upstream location. This decrease in pressure fluctuation of $D/\delta_0 = 0.25$ case is linked to the attenuated footprint of the separation shock low-frequency unsteadiness upon inspection of the pre-multiplied power spectral density contours of wall-pressure signals in the interaction region as shown in Fig.4(a). The spectra at the separation lines are further compared in Fig.4(b), and the spectra magnitude of case $D/\delta_0 = 0.25$ drops significantly compared with that of the smooth wall case near $fL_{sep}/u_\infty = 0.1$. Results from dynamic mode decomposition(DMD) also provide supportive evidence for this claim.

Further investigation into the effect of spanwise heterogeneous roughness on STBLI under a higher Reynolds number is ongoing and will be elaborated in the full-length paper and discussed during the conference, as well as the influence of another geometric parameter ridge height H/δ_0.

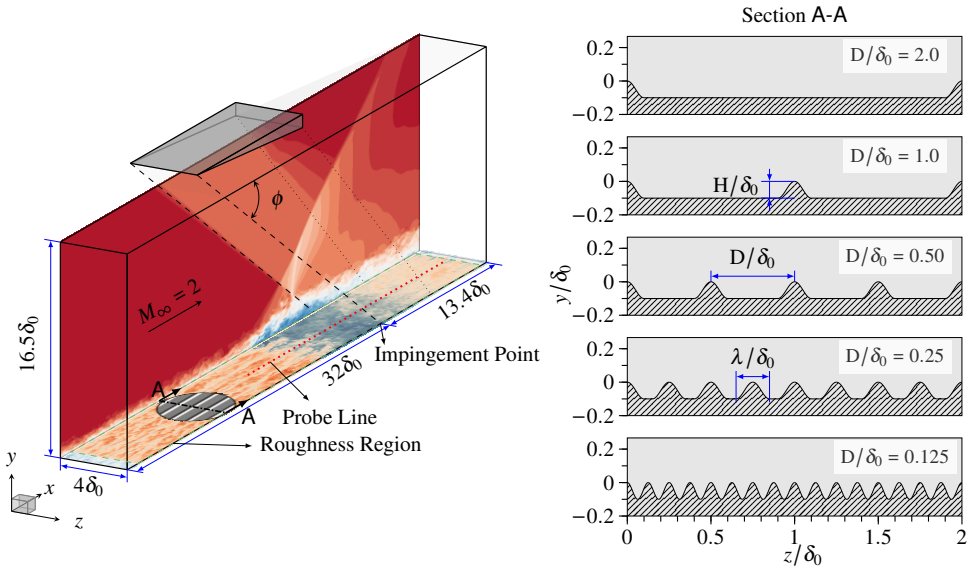

Figure 1: (a) Schematic of the computation domain, and (b) schematic view of the ridge-type rough walls with relevant definitions

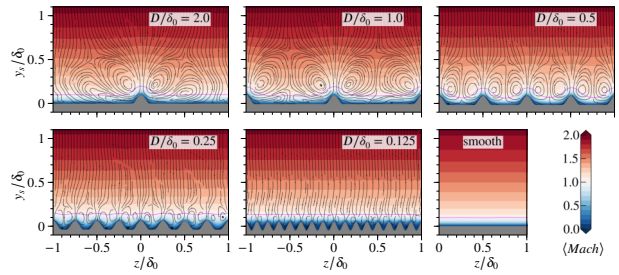

Figure 2: Streamlines and Mach number distribution in a cross-stream plane at $(x - x_{imp})/\delta_0 = -20$. The magenta line represents the location of the sonic line.

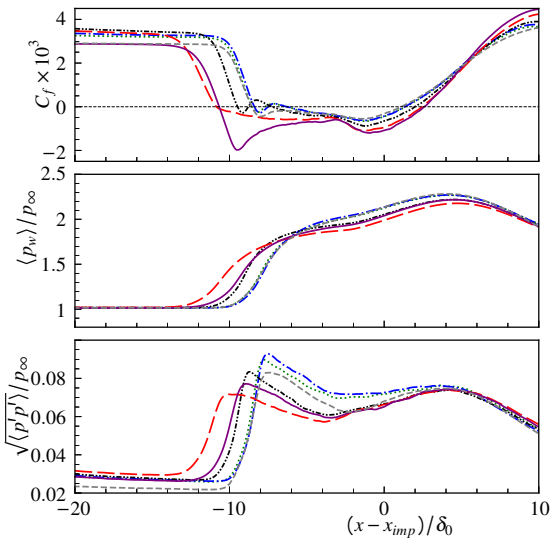

Figure 3: Spanwise averaged (a) friction coefficient (b) wall pressure and (c) wall pressure fluctuation along streamwise direction. ----, smooth wall; ·····, $D/\delta_0 = 2.0$; -·-·-,$D/\delta_0 = 1.0$; -··-··-,$D/\delta_0 = 0.5$; — —,$D/\delta_0 = 0.25$; ——,$D/\delta_0 = 0.125$.

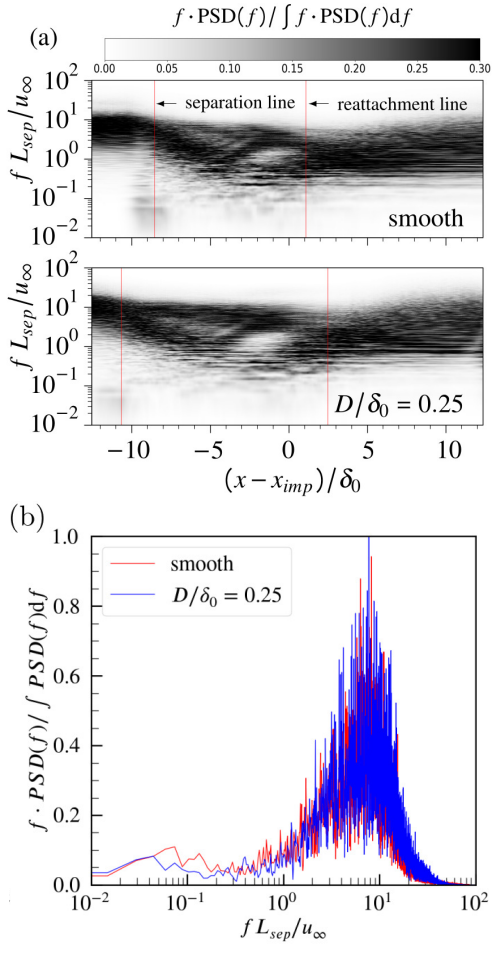

Figure 4: (a) Pre-multiplied power spectral density (PSD) of wall pressure signals at the mid-plane for the smooth wall and $D/\delta_0 = 0.25$ case, and (b) comparison of pre-multiplied PSD at the separation lines.

WORKSHOP
Direct and Large-Eddy Simulation 14
April 10-12 2024, Erlangen, Germany

DIRECT NUMERICAL SIMULATION OF SMOOTH AND ROUGH WALL TURBULENT BOUNDARY LAYERS WITH HEAT TRANSFER

F. Secchi[1], J. Yang[1], D. Gatti[1], A. Stroh[1], P. Schlatter[2], B. Frohnapfel[1]
[1]Institute of Fluid Mechanics (ISTM), Karlsruhe Institute of Technology, Germany
[2]Chair of Fluid Mechanics, Friedrich-Alexander-Universität Erlangen-Nürnberg, Germany
francesco.secchi@kit.edu

INTRODUCTION

Boundary layers are ubiquitous as they form around any solid body moving relative to a fluid. By definition, heat and momentum are exchanged between the moving body and the free-stream flow within the boundary layer thickness. In most engineering applications, the flow within the boundary layer is turbulent, and the surface over which the boundary layer develops is rough. Even though many aspects on the nature of turbulent boundary layers over smooth walls are currently well-established, a greater understanding gap is still present when surface roughness comes into play. Rough wall-bounded turbulence has been extensively studied in the literature, but only a limited number of investigations address spatially developing rough wall flows and experimental efforts on the topic are not equally supported by high fidelity numerical studies [1, 2]. In fact, due to the extensive computational demands required to simulate such flows, just a few investigations in the literature report studies of rough wall turbulent boundary layers and, most of available results are limited to momentum transfer and little is known regarding heat transfer [3, 4, 5, 6].

In this study we present direct numerical simulation (DNS) results of smooth and rough wall zero pressure gradient turbulent boundary layers with heat transfer. The boundary layer develops along a smooth plate before entering a region with homogeneous surface roughness. The plate is kept at a constant and uniform temperature, which is greater than the temperature of the free-stream flow. The study assesses the effects of surface roughness by comparing mean flow statistics with smooth wall turbulent boundary layer data obtained using the same DNS framework.

PROBLEM FORMULATION

The incompressible Navier-Stokes equations are numerically integrated using the pseudo-spectral flow solver `SIMSON` [7], in which Fourier space and Chebyshev polynomials are used for discretizing flow variables in the wall-parallel and wall-normal directions, respectively. The domain of the simulations is sketched in figure 1. The computational box has size $L_x = 3000\delta_{1,in}$, $L_z = 124\delta_{1,in}$, and $L_y = 100\delta_{1,in}$ in the streamwise, spanwise and wall-normal directions, respectively. Here $\delta_{1,in}$ indicates the displacement thickness of the Blasius boundary layer at the inlet section of the computational domain. A homogeneous surface roughness patch of length $L_R = 2350\delta_{1,in}$ is laid over the bottom wall of the computational domain starting at $x = L_T = 150\delta_{1,in}$. A sigmoid

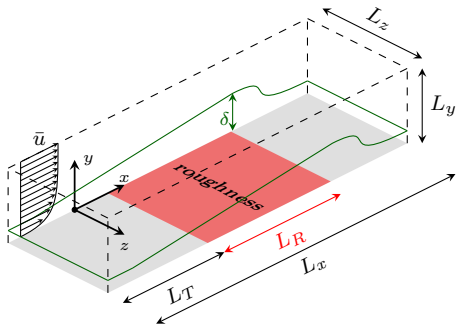

Figure 1: View of the computational domain. The red area represents the region where surface roughness is present. The aspect ratio of the figure is not representative of the actual simulation.

scaling function is employed on the roughness height distribution in the vicinity of $x = L_T$ to facilitate a gradual transition from smooth to rough wall. The length L_T is designed to reach a turbulent state at the beginning of the roughness patch that is independent on the tripping used to make the boundary layer turbulent. Periodic boundary conditions are applied in both wall-parallel directions for all flow variables. To cope with the flow development in the streamwise direction, the re-scaling strategy presented in [7] is applied. No-slip and no-penetration boundary conditions are applied at the bottom wall using an immersed boundary method based on the method of [8]. A similar approach is applied to enforce a Dirichlet boundary condition for the temperature field with a uniform temperature T_w. On the top plane of the computational domain, the velocity field is prescribed to match the free-stream velocity u_∞ in the streamwise direction and allowed to have transpiration in the wall-normal direction [7]. On the other hand, the temperature is prescribed to be that of the free-stream flow T_∞, with $T_\infty < T_w$. The Prandtl number is set to $Pr = 1$.

Surface roughness is a filtered three-dimensional scan of a real sandpaper rough surface. The characteristic size k of the roughness topography is defined to be $k_t = 4\delta_{1,in}$, where k_t is the peak-to-trough height of the roughness.

RESULTS

The friction coefficient $C_f = 2\tau_w/(\rho u_\infty^2)$ and Stanton number $St = 2q_w/(\rho c_p u_\infty \Delta T)$ distributions for the smooth and

rough wall cases are shown in figure 2. Here τ_w is the wall-shear stress, q_w the wall-heat flux, ρ is the fluid density, c_p is the heat capacity at constant pressure, and $\Delta T = T_w - T_\infty$. The skin friction coefficient and Stanton number attain very similar values along the boundary layer, except for the rough wall case near the roughness leading edge (approximately for $x < 500\delta_{1,in}$). In this region, the rough wall induced increase in skin friction exceeds significantly the wall-heat flux enhancement. This is consistent with the pressure drag introduced by roughness elements which does not play a direct role in increasing the wall-heat flux. Compared to the smooth-wall case, skin-friction and Stanton number decrease faster along the boundary layer and, for $x > 1500\delta_{1,in}$, a local net decrease is observed in both the skin-friction coefficient and Stanton number for the rough wall case.

The roughness Reynolds number $k^+ = k/\delta_\nu$ (a plus superscript indicates viscous units scaled quantities, δ_ν indicates the viscous length scale and ν is the kinematic viscosity), is reported in figure 3. In the same figure, the boundary layer thickness is also shown in terms of displacement δ_1, momentum δ_2 and thermal-energy δ_T thickness. k^+ ranges from approximately $k^+ = 200$ close to the roughness leading edge to approximately $k^+ = 40$ near the end of the roughness region. As such, the flow moves from a fully-rough to a transitionally rough condition along the boundary layer. As a result of this flow transition, viscous units scaled mean velocity and temperature profiles at different streamwise locations, which are reported in figure 4, display a visible scatter compared to the smooth wall case mean profiles.

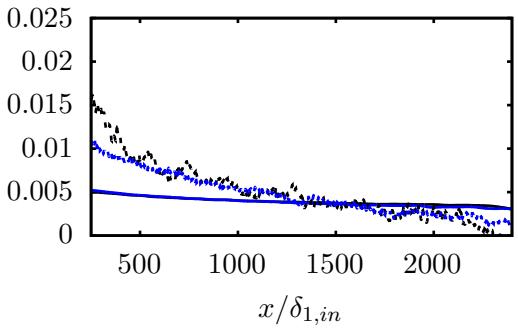

Figure 2: Friction coefficient and Stanton number distributions along the boundary layer. Smooth wall: ——, C_f; ——, St. Rough wall: - - - - -, C_f; - - - - -, St.

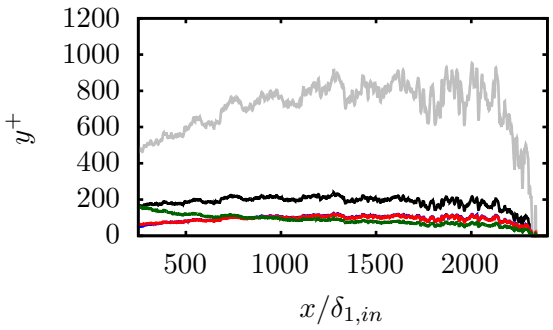

Figure 3: Roughness Reynolds number and boundary layer thicknesses distributions along the rough wall boundary layer. ——, δ_{99}^+; ——, δ_1^+; ——, δ_2^+; ——, δ_T^+; ——, k^+.

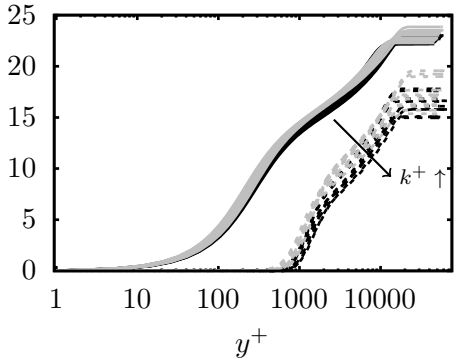

Figure 4: Viscous units scaled mean velocity and temperature profiles. Smooth wall: —— $\langle\overline{u}\rangle^+$; —— $(T_w - \langle\overline{T}\rangle)^+$. Rough wall: - - - - - $\langle\overline{u}\rangle^+$; - - - - - $(T_w - \langle\overline{T}\rangle)^+$.

ACKNOWLEDGEMENTS

We greatly acknowledge the support by the German Research Foundation (DFG) under the Collaborative Research Centre TRR150 (project number 237267381). The simulations presented in this work were performed on the HPE Apollo (Hawk) supercomputer at the High Performance Computing Center Stuttgart (HLRS) under the grant number zzz44198.

REFERENCES

[1]D. Chung, N. Hutchins, M. Schultz, and K. Flack, "Predicting the drag of rough surfaces," *Annual Review of Fluid Mechanics*, vol. 53, no. 1, pp. 439–471, 2021.

[2]M. Kadivar, D. Tormey, and G. McGranaghan, "A review on turbulent flow over rough surfaces: Fundamentals and theories," *International Journal of Thermofluids*, vol. 10, p. 100077, 2021.

[3]J. Cardillo, Y. Chen, G. Araya, J. Newman, K. Jansen, and L. Castillo, "DNS of a turbulent boundary layer with surface roughness," *Journal of Fluid Mechanics*, vol. 729, p. 603–637, 2013.

[4]J. Yuan and U. Piomelli, "Numerical simulation of a spatially developing accelerating boundary layer over roughness," *Journal of Fluid Mechanics*, vol. 780, p. 192–214, 2015.

[5]A. Doosttalab, G. Araya, J. Newman, R. Adrian, K. Jansen, and L. Castillo, "Effect of small roughness elements on thermal statistics of a turbulent boundary layer at moderate reynolds number," *Journal of Fluid Mechanics*, vol. 787, p. 84–115, 2016.

[6]I. K. Kaminaris, E. Balaras, M. P. Schultz, and R. J. Volino, "Secondary flows in turbulent boundary layers developing over truncated cone surfaces," *Journal of Fluid Mechanics*, vol. 961, p. A23, 2023.

[7]M. Chevalier, P. Schlatter, A. Lundbladh, and D. Henningson, "SIMSON–A pseudo-spectral solver for incompressible boundary layer flow.," *Technical Report TRITA-MEK*, pp. 1–100, 2007.

[8]D. Goldstein, R. Handler, and L. Sirovich, "Modeling a no-slip flow boundary with an external force field," *Journal of Computational Physics*, vol. 105, no. 2, pp. 354–366, 1993.

Turbulent flow of Herschel-Bulkley Fluids in Rough Channels

Chidambaram Narayanan†, Djamel Lakehal†, Roel Belt* and Thierry Palermo+

† Advanced Modelling & Simulation (AMS)
AFR, Switzerland
e-mail: djamel.lakehal@afry.com

* TotalEnergies, Pôle d'Etudes et de Recherche de Lacq, France
+ TotalEnergies, Centre Scientifique et Technique Jean Féger, Pau, France

ABSTRACT

DNS of turbulent channel flow at a shear Reynolds number of $Re^* = 360$ for Newtonian and Herschel-Bulkley fluids in smooth and rough channels has been performed. The rough surface was made of irregular undulations modeled with the immersed surface method. The presentation will center around the Newtonian-fluid flows in the rough surface channel (CASE 1; (Narayanan et al. 2023), albeit selected results of the non-Newtonian case (Narayanan et al. 2024) will also be discussed.

For CASE 1, the results confirm that turbulence in the outer layer is not directly affected by the rough surface. The roughness effects on the turbulent stresses, the mean momentum balance and the budget of turbulence kinetic energy are confined to the layer < 25 wall units; beyond, the profiles collapse with those for smooth pipes. In the roughness sublayer, the streamwise normal Reynolds stress is reduced while the spanwise and wall-normal components are increased. The largest increase is for the Reynolds shear stress, resulting in a significant increase in the turbulence production near the wall even though the velocity gradient is decreased. The kinetic energy budget shows that turbulence production dominates the mean viscous diffusion of turbulence kinetic energy and both mechanisms are balanced by turbulent dissipation. The friction factor using the Colebrook-White correlation calculated by specifying the sand-grain roughness as 7.5 wall units predicts the friction velocity and the bulk velocity accurately. The streaky structures that exist near smooth walls were observed to be broken by the roughness elements, leading to a denser population of coherent structures near the wall, which increase the velocity fluctuations. The coherent structures developed in the roughness layer do not seem to penetrate in to the outer layer, and no evidence could be found as to the direct impact of the roughness layer on the outer one.

References:

- Narayanan et al., 2023 (arXiv preprint arXiv:2312.05168: submitted to JFM)
- Narayanan et al., 2024 (submitted to JFM)

SESSION: Particle-laden flows

Friday, April 12, 2024

11:00- 12:30

WORKSHOP
Direct and Large-Eddy Simulation 14
April 10-12 2024, Erlangen, Germany

EFFECTS OF FILTERING ON PARTICLES CLUSTERING IN TURBULENCE

Lukas A. Codispoti, Daniel W. Meyer, Patrick Jenny
Institute of Fluid Dynamics (IFD)
ETH Zürich, Switzerland
lukasco@ethz.ch

INTRODUCTION

Clustering in particle-laden turbulent flows typically takes place or is largely influenced by the smallest scales of the turbulent flow field. As a result, large eddy simulations (LES) of such flows require adequate subgrid-scale models. The development of these models require a thorough understanding of the mechanisms of particle clustering, which is still lacking. The challenge is especially pronounced in the case of light particles, since most conventional models cannot reconstruct coherent motion at the smallest scales. In this work, we take a first step towards the development of new SGS models for particle-laden turbulence by performing direct numerical simulations (DNS) of homogeneous isotropic turbulence at $Re_\lambda = 418$ laden with $N_p = 5.4 \times 10^9$ inertial point particles and then repeating them with sharp spectrally filtered fields to mimic 'perfect' LES.

NUMERICAL SIMULATIONS

DNS data is acquired from the Johns Hopkins Turbulence Database (JHTDB) [1]. The flow field is a homogeneous isotropic turbulent flow computed by a pseudo-spectral method on an $M^3 = 1024^3$ grid of a periodic box of side length $L = 2\pi$. The large-eddy turnover time is $T_L = 1.99$ Additional parameters of the dataset are provided in Table 1. In the cases LES1 and LES7, a *sharp spectral filter* is used to truncate the turbulent energy spectrum, resulting in a model-free LES field. We use a Lagrangian particle tracking method

Case	Re_λ	κ_{max}	η	τ_η	τ_p	St
DNS1	418	512	0.0028	0.0424	0.0424	1
DNS7	418	512	0.0028	0.0424	0.2968	7
LES1	-	8	0.0081	0.3560	0.0424	0.12
LES7	-	8	0.0081	0.3560	0.2968	0.83

Table 1: Summary of simulation cases.

to simulate the motion of one-way coupled, monodispersed point particles, effectively reducing the complexity to a single parameter - the Stokes number, $St = \tau_p/\tau_\eta$, where τ_η is the Kolmogorov time scale and τ_p is the particle response time. The particle equations of motion

$$\dot{\boldsymbol{x}} = \boldsymbol{v}, \quad \dot{\boldsymbol{v}} = (\boldsymbol{u}(\boldsymbol{x}, t) - \boldsymbol{v})/\tau_p \tag{1}$$

are integrated in time with an exact integration scheme using an in-house parallel solver.

We compute Eulerian fields of the particle number density n and particle velocity $\boldsymbol{u}_p$ using grid projection with the cloud-in-cell (CIC) method [2]. The intensity of particle clustering is then expressed as the variance of the particle number density, $\langle n^2 \rangle$, which, as we will show, can take longer than $4T_L$ to reach steady state.

PHYSICAL SPACE

Depending on the Stokes number, filtering out small-scale turbulent flow structures attenuates or intensifies particle clustering. This is clearly demonstrated in Fig. 1. In the DNS1 case, the particles resonate most strongly with eddies of size η and the resulting clusters are sharp patterns that are elongated in the direction of local vorticity. The presence of larger voids implies multiscale clustering, as formerly noted by Matsuda *et al.* [3]. In the LES1 case, on the other hand, fine-scale patterns are missing completely. The particles are distributed more uniformly, yet still avoid regions of high vorticity and form sheet-like clusters. In the DNS7 case, clustering takes place at larger length scales, but small-scale velocity fluctuation act to randomize the motion of the particles, which results in significantly less well-defined patterns. Here, the effect of the sharp spectral filter is to intensify clustering: particles in the LES7 case exhibit strong preferential concentration with clusters that are separated from void regions with sharp edges. We identify warped manifolds of increased number density that resemble *caustics*, which have been reported previously by e.g. Wilkinson and Mehlig [4] in two-dimensional synthetic turbulence. According to this mechanism, particles cluster as a result of folds in phase space, i.e. when particles at the same location have different velocities. This notion is particularly compelling due to the fact that while in all cases, the particles tend to accumulate outside high-vorticity regions, the centrifuge mechanism alone appears to be insufficient in explaining the observed particle distributions.

FOURIER SPACE

With $\hat{n}(\kappa)$ denoting the Fourier mode of the particle number density, we compute the particle density power spectrum $E_n(\kappa) = \frac{1}{2}\langle \hat{n}(\kappa)\hat{n}^*(\kappa) \rangle$, which quantifies the distribution of $\langle n^2 \rangle$ in wavenumber space (Fig. 2). The tendency of the $St = 1$ particles of the DNS1 case to cluster at small length scales is reflected in the increased density at larger wavenumbers, but clustering is clearly taking place on multiple length scales. A single *'typical cluster size'*, that one would expect to obtain from dimensional analysis, cannot be observed. Interestingly, the clusters that form in the LES7 case span a range of wavenumbers largely exceeding the energy spectrum of the

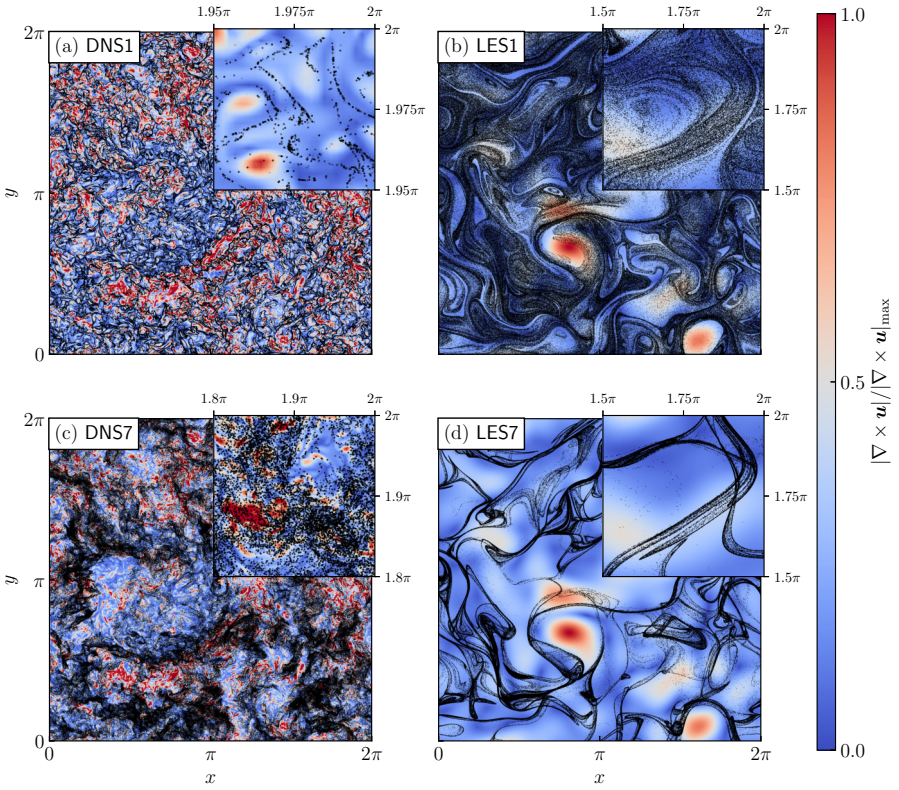

Figure 1: Scatters of particles inside the slice $\pi - \eta/4 < z < \pi + \eta/4$ over contours of the flow vorticity (normalized and clipped by $|\nabla \times \boldsymbol{u}|_{\max} = 50$ and 7.5 in the DNS and LES, respectively) with insets showing the upper right-hand side corner magnified. The transparency of the particles is linearly scaled with the distance to the center slice $z = \pi$.

flow field, which is cut off at $\kappa_{max} = 8$, meaning that the particles cluster at length scales smaller than the Kolmogorov eddies.

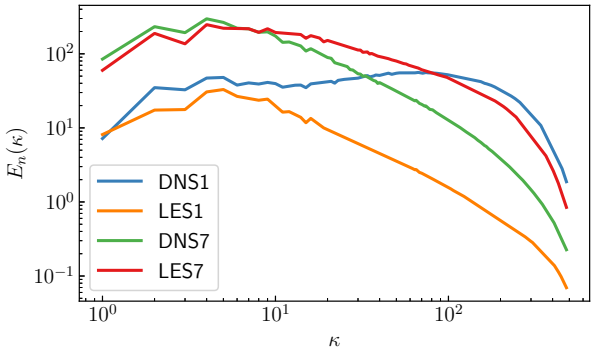

Figure 2: Particle number density power spectra.

Figure 2 by itself is, however, limited in its usefulness. Clearly, $E_n(\kappa)$ is not a good measure to compare the preferential concentration of the cases DNS7 and LES7, which look very different in physical space, but have qualitatively almost identical density spectra. Due to its non-local nature, the Fourier analysis is also unable to capture the caustic-like structures that are observed in the LES7 case. For this, we will resort to other measures, e.g. box-counting to compute the fractal dimension.

A more insightful analysis in Fourier space is performed by quantifying the transfer and production of $E_n(\kappa)$. To achieve this, we separate the contributions of transport and source terms in the conservation of the particle number density

$$\frac{\partial n}{\partial t} + \boldsymbol{u}_p \cdot \nabla n = -n \nabla \cdot \boldsymbol{u}_p. \tag{2}$$

Here, it is evident that the compressibility of $\boldsymbol{u}_p$ acts as a source term and is therefore responsible for producing variance in n. This allows us to derive an equation of the form $\frac{\partial E_n(\kappa)}{\partial t} = \mathcal{P}(\kappa) + \mathcal{T}(\kappa)$, enabling an investigation of the production of $\langle n^2 \rangle$ in Fourier space and its transfer between wavenumbers.

REFERENCES

[1]Y. Li, E. Perlman, M. Wan, Y. Yang, C. Meneveau, R. Burns, S. Chen, A. Szalay, and G. Eyink, "A public turbulence database cluster and applications to study Lagrangian evolution of velocity increments in turbulence," *Journal of Turbulence*, vol. 9, p. N31, Jan. 2008.

[2]C. K. Birdsall and D. Fuss, "Clouds-in-clouds, clouds-in-cells physics for many-body plasma simulation," *Journal of Computational Physics*, vol. 3, pp. 494–511, Apr. 1969.

[3]K. Matsuda, K. Yoshimatsu, and K. Schneider, "Large-scale clustering of inertial particles in homogeneous isotropic turbulence," in *12th International Symposium on Turbulence and Shear Flow Phenomena (TSFP12)*, (Osaka, Japan), July 2022.

[4]M. Wilkinson and B. Mehlig, "Caustics in turbulent aerosols," *Europhysics Letters (EPL)*, vol. 71, pp. 186–192, July 2005.

WORKSHOP
Direct and Large-Eddy Simulation 14
April 10-12 2024, Erlangen, Germany

TURBULENT FLOWS OF DILUTE POLYMER SOLUTIONS: COMPARING DNS WITH EXPERIMENTS

F. Serafini[1], **F. Battista**[1], **P. Gualtieri**[1], **C.M. Casciola**[1]
[1]Department of Mechanical and Aerospace Engineering
Sapienza, University of Rome, Italy
francesco.serafini@uniroma1.it

The transition from the laminar to the turbulent regime is responsible for a significant increase in friction drag in wall-bounded flows [1]. Among the many possibilities to mitigate the phenomenon, the addition of a tiny amount of long-chain polymers to a Newtonian solvent is known to be one of the most efficient ways to reduce friction [2]. Despite more than 70 years since the first experimental evidence, the polymer drag reduction phenomenon is still not fully understood and the mechanism behind it is still debated [3]. The experiments suggest that the mechanical interaction between polymer chains and turbulence dynamics is at the basis of drag reduction (DR) [4], they characterised the role of polymer and solvent parameters [5], but they cannot provide many details about the polymer-turbulence interaction and sometimes give contrasting information that does not allow for a unique interpretation of the phenomenon.

Direct numerical Simulation (DNS) has been used since the 90s to investigate the dynamics of polymeric flows [6] but a quantitative agreement between DNS and the experiments has not been achieved yet. The main reason is that the classical polymer modelling (i.e. the Eulerian FENE-P model [7]) has been unable to reproduce the real polymer parameters [8]. Only recently hybrid Eulerian-Lagrangian simulations of polymer-laden flows have been developed, showing the capability of reproducing polymer systems with realistic concentrations and molecular weights [9].

These hybrid simulations couple the Navier-Stokes equation for a Newtonian solvent with the Lagrangian evolutions of millions, or even billions, of polymer molecules. The polymer chains are modelled as FENE dumbbells, namely two massless beads connected by a nonlinear entropic spring that accounts for the polymer relaxation and the polymer finite extensibility. The dimensionless system of equations describing the polymer solutions is

$$\begin{aligned}
\boldsymbol{\nabla}\cdot\boldsymbol{u} &= 0 \\
\frac{\partial \boldsymbol{u}}{\partial t} + \boldsymbol{\nabla}\cdot(\boldsymbol{u}\otimes\boldsymbol{u}) &= -\boldsymbol{\nabla}p + \frac{1}{\mathrm{Re}}\boldsymbol{\nabla}^2\boldsymbol{u} + \boldsymbol{F} \\
\frac{d\boldsymbol{x}_c^{(j)}}{dt} &= \frac{\boldsymbol{u}_1^{(j)}+\boldsymbol{u}_2^{(j)}}{2} + \frac{L h_{eq}}{\sqrt{3\mathrm{Wi}}}\frac{\boldsymbol{\xi}_1^{(j)}+\boldsymbol{\xi}_2^{(j)}}{2}\,. \\
\frac{d\boldsymbol{h}^{(j)}}{dt} &= \frac{\boldsymbol{u}_2^{(j)}-\boldsymbol{u}_1^{(j)}}{L} - \frac{\boldsymbol{h}^{(j)}}{\mathrm{Wi}(1-H^{(j)2})} + \frac{h_{eq}\left(\boldsymbol{\xi}_2^{(j)}-\boldsymbol{\xi}_1^{(j)}\right)}{\sqrt{3\mathrm{Wi}}}
\end{aligned} \tag{1}$$

In eq. (1) $\boldsymbol{u}$ the fluid velocity, p the hydrodynamic pressure, $\boldsymbol{F}$ the polymers' force density exerted on the solvent. The dimensionless form is obtained using as reference quantities the solvent density ρ^* and viscosity μ^*, the pipe radius ℓ_0^*, and the bulk velocity $U_b^* = Q_b^*/(\pi\ell_0^{*2})$. $\mathrm{Re} = \rho^* U_b^* \ell_0^*/\mu^*$ is the Reynolds number (the asterisks denote dimensional quantities). As far as polymer are concerned, $\boldsymbol{x}_c^{(j)} = (\boldsymbol{x}_1^{(j)} + \boldsymbol{x}_2^{(j)})/2$ is the polymer centre, $\boldsymbol{h}^{(j)} = (\boldsymbol{x}_2^{(j)} - \boldsymbol{x}_1^{(j)})/L$ is the end-to-end vector normalised by the polymer contour length L ($H = \|\boldsymbol{h}\|$), and $\boldsymbol{u}_{1/2}$ is the fluid velocity at the position of the beads. The equilibrium polymer size in a still solvent, h_{eq}, is set through the white noise terms $\boldsymbol{\xi}_{1/2}^{(j)}$. $\mathrm{Wi} = \tau^*/(\ell_0^*/U_b^*)$ is the Weissenberg number, the ratio of the polymer relaxation time τ^* and the fluid time scale. The Weissenberg number is the relevant parameter controlling the interaction between polymers and turbulence since it determines the polymer stretching distributions. The polymers exert the backreaction $\boldsymbol{F}$ on the solvent, written as follows

$$\boldsymbol{F} = \frac{\gamma L}{2\mathrm{Wi}}\sum_{j=1}^{N_p}\frac{\boldsymbol{h}^{(j)}}{1-H^{(j)2}}\left[\delta(\boldsymbol{x}-\boldsymbol{x}_1^{(j)}) - \delta(\boldsymbol{x}-\boldsymbol{x}_2^{(j)})\right]. \tag{2}$$

In (2) γ is the dimensionless friction coefficient of the beads, while the singularity in the polymer forcing is regularised according to the Exact Regularised Point Particle method [10].

Figure 1 shows the magnitude of the instantaneous velocity and the instantaneous polymer configuration in a portion of the pipe, as an example of the geometry and flow configuration.

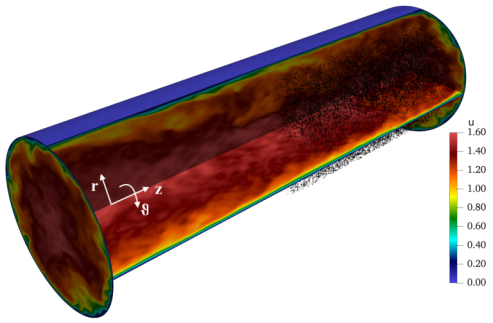

Figure 1: Example of the flow configuration [11]: magnitude of the instantaneous velocity (coloured contour) and instantaneous polymer configuration (black lines) in a portion of the pipe.

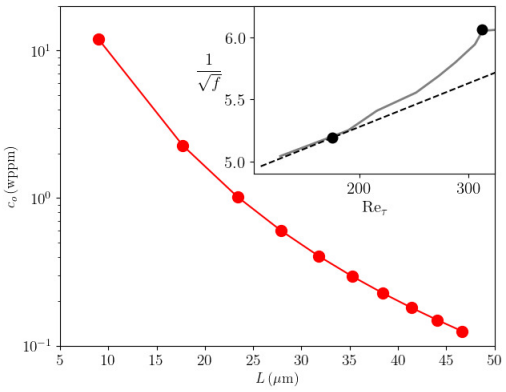

Figure 2: Concentration of polymers of different contour lengths needed to reproduce the experimental molecular weight distribution [13]. Inset: inverse of the square root of the friction factor f vs friction Reynolds number Re_τ compared to the experimental curve [13] (black dots vs grey line).

Reproducing an actual experiment requires an accurate characterization of the polymer used as drag reducing additive. The main issue is that most of the experimental works are performed using synthetic polymers [12]. Synthetic polymers are generally characterised by a large polydispersity, namely polymers have a rather broad distribution of molecular weight and thus they have different lengths. Since the Weissenberg number Wi depends almost quadratically on L, polymers of different lengths experience different levels of stretching (the probability of large stretching increases with Wi) and must be simulated simultaneously if one aims at a one-to-one matching of the experimental conditions.

DNS data are compared with the experimental results of Berman [13], who analysed the friction scaling law of dilute solutions of Polyethylene oxide (PEO) and estimated the molecular weight distribution by gel chromatography. The molecular weight (or contour length) distribution is reproduced in our simulation by considering ten polymer populations with different contour lengths. In particular, fig. 2 reports the concentration of polymer (in terms of part per million in weight) with different lengths that reproduce the molecular weight distribution of Berman's experiment. Inset of fig. 2 shows the friction factor obtained by numerical simulations at two different Reynolds numbers, $\mathrm{Re}_\tau = 180$ and $\mathrm{Re}_\tau = 320$, exhibiting excellent agreement with the experimental curve (solid grey line).

During the oral presentation, results from Direct Numerical Simulations will be presented, providing methodological details and a physical interpretation of the polymer turbulence interaction at the basis of the drag reduction phenomenon.

*

References

[1] B. Frohnapfel, Y. Hasegawa, and M. Quadrio, "Money versus time: evaluation of flow control in terms of energy consumption and convenience," *Journal of fluid mechanics*, vol. 700, pp. 406–418, 2012.

[2] I. Procaccia, V. S. L'vov, and R. Benzi, "Colloquium: Theory of drag reduction by polymers in wall-bounded turbulence," *Reviews of Modern Physics*, vol. 80, no. 1, p. 225, 2008.

[3] R. Benzi and E. S. Ching, "Polymers in fluid flows," *Annual Review of Condensed Matter Physics*, vol. 9, pp. 163–181, 2018.

[4] L. Xi, "Turbulent drag reduction by polymer additives: Fundamentals and recent advances," *Physics of Fluids*, vol. 31, no. 12, p. 121302, 2019.

[5] P. Virk, "Drag reduction fundamentals," *AIChE Journal*, vol. 21, no. 4, pp. 625–656, 1975.

[6] R. Sureshkumar, A. Beris, and R. Handler, "Direct numerical simulation of the turbulent channel flow of a polymer solution," *Physics of Fluids*, vol. 9, no. 3, pp. 743–755, 1997.

[7] R. B. Bird, C. F. Curtiss, R. C. Armstrong, and O. Hassager, *Dynamics of Polymeric Liquids, Volume 2: Kinetic Theory*. Wiley, 1987.

[8] Y. Dubief, V. E. Terrapon, and B. Hof, "Elasto-inertial turbulence," *Annual Review of Fluid Mechanics*, vol. 55, p. 2023, 2022.

[9] F. Serafini, F. Battista, P. Gualtieri, and C. Casciola, "Drag reduction in turbulent wall-bounded flows of realistic polymer solutions," *Physical Review Letters*, vol. 129, no. 10, p. 104502, 2022.

[10] F. Battista, J.-P. Mollicone, P. Gualtieri, R. Messina, and C. M. Casciola, "Exact regularised point particle (erpp) method for particle-laden wall-bounded flows in the two-way coupling regime," *Journal of Fluid Mechanics*, vol. 878, pp. 420–444, 2019.

[11] F. Serafini, F. Battista, P. Gualtieri, and C. M. Casciola, "Drag reduction in polymer-laden turbulent pipe flow," *Fluids*, vol. 7, no. 11, p. 355, 2022.

[12] J. Lumley, "Drag reduction by additives," *Annual review of fluid mechanics*, vol. 1, no. 1, pp. 367–384, 1969.

[13] N. Berman, "Drag reduction of the highest molecular weight fractions of polyethylene oxide," *The Physics of Fluids*, vol. 20, no. 5, pp. 715–718, 1977.

WORKSHOP
Direct and Large-Eddy Simulation 14
April 10-12 2024, Erlangen, Germany

VALIDATION OF AN ENHANCED MODEL FOR PARTICLE-BUBBLE COLLISIONS IN FLOTATION BY DNS

B. Tiedemann, M. Kreuseler, J. Fröhlich
Institute of Fluid Mechanics (ISM)
Technische Universität Dresden, Germany
benedikt.tiedemann@tu-dresden.de

INTRODUCTION

Flotation is a highly complex process involving a wide variety of physicochemical subprocesses. One of the most important subprocesses is the collision of mineral particles and bubbles, because of its direct effect on the recovery and performance of flotation [1]. In addition, collisions between pairs of bubbles and pairs of mineral particles also play a vital role in flotation dynamics. These collisions are a key factor influencing the trajectories and movements of mineral particles and bubbles within the flotation cell. It is, therefore, vital to know the frequency of these three types of collision events to predict the behaviour and performance of flotation equipment. Due to the high loading of the three-phase flows in flotation, collisions are inherently difficult to study experimentally [2]. Furthermore, existing numerical approaches are limited and their use is often very costly [3]. Therefore, a reliable model for predicting the collision process is needed for computations in an Euler-Euler framework or for use in global modelling of flotation processes or in other multiphase flows.

PROPOSED COLLISION MODEL

Existing, widely used collision models are based on assumptions that are not really fulfilled in flotation [4, 5]. Thus, the authors propose a new Integrated Multi Size Collision model (IMSC). The IMSC provides an analytical description of the collision kernel Γ in a turbulent, bidisperse suspension with particles and/or bubbles of different sizes. Using a spherical collision kernel, as proposed by Saffman and Turner [6], the main modelling quantity is the root mean square radial relative velocity w_{rms} between two representative particles of class i and j. The proposed modelling framework extends, refines, and combines proven and existing approaches for the modelling of collisions [6, 8, 9]. Additionally, new items such as consideration of swarm effects and an iterative drag correction are introduced. Figure 1 shows an overview of the proposed IMSC model.

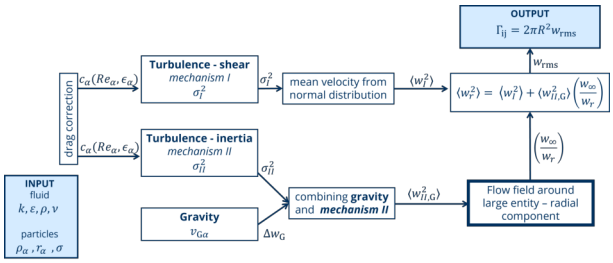

Figure 1: Overview of the proposed IMSC model

SIMULATIONS CONDUCTED

As a reference for validation, three-phase Direct Numerical Simulations with mono-sized air bubbles and mineral particles were performed. The continuous fluid phase is governed by the unsteady, three-dimensional Navier-Stokes equations for incompressible fluids discretized with a second-order finite-volume scheme on a staggered, Cartesian grid.

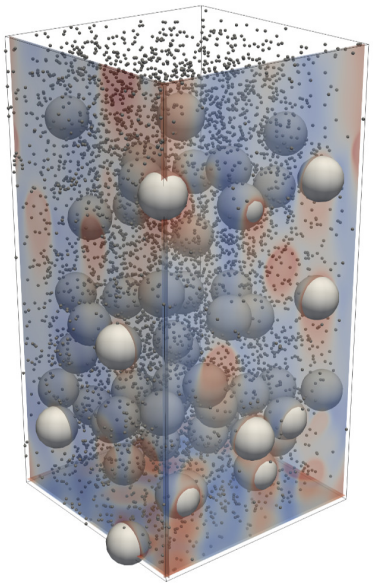

Figure 2: Instantaneous snapshot of the reference case with gravity as main driver of particle and bubble movement. The contour depicts the vertical fluid velocity v. The number of particles is reduced for better visibility.

Air bubbles are modelled as rigid spheres represented by their equations of motion and coupled to the fluid by the immersed boundary method of Tischisgale et. al. [10]. The solid particles are two-way coupled point particles with their motion being governed by the sum of forces acting on them. A representative region of a flotation cell was defined with a size of $5.5 \times 11 \times 5.5$ times the bubble diameter with triperiodic boundary conditions. Key influencing parameters for the particle-bubble encounter were varied. This includes, but is not limited to, the bubble diameter, the diameter of the mineral particles, particle and bubble concentration, as well as the turbulence intensity. All parameters were chosen to match real world conditions in mechanical flotation cells. An impression of the results is provided in Figure 2.
A more detailed overview of the simulation setup is given in Tiedemann and Fröhlich [11], together with results for a reference case. Further simulations, used for validation here, will be presented in a forthcoming paper together with a detailed analysis.

VALIDATION

Figure 3 shows the simulated and modelled particle-bubble collision kernel. Simulation data for different parameter combinations and the corresponding results of the new model and other models are shown. The new IMSC model fits both the simulated collision kernel and the simulated relative velocity substantially better than the reference models. All other models shown, drastically overpredict the collision kernel. Overall, the proposed approach is promising for modelling of collisions between collision partners of different sizes. The proposed model is, hence, highly suitable for use in a wide range of modelling and simulation approaches for flotation and multiphase flow applications. The final contribution will highlight the proposed model in more detail, and show further validations, including literature data.

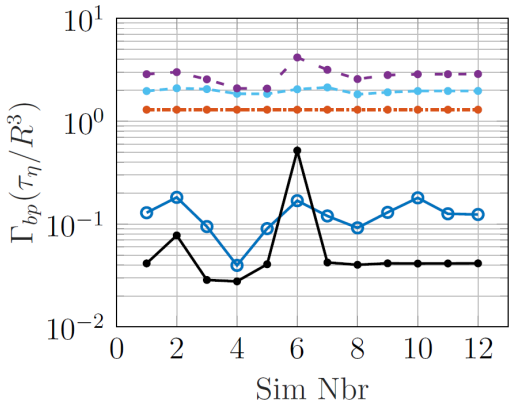

Figure 3: Particle-bubble collision kernels of DNS (—o—), Abrahamson [7] (- -•- -), Saffman and Turner [6] (-·-·-), Zaichik et al. [12] (- -•- -), IMSC (—•—)

REFERENCES

[1]Jameson, G.J., Narn, S., Young, M. : Physical factors affecting recovery rates in flotation, *Mineral Science Engineering*, **9**, 103–118 (1977).
[2]Lee, C.H., Erickson, L.E., Glasgow, L.A. : Dynamics of bubble size distribution in turbulent gas-liquid dispersions, *Chem Eng Commun*, **61**, 181–195 (1987).
[3]Chan, T.T.K., Ng, C.S., Krug, D. : Bubble–particle collisions in turbulence: insights from point-particle simulations, *J. Fluid Mech.*, **959**, A6 (2023).
[4]Kruis, F.E., Kusters, K.A. : The collision rate of particles in turbulent flow, *Chem Eng Commun*, **158**, 201–203 (1997).
[5]Kostoglou, M., Karapantsios, T.D., Evgenidis, S. : A critical review on turbulent collision frequency/efficiency models in flotation: Unravelling the path from general coagulation to flotation, *Adv. Colloid Interface Sci.*, **279** (2020).
[6]Saffman, P.G., Turner, J.S. : On the collision of drops in turbulent clouds. *J. Fluid Mech.*, **1**, 16–30 (1956).
[7]Abrahamson, J. : Collision rates of small particles in a vigorously turbulent fluid, *Chem. Eng. Sci.*, **30**, 1371–1379 (1975).
[8]Kostoglou, M., Karapantsios, T.D., Evgenidis, S. : On a generalized framework for turbulent collision frequency models in flotation: The road from past inconsistencies to a concise algebraic expression for fine particles, *Adv. Colloid Interface Sci.*, **284**, 102270 (2020).
[9]Yuu, S. : Collision rate of small particles in a homogeneous and isotropic turbulence. *AIChE Journal*, **30**, 802–807 (1984).
[10]Tschisgale, S. Kempe, T., Fröhlich, J. : A general implicit direct forcing immersed boundary method for rigid particles, *Comput. Fluids*, **170**, 285–298 (2018).
[11]Tiedemann, B., Fröhlich, J. : Collision dynamics of particles and bubbles in gravity-driven flotation: A DNS investigation, *PAMM*.
[12]Zaichik, L.I., Simonin, O., Alipchenkov, V.M. : Turbulent collision rates of arbitrary-density particles, *Int. J. Heat Mass Transf.*, **53**, 1613–1620 (2010).

WORKSHOP
Direct and Large-Eddy Simulation 14
April 10-12 2024, Erlangen, Germany

SLENDER FLEXIBLE FIBERS IN TURBULENT CHANNEL FLOW

D.J.D. Sam[1], **D. Di Giusto**[1], **C. Marchioli**[1]
[1]Dept. Engineering and Architecture University of Udine, Italy
darishjeswindhas.sam@uniud.it, davide.di-giusto@etu.univ-amu.fr, marchioli@uniud.it

INTRODUCTION

Suspensions of fibers are a matter of great scientific interest because of their importance in the production of paper [1], their effectiveness as drag-reducing agents [2] and their relevance in understanding the microplastics cycle in the oceans [3]. The viscous theory of Jeffery [4] has been the foundation in understanding how rigid fibers reorient when suspended in turbulence, finding that these particles not only express a preferential alignment within the flow but also filter out small-scale contributions as their length becomes comparable to that of the eddies in the inertial range [5, 6]. In several biological and industrial applications, fibers are flexible and deform within the flow [7]. The effect of flow rotation and strain on the dynamics of flexible fibers is modified by the competition between viscous and elastic forces, their ratio determining the viscous-elastic number, $\mathbb{B} = (8\pi\ell^4\rho u_\tau^2)/(E_Y \cdot \pi/4a^4)$, where ρ the density of the fluid, u_τ the shear velocity, ℓ and a the particle half-length and radius and E_Y the Young's modulus of the material. In a turbulent flow, flexible fibers are intermittently stretched and compressed, depending on $\mathbb{B}$ but also on their relative length with regard to the turbulent scales. Sub-Kolmogorov flexible fibers suspended in Homogeneous Isotropic Turbulence (HIT hereinafter) are stretched at most times regardless of their bending stiffness, experiencing rapid buckling as they tumble [8]. Instead, long and flexible fibers start aligning inside eddies of comparable size [9] and respond more or less coherently to these structures depending on their bending stiffness [10]. In this study, we look at the rotations and deformations of long and flexible fibers, especially focusing on their bending dynamics. We will evaluate the influence of the flexibility of the fibers ($\mathbb{B} >> 1$) on their dynamics, performing two-way coupled Euler-Lagrangian point particle Direct Numerical Simulations of a turbulent channel flow.

PHYSICAL PROBLEM AND METHODOLOGY

We perform DNS of a pressure-imposed turbulent channel flow laden with fibers in the two-way coupling regime. The flow field $\mathbf{u}$ is calculated on an Eulerian grid by solving the Continuity and Navier-Stokes equations:

$$\nabla \cdot \mathbf{u} = 0 \quad , \quad \frac{\partial \mathbf{u}}{\partial t} + (\mathbf{u} \cdot \nabla)\mathbf{u} = -\nabla P + \frac{1}{Re_\tau}\nabla^2\mathbf{u} + \mathbf{f}_{2w} \quad (1)$$

where ∇P is the equivalent pressure gradient that drives the flow and $\mathbf{f}_{2w}$ is the two-way coupling momentum term determined by the fibers. The shear Reynolds number is $Re_\tau = \rho u_\tau h/\mu = 300,\ 1200$, being ρ the fluid density, μ the fluid dynamic viscosity, u_τ the shear velocity and h the half-height of the channel. The computational domain is a rectangular box of size $L_x^+ \times L_y^+ \times L_z^+ = 4\pi Re_\tau \times 2\pi Re_\tau \times 2Re_\tau$ in the stream-wise x, span-wise y and wall-normal z coordinates, where the superscript $^+$ indicates wall units. The flow equations are resolved following a classical pseudo-spectral algorithm. Simulations are performed at imposed particle volume fraction $\Phi = 0.0001$, by dispersing 2.5 million point-wise rod elements of aspect ratio $r = 5$ in the turbulent channel flow. Their diameter and length are $2a^+ = 0.36$ and $2\ell = 1.79$. The latter is explicitly chosen to be comparable to the Kolmogorov length scale of the unladen flow at the wall $\eta_{k,w} = 1.51$, making viscous flow theory the best approximation to accurately model the drag force that the flow determines on the point-wise rods [11]. Fibers are modelled as chains of up to 40 sub-Kolmogorov inextensible rods interconnected by holonomic constraints that enable relative rotation of neighboring elements. The motion of each constrained rod is computed in time using the Lagrangian approach described in [12]. Fibers are classified according to their total length L_0^+ and total aspect ratio r_{tot} into short ($L_0^+ = 17.91, r_{tot} = 50$), intermediate ($L_0^+ = 35.81, r_{tot} = 100$) and long fibers ($L_0^+ = 71.62, r_{tot} = 200$). The fiber Stokes number is defined as:

$$St_f^+ = \frac{2(a^+)^2\rho^+}{9}\frac{r_{tot}\ln(r_{tot} + \sqrt{r_{tot}^2 - 1})}{\sqrt{r_{tot}^2 - 1}} \ , \quad (2)$$

where $\rho^+ = 3$ is the ratio between the density of the fibers ρ_p and that of the fluid ρ. The characteristic time of the fibers ($[0.1; 0.11; 0.13]$) is not particularly high, therefore the resulting inertial effects should be secondary. Following [13], the bending stiffness of the fibers is modelled as a torque acting to align two constrained rods:

$$Y_b^+ = \frac{\pi E_Y^+ {a^+}^3}{8r}\cos^{-1}(\mathbf{o}_n \cdot \mathbf{o}_{n-1})\frac{\mathbf{o}_n \times \mathbf{o}_{n-1}}{|\mathbf{o}_n \times \mathbf{o}_{n-1}} \ , \quad (3)$$

where $E_Y^+ = E_Y/(\rho^2 u_\tau)$ is the dimensionless Young's modulus of the fibers and $\mathbf{o}_n$ is the orientation vector of the n^{th} rod of the given chain. Two different values of Young's modulus will be considered in this study, determining stiff-less ($E_Y^+ = 0$) and stiff ($E_Y^+ = 10^4$) fibers. Short ($\mathbb{B} = 20.000$), intermediate ($\mathbb{B} = 320.000$) and long ($\mathbb{B} = 5.120.000$) stiff fibers ($E_Y^+ = 10^4$) as well as all the stiff-less chains ($\mathbb{B} \sim \infty$) correspond to very flexible objects in a turbulent flow. The hydro-dynamical disturbance determined by the point-wise rods on the flow is restored through the Exact Regularized Point Particle (ERPP) method [14], which required a computational grid made of $N_x \times N_y \times N_z = 1024 \times 512 \times 513$

points at $Re_\tau = 300$. This corresponds to a grid resolution of $\left(dx^+ = dy^+ \sim 3.7; dz^+_{max} \sim 1.8\right)$ wall units, allowing us to set the regularisation time-scale of the ERPP method to $\epsilon^+_R = 1.8^2/2 = 1.62$. As a consequence, the rods information is stored for $\epsilon^+_R/dt^+ = 1.62/0.015 = 108$ time-steps δ^+_t before diffusing to the Eulerian grid discretizing the flow. Initially, fibers are randomly dispersed into a fully-developed turbulent channel flow, oriented along the stream-wise direction and fully stretched. Statistics are collected at steady state every 7.5 t^+ and averaged over 100 different samples, sorting fibers according to their wall-normal position.

RESULTS

In this abstract, we focus on the tumbling rate of the flexible fibers $|\dot{\mathbf{n}}| = \omega \times \mathbf{n}$, which is calculated by averaging the rotational velocity ω and the orientation $\mathbf{n}$ among all the rods of a chain. The statistics of the calculated tumbling rate are displayed in Figure 1, for the $Re_\tau = 300$ simulations. By considering only fibers that lie within 30 wall units from the half-height of the channel, we compare their mean squared tumbling rate $\langle \dot{n}^+ \dot{n}^+ \rangle$ to those of rigid fibers in Homogeneous Isotropic Turbulence (HIT hereinafter), normalized by the local Kolmogorov time scale τ^+_k and displayed against the fiber length L^+_0 relative to the local Kolmogorov length scale η^+_k in panel (a) of figure 1. Interestingly, although the bulk of the turbulent channel flow is not a region of perfect turbulence isotropy, the influence of the walls on the considered flexible fibers is not relevant as their mean squared tumbling rate is comparable to experimental observations [5, 6] with rigid fibers in HIT. This has been explained in terms of a preferential alignment with the local vorticity and we speculate that the low bending stiffness of our chains does not have an important influence on this phenomenology. Therefore, flexible fibers do not correlate with turbulence as if they were randomly aligned short rods (black dashed line) or had a finite length (purple line), as modelled by Parsa & Voth [5]. Moreover, the considered fibers are not long enough to observe the filtering effect of small turbulent scales beyond a certain relative length, well captured by the scaling expression of Oehmke et al. [6] (dashed grey line), yet a relevant influence of the particle length is observed for the longest chains (brown left triangles), whose mean squared tumbling rate is higher when they are completely stiff-less ($\mathbb{B} = \infty$). A clear influence of the viscous-elastic number $\mathbb{B}$ emerges when we display the normalized mean squared tumbling rate $\langle \dot{n}^+ \dot{n}^+ \rangle$ against the wall-normal coordinate z^+ in panel (b) of Figure 1, comparing with the experiments of Shaik et al. [15] and Alipour et al. [16] with rigid fibers ($\mathbb{B} \sim 1$) in a similar flow geometry. Despite a general qualitative agreement, our results indicate a remarkable influence of the particle deformability ($\mathbb{B} >> 1$) on the mean squared tumbling rate, which is higher than what is observed for rigid fibers [15, 16]. Again, an influence of the particle length emerges only for the longest chains, which tumble with larger dispersion at infinite $\mathbb{B}$ (brown left triangles).

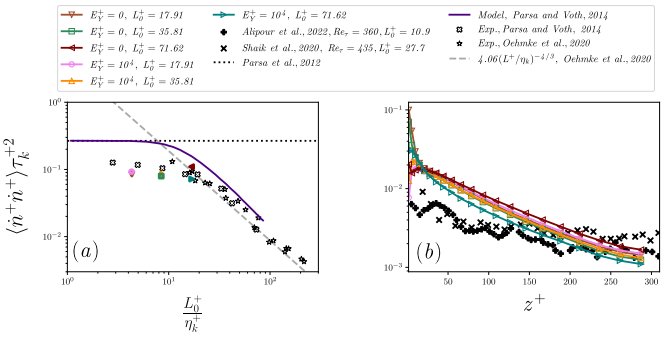

Figure 1: Dimensionless mean squared tumbling rate $\langle |\dot{\mathbf{n}}\dot{\mathbf{n}}| \rangle$, normalized by the local Kolmogorov time scale τ^+_k. Panel (a): $\langle |\dot{\mathbf{n}}\dot{\mathbf{n}}| \rangle$ against the stretched fiber length L^+_0, normalized by the local Kolmogorov length scale η^+_k at the half-height of the turbulent channel flow. The HIT models for randomly oriented sub-Kolmogorov rods (dotted black line), randomly oriented long fibers (solid purple line), the experimental results (empty black exes and empty black stars) as well as their scaling law (dashed grey line) are displayed for comparison. Panel (b): $\langle |\dot{\mathbf{n}}\dot{\mathbf{n}}| \rangle$ against the dimensionless wall normal coordinate z^+.

In the final paper, we will also discuss the effects of fluid inertia on the forces and torques experienced by the fibers, thus going beyond the commonly used Jeffery torques [4]. We do this using the model proposed by [17] and study how incorporating fluid-inertial forces and torques affects the collective dynamics of the fibers. We will examine the conditions under which the inertial contribution becomes relevant given the intermittent nature of the flow, comparing the drift time (of typical order of a few periods of rotation) with the typical time of the flow velocity fluctuations. We will show that the fibers in the bulk of the flow orient with the local strain, align with the vorticity - as in HIT - and experience a tumbling rate comparable to that of rigid fibers. Near the walls, vorticity orients with the spanwise direction while flexible fibers align with the mean flow. This orthogonality determines a stronger contribution of the flow rotation to the tumbling rate. The most probable deformed shapes define a bi-variate probability space, suggesting that two main deformation patterns exist: eyelash bending and compressive buckling.

REFERENCES

[1]Lundell, F., Söderberg, L.D., Alfredsson, P.H., 2011. Annu. Rev. Fluid Mech. 43, 195–217.

[2]Hoyt, J.W., 1972. Technical Report. Naval Undersea Center San Diego CA.

[3]Ross, P.S., et al., Nature Commun. 12, 1–9, 2021.

[4]Jeffery, G. B. Proc. R. Soc. Lond. A **102.715**, pp. 161–179, 1922.

[5]Parsa, S., Voth, G.A., 2014. Phys. Rev. Lett. 112, 024501.

[6]Oehmke, T.B., Bordoloi, A.D., Variano, E.A., Verhille, G., 2021. Phys. Rev. Fluids 6, 044610.

[7]Du Roure, O., Lindner, A., Nazockdast, E.N., Shelley, M.J., 2019. Annu. Rev. Fluid Mech. 51, 539–572.

[8]Allende, S., Henry, C., Bec, J., 2018. Phys. Rev. Lett. 121, 154501.

[9]Picardo, J.R., Singh, R., Ray, S.S., Vincenzi, D., 2020. Phil. Trans. R. Soc. A 378, 20190405.

[10]Rosti, M.E., Banaei, A.A., Brandt, L., Mazzino, A., 2018. Lett. 121, 044501.

[11]Kim, S., Karrila, S.J., 2013. Microhydrodynamics: principles and selected applications. Courier Corporation.

[12]Dotto, D., Soldati, A., Marchioli, C., 2020. Meccanica 55, 343–356.

[13]Lindström, S.B., Uesaka, T., 2007. Phys. Fluids 19, 113307.

[14]Gualtieri, P., et al., 2015 J. Fluid Mech. 773, 520–561.

[15]Shaik, S., Kuperman, S., Rinsky, V., van Hout, R., 2020. Phys. Rev. Fluids 5, 114309.

[16]Alipour, M., De Paoli, M., Soldati, A., 2022. J. Fluid Mech. 934.

[17]Dabade, V.,Marath, N. K., Subramanian, G. J. Fluid Mech., **791**, pp. 631–703, 2016.

WORKSHOP
Direct and Large-Eddy Simulation 14
April 10-12 2024, Erlangen, Germany

INFLUENCE OF MAXEY–RILEY TERMS ON THE MICROPLASTIC PARTICLE DISTRIBUTIONS IN OPEN CHANNEL TURBULENCE

Y. Sakai[1], **M. Manhart**[1]

[1]TUM School of Engineering and Design, Professorship of Hydromechanics
Technical University of Munich (TUM) Munich, Germany
yoshiyuki.sakai@tum.de

INTRODUCTION

Microplastic (MP) fragments in the aquatic environment are believed to be a major health concern to aquatic organisms. When sampling methods are used to estimate MP loads in a river, then several uncertainties arise, one of them is the uncertainty in the vertical concentration profile. It is therefore important to understand the impact of hydraulic conditions on MP particles' dynamics in surface waters. During their ageing, MP particles are fragmented and can be found in a wide range of particle diameters ranging from the nanometre size to several millimetres. Furthermore, their density can vary due to possible accumulation of biofilm around their core which leads to (i) increasing sphericity of the particles and (ii) a density tending towards the one water. For MP particles being smaller than the Kolmogorov length, the point particle method is the method of choice. In exchange for the model uncertainties, this type of numerical methods enables us to predict the motions of many particles subjected to the turbulence at a reasonable computational cost.

In the literature, it is well-documented that all of the hydrodynamic forces need to be considered in the dynamics of (nearly) neutrally buoyant particles subjected to turbulence [1, 2]. This is in contrast to the situation of the particles that are significantly heavier or lighter than the transporting fluids, where many of the hydrodynamic forces can be neglected. In [3], a high sensitivity of the steady-state MP concentrations to inclusion of certain forces was found. Our aim of this contribution is therefore to document and analyse our findings to serve as a guidance towards the future MP simulation works.

NUMERICAL METHODS & SIMULATION SET-UP

We perform open-channel DNS by means of the CFD code MGLET, which solves the incompressible Navier-Stokes equations without any turbulence models.

A second-order central finite volume scheme is used to discretise the equations based on a Cartesian staggered grid arrangement, whilst a third-order low-storage Runge-Kutta scheme [4] integrates in time. The projection method of [5] is used to decouple the velocity/pressure computations, whilst the resulting Poison problem is solved by a SIP solver [6].

One-way coupled point-particle approach is used to approximate the MP particle dynamics, in which the momentum balance for a particle is modelled based on individual forces, namely: *buoyancy*, *fluid acceleration*, *Stokes drag*, *added mass*, and *Basset history*. Accordingly, the governing equation of particle motions called Maxey-Riley equation can be formulated (eqn. 1), where $u_{\mathrm{p},i}$ is particle velocity in i-th direction, ρ_p is particle density, ρ_f and ν are the fluid density and kinematic viscosity, g_i is gravitational acceleration that is nonzero in $i = 3$, and $u_{@\mathrm{p},j}$ is the fluid velocity at the particle location, and $\tau_\mathrm{p} = \beta d_\mathrm{p}^2/(18\nu)$ is the particle timescale. The Stokes term in eqn. 1 contains the so-called Faxén correction, which takes into account the finite-size effect in low particle Reynolds number (Re_p) limit. Instead, the finite Re_p effect can be incorporated by replacing the expression by $\frac{C_\mathrm{D} Re_\mathrm{p}}{24\tau_\mathrm{p}}\left(u_{@\mathrm{p},i} - u_{\mathrm{p},i} + \frac{d_\mathrm{p}^2}{24}\frac{\partial^2 u_i}{\partial x_j^2}\right)$ where the drag coefficient C_D depends on Re_p. In the current method, C_D is set according to [7]. The implementation of the history term is done via the efficient second-order method of [8]. In the current set-up, all of the above forces are expected to play non-negligible roles in the dynamics of (nearly) neutrally buoyant particles subjected to turbulence [1].

Table 1: Flow simulation parameters

Δx^+, Δy^+	$\Delta z^+_{\{\mathrm{min,max}\}}$	$N_x \times N_y \times N_z$	$\Delta T u_\tau^2/\nu$
8.44, 4.22	0.9, 3.3	$256 \times 256 \times 96$	15310

We consider an infinitely long/wide open channel turbulence with a smooth bottom wall. The flow is realised by doubly-periodic boundary condition in streamwise (x) and spanwise (y) directions respectively, whereas in the wall-normal direction (z), impermeable rigid free-slip and no-slip planes represent the top and the bottom boundaries. Approximation by the rigid free-slip implies that the Froude number is at zero, therefore the friction Reynolds number $Re_\tau = \frac{u_\tau h}{\nu}$ solely characterises the flow, where u_τ is the friction velocity, which is defined as $u_\tau = (\tau_w/\rho_\mathrm{f})^{0.5}$ with the average wall shear stress τ_w, and h is the channel full height. Due to the high computational effort required for DNS, a relatively low Reynolds number flow $Re_\tau = 180$ is simulated in a numerical domain of $[L_x, L_y, L_z]/h = [12, 6, 1]$ (see also table 1).

On the other hand, the following particle-related dimensionless numbers describe the dynamics, namely a dimensionless particle diameter $d_\mathrm{p}^+ = d_\mathrm{p} u_\tau/\nu$, the Stokes number $St = \frac{\beta}{18}\left(\frac{d_\mathrm{p} u_\tau}{\nu}\right)^2$, and the Galileo number $Ga = \sqrt{|1-\beta| g d_\mathrm{p}^3}/\nu$, where $\beta = \rho_\mathrm{p}/\rho_\mathrm{f}$. In this study the density ratio is fixed at $\beta = 0.95$, whereas nine configurations in the St–Ga parameter space are chosen ($St = \{0.05, 0.5, 5\}$, $Ga = \{0.316, 1, 3.16\}$),

$$\frac{\mathrm{d}u_{\mathrm{p},i}}{\mathrm{d}t} = \underbrace{\frac{\rho_\mathrm{p}-\rho_\mathrm{f}}{\rho_\mathrm{p}}g_i}_{\text{buoyancy}} + \underbrace{\frac{\rho_\mathrm{f}}{\rho_\mathrm{p}}\left(\frac{\partial u_i}{\partial t}+u_{@\mathrm{p},j}\frac{\partial u_i}{\partial x_j}\right)}_{\text{fluid acceleration}} + \underbrace{\frac{1}{\tau_\mathrm{p}}\left(u_{@\mathrm{p},i}-u_{\mathrm{p},i}+\frac{d_\mathrm{p}^2}{24}\frac{\partial^2 u_i}{\partial x_j^2}\right)}_{\text{Stokes drag}}$$
$$+ \underbrace{\frac{\rho_\mathrm{f}}{2\rho_\mathrm{p}}\frac{\mathrm{d}}{\mathrm{d}t}\left(u_{@\mathrm{p},i}-u_{\mathrm{p},i}+\frac{d_\mathrm{p}^2}{40}\frac{\partial^2 u_i}{\partial x_j^2}\right)}_{\text{added mass}} + \underbrace{\frac{d_\mathrm{p}}{2\tau_\mathrm{p}}\frac{\int_0^t \frac{\mathrm{d}}{\mathrm{d}t}\left(u_{@\mathrm{p},i}-u_{\mathrm{p},i}+\frac{d_\mathrm{p}^2}{24}\frac{\partial^2 u_i}{\partial x_j^2}\right)}{\sqrt{\pi\nu(t-\tau)}}\mathrm{d}\tau}_{\text{Basset history}} \quad (1)$$

based on the order of magnitude analysis in [3].

PRELIMINARY RESULTS

In figure 1, the vertical distributions of the steady-state particle concentration of the cases with $St = 5$ are shown. As discussed in [3], when all the forces are included, the mean concentration profiles show largely homogeneous distributions in this largest Stokes number group (green lines in figure 1), which is especially true for the lower Ga cases. At the largest Ga (case I), a slight accumulation of particles can be observed towards the free surface, together with a noticeable concentration reduction near the bottom wall. Moreover, so-called *turbophoresis* —migration of light inertial particles towards the regions of lower turbulent diffusivity [9]— can be observed specifically in the case G.

By alternating the force combinations, this turbophoresis appears even at more exaggerated intensities for all the cases in this St group when the fluid acceleration term is excluded (see blue and yellow lines). Notice that this pseudo-physical turbophoresis emerges not only near the bottom no-slip wall, but also in the vicinity of the free surface. On the other hand, if we consider all the forces except the history term, the apparent turbophoresis disappears entirely, and it only re-appears in the case G once the history term is incorporated.

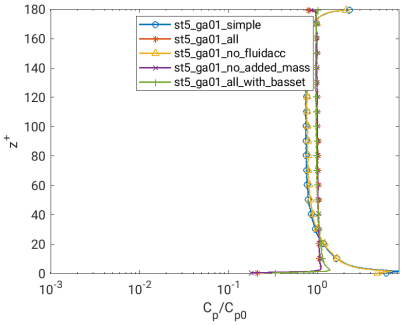

(a) Case G ($St = 5$, $Ga = 0.316$)

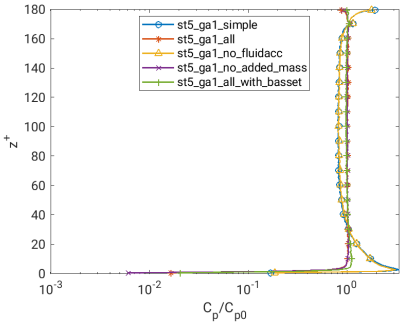

(b) Case H ($St = 5$, $Ga = 1$)

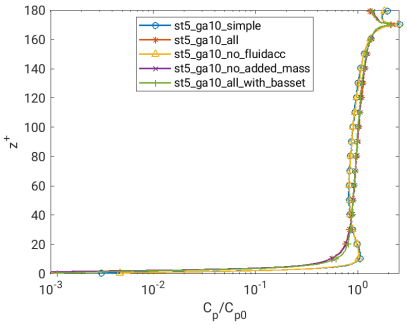

(c) Case I ($St = 5$, $Ga = 3.16$)

Figure 1: Mean particle concentration over the flow depth $C_\mathrm{p}(z)$, normalised by the bulk concentration C_p0. Different colours/symbols represent the modelled force combinations being included. In addition to buoyancy term, the following terms are included for: "simple", Stokes; "all", all terms except Basset history term; "no_fluidacc", "all" except fluid acceleration; "no_added_mass", "all" except added mass; "all_with_basset", "all" and Basset history

REFERENCES

[1], Kuerten, J.G.: Point-Particle DNS and LES of Particle-Laden Turbulent flow – a state-of-the-art review,*Flow, Turbul. Combust.*,**97**,689–713 (2016)

[2], Daitche, A.: On the role of the history force for inertial particles in turbulence,*J. Fluid Mech.*,**782**,567–593 (2015)

[3], Sakai, Y.,Manhart, M.: Direct numerical simulation of the distribution of floating microplastic particles in an open channel flow,*Appl. Res.*,**Feb.**,1–13 (2023)

[4], Williamson, J. H.: Low-storage Runge-Kutta schemes,*J. Comput. Phys.*,**35**,48–56 (1980)

[5], Chorin, A. J.: Numerical Solution of the Navier-Stokes Equation,*Math. Comput.*,**42**,490–507 (1968)

[6], Stone, H. L.: Multidimensional Partial Differential Equations, *SIAM J. Numer. Anal.*,**5**, 530–558 (1968)

[7], Clift, R., Grace, J. R., Weber, M. E.: *Bubbles, Drops, and Particles*, Mineola, New York: Dover, 2005

[8], van Hinsberg, M. A.T., ten Thije Boonkkamp, J. H.M., Clercx, H. J.H.: An efficient, second order method for the approximation of the Basset history force, *J. Comput. Phys.*,**230**, 1465–1478 (2011)

[9], De Lillo, F., Cencini, M., Musacchio, S., Boffetta, G.: Clustering and turbophoresis in a shear flow without walls, *Phys. Fluids*,**28**, (2016)

WORKSHOP
Direct and Large-Eddy Simulation 14
April 10-12 2024, Erlangen, Germany

SIMULATING THE SETTLING OF FINITE-SIZE PARTICLES IN A VERTICALLY NON-PERIODIC CONFIGURATION

Manuel Moriche [1], **Manuel García-Villalba** [1] **and Markus Uhlmann** [2]
[1] Institute of Fluid Mechanics and Heat Transfer ,TU Wien, Austria
[2] Karlsruhe Institute of Technology, Germany

INTRODUCTION

The settling of particles in a fluid is a process in which hydrodynamic forces and contact forces are coupled in a very complex fashion. These type of flows present a challenge for the scientific community, independently on the particular approach: experiments, theory or numerical simulations. However, direct numerical simulations have gained popularity in the last decades because of the establishment of non-conforming grid algorithms and the increased computational power available in supercomputing centers.

One of the main issues when simulating particles settling under gravity is that the vertical velocity of the particles is not known a-priori. Therefore, one must find a way to overcome the fact that particles could, eventually, leave the computational domain. One possible solution is to solve the governing equations on a grid which is moving at some predetermined translational velocity. This is typically used by the group of Dušek for single particles [1, 2] and can also implemented for many particles. However, we aim for an algorithm with which obtain a similar behavior as when using a non-inertial reference frame (track the particles), but using an algorithm based in an inertial reference frame. Therefore, we will restrict our discussion to algorithms in which the governing equations are solved in an inertial reference frame

When dealing with few particles, authors use different approaches to overcome the issue of keeping the particles inside the computational domain: some use very large computational domains [3] to accommodate the vertical displacement of the particle, and others use good estimations of the vertical velocity together with small adjustments of the problem parameters [1]. The former is hardly extendable to many particles because of the increased computational cost associated with an extra large domain. Regarding the latter, its main inconvenience is that it is heavily based on experience and lacks of a systematic approach. Furthermore, in both approaches the integration time is somehow constrained either by the finite size of the domain in the vertical direction or because small drifts can lead to large displacements for long time intervals.

If the number of particles in the problem is increased the above-mentioned techniques are not sufficient and the majority of the authors rely on a triply periodic configuration, where particles are always by definition inside the computational domain. This approach presents clear advantages, but there are also some inconveniences like the influence of periodic repetitions in the vertical direction (see the work of Kajishima [4] for a detail analysis of this issue in the case of a single particle). The influence of periodic repetitions is aggravated when

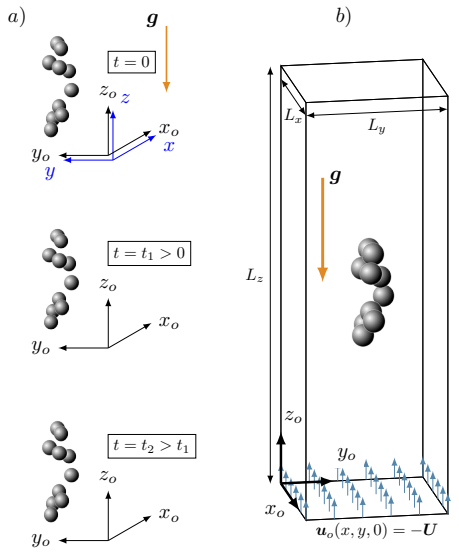

Figure 1: a) Sketch of the problem with the global (x,y,z) and observer (x_o, y_o, z_o) reference frames. b) Computational setup.

particles form clusters, whose size is typically very large and can fill, in the context finite-size direct numerical simulations, the entire domain. As a result, the solution is strongly correlated and we cannot, for example, analyze cluster dynamics once these are of the size of the computational domain.

In the talk we present an algorithm to track the particles by an iterative update of the configuration when solving the governing equations in an inertial reference frame. We believe that the proposed algorithm would be beneficial for the scientific community to solve problems with moving particles, without having to modify their already working implementations.

METHODOLOGY

We consider the settling of a set of particles under the action of gravity in an unbounded domain. The flow is assumed to be incompressible and the fluid Newtonian with density ρ_f and kinematic viscosity ν. Each particle is a rigid sphere of uniform density ρ_p with diameter D. The algorithm uses two inertial reference frames which we refer as global and observer, respectively. The global reference frame is defined as

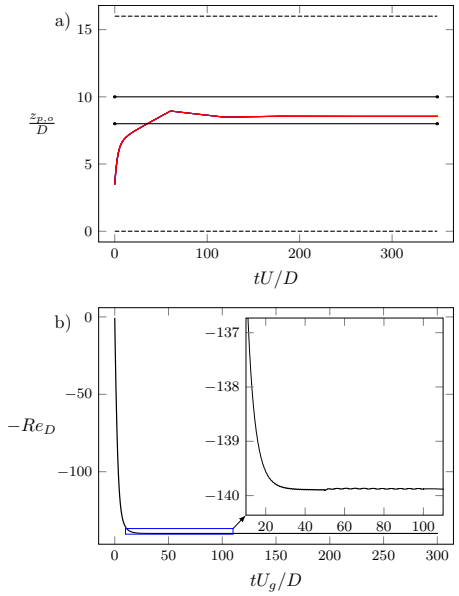

Figure 2: Time history of a) the vertical position of the particle in the observer reference frame versus the time scaled with the observer velocity U and b) the particle Reynolds number versus the time scaled with the gravity-scaled velocity U_g, for a single particle with $\tilde{\rho} = 1.5$ and $Ga = 121$.

the frame in which the fluid velocity is zero in the absence of particles and its vertical axis, z, is given by the unit vector $\boldsymbol{e}_z = -\boldsymbol{g}/g$, where $g = |\boldsymbol{g}|$ is the magnitude of the gravitational acceleration vector $\boldsymbol{g}$ (see Figure 1a). The observer reference frame is aligned with the global reference frame, but translates with a velocity $\boldsymbol{U} = -U\boldsymbol{e}_z$ with respect to it. We then proceed to solve the Navier-Stokes equations for the flow and the Newton-Euler equations for the particles in the observer reference frame (see Figure 1b). The success of the algorithm can be summarized in finding a very good approximation the time-averaged mean settling velocity of the particles $\langle w_p \rangle_{pt}$. Making $U = \|\langle w_p \rangle_{pt}\|$ will allow for very long time intervals. In the talk we will discuss the details of the method.

RESULTS

As a validation case we first analyze the settling of a single sphere with density ratio between the particle and the fluid $\tilde{\rho} = \rho_p/\rho_f = 1.5$ at a Galileo number $Ga = U_g D/\nu = 121$ inspired by the work of Uhlmann & Doychev [1], where $U_g = \sqrt{(\tilde{\rho} - 1)\, gD}$ is a gravitationally-scaled velocity. We release the particle from rest and thanks to the proposed algorithm we track the evolution of the particle incurring in minimum errors (to be discussed in the talk). This case shows a vertical steady regime fully characterized by the particle Reynolds number $Re_D = -w_p D/\nu$, where w_p is the settling velocity of the particle in the global reference frame. The vertical position of the particle in the observer reference frame, $z_{p,o}$, is shown together with Re_D in Figure 2.

As a proof of the success of the algorithm we also show results for a case with with 1791 particles in a computational domain of $[42.7 \times 42.7 \times 128]D^3$ in which particles the same density ratio ($\tilde{\rho} = 1.5$), but the Galileo number $Ga = 178$ is such that a single particle follows a steady-oblique path and many particles do form clusters in a triply periodic configuration [5]. Figure 3 shows one snapshot of the initial condition (particles uniformly distributed with a horizontally-averaged solid volume fraction of $\langle \phi \rangle_{xy} = 5 \cdot 10^{-3}$ along a length of approximately $100D$), and a final state where it can be seen that the particle distribution clearly differs from the initial solution.

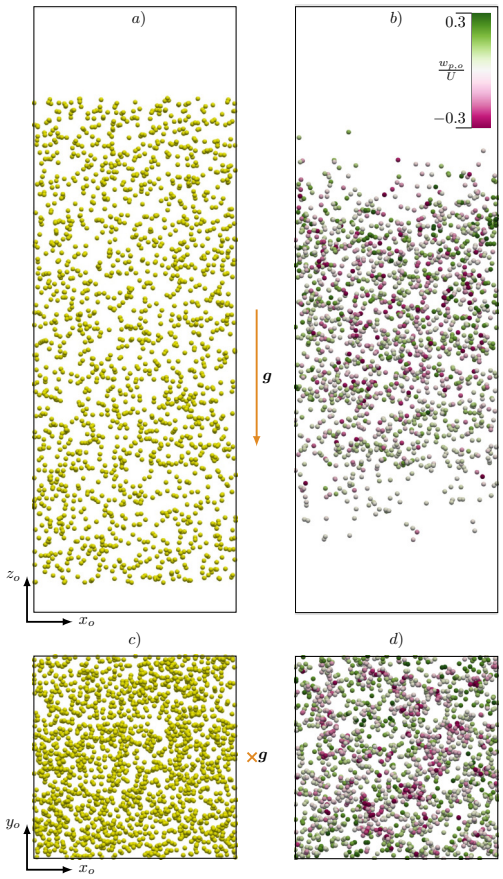

Figure 3: a) Initial and b) final state of a many-particles simulation with $\tilde{\rho} = 1.5$, $Ga = 178$ and an initial uniform particle distribution of $\langle \phi \rangle_{xy} = 5{\cdot}10^{-3}$. In b) the particles are coloured by their settling velocity in the observer's reference frame.

REFERENCES

[1] M. Uhlmann and J. Dušek, "The motion of a single heavy sphere in ambient fluid: a benchmark for interface–resolved particulate flow simulations with significant relative velocities," *Intl. J. Multiphase Flow*, vol. 59, pp. 221 – 243, 2014.

[2] W. Zhou, M. Chrust, and J. Dušek, "Path instabilities of oblate spheroids," *J. Fluid Mech.*, vol. 833, p. 445–468, 2017.

[3] M. N. Ardekani, P. Costa, W. P. Breugem, and L. Brandt, "Numerical study of the sedimentation of spheroidal particles," *Intl. J. Multiph. Flow*, vol. 87, pp. 16 – 34, 2016.

[4] T. Kajishima and S. Takiguchi, "Interaction between particle clusters and particle–induced turbulence," *Int. J. Heat Fluid Fl.*, vol. 23, no. 5, pp. 639 – 646, 2002.

[5] M. Uhlmann and T. Doychev, "Sedimentation of a dilute suspension of rigid spheres at intermediate Galileo numbers: the effect of clustering upon the particle motion," *J. Fluid Mech.*, vol. 752, p. 310–348, 2014.

SESSION: Hybrid LES/RANS

Friday, April 12, 2024

13:30- 14:30

WORKSHOP
Direct and Large-Eddy Simulation 14
April 10-12 2024, Erlangen, Germany

ANISOTROPIC MESH REFINEMENT IN AUTOMOTIVE FLOW AND HYBRID RANS-LES MODELS

E. Guilmineau[1]
[1]LHEEA, CNRS UMR 6598
Centrale Nantes, France
emmanuel.guilmineau@ec-nantes.fr

INTRODUCTION

A prediction of aerodynamic coefficients on road vehicles is crucial for an efficient design and optimization process. One critical aspect of CFD modeling is the selection of turbulence models, which play a important role in accurately capturing the complex flow phenomena around vehicles. The objective of the Automotive CFD Prediction Workshop is to assess the predictive capability of CFD codes for road-cars geometries. The third edition of this workshop held at Barcelona in 2022 and two test-cases were studied: the Windsor body at yaw and the notchback version of the DrivAer.

For this workshop, several meshes were generated by the organizing committee. But the solution was not mesh-converged, despite the fine mesh generated, 197 million cells. One solution may be to use automatic grid refinement and vary its parameters to converge into a mesh. Automatic grid refinement algorithms dynamically adapt the mesh based on the local flow conditions, concentrating computational resources where they are most needed. This adaptive approach allows for a more accurate representation of critical flow features without unnecessarily refining regions where the flow is relatively simple.

TEST CASE

In this paper, the so-called Windsor is considered, see Figure 1. This model preserves the dimensions and aspect ratio of the Ahmed body but also presents a slanted front-end that is more representative of passenger cars. The model is 1.04425 m in length (L), 0.288 m in height (H) and 0.290 m in width (W), supported by four cylindrical struts of 50 mm in diameter. The ground clearance (G) is 0.050 m. The frontal area is rounded to be 0.112 m^2. The reference length used for pitching moment is the wheelbase 0.6375 m. The model has its origin on the ground plane, in the symmetry plane midway between the feet. The coordinate system has X in the streamwise direction, Z upwards and hence positive Y is towards the right of the model. The model is yawed by -2.5 degrees around the Z-axis. The forces and moments are in the coordinate system of the yawed model. The inlet velocity condition is $U_\infty = 40$ m/s which corresponds to a Reynolds number, based on the vehicle length, of 2.9×10^6. Measurements were taken at the Loughborough University wind tunnel by Varney [1].

FLOW SOLVER

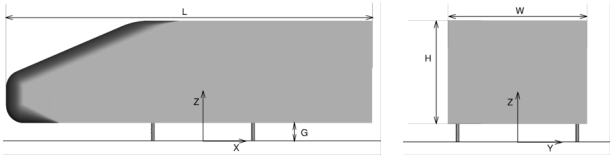

Figure 1: Windsor model squareback.

The in-house solver ISIS-CFD developed by CNRS and Centrale Nantes, also available as a part of the FINE™/Marine computing suite worldwide distributed by Cadence Design Systems, is an incompressible multiphase unsteady Reynolds-averaged Navier-Stokes (URANS) solver mainly devoted to marine hydrodynamics. It is based on a fully-unstructured (face-based) finite volume discretization with specific functionalities needed for multiphase flows [2, 3].

The method features several sophisticated turbulence models: apart from the classical two-equation k-ϵ and k-ω models, the anisotropic two-equation Explicit Algebraic Reynolds Stress Model (EARSM), as well as Reynolds Stress Transport Models (RSTM), are available [4, 5]. Hybrid RANS/LES turbulence models based on Detached Eddy Simulation (DES-SST, DDES-SST, IDDES-SST) are also implemented and have been thoroughly validated on automotive flows characterized by large separations [6] and ships at steady drift [7]. All models are available with wall-function or low-Reynolds near wall formulations.

Moreover, the solver accepts sliding and overset grids and features an anisotropic adaptive grid refinement functionality [8, 9] applied to unstructured hexahedral meshes. The automatic grid refinement performs by local division of meshes. The decision where to refine is based on a metric refinement criterion, a tensor field computed from the flow. The tensor is based on second derivatives of the flow variables. The refinement criterion is the flux-component Hessian. The grid is refined until the dimension of each cell satisfy the threshold Tr.

NUMERICAL SIMULATION SET-UP

The computational domains extends from X = -5 m to X = +6 m. The model nose is located at X = -0.56 m and the base at X = +0.48 m. The width and height of the domain matches the wind tunnel for which the cross section is 1.92 m wide × 1.32 height.

In this paper, two types of mesh are used. The first mesh is

generated by the organizers of the workshop AutoCFD 3 using the trimmer mesh and prism layer approach from Simcenter STAR-CCM+. Three grids are created: baseline g2, coarse g1 and fine g3. All three meshes have the same wall normal grid spacing and prism layer thickness and vary the number of cells by adjusting all other cell dimensions consistently. The second mesh is generated by using Fidelity™. This mesh is similar to the coarse mesh proposed by the organizers of the workshop. Then the automatic grid refinement is used from this mesh. To obtain several meshes, the value of the threshold Tr is modified which is in the range $Tr \in$ [0.4L, 0.025L] for coarse to fine grids.

RESULTS

Figure 2 shows convergence of the aerodynamic coefficients, drag coefficient see Figure 2a and lift coefficient see Figure 2b, for both sets of meshes. The characteristic mesh size is computed as h = $N^{-1/3}$, where N is the number of cells. A first observation is that all simulations underestimate the coefficient obtained in the experiments. These results are consistent with those presented during the workshop using the same turbulence models. A second observation is the converged solution for the aerodynamic coefficient depends on the turbulence model. With the k-ω SST turbulence model, both mesh types converge to the same solution. However, the solution obtained with automatic mesh refinement converges much faster. The difference in drag between the two final solutions is 0.8%. However, only 15.1 million cells, mesh $Tr = 0.1$L, are used with the adapted mesh instead of the 197.5 million cells, mesh g3, of the committee mesh. With the DDES-SST and IDDES-SST models, the solution is not yet converged with the committee meshes while using the automatic grid refinement, the solution converges towards a mesh with 24.7 million cells for the DDES-SST and 27.8 million cells for the IDDES-SST, mesh $Tr = 0.2L$. The use of automatic mesh refinement allows to converge faster in mesh.

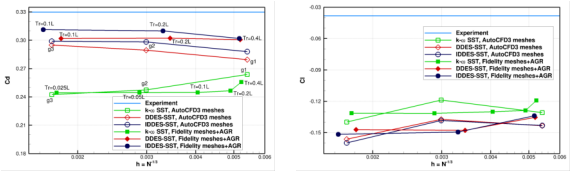

(a) Cd (b) Cl

Figure 2: Grid convergence of aerodynamic coefficients.

Figure 3 presents a comparison of the base pressure coefficient, Cp. For a given turbulence model, the solution is mesh-independent. The flow predicted with the k-ω SST turbulence model is not in agreement with the experiments. The shape of the RANS contours is different from the experiment and it is indicative of a toroidal vortex structure in the wake. With the hybrid RANS/LES models, the base pressure is in agreement with the experiment. However, the Cp level on the leeward side is overestimated.

REFERENCES

[1]Varney, M. : Base drag reduction for squareback road vehicle, *PhD thesis, Loughborough University* (2020).

[2]Leroyer, A. and Visonneau, M. : Numerical methods for RANSE simulations of a self-propelled fish-like body, *Journal of Fluids and Structures*, **20**, 975–991 (2005).

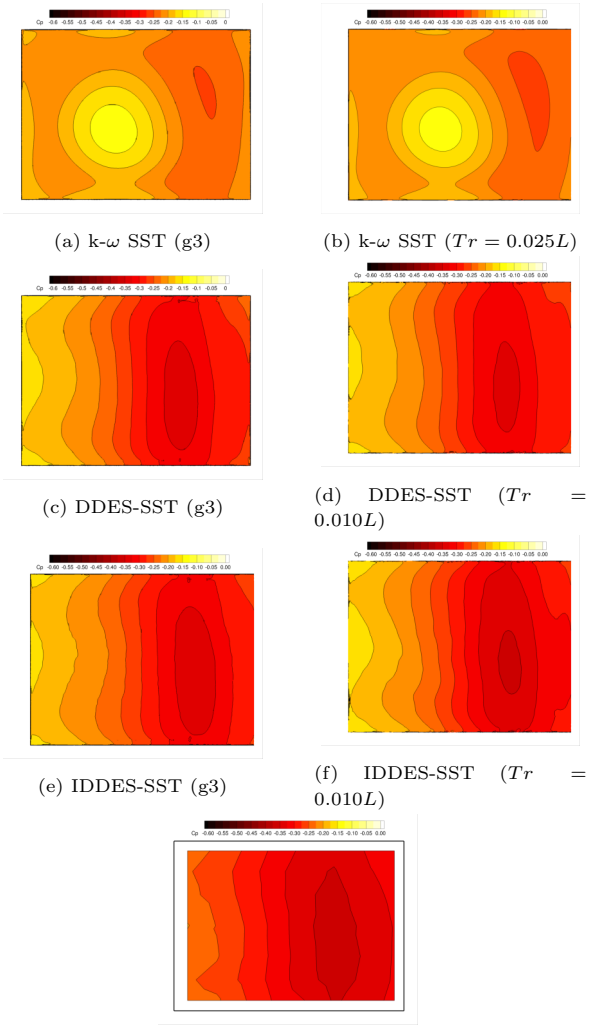

(a) k-ω SST (g3) (b) k-ω SST ($Tr = 0.025L$)

(c) DDES-SST (g3) (d) DDES-SST ($Tr = 0.010L$)

(e) IDDES-SST (g3) (f) IDDES-SST ($Tr = 0.010L$)

(g) Experiment

Figure 3: Base pressure coefficient.

[3]Queutey, P. and Visonneau, M. : An Interface Capturing Method for Free-Surface Hydrodynamic Flows, *Computers & Fluids*, **36**, 1481–1510 (2007).

[4]Deng, G.B. and Visonneau, M. Comparison of explicit algebraic stress models and second-order turbulence closures for steady flow around ships, *Proc. of 7th Symposium on Numerical Ship Hydrodynamics, July, Nantes, France*, (1999).

[5]Cecora, R.-D., Radespiel, R., Eisfeld, B. and Probst, A. : Differential Reynolds-Stress Modeling for Aeronautics, *AIAA Journal*, **53**(3), 48–65 (2015).

[6]Guilmineau, E. Deng, G.B., Leroyer, A., Queutey, P., Visonneau, M. and Wackers, J. : Assessment of hybrid RANS-LES formulations for flow simulation around the Ahmed body, *Computers & Fluids*, **178**, 302–319 (2018).

[7]Visonneau, M., Guilmineau, E. and Rubino, G. : Local flow around a surface combatant at various static drift conditions: The role played by turbulence closures, *Proc. of 33rd Symposium on Naval Hydrodynamics, Osaka, Japan*, (2020).

[8]Wackers, J., Deng, G.B., Guilmineau, E., Leroyer, A., Queutey, P., Visonneau, M. and Liverani, A. : Can adaptive grid produce grid-independent solutions for incompressible flows?, *Journal of Computational Physics*, **244**, 364–380 (2017).

[9]Mozaffari, S., Guilmineau, E., Visonneau, M. and Wackers, J. : Average-based mesh adaptation for hybrid RANS/LES simulation of complex flows, *Computers & Fluids*, **232**, 105202 (2022).

WORKSHOP
Direct and Large-Eddy Simulation 14
April 10-12 2024, Erlangen, Germany

A METHOD FOR ZONAL HYBRID RANS-LES SIMULATIONS IN MULTI-STAGE TURBOMACHINERY APPLICATIONS

J. Buchmeier[1], **C. Morsbach**[2]
[1]Department of Virtual Engine and Numerical Methods, Institute of Test and Simulation for Gas Turbines
[2]Department of Numerical Methods, Institute of Propulsion Technology
[1,2]German Aerospace Center
jonas.buchmeier@dlr.de

INTRODUCTION

Despite growing computational resources, large eddy simulations (LES) as a tool to conduct aerodynamic assessments of turbomachinery blade profiles at relevant Reynolds numbers are often limited to single-row, single-passage simulations, especially if end walls are present [1]. A pure LES of a blade row passage requires boundary conditions of either numerical or experimental origin which closely match the physical conditions present in the surroundings of the blade. Due to the inherently unsteady nature of multi-stage turbomachinery applications, those conditions are time-dependent, which complicates the assessment of the blade profile in a multi-stage context.

In fact, steady simulations are still widely used in industrial contexts for design processes of multi-stage configurations. The mixing plane approach [2], which couples adjacent blade rows by exchanging circumferentially averaged radial profiles, is a well established method to obtain a steady, single-passage solution in each blade row. However, the usage of the mixing plane method can be extended to provide interface conditions for a LES domain of a blade row embedded in Reynolds averaged Navier–Stokes (RANS) blade row domains. A method for this two-way axial coupling of RANS and LES domains in turbomachinery via a mixing plane approach is presented in this paper.

The presented method of embedded LES is seen as an alternative to pure LES of a single blade with prescribed, steady inlet and outlet boundary conditions and as a step towards scale-resolving multi-stage investigations. The method aims to overcome predictive deficits of multi-stage RANS simulations and to provide in depth flow physics insights of the blade profile of interest by utilizing LES capabilities while keeping the computational cost manageable.

NUMERICAL METHODOLOGY

The presented zonal hybrid RANS-LES simulations are conducted by utilizing the multi-block structure of DLR's turbomachinery flow solver TRACE. This structure allows to solve either the RANS or LES governing equations in a specified block group. For both approaches, a second order accurate finite volume (FV) discretization method is used, where Roe's numerical flux is added to the central flux by a fraction of $\phi = 10^-3$. In unsteady block groups time integration is achieved by deploying an implicit Runge-Kutta method of second order accuracy.

Following the mixing plane approach, the sub-domains are coupled by exchanging radial profiles. While instantaneous profiles of the steady RANS mixing plane sides are exchanged, an exponential moving average (EMA) technique is applied to the profiles obtained at the LES sides of mixing planes. The smoothing factor of the temporal EMA is defined in each radial band of the mixing plane and based on a band-wise time scale $\alpha\Delta/\sqrt{k_m}$, where α is a user-provided pre-factor, Δ is the grid size characteristic for the band and k_m the mean kinetic energy of the band.

In addition to the flow state and direction, the turbulence state is required at inlet boundaries of the multi-domain method. In particular, the necessary input information to the synthetic turbulence generator (STG) [3] deployed at the inlet of the LES need to be obtained from the upstream RANS domain. Depending on the type of turbulence model used in the upstream RANS domain, the required radial profiles of Reynolds stresses are either inputted directly from the RANS mixing plane side into the STG or are assumed to be isotropic and reconstructed from the turbulent kinetic energy k (TKE) modeled on the RANS side. Required as additional STG input, the turbulent length scale is computed as $l_t = k^{1/2}/(C_\mu\omega)$, where $C_\mu = 0.09$ and ω is the turbulent dissipation rate of the RANS model. While radial profiles are exchanged at every time step, the input to the STG is updated in user-defined intervals by averages of the radial profiles within the time step interval. To avoid spurious waves originating from the STG, the bulk state is kept constant throughout the simulation. To complete the RANS to LES interface, radial profiles of the static pressure are prescribed to the upstream RANS side by the LES side.

The mean flow state required at an downstream RANS side of a zonal interface is obtained by circumferentially averaging and applying the temporal EMA technique to the upstream LES side of the mixing plane interface. The required boundary values for the RANS turbulence model are reconstructed from the LES by using the resolved TKE or Reynolds stresses and the mean strain rate tensor [4]. Instantaneous radial profiles from the RANS side are used to set an outflow boundary condition on the LES side.

VALIDATION VIA TURBULENT CHANNEL FLOW

The proposed zonal coupling method is validated by sim-

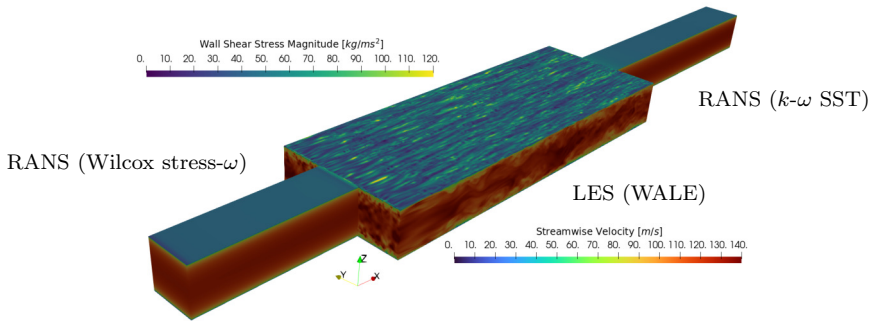

Figure 1: Instantaneous flow field of a LES domain embedded in an upstream and downstream RANS domain of a turbulent channel. The domains exhibit varying spanwise extent (pitch) and are 2-way coupled via mixing planes at the zonal interfaces.

ulating fully developed turbulent flow of $Re_\tau = u_\tau \delta/\nu = 590$ in a plane channel, where $u_\tau = \sqrt{\tau_w/\rho}$ is the friction velocity with τ_w as the wall shear stress and δ is the channel half-height. The domain is split into an upstream RANS zone deploying the Wilcox's stress-ω full Reynolds stress model, a middle section simulated in explicit LES using the WALE SGS model and a downstream RANS region, where the k-ω SST model is used, as shwon in Fig. 1. Comparisons with DNS results in Fig. 2(b) indicate a development length of the resolved and modeled TKE behind the RANS to LES and LES to RANS interface. The overestimation of the TKE peak in the LES zone can be attributed to overestimating the streamwise normal Reynolds stress [5].

PLANNED APPLICATION TO A 1,5-STAGE TURBINE

For the final paper of the DLES 14 workshop, an application of the zonal method to the 1.5-stage Aachen turbine [7] is planned. While the stators in rows 1 and 3 will be simulated as RANS domains, an LES with an STG applied in the rotational reference frame will be used for the rotor in row 2.

REFERENCES

[1]Morsbach, C., Bergmann, M., Tosun, A., Klose, B. F., Kügeler, E. and Franke, M.: Large eddy simulation of a low-pressure turbine cascade with turbulent end wall boundary layers, *Flow Turbulence Combust*, (2023).

[2]Denton, J.D. and Singh, U.K.: Time marching methods for turbomachinery flow calculation, *In Von Karman Inst. for Fluid Dyn. Appl. of Numerical Methods to Flow Calculations in Turbomachines 47 p (SEE N80-12365 03-34)* (1979)

[3]Shur, M. L. and Spalart, P. R. and Strelets, M. K. and Travin, A. K.: Synthetic turbulence generators for RANS-LES interfaces in zonal simulations of aerodynamic and aeroacoustic problems, *Flow, turbulence and combustion*, **93**, 63–92 (2014)

[4]König, D. and Meinke, M. and Schröder, W.: Embedded LES-to-RANS boundary in zonal simulations, *J. of Turb., nr. 11* (2010)

[5]Matha, M. and Morsbach, C. and Bergmann, M.: A comparison of methods for introducing synthetic turbulence, ECCOMAS–ECFD 2018-6th European Conference on Computational Mechanics (Solids, Structures and Coupled Problems)/7th European Conference on Computational Fluid Dynamics (2018)

[6]Moser, R. D. and Kim, J. and Mansour, N. N.: Direct numerical simulation of turbulent channel flow up to Re τ= 590, *Physics of fluids*, **vol. 11 nr. 4**, 943–945 (1999)

[7]Restemeier, M. and Jeschke, P. and Guendogdu, Y. and Gier, J.: Numerical and experimental analysis of the effect of variable blade row spacing in a subsonic axial turbine, *Journal of turbomachinery, vol. 135, nr. 2* 21–31 (2013)

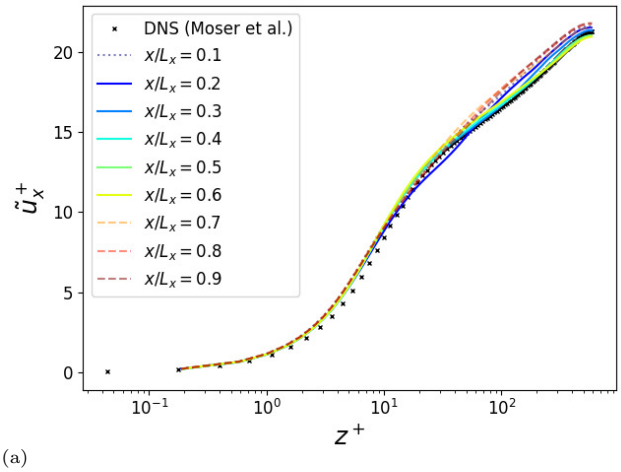

(a)

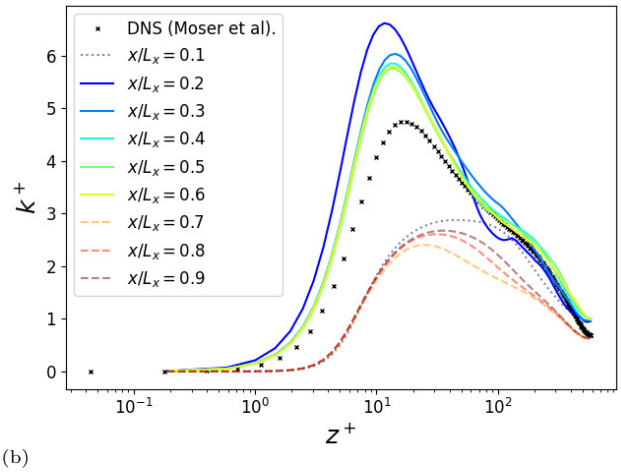

(b)

Figure 2: Profiles of streamwise velocity (a) and turbulent kinetic energy (b) at various downstream positions of the channel. Dotted lines indicate profiles in the upstream RANS zone, solid lines LES profiles and dashed lines profiles of the downstream RANS region.

WORKSHOP
Direct and Large-Eddy Simulation 14
April 10-12 2024, Erlangen, Germany

HYBRID HIGH-ORDER METHODS WITH TURBULENCE MODELLING CAPABILITIES

Lorenzo Botti[1], **Francesco Carlo Massa**[1]
[1]Dipartimento di Ingegneria e Scienze Applicate (DISA)
Universitá degli Studi di Bergamo, Dalmine, Italy
francescocarlo.massa@unibg.it

INTRODUCTION

Recently, the development of CFD solvers featuring high-fidelity turbulence modeling capabilities has focused on the reliable reproduction of the prominent physical phenomena and on the mimicking of relevant properties of the continuous problem at the discrete level. In incompressible flow computations, for example, one of the most sought-after features is the *preservation of kinetic energy*, pursued in the sense that the discretization of the convective term should be guaranteed not to alter the balance of kinetic energy in the case of passive boundary conditions. Indeed, wavenumber Fourier analysis of the Navier Stokes equations shows that the convective term causes redistribution of kinetic energy among different wavenumber modes, without being dissipative. Similarly, the key property that a modification of the irrotational part of body forces only affects the pressure, leaving the velocity field unaltered, has been demonstrated to be closely linked to the discretization of the divergence free constraint. Contextually, an estimate of the velocity independent of both the pressure and the viscosity can be attained.

From the numerical formulation viewpoint, the development of Hybrid High-Order (HHO) and Hybridizable Discontinuous Galerkin methods (HDG) has provided a new ground to pursue the development of high-fidelity computational modelling tools for turbulent flows. As opposite to DG, which solely employs broken polynomials on the mesh, HHO and HDG methods are based on degrees of freedom that are broken polynomials on the mesh and on its skeleton. Hybrid formulations allow to reproduce key continuous properties at the discrete level by introducing physics dependent local reconstructions of discrete operators. Relevant features are 1) local (element-by-element) conservation of physical quantities, 2) increased convergence rates thanks to higher-order stabilization terms penalizing face residuals, 3) robustness with mesh distortion and grading 4) reduced memory footprint of Jacobian matrix operators as compared with DG.

The latter feature is of crucial practical importance in the context of implicit time integration strategies. Since the face based stencil of HHO and HDG consist of all mesh faces belonging to the boundary of the two elements sharing the face, elemental degrees of freedom can be eliminated by computing the Schur complement. As a result, Jacobian matrices are sparse block matrices whose block size is driven by the dimension of polynomial spaces in $d-1$ variables when considering a d-dimensional flow problem. Accordingly, when accuracy is improved by means of higher-degree p-type expansions, the number of Jacobian matrix non-zero entries grows slower than DG methods, thereby reducing the computational cost associated to matrix-vector products as well as matrices memory footprint.

Among the two Hybrid High-Order formulations of the incompressible Navier-Stokes equation we recently proposed in [1] the, so-called, `HHO-Hdiv` formulation is kinetic energy preserving and pressure-robust but fails in the inviscid limit, and the, so-called, `HHO-HLL` formulation is able to cope with the incompressible Euler equations but is based on a inherently dissipative Godunov flux for pressure-velocity coupling. In this work we propose to further improve the aforementioned HHO discretizations with the goal of devising a numerical scheme that is capable of dealing with high-Reynolds turbulent flows and provides trustworthy reproduction of the phenomena involved in the energy cascade. In particular, we plan to replace the Harten, Lax and van Leer (HLL) approximated Riemann solver of `HHO-HLL` with an exact Riemann solver for the artificial compressibility perturbation of the Euler equations devised by Bassi, Massa, Botti and Colombo [2]. Based on the experience with Godonuv fluxes in the context of DG methods, we ought to further reduce dissipation without compromising robustness in the inviscid limit. Alongside, we also plan to investigate the lack of robustness of `HHO-Hdiv` in the inviscid limit, the scheme is based on the non-dissipative skew-symmetric convective term formulation introduced by Botti, Di Pietro and Droniou in [3] and the pressure-velocity coupling proposed by Rhebergen and Wells in [4].

REFERENCES

[1]L. Botti, F. C. Massa: HHO Methods for the Incompressible Navier-Stokes and the Incompressible Euler Equations, *Journal of Scientific Computing 92, 28 (2022)*, 10.1007/s10915-022-01864-1.

[2]F. Bassi, F. C. Massa L. Botti, A. Colombo: Artificial compressibility Godunov fluxes for variable density incompressible flows, *Computers & Fluids, 169 (2018)*, 10.1016/j.compfluid.2017.09.010.

[3]L. Botti, D. A. Di Pietro, J. Droniou: A Hybrid High-Order method for the incompressible Navier–Stokes equations based on Temam's device. *Journal of Computational Physics 376, 786–816 (2019)*, /10.1016/j.jcp.2018.10.014.

[4]S. Rhebergen, G. N. Wells: A Hybridizable Discontinuous Galerkin method for the Navier-Stokes equations with pointwise divergence-free velocity field. *J. Sci. Comput. 76(3), 1484–1501 (2018)*, 10.1007/s10915-018-0671-4.

WORKSHOP
Direct and Large-Eddy Simulation 14
April 10-12 2024, Erlangen, Germany

A PRIORI VALIDATION OF A GENERALIZED WALL STRESS FUNCTION WITH THE FLOW OVER A PERIODIC HILL

K. Xue[1,2], D. Quosdorf[2], L. Zhao[1], M. Manhart[2]
[1]School of Aerospace Engineering
Beijing Institute of Technology (BIT), P. R. China
[2]Professorship of Hydromechanics
Technical University of Munich(TUM), Germany
michael.manhart@tum.de

INTRODUCTION

Equilibrium wall functions are widely used in wall-modelled large eddy simulation (LES) due to its simplicity and low computational cost. Unfortunately, equilibrium models have problems to predict wall shear stress distributions for complex flows with pressure gradients, acceleration, deceleration or separation of the flow. To take non-equilibrium effect into account, Stratford [1] suggested that the velocity profile near the wall must be described by both the wall shear stress velocity scaling $u_\tau = \sqrt{|\tau_w|/\rho}$ and the pressure gradient velocity scaling $u_p = (\frac{\nu}{\rho}|\frac{\partial P_w}{\partial x}|)^{\frac{1}{3}}$, where ρ is the density of flow, P_w is the wall pressure and ν is the kinematic viscosity. Manhart et al. [2] proposed a model for the viscous sublayer that takes both contributions into account. Later Duprat et al. [3] extended this model and made it applicable to the inertial layer. Shih [4] on the other hand proposed to express the velocity profile as the superposition of the asymptotic solutions for zero pressure gradient and zero wall stress boundary layers, respectively, which are based on Tennekes and Lumley [5].

In the present study, we revisit the model of Shih [4] and test it in an a priori way along the windward side of a hill at which a strong acceleration of the flow leads to large wall shear stresses. We evaluate how well the velocity profiles of Shih's model fit with the experimental data obtained by PIV measurements [6] along the windward side of the hill at $Re_h = 10.595$.

METHODOLOGY

By matching the wall functions of the viscous, buffer, and inertial layers, the simplest dimensionless forms at zero pressure gradient and zero wall stress were suggested by Spalding [7] and Shih [4], respectively:

$$Y_\tau^+ = U_1^+ + \exp(-\kappa C)\left[\exp\left(\kappa U_1^+\right) - 1 - \kappa U_1^+ - \frac{1}{2}\left(\kappa U_1^+\right)^2 - \frac{1}{6}\left(\kappa U_1^+\right)^3\right] \quad (1)$$

and

$$\left(Y_p^+\right)^2 = U_2^+ + \exp(-2\alpha/\beta)\left[\exp\left(U_2^+/\alpha\right) - 1 - U_2^+/\alpha\right] \quad (2)$$

Here, U_1^+ depends solely on the wall stress τ_w/ρ, and U_2^+ is associated with the pressure gradient. Since the profile of the total velocity U varies with the ratio of the pressure gradient velocity u_p to the wall stress velocity u_τ, the proportionality coefficient λ is first defined as follows:

$$\lambda = -\frac{\boldsymbol{U_t}\cdot\partial P_w/\partial s_w}{|\boldsymbol{U_t}\cdot\partial P_w/\partial s_w|}\frac{u_p}{u_\tau} \quad (3)$$

For a favourable pressure gradient the sign of λ is positive and for an adverse pressure gradient it is negative. By substituting ${Y_p}^+ = \lambda {Y_\tau}^+$ into Eq. (2) the velocity ${U_2}^+$ can be determined. Then we can obtain the dimensionless velocity U^+ as:

$$U^+ = \frac{U}{u_\tau} = {U_1}^+ - \lambda {U_2}^+ \quad (4)$$

The profiles of U^+ over Y_τ^+ under the influence of favorable pressure gradients are plotted in Fig. 1 for $\alpha = 5$ and $\beta = 8$ which are the asymptotic profile parameters for high Reynolds number zero wall stress profiles [5]. Compared to the zero pressure gradient law of the wall, the velocity profiles are shifted upwards by an adverse and downwards by a favourable pressure gradient. Under favourable pressure gradient conditions, the velocity profile develops an undulation with a local maximum and a subsequent minimum in the buffer layer. As for the effect of adverse pressure gradients, the profiles of U^+ over Y_τ^+ are shifted upwards, which will be shown in the presentation.

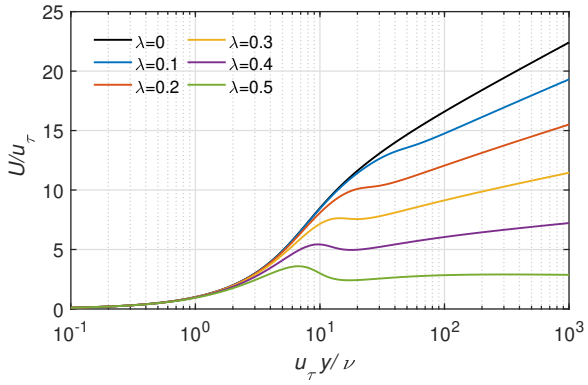

Figure 1: Effect of both favorable pressure gradients on the near wall flow ($\alpha = 5$, $\beta = 8$).

A priori validation with flow over periodic hill

Experimental velocity data around the windward side of the hill at $Re = 10595$ (Quosdorf et al. [6]) are used to evaluate the wall function in an a priori way. In Fig. 2 we compare velocity profiles of U_2 scaled in terms of u_p to Eq. 2. From the figure, we can conclude that the profile of the velocity U_2 does follow a logarithmic law when $u_p y/\nu$ is greater than a certain value. However, compared to the profile of Eq. 2 with $\beta = 8$, the slope of the experimental curve in the logarithmic region is the same, but shifted downwards. If the constant β is reduced to 3, it would fit the experimental data more accurately.

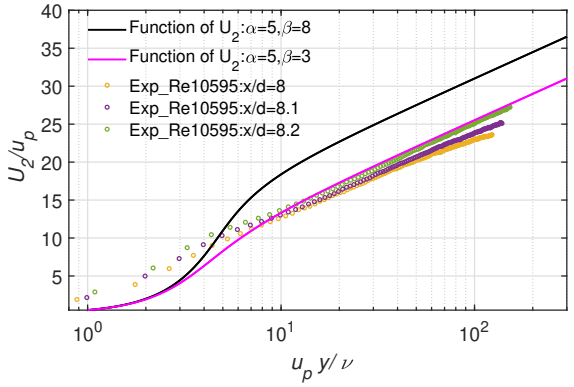

Figure 2: Profile of $U_2{}^+$ with $Y_p{}^+$, $Re = 10595$, $x/h = 8.0, 8.1, 8.2$.

Next, the profiles of the dimensionless velocity U/u_τ obtained from experimental data [6] over $u_\tau y/\nu$ at several positions around the windward side of the hill are presented. Since Fig. 1 has already shown that the total velocity profile varies with different ratios of λ, the distribution of λ along the lower wall needs to be clarified first. In Fig. 3, we calculated the distribution of λ along the lower wall using the wall shear stress and pressure obtained from a wall-resolved LES results (the simulation will be introduced in the presentation) of the present work. It is evident that the value of λ remains relatively constant around 0.4 within the range $7.8 < x/h < 8.6$.

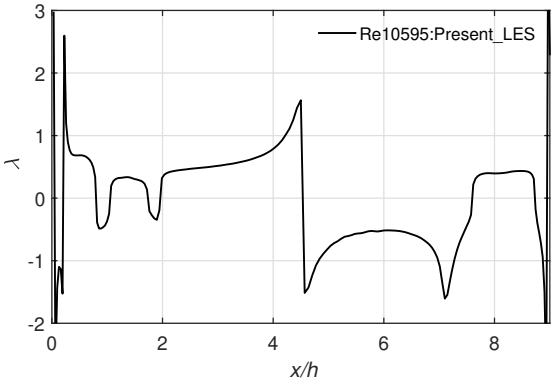

Figure 3: Distribution of λ along the lower wall

Wall normal profiles of U/u_τ with $u_\tau y/\nu$ obtained from the experiment [6] at $x/h = 8.0$, $x/h = 8.1$ and $x/h = 8.2$ are presented in Fig. 4. The wall function of zero pressure gradient as well as the original and modified wall functions at $\lambda = 0.4$ and $\lambda = 0.45$ are also depicted in the same figure. The measured velocity profiles deviate strongly from the zero pressure gradient law of the wall, indicating a strong effect of the pressure gradient. The original function ($\beta = 8$) overestimates the impact of the pressure gradient, whereas the modified function ($\beta = 3$) aligns well with the experimental data.

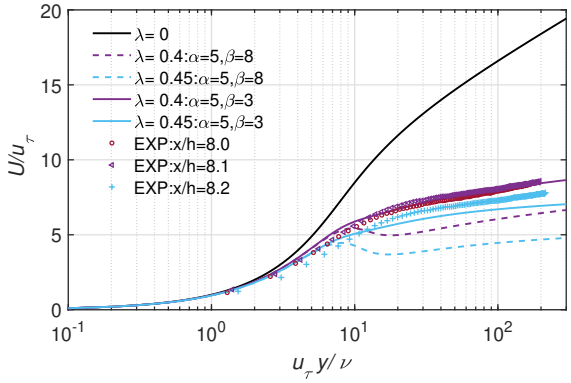

Figure 4: Profile of U^+ with $Y_\tau{}^+$, $Re = 10595$, $x/h = 8.0$, $x/h = 8.1$ and $x/h = 8.2$.

This evaluation demonstrates that in the situation considered, the functional form of the model is able to represent the velocity profiles which are strongly influenced by the favourable pressure gradient. And it was confirmed in subsequent simulations. However, it is necessary to adapt the constants to the particular flow situation to avoid undulations in the modelled profiles and to adapt the constant in the logarithmic part of the "pressure gradient" profile U_2. In the presentation, we will have a deeper dive into other positions and a higher Reynolds number $Re_h = 37.000$.

ACKNOWLEDGEMENTS

This work has been carried out with the support of China Scholarship Council (202006030033). Computing time for the project was granted by the Leibniz Supercomputing Centre on its Linux Cluster.

REFERENCES

[1]Stratford B. S.: The prediction of separation of the turbulent boundary layer, *Journal of Fluid Mechanics*, **5(1)**, 1-16 (1959).

[2]Manhart, M., Peller, N., Brun, C.: Near-wall scaling for turbulent boundary layers with adverse pressure gradient: A priori tests on DNS of channel flow with periodic hill constrictions and DNS of separating boundary layer, *Theoretical and Computational Fluid Dynamics*, **22**, 243-260 (2008).

[3]Duprat, C., et al.: A wall-layer model for large-eddy simulations of turbulent flows with/out pressure gradient, *Physics of Fluids*, **23**, (2011).

[4]Shih, T.H.: A generalized wall function, *National Aeronautics and Space Administration, Glenn Research Center*, (1999).

[5]Tennekes, H., Lumley, J. L.: A first course in turbulence, *MIT press*, (1972).

[6]Quosdorf, D. and Unglehrt, L. and Manhart, M. : Approximation of Near-wall Velocity Profiles at Flow Over Periodic Hills Using the Falkner-Skan Solutions, *13th International ERCOFTAC Symposium Engineering, Turbulence, Modelling and Measurements (ETMM13) Conference Proceedings* (2021).

[7]Spalding, D. B.: A single formula for the law of the wall, *Journal of Applied Mechanics.*, **28**, 455–458 (1961).

SESSION: Multiphase and complex flows

Friday, April 12, 2024

13:30- 14:30

WORKSHOP
Direct and Large-Eddy Simulation 14
April 10-12 2024, Erlangen, Germany

DNS OF A TURBULENT POLYMERIC FLOW AT HIGH FRICTION REYNOLDS NUMBER

E. Massarelli[1], F. Serafini[1], F. Battista[1], P. Gualtieri[1], C.M. Casciola[1]
[1]Department of Mechanical and Aerospace Engineering
Sapienza, University of Rome, Italy
elena.massarelli@uniroma1.it

INTRODUCTION

Turbulent flows play an important role in numerous engineering applications, involving the transport and mixing of fluids. A fundamental characteristic of turbulence is in fact the increment of mixing velocity, rate of mass transport, momentum and energy inside the fluid. However, since a turbulent flow is also associated with an increased drag, the reduction of this term represents one of the most active areas of research because it would permit a remarkable energy saving [1]. In 1948 Toms [2] discovered that by adding a small amount of polymers in a fully developed turbulent pipe flow, a decrease of the pressure drop was generated as a direct consequence of the reduction of the friction [3]. In the latest years, thanks to the development of High Performance Computing (HPC), Direct Numerical Simulation (DNS) assumed a central role, allowing a more detailed analysis of the mechanical interaction between polymers and turbulence structures, an interaction that the experiments cannot fully characterise. Defining a model that could replicate the experimental conditions in the simulations, is thus of fundamental importance, to better investigate the phenomenology of DR [4].

GOVERNING EQUATIONS

In the numerical simulations, polymers are modeled as dumbbells, made of 2 beads, connected by a spring [5]. Each bead is considered inertialess and is subjected to a friction force from the side of the solvent, a random Brownian force and an elastic force. Starting from the Newtonian balance of forces for each bead it is possible to obtain a non-dimensional equation for the polymer centre x_c and the connector vector r evolution

$$\begin{aligned} \frac{d\mathbf{x}_c^j}{dt} &= \frac{\mathbf{u}_j^1 + \mathbf{u}_j^2}{2} + \sqrt{\frac{a^2}{3Wi}}\frac{\boldsymbol{\epsilon}^1 + \boldsymbol{\epsilon}^2}{2} \\ \frac{d\mathbf{r}_j}{dt} &= \mathbf{u}_j^2 - \mathbf{u}_j^1 + \frac{1}{Wi}\frac{\mathbf{r}_j}{1-\frac{{r_j}^2}{L^2}} + \sqrt{\frac{a^2}{3Wi}}(\boldsymbol{\epsilon}^1 - \boldsymbol{\epsilon}^2) \end{aligned} . \tag{1}$$

In eq. (1), u_j^2 and u_j^1 represent the bead velocity of the j-th polymer, a its equilibrium length in a quiet solvent, Wi the Weissenberg number (ratio between the polymer relaxation time and a characteristic time scale of the flow), L the polymer contour length and ϵ^1 and ϵ^2 the Brownian term for the beads setting the equilibrium configuration in a still solvent. The term

$$f = \frac{1}{1-\frac{{r_j}^2}{L^2}}$$

is used to impose a finite extensibility for the spring (FENE model) [6].

These equations are coupled with the Navier-Stokes equation for an incompressible flow:

$$\begin{aligned} \nabla \cdot \mathbf{u} &= 0 \\ \frac{\partial \mathbf{u}}{\partial t} + \nabla \cdot (\mathbf{u} \otimes \mathbf{u}) &= -\nabla p + \frac{1}{Re}\nabla^2 \mathbf{u} + \mathbf{F} \end{aligned} \tag{2}$$

where u is the fluid velocity, k is the spring stiffness p is the pressure. F is the polymer forcing on the solvent and, given the friction coefficient γ of the beads, is expressed as follows

$$\mathbf{F} = \frac{\gamma}{2Wi}\sum_{j=1}^{N_p}\frac{\mathbf{r}_j}{1-\frac{{r_j}^2}{L^2}}\left[\delta(\mathbf{x}-\mathbf{x}_j^1) - \delta(\mathbf{x}-\mathbf{x}_j^2)\right]. \tag{3}$$

All the equations presented above are in the dimensionless form, obtained used as reference quantities the pipe radius $\hat{R}$, the kinematic viscosity $\hat{\nu}$, and the bulk velocity $\hat{U}_b$.

The system of equations is discretized on a staggered grid with cylindrical coordinates (r, θ, z), a second-order scheme in space and a semi-spectral projection method are used to impose the solenoidality of the velocity field. Temporal integration is performed by means of a four-step third-order Runge-Kutta scheme. Given the discrete representation of

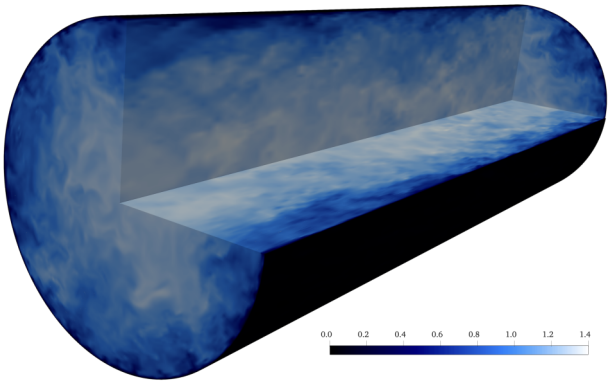

Figure 1: Snapshot of the velocity magnitude in the pipe at $Re_\tau = 1000$.

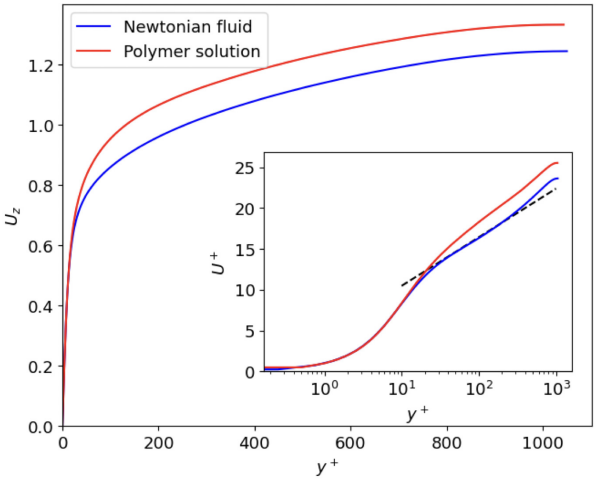

Figure 2: Axial mean velocity profile U_z as a function of the normalized distance from the wall y^+, in the case of a Newtonian fluid and a polymer solution.

polymers as two pointwise beads, F is singular and it is necessary to apply the ERPP method to regularize it [7] in a physically consistent way. The system can be directly solved through Direct Numerical Simulations with no need for turbulence models; the grid points are homogeneously distributed in the azimuthal and axial directions while in the radial one a higher resolution is ensured close to the wall where the largest gradients of velocity are expected.

DNS OF A POLYMERIC SOLUTION AT $Re_\tau = 1000$

In 2023, Leonardo, hosted by Cineca, classified in the 4° position among the most powerful supercomputers in the world has been made available in the preproduction phase for calculations on the DR problem. With a computational power of 255 PetaFLOPS, it is a fundamental resource, to model, simulate, and thus help understanding the complex interaction phenomenon between polymers and the turbulent field. Thanks to High Performance Computing it is possible to conduct numerical simulations of polymeric solutions at high values of $Re_\tau = Ru_\tau/\nu$, where R is the pipe radius, ν is the solvent kinematic viscosity, $u_\tau = \sqrt{\tau_w/\rho}$ the friction velocity (τ_w is the the shear stress at the wall and ρ the fluid density). The use of HPC allows exploiting the hybrid Eulerian–Lagrangian approach summarised above, considering very large number of polymers to match the concentrations used in the experiments. In particular, a drag-reducing polymer solution in a turbulent pipe flow at a friction Reynolds number of $Re_\tau = 1000$ is investigated. The flow is simulated in a domain of dimensions $(L_\theta, R, L_z) = (2\pi, 1, 6\pi)$, on a grid of $(N_\theta, N_r, N_z) = (3072, 519, 9216)$ for an overall number of cells of about 15 billion. The simulation involves the Lagrangian evolution, and feedback reaction of 1.1 billion of polymer molecules.

A representation of the flow configuration is depicted in fig. 1, reporting the contour of the instantaneous velocity magnitude inside the pipe. Figure 2 reports the radial profile of the mean axial velocity of the Newtonian solvent, showing an increase since the buffer layer when the polymers are added. According to many experimental observations of polymers drag reduced flows, the slope of the mean velocity profile increases in the buffer layer, to return parallel to the Newtonian line in the log layer.

During the talk, additional methodological information will be provided, with particular emphasis on polymer modelling and the role of HPC in such high-fidelity simulations.

*

References

[1] J. Lumley, "Drag reduction by additives," *Annual review of fluid mechanics*, vol. 1, no. 1, pp. 367–384, 1969.

[2] B. Toms, "On the early experiments on drag reduction by polymers," *The Physics of Fluids*, vol. 20, no. 10, pp. S3–S5, 1977.

[3] P. Virk, "Drag reduction fundamentals," *AIChE Journal*, vol. 21, no. 4, pp. 625–656, 1975.

[4] F. Serafini, F. Battista, P. Gualtieri, and C. Casciola, "Drag reduction in turbulent wall-bounded flows of realistic polymer solutions," *Physical Review Letters*, vol. 129, no. 10, p. 104502, 2022.

[5] R. B. Bird, C. F. Curtiss, R. C. Armstrong, and O. Hassager, *Dynamics of Polymeric Liquids, Volume 2: Kinetic Theory*. Wiley, 1987.

[6] F. Serafini, F. Battista, P. Gualtieri, and C. Casciola, "The role of polymer parameters and configurations in drag-reduced turbulent wall-bounded flows: Comparison between fene and fene-p," *International Journal of Multiphase Flow*, vol. 165, p. 104471, 2023.

[7] F. Battista, J.-P. Mollicone, P. Gualtieri, R. Messina, and C. M. Casciola, "Exact regularised point particle (erpp) method for particle-laden wall-bounded flows in the two-way coupling regime," *Journal of Fluid Mechanics*, vol. 878, pp. 420–444, 2019.

WORKSHOP
Direct and Large-Eddy Simulation 14
April 10-12 2024, Erlangen, Germany

TURBULENT MAGNETIC FIELD AMPLIFICATION IN BINARY NEUTRON STAR MERGERS USING THE GRADIENT SGS MODEL

R. Aguilera-Miret[1,3], C. Palenzuela[2,3,4], D. Viganò[6,4,3], F. Carrasco[5,3]
[1]University of Hamburg, Hamburger Sternwarte, Gojenbergsweg 112, 21029, Hamburg, Germany
ricard.aguilera.miret@hs.uni-hamburg.de
[2]Departament de Física, Universitat de les Illes Balears, Palma de Mallorca, E-07122, Spain
[3]Institute of Applied Computing & Community Code (IAC3)
Universitat de les Illes Balears, Palma de Mallorca, E-07122, Spain
[4]Institut d'Estudis Espacials de Catalunya (IEEC), 08034 Barcelona, Spain
[5]Instituto de Física Enrique Gaviola, CONICET-UNC, 5000 Córdoba, Argentina
[6]Institute of Space Sciences (IEEC-CSIC), E-08193 Barcelona, Spain

INTRODUCTION

The tremendous scientific potential of binary neutron star (BNS) mergers, detected simultaneously through gravitational waves (GW) and electromagnetic (EM) counterparts, was confirmed with the event GW170817 [1]. Among other astrophysical information, this event provided the most compelling evidence that BNS mergers can produce powerful jets and short Gamma-Ray bursts (SGRBs [2]), as well as copious amounts of heavy r-process elements. Although the binary inspiral is mostly driven by gravitational wave emission, several non-linear magnetohydrodynamic (MHD) processes and instabilities affects the post-merger dynamics. For this reason, some key elements of the matter and magnetic fields remnant's evolution remain still uncertain, including the actual mechanisms behind jet formation and matter ejection.

The only way to accurately model the remnant's dynamics in a realistic manner is through numerical relativity simulations of merging BNSs. Here we focus on the influence of the magnetic fields, which are known to play an important key role in the remnant's evolution and in shaping the electromagnetic counterpart signals. Strong, large-scale magnetic fields (up to 10^{51} ergs or even higher) are believed to be necessary to power relativistic jets. This magnetic field amplification relies on different mechanisms, one of them being the Kelvin-Helmholtz instability (KHI, e.g., [3]). This instability generally happens at (very) small scales which cannot be fully captured with the standard resolutions currently used in numerical simulations.

An interesting alternative to compensate for the lack of resolution relies on the use of Large-Eddy Simulations (LESs), a technique in which the general relativistic MHD (GRMHD) evolution equations are modified by including new terms to account for the unresolved subgrid-scale (SGS) dynamics. In particular, the gradient SGS model [4] is a sophisticated choice, conceptually similar to a numerical mathematically-informed flux reconstruction, with no a-priori physical assumptions. By including these SGS terms in the equations one can recover, at least partially, the effects induced by the unresolved SGS dynamics over the resolved scales. Here we will present some results combining high-order numerical schemes, high-resolution and LES with the gradient SGS model to obtain an amplification of the magnetic field in a turbulent regime, something that has been tested in box simulations [5, 6]. In particular, we found convergence on the (averaged) magnetic fields reached after the KHI amplification phase [7].

Case	Refinement levels	ΔL_{min} [km]	Δ_{min} [m]
`LR`	7 FMR	[-28,28]	120
`MR`	7 FMR + 1 AMR	[-13,13]	60
`HR`	7 FMR + 2 AMR	[-11,11]	30
`LR LES`	7 FMR	[-28,28]	120
`MR LES`	7 FMR + 1 AMR	[-13,13]	60
`HR LES`	7 FMR + 2 AMR	[-11,11]	30

Table 1: *Parameters of the simulations:* Different resolutions and mesh refinement setup (with the finest grid spacing Δ_{min} covering a region of size ΔL_{min}). Each setup is adopted at the merger time, while the inspiral phase is common to all of them and is run under the `LR` configuration.

AMPLIFICATION OF THE MAGNETIC FIELD

We perform some simulations (summarized in Table 1) including (or not) the gradient SGS model for resolutions that are $\{120, 60, 30\}$ meters, called low resolution (LR), medium resolution (MR) and high resolution (HR) from now on, respectively. One of these simulations is shown in Fig. 1, where it is shown the orbital plane at $z = 0$. The system performs 5 orbits before the merger occurs, producing gravitational waves while stretching the orbit. A thin, rotating shear layer is produced at the time of the merger between the colliding cores that move in opposite directions. This is the perfect premise to develop the KHI, manifested by the typical curly structures at small scales. These small eddies twist and stretch the magnetic field of the remnant, increasing quickly the magnetic energy at the expenses of the kinetic one, reaching values of 10^{17} G.

Our simulations show, for the first time, convergent results on the volume averaged turbulent amplification of the magnetic field in BNS mergers between MR LES, HR and HR LES,

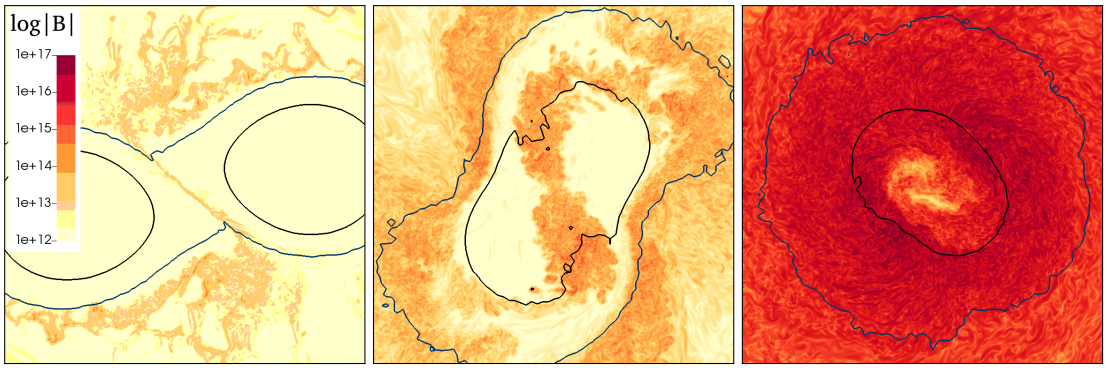

Figure 1: *Evolution of the magnetic field intensity in the orbital plane.* Snapshots at $t = (0.5, 1.5, 5)$ ms after the merger, displaying the magnetic field strength in Gauss, together with constant density contours at $\rho = (10^{13}, 5 \times 10^{14})$g/cm^3. The amplification is mostly driven by the KHI.

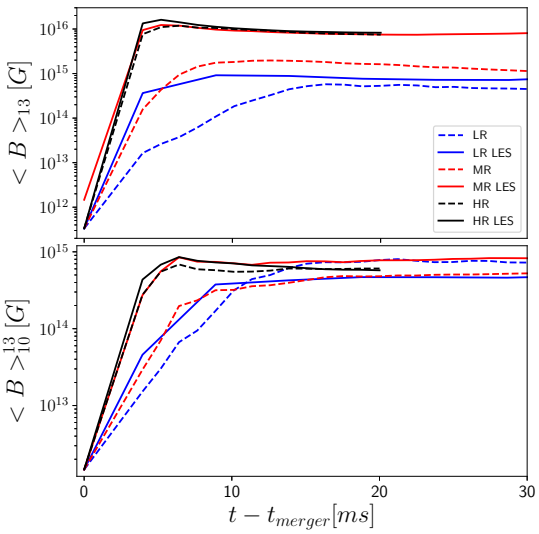

Figure 2: *Evolution of the average magnetic field.* Volume-average of the magnetic field intensity either in the bulk (top) or in the envelope (bottom) of the remnant. These averages are calculated for all the resolutions (identified by colours), both for the LES (solid lines) and for the standard simulations (dashes). Clearly, the averages in the bulk calculated with LES converge to a well-defined value.

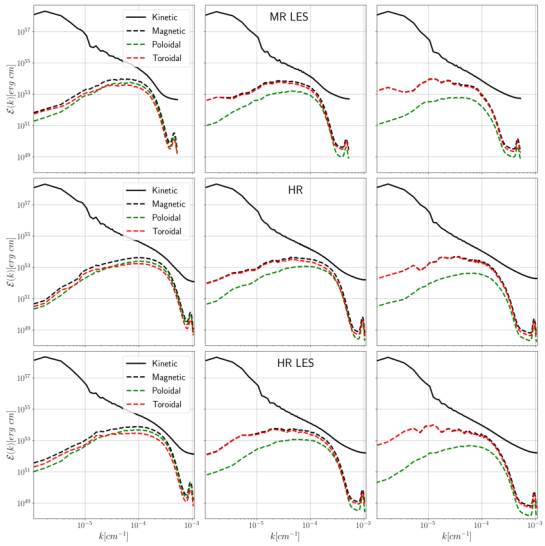

Figure 3: *Evolution of the energy spectra.* Spectra of the kinetic (solid) and magnetic energy (dashed) at $t = \{5, 10, 20\}$ ms after the merger, for the MR LES and the HR simulations. The kinetic and magnetic energies almost reach equipartition at high wave-numbers (i.e., before the decay induced by numerical dissipation, which is much more prominent in the magnetic spectra).

as seen in Fig. 2 both in the bulk region of the remnant (top) and the envelope (bottom). This amplification is produced in less than 5 ms.

Fig. 3 shows the spectra energy for these convergent simulations at $t = \{5, 10, 20\}$ ms after the merger. The solid line corresponds to kinetic energy and the dashed ones correspond to total (black), toroidal (red) and poloidal (green) components of the magnetic energy. We can see that the isotropic turbulent state driven by the KHI produces a similar spectra of the poloidal and toroidal components at 5 ms. The magnetic energy approaches equipartition with the kinetic one at high wave-numbers k.

REFERENCES

[1]B. P. Abbott, and et al. GW170817: Observation of Gravitational Waves from a Binary Neutron Star Inspiral. *Phys. Rev. Lett.*, **119**(16):161101, October (2017).

[2]B. P. Abbott, and et al. Gravitational Waves and Gamma-Rays from a Binary Neutron Star Merger: GW170817 and GRB 170817A. *Astrophys. J. Lett.*, **848**:L13, October (2017).

[3]D. J. Price and S. Rosswog. Producing Ultrastrong Magnetic Fields in Neutron Star Mergers. *Science*, **312**:719–722, May (2006).

[4]P. Grete. Large eddy simulations of compressible magnetohydrodynamics PhD thesis, *Max-Planck-Institut für Sonnensystemforschung*, (2017).

[5]Federico Carrasco, and et al. Gradient subgrid-scale model for relativistic mhd large-eddy simulations. *Phys. Rev. D*, **101**(6):063003, (2020).

[6]Daniele Viganò, and et al., General relativistic MHD large eddy simulations with gradient subgrid-scale model. *Phys. Rev. D*, 101(12):123019, June (2020).

[7]C. Palenzuela, and et al. Turbulent magnetic field amplification in binary neutron star mergers. *Phys. Rev. D*, **106**(2):023013, July (2022).

WORKSHOP
Direct and Large-Eddy Simulation 14
April 10-12 2024, Erlangen, Germany

DNS OF SHEAR TURBULENCE INTERACTING WITH A MELTING-FREEZING ICE LAYER

Diego Perissutti[1], **Francesco Zonta**[2], **Alessio Roccon**[1,2], *__Cristian Marchioli__[1], **Alfredo Soldati**[1,2]
[1]Polytechnic Department of Engineering and Architecture
University of Udine, Udine, Italy
[2]Institute of Fluid Mechanics and heat transfer
Technische Universität Wien (TUW), Vienna, Austria
*cristian.marchioli@uniud.it

INTRODUCTION

When a turbulent flow of water interacts with an ice boundary at near-freezing temperature, the fluid can undergo freezing or melting, depending on the local temperature. The turbulence structures that develop in proximity to the ice layer can affect the convective heat transport patterns, leading to the formation of complex phase-boundary morphologies. The ice layer evolves as part of the solution and modifies the near-boundary fluid structures, resulting in heat transfer perturbations. We investigate this problem by performing DNS of an open channel flow at shear Reynolds number in the range $\mathrm{Re}_\tau = 10^2 \div 10^3$.

METHODOLOGY

The DNS are performed in a rectangular domain where the upper section of the channel is occupied by ice, while free shear conditions are applied at the bottom. Temperature is imposed on both walls. Periodic conditions are applied in the streamwise and spanwise directions. The ice melting/freezing is simulated using a phase field method [1]:

$$\frac{\partial \theta}{\partial t} = \frac{5}{6C\mathrm{St}\mathrm{Re}_\tau \mathrm{Pr}} \left[\nabla^2 \phi - \frac{1}{\epsilon^2} \phi \left(1-\phi\right)\left(1-2\phi+C\theta\right) \right], \quad (1)$$

where ϕ is the phase variable and St is the Stefan number, which is defined as the ratio between the latent heat and the sensible heat that characterizes the system. A volume-penalization immersed boundary method is employed to account for the presence of the solid ice boundary:

$$\begin{cases} \nabla \cdot \mathbf{u} = 0 \\ \dfrac{\partial \mathbf{u}}{\partial t} + \mathbf{u} \cdot \nabla \mathbf{u} = -\nabla p + \dfrac{1}{\mathrm{Re}_\tau} \nabla^2 \mathbf{u} - \mathbf{g} \dfrac{\mathrm{Ra}}{16 \mathrm{Pr} \mathrm{Re}_\tau^2} \theta - \dfrac{\phi}{\eta_s} \mathbf{u}. \end{cases} \quad (2)$$

The system is closed by the energy equations, which includes also the contribution of the latent heat:

$$\frac{\partial \theta}{\partial t} + \mathbf{u} \cdot \nabla \theta = \frac{1}{\mathrm{Re}_\tau \mathrm{Pr}} \nabla^2 \theta + \mathrm{St} \frac{\partial \phi}{\partial t}, \quad (3)$$

where θ is the temperature field. The governing equations are solved using a pseudo-spectral scheme based on the Chebyshev-tau method [2].

RESULTS

We investigated how the behavior of the system changes with the flow conditions (i.e. Reynolds number), with a specific focus on characterizing the features of the ice morphology through spectral analysis. In particular, we observed a remarkable influence of Re_τ on the ice morphology: at low Re_τ, the typical streamwise-oriented canyons already reported in similar studies [3] are present. However, at higher Re, spanwise instabilities are triggered, making the final ice morphology more complex.

REFERENCES

[1]R. Yang et al., Morphology evolution of a melting solid layer above its melt heated from below, *Journal of Fluid Mechanics*, **956**, A23, 2023.
[2]F Zonta et al., Modulation of turbulence in forced convection by temperature-dependent viscosity, *Journal of Fluid Mechanics*, **697**, pp. 150–174, 2021.
[3]L. A. Couston et al., Topography generation by melting and freezing in a turbulent shear flow, *Journal of Fluid Mechanics*, **911**, A44, 2021.

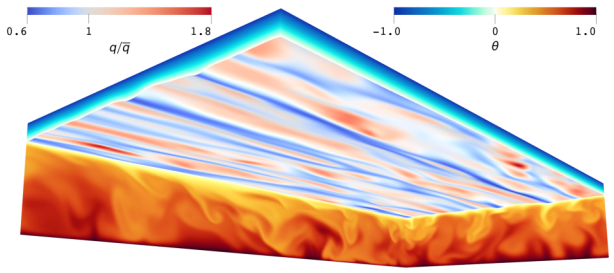

Figure 1: Render view from below of the open channel flow at a low Reynolds number. On the top section of the channel, the corrugated ice layer is shown. On the ice boundary, the normalized heat flux passing through it is displayed (high heat flux is shown in red, low heat flux in blue). The local temperature field is reported on the side domain boundaries. The typical streamwise-oriented canyons at the ice interface are visible and the heat flux correlates well with those patterns (the heat flux is higher inside the canyons).

WORKSHOP
Direct and Large-Eddy Simulation 14
April 10-12 2024, Erlangen, Germany

EFFECT OF ABLATION ON LAMINAR-TURBULENT TRANSITION OVER COMPRESSION RAMP AT MACH 8

A. O. Başkaya[1], **S. Hickel**[1]
[1]Faculty of Aerospace Engineering, Delft University of Technology, Delft, The Netherlands
a.o.baskaya@tudelft.nl

INTRODUCTION

Vehicles traveling at hypersonic speeds operate in extreme flight environments. Ablative surface materials are used for ensuring the integrity of the vehicle and the survival of the payload onboard. When exposed to high temperatures, the ablative surface material undergoes physicochemical decomposition. Ablation products blow out of the surface into the boundary layer and the material itself erodes away. The ablative recession of the surface affects the aerothermodynamics of the vehicle. This interaction becomes more complex when the surrounding flow is transitioning from a laminar to a turbulent state [1]. The turbulent flow enhances heat transfer and consequently the ablation rate. Larger heat and mass transfer results in rapid evolution of the shape, constructing a feedback cycle, which persists throughout the high-temperature flight duration. Such phenomena in this flow regime are critical since delaying or promoting earlier transition holds important implications for the thermal and mechanical loads imposed on the vehicle.

In this work, direct numerical simulations (DNS) are performed over a 15° compression ramp undergoing ablation at Mach 8. The setup is validated against experiments [2] and simulations [3] that considered the laminar flow over an inert ramp. Streamwise vortices, which generate heating streaks through the lift-up effect, are introduced by perturbing the base flow [4]. The ramp is then replaced by a low-temperature ablator in our DNS and the interaction of the streaks with the recessing ablator surface is examined. We present the first findings regarding the influence of ablation on the perturbation evolution and transition to turbulence for this configuration.

PRELIMINARY RESULTS

The laminar base flow is perturbed by a forcing function with wavelength $\lambda = 0.003$ m to obtain steady streaks over the ramp. The rigid ramp is then numerically replaced by solid camphor, allowing it to undergo ablative recession as a result of sublimation reactions.

Solutions obtained with our in-house flow solver INCA [5] are presented in Fig. 3. Entrainment from the counter-rotating vortices of the steady streaks leads to the formation of alternating heating and cooling streaks on the surface along the spanwise direction. Influence of ablation on perturbation growth is quantified by comparing the results obtained with inert and ablative boundary conditions in Fig. 1, where maximum spanwise speeds along streamwise locations are shown. These values are normalized with the amplitude at the forcing location. Amplitudes for the inert and ablative cases mostly match until around 0.15 m; further downstream, a rapid amplification of the total perturbation is observed for the ablative case. This higher amplification rate under the influence of ablation is expected in the absence of complex gas-phase chemistry. Effect of these steaks on the surface can also be observed from the recession patterns shown in Fig. 2.

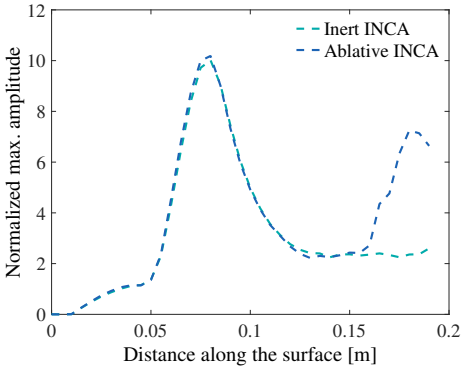

Figure 1: Comparison of perturbation amplitudes for the inert and ablative solutions.

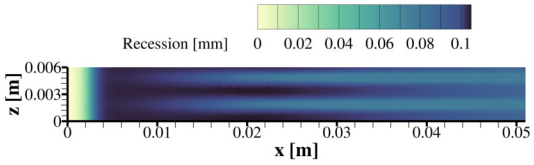

Figure 2: Recession patterns due to steady streaks over the ablating camphor wall.

CONCLUSION

Following the preliminary results presented here, the full paper will further analyze the sensitivity of the transitional boundary layer to the ablation of the surface.

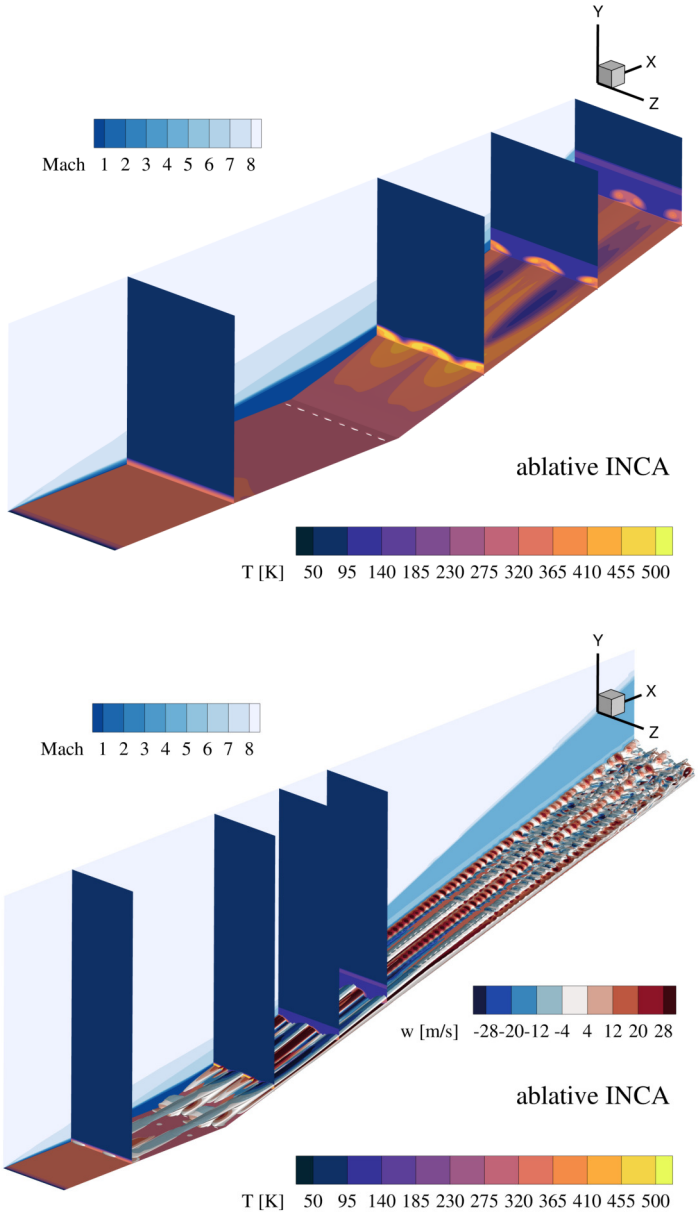

Figure 3: Isometric views of ablative solutions. Background slice in the spanwise direction shows Mach number contours. Slices in the streamwise plane at $x = [0.023, 0.030, 0.070, 0.1]$ m show temperature contours. While the top figure shows the domain until 0.1 m in the streamwise direction, bottom figure extends to 0.2 m. Iso-surface of vorticity at $1 \times 10^4\,\mathrm{s}^{-1}$ is colored with the spanwise velocity in the bottom figure.

REFERENCES

[1] S. P. Schneider, "Hypersonic boundary-layer transition with ablation and blowing," *Journal of Spacecraft and Rockets*, vol. 47, no. 2, pp. 225–237, 2010.

[2] P. V. Chuvakhov, V. Y. Borovoy, I. V. Egorov, V. N. Radchenko, H. Olivier, and A. Roghelia, "Effect of small bluntness on formation of Görtler vortices in a supersonic compression corner flow," *Journal of Applied Mechanics and Technical Physics*, vol. 58, pp. 975–989, 2017.

[3] A. Dwivedi, G. S. Sidharth, J. W. Nichols, G. V. Candler, and M. R. Jovanović, "Reattachment streaks in hypersonic compression ramp flow: An input-output analysis," *Journal of Fluid Mechanics*, pp. 113–135, 2019.

[4] A. O. Başkaya, S. D. Dungan, S. Hickel, and C. Brehm, "Fluid-ablation interactions on a compression ramp at Mach 8," in *AIAA SciTech 2024 Forum*, 2024.

[5] A. O. Başkaya, M. Capriati, A. Turchi, T. Magin, and S. Hickel, "Assessment of immersed boundary methods for hypersonic flows with gas-surface interactions," *Computers & Fluids*, vol. 270, p. 106134, 2024.